

AD 607252

RTD TDR 63-4098

## RESEARCH ON PHOTOGRAPHIC WINDOW PROBLEM IN SUPERSONIC AND HYPERSONIC AIRCRAFT

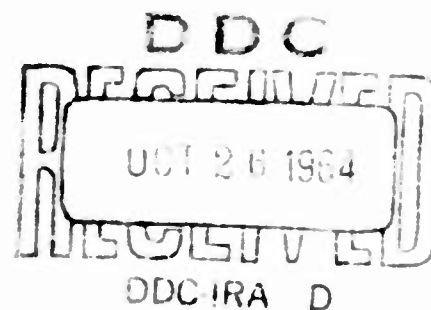
TECHNICAL DOCUMENTARY REPORT No. RTD TDR 63-4098

MARCH 1964

COPY	2	OF	3	1 copy
HARD COPY				\$ .600
MICROFICHE				\$ .125

250p

AF AVIONICS LABORATORY  
RESEARCH AND TECHNOLOGY DIVISION  
AIR FORCE SYSTEMS COMMAND  
WRIGHT-PATTERSON AIR FORCE BASE, OHIO



(Prepared under Contract No. AF 33(657)-8013 by  
North American Aviation, Inc., Los Angeles, Calif.)

**Best  
Available  
Copy**

**CLEARINGHOUSE FOR FEDERAL SCIENTIFIC AND TECHNICAL INFORMATION CFSTI  
DOCUMENT MANAGEMENT BRANCH 410.11**

**LIMITATIONS IN REPRODUCTION QUALITY**

ACCESSION # *AD 607 252*

- ☒ 1. WE REGRET THAT LEGIBILITY OF THIS DOCUMENT IS IN PART UNSATISFACTORY. REPRODUCTION HAS BEEN MADE FROM BEST AVAILABLE COPY.
- ☐ 2. A PORTION OF THE ORIGINAL DOCUMENT CONTAINS FINE DETAIL WHICH MAY MAKE READING OF PHOTOCOPY DIFFICULT.
- ☐ 3. THE ORIGINAL DOCUMENT CONTAINS COLOR, BUT DISTRIBUTION COPIES ARE AVAILABLE IN BLACK-AND-WHITE REPRODUCTION ONLY.
- ☐ 4. THE INITIAL DISTRIBUTION COPIES CONTAIN COLOR WHICH WILL BE SHOWN IN BLACK-AND-WHITE WHEN IT IS NECESSARY TO REPRINT.
- ☐ 5. LIMITED SUPPLY ON HAND: WHEN EXHAUSTED, DOCUMENT WILL BE AVAILABLE IN MICROFICHE ONLY.
- ☐ 6. LIMITED SUPPLY ON HAND: WHEN EXHAUSTED DOCUMENT WILL NOT BE AVAILABLE.
- ☐ 7. DOCUMENT IS AVAILABLE IN MICROFICHE ONLY.
- ☐ 8. DOCUMENT AVAILABLE ON LOAN FROM CFSTI ( TT DOCUMENTS ONLY).
- ☐ 9.

PROCESSOR: *Pm*

## FOREWORD

This is the final Technical Documentary Report for ASD Contract AF 33(657)-8103, summarizing all activities pertinent to the contract. Essential information included in monthly status letter reports prepared during the course of the contract (May 1962 through July 1963) has been incorporated in this report, so that it may be utilized as a single entity.

The work described was performed, for the most part, by Donald Koch of the Optics Laboratory, James Nixon of Thermal Analysis, and Raymond Wykes of Structural Sciences at the Los Angeles Division of North American Aviation, Inc. Responsibility for supervising the program was assigned to Seymour Konopken (during the early months) and, later, Robert Klemm, under overall management of R. R. Janssen, Director, Laboratories.

Direction and guidance by the ASD Program Manager, Mr. H. R. Gedling, and his predecessor, Lt. L. Reynolds, during the contract period are gratefully acknowledged.

The Contractor's assigned number for this report is NA-63-717.



# **ABSTRACT**

The purpose of this contract was twofold: (1) to attempt laboratory verification of the analytically predicted effects of environmentally-stressed windows on photographic image quality, and (2) to perform an engineering investigation directed toward the more precise determination of the window environment to be expected in a hypersonic vehicle, and the feasibility of reducing the severity of such an environment. Both objectives have been fulfilled. It is recommended that flight tests be considered in any subsequent program, in order to more closely simulate the environmental factors which affect window performance. It is further recommended that research be directed toward the attainment of a suitable method for direct measurement of temperature distributions within glass panels.

Publication of this technical documentary report does not constitute Air Force approval of the report's findings or conclusions. It is published only for the exchange and stimulation of ideas.

# TABLE OF CONTENTS

	<u>Page No.</u>
FOREWORD	
ABSTRACT	111
TABLE OF CONTENTS	lv
LIST OF ILLUSTRATIONS	vi
LIST OF TABLES	xv
I. INTRODUCTION	1
II. SUMMARY	2
III. PROGRAM OBJECTIVES	3
IV. <u>AEROTHERMODYNAMIC ANALYSIS</u>	4
Section Summary	4
Trajectory Selection	5
Incident Heat Flux To Window	7
Effect of Window Location	7
Effect of Air Expansion	8
Outside Surface Pressure On Window	10
Temperature of Window	10
High Angle Re-entry	11
Low Angle Re-entry	12
Thermal Lag	13
Compartment Heat Transfer	13
Concluding Remarks	14
V. <u>OPTICAL ANALYSIS AND TESTS</u>	71
Section Summary	71
Discussion of Window Quality	71
Required Test Window Quality	71
Optical Quality Necessary For Laboratory Tests	80
Quality of Glass Test Panels as Received	82
Relationship Between Deviation and Resolution	84
Deviation Differential	84
Analytical Assumptions	86
Modified Theory	93
Unequal Curvatures	93
Sample Calculations	100
Optical Tests	103
Pressure Test Equipment	103
Pressure Test Results	104
Conclusions	104
Temperature Test Equipment	104
Temperature Test Results	105
Conclusions	105
VI. <u>LUMINOSEITY TEST PROGRAM</u>	172
Test Conditions	172
Test Procedure	173
VII. <u>STRUCTURAL DESIGN</u>	174
Section Summary	174
Design Criteria	174
Window Mount Design	175

TABLE OF CONTENTS (Continued)

	<u>Page No.</u>
VII. <u>STRUCTURAL DESIGN</u> (Continued)	
Basic Mount	175
Extensions of Basic Design	176
Conclusions	176
Proposed Method for Protecting Window	176
Feasibility of Window Protection	177
VIII. <u>CONCLUSIONS AND RECOMMENDATIONS</u>	184
Hypersonic Reconnaissance Photography	184
Summary of Program Accomplishments	184
Recommendations	185
IX. <u>REFERENCES</u>	188

## LIST OF FIGURES

Figure No.	Description	Page
<b><u>Section IV</u></b>		
1.	Trajectories Selected for Photographic Window Study	16
2.	Typical Photographic Window Temperature for Trajectories Selected	16
3.	Trajectory 1 Flight Parameters Versus Time	17
4.	Trajectory 1 Fuselage Thin Skin Convective Heating Rate Versus Time (TSTP)	18
5.	Trajectory 1 Fuselage Thin Skin Net Heating Rate Versus Time (TSTP)	19
6.	Trajectory 1 Fuselage Thin Skin Temperature Versus Time (TSTP)	20
7.	Trajectory 1 Temperature-Time Distribution Through an Opaque Fused Silica Window 1-1/2" Thick Mounted as Shown Located One-Foot Aft on Lower Fuselage Surface Parallel to Vehicle Centerline (TSTP)	21
8.	Trajectory 2A Flight Parameters Versus Time (H.S. Flt. 2-21)	22
9.	Trajectory 2A Local Pressure Coefficient Versus Time (H.S. Flt. 2-21)	23
10.	Trajectory 2A Fuselage Thin Skin Net Heating Rate Versus Time (H.S. Flt. 2-21) (TSTP)	24
11.	Trajectory 2A Fuselage Thin Skin Temperature Versus Time (H.S. Flt. 2-21) (TSTP)	25
12.	Trajectory 2B Flight Parameters Versus Time (Typical High Speed Flight)	26
13.	Trajectory 2B Temperature-Time Distribution Through an Opaque Fused Silica Window 3/8" Thick Mounted as Shown, Located Twelve Feet Aft on Lower Fuselage Centerline (TSTP)	27
14.	Trajectory 2B Temperature-Time Distribution Through an Opaque Fused Silica Window 1-1/2" Thick Mounted as Shown Located Twelve Feet Aft on Lower Fuselage Centerline (TSTP)	28

# LIST OF FIGURES (Continued)

Figure No.	Description	Page
<b>Section IV (Continued)</b>		
15.	Trajectory 2C Flight Parameters Versus Time (High Altitude Flight)	29
16.	Trajectory 2C Local Pressure Coefficient Versus Time (High Altitude Flight)	30
17.	Trajectory 2C Fuselage Thin Skin Net Heating Rate Versus Time (High Altitude Flight) (TSTP)	31
18.	Trajectory 2C Fuselage Thin Skin Temperature Versus Time (High Altitude Flight) (TSTP)	32
19.	Trajectory 3A Flight Parameters Versus Time (Angle of Attack = $50^\circ$ )	33
20.	Trajectory 3B Flight Parameters Versus Time (Angle of Attack = $15^\circ$ )	34
21.	Summary of Trajectory 3A Convective Heating Rates Versus Time, Laminar and Turbulent Flow, Compared at Locations of One-Foot and Six-Foot Aft on Vehicle Lower Wing Surface (HASTE)	35
22.	Summary of Trajectory 3B Convective Heating Rates Versus Time, Laminar and Turbulent Flow, Compared at Locations of One-Foot and Six-Foot Aft on Vehicle Lower Wing Surface (HASTE)	36
23.	Trajectory 3A11 Convective Heating Rate Versus Time, Laminar Flow, One-Foot Aft, on Wing Surfaces at Various Local Expansion Angles (HASTE)	37
24.	Trajectory 3A16 Convective Heating Rates Versus Time, Laminar Flow, Six-Foot Aft, on Wing Surfaces at Various Local Expansion Angles (HASTE)	38
25.	Trajectory 3B11 Convective Heating Rate Versus Time, Laminar Flow, One-Foot Aft, on Wing Surfaces at Various Local Expansion Angles (HASTE)	39
26.	Trajectory 3B16 Convective Heating Rates Versus Time, Laminar Flow, Six-Foot Aft, on Wing Surfaces at Various Local Expansion Angles (HASTE)	40
27.	Trajectory 3AT1 Convective Heating Rate Versus Time, Turbulent Flow, One-Foot Aft, on Wing Surfaces at Various Local Expansion Angles (HASTE)	41

# LIST OF FIGURES (Continued)

Figure No.	Description	Page
<u>Section IV(Continued)</u>		
28.	Trajectory 3AT6 Convective Heating Rate Versus Time, Turbulent Flow, Six-Foot Aft, on Wing Surfaces at Various Local Expansion Angles (HASTE)	42
29.	Trajectory 3BT1 Convective Heating Rate Versus Time, Turbulent Flow, One-Foot Aft, on Wing Surfaces at Various Local Expansion Angles (HASTE)	43
30.	Trajectory 3BT6 Convection Heating Rate Versus Time, Turbulent Flow, Six-Foot Aft, on Wing Surfaces at Various Local Expansion Angles (HASTE)	44
31.	Trajectory 3AL Local Pressure Versus Time, Laminar Flow, One-Foot and Six-Foot Aft, on Wing Surfaces at Various Local Expansion Angles.	45
32.	Trajectory 3BL Local Pressure Versus Time, Laminar Flow, One-Foot and Six-Foot Aft, on Wing Surfaces at Various Local Expansion Angles	46
33.	Trajectory 3AL12E Temperature-Time Distribution Through an Opaque Fused Silica Window, 1-1/2" Thick, Mounted as Shown, Located One-Foot Aft, Flush with Lower Wing Surface, Laminar Flow	47
34.	Trajectory 3AL62E Temperature-Time Distribution Through an Opaque Fused Silica Window, 1-1/2" Thick, Mounted as Shown, Located Six-Foot Aft, Flush with Lower Wing Surface, Laminar Flow	48
35.	Trajectory 3AT12E Temperature-Time Distribution Through an Opaque Fused Silica Window, 1-1/2" Thick, Mounted as Shown, Located One-Foot Aft, Flush with Lower Wing Surface, Turbulent Flow	49
36.	Summary of Trajectory 3A Temperature Versus Time on Outer Surface of an Opaque Fused Silica Window, 1-1/2" Thick, Located One-Foot and Six-Foot Aft, Flush with Lower Wing Surface, Laminar and Turbulent Flow	50
37.	Effect of Location Along the Lower Surface Upon the Maximum Opaque Window Surface Temperature Calculated for 3A Trajectory with Turbulent and Laminar Flow	51
38.	Trajectory 3AT6 Temperature Versus Time on Outer Surface of an Opaque, Fused Silica Window, 1-1/2" Thick, Six-Foot Aft on Lower Wing Surface, Turbulent Flow, at Various Local Expansion Angles	52

# LIST OF FIGURES (Continued)

Figure No.	Description	Page
<b>Section IV (Continued)</b>		
39.	Trajectory 3AT6 Temperature Differences Versus Time for Outer Surface of an Opaque Fused Silica Window, 1-1/2" Thick, Six-Foot Aft on Lower Wing Surface, Turbulent Flow, at Various Local Expansion Angles Compared to the Flush Condition	53
40.	Effect of Local Expansion Angle Upon the Temperature Difference at Maximum Surface Temperature of a Fused Silica Window, 1-1/2" Thick, During 3A Trajectory	54
41.	Trajectory 3AT62D Temperature-Time Distribution Through a Diathermanous Fused Silica Window, 1-1/2" Thick, Located Six-Foot Aft, Flush with Lower Wing Surface, Turbulent Flow	55
42.	Trajectory 3AT66D Temperature-Time Distribution Through a Diathermanous Fused Silica Window, 1-1/2" Thick, Located Six-Foot Aft, at $\nu = 30^\circ$ (Local Expansion Angle), Turbulent Flow	56
43.	Trajectory 3AL62D Temperature-Time Distribution Through a Diathermanous Fused Silica Window 1-1/2" Thick, Located Six-Foot Aft, Flush with Lower Wing Surface, Laminar Flow	57
44.	Temperature Distribution Through a Diathermanous Fused Silica Window, 1-1/2" Thick, Located Six-Foot Aft, Turbulent Flow at Instant of Maximum Temperature Difference Through the Window and at Maximum Temperature of Outer Surface, 3AT6 Trajectory	58
45.	Comparison of Diathermanous and Opaque Temperature-Time Distributions Through a Fused Silica Window, 1-1/2" Thick, Exposed to a Heating Rate of 4.25 BTU/Sec.ft <sup>2</sup>	59
46.	Trajectory 3BL12E Temperature-Time Distribution Through an Opaque Fused Silica Window, 1-1/2" Thick, Mounted as Shown, Located One-Foot Aft, Flush with Lower Wing Surface, Laminar Flow	60
47.	Trajectory 3BL62E Temperature-Time Distribution Through an Opaque Fused Silica Window, 1-1/2" Thick, Mounted as Shown, Located Six-Foot Aft, Flush with Lower Wing Surface, Laminar Flow	61
48.	Trajectory 3BT12E Temperature-Time Distribution Through an Opaque Fused Silica Window, 1-1/2" Thick, Mounted as Shown, Located One-Foot Aft, Flush with Lower Wing Surface, Turbulent Flow	62



## LIST OF FIGURES (Continued)

Figure No.	Description	Page
<b><u>Section IV(Continued)</u></b>		
49.	Summary of Trajectory 3B Temperature Versus Time on Outer Surface of an Opaque Silica Window, 1-1/2" Thick, Located One-Foot and Six-Feet Aft, Flush with Lower Wing Surface, Laminar and Turbulent Flow	63
50.	Effect of Location Along the Lower Surface Upon the Maximum Opaque Window Surface Temperature Calculated for 3B Trajectory with Turbulent and Laminar Flow	64
51.	Effect of Local Expansion Angle Upon the Temperature Difference at Maximum Surface Temperature of a Fused Silica Window, 1-1/2" Thick, During a 3B Trajectory	65
52.	Trajectory 3BT62D Temperature-Time Distribution Through a Diathermanous Fused Silica Window, 1-1/2" Thick, Located Six-Feet Aft, Flush with Lower Wing Surface, Turbulent Flow	66
53.	Trajectory 3BT63D Temperature-Time Distribution Through a Diathermanous Fused Silica Window, 1-1/2" Thick, Located Six-Feet Aft, at $\nu = 10^\circ$ (Local Expansion Angle), Turbulent Flow	67
54.	Temperature Distribution Through a Diathermanous Fused Silica Window, 1-1/2" Thick, Located Six-Feet Aft, Turbulent Flow, at Instant of Maximum Temperature Difference Through the Window and at Maximum Temperature of Outer Surface. 3BT6 Trajectory	68
55.	Comparison Between Opaque and Diathermanous Temperature Distributions Through a Fused Silica Window, 1-1/2" Thick, Located Six-Feet Aft, Flush with Lower Wing Surface, Laminar Flow at Given Times During 3BT6 Trajectory	69
56.	Heat Trajectory Rates to the Compartment (Radiation and Convection) Through a Fused Silica Window, 1-1/2" Thick, During 3BT6 Trajectory with Window Flush and at a Local Expansion Angle of $10^\circ$	70
<b><u>Section V</u></b>		
57.	Schematic Drawing of the Image Space Showing the Back Principal Plane and the Focal Point, Before and After Power is Introduced to the System	108
58.	Schematic Drawing of the Image Space Showing the position and Diameter of the Exit Pupil, the Angle of Convergence, the Radius of The Blur Circle, and the Position of the Image Plane	109



# LIST OF FIGURES (Continued)

Figure No.	Description	Page
<b>Section V (Continued)</b>		
59.	Intensity Distribution Functions for Single Point Response and the Composite Functions	110
60.	Graphical Presentation of Tolerable Window Power, for Various Focal Lengths at $f/2$	111
61.	Graphical Presentation of Tolerable Window Power, for Various Focal Lengths at $f/4$	112
62.	Graphical Presentation of Tolerable Window Power, for Various Focal Lengths at $f/6$	113
63.	Graphical Presentation of Tolerable Window Power, for Various Focal Lengths at $f/8$	114
64.	(This illustration deleted)	
65.	Test Arrangement to Check the Effect of Window Samples on the Image Formed from a Collimator Beam	116
66.	Interferometer with Window Sample in Test Position	116
67.	Interferometer Fringe Pattern without Window Glass in Test Position	117
68.	Window Sample A in Test Position	117
69.	Window Sample Bin Interferometer Test Position	118
70.	Window Sample C in Interferometer Test Position	118
71.	Interferometer Pattern for Window Sample D	119
72.	Interferometer Pattern for Window Sample E	119
73.	Interferometer Pattern for Glass Sample F	120
74.	Interferometer Pattern for Glass Sample G	120
75.	Interferometer Pattern for Glass Sample H	121
76.	Test Setup for Photographing Test Flat Fringe Pattern	122
77.	Fringe Pattern Produced by Two Test Flats	123
78.	Fringe Pattern Produced by Test Flat and Uncoated Surface of Window Sample A	123

## LIST OF FIGURES (Continued)

Figure No.	Description	Page
<b>Section V (Continued)</b>		
79.	Fringe Pattern Produced by Test Flat and Window Sample B	124
80.	Fringe Pattern Produced by Test Flat and Window Sample C	124
81.	Fringe Pattern Produced by Test Flat and Window Sample D	125
82.	Fringe Pattern Produced by Test Flat and Window Sample E	125
83.	Fringe Pattern Produced by Test Flat and Window Sample F	126
84.	Fringe Pattern Produced by Test Flat and Window Sample G	126
85.	Fringe Pattern Produced by Test Flat and Window Sample H	127
86.	Geometry of the Optical System for Deviated and Undeviated Rays	128
87.	Geometry of the Deviated and Undeviated Rays in The Image Space	128
88.	Graph of the Product of Resolution and Focal Length as Function of the Difference in Deviation	129
89.	Graph of Index of Refraction versus Temperature for Fused Silica Glass #7940	130
90.	Graphs of Thermal Expansion Coefficient, Modulus of Elasticity, and Poisson's Ratio versus Temperature for Fused Silica Glass #7940	131
91.	Diagram of Ray Trace Showing Propagation Vectors, Normal Vectors, the Coordinate System, and the Angle of Deviation	132
92.	Curve of the Equation of Curvature for a Square Plate	133
93.	Curve of the Equation of Curvature for a Circular Plate	134
94.	Schematic Diagram of Pressure Test Setup, Showing Location of Collimators in Pressure Vessel	135

# LIST OF FIGURES (Continued)

Figure No.	Description	Page
<b>Section V (Continued)</b>		
95.	Test Collimator	136
96.	Light Deviation versus Pressure for Fused Silica #7940 Glass, 9" x 9" x 1", at Zero Angle of Incidence, for a Point 3" from Vertex	137
97.	Light Deviation versus Pressure for Fused Silica #7940 Glass, 9" x 9" x 1", at 22.5 Degrees Angle of Incidence, for a Point 1" from Vertex	138
98.	Light Deviation versus Pressure for Fused Silica #7940 Glass, 9" x 9" x 1", at 45 Degrees Angle of Incidence, for a Point 3" from Vertex	139
99.	Light Deviation versus Pressure for Fused Silica #7940 Glass, 9" x 9" x 1", at 45 Degrees Angle of Incidence, for a Point 1" from Vertex	140
100.	Light Deviation versus Pressure for Aluminosilicate #1723 Glass, 9" x 9" x 1", at 22.5 Degrees Angle of Incidence, for a Point 3" from Vertex	141
101.	Light Deviation versus Pressure for Aluminosilicate #1723 Glass, 9" x 9" x 1", at 22.5 Degrees Angle of Incidence, for a Point 1" from Vertex	142
102.	Light Deviation Versus Pressure for Fused Silica #7940 Glass, 9" x 9" x 1", at 22.5 Degrees Angle of Incidence, for A Point 1" from Vertex (Second Chamber)	143
103.	Temperature Test Setup	144
103a.	Temperature Test Setup	145
104.	Collimator inside Vacuum Chamber	146
105.	Heater Inside Vacuum Chamber	147
106.	Temperature and Light Deviation versus Time, Test #1	148
107.	Temperature and Light Deviation versus Time, Test #2	149
108.	Temperature and Light Deviation versus Time, Test #3	150
109.	Temperature and Light Deviation versus Time, Test #4	151
110.	Temperature and Light Deviation versus Time, Test #5	152
111.	Temperature and Light Deviation versus Time, Test #6	153
112.	Temperature and Light Deviation versus Time, Test #7	154

# LIST OF FIGURES (Continued)

Figure No.	Description	Page
<u>Section V (Continued)</u>		
113.	Temperature and Light Deviation versus Time, Test #8	155
114.	Temperature and Light Deviation versus Time, Test #9	156
115.	Temperature and Light Deviation versus Time, Test #10	157
116.	Temperature and Light Deviation versus Time, Test #11	158
117.	Temperature and Light Deviation versus Time, Test #12	159
118.	Temperature and Light Deviation versus Time, Test #13	160
119.	Temperature and Light Deviation versus Time, Test #14	161
120.	Temperature and Light Deviation versus Time, Test #15	162
121.	Temperature and Light Deviation versus Time, Test #16	163
122.	Temperature and Light Deviation versus Time, Test #19	164
123.	Temperature and Light Deviation versus Time, Test #20	165
124.	Temperature and Light Deviation versus Time, Test #21	166
125.	Temperature and Light Deviation versus Time, Test #22	167
126.	Temperature and Light Deviation versus Time, Test #23	168
127.	Temperature and Light Deviation versus Time, Test #24	169
128.	Temperature and Light Deviation versus Time, Test #25	170
129.	Schematic Diagram Showing Location of Thermocouples on Typical Test Panel	171
<u>Section VII</u>		
130.	Basic Window Mount Design	178
131.	Window Mount Design #2	179
132.	Window Mount Design #3	180
133.	Window Mount Design #4	181
134.	Window Mount Design #5	182
135.	Schematic Diagram Illustrating a Possible Means of Protecting a Photographic Window from the Heat Generated During Hypersonic Re-entry	183

# LIST OF TABLES

Table No.	Description	Page
I	Hypersonic Heating Rates and Temperatures	15
II	Description of Glass Test Panels	107

## **Section I**

### **INTRODUCTION**

Photographic reconnaissance has for many years been one of the most effective means for the collection of intelligence information. With the advent of supersonic and hypersonic vehicles, the environmental conditions to which the camera systems are exposed have become more severe. At the same time, because of the higher velocities and altitudes, the requirements for optical quality and precision are more stringent.

The photographic window, separating the camera compartment from the external environment, performs several necessary functions:

- (a) It protects the camera from excessive heat.
- (b) It helps maintain an aerodynamically acceptable moldline.
- (c) It acts as a pressure seal for the camera compartment.

It should perform these functions while not adversely affecting the performance of the camera.

The heat generated at the skin of a supersonic vehicle is absorbed by the window. The part of the glass which is nearer the outer surface absorbs more heat than the inner portions. Since the glass expands as a function of temperature, the temperature differential through the glass induces a bowing (bending) of the window. The stressed window then acts as an additional, unwanted "diffusing lens" in front of the camera, causing distortion of the image and a general reduction in clarity of the photographs. This degradation of image quality can mean the difference between effective reconnaissance and a wasted mission.

While the effects of stressed windows on photographic image quality have been analyzed to some extent in the past, little or no experimental verification of the phenomena has been attempted. It is the purpose of this contract to perform a laboratory investigation of the effects, and to evolve design techniques for the partial protection of photographic windows from the severities of hypersonic vehicle environments.

Manuscript released by the author 30 March 1964 for publication as an RTD Technical Report.

## Section II

### SUMMARY

Results of a research program on photographic windows for use in supersonic and hypersonic vehicles are presented in this report. Previous analytical predictions concerning the effects of induced window curvature on optical quality have been found to be questionable. Certain assumptions upon which the predictions were based were found to be somewhat inadequate, and the equations were modified accordingly. Good qualitative agreement between experimental results and the modified theory was then established.

Investigations of several typical aircraft trajectories has yielded useful information concerning heat transfer through camera windows, temperature distributions within the windows, and pressure differentials, as functions of time. Particularly for a high-angle and a low-angle re-entry trajectory for a Dynasoar-type vehicle, a great deal of thermal data was generated during the program, for evaluation of Dynasoar as a possible reconnaissance vehicle.

Design criteria and techniques for thermal protection of camera windows have been evolved. Several designs for camera window mounts suitable for use in a high-temperature (2500 F) environment are included in this report. In addition, the efficacy of protecting the window from the thermal environment has been investigated. Two methods, separation of aerodynamic flow (recessing the window) and controlled expansion flow (tilting the window) have been found to be feasible. Controlled expansion flow can reduce the heat input to the window by 30 to 50 percent, reducing the window temperature correspondingly.

Cancellation of the Dynasoar program negates the usefulness of a portion of the data presented herein. But the analytical procedures for obtaining that data, developed during the course of this contract, are obviously applicable to the generation of analogous data for other advanced vehicles.

## Section III

### PROGRAM OBJECTIVES

The general objectives of the program were "to provide for the experimental verification (or contradiction) of the calculated effects of supersonic and hypersonic speed on an unprotected photographic window, and to evolve methods of installation and thermal protection," Reference 4.

The specific objectives were as follows:

(a) Literature Survey

(b) Parameter Analysis

Establishment of reliable optical methods for evaluation of photographic quality.

Selection of photographic missions based on existing or planned vehicles.

Determination of expected window temperature gradients and pressure differentials.

(c) Verification of Analysis

Experimental determination of the dependence of optical deviation and resolution on temperature and pressure differences, glass type, shape, and thickness.

Experimental determination of the dependence of optical deviation and resolution on boundary layer refraction, shock wave interference, and luminosity.

(d) Design Recommendations

Establishment of three mission profiles covering the range of supersonic, high supersonic, and hypersonic aircraft.

Design of representative window mountings.

Recommendations and conclusions based on the results of the program.

The objectives of the engineering program were used for defining the separate tasks chronologically, and for maintaining schedule control. Organizationally, however, the work was divided into four distinct areas of effort:

- A. Aerothermodynamic Analysis
- B. Optical Analysis and Tests
- C. Luminosity Test
- D. Structural Design

In collating the results of the program, these organizational subdivisions provide a clearer perspective of the overall research than does the chronological outline, and the technical portion of this report will be subdivided accordingly.



## **Section IV**

### **AEROTHERMODYNAMIC ANALYSIS**

#### **SECTION SUMMARY**

The theoretical work done by Vidya, Inc., References 1 and 2, and others has provided tentative data on expected flow characteristics in the vicinity of an aircraft camera window, and on effects of the presence of the boundary layer and shock wave on photographic quality. It is the purpose of the present work to supply more definitive information.

A literature search was conducted to provide background for this study. The range of interest was divided into two general realms, namely, the hypersonic region above  $M 5.0$  ( $M$  is used in this report to indicate Mach number) and the supersonic regime below  $M 5.0$ . The requirements for operation below  $M 5.0$  are not concerned with structural and material temperature limits, but rather with the thermal distributions and environment which cause distortion and resolution problems in the camera window. The hypersonic regime has another order of problems which stem from the thermal limits of the materials involved as well as the highly excited state of the thermal environment along the surface of the vehicle outside of the window. The theoretical analysis was directed largely toward the hypersonic problems, since this area is not as well defined and appears to impose severe structural and temperature limitations on materials, as well as exhibiting a high-temperature flow field.

Two specific areas of study were pursued, namely, (1) simple methods of aerodynamic protection of the camera window, and (2) calculation of the temperature distribution through a diathermanous material. A diathermanous material allows radiation exchange directly to and from points within the material. In the case of an opaque material, on the other hand, the radiation exchange is assumed to be solely a surface function.

Two methods of aerodynamic protection have been considered. These are (1) separation (by means of a cavity), and (2) expansion of the flow over the window outer surface. The calculated environmental conditions consider a re-entering vehicle wing with trajectories at two angles of attack, for two locations on the assumed vehicle, for both laminar and turbulent flow. It is expected that the major points of interest are thereby approximated, and an estimate of the magnitude of importance of the location, expansion or separation surface, and type of flow can be made. Other effects, such as the temperature distribution through an edge mount, the heat load to the camera compartment, and the effect of an opaque window versus a diathermanous window are also considered. The data presented compare the aerodynamic conditions which may be expected for the trajectories selected. The condition of turbulent flow at one foot aft of the nose is an unrealistic condition. However, this curve is included in order to complete the map of conditions. It is thus assumed that the actual flow conditions are contained within the bounds of the conditions plotted. The effects of expansion on the window surface have been analyzed by comparing the computed heating rates with various expansion angles during a hypersonic re-entry trajectory.

## TRAJECTORY SELECTION

Three basic trajectories, covering a wide range of vehicle performance, were selected for study:

1. Supersonic flight at sea level
2. Hypersonic flight at high altitude
3. Hypersonic re-entry

Trajectories 2 and 3 were further subdivided:

- 2A. X-15 aircraft, flight #2-21 (high-speed)
- 2B. Typical X-15 high-speed flight
- 2C. Typical X-15 high-altitude flight
- 3A. High angle of attack hypersonic re-entry
- 3B. Low angle of attack hypersonic re-entry

Altitude-velocity curves, defining the five trajectories are shown in Figure 1. Typical temperature-time histories for these trajectories are given in Figure 2.

Several important flight parameters for trajectory #1 are given as functions of time in Figure 3: These include:

- (a) Altitude
- (b) Mach number
- (c) Angle of attack
- (d) Dynamic Pressure
- (e) Axial load factor
- (f) Normal load factor

In this trajectory the convective heating rate and net heating rate, Figure 4 and 5 respectively, are characterized by a single, quick impulse of heat flux followed by a long period during which the heating rates are very small. Two graphs are shown in each figure, corresponding to two different points on the fuselage, one at the nose and the other one foot aft of the nose. Thermal emissivities of 0.80 were assumed for the skin material in each case. Calculated skin temperatures (assuming a thin skin) for each of the two locations selected are given in Figure 6. At the front of the vehicle the temperature levels off at about 975 F, while at a position one foot aft of the nose the temperature is down to 870 F.

Temperature-time histories for a fused silica photographic window during trajectory #1 were calculated, and are shown in Figure 7. The window is assumed to be one foot aft of the nose, and its thermal properties are assumed to be equivalent to an opaque material. This particular window is 1-1/2 inches thick, and is mounted with a columbium-Inconel X edge attachment. Index numbers on the curves in the upper chart correspond to relative locations inside the window and mount, as indicated in the lower schematic diagram. It is seen that the outer surface of the glass never reaches a temperature higher than 830 F, but a portion of the metal mount may go considerably higher. The temperature gradient through the window can be determined from curves 1, 2, 4, and 7 of this figure. It varies considerably with time, decreasing as the inner portions of the glass absorb heat.

Flight parameters for X-15 high-speed flight #2-21 (trajectory 2A in this report) have been included for information purposes, Figure 8 through 11. The parameters are all given as functions of time, and include:

- (a) Altitude
- (b) Mach number
- (c) Angle of Attack
- (d) Dynamic pressure
- (e) Longitudinal acceleration
- (f) Normal acceleration
- (g) Local pressure coefficient  
(nose and six feet aft)
- (h) Net heating rate  
(nose and six feet aft)
- (i) Skin temperature  
(nose and six feet aft)

Skin temperature at a point six feet aft of the nose rises steadily to about 900 F in a matter of minutes, then drops rapidly as the aircraft velocity is reduced.

The flight parameters (Figure 8) for the actual X-15 high-speed flight have been smoothed in Figure 12 to define a typical high-speed flight, trajectory 2B. These data can then be used to calculate temperature-time histories of various points within a window, as was done previously for the supersonic, sea level trajectory #1 (Figure 7). Two thicknesses of window are considered, 3/8 inch and 1-1/2 inches, Figures 13 and 14 respectively. Each of the windows is considered to be thermally opaque, and located 12 feet aft of the nose. The window mount is similar in configuration to that of the vehicle in trajectory #1 (Figure 7), except that titanium can be used at the lower temperature. It is seen that neither window ever reaches a temperature above 350 F at the outer surface. It is also obvious that the temperature gradient through the thicker window is much less uniform than that of the thinner window, as would be expected.

Flight parameters for a typical X-15 high-altitude flight are presented in Figures 15 through 18, and include:

- (a) Altitude
- (b) Mach number
- (c) Angle of attack
- (d) Dynamic pressure
- (e) Normal acceleration
- (f) Local pressure coefficient  
(two locations)
- (g) Net heating rate (two locations)
- (h) Skin temperature (two locations)

The two locations on the aircraft considered here are about six feet aft of the nose and the ventral leading edge. The sudden increase in skin temperature at 300 seconds is due to an increase in velocity at a lower altitude.

The above data were all calculated utilizing perfect gas relationships. These are considered reasonably satisfactory for trajectories 1 and 2, but are not realistic enough for the hypersonic re-entries (trajectories 3A and 3B). In trajectories 3A and 3B real gas relationships are used in order to provide data which should more closely describe the actual local conditions on the vehicle surfaces in question. The figures are identified according to the method used. The code TSTP indicates Transient Skin Temperature Program (perfect gas), Reference 6. The code HASTE refers to Hypersonic and Supersonic Temperature Evaluation Program (real gas), References 7 and 14.

Flight parameters for trajectories 3A and 3B are given in Figures 19 and 20. Both trajectories are considered to have a constant angle of attack, one being nominally high (50 degrees) and the other low (15 degrees). The 50 degree re-entry, trajectory 3A, is subject to heating conditions over a time period only half as long as trajectory 3B, and therefore the heating problems are not as severe. Typical temperature-time curves to illustrate this were shown in Figure 2.

Trajectories 3A and 3B are further subdivided by location of the point of interest on the vehicle, and according to whether laminar or turbulent boundary layer flow is being considered. Thus 3AL6 refers to a point six feet aft of the nose, with laminar flow, in trajectory 3A (50 degree angle re-entry). Similarly, 3BT1 refers to a point one foot aft, with turbulent flow, in the 15 degree angle re-entry. In the following paragraphs these variations are discussed in detail.

## INCIDENT HEAT FLUX TO THE WINDOW

### Effect of Window Location

The effect of window location along the vehicle surface may be considered by referring to Figure 21, which is a graph of convective heating rates resulting from laminar and turbulent flow, one foot aft and six feet aft, in the 3A trajectory (50 degree angle of attack). It is observed that, for both the laminar and the turbulent condition, the heating rate is considerably less at the locations farthest from the nose. Locating a photographic window as far aft as possible, therefore, is of obvious benefit, particularly in the case of laminar flow where a reduction of more than 50 percent can be achieved by locating the window at the six-foot position instead of the one-foot position. As may be expected when the Reynolds number is sufficiently low, the maximum heating rate for turbulent flow is less than that of the laminar at one foot, but is considerably more than the laminar at six feet.

The 3B trajectories show a considerably different trend in the time at which peak heating occurs. Referring to Figure 1 the 3B trajectory is at much lower altitudes for equivalent Mach numbers. During the early part of the 3B trajectory, Figure 22, the one-foot aft location with laminar flow is subjected to the highest heating rate, as in the 3A trajectory. But, since the 3B trajectory is much longer in duration, and the peak heating occurs at a lower altitude (and higher Reynolds number), the turbulent flow soon produces a higher rate than the laminar flow. This is true for both locations. The maximum heating rate in the 3B trajectory is, in all cases, higher than that in trajectory 3A.

#### Effect of Air Expansion

As stated before, Figures 21 and 22 show a summary of theoretical comparisons between heating rates at two locations for two flow conditions, in two trajectories. The vehicle nose radius is considered to be 7.5 inches at zero sweep angle. The six foot aft location is most pertinent to possible photographic window locations. Only the downward-looking surface was considered. In the paragraphs that follow, angles of expansion are listed with reference to a zero angle such that the surface of interest is parallel to the vehicle centerline.

#### Laminar Flow Region

Convective heating rates versus time are presented in Figure 23 for various angles of expansion from minus ten degrees to plus 30 degrees. The -10 degree angle is included in order to extend the study to a point on the vehicle which may be oriented at +10 degrees angle of attack when the vehicle centerline is parallel to the direction of flow. This is represented as a negative expansion angle. From Figure 23 it is evident that expansion angles of more than ten degrees result in a significant reduction in the convective heating rate. The same effect is evident at the six foot aft location, Figure 24. These are controlled expansions, not separation.

Chapman, Reference 9, has provided a theoretical analysis of heat transfer in regions of separated flow. The paper by Larson, Reference 8, supplies data for correlation of Chapman's theory for laminar flow separation heat transfer. This analysis indicates a theoretical reduction of approximately 44 percent for two-dimensional bodies, and is apparently independent of the temperature of the surface area beneath the separated boundary layers. The investigation of Charwat, Reference 10, concurs with the results reported by Larson for laminar flow if the boundary layer up-stream of the cavity is thin. Comparison of this reduction of 44 percent in heat flux due to laminar region separation with that theoretically available from controlled expansion is of interest. The theoretically available reductions for controlled expansion depend upon the assumption that the flow will follow the expansion angle without separation. The expansion angles plotted are either parallel to or "see" the oncoming flow. They are not larger than the angle of attack of the vehicle. This would tend to stabilize the flow and, therefore, make separation less likely.



By referring to Figure 23 it is seen that a 30 degree expansion angle is not sufficient to produce a 44 percent reduction in maximum heat flux, and so this angle of expansion is not as efficient as a complete separation of flow. It is estimated from cross plots that an angle of approximately 35 degrees would be required, for both the one-foot and six-foot position in the 3A trajectory, to provide protection equal to that provided by separated flow regions. Whether the controlled expansion can provide even more protection than the fully separated region remains to be investigated.

The heating rates calculated for the 3B trajectory with laminar flow are given in Figures 25 and 26 for the one-foot and six foot position. For this trajectory, with an angle of attack of 15 degrees, an expansion angle of only ten degrees provides a relatively large amount of protection. The heating rates are reduced by approximately 40 percent. At the six-foot location an expansion angle of 15 degrees theoretically provides the same amount of thermal protection as that which would be expected from a cavity with complete flow separation.

#### Turbulent Flow Region

The data of Charwat et al, Reference 10, concludes that the turbulent heat transfer to a cavity is a function of the boundary layer thickness of the incoming stream. If the boundary layer is thin (less than the depth of the cavity), the heat transfer is reduced by a factor of approximately two. If it is thick, the heat transfer can even be increased. The effect of the expansion angle when the flow is turbulent is shown in Figures 27 and 28, again for a one-foot and a six-foot location, 3A trajectory. It is quite unlikely that the flow would be turbulent at the one-foot location during the re-entry time of interest. However, this one-foot turbulent study shows approximately the same effectiveness in reducing convective heat flux to the surface as that of the six-foot location. Therefore, the effectiveness may be assumed to be nearly constant at any location between one-foot and six-feet aft.

Similar charts, for the 3B trajectory, are shown in Figures 29 and 30. The same general trend observed in the 3A trajectory is also evident here. It is interesting to note that, in the 15 degree angle of attack trajectory 3B, a negative expansion angle shows an increased heating rate, as would be expected, Figures 25, 29, and 30. But, in the 50 degree trajectory 3A, a negative expansion angle shows a lower heating rate than a zero angle (where the window is flush with the moldline), Figures 23, 27, and 28. This may be a result of the particular calculation methods which were selected, since the very large angle of attack combined with an additional expansion angle places the window at an angle of 60 degrees to the oncoming flow. A reduction in calculated local velocity on the surface at this extreme angle would probably account for the reduced heating rate.

#### Conclusions

The first order of importance in window protection is the location of any photographic window as far aft as would be practical. The next order of importance is to maintain laminar flow over the surface, if possible.

A controlled expansion flow would have an advantage over separated flow in that, should the flow become turbulent, a small angle of expansion is quite effective in reducing heat flux to the window. This is especially true during the low-angle re-entry (3B), which requires a greater amount of protection over a longer period of time than the high-angle re-entry (3A) trajectory. If the window could be made variable in angle, to keep it more nearly parallel to the ground at all times, window heating rates could be maintained at a more constant level.

#### OUTSIDE SURFACE PRESSURE ON WINDOW

Local pressures were computed by a modification of Creager's method Reference 11, which includes blast wave and boundary layer convections. The adequacy of this method for describing the actual situation is discussed in Reference 14. The following calculated results were obtained.

The effect of location of the window upon the local pressure along the wing surface is shown to be negligible, within the considerations of this study. This may be seen by comparison of 3AL12H and 3AL62H in the left hand chart of Figure 31.

The effect of local expansion angle upon this local pressure is considerably more pronounced, as seen in the right hand chart of the same Figure 31. These curves show local pressure vs. time at a point six feet aft of the nose, in a laminary flow 3A trajectory. The pressure may be theoretically reduced to one-fifth the flush value by using an expansion angle of 30 degrees. The same effect holds true for the laminar 3B trajectory, Figure 32. The effect of expansion is even more pronounced in this trajectory. In addition, it is advantageous to place the window as far aft as possible, as seen by comparison of the one-foot and six-foot pressure curves in the left-hand chart (Figure 32).

#### TEMPERATURE OF WINDOW

Maximum heating rates and window temperatures for hypersonic re-entry trajectories 3A and 3B have been tabulated for convenience in Table I. The most likely window locations are aft of the one-foot condition. The flow at one foot aft would not be expected to be turbulent for the re-entry conditions considered. But these data do allow an estimate of the limitations that must be exercised upon the vehicle flight path in order to keep the local window temperatures from becoming excessive.

The data in Table I indicate that the longer duration, low angle of attack re-entry trajectory (3B) is characterized by a much higher heat flux and higher maximum window temperature than the shorter duration, high angle trajectory (3A). The temperature of an unprotected diathermanous window re-entering along a 3B trajectory would theoretically reach a temperature above the nominal limit of 2000 F which is considered to be the maximum safe temperature for fused silica in this study. This maximum temperature may be reduced, theoretically, by locating the window at a ten degree expansion angle. In Table I, 3ET63 is a ten degree surface, and the maximum window temperature is less than 1600 F.

Because of the longer machine time required to run the diathermanous analysis, the aerodynamic comparisons were made with an opaque glass analysis. It is expected that the approximate relationships between the opaque and the diathermanous methods of analysis would hold true throughout the whole spectrum of this study. Therefore, direct comparisons have been made for a minimum number of diathermanous calculations. The diathermanous temperature analysis machine program, Reference 7, was based on the theory of Gardon, Reference 13.

### High Angle Re-entry

Typical temperature-time distributions through an opaque fused silica window are given for the 3A trajectory, Figures 33, 34, and 35. These are, respectively, laminar one-foot, laminar six-foot, and turbulent one-foot flow conditions. The schematic window mounting shown is similar to that assumed for the supersonic, sea level trajectory. In each of the figures, the temperature gradient through the glass is seen to increase with time until 3000 seconds after start of re-entry, at which point the vehicle velocity is reduced to M 10. The outer surface temperatures for these three trajectories have been replotted in Figure 36, together with data for the turbulent six-foot flow condition. The same trends noted for the heating rates are reflected in the computed temperatures. For further comparison, a crossplot of temperature vs window location has been drawn for both laminar and turbulent flow, Figure 37. Again, it is obvious that window temperature can be reduced by locating it as far aft of the nose as is practicable.

The effect of expansion angle on window surface temperature is illustrated in Figure 38, which is typical of the data that could be plotted for each flow condition and surface location. This particular graph is for a six-foot aft position, with turbulent flow. The effect of expansion angle upon maximum window temperature for other flow conditions may be determined from Table I.

A more graphic presentation of the effectiveness of expansion angle in reducing window temperature is given in Figure 39. Here the reference is a flush window, and reductions in temperature are plotted with time, for various expansion angles. A rather large expansion angle (30 degrees) is required to produce an appreciable amount of thermal protection. This chart is for a 3A condition (turbulent flow, six feet aft). A crossplot, Figure 40, shows the effectiveness of expansion angle for other flow conditions, at the time of maximum window temperature. The four curves were derived for opaque windows. The single point below the curves illustrates the effectiveness of expansion angle for a diathermanous window. The protection appears to be greater for the diathermanous window, but it should be noted that the maximum surface temperatures are higher for diathermanous than for opaque windows, as will be seen presently.

Typical temperature-time distributions, calculated one-dimensionally through a diathermanous window, are shown in Figures 41, 42, and 43. These are, respectively, turbulent flow with flush window, turbulent flow with a 30 degree expansion angle, and laminar flow with flush window. Figure 43 is directly comparable with Figure 34, which represents the same conditions except with a thermally opaque window. The window temperatures derived from



diathermanous calculations are some 200 F higher. A crossplot of Figures 41 and 42 is given in Figure 44, where typical temperature distributions through the window are shown at (1) the time of maximum temperature difference, and (2) the time of maximum surface temperature, for both flush and 30 degree expansion angle conditions. As additional information, Figure 45 compares the temperatures of diathermanous and opaque windows directly. In all cases the diathermanous is hotter.

#### Low Angle Re-entry

Typical temperature-time distributions through an opaque fused silica window are given for the 3B trajectory, Figures 46, 47, and 48. These are, respectively, laminar one-foot, laminar six-foot, and turbulent one-foot flow conditions. The equivalent graphs for the 3A trajectory are Figures 33, 34, and 35. In each of the figures the temperature gradient is seen to increase with time until 6000 seconds after re-entry. The outer surface temperatures for these three trajectories have been plotted in Figure 49, together with data for the turbulent six-foot flow condition.

The effect of location along the surface is, in this trajectory, quite similar to that of the 3A trajectory. As shown in Figure 50 the maximum window temperature becomes lower as the location of the window is moved aft. Here, however, the two curves never cross.

The effect of local expansion angle upon temperature difference at maximum temperature is shown in Figure 51. As mentioned before, the diathermanous calculations would indicate a somewhat greater effectiveness than the opaque calculation, but this should be weighted against the higher maximum temperature of the diathermanous window. The completely different shape of the curves for this trajectory (compare Figure 40 for the other trajectory) is due to the greatly different angle of attack. In this trajectory an increase in the angle serves to increase the velocity and, therefore, the heating rate to the surface is also raised. The negative expansion angle produces the same effect. In the 3A trajectory with its 50 degree angle of attack, on the other hand, an increase in angle only brings the surface in question to an angle which is closer to the stagnation region. (The model under consideration is a two-dimensional blunt wing of constant radius.) The result is a greatly reduced local velocity which, in turn, reduces the heat transfer rate.

The temperature-time distribution through a diathermanous window, six feet aft, with turbulent flow, is given in Figure 52. The window is flush with the moldline. At the time of peak temperature (2100 F) the temperature difference through the window is approximately 550 F. As shall be proved in subsequent sections of this report, photography through such a window is almost impossible. The point to be made in Figure 52 is that the thermal environment is so severe that the structural integrity of the window would be extremely difficult to maintain, without protection. Fortunately, such protection is feasible, by means of controlled-expansion flow. Figure 53 shows the remarkable reduction in temperature that can be achieved by tilting the window to produce a ten degree expansion angle. The outer surface temperature is reduced by some 530 F, the inner by 340 F. The

temperature difference through the window is reduced by 150 F (30 percent). This improvement may not be sufficient to guarantee good photographs, but the structural problems have been diminished significantly.

A direct comparison of the instantaneous distribution through the glass, at the times of maximum temperature and maximum temperature difference, is presented in Figure 54, for both a flush window and a ten degree expansion angle (cf. Figure 44 for equivalent data on trajectory 3A). Using the same location, six feet aft, but with laminar instead of turbulent flow, distributions through a diathermanous window are given for various specific times after start of re-entry in Figure 55. These are shown in comparison with opaque window data, so that the difference in the two computational methods may be appraised. Figure 55 illustrates quite readily the greater temperature difference, lower maximum temperature, and linear temperature distribution at equilibrium, all of which are characteristics of the opaque method of calculation.

#### Thermal Lag

The time lag of temperature rise in various parts of the window can be grossly evaluated by comparison of temperature-time distributions as shown in Figure 43. A special machine run was made to evaluate this lag for a specific set of conditions. Both the opaque and the diathermanous window were assumed to be normalized at 600 R and instantly subjected to a heating rate of 4.25 BTU/sec ft<sup>2</sup>. This approximates the maximum heating rate of the 3A16 trajectory. The outside surface temperature-time histories and instantaneous distributions through the glass at 1000 seconds and 5000 seconds are shown in Figure 45. In neither case can the distribution through the diathermanous window be adequately described by the opaque analysis. The outstanding characteristics of the opaque analysis are internal lag at the 1000 second mark and straight-line equilibrium temperatures at the 5000 second mark. The diathermanous calculation shows a steeper temperature gradient at each surface in both cases, and still presents a lower over-all temperature difference. The maximum outer surface temperature of the diathermanous material also reaches a much higher value at stabilization than the opaque analysis would predict. This is explained by the fact that the opaque analysis neglects the radiant exchange of energy within the material itself.

#### COMPARTMENT HEAT TRANSFER

The machine program written for this study made provision for the investigation of various methods of cooling the inner surface of the window. These investigations were not pursued, because of budget limitations. However, some understanding of the relative importance of such a study may be obtained by observing the effectiveness of controlled expansion flow on the rate of heat transfer to the camera compartment. Figure 56 shows the relative transfer rates for expansion angles of zero and ten degrees, in a 3BT6 trajectory. It is seen that the heat transfer rate is reduced by more than 50 percent, during the entire trajectory, when the ten degree expansion is utilized.

## CONCLUDING REMARKS

The analysis presented here is an example of the type of aerothermodynamic study which can be provided for any specific vehicle. The machine programs which have been developed are not restricted to the conditions considered for this study.

If a particular vehicle and mission were specified, a more definitive selection of glass type and thickness could be made. The heat transfer to the compartment, and the weight of the window, could be optimized, and the reduced temperature gradients would provide an improvement in photographic capabilities.

Protection of the window by means of controlled expansion flow has been shown to be feasible on a theoretical basis. It would be valuable to investigate this further in laboratory tests.

Protection of the window by means of separated flow can be accepted as feasible for a laminar flow field, but the turbulent case is less easily defined. Laboratory tests might be extended into the realm of basic data on the effects of local surface deflections on heat transfer.

These studies have been largely confined to a blunted two-dimensional wing problem. The specific flow characteristics of a three-dimensional body will not necessarily produce the same results.

Traj.	Expansion Angle $\alpha$	( $Q_c$ ) <sub>max</sub> BTU/SEC-FT <sup>2</sup>	Columno. Frame (T <sub>#22</sub> ) <sub>max</sub> °R	Inconel Thin Skin (T <sub>#34</sub> ) <sub>max</sub> °R	Opaque Glass (T <sub>#1</sub> ) <sub>max</sub> °R	Diathermanous Glass (T <sub>w</sub> ) <sub>max</sub> °R	Comment
3AL12	0	9.374	1978	2247	2036		Not likely window location
3	10	9.059			2011		
5	20	8.032					
6	30	6.555			1824		
3AT12	0	8.416	1908	2206	1963		Not feasible flow condition
3	10	8.120					
5	20	6.892					
6	30	5.119			1698		
3AL62	0	4.098	1510	1806	1538	1741	
3	10	3.904			1503		
5	20	3.405					
6	30	2.649	1315	1619	1323		
3AT62	0	5.922			1738	2015	
3	10	5.557			1703		
5	20	4.555			1591		
6	30	3.128	1181	1739	1410	1540	
3BL12	0	14.443	2216	2461	2276		Not likely window location
3	10	11.297			2124		
4	15	10.713			2090		
3BT12	0	19.219	2396	2629	2456	3117	Not feasible flow condition
3	10	13.494			2190		
4	15	12.553					
3BL62	0	4.724	1665	1896	1703	2066	
3	10	2.942			1475		
4	15	2.575			1419		
3BT62	0	10.304			2073	2572	
3	10	5.113	1386	1904	1710	2041	
4	15	4.207			1628		

Table I  
Hypersonic Heating Rates and Temperatures

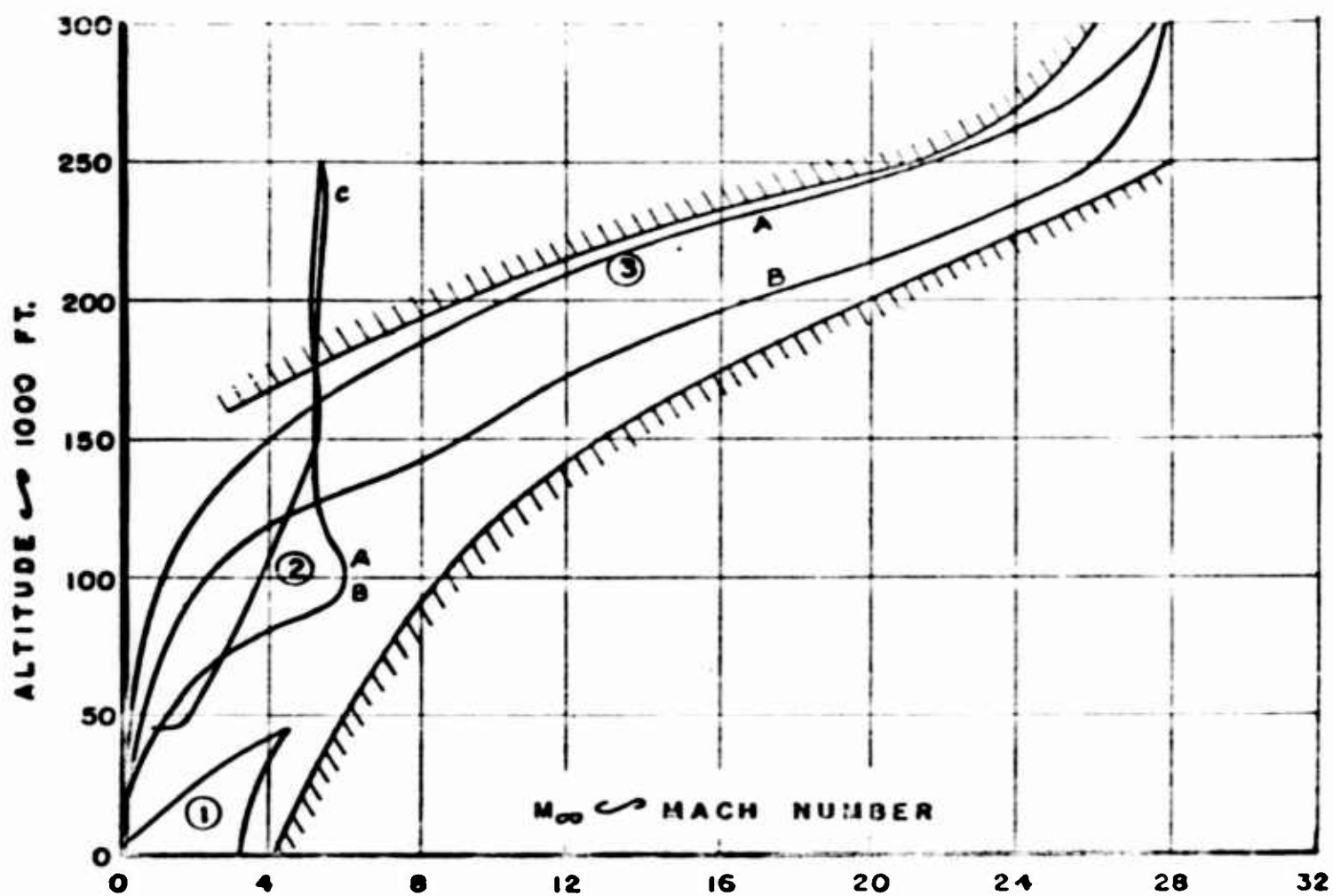


Figure 1 Trajectories Selected for Photographic Window Study

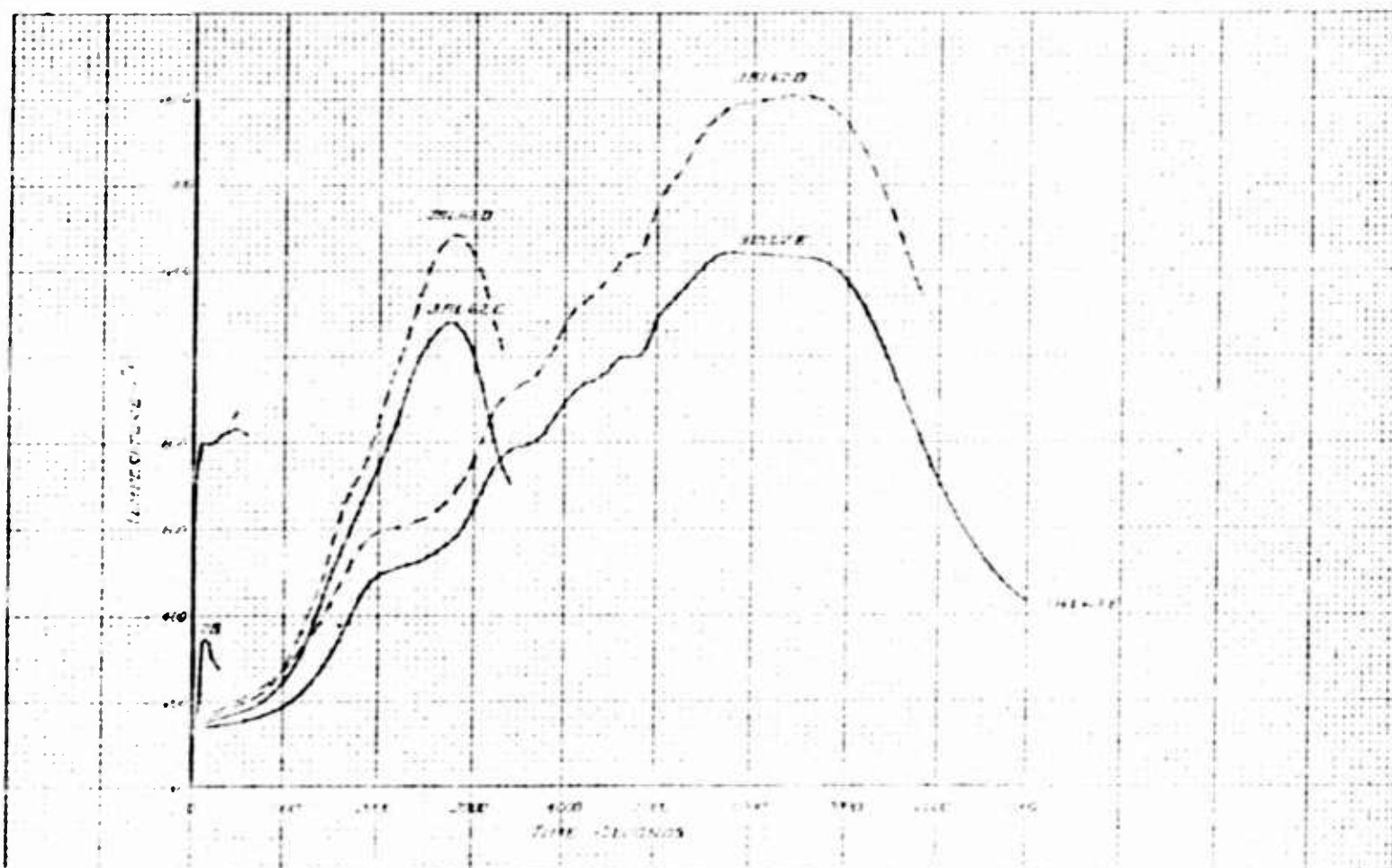


Figure 2 Typical Photographic Window Temperature for Trajectories Selected



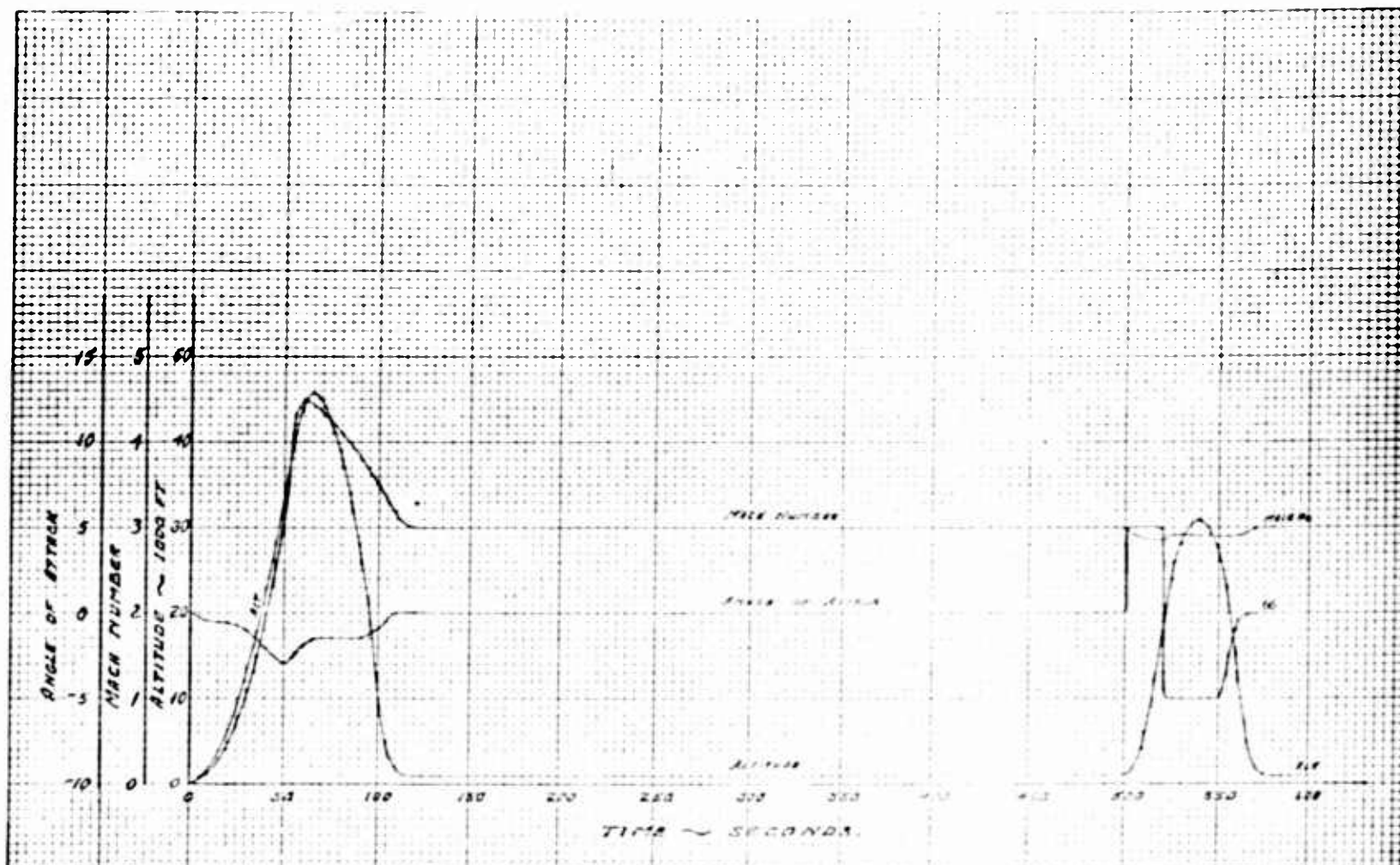
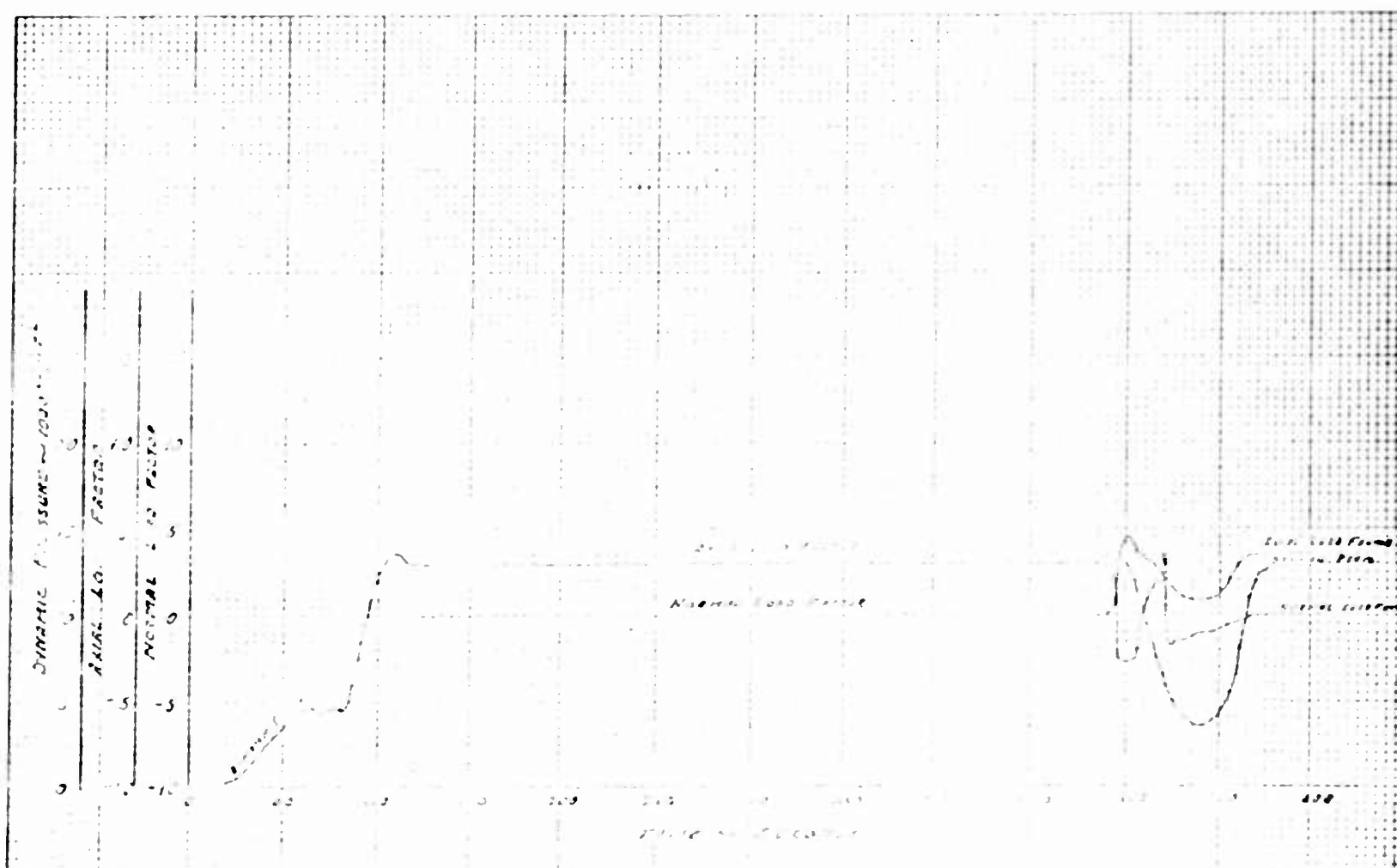


Figure 3 Trajectory 1 Flight Parameters Versus Time



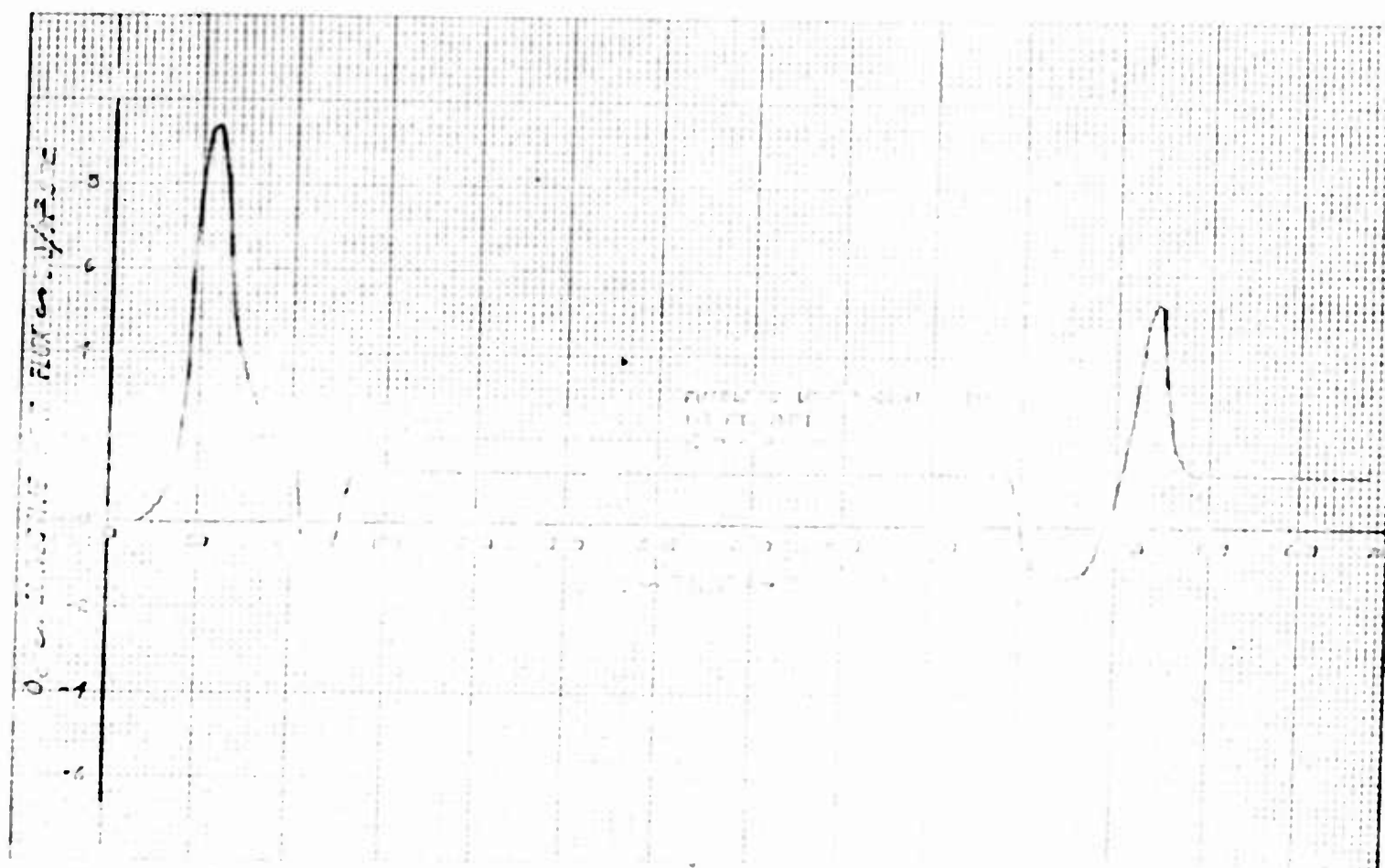
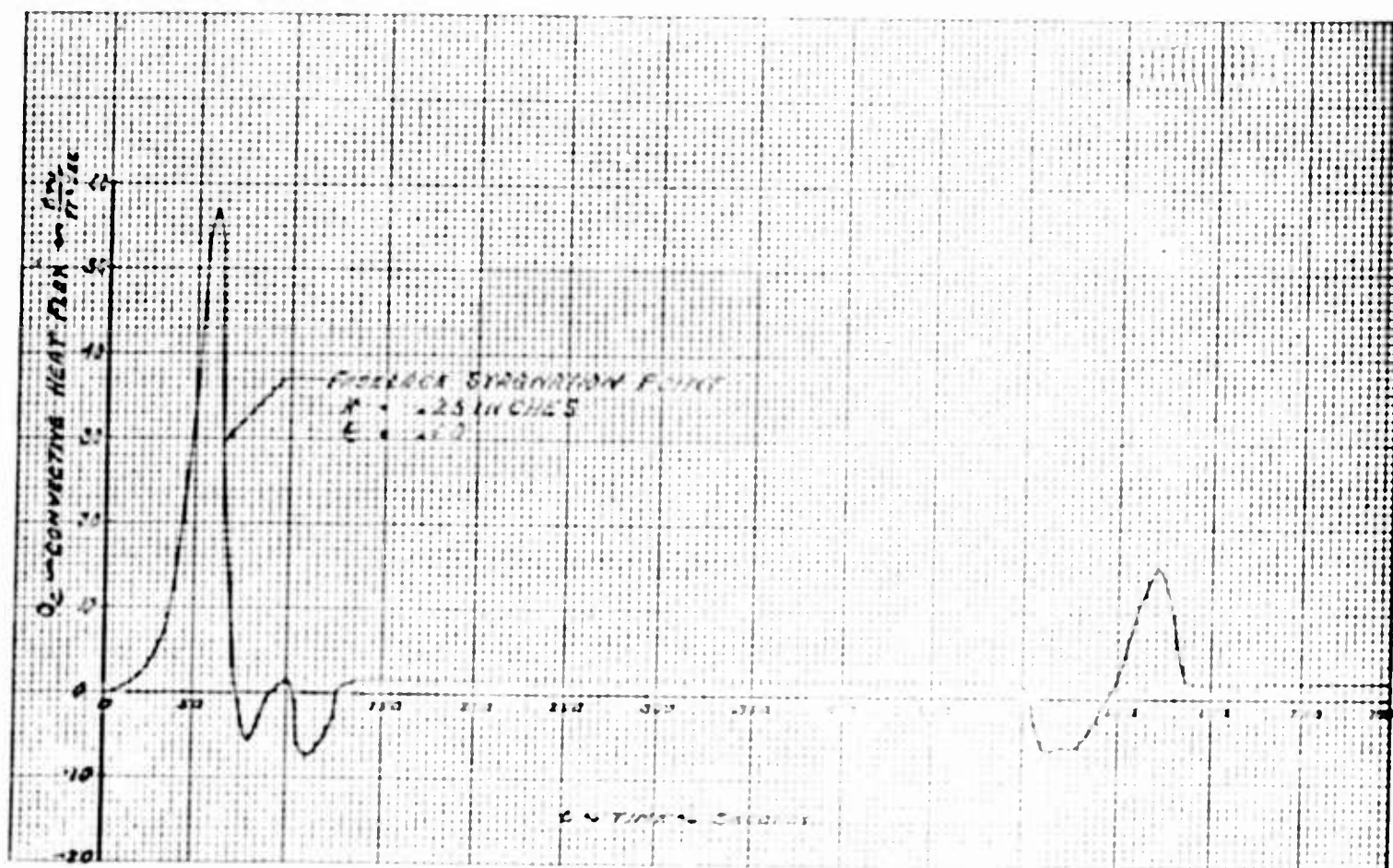


FIGURE 1. Convective Heat Flux vs. Time for a Free-Surface Stratification Experiment (TSP)

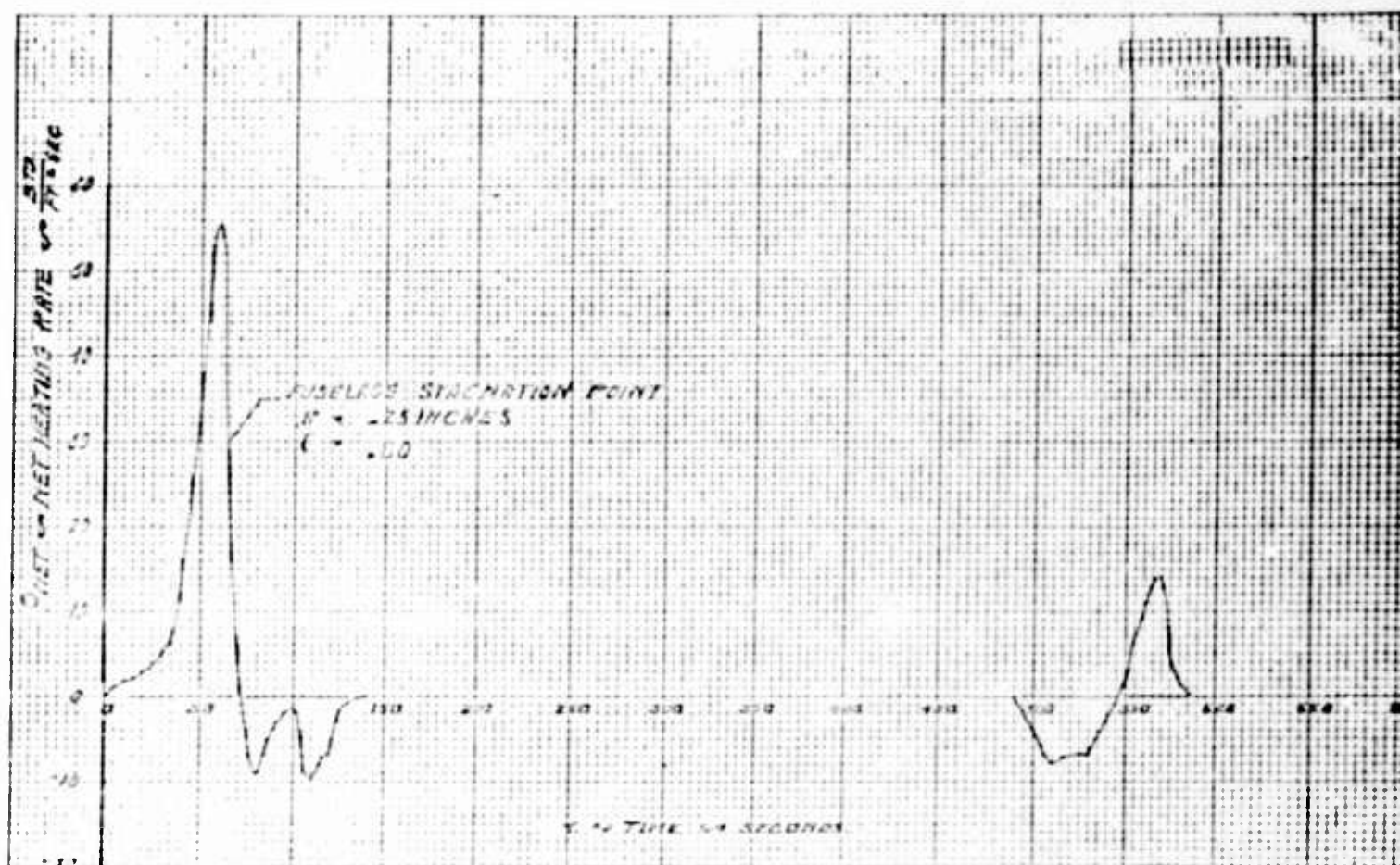


FIGURE 5. Net Heating Rate vs Time for a Fibered Synchronization Point (RSTP)



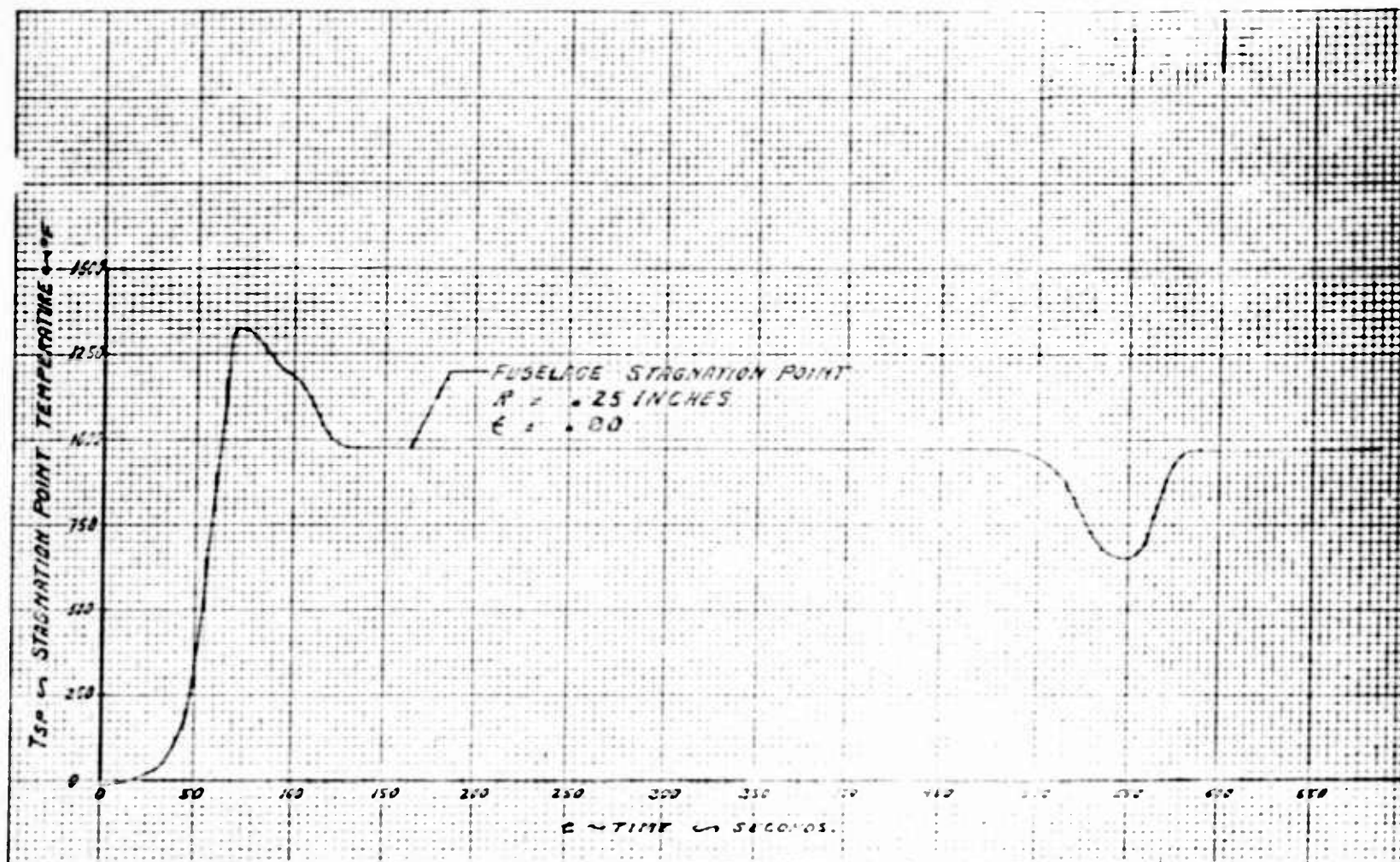
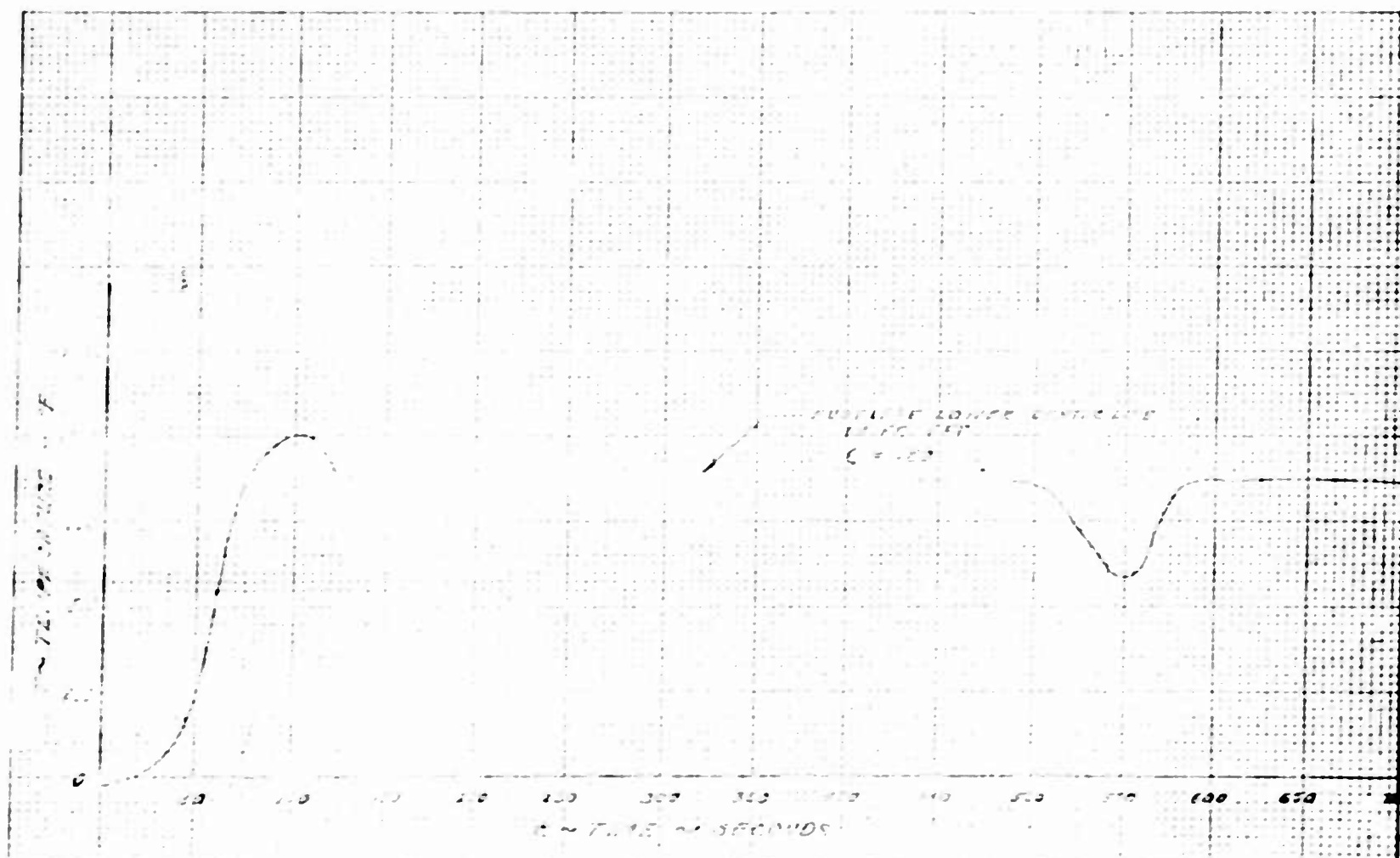


Figure 6 Trajectory 1 Fuselage Thin Skin Temperature Versus Time (TSTP)



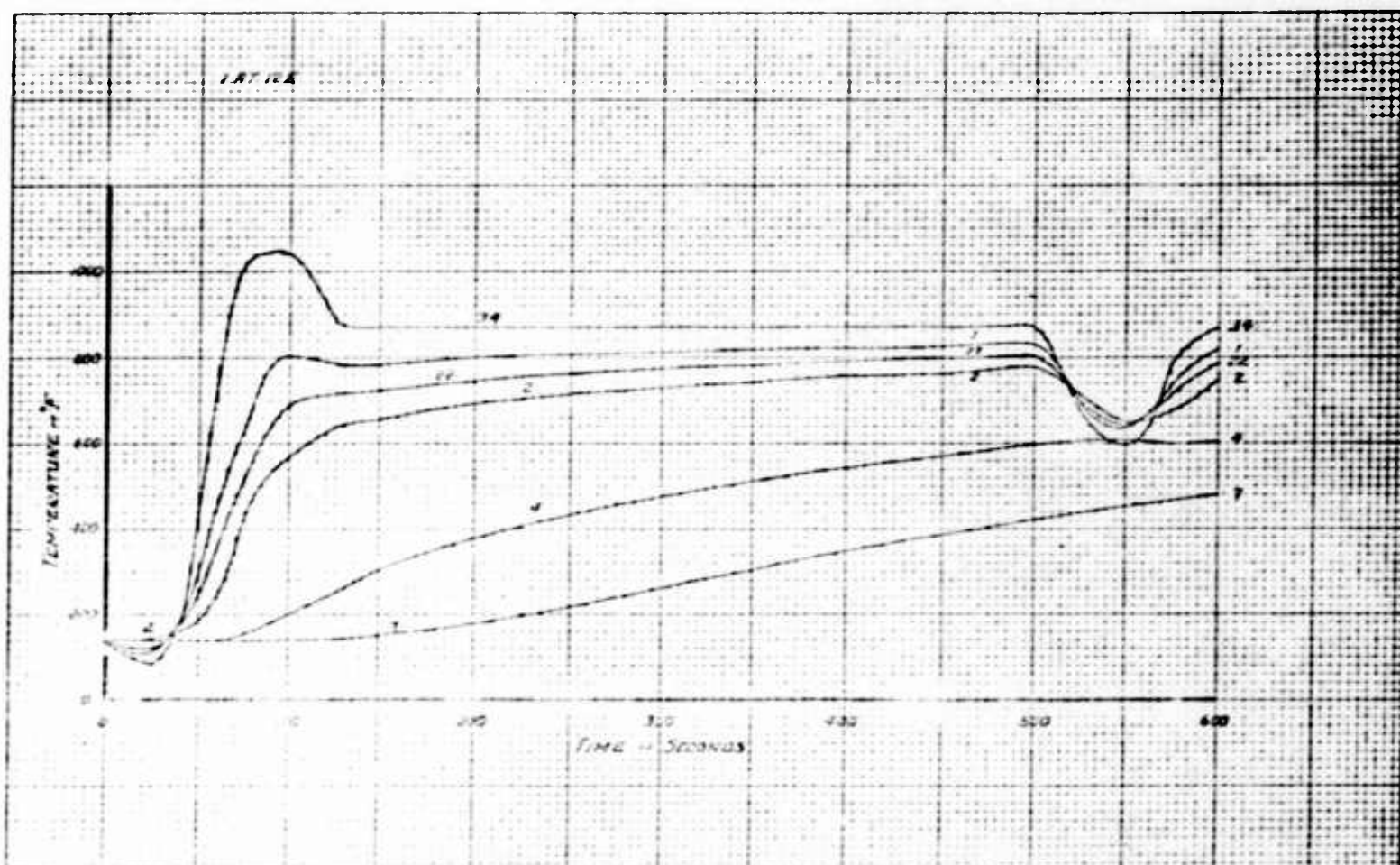
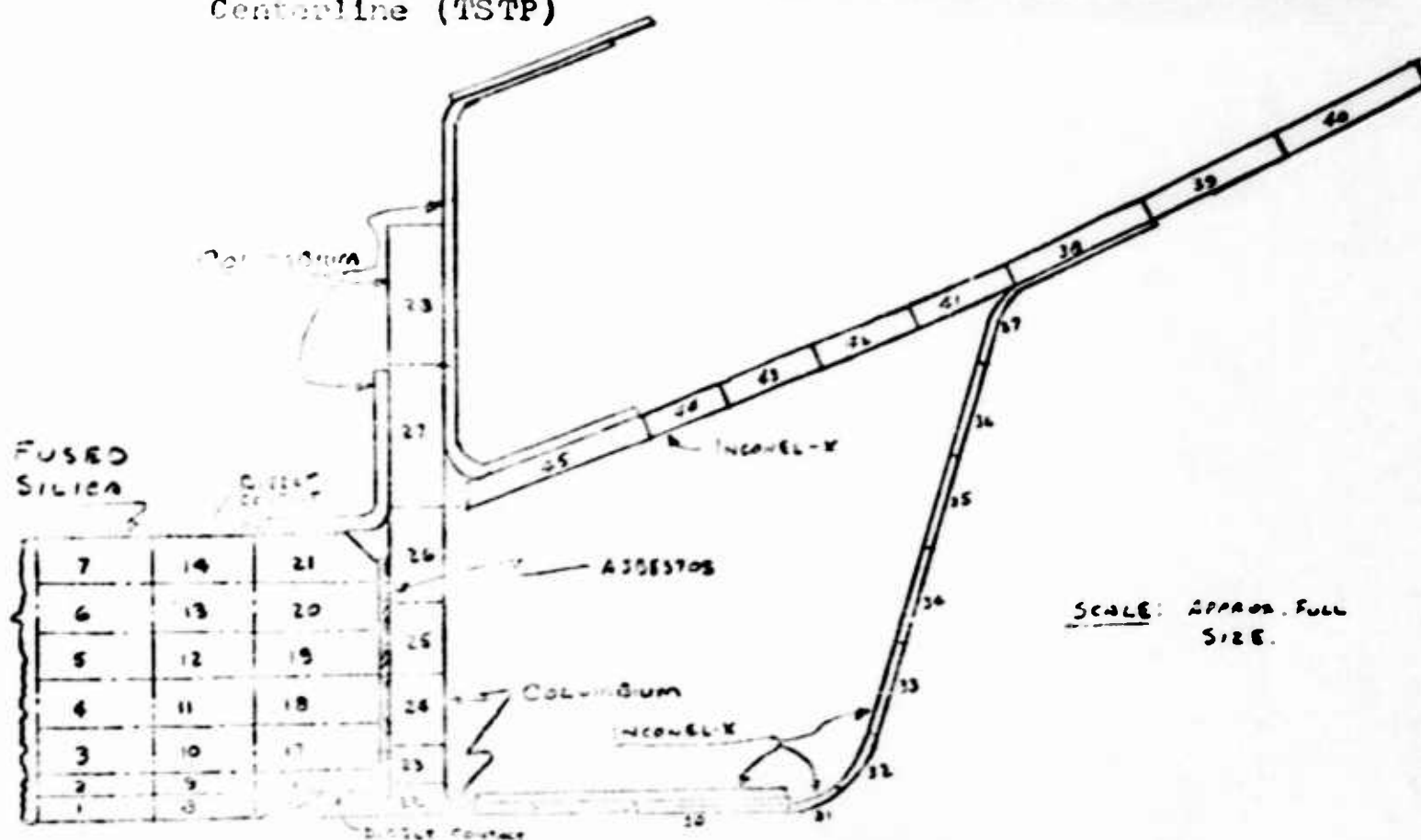


Figure 7 Trajectory 1 Temperature-Time Distribution Through an Opaque Fused Silica Window 1-1/2" Thick Mounted as Shown Located One-Foot Aft on Lower Fuselage Surface Parallel to Vehicle Centerline (TSTP)



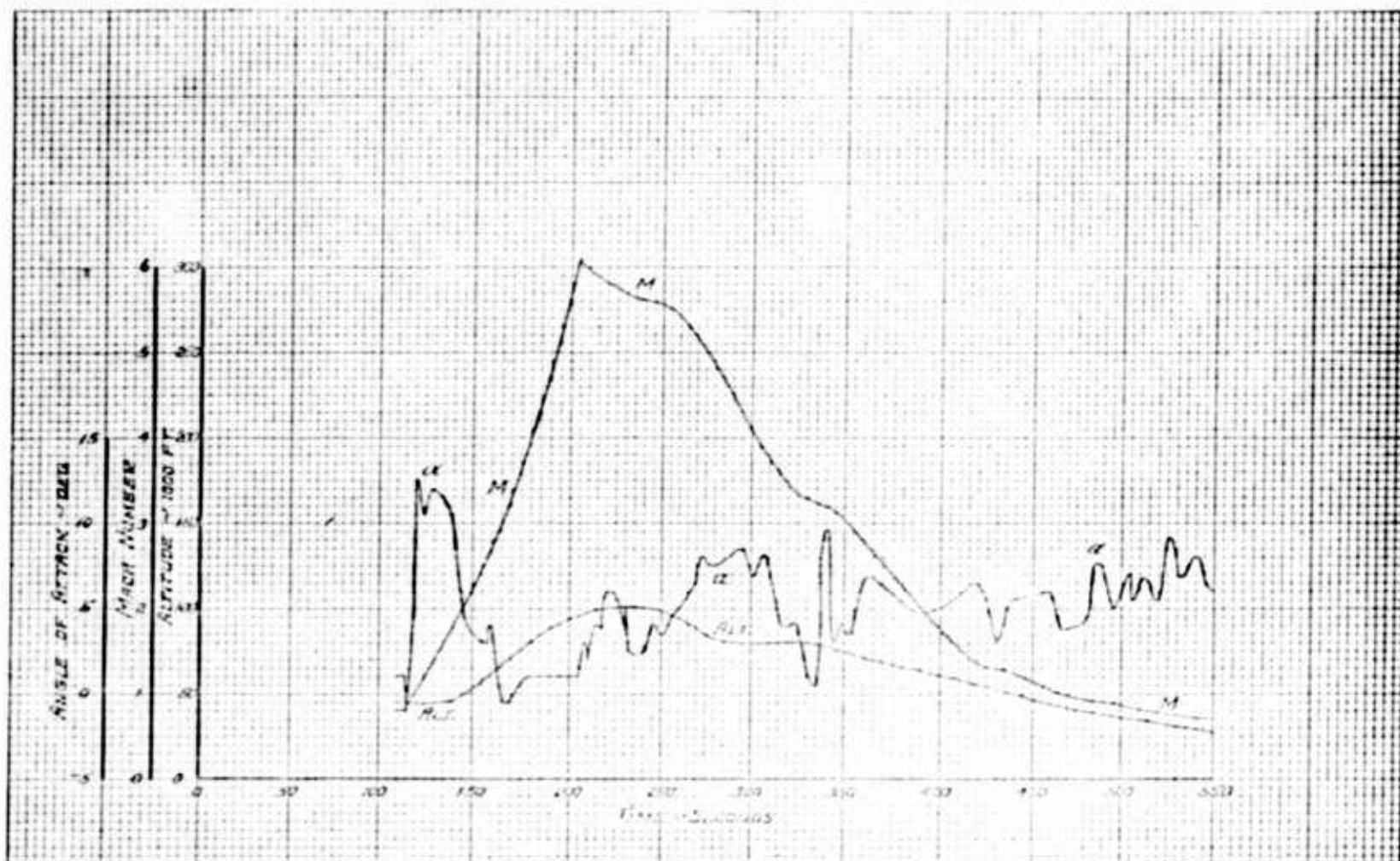
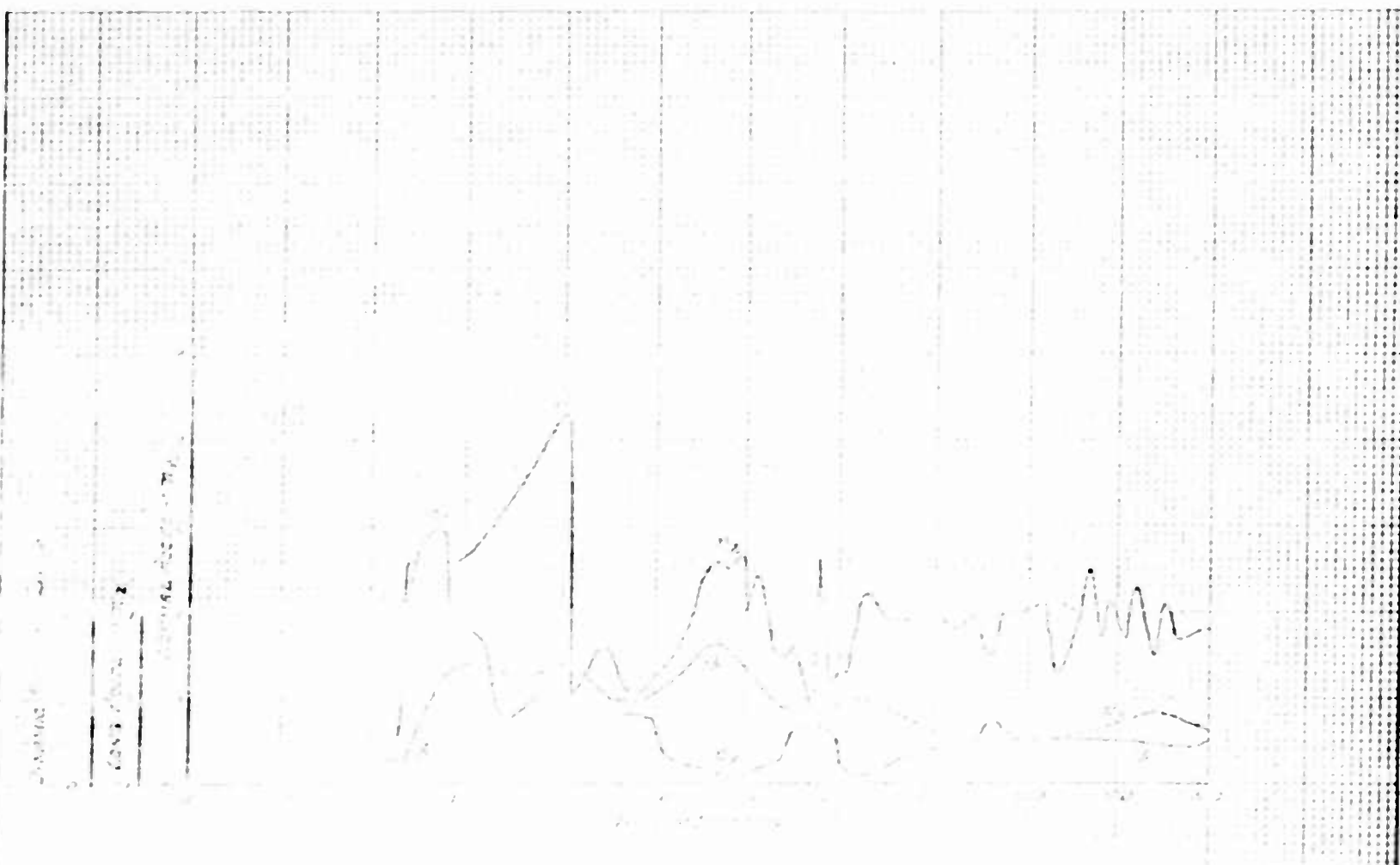


Figure 8 Trajectory 2A Flight Parameters Versus Time (H.S. Flt. 2-21)





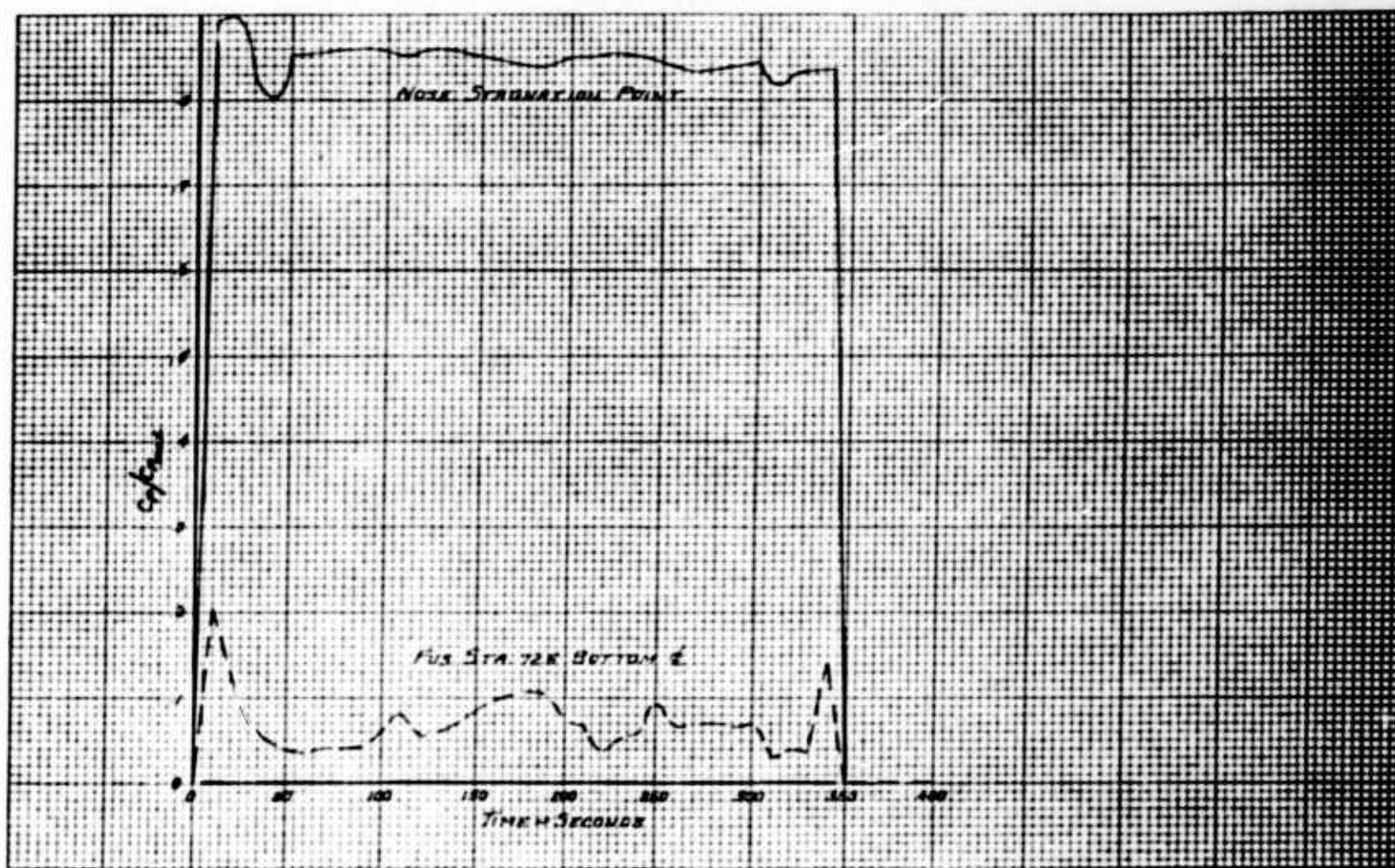


Figure 9 Trajectory 2A Local Pressure Coefficient Versus Time  
(H.S. Flt. 2-21)

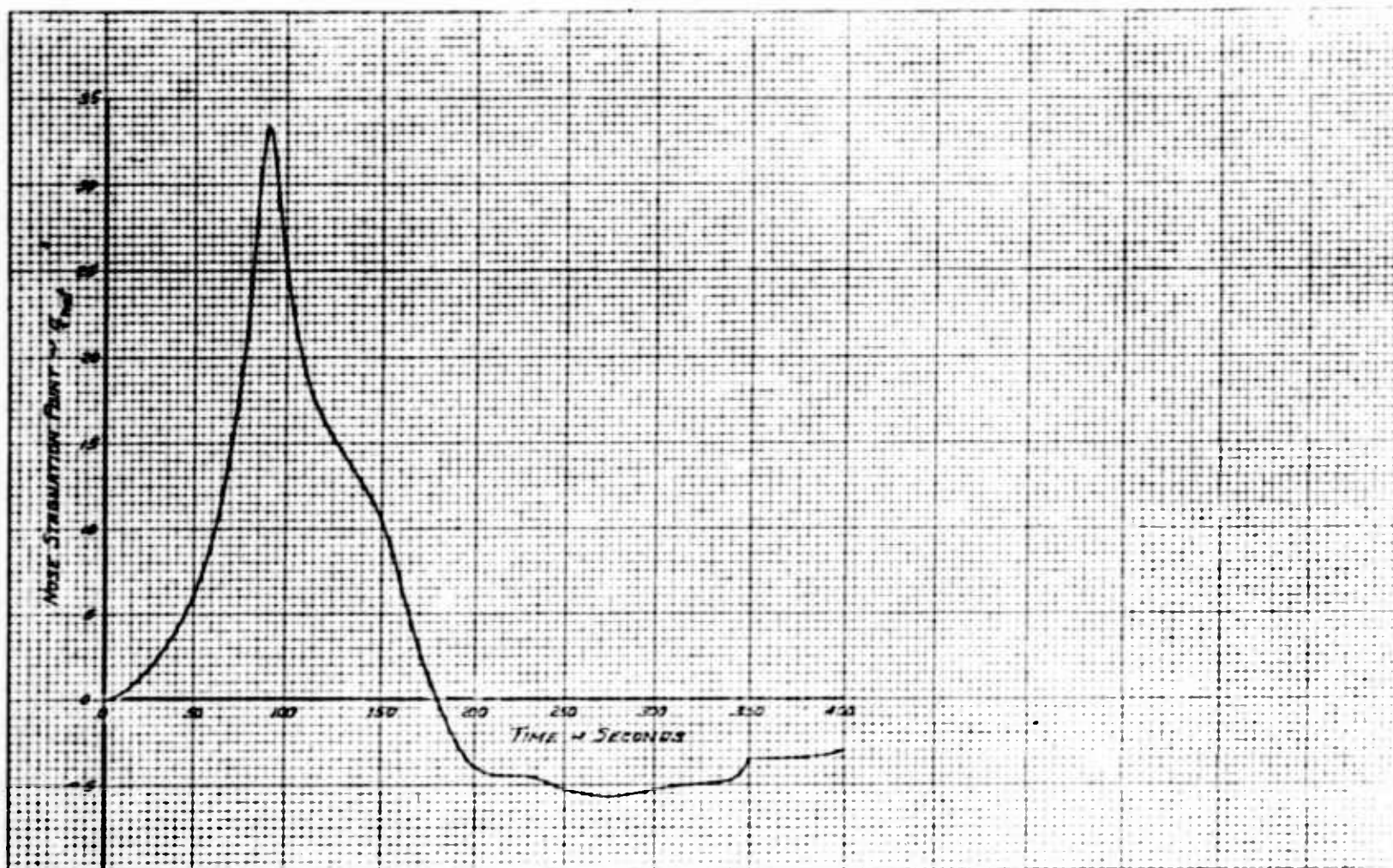
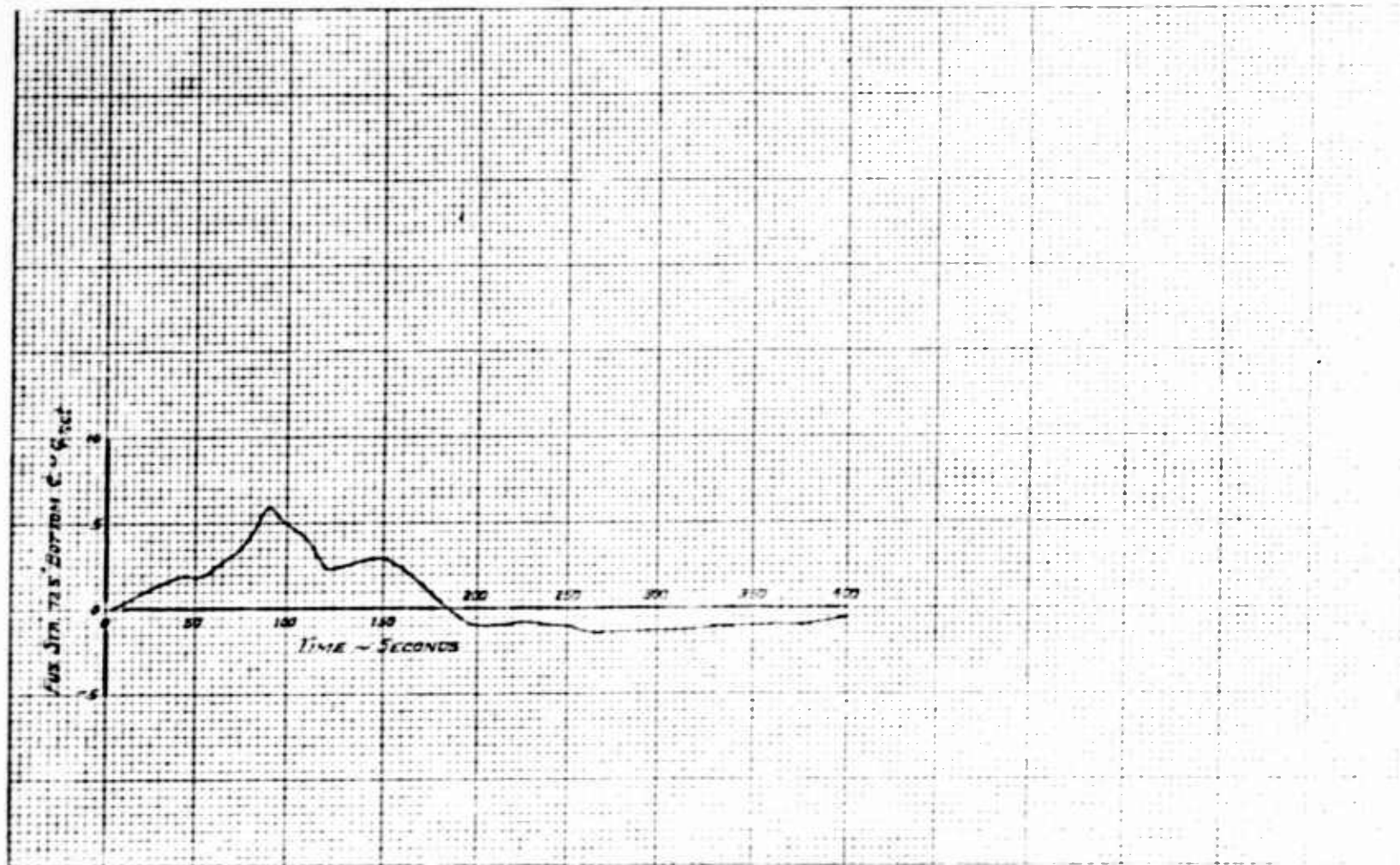


Figure 10 Trajectory 2A Fuselage Thin Skin Net Heating Rate Versus Time (H.S. Flt. 2-21) (TSTP)





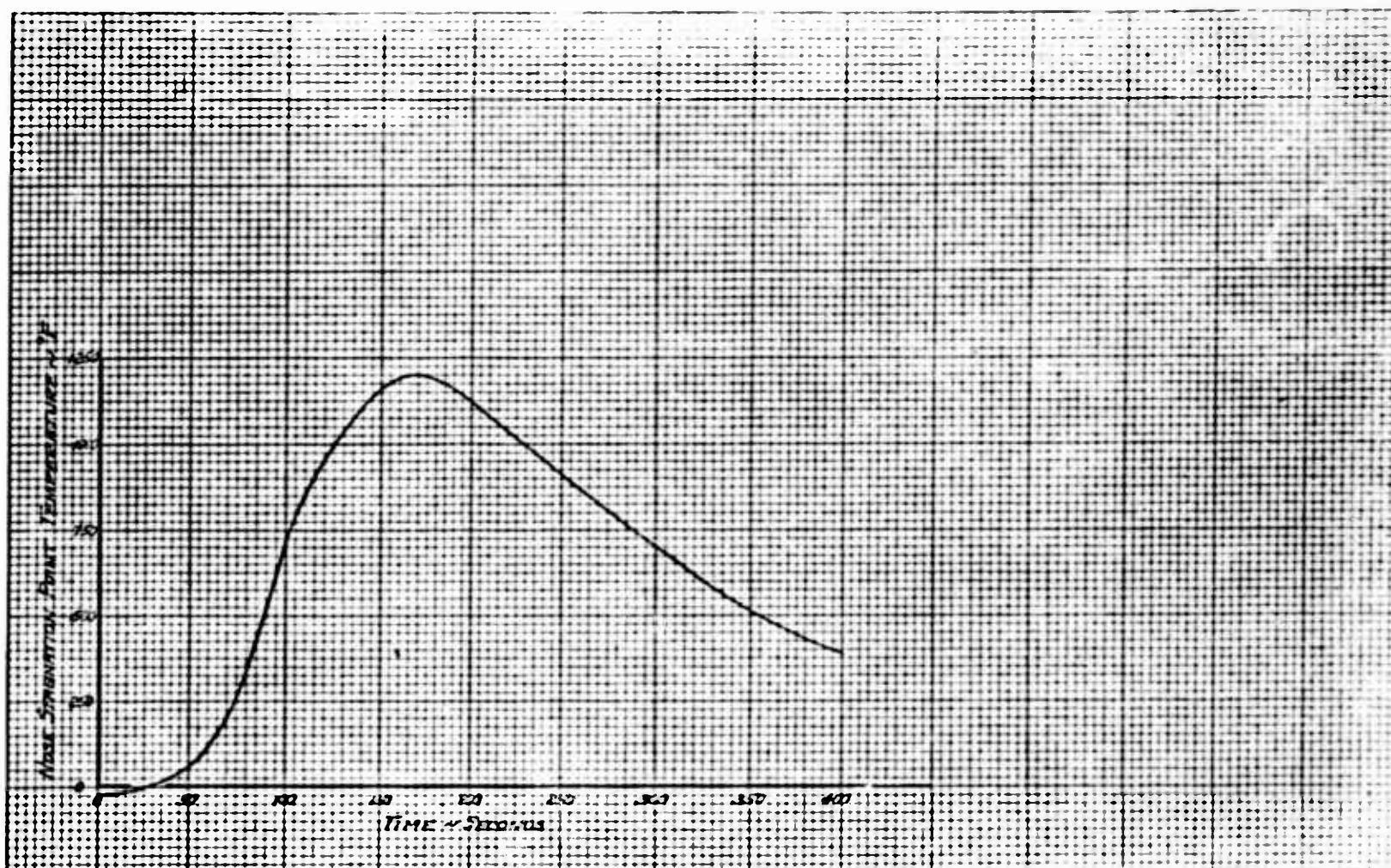
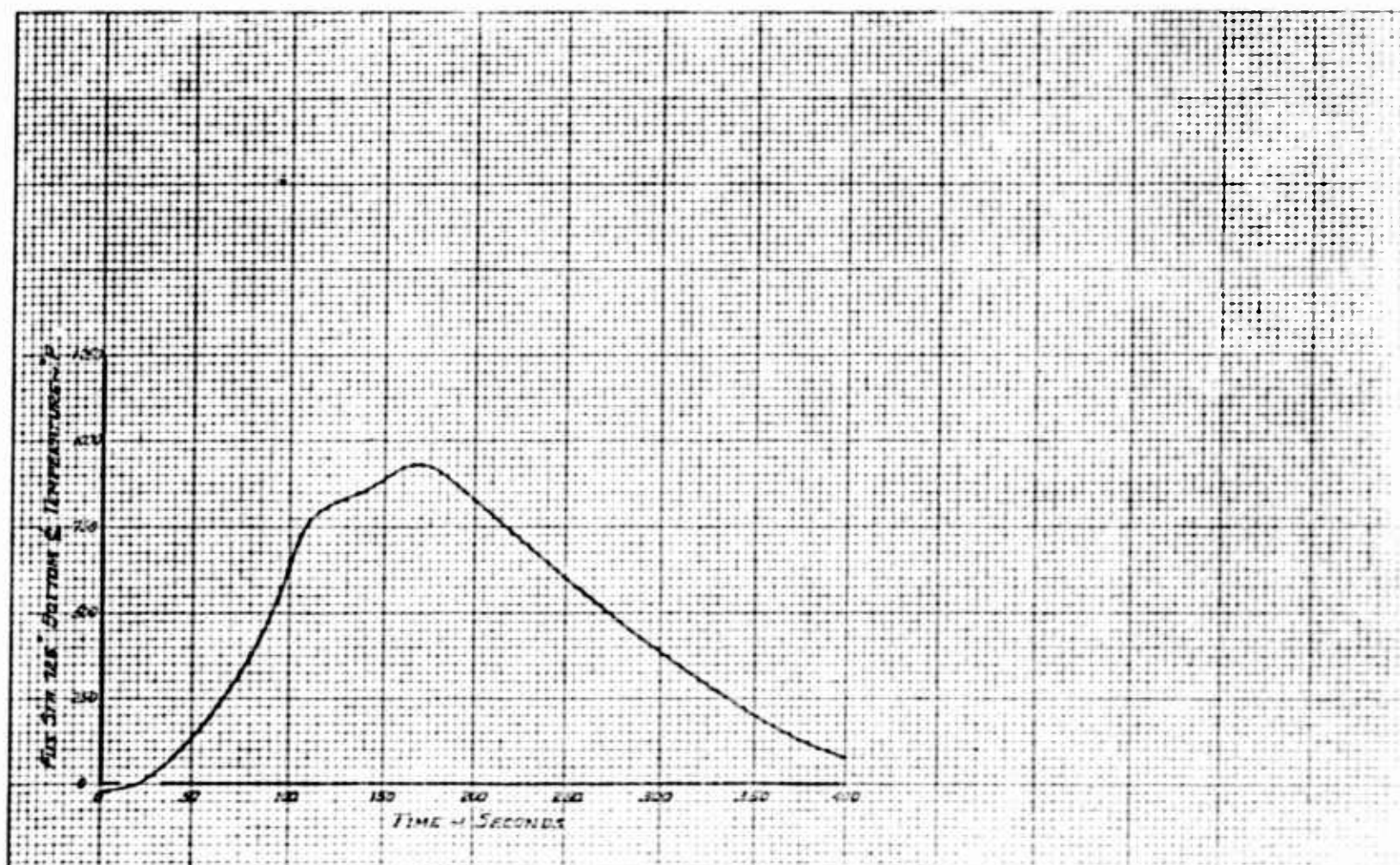


Figure 11 Trajectory 2A Fuselage Thin Skin Temperature Versus Time  
(H.S. Flt. 2-21) (TSTP)



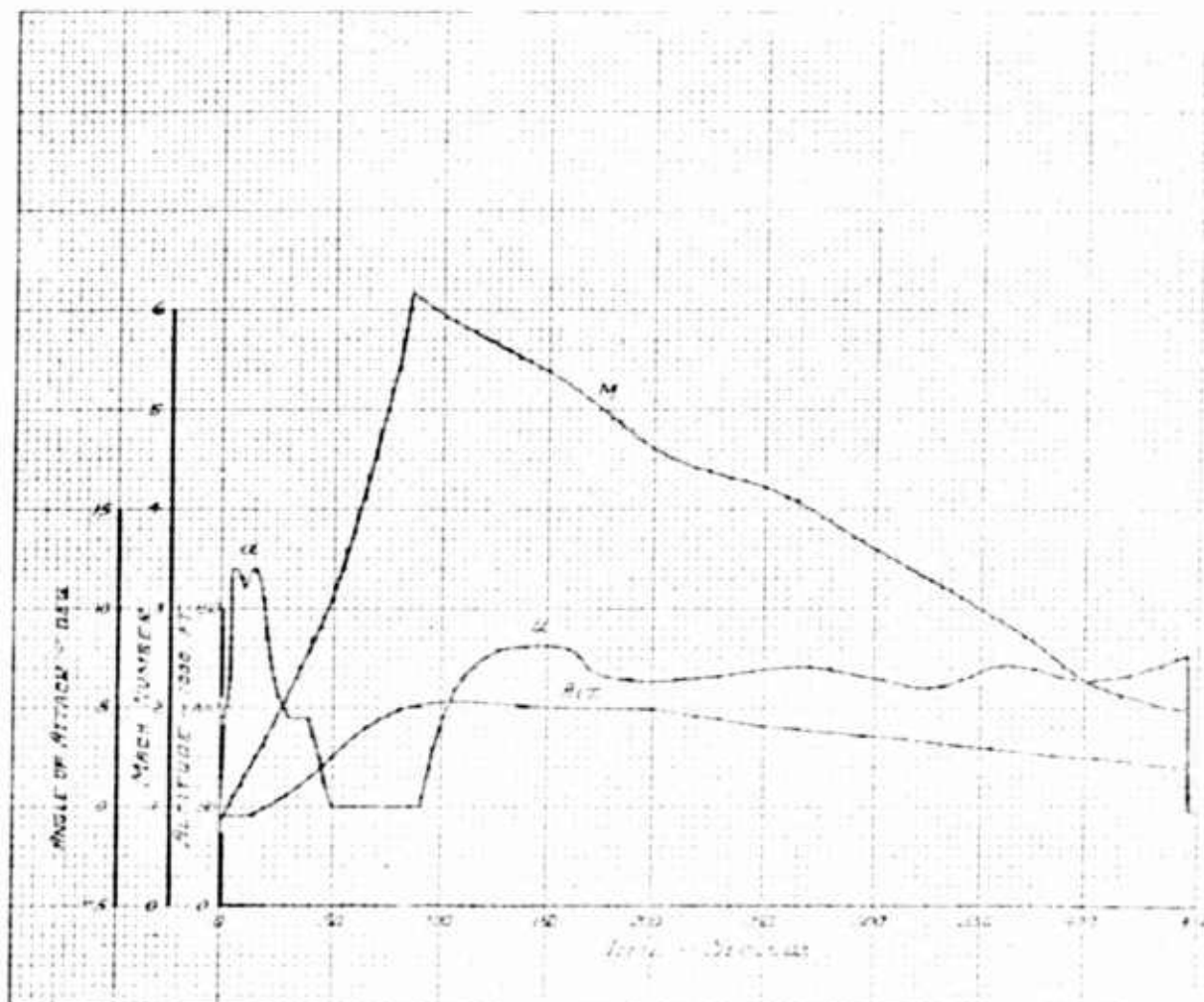
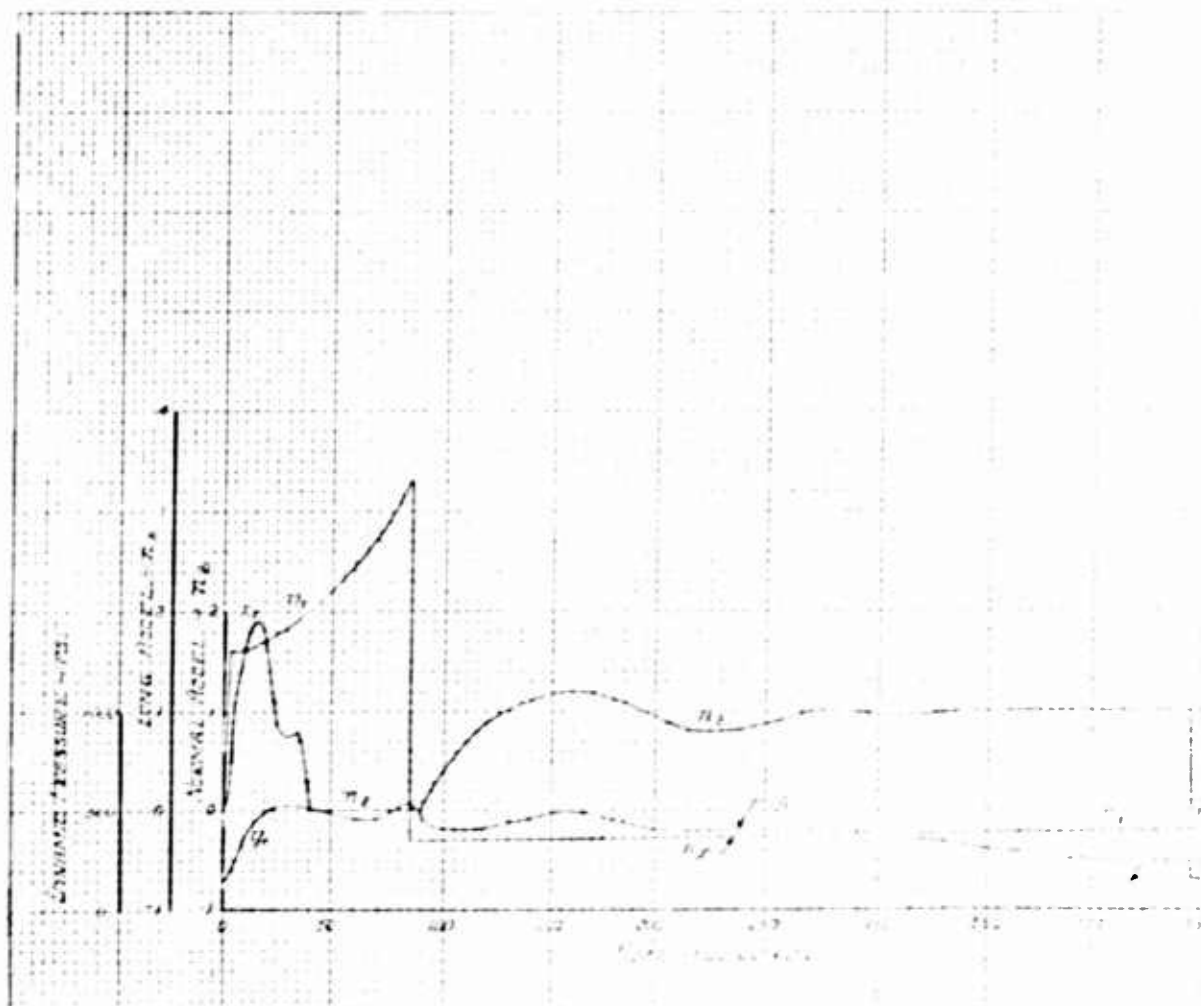
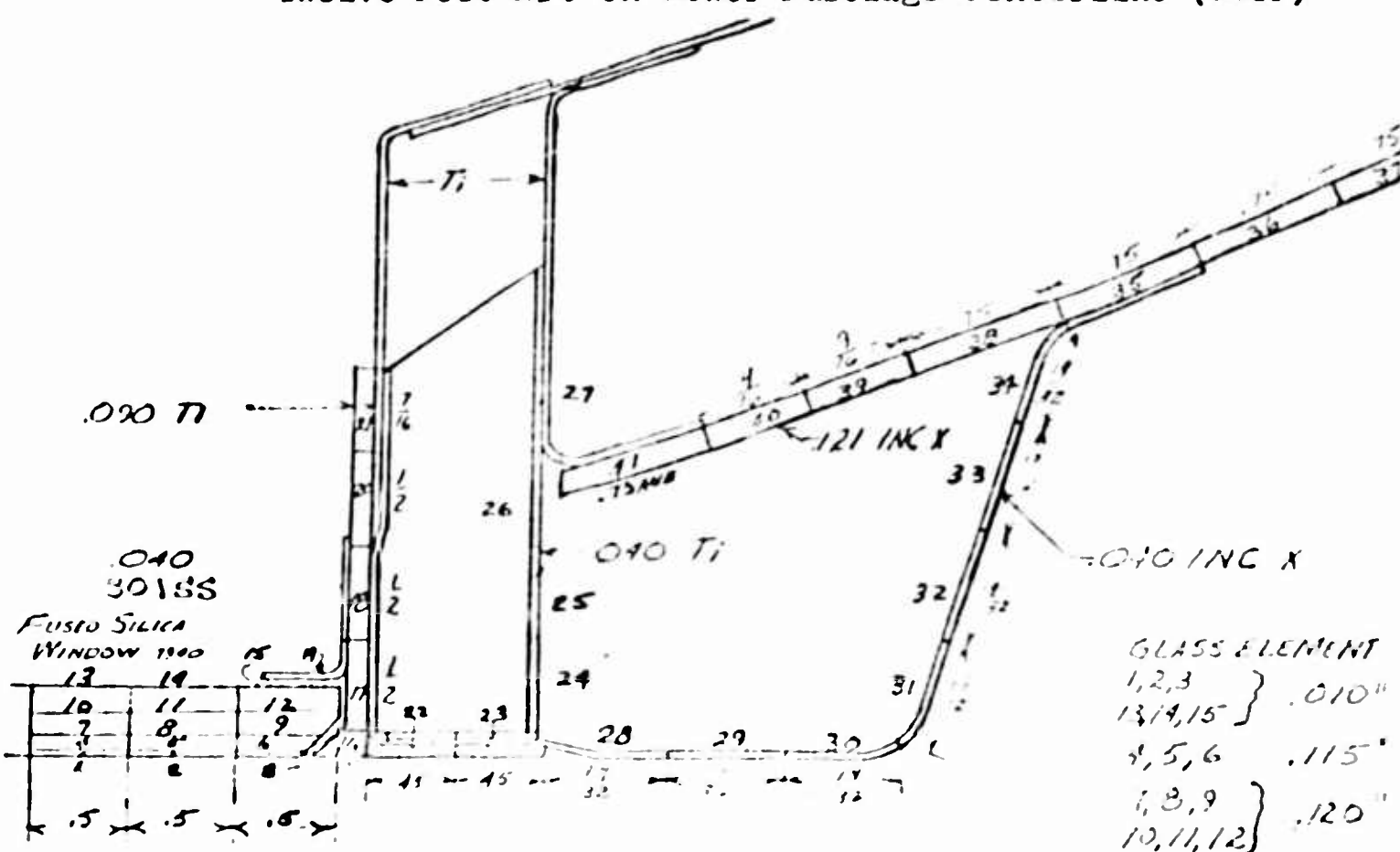
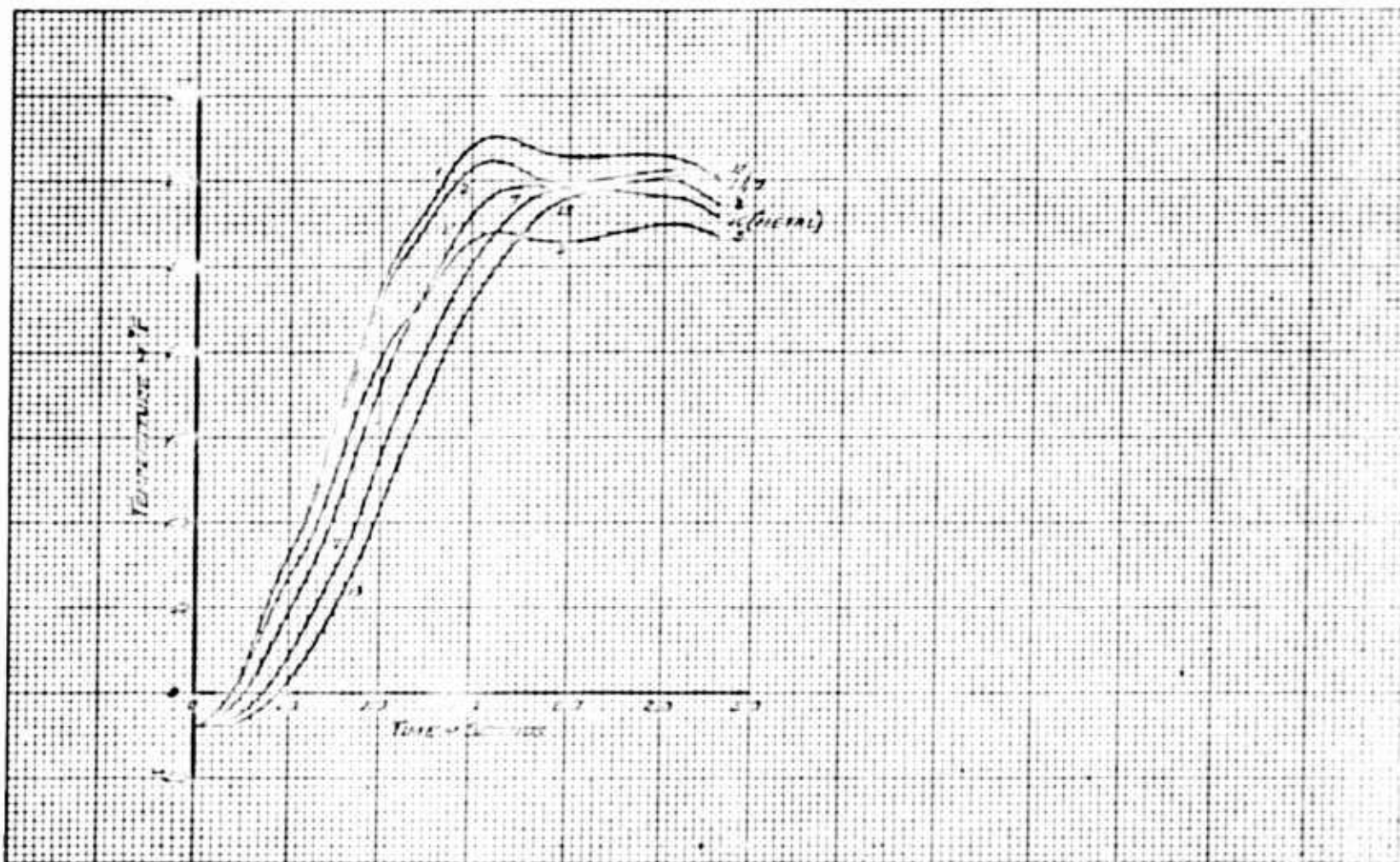


Figure 12 Trajectory 2B Flight Parameters Versus Time (Typical High Speed Flight)







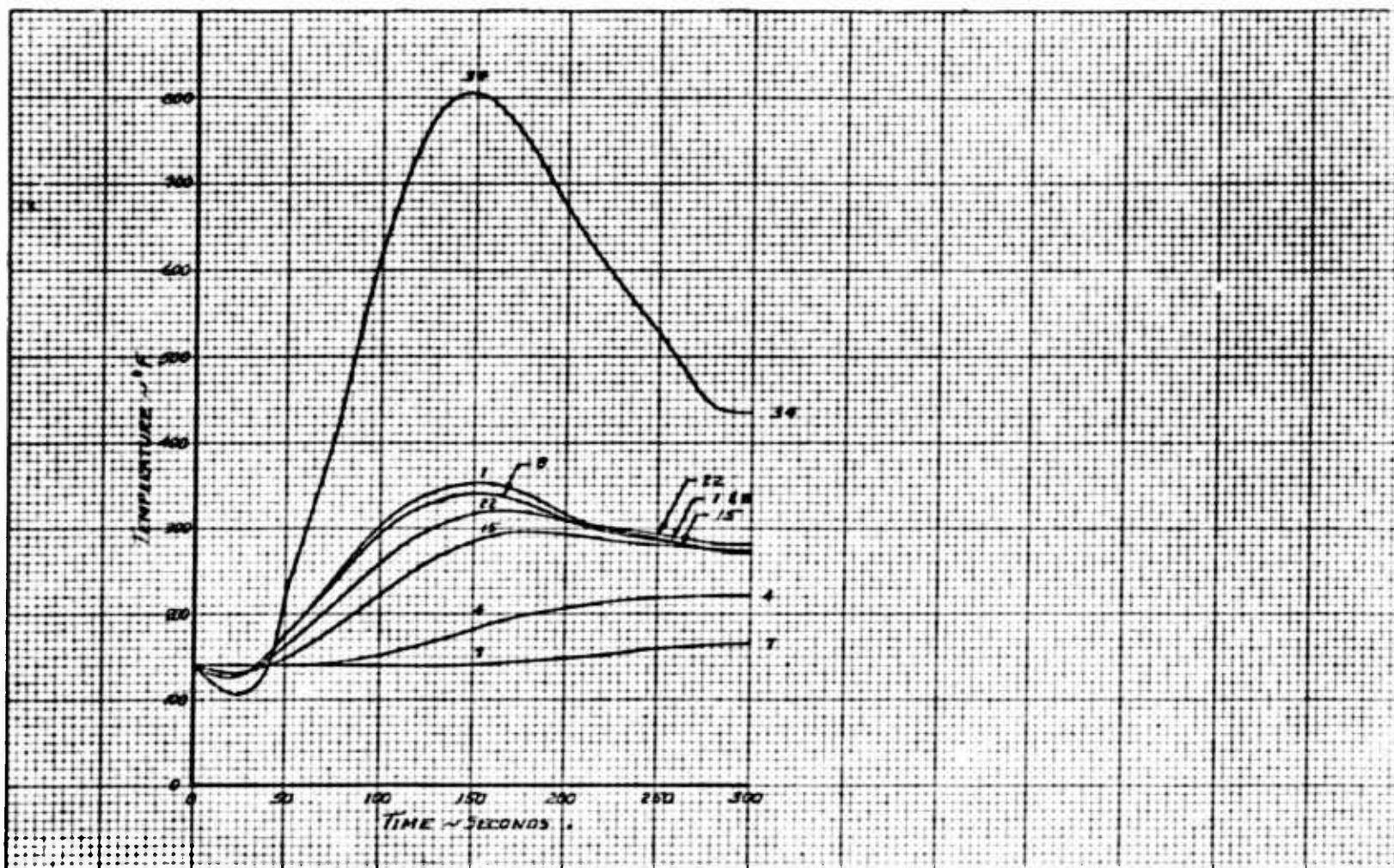
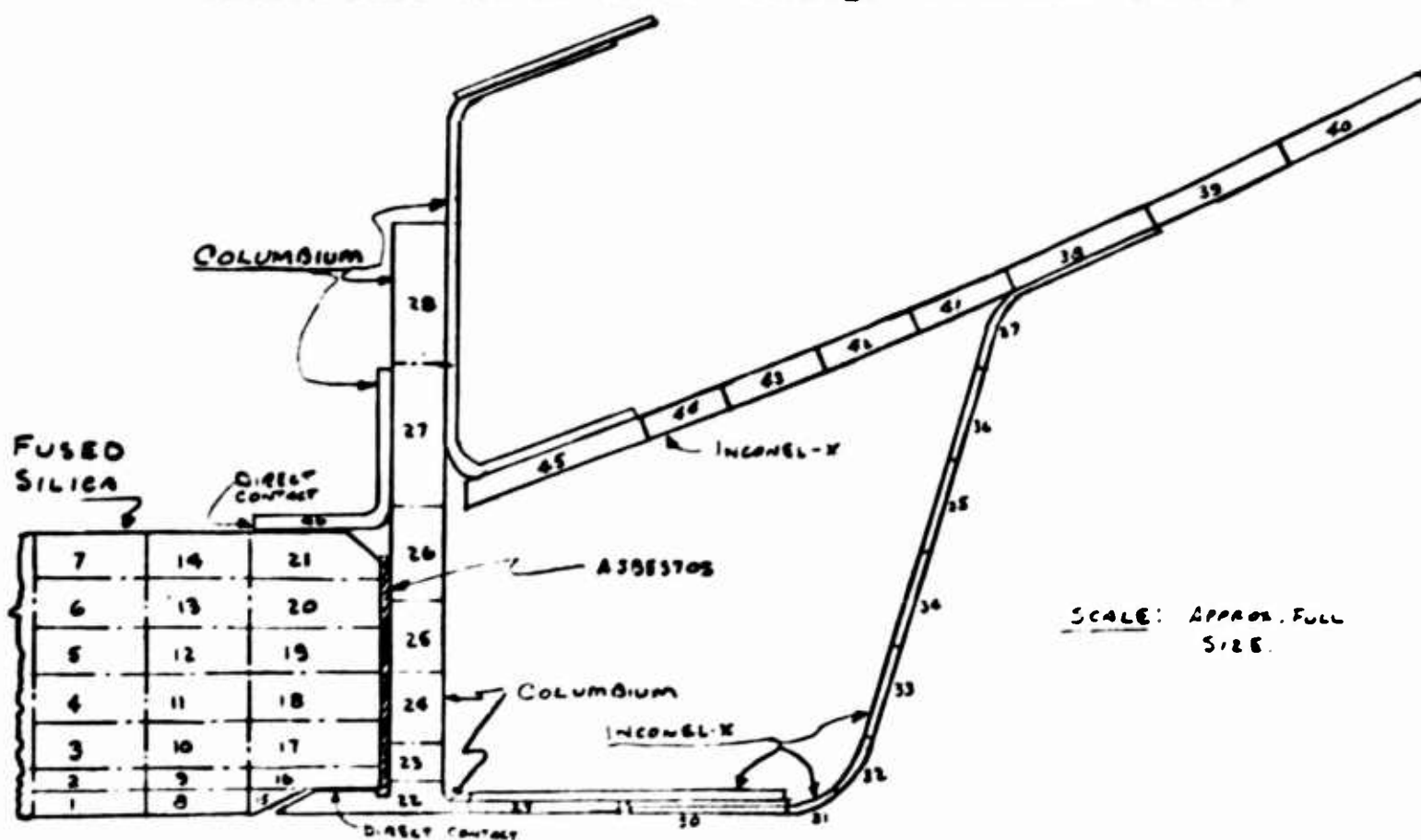


Figure 14 Trajectory 23 Temperature-Time Distribution Through an Opaque Fused Silica Window 1-1/2" Thick Mounted as Shown Located Twelve Feet Aft on Lower Fuselage Centerline (TSTP)





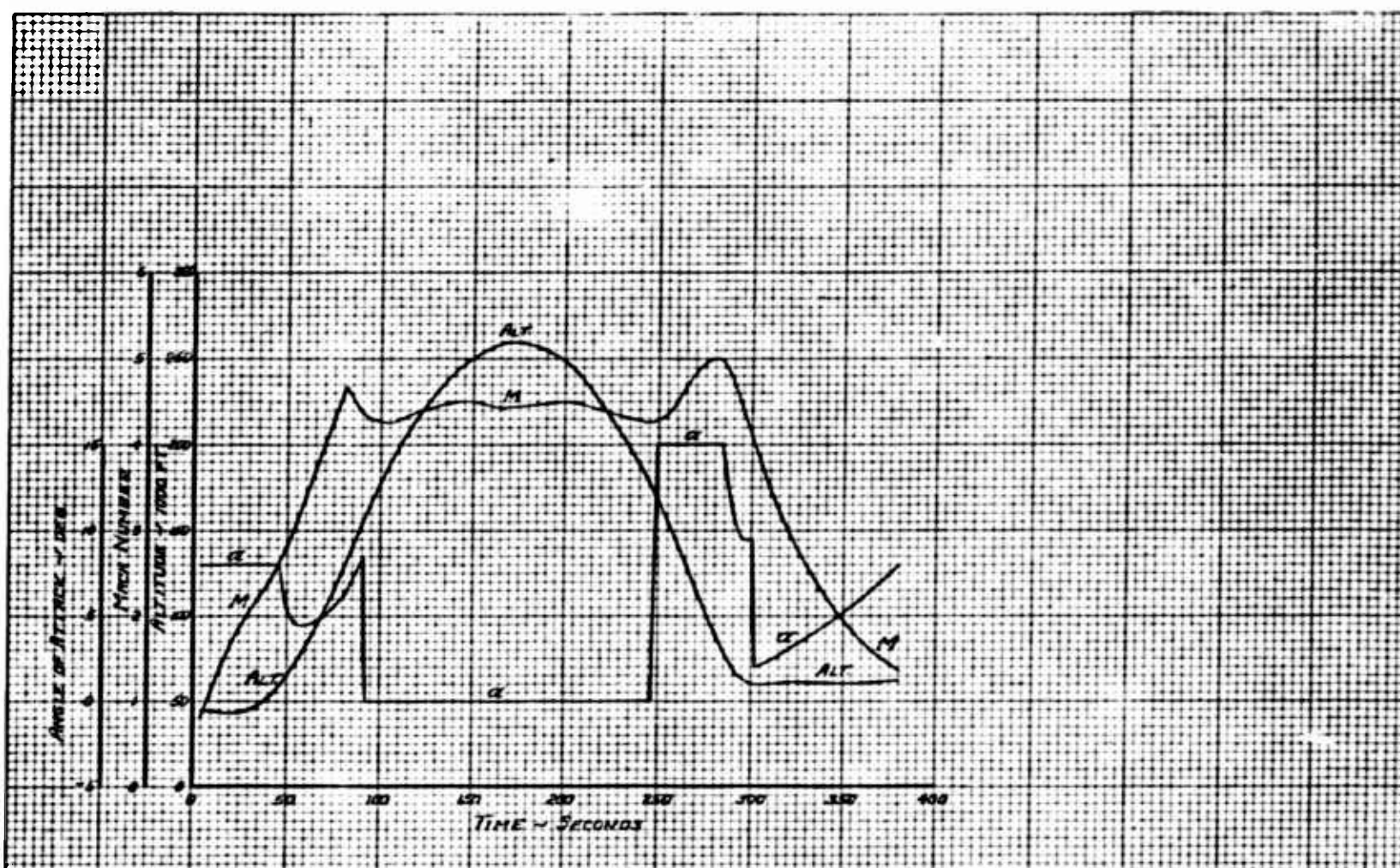
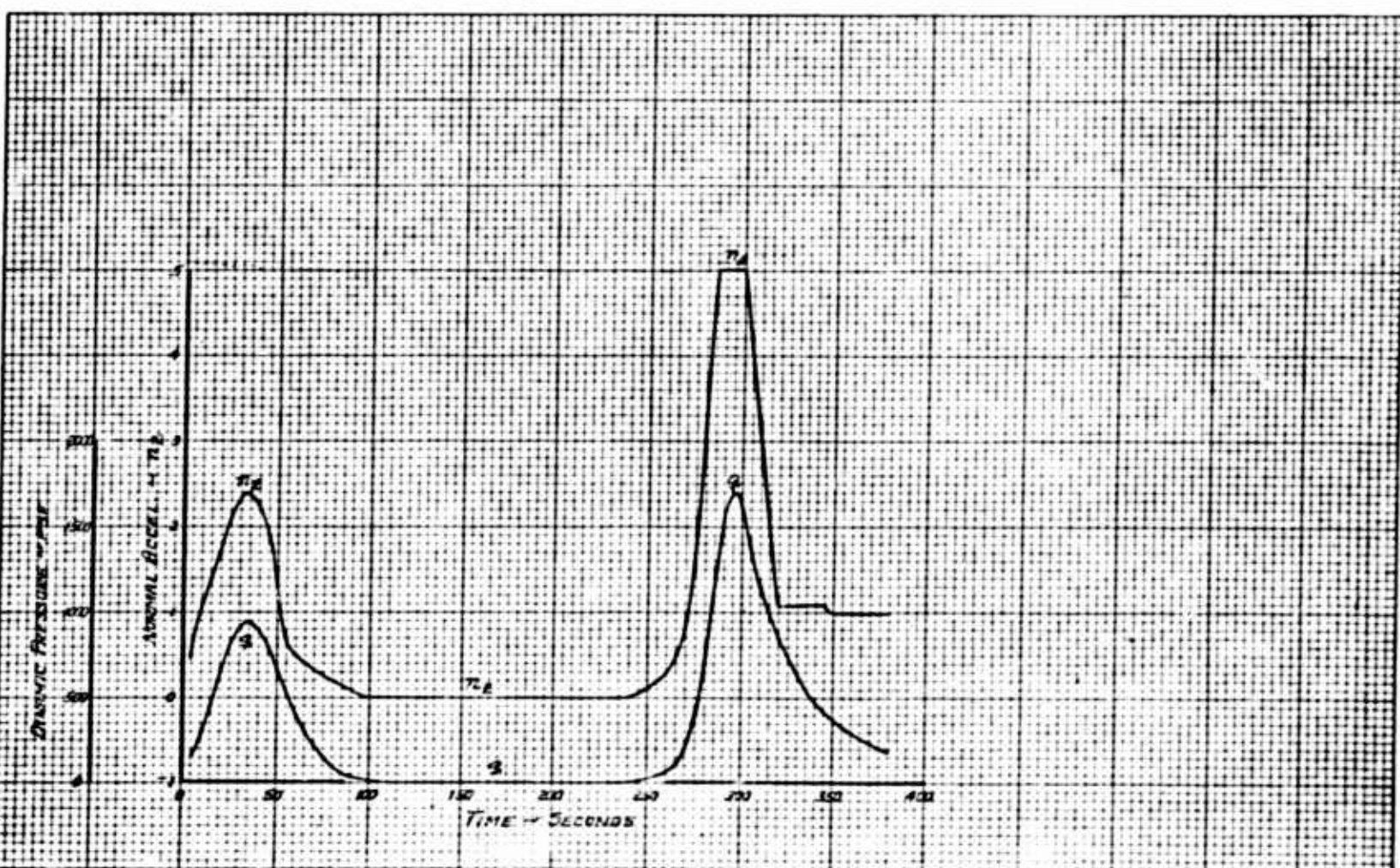


Figure 15 Trajectory 2C Flight Parameters Versus Time (High Altitude Flight)



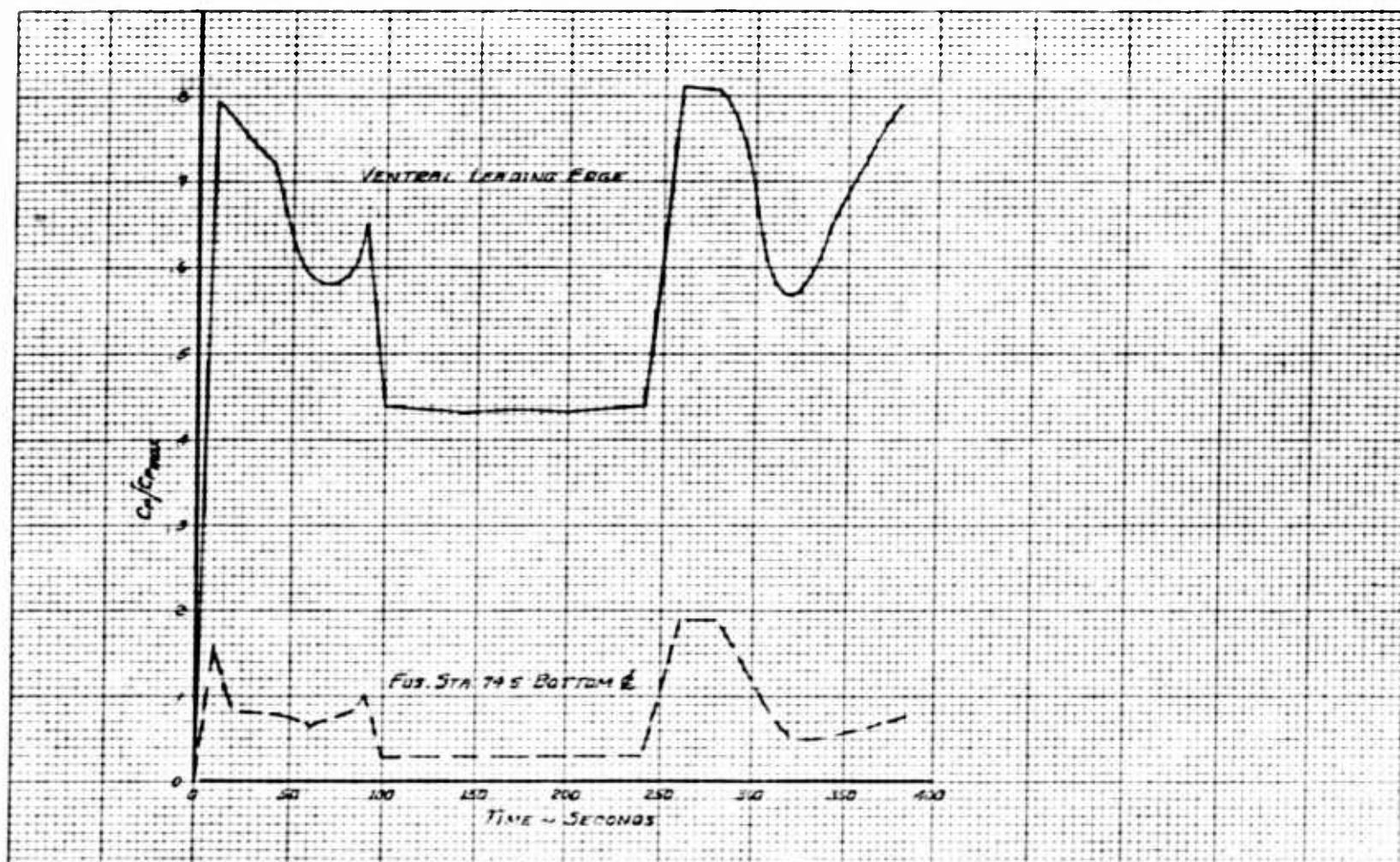
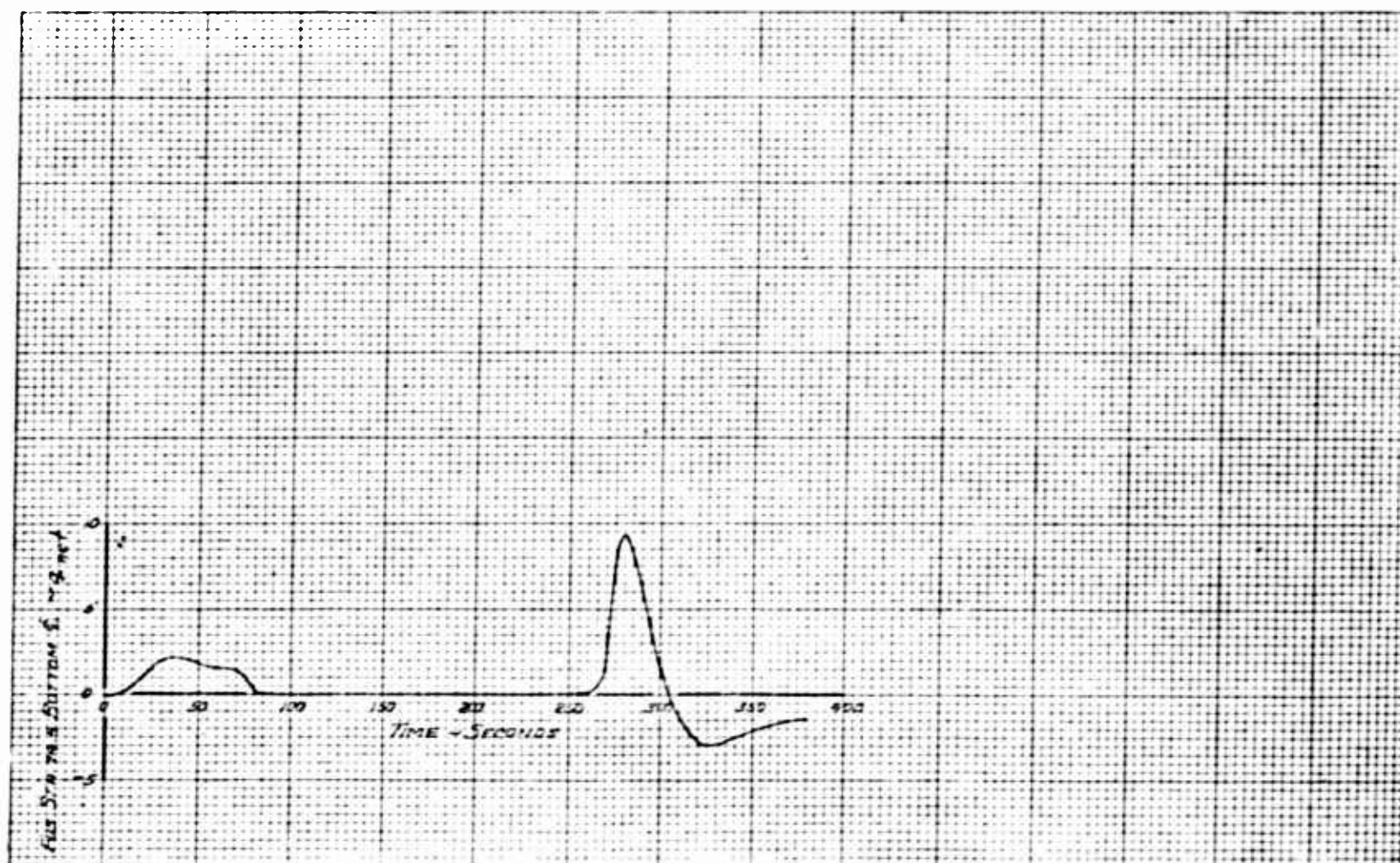


Figure 16 Trajectory 2C Local Pressure Coefficient Versus Time (High Altitude Flight)





Figure 17 Trajectory 2C Fuselage Thin Skin Net Heating Rate Versus Time (High Altitude Flight) (TSTP)





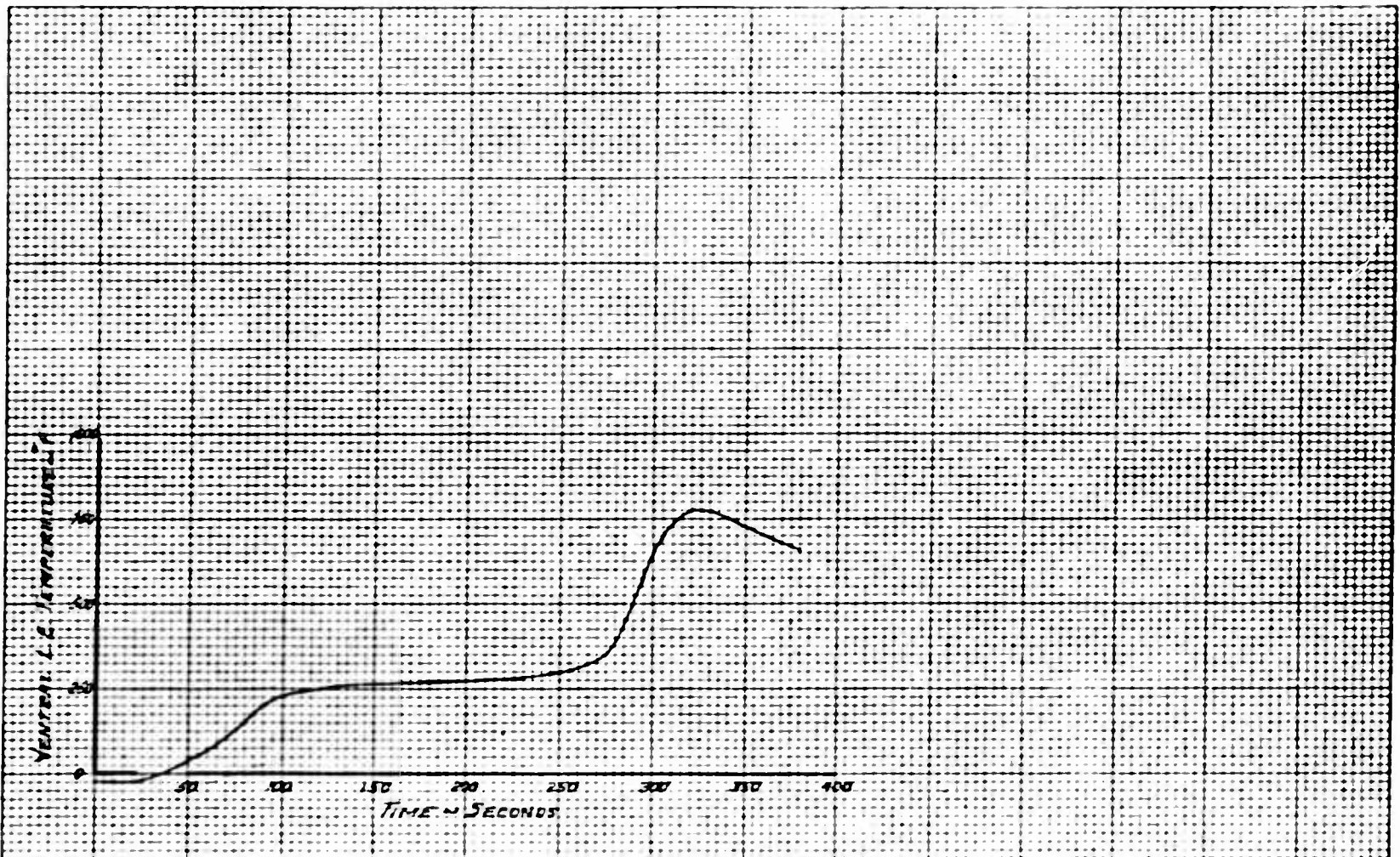
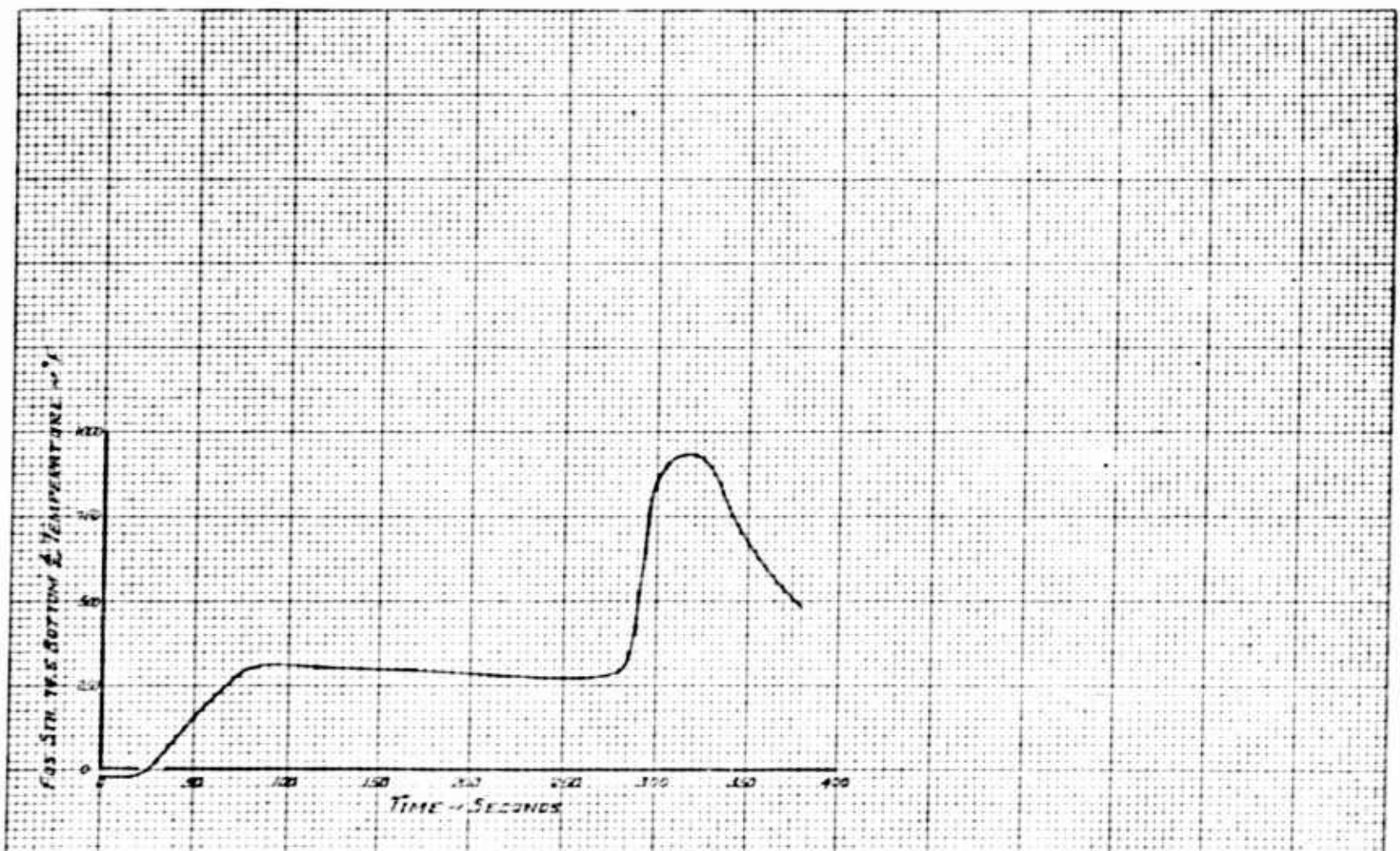


Figure 18 Trajectory 2C Fuselage Thin Skin Temperature Versus Time (High Altitude Flight) (TSTP)





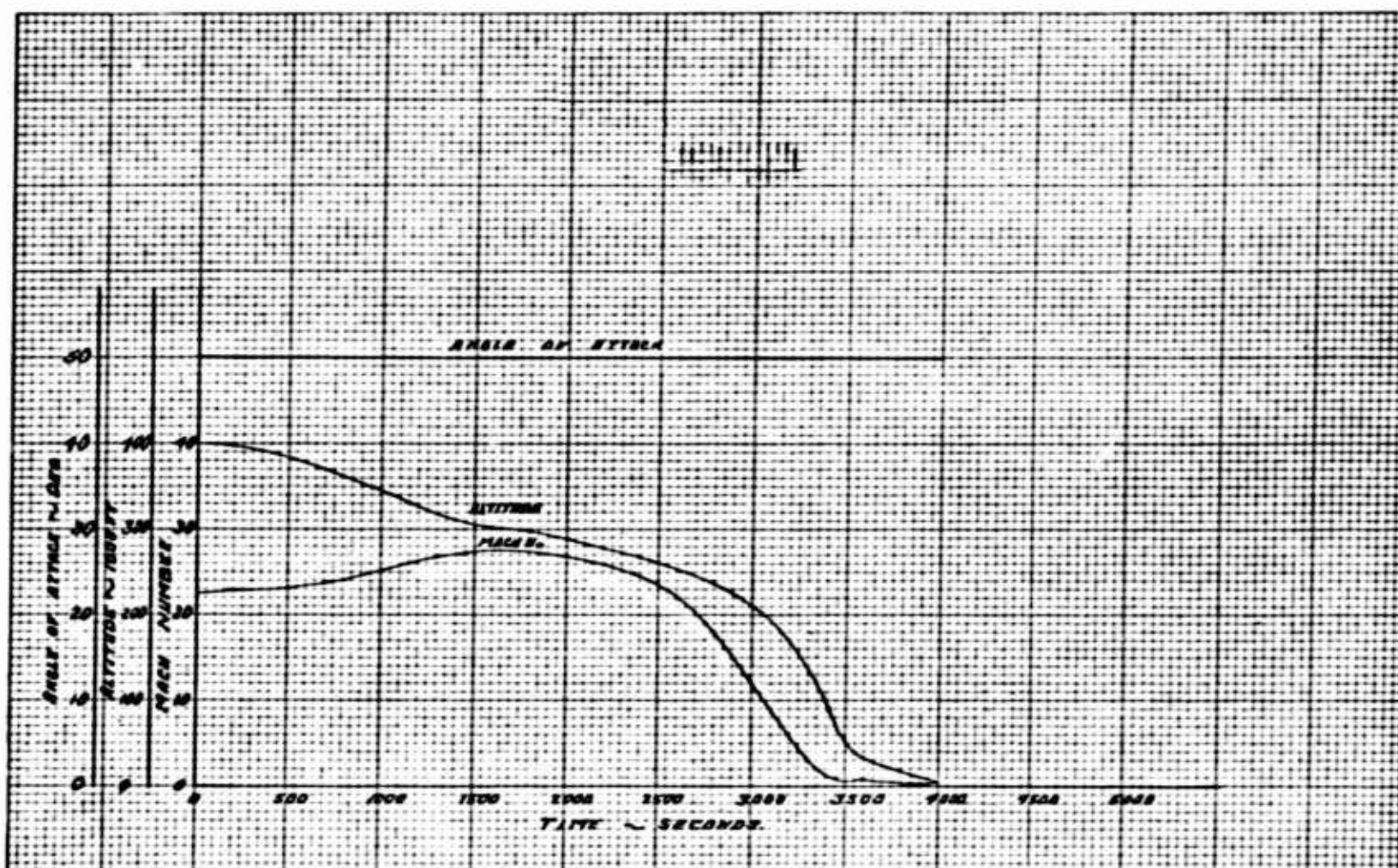
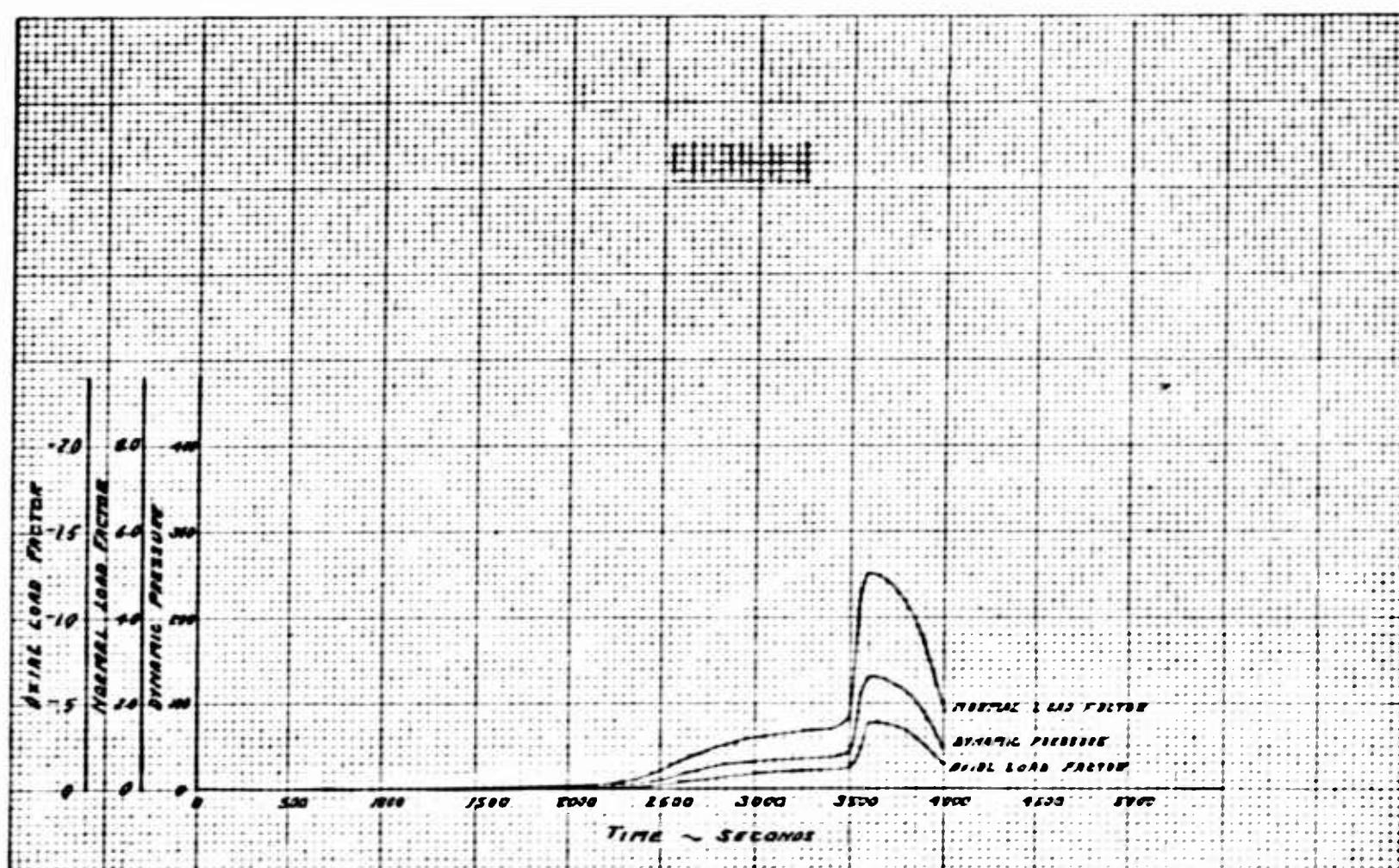


Figure 19 Trajectory 3A Flight Parameters Versus Time (Angle of Attack = 50°)





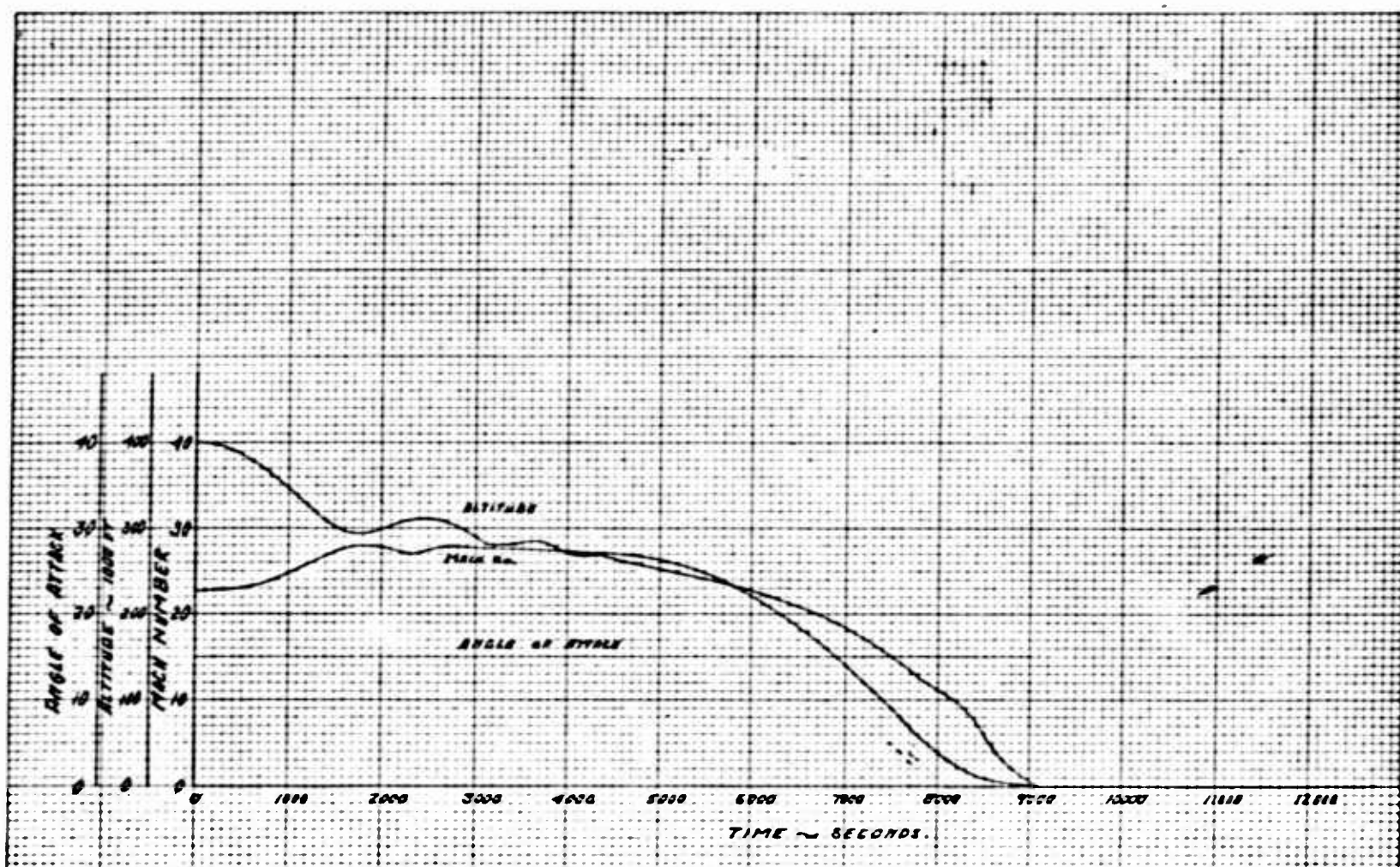
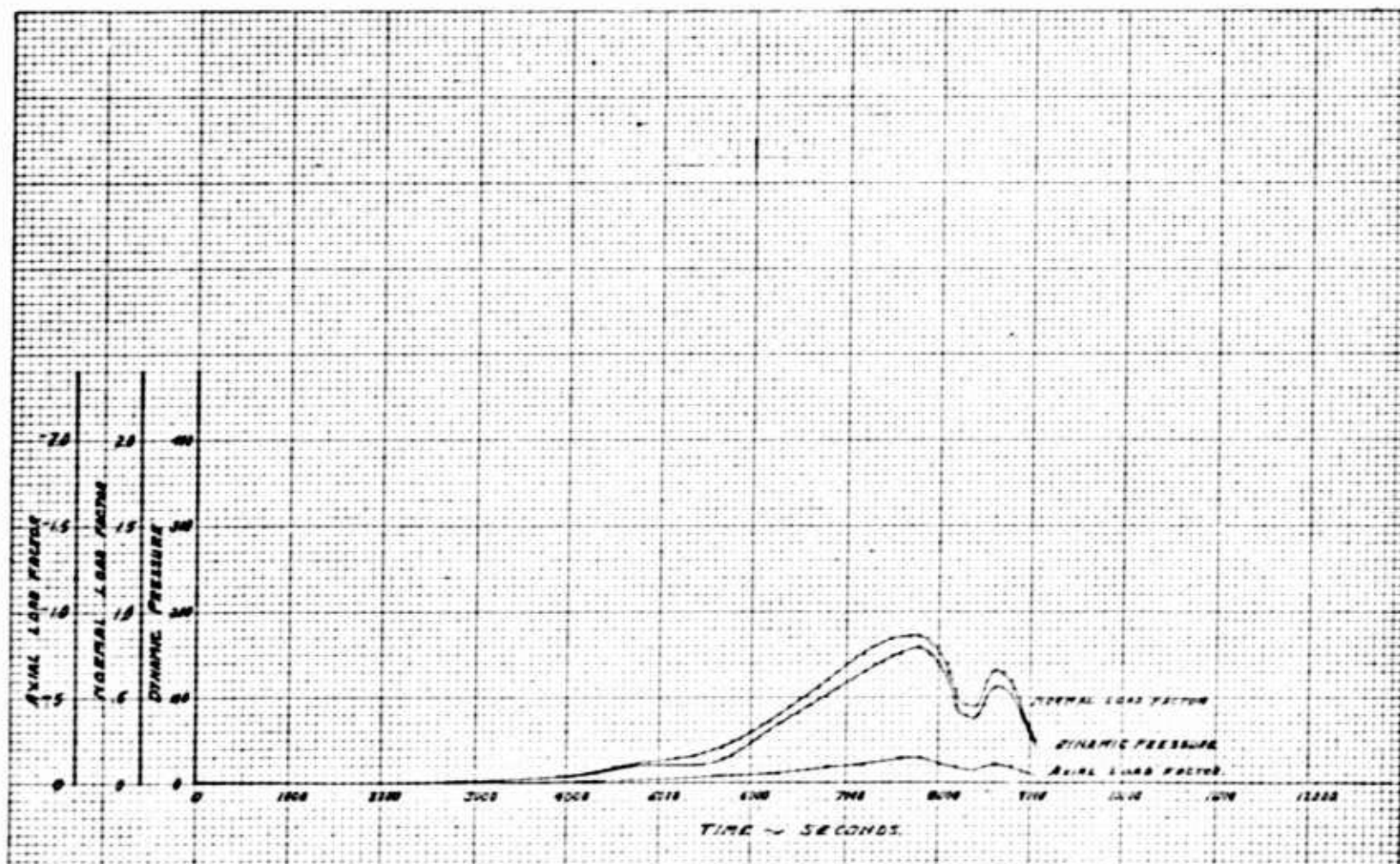


Figure 20 Trajectory 3B Flight Parameters Versus Time (Angle of Attack =  $15^\circ$ )



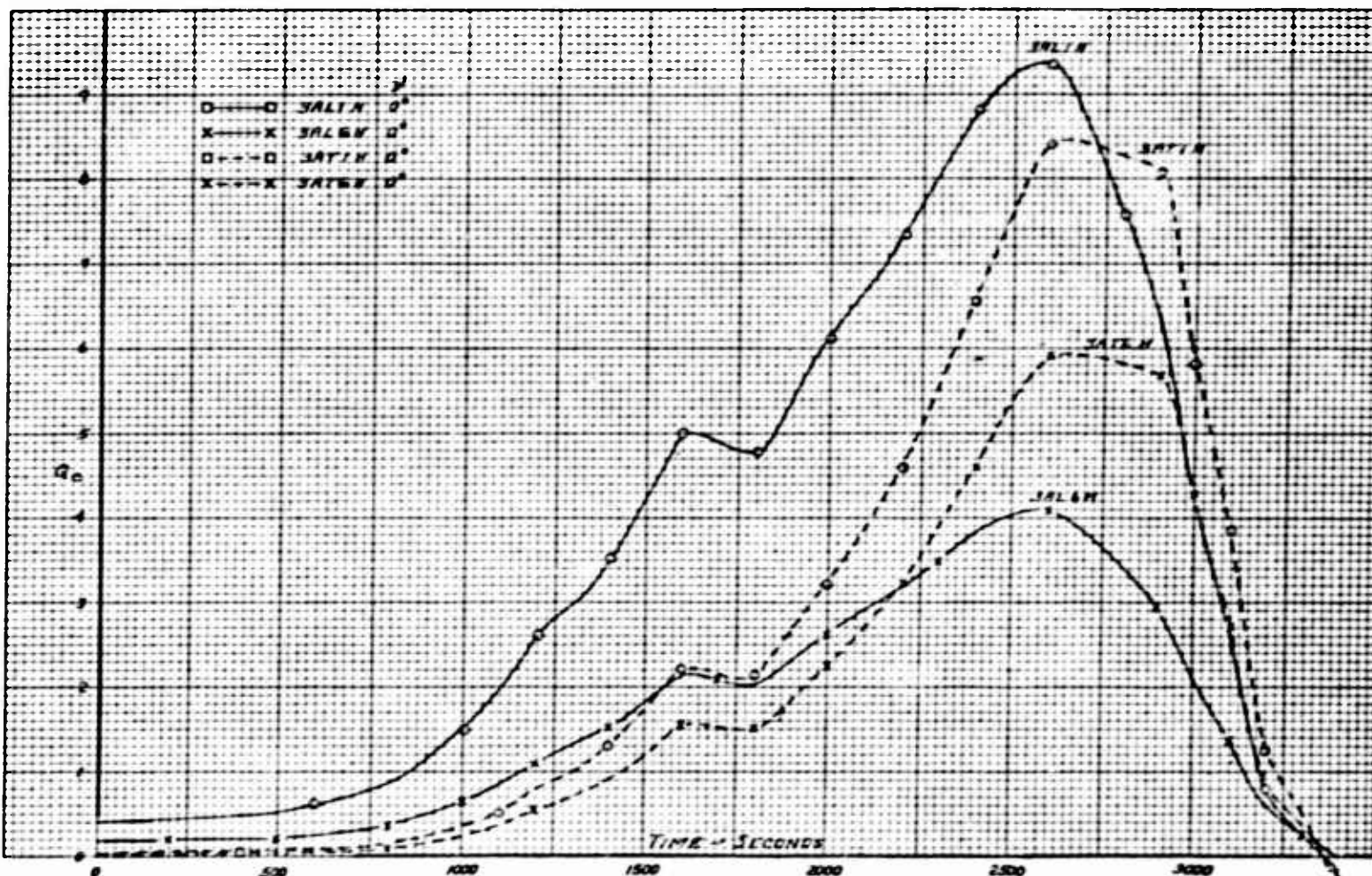
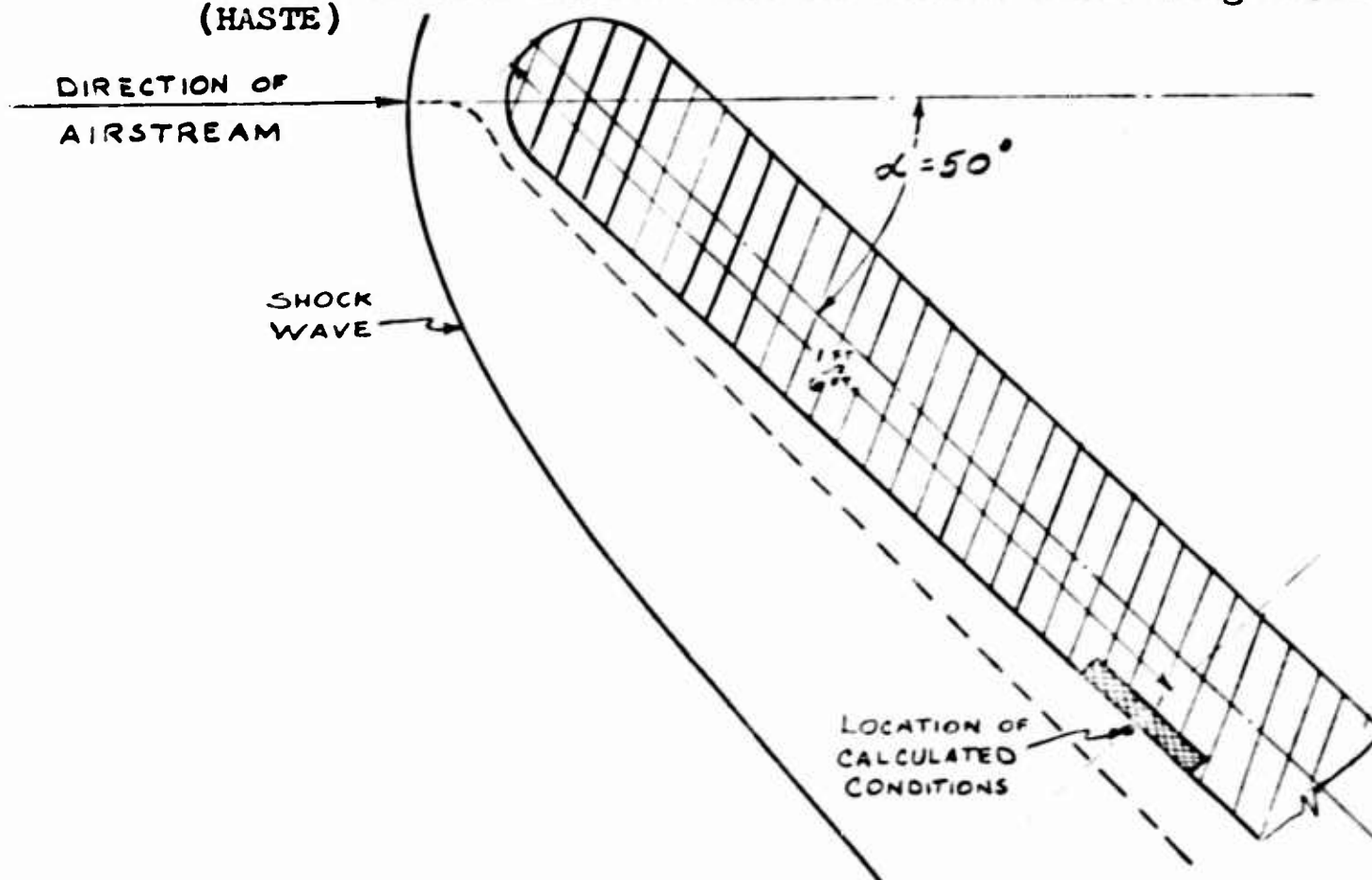


Figure 21 Summary of Trajectory 3A Convective Heating Rates Versus Time, Laminar and Turbulent Flow, Compared at Locations of One-Foot and Six-Foot Aft on Vehicle Lower Wing Surface (HASTE)





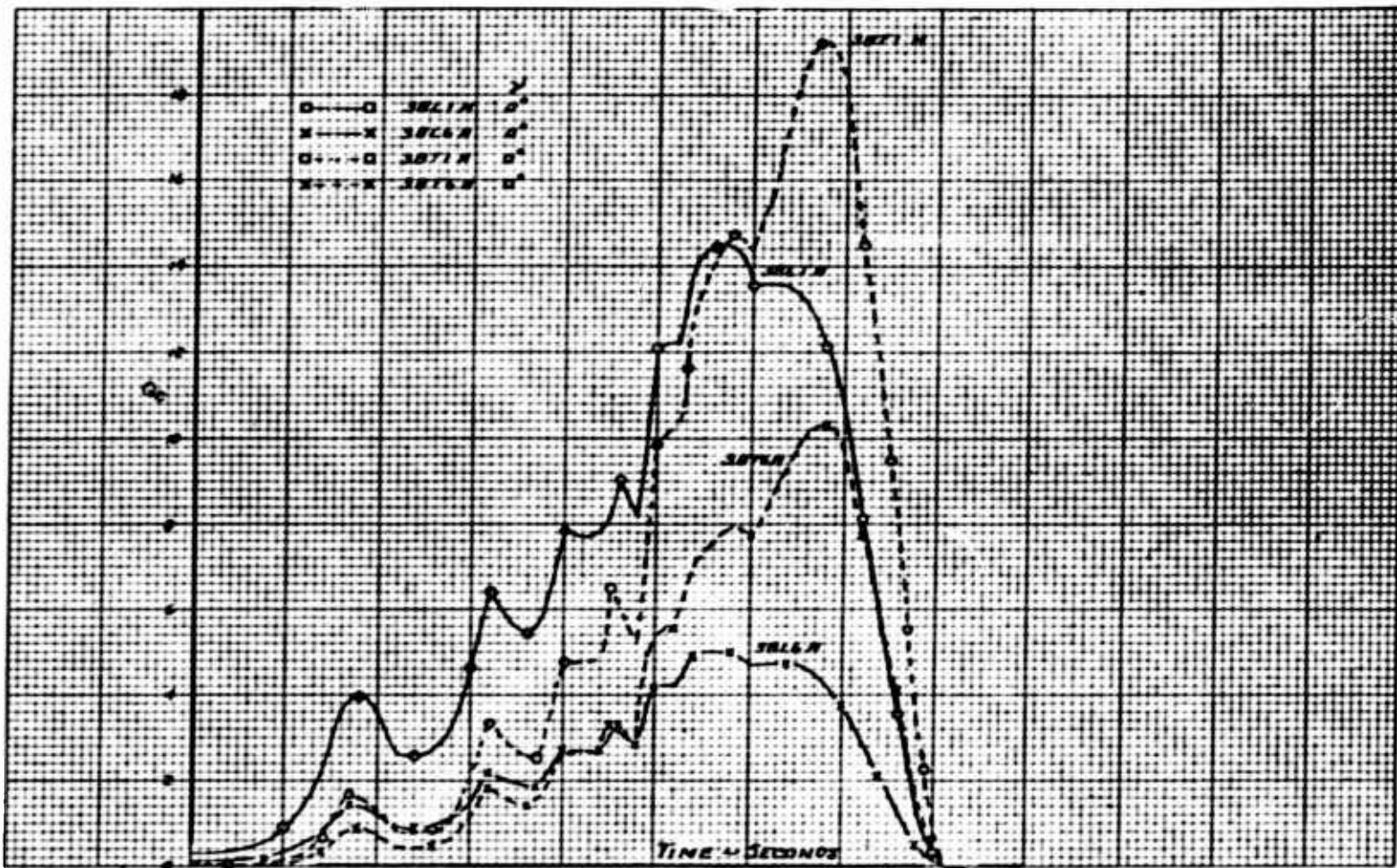
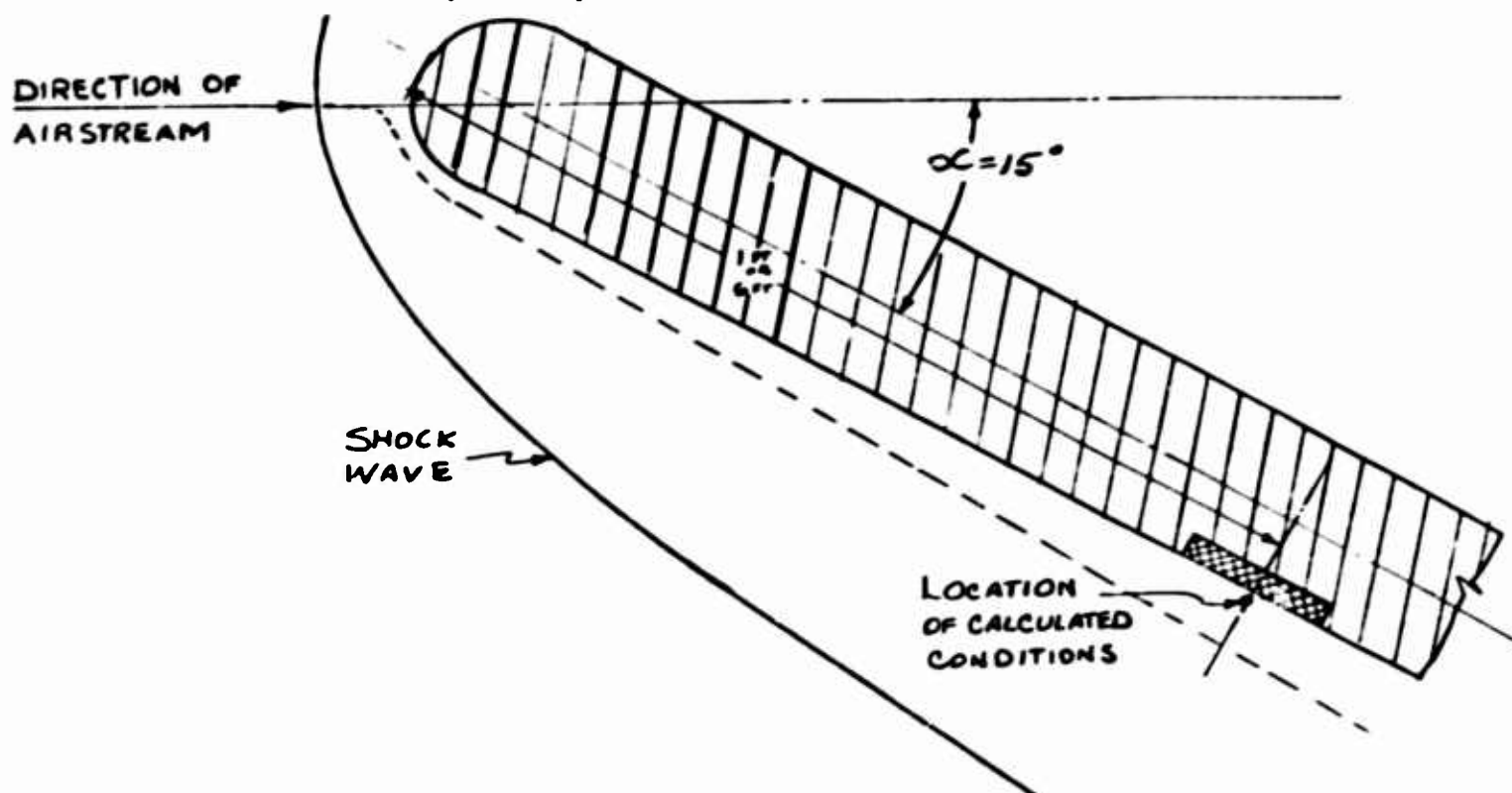


Figure 22 Summary of Trajectory 3B Convective Heating Rates Versus Time, Laminar and Turbulent Flow, Compared at Locations of One-Foot and Six-Foot Aft on Vehicle Lower Wing Surface (HASTE)



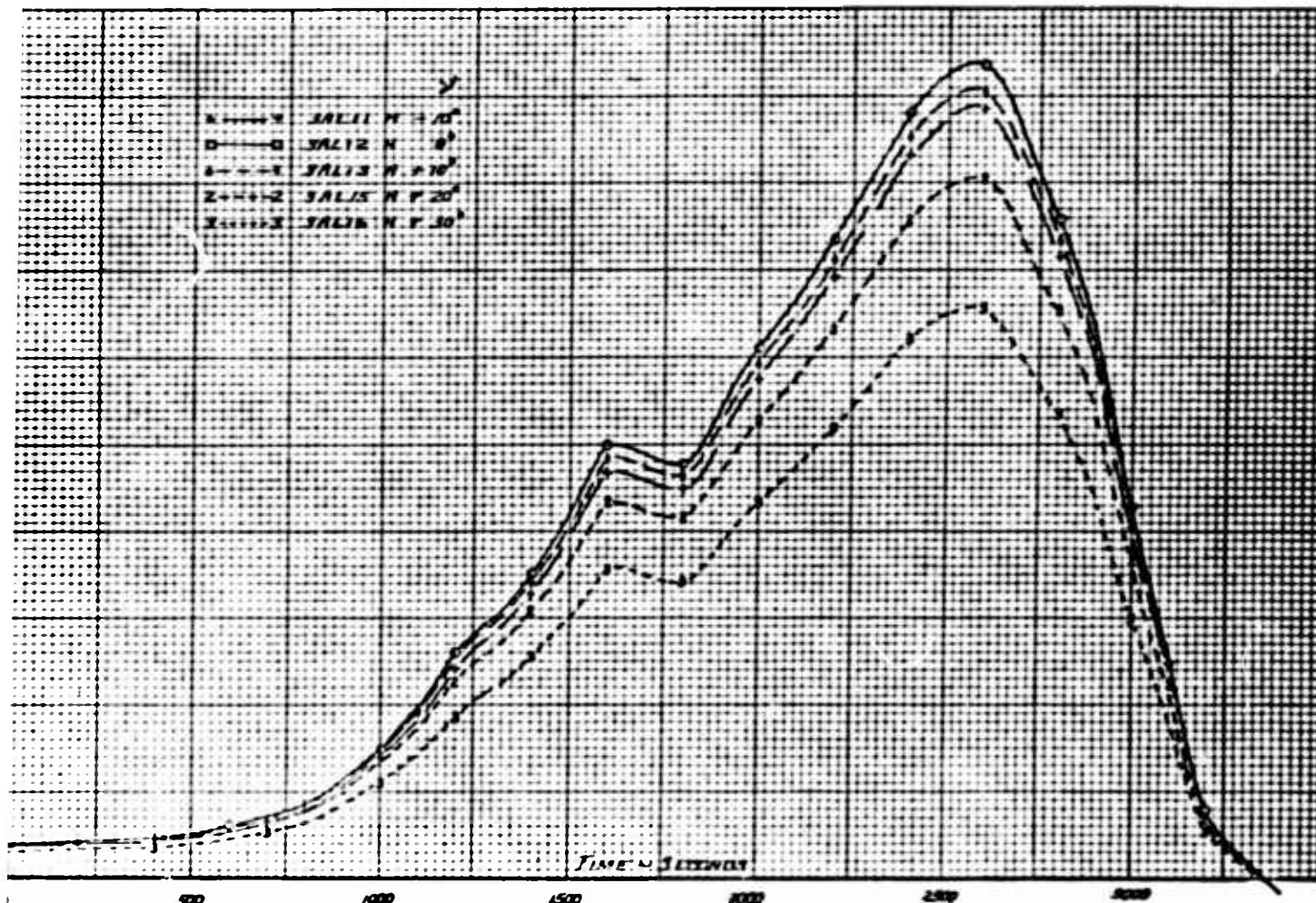
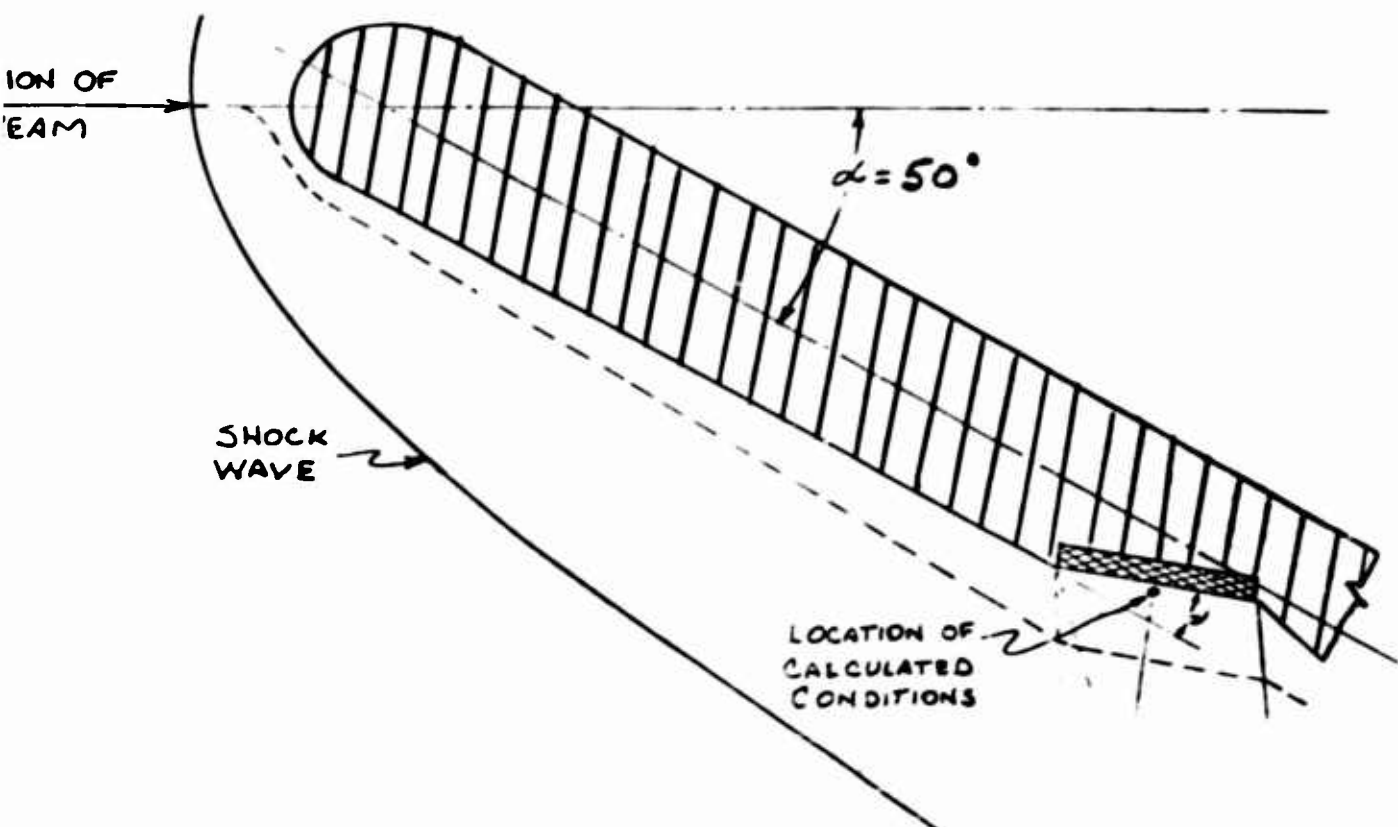


Figure 23 Trajectory 3All Convective Heating Rates Versus Time, Laminar Flow, One-Foot Aft, on Wing Surfaces at Various Local Expansion Angles (HASTE)



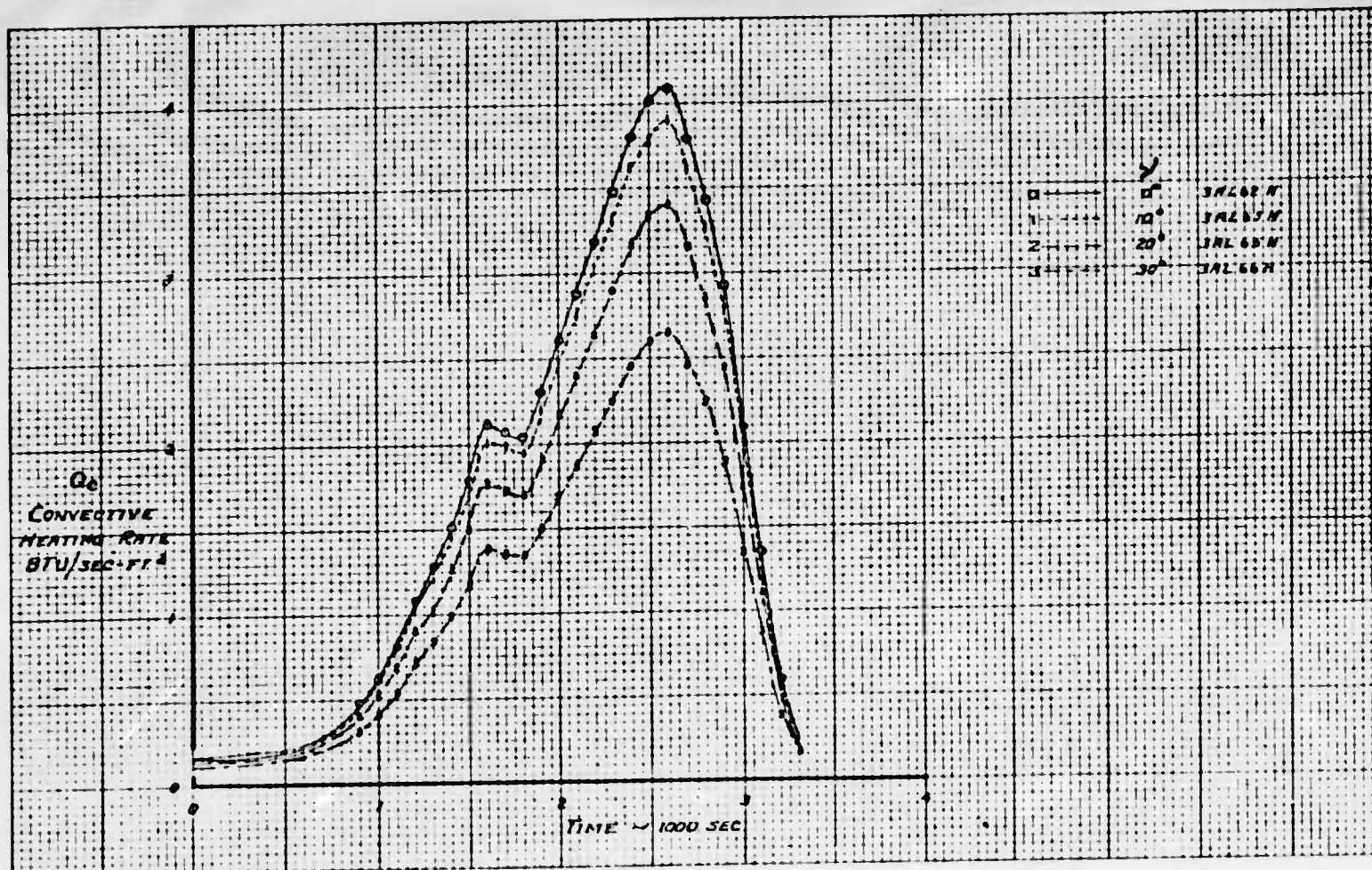
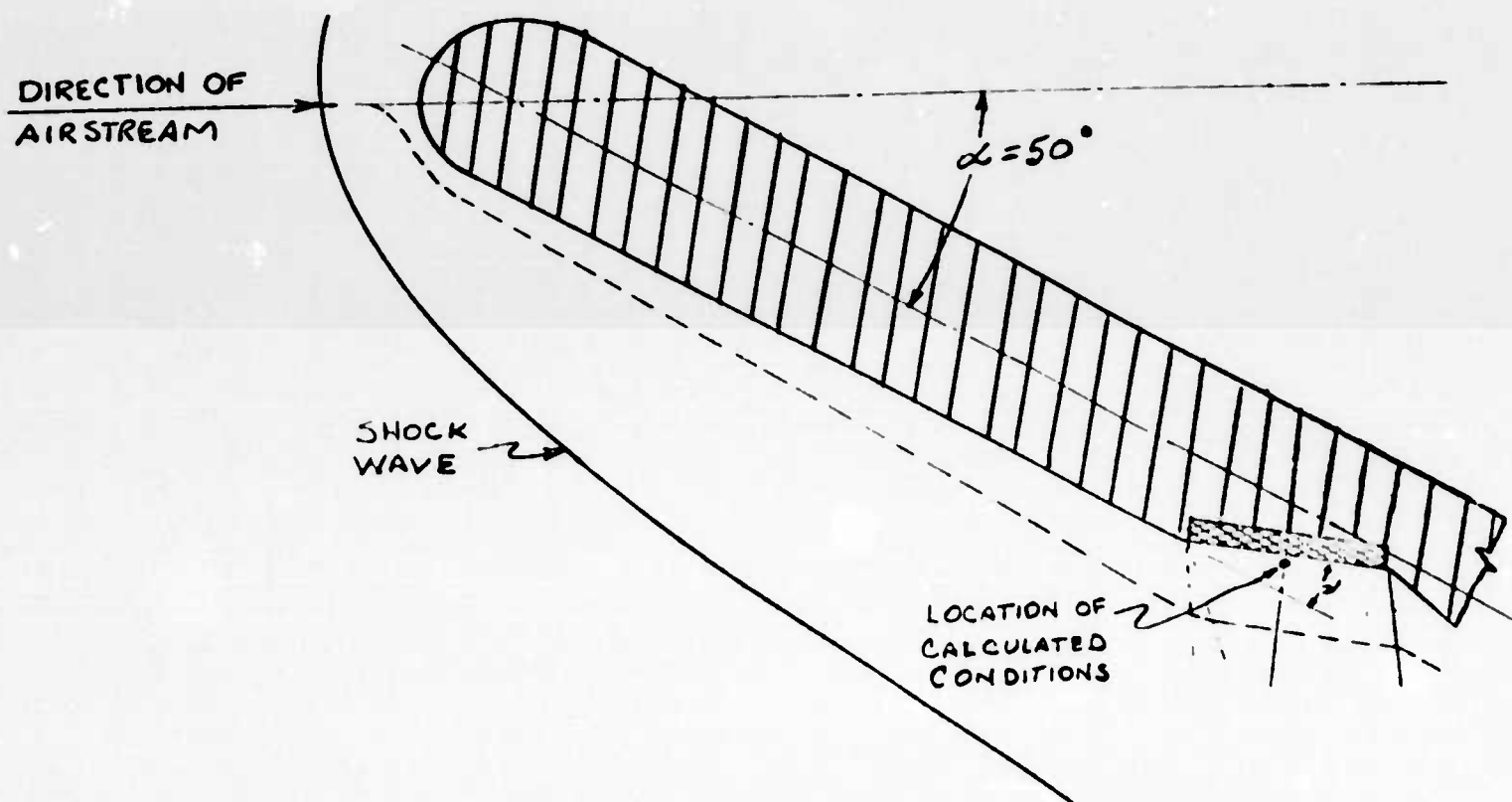


Figure 24 Trajectory 3AL6 Convective Heating Rates Versus Time, Laminar Flow, Six-Foot Aft, on Wing Surfaces at Various Local Expansion Angles (HASTE)





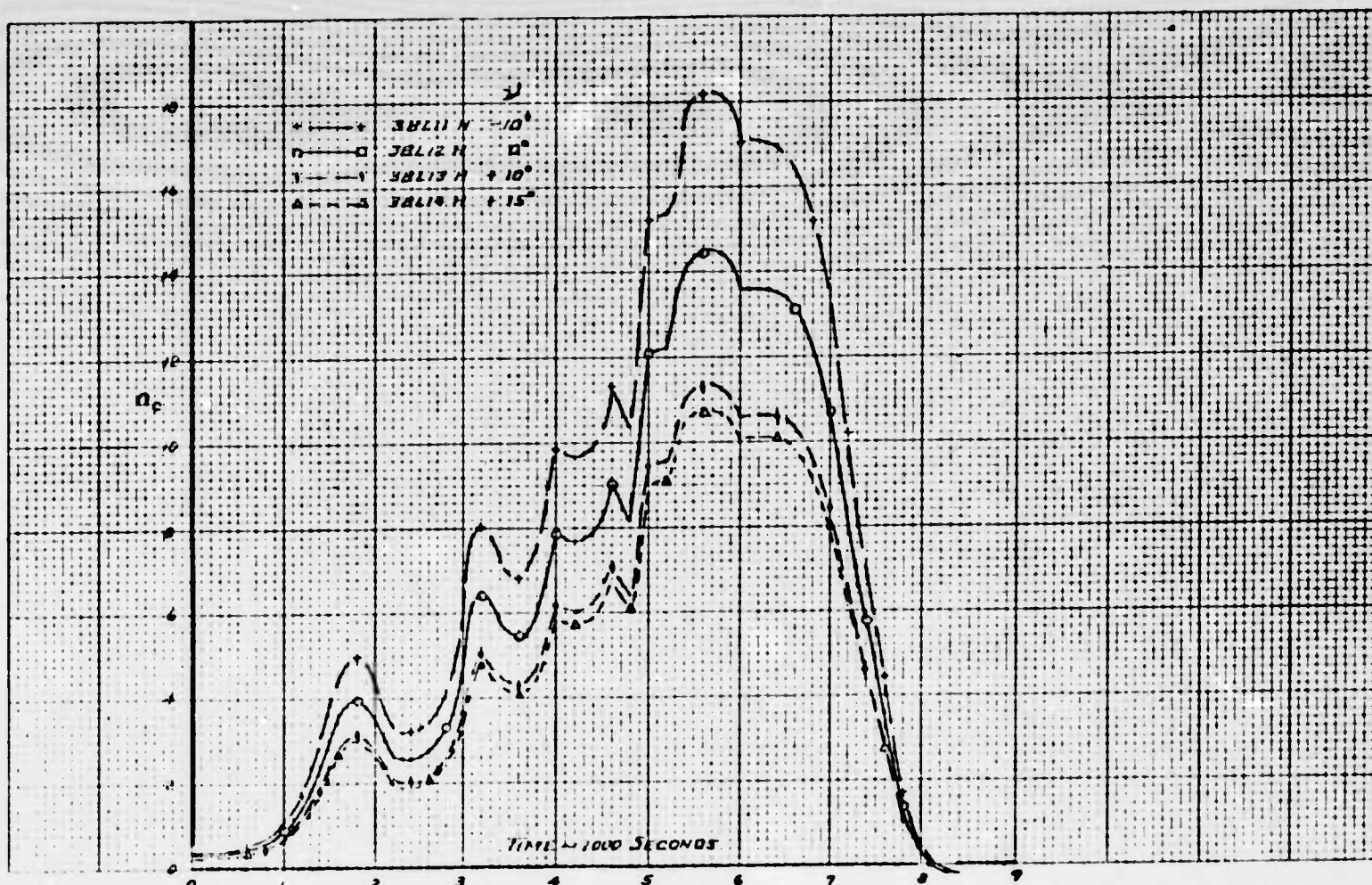


Figure 25 Trajectory 3BL1 Convective Heating Rate Versus Time, Laminar Flow, One-Foot Aft, on Wing Surfaces at Various Local Expansion Angles (HASTE)

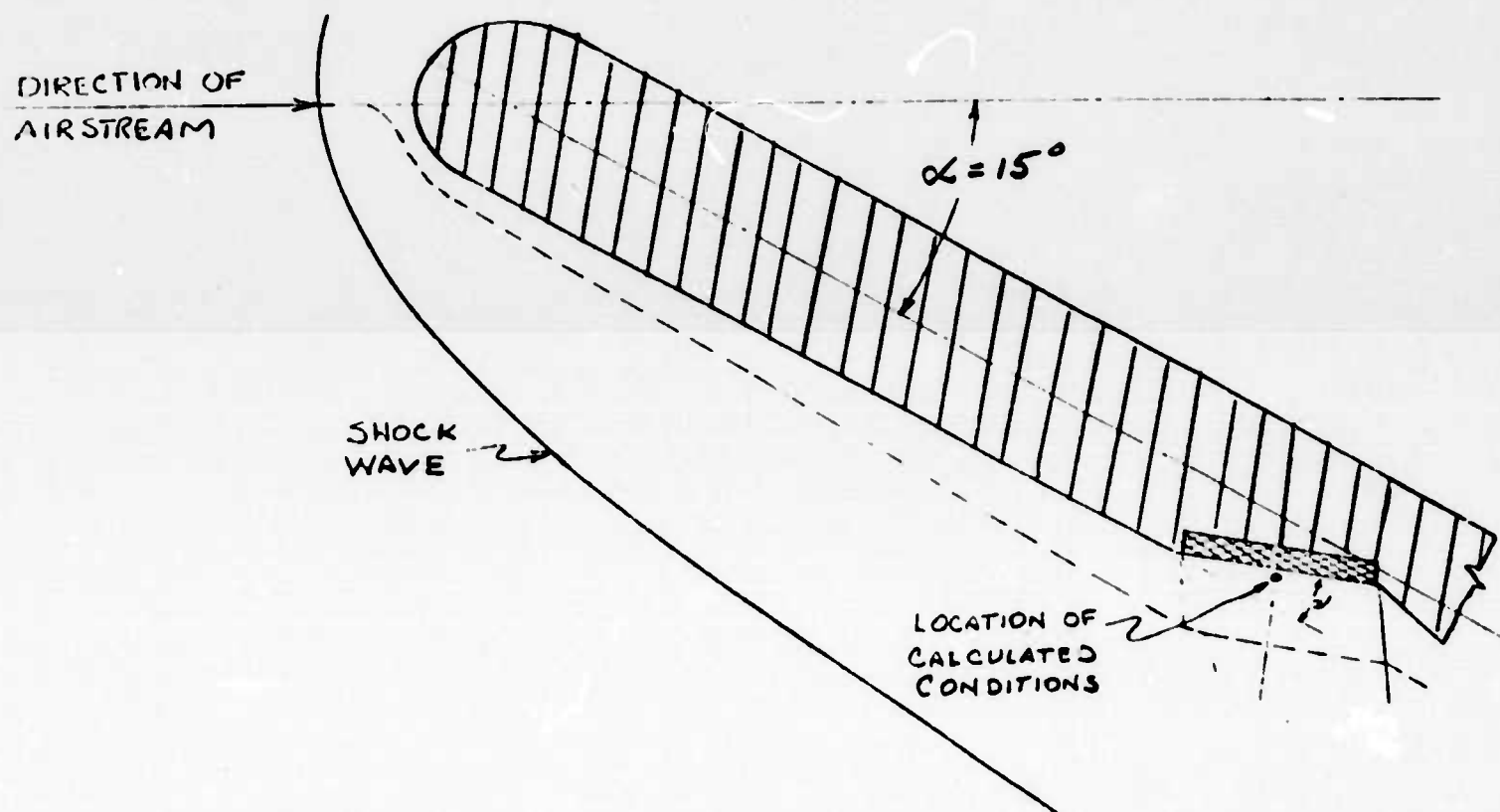
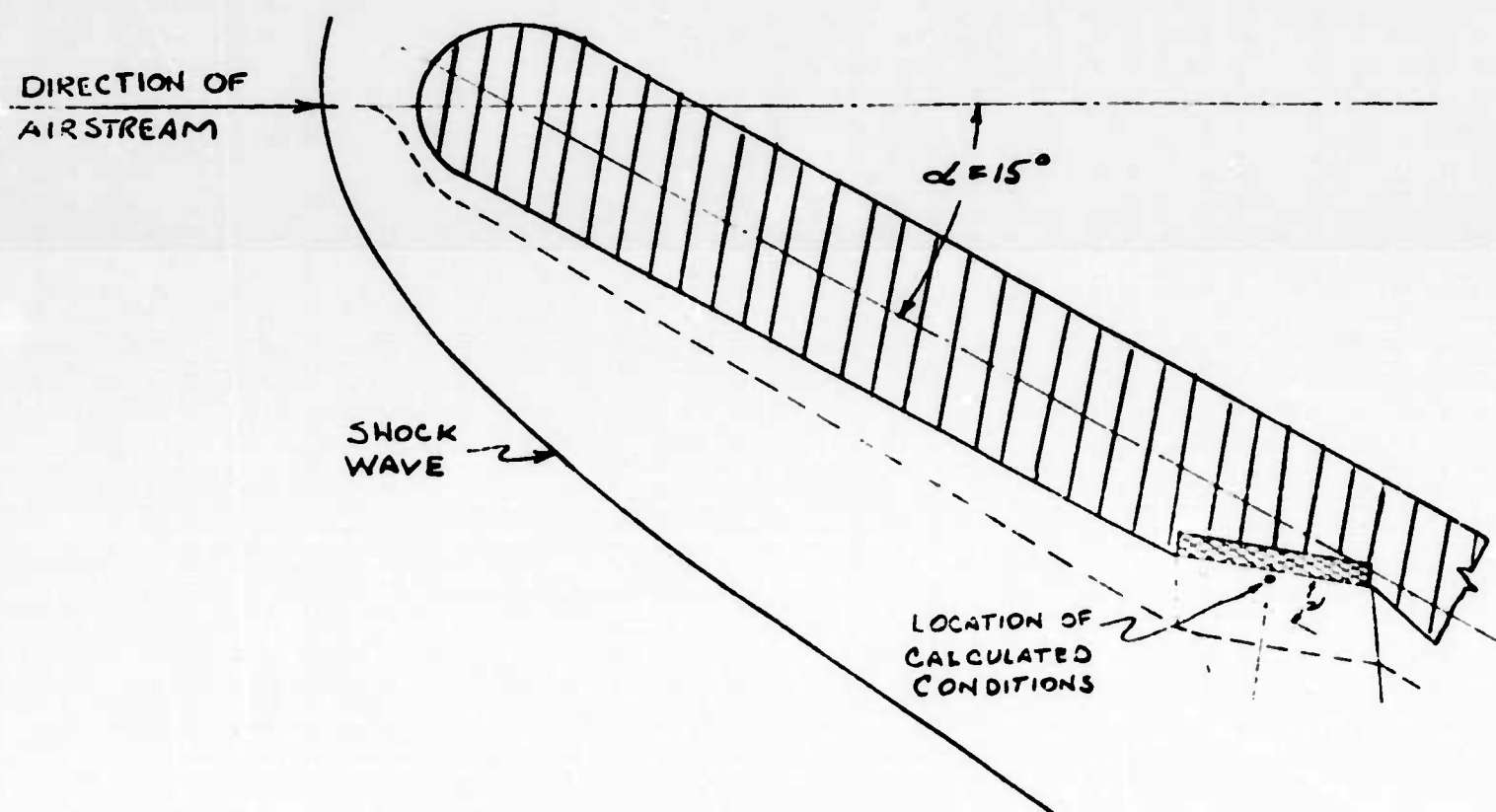




Figure 26 Trajectory 3BL6 Convective Heating Rates Versus Time, Laminar Flow, Six-Foot Aft, on Wing Surfaces at Various Local Expansion Angles (HASTE)





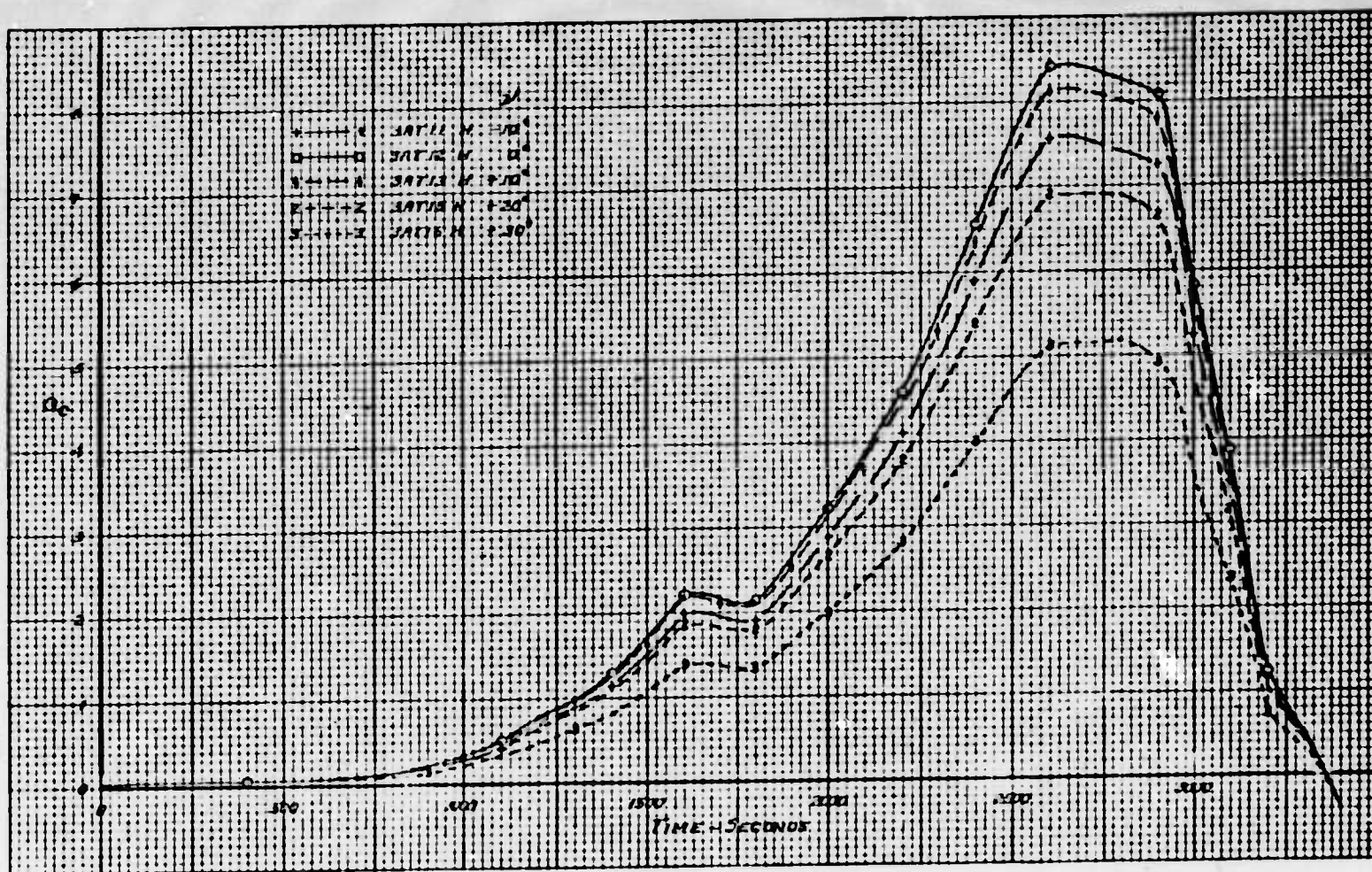
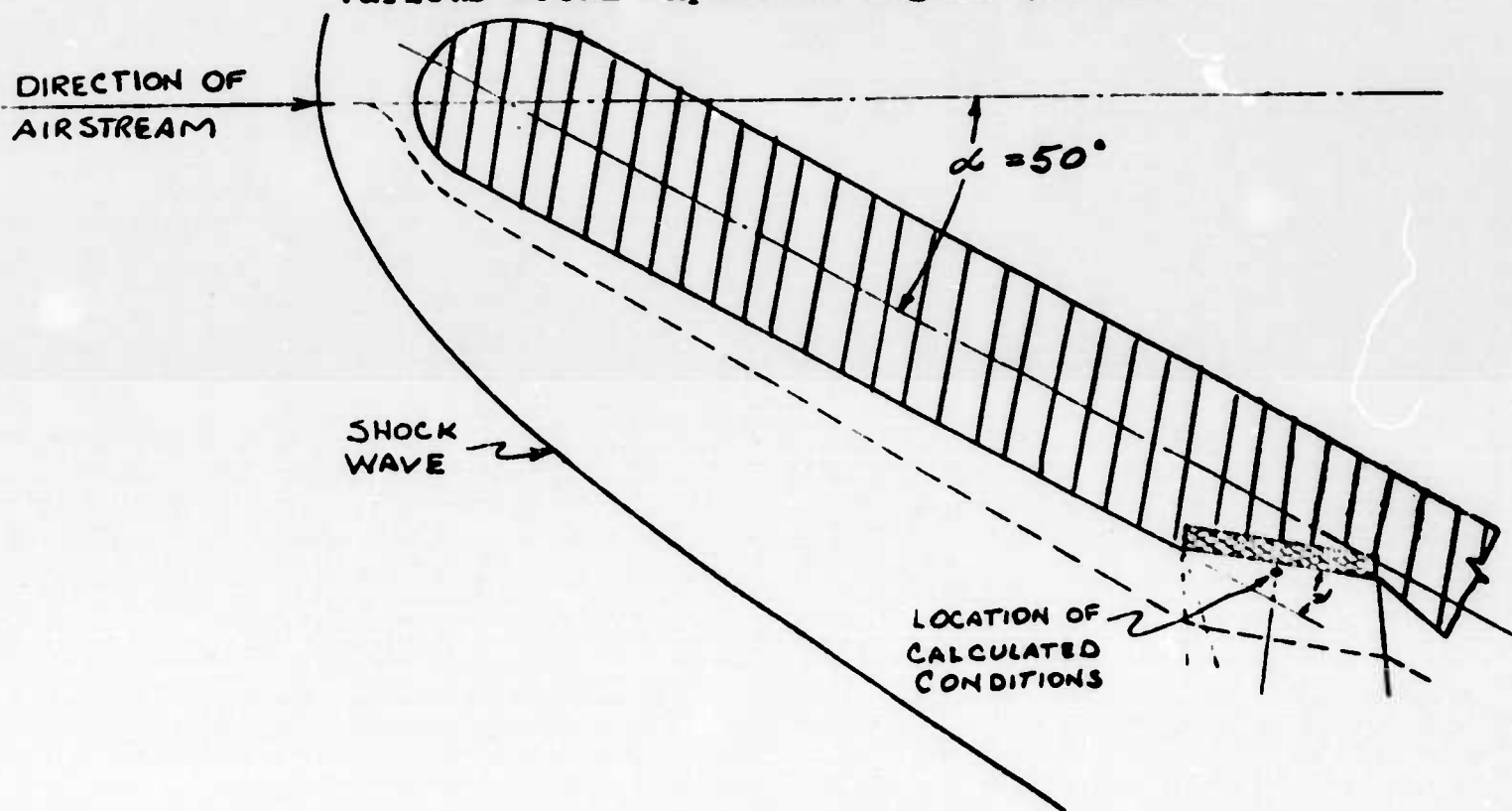


Figure 27 Trajectory 3AT1 Convective Heating Rate Versus Time, Turbulent Flow, One-Foot Aft, on Wing Surfaces at Various Local Expansion Angles (HASTE)



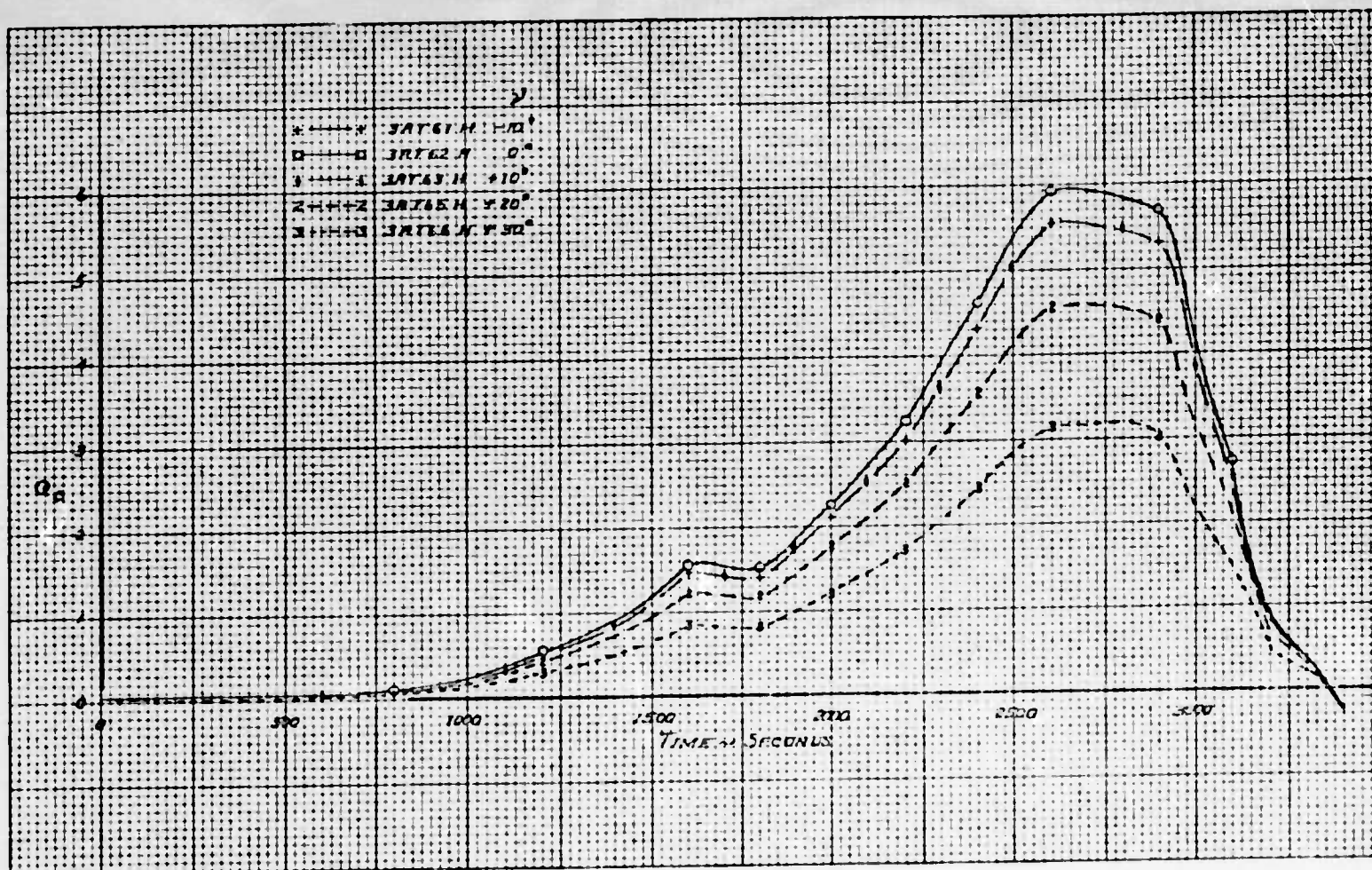
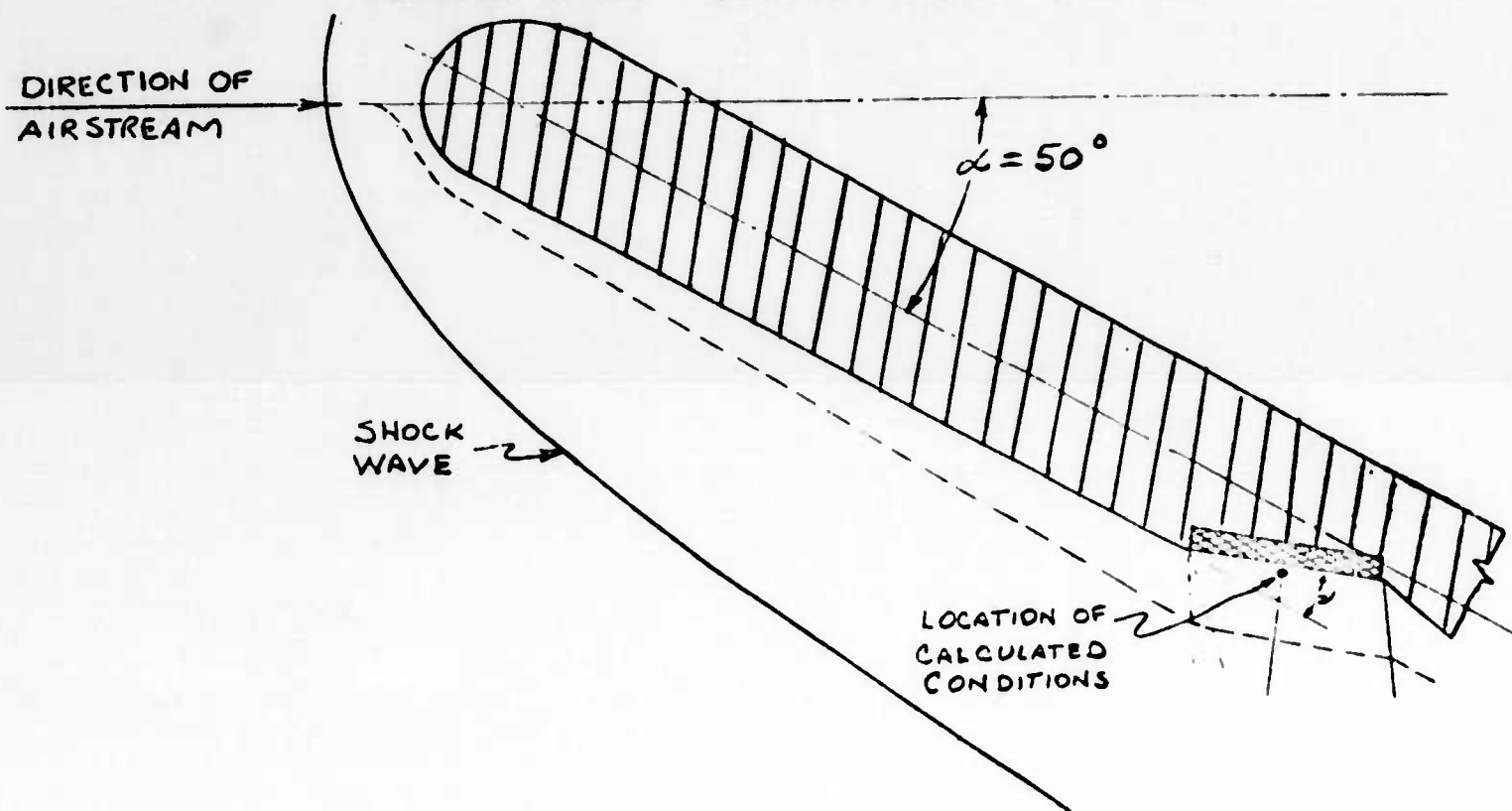


Figure 28 Trajectory 3AT6 Convective Heating Rate Versus Time, Turbulent Flow, Six-Foot Aft, on Wing Surfaces at Various Local Expansion Angles (HASTE)





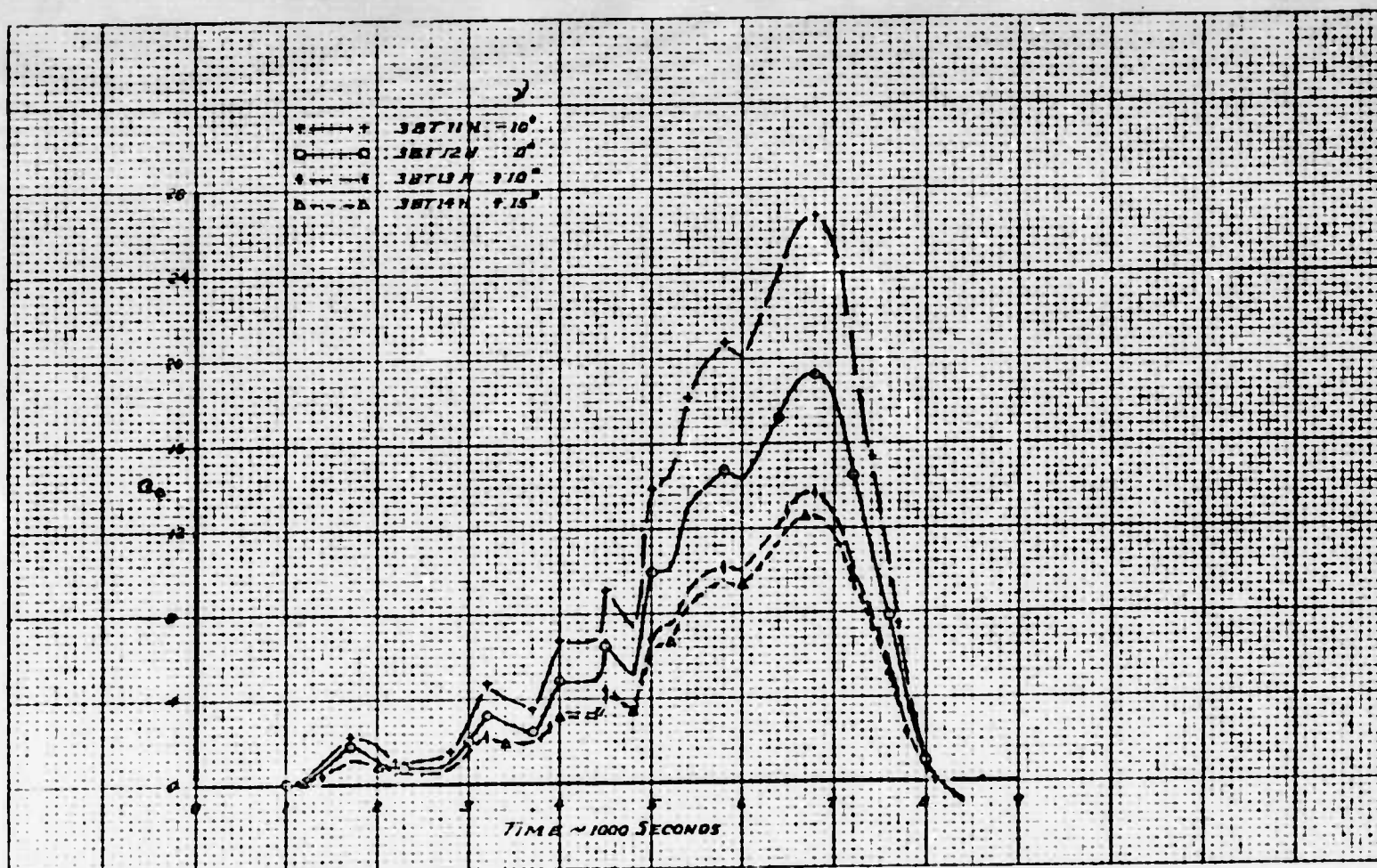
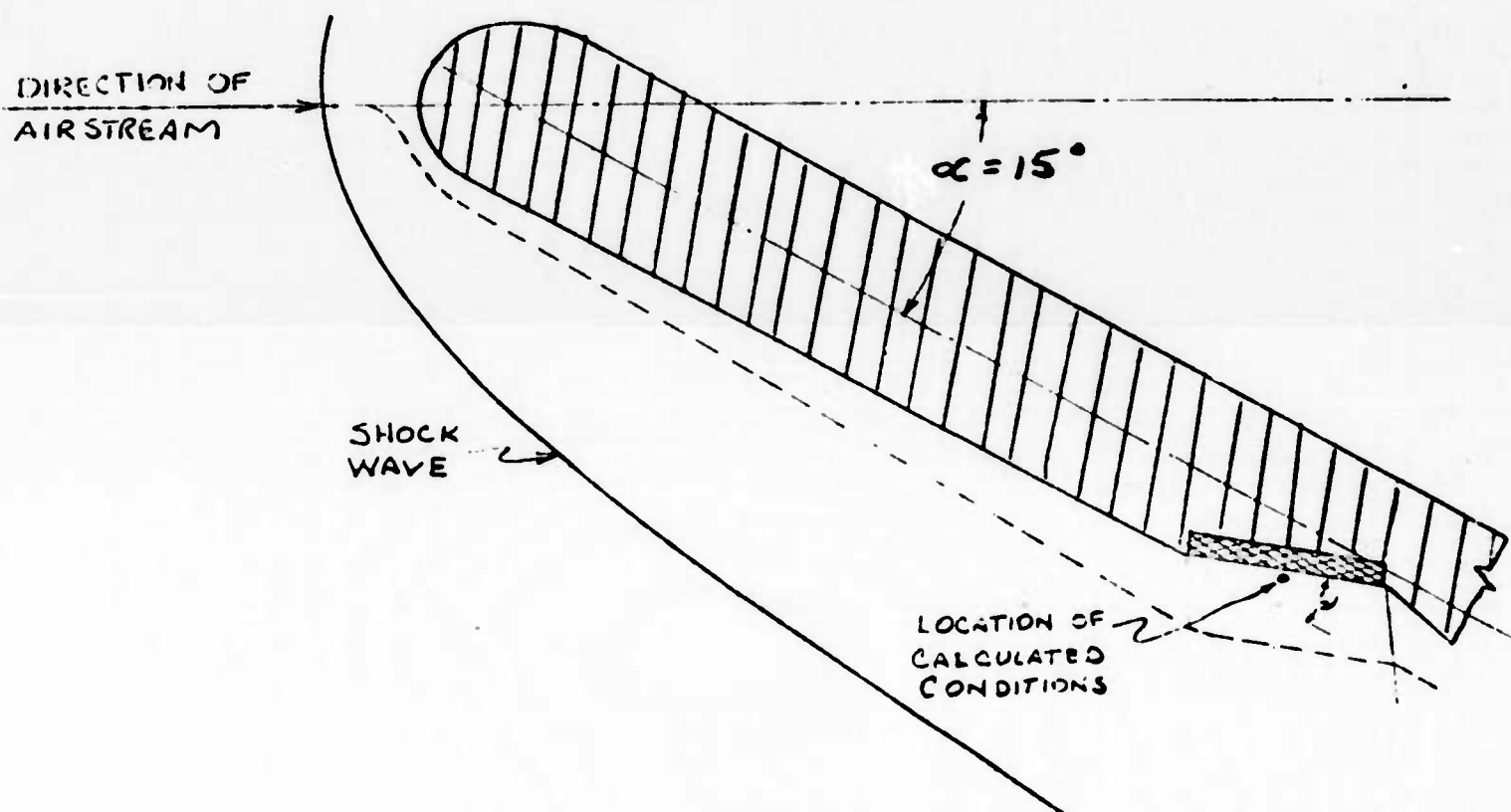


Figure 29 Trajectory 3BT1 Convective Heating Rate Versus Time, Turbulent Flow, One-Foot Aft, on Wing Surfaces at Various Local Expansion Angles (HASTE)



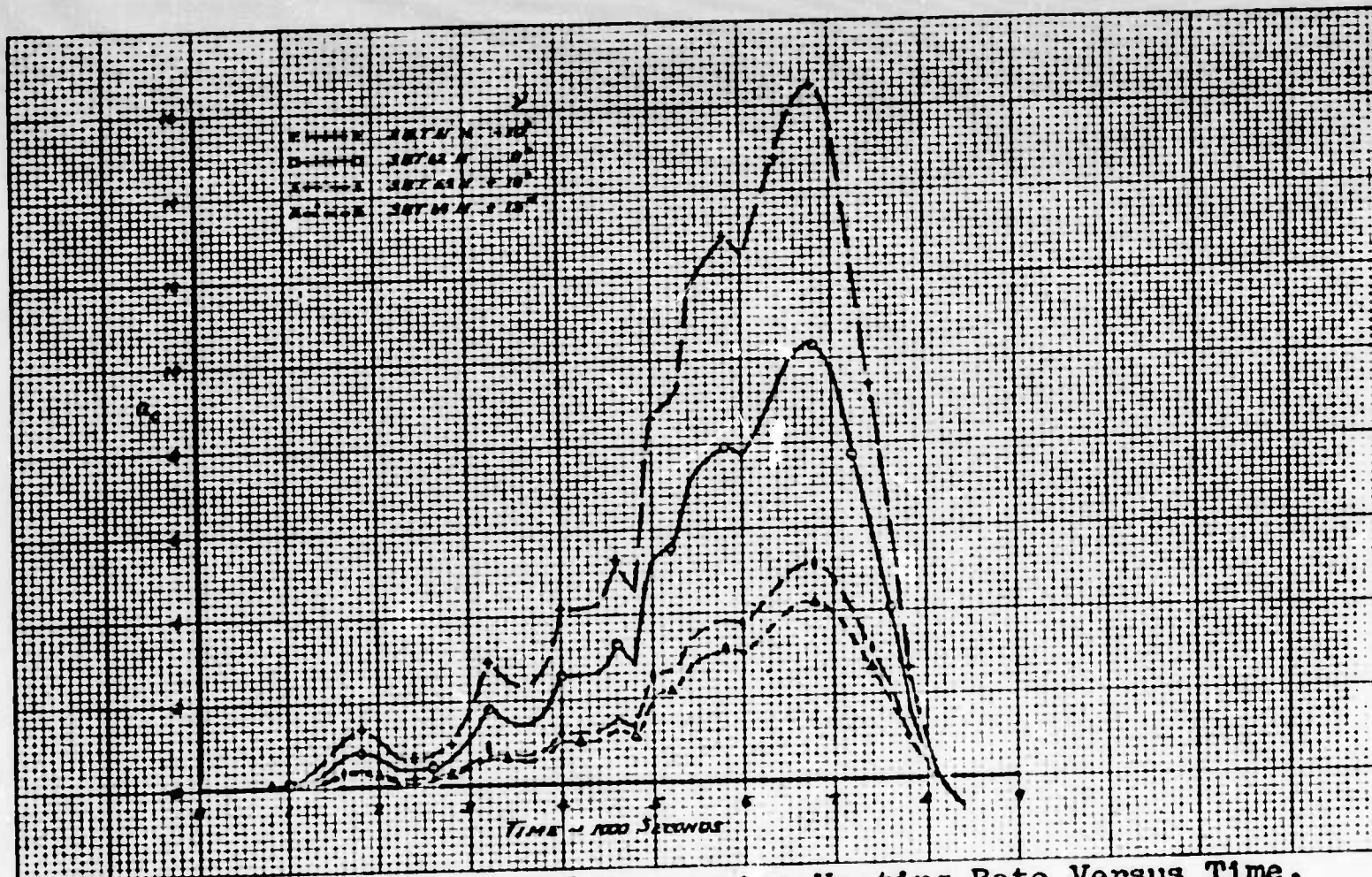
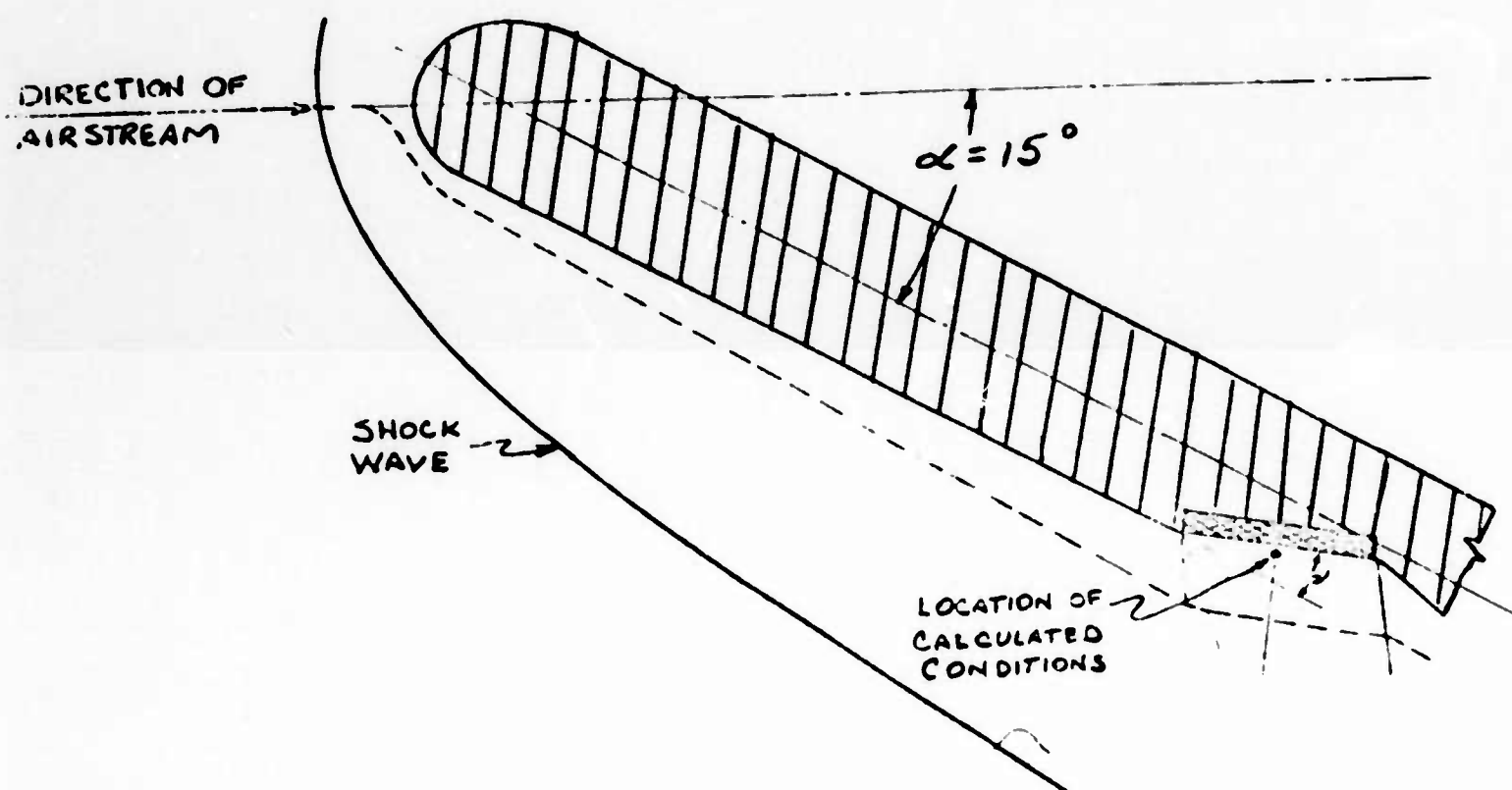


Figure 30 Trajectory 3BT6 Convective Heating Rate Versus Time, Turbulent Flow, Six-Foot Aft, on Wing Surfaces at Various Local Expansion Angles (HASTE)



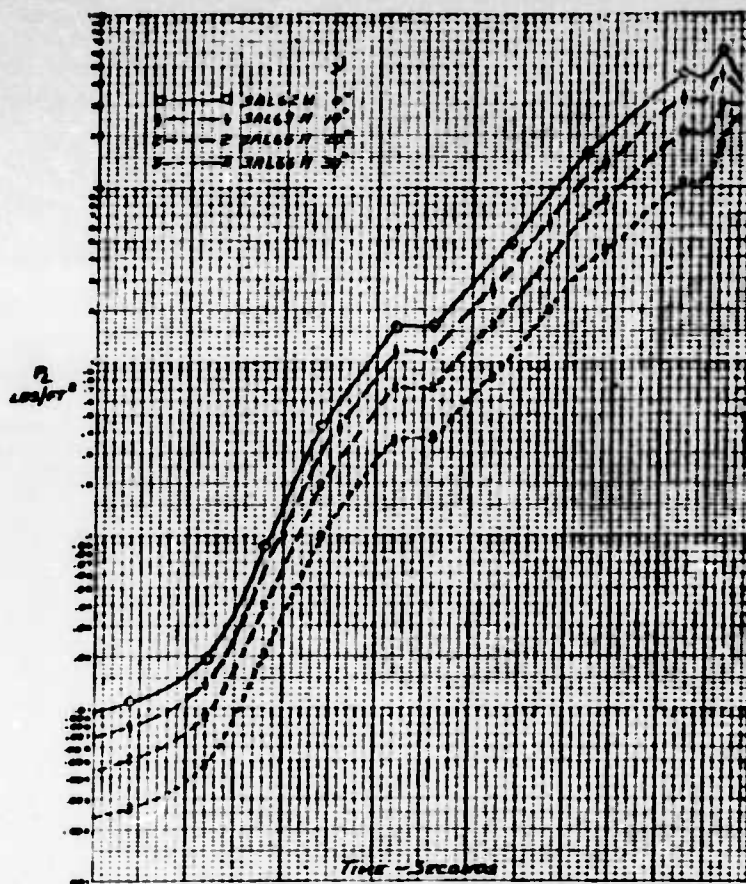
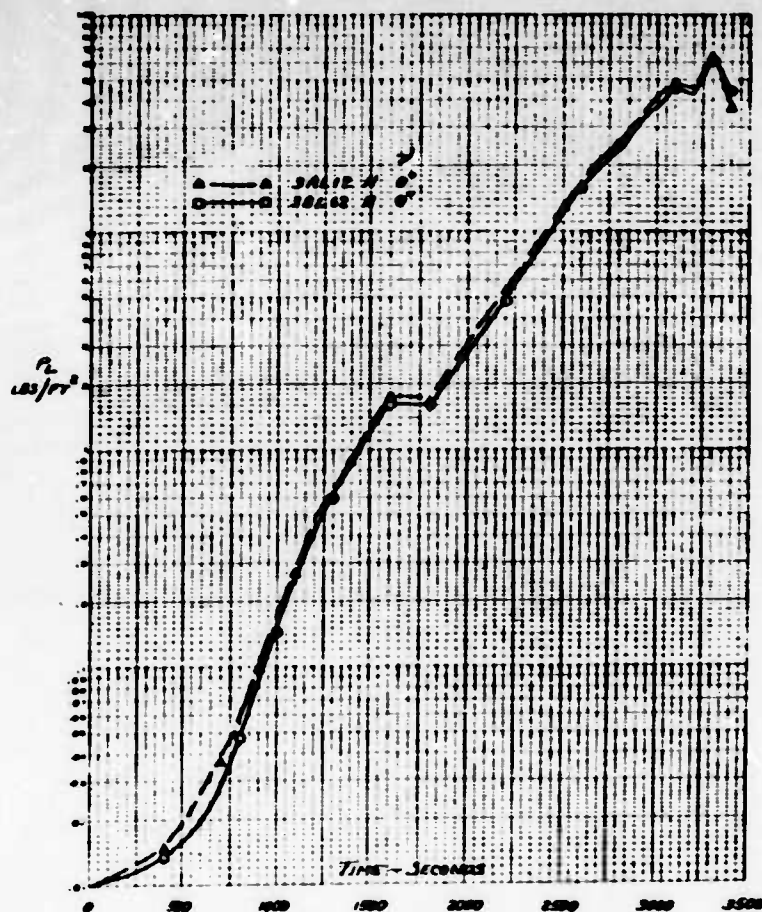
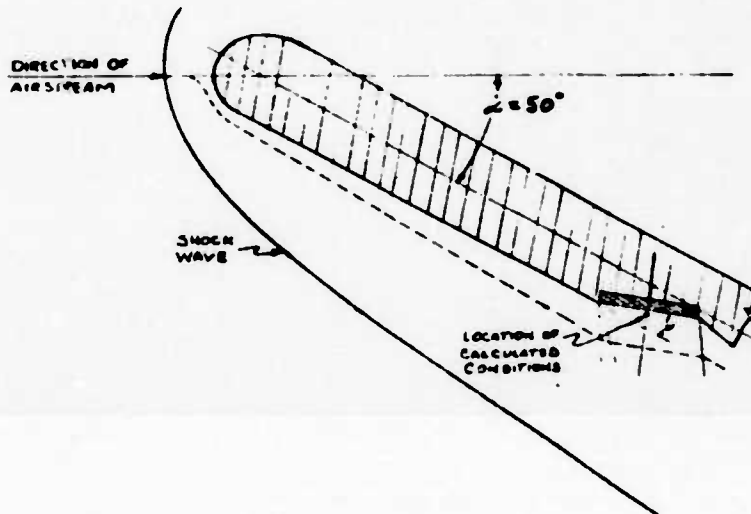
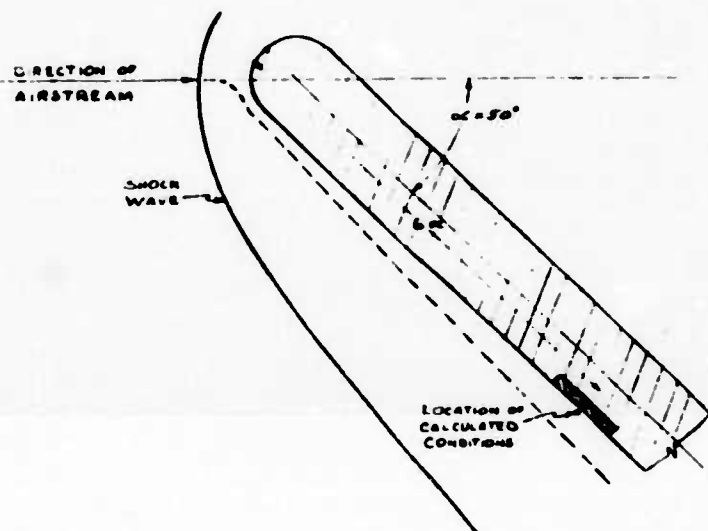


Figure 31 Trajectory 3AL Local Pressure Versus Time, Laminar Flow, One-Foot and Six-Foot Aft, on Wing Surfaces at Various Local Expansion Angles





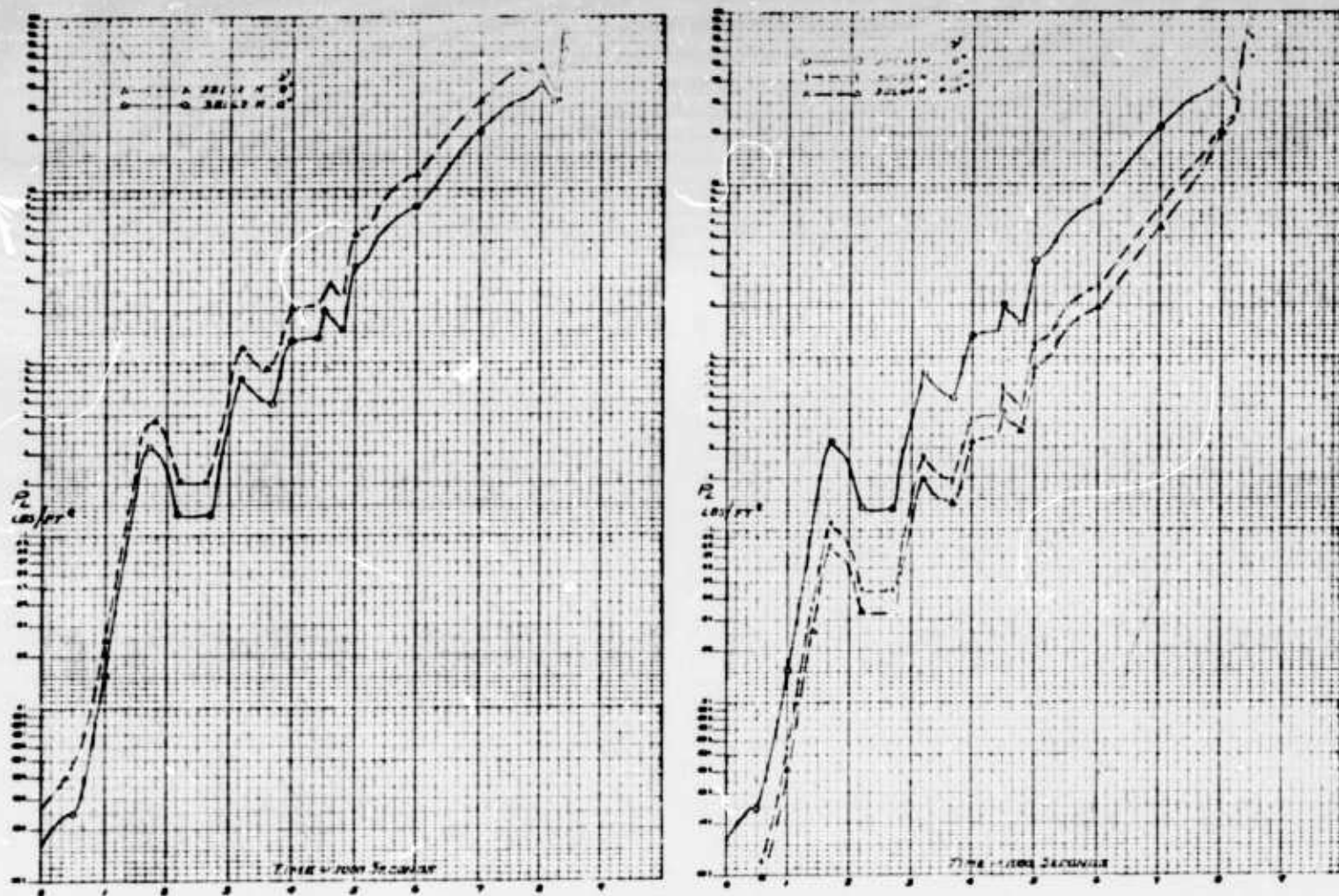
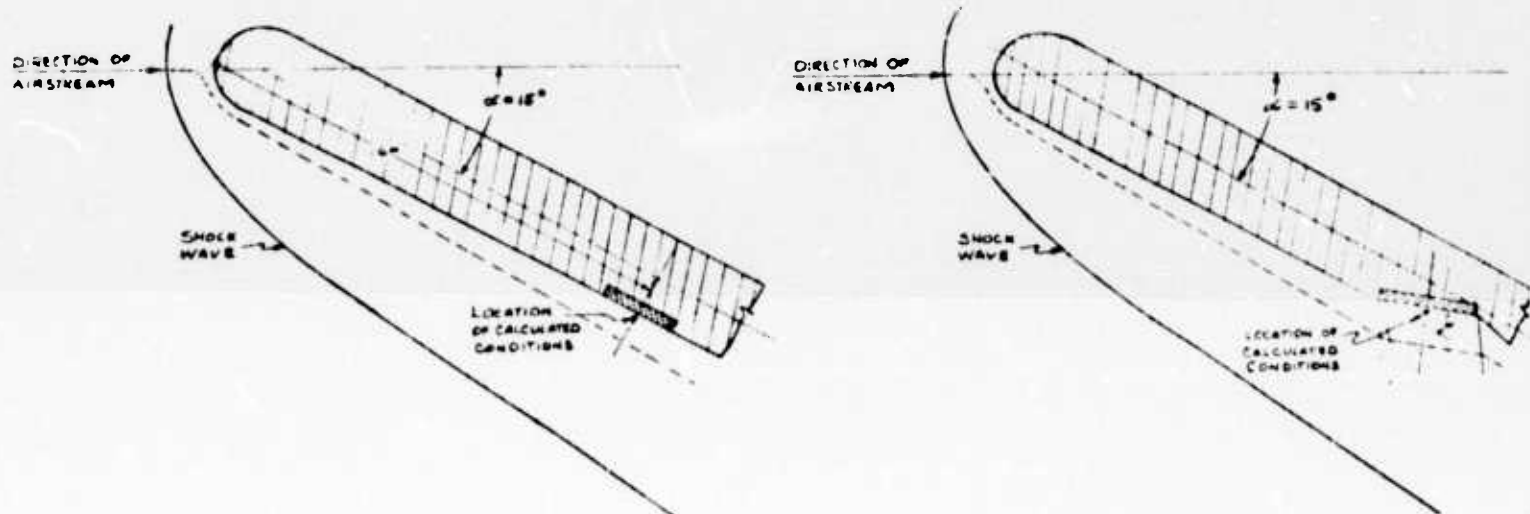


Figure 32 Trajectory 3BL Local Pressure Versus Time, Laminar Flow, One-Foot and Six-Feet Aft, on Wing Surfaces at Various Local Expansion Angles





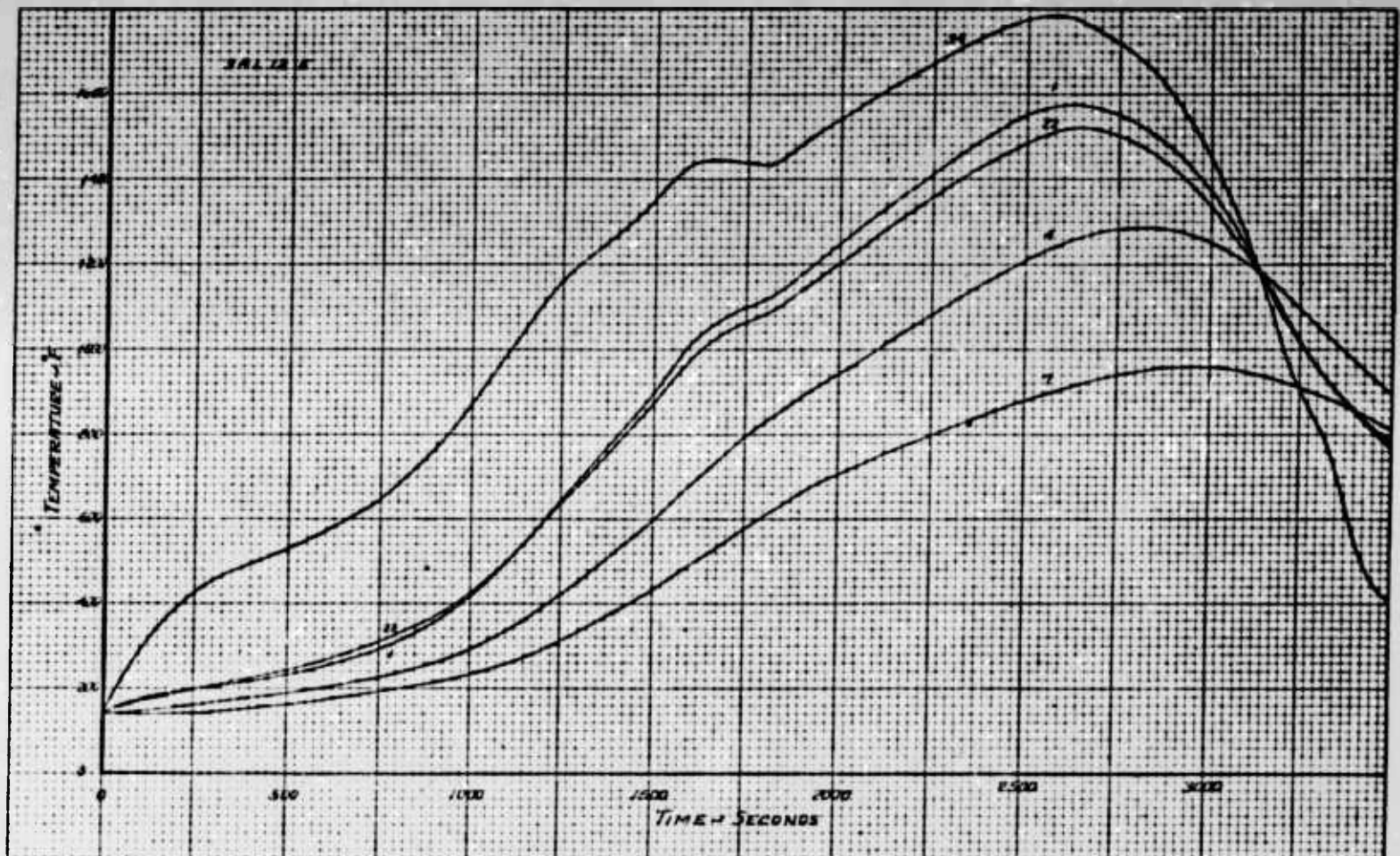
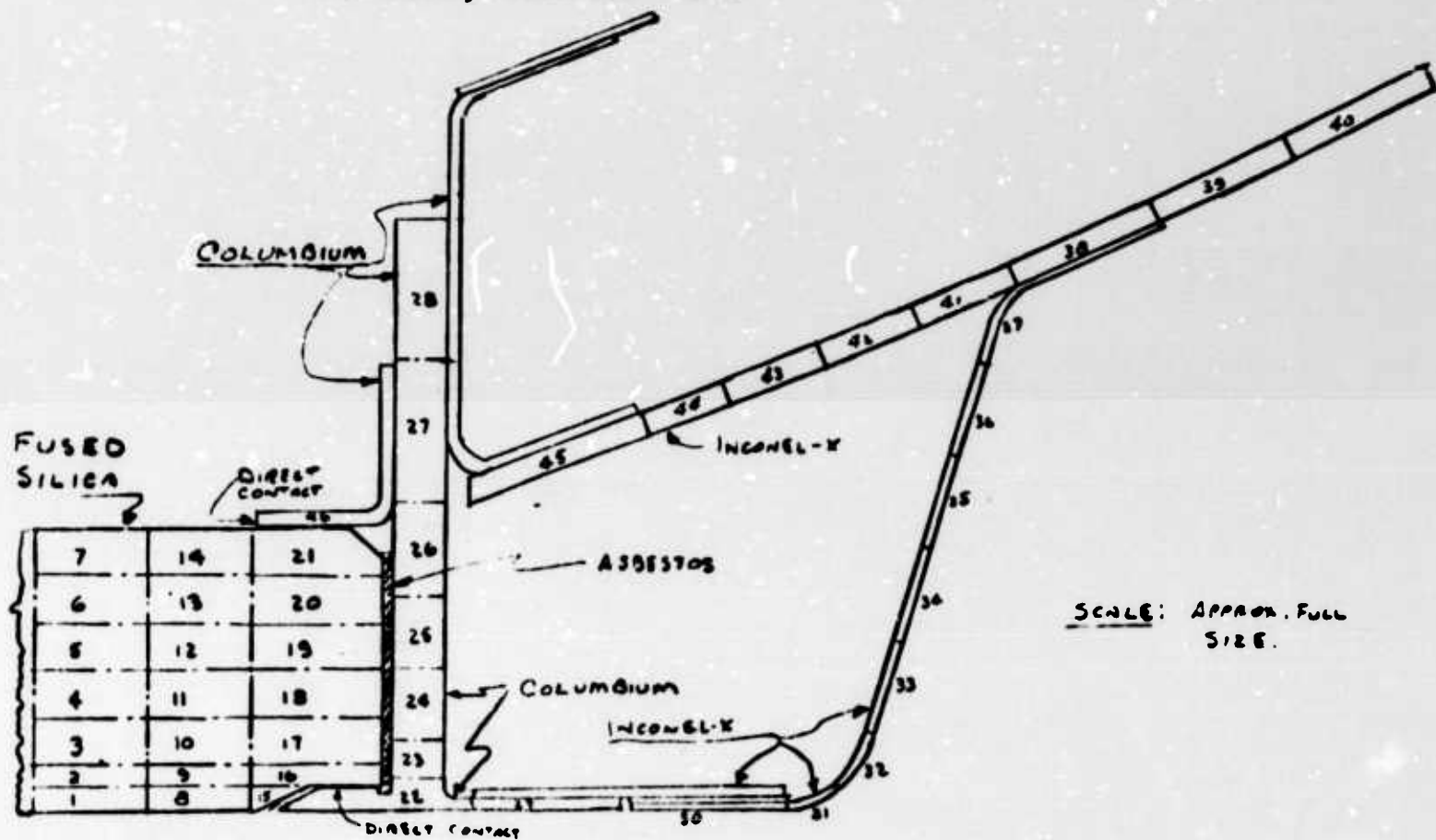


Figure 33 Trajectory 3AL12E Temperature-Time Distribution Through an Opaque Fused Silica Window, 1 1/2" Thick, Mounted as Shown, Located One-Foot Aft, Flush with Lower Wing Surface, Laminar Flow



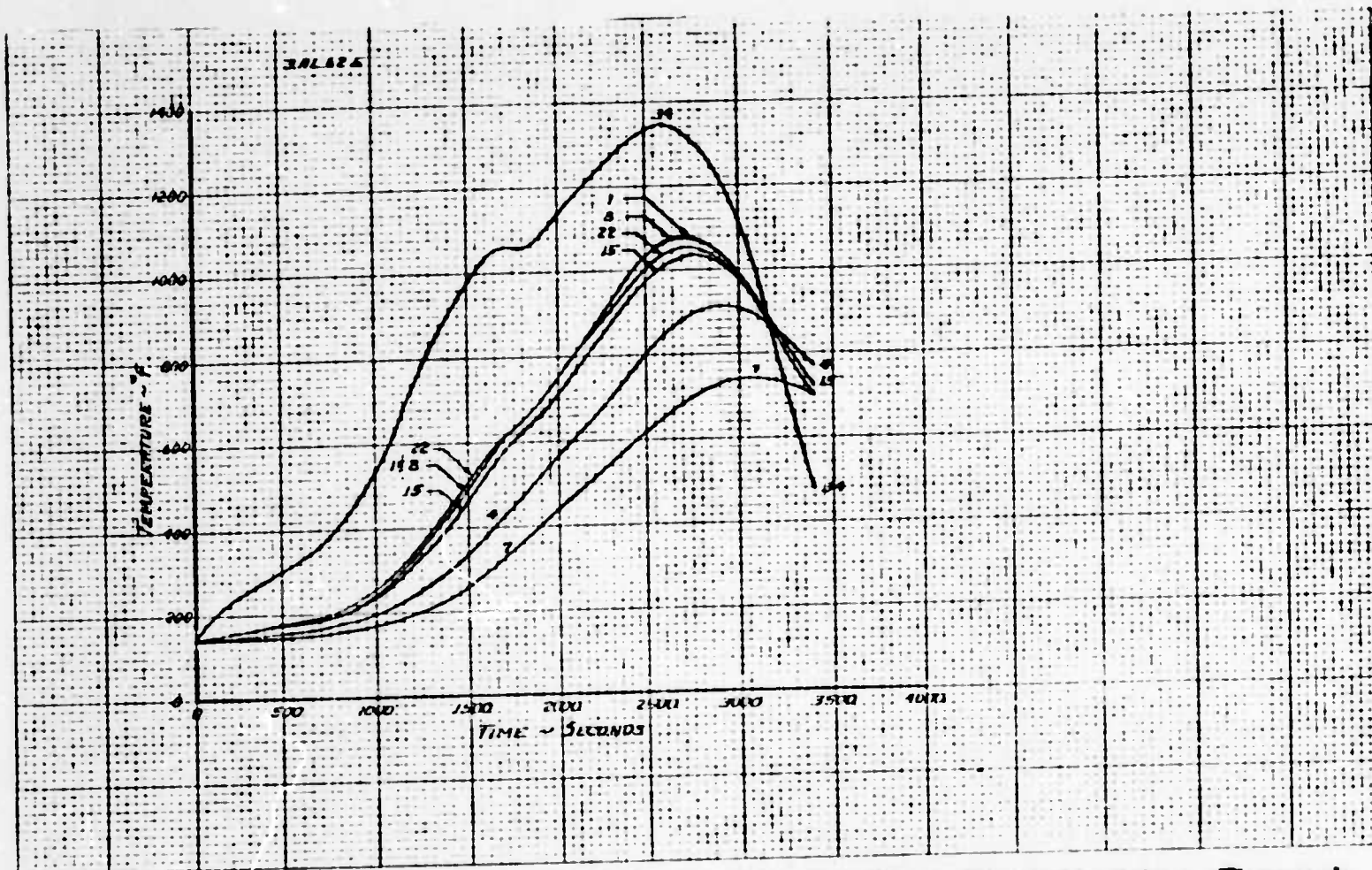
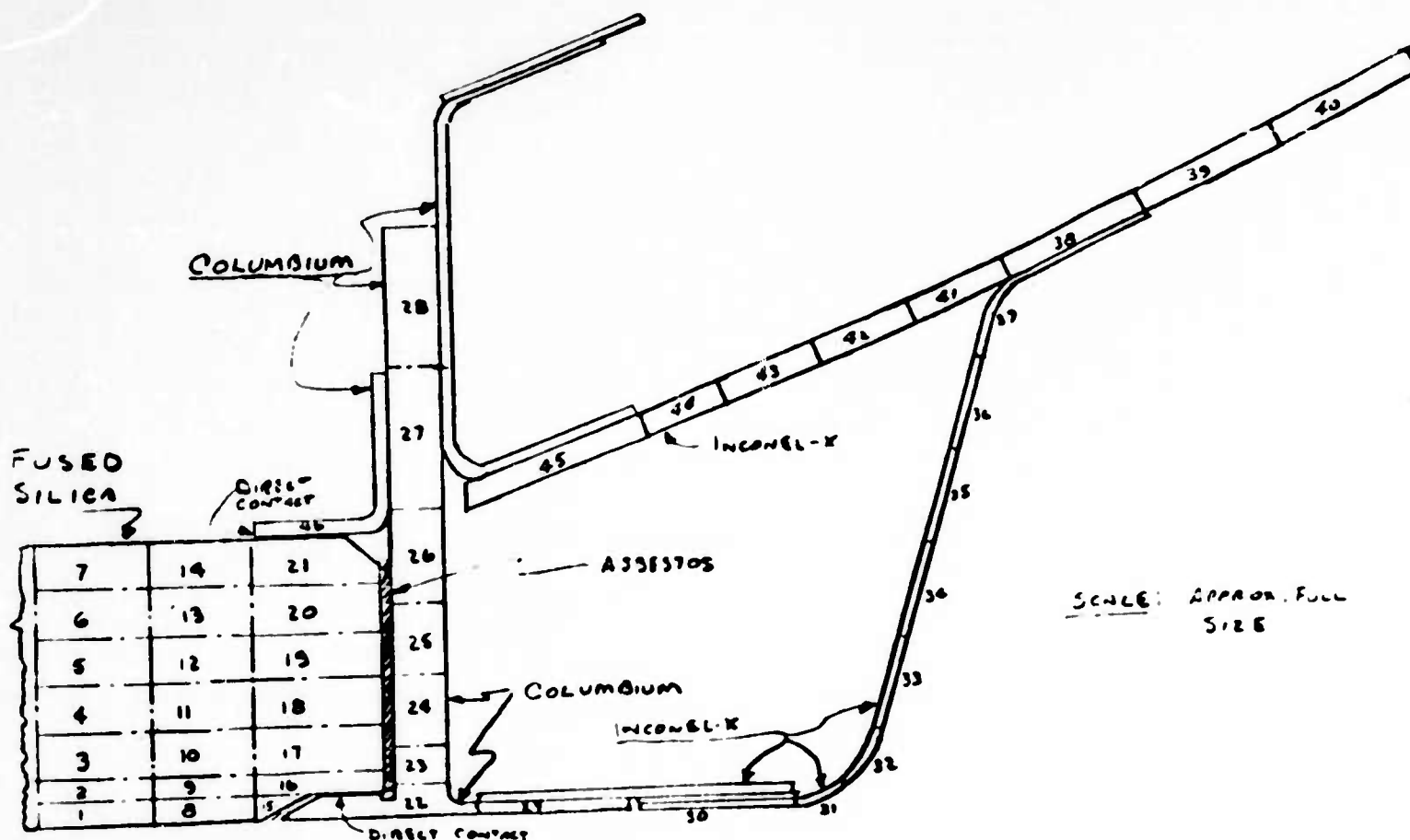
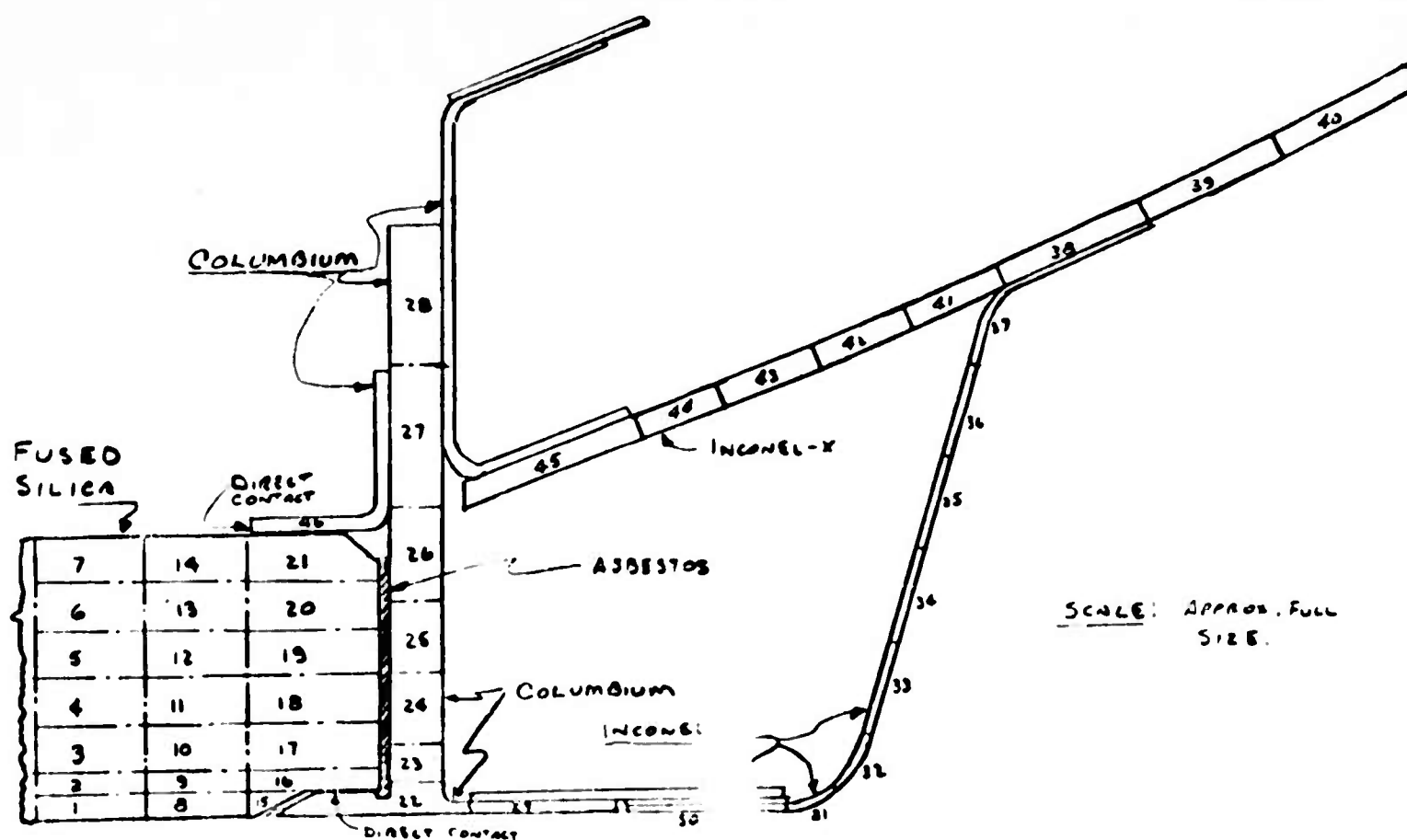
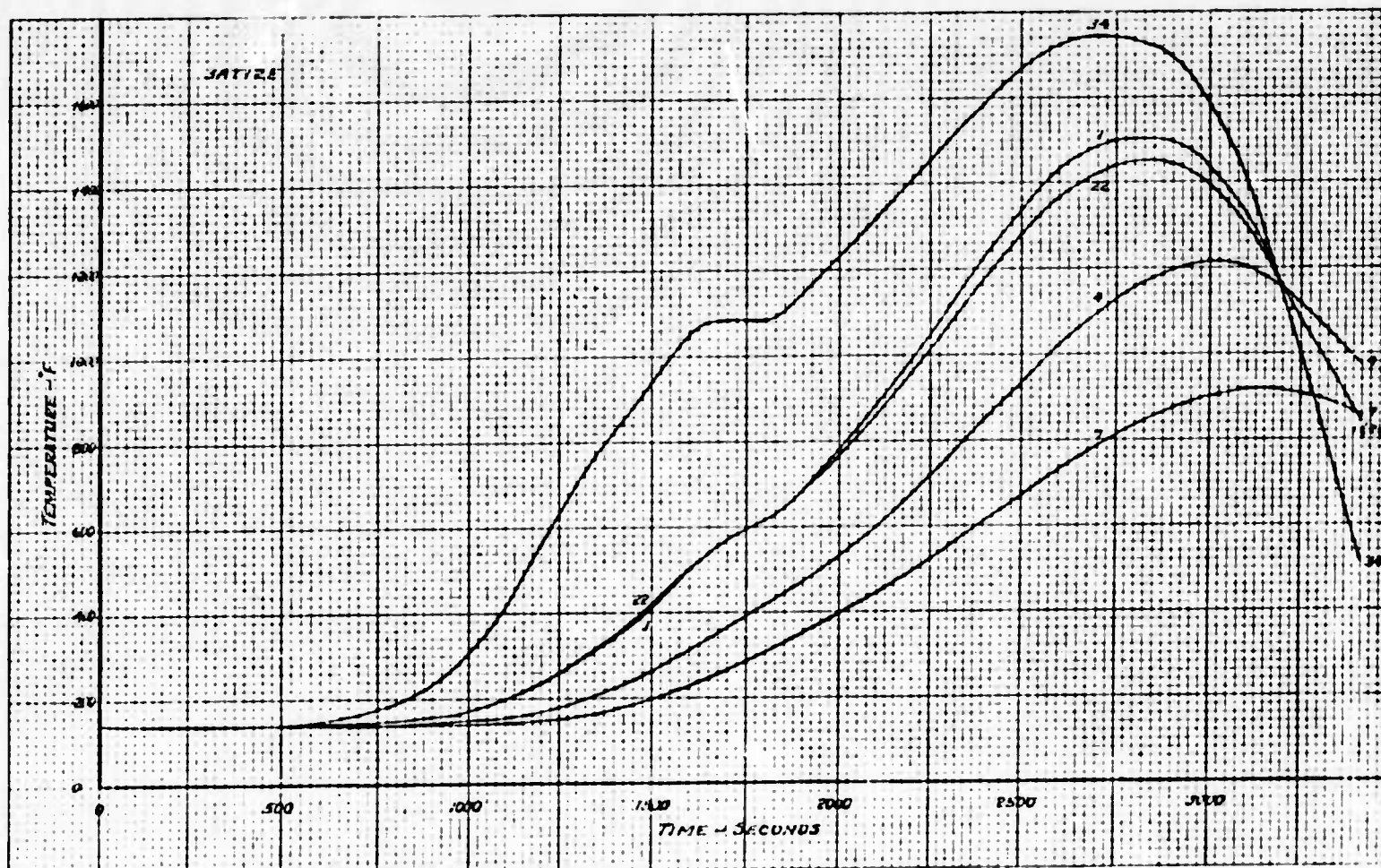


Figure 34 Trajectory 3AL62E Temperature-Time Distribution Through an Opaque Fused Silica Window, 1 1/2" Thick, Mounted as Shown, Located Six-Foot Aft, Flush with Lower Wing Surface, Laminar Flow







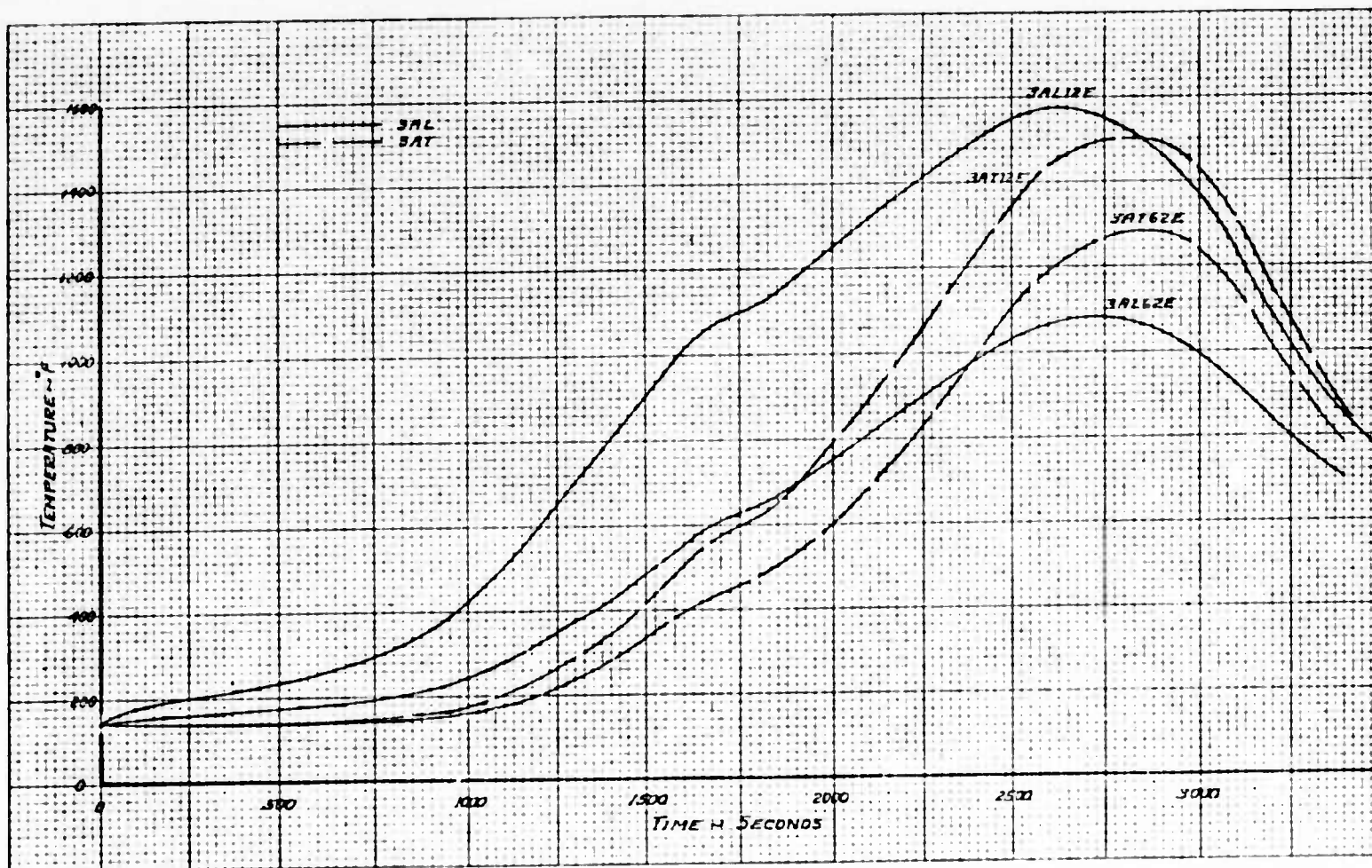
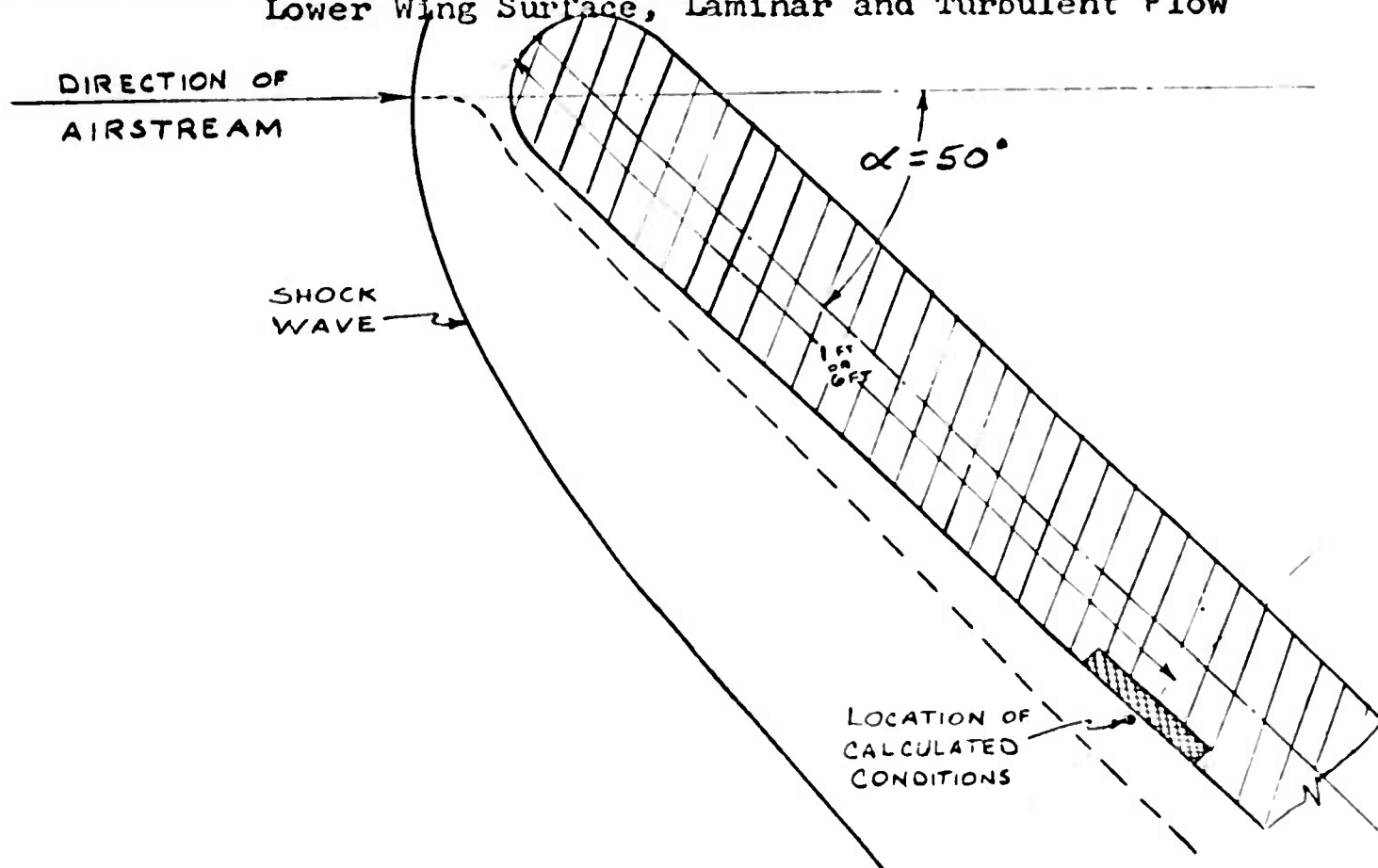


Figure 36 Summary of Trajectory 3A Temperatures versus Time on Outer Surface of an Opaque Fused Silica Window, 1 1/2" Thick, Located One-Foot and Six-Foot Aft, Flush with Lower Wing Surface, Laminar and Turbulent Flow





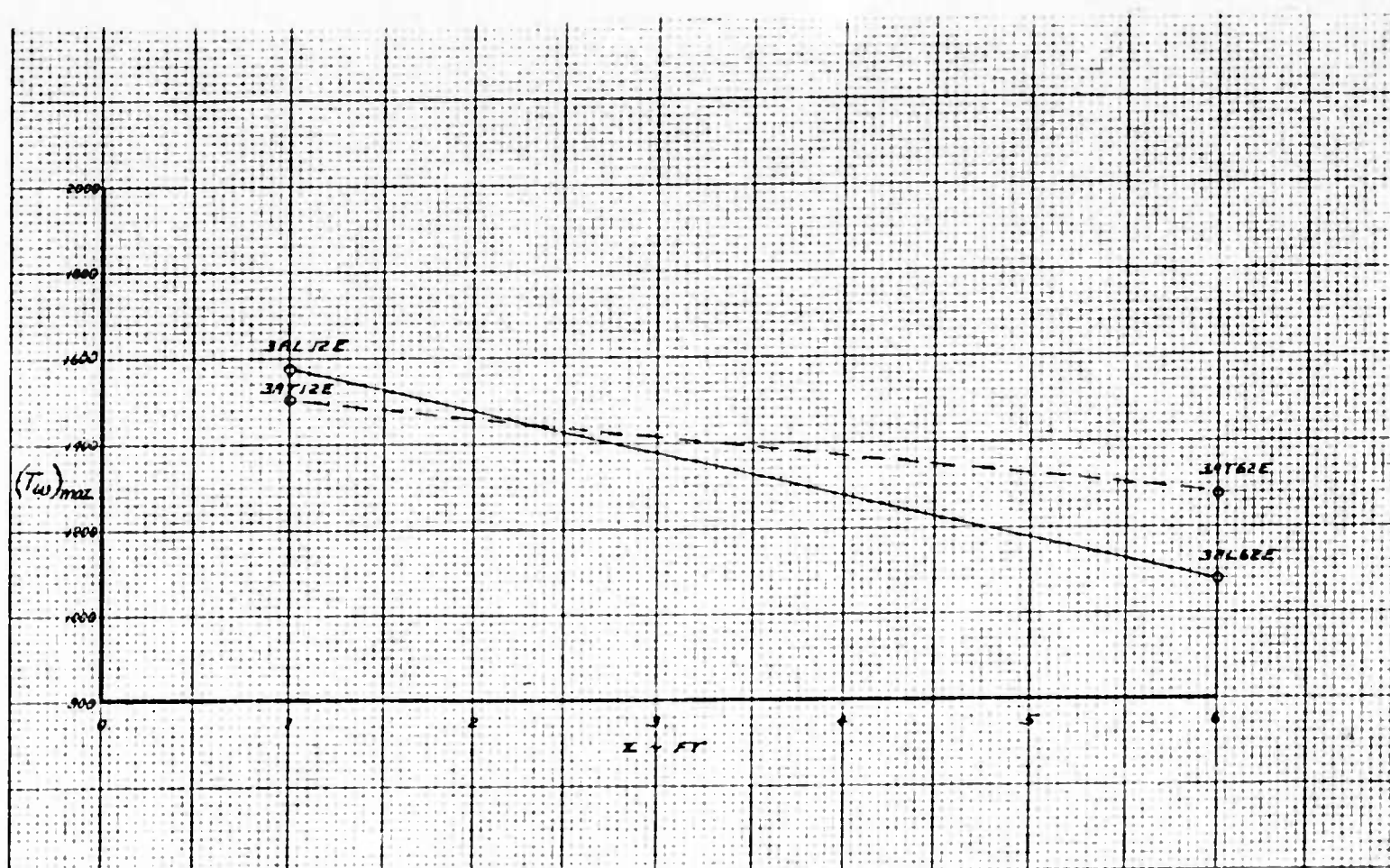
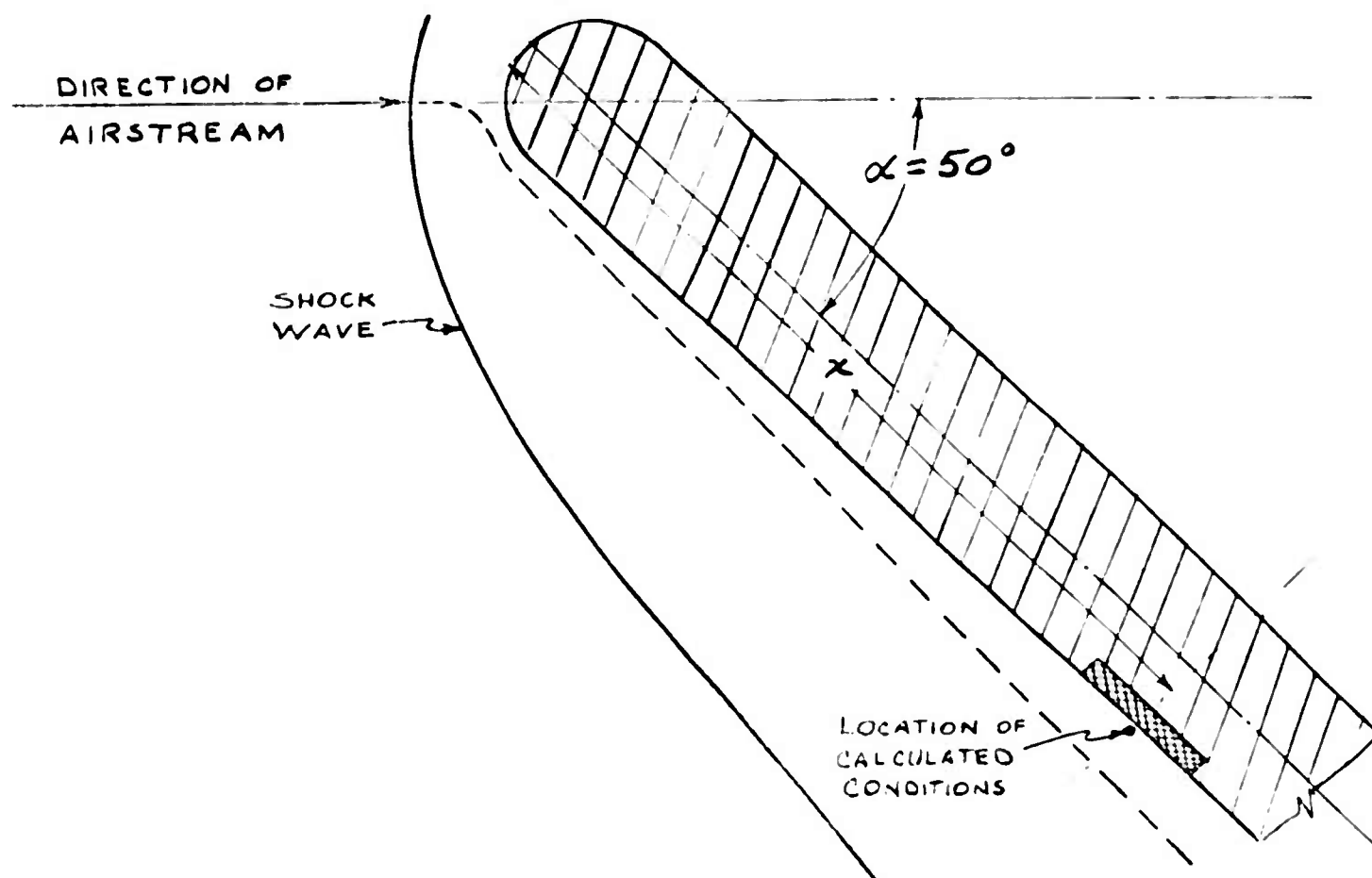


Figure 37 Effect of Location Along the Lower Surface Upon the Maximum Opaque Window Surface Temperature Calculated for 3A Trajectory with Turbulent and Laminar Flow



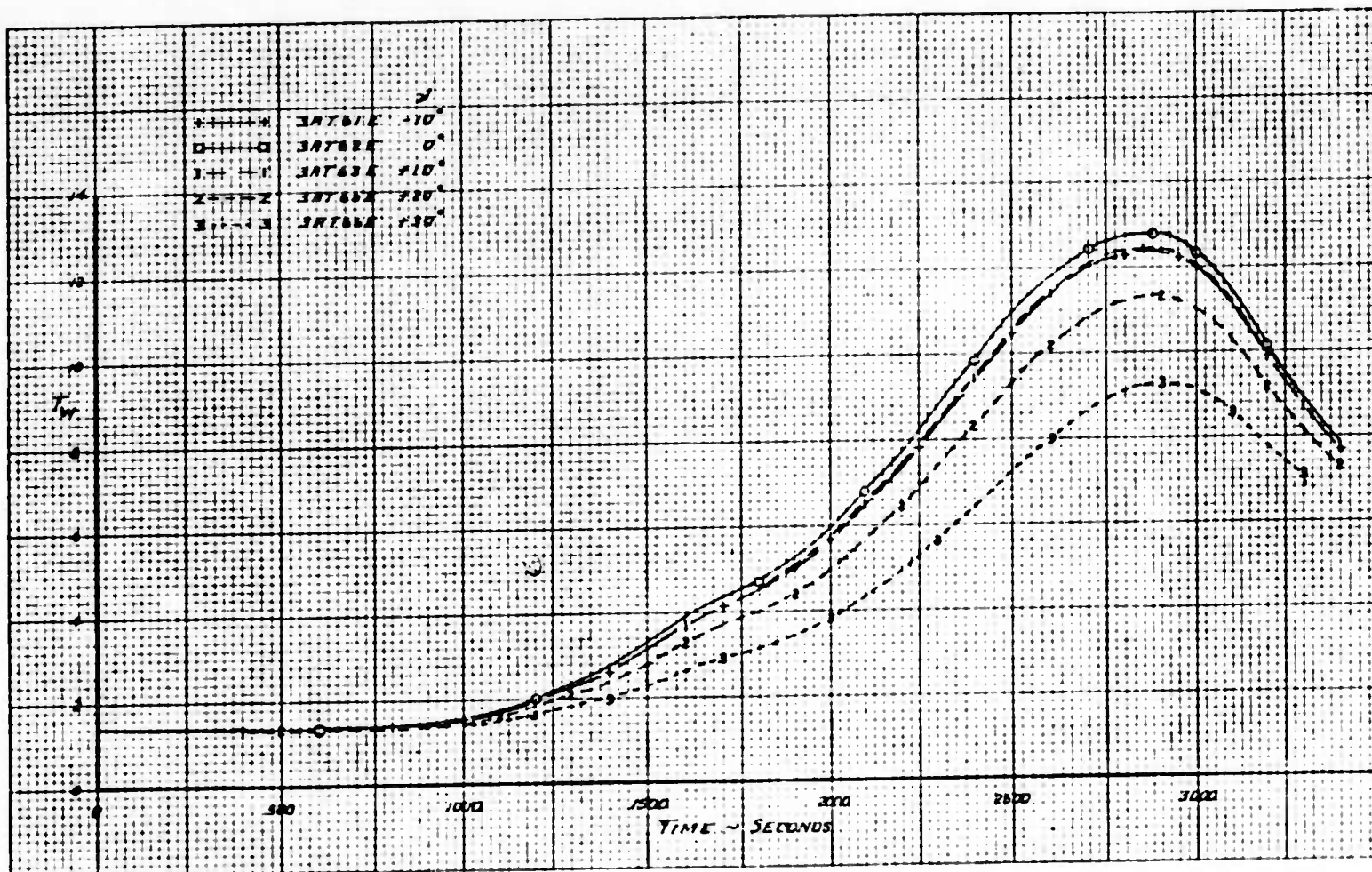
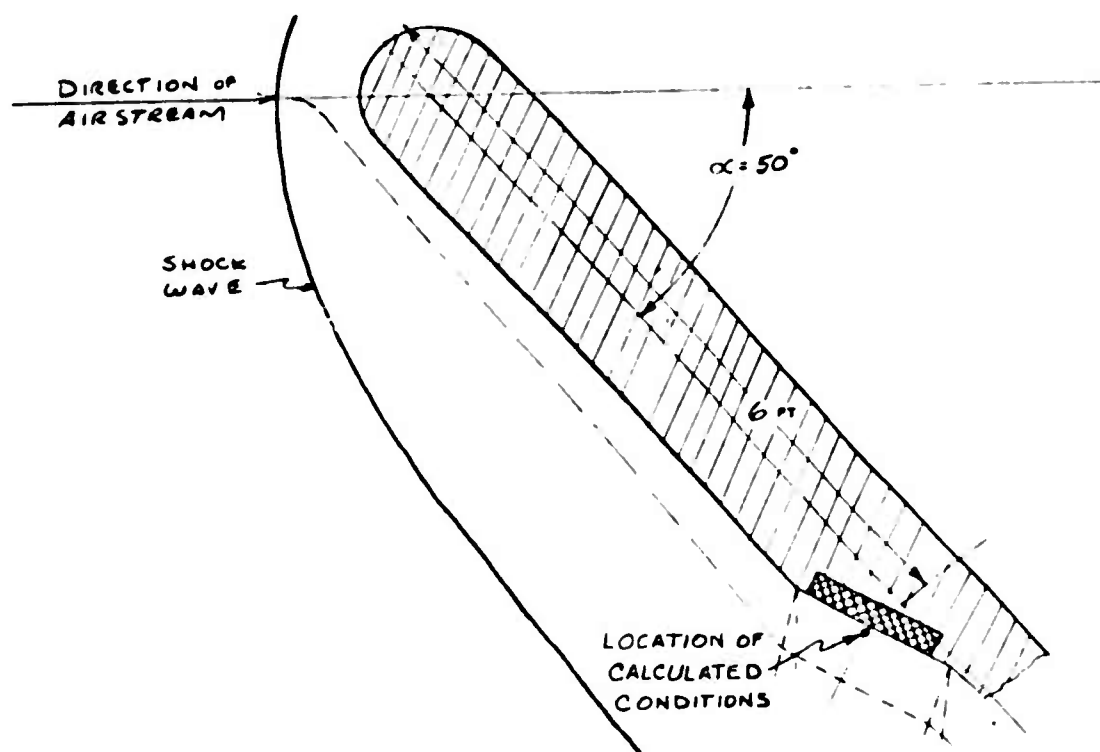


Figure 38 Trajectory 3AT6 Temperature Versus Time on Outer Surface of an Opaque, Fused Silica Window, 1 1/2" Thick, Six-Foot Aft on Lower Wing Surface, Turbulent Flow, at Various Local Expansion Angles



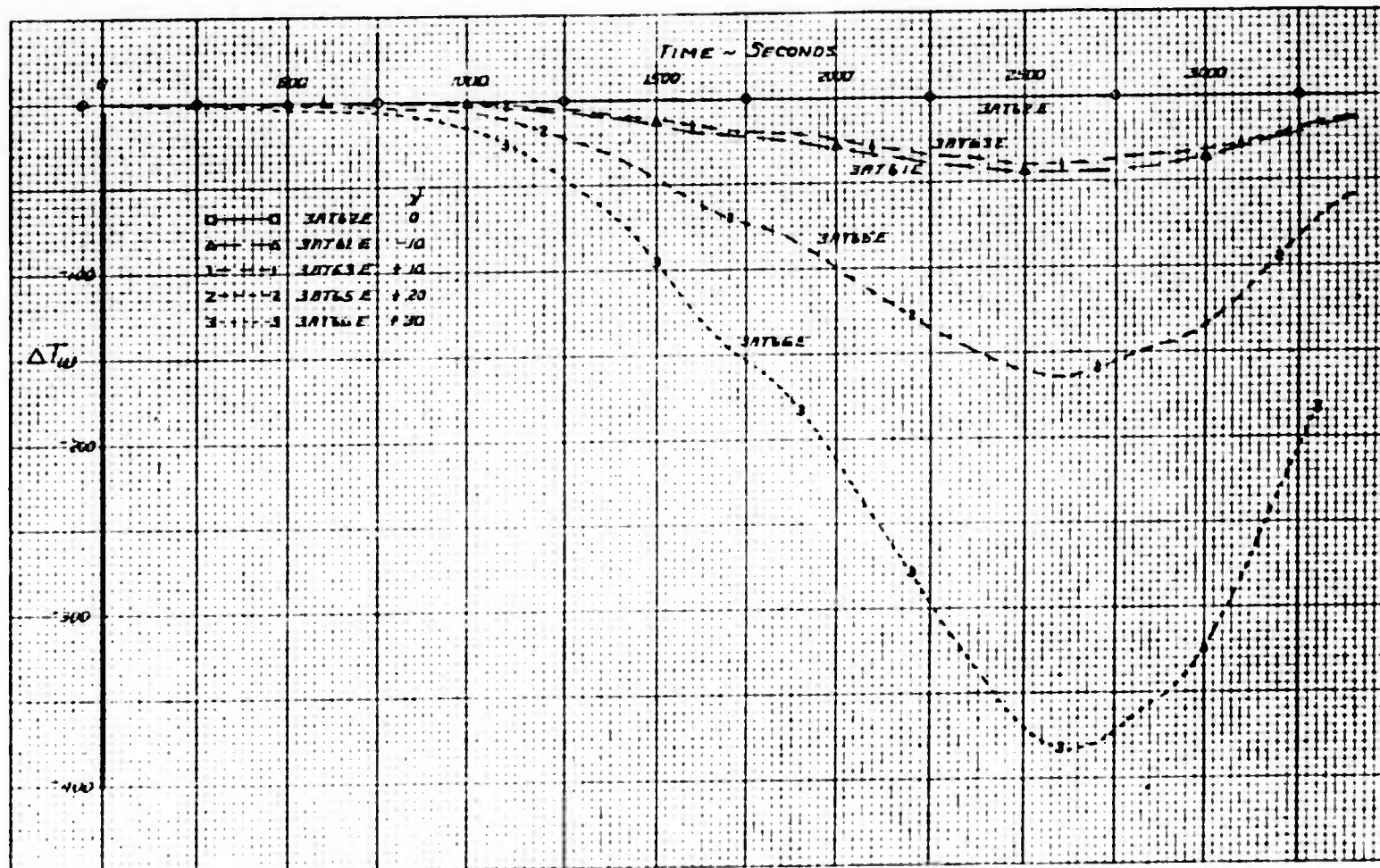
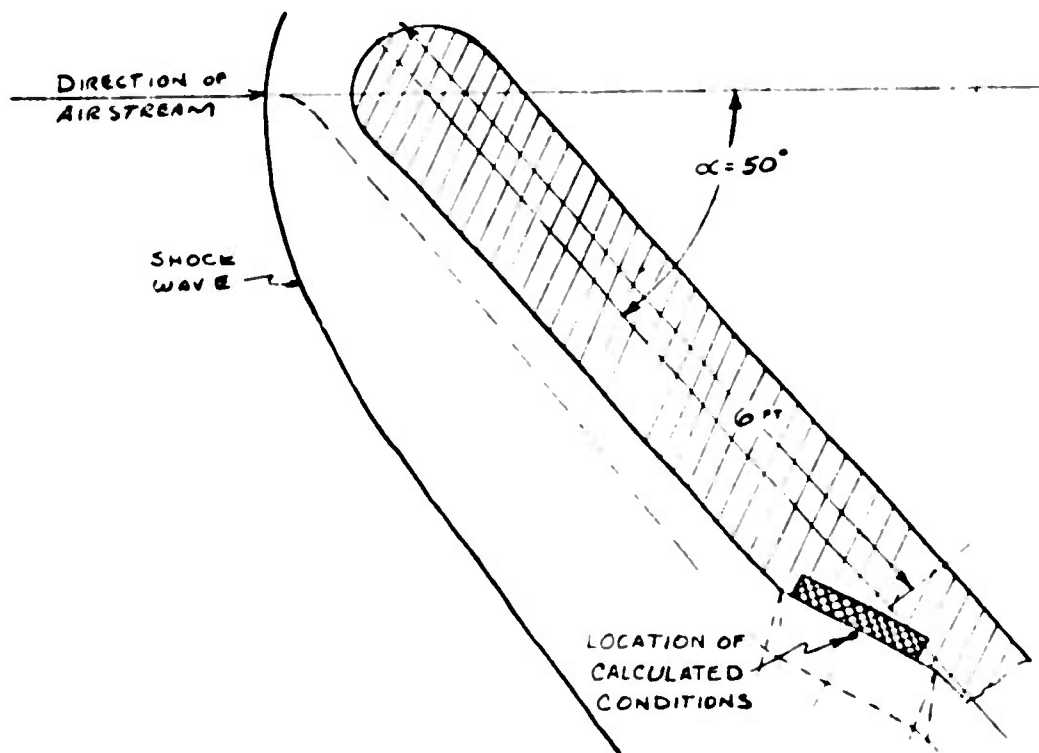


Figure 39 Trajectory 3AT6 Temperature Differences Versus Time for Outer Surface of an Opaque Fused Silica Window, 1 1/2" Thick, Six-Feet Aft on Lower Wing Surface, Turbulent Flow, at Various Local Expansion Angles Compared to the Flush Condition



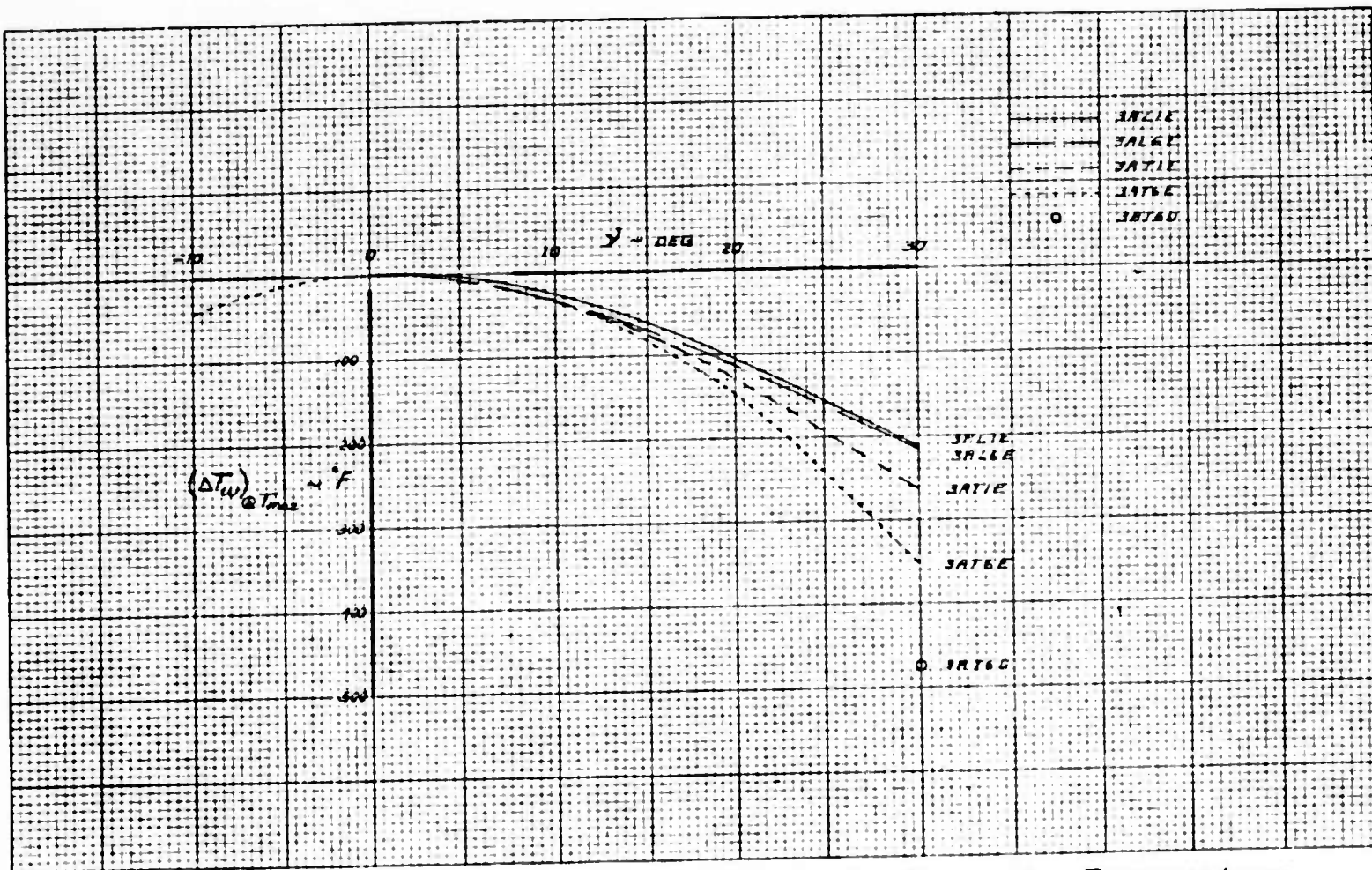
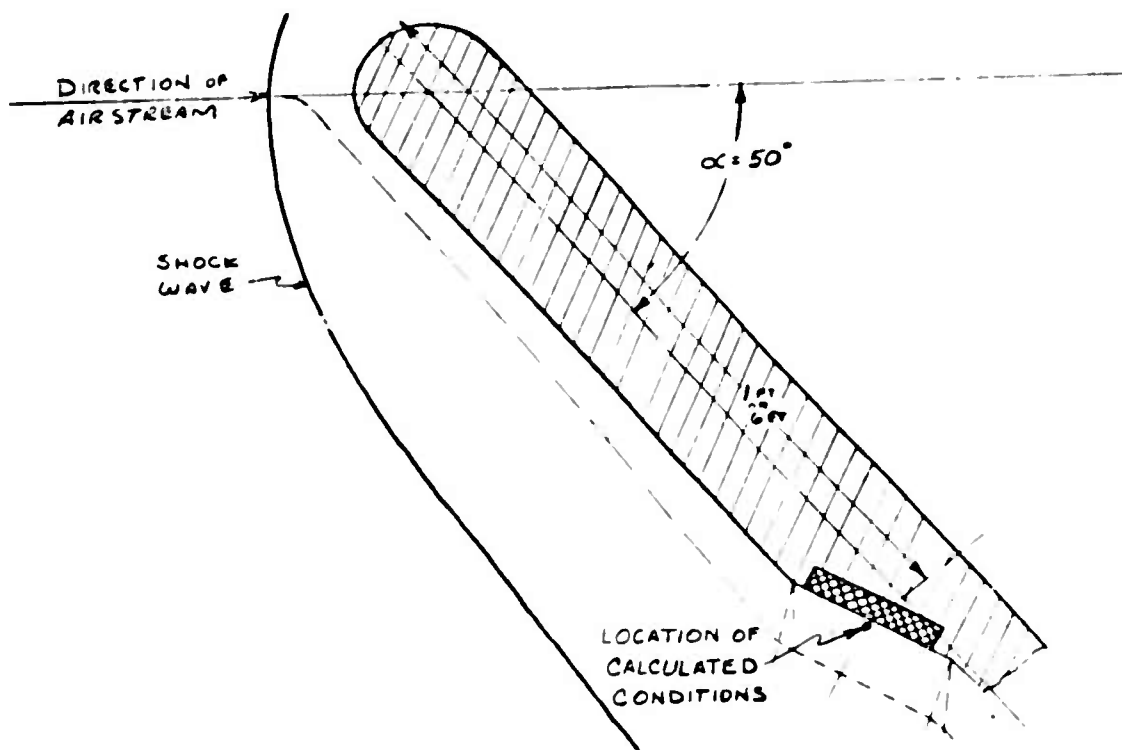


Figure 40 Effect of Local Expansion Angle Upon the Temperature Difference at Maximum Surface Temperature of a Fused Silica Window, 1 1/2" Thick, During 3A Trajectory





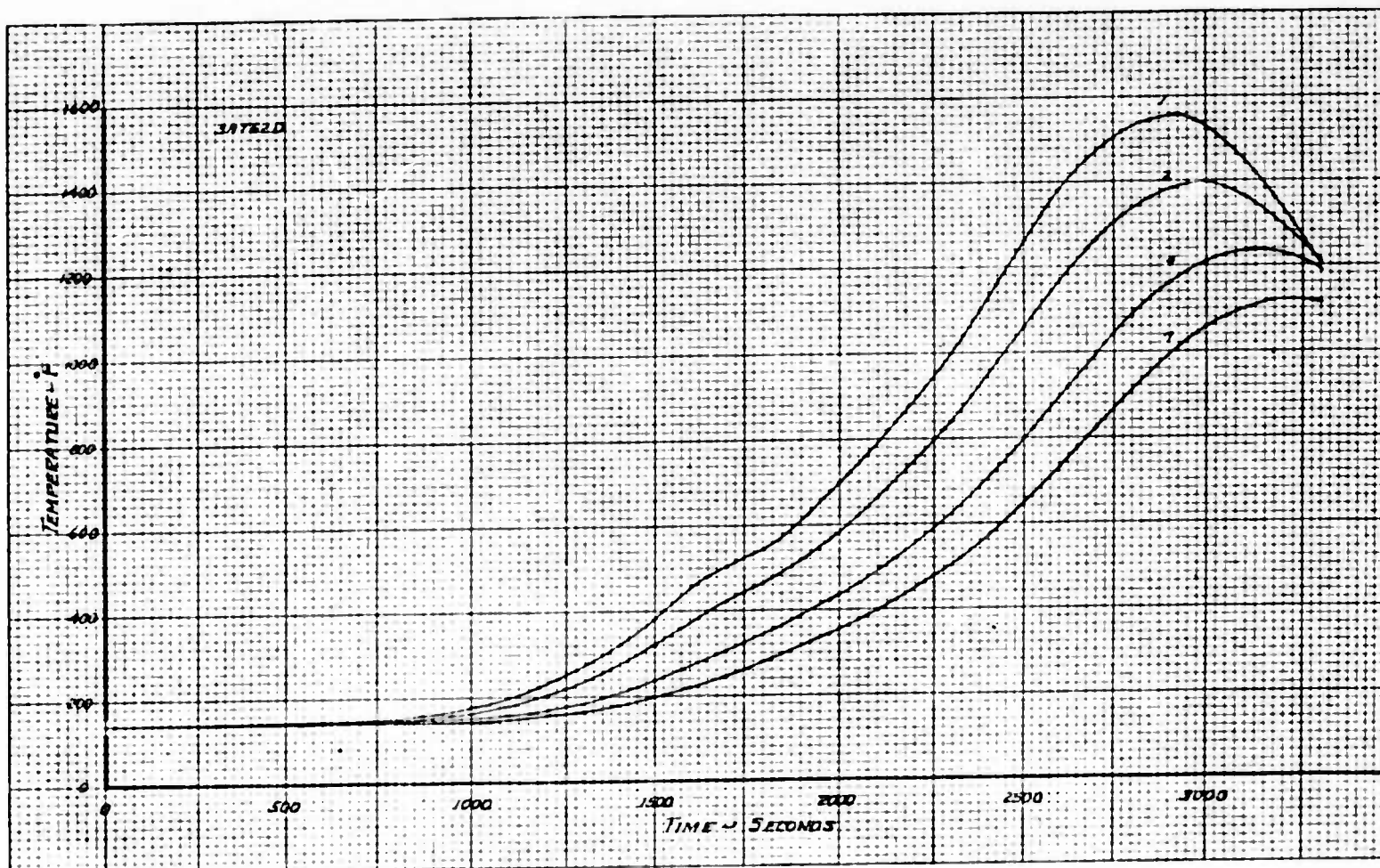
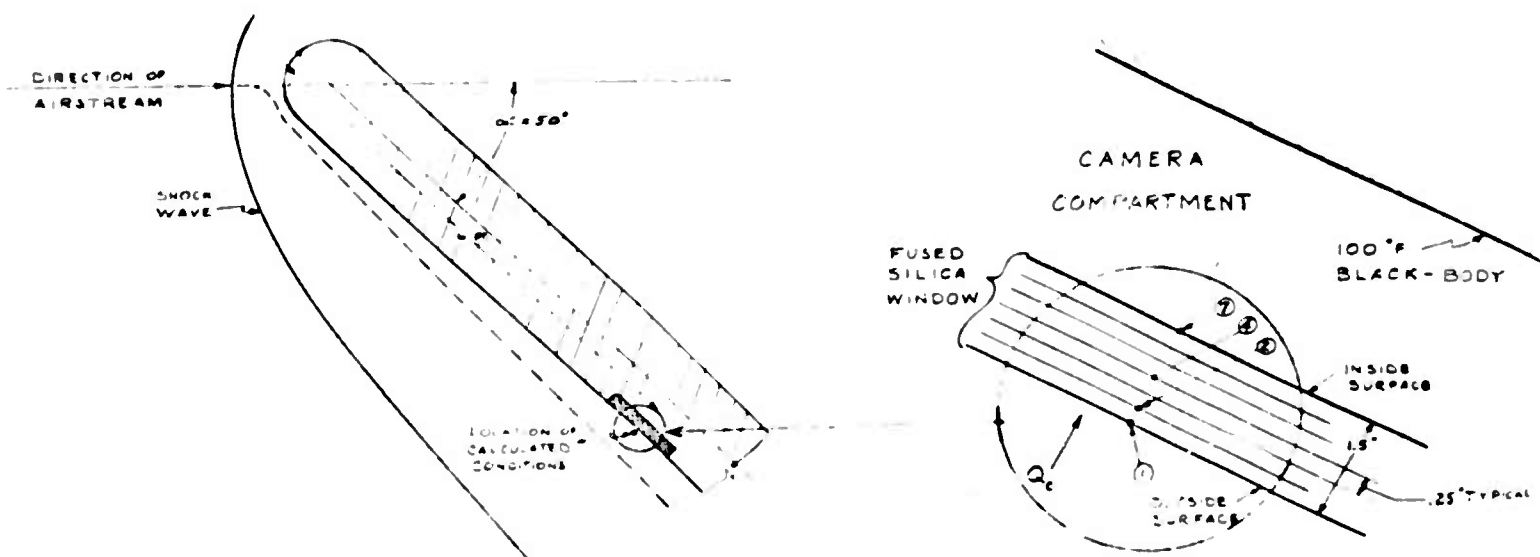


Figure 41 Trajectory 3AT62D Temperature-Time Distribution Through a Diathermanous Fused Silica Window, 1 1/2" Thick, Located Six-Foot Aft, Flush with Lower Wing Surface, Turbulent Flow



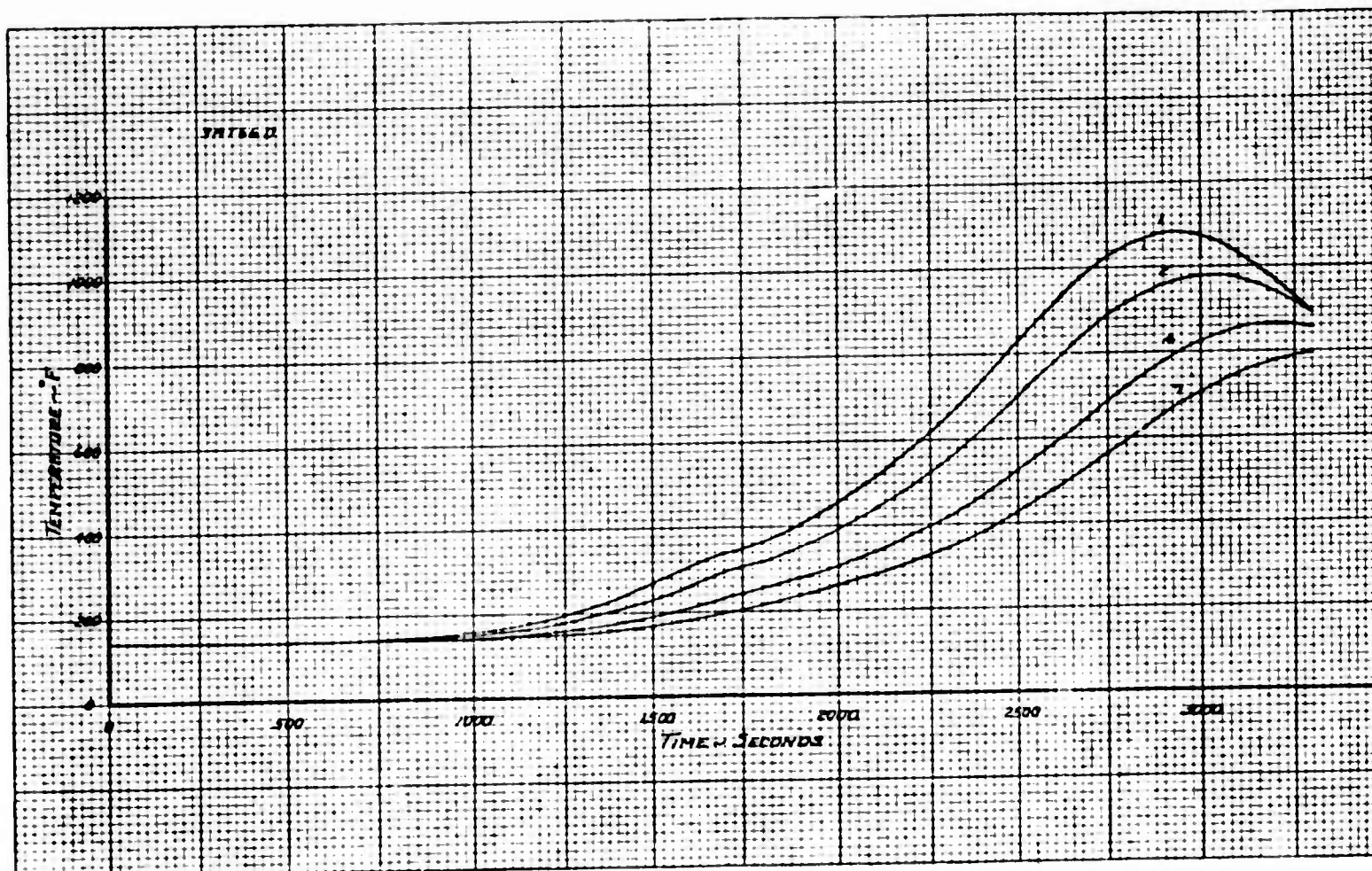
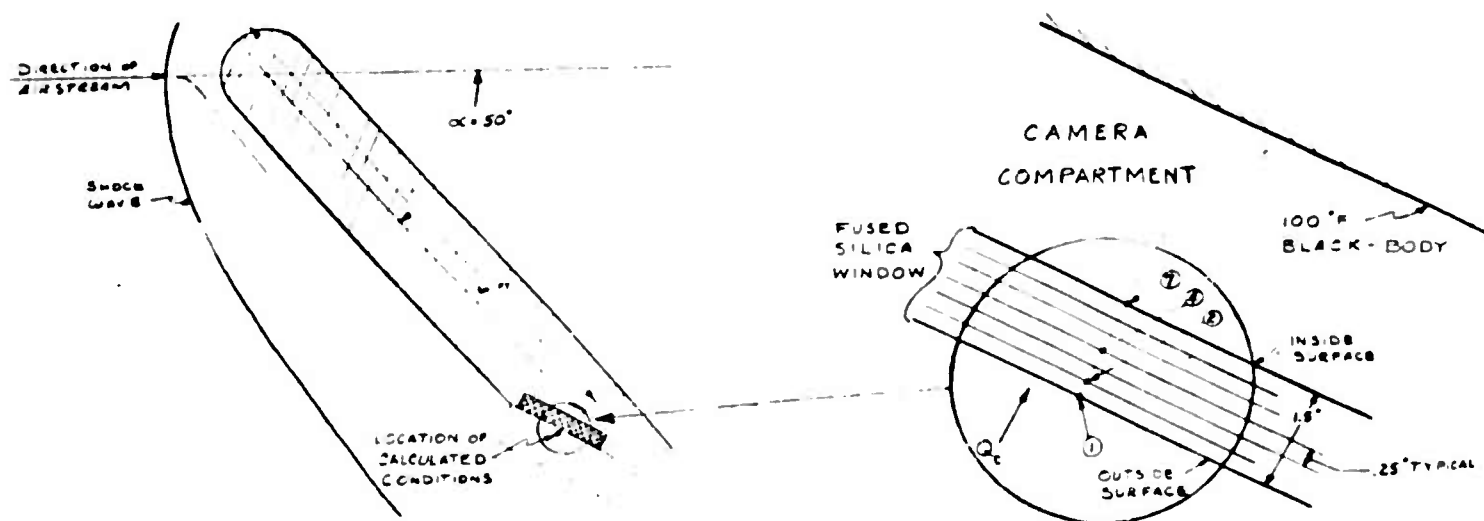


Figure 42 Trajectory 3AT66D Temperature-Time Distribution Through a Diathermanous Fused Silica Window, 1 1/2" Thick, Located Six-Feet Aft, at  $\alpha = 30^\circ$  (Local Expansion Angle), Turbulent Flow



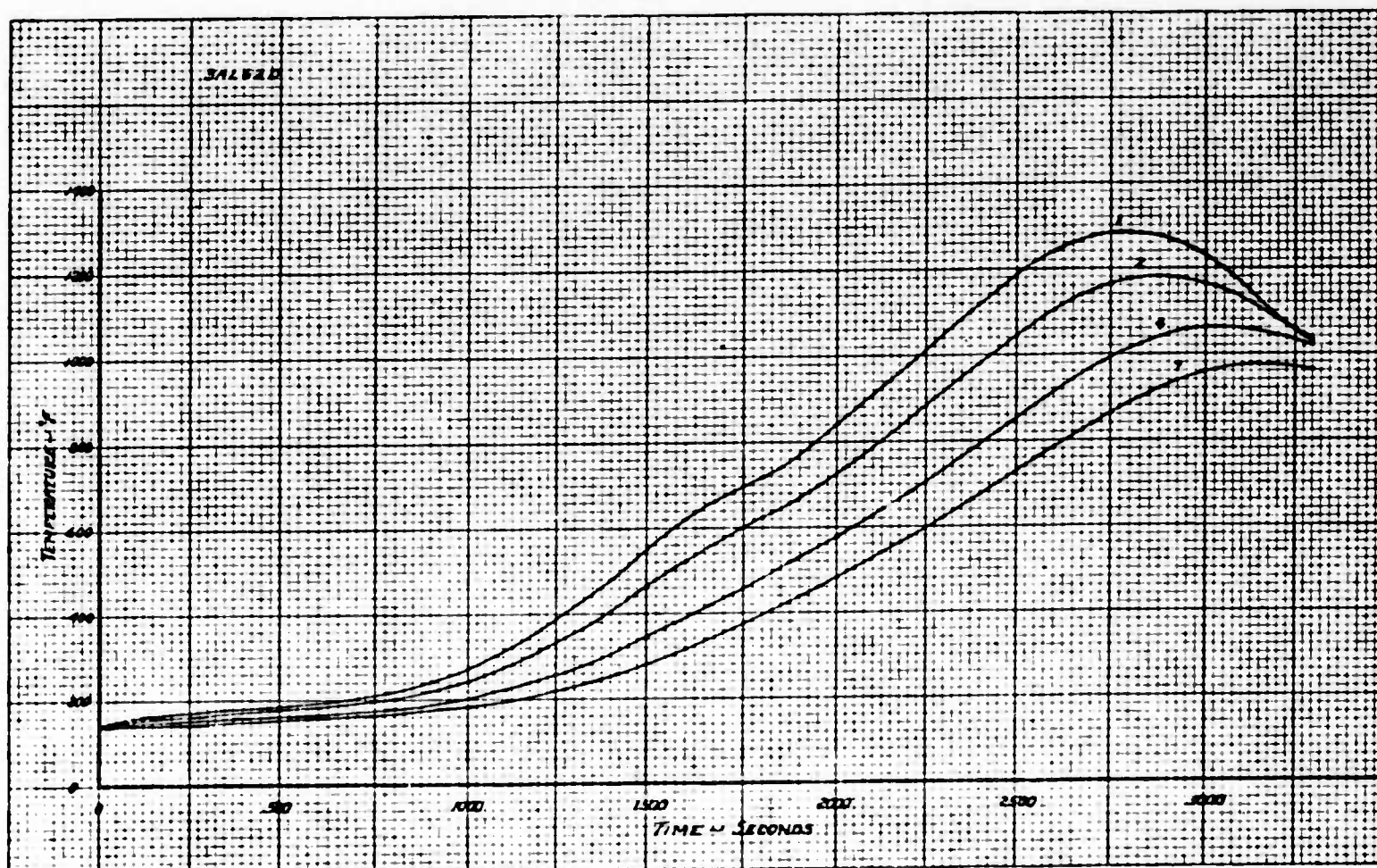
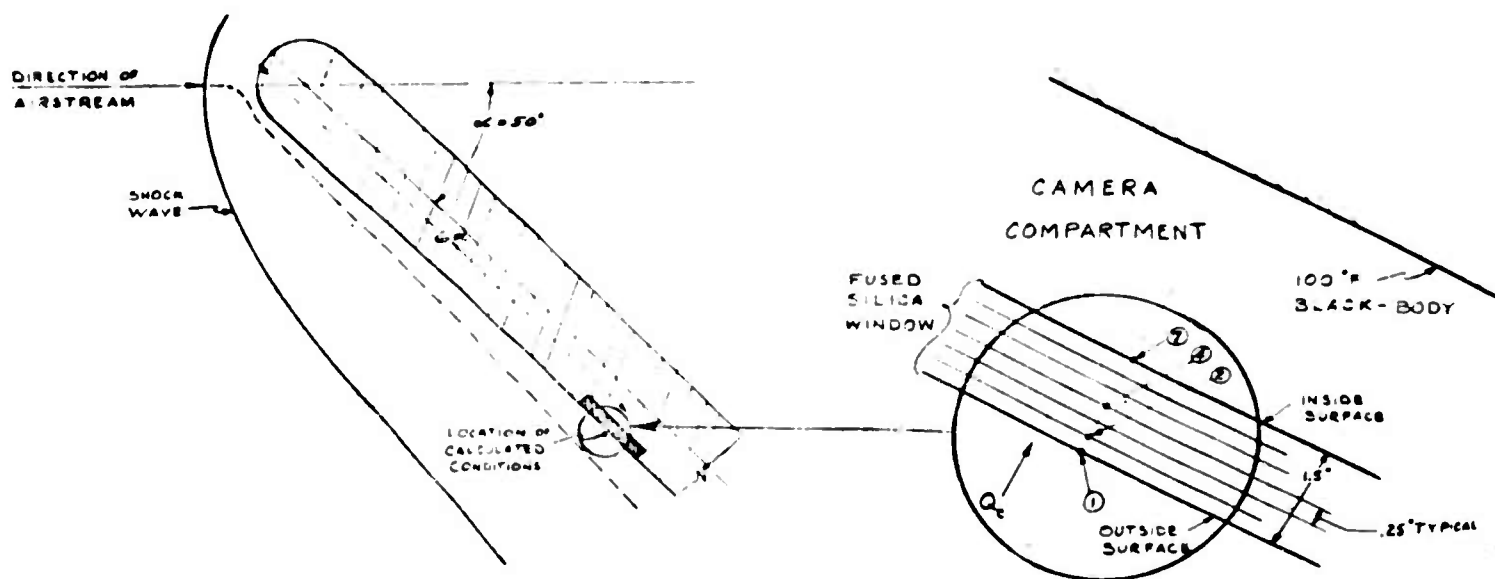


Figure 43 Trajectory 3A162D Temperature-Time Distribution Through a Diathermanous Fused Silica Window, 1 1/2" Thick, Located Six-Foot Aft, Flush with Lower Wing Surface, Laminar Flow





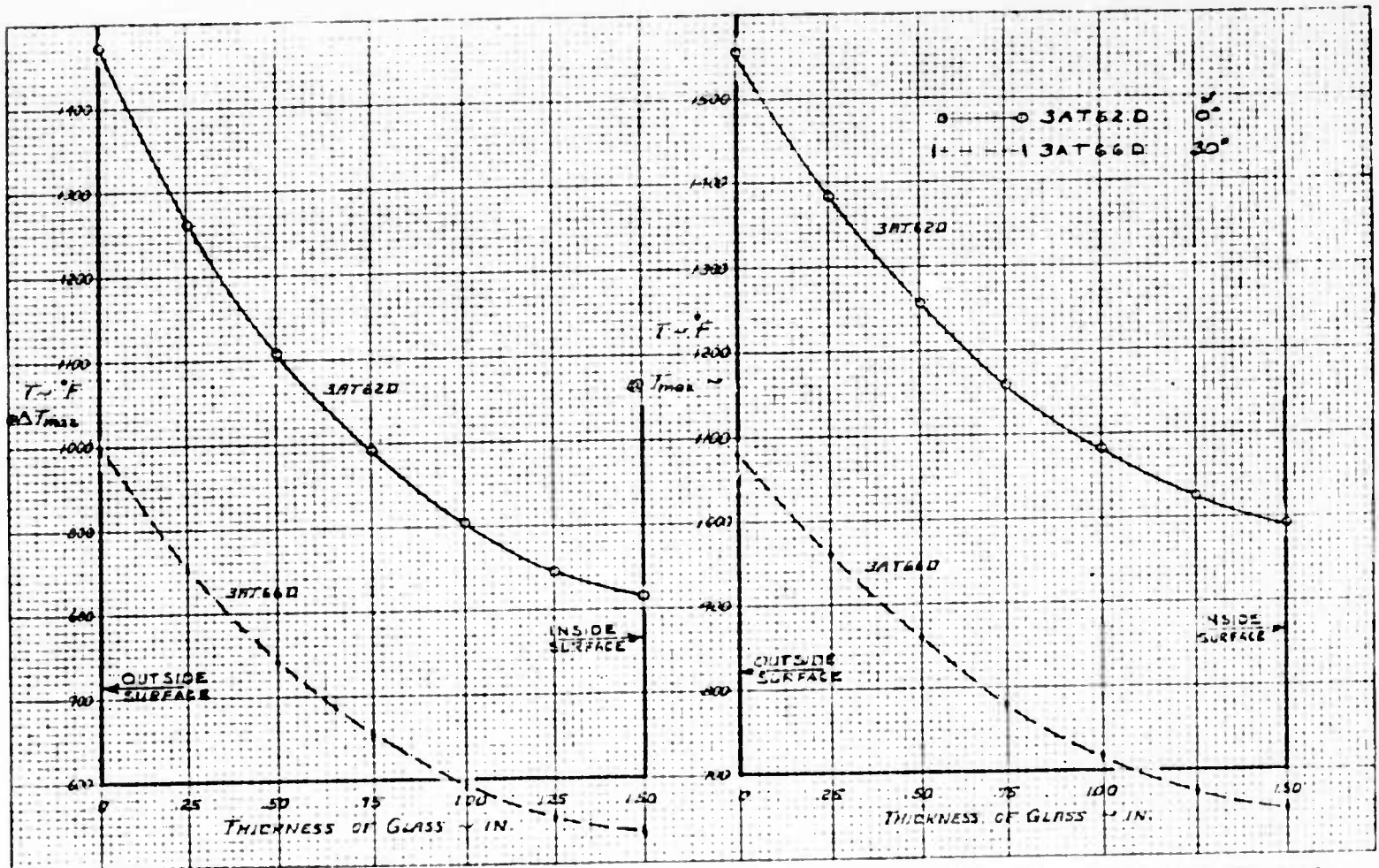
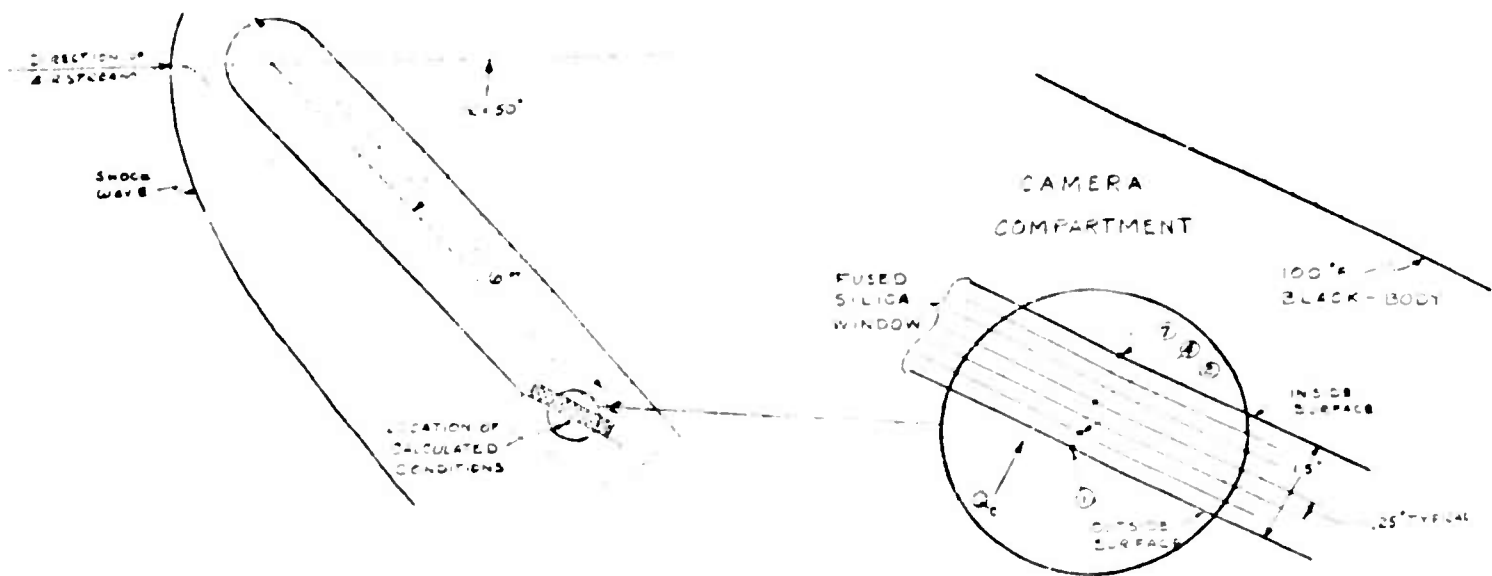


Figure 44 Temperature Distribution Through a Diathermanous Fused Silica Window, 1 1/2" Thick, Located Six-Foot Aft, Turbulent Flow at Instant of Maximum Temperature Difference Through the Window and at Maximum Temperature of Outer Surface. 3AT6 Trajectory





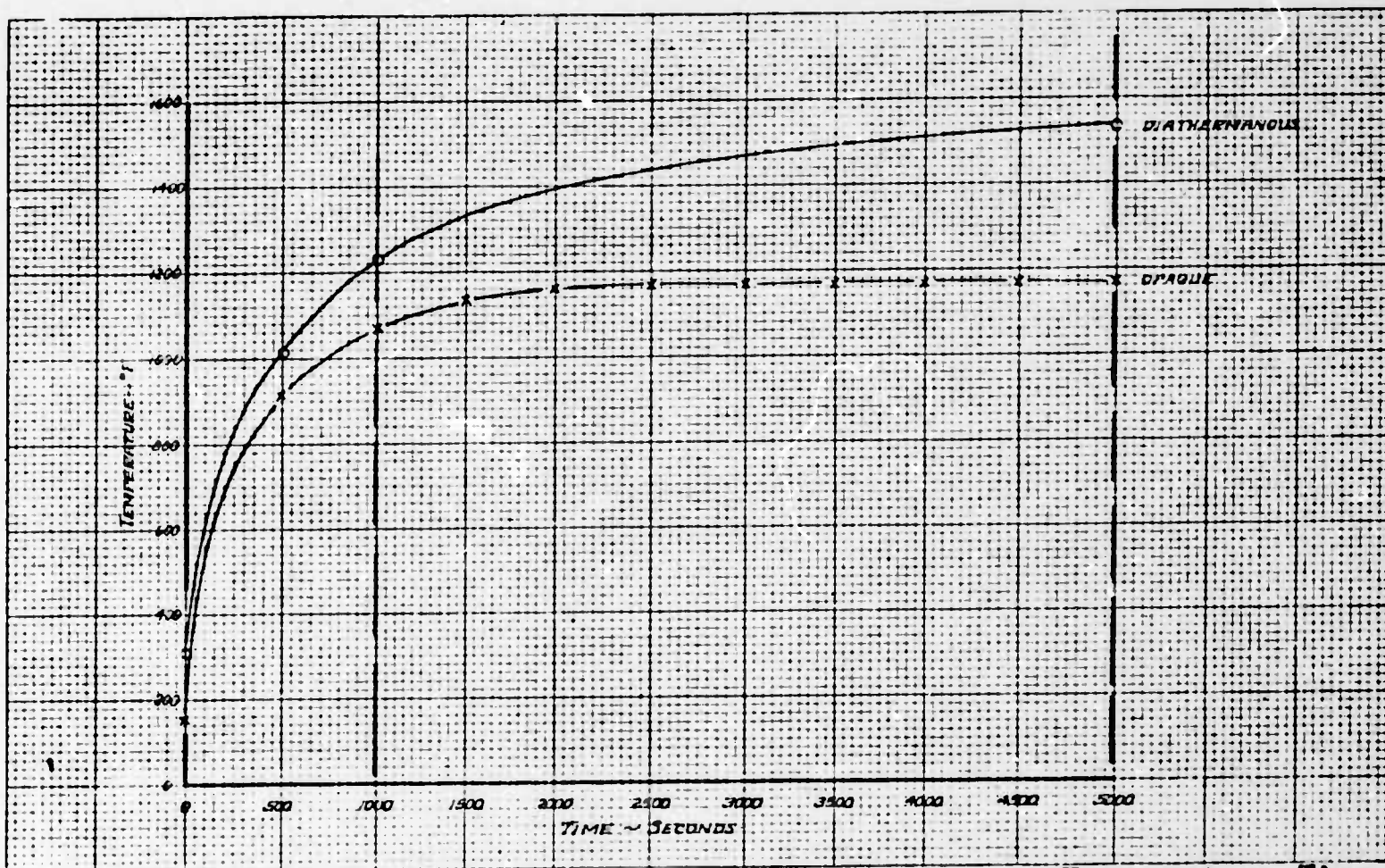
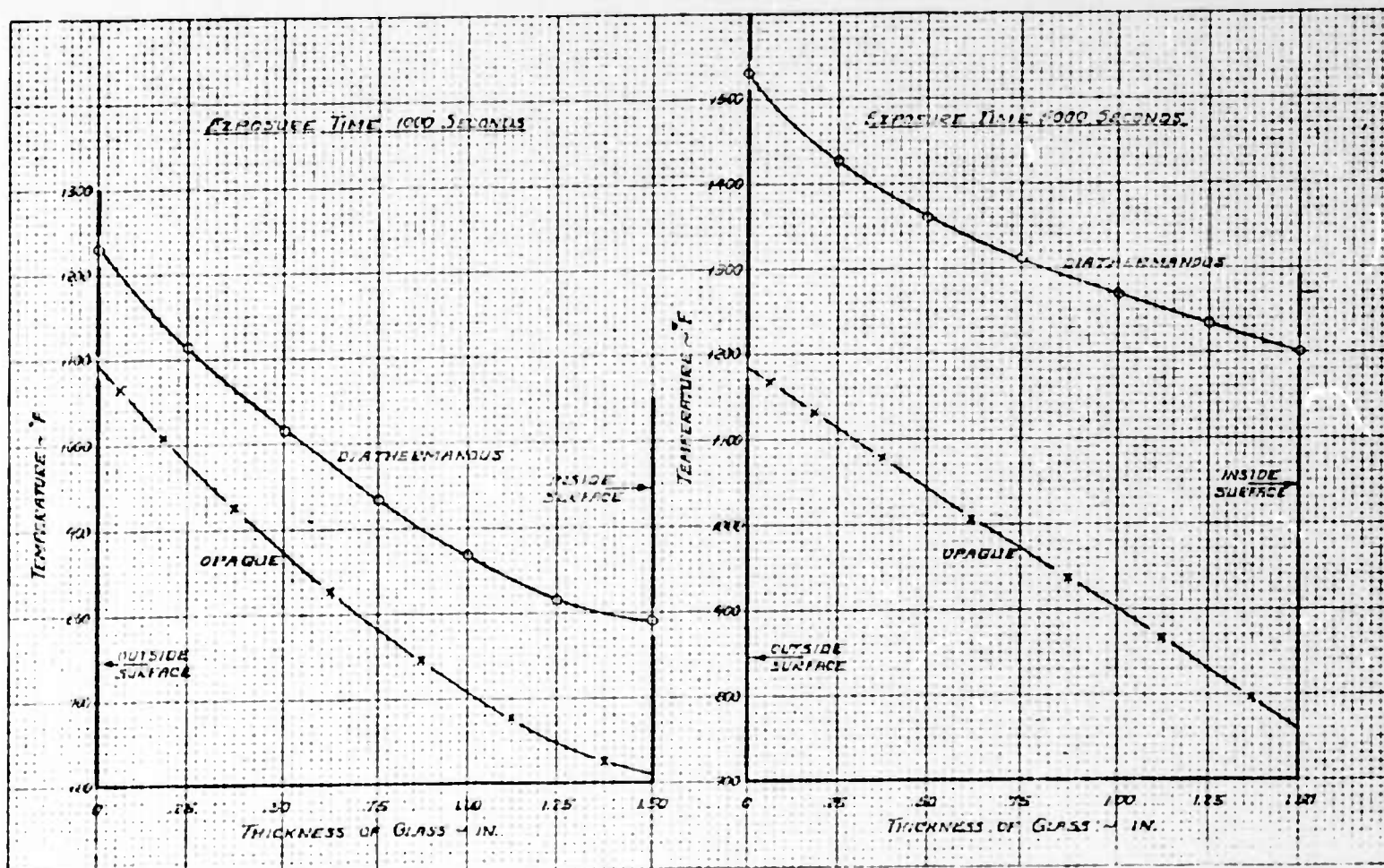


Figure 45 Comparison of Diathermanous and Opaque Temperature-Time Distributions Through a Fused Silica Window, 1 1/2" Thick, Exposed to a Heating Rate of 4.25 BTU/Sec ft<sup>2</sup>



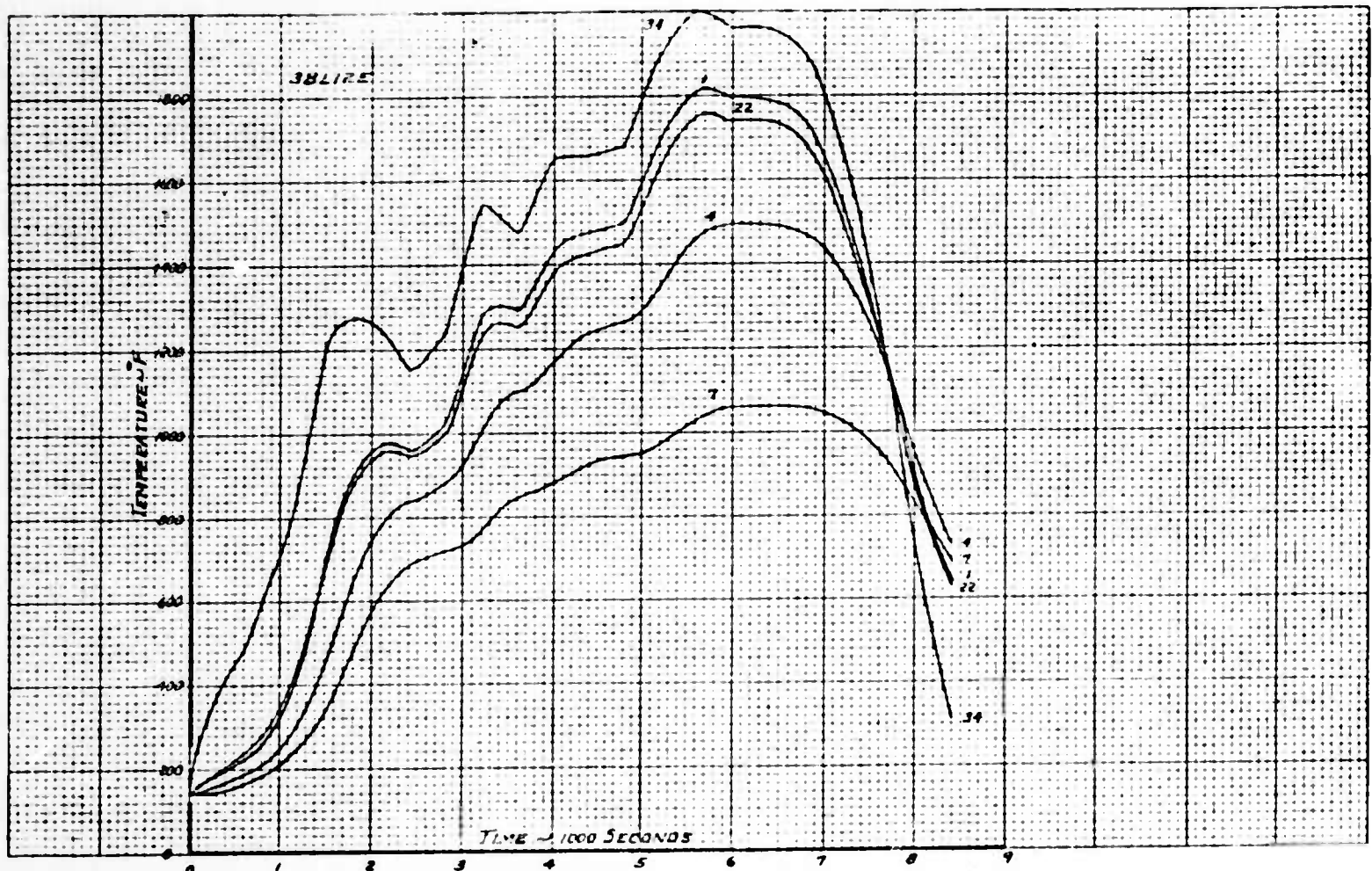
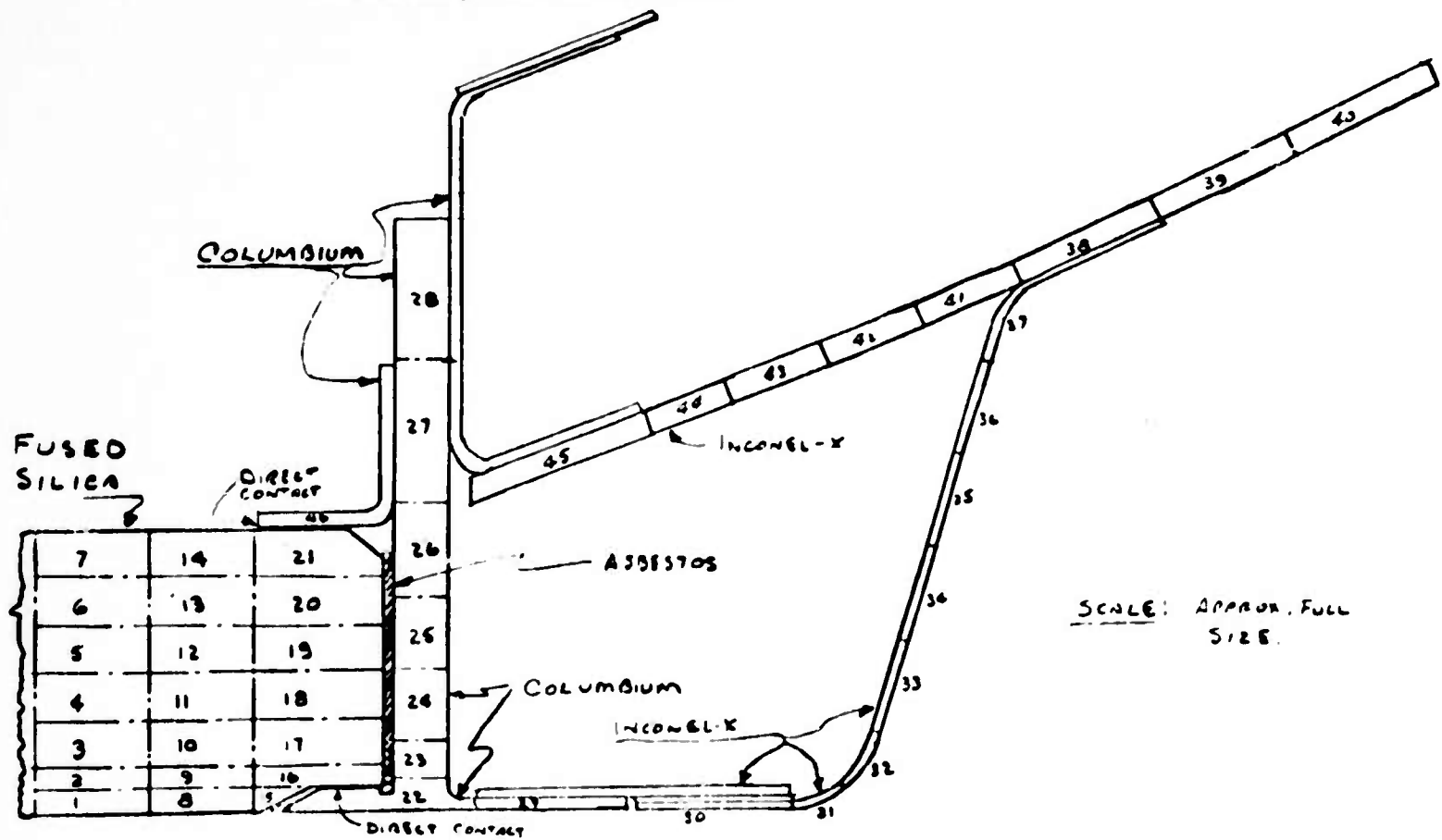


Figure 46 Trajectory 3BL12E Temperature-Time Distribution Through an Opaque Fused Silica Window, 1 1/2" Thick, Mounted as Shown, Located One-Foot Aft, Flush with Lower Wing Surface, Laminar Flow



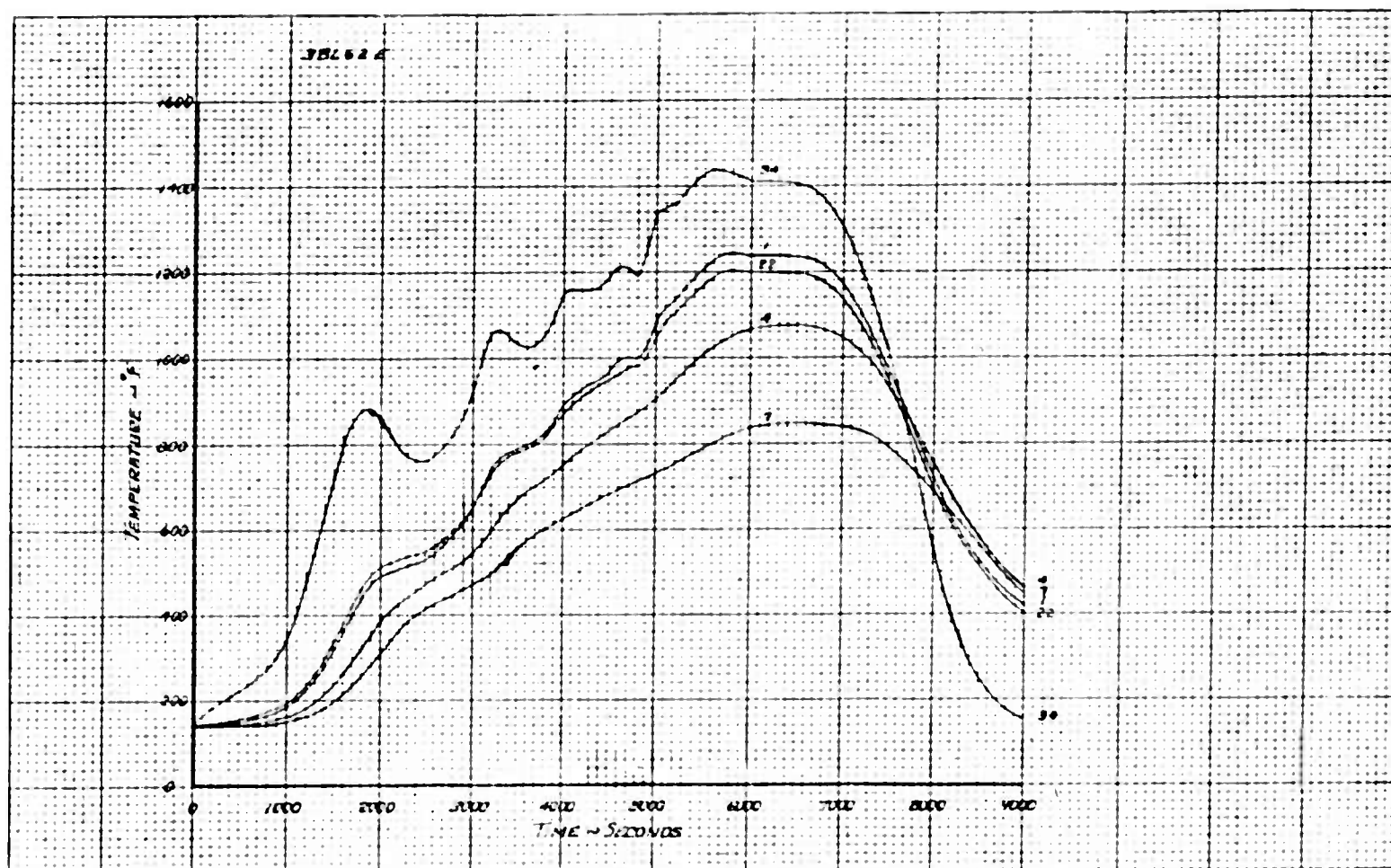
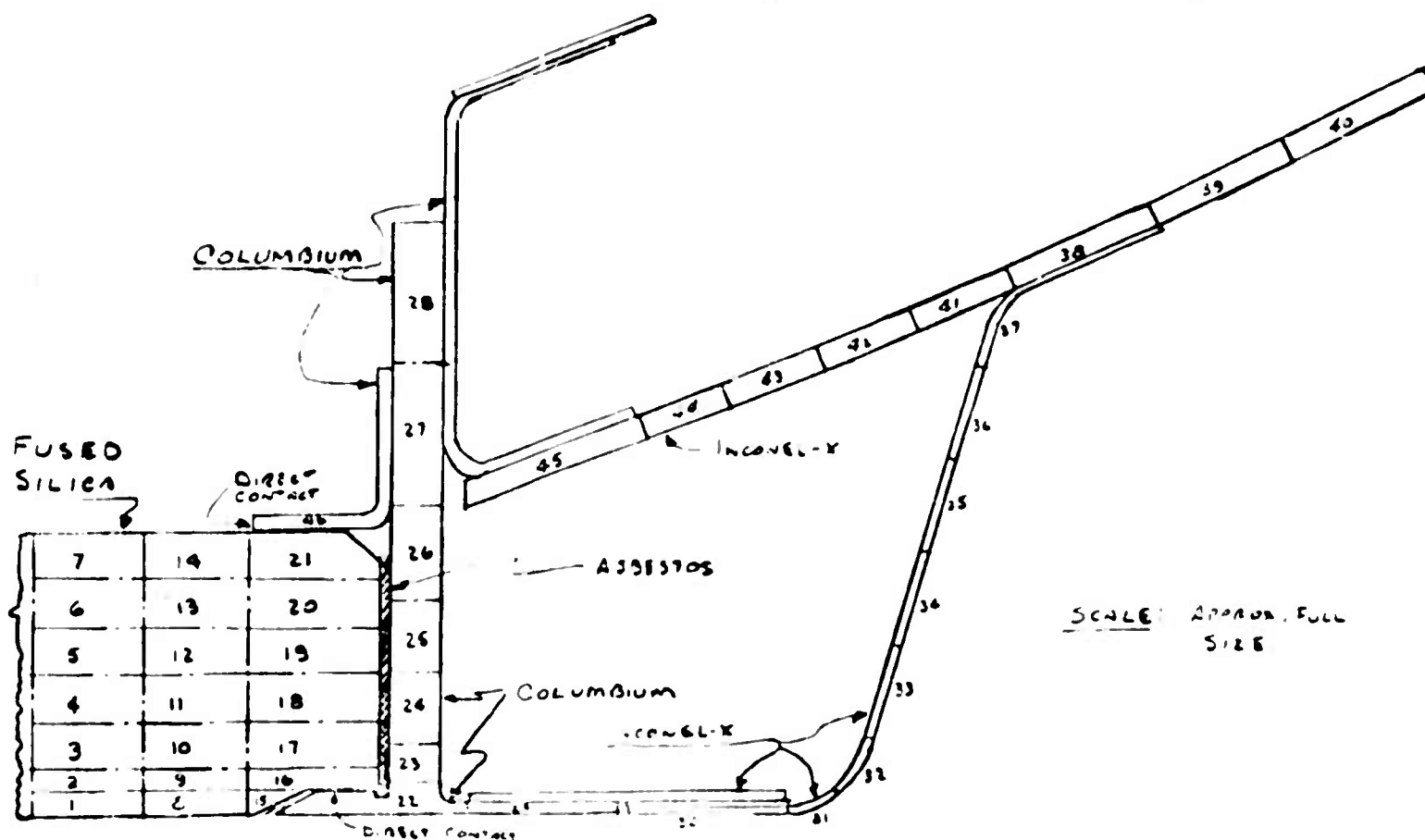


Figure 47 Trajectory 3BL62E Temperature-Time Distribution Through an Opaque Fused Silica Window, 1 1/2" Thick, Mounted as Shown, Located Six-Foot Aft, Flush with Lower Wing Surface, Laminar Flow





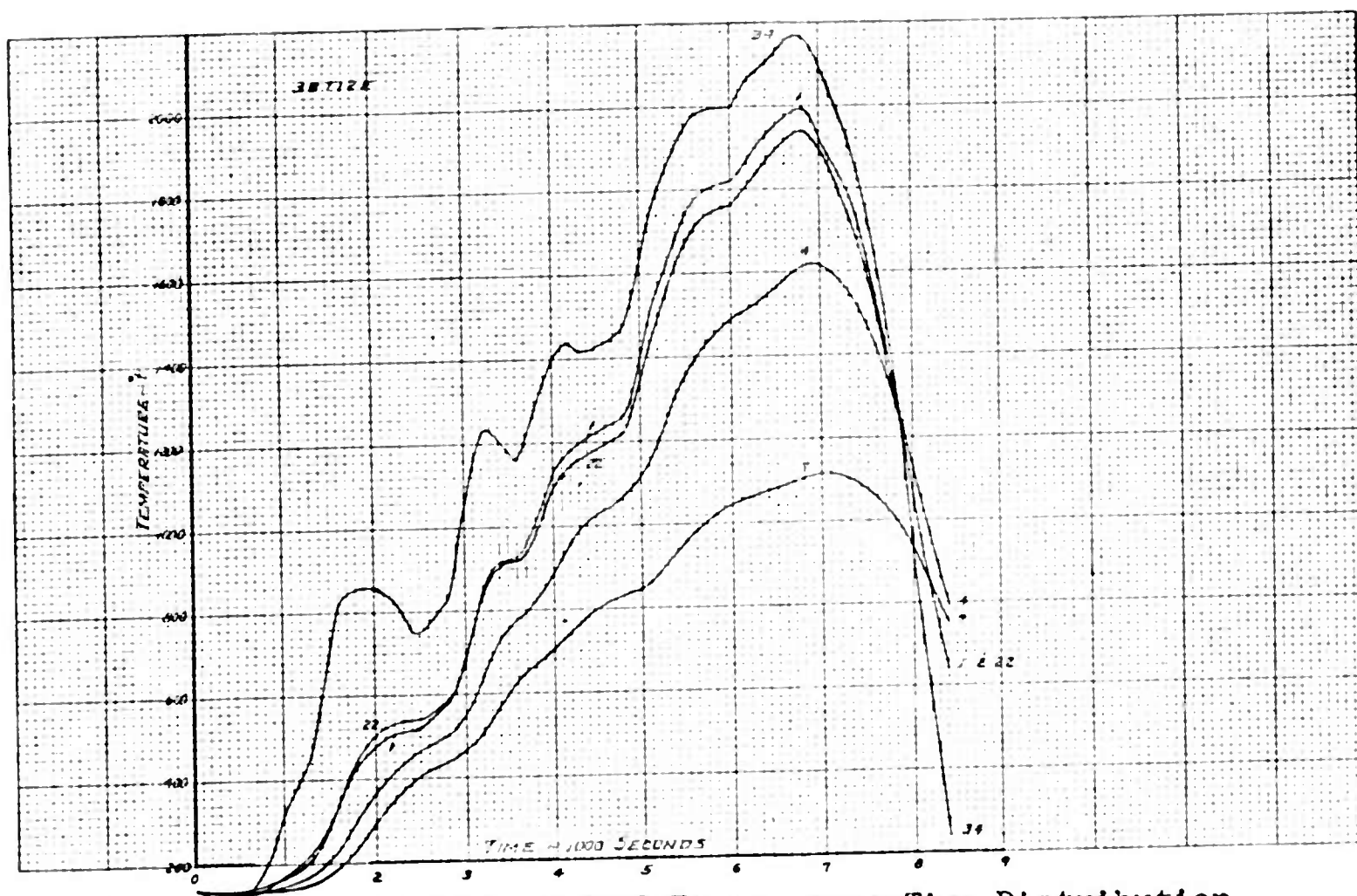
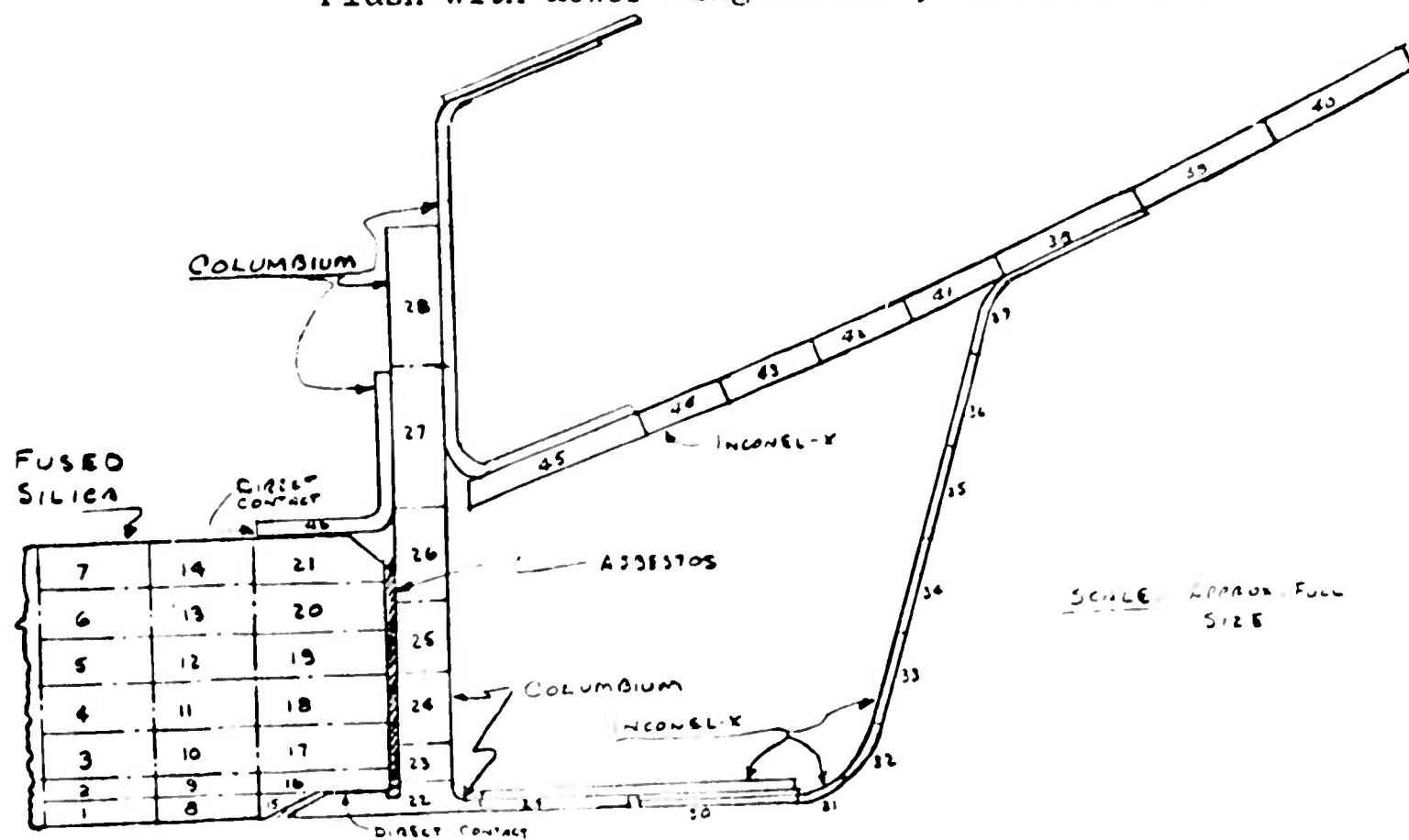


Figure 48 Trajectory 3BT12E Temperature-Time Distribution Through an Opaque Fused Silica Window, 1 1/2" Thick, Mounted as Shown, Located One-Foot Aft, Flush with Lower Wing Surface, Turbulent Flow





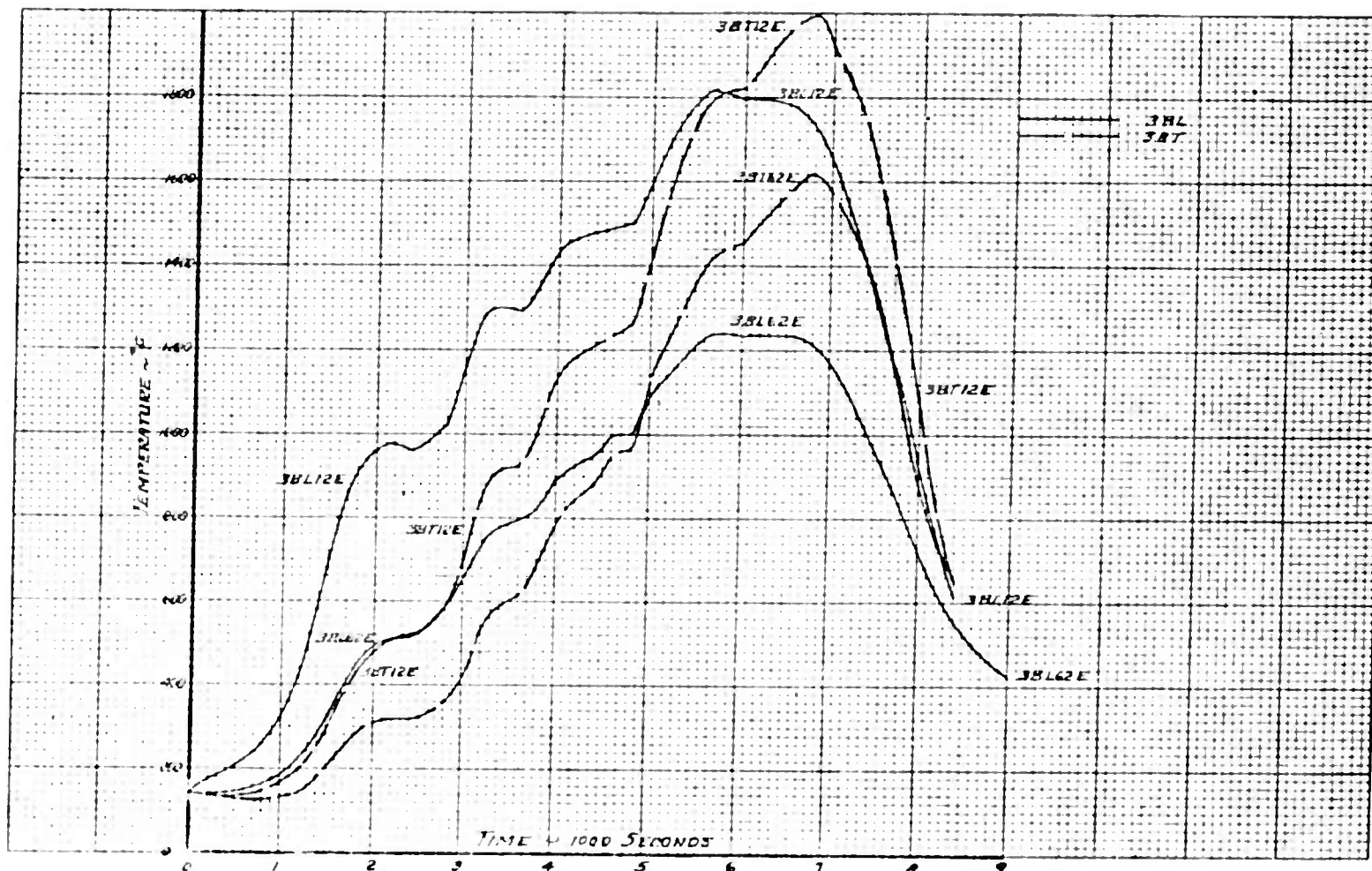
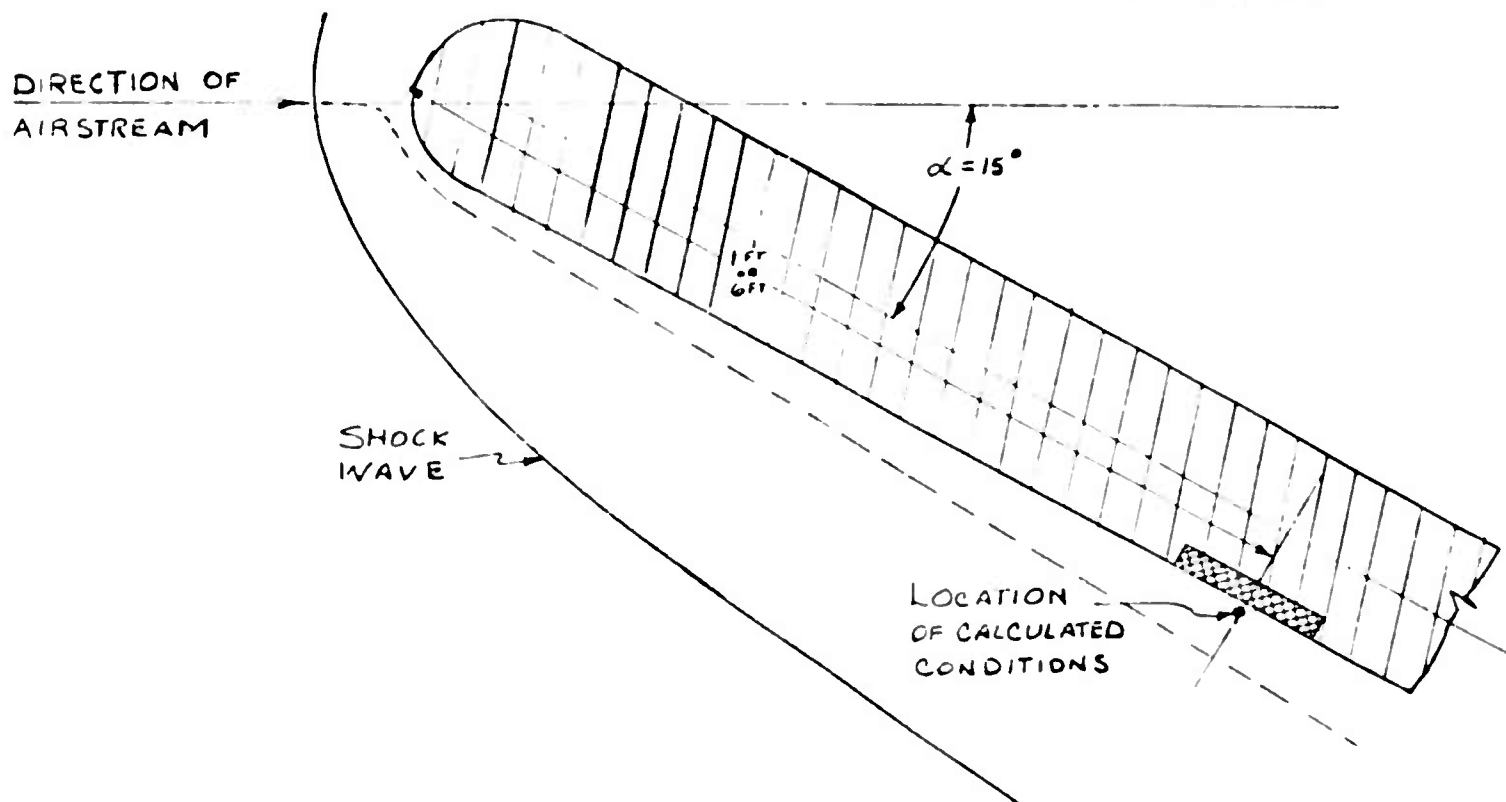


Figure 49 Summary of Trajectory 3B Temperature Versus Time on Outer Surface of an Opaque Fused Silica Window, 1 1/2" Thick, Located One-Foot and Six-Feet Aft, Flush with Lower Wing Surface, Laminar and Turbulent Flow



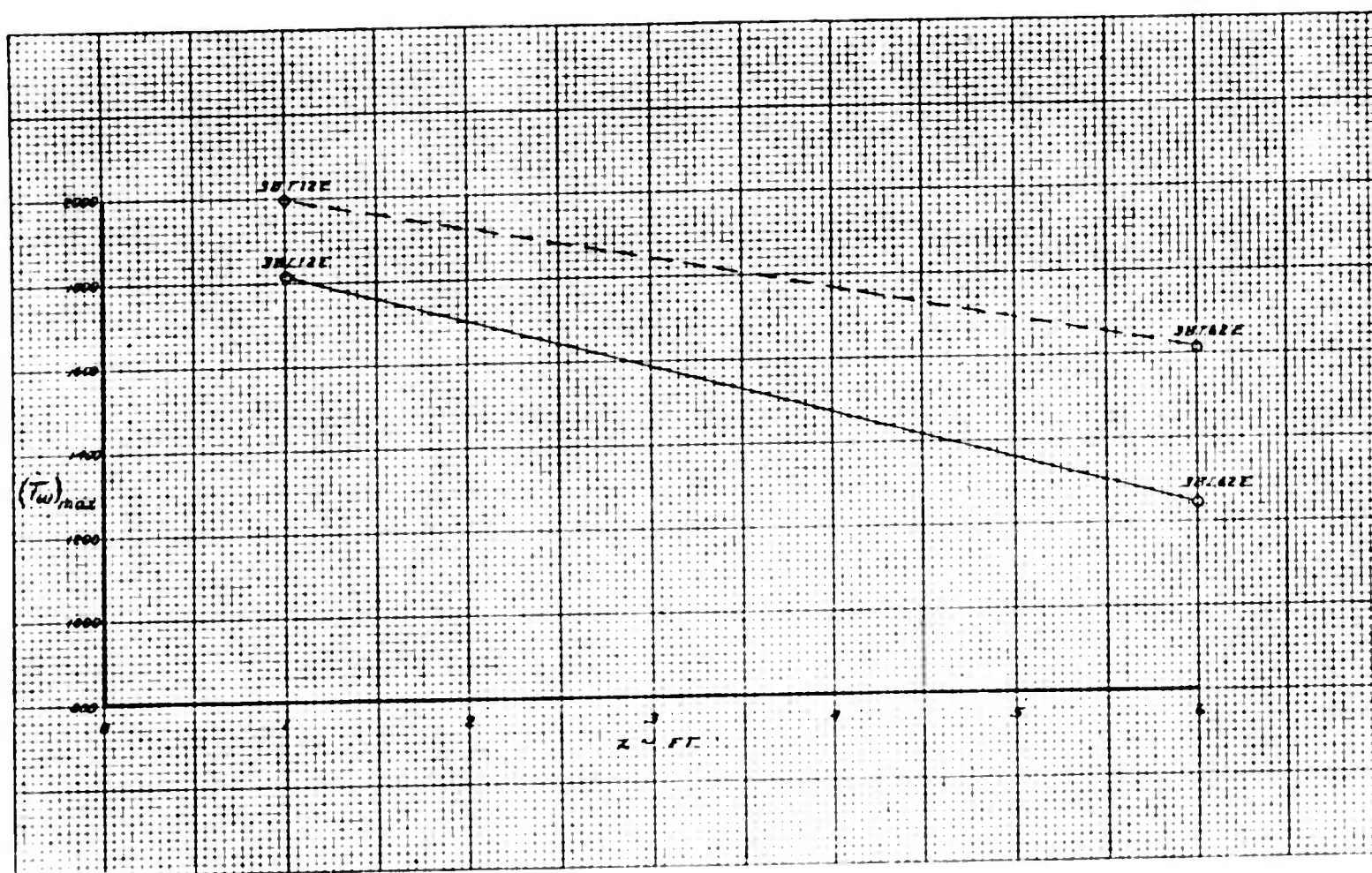
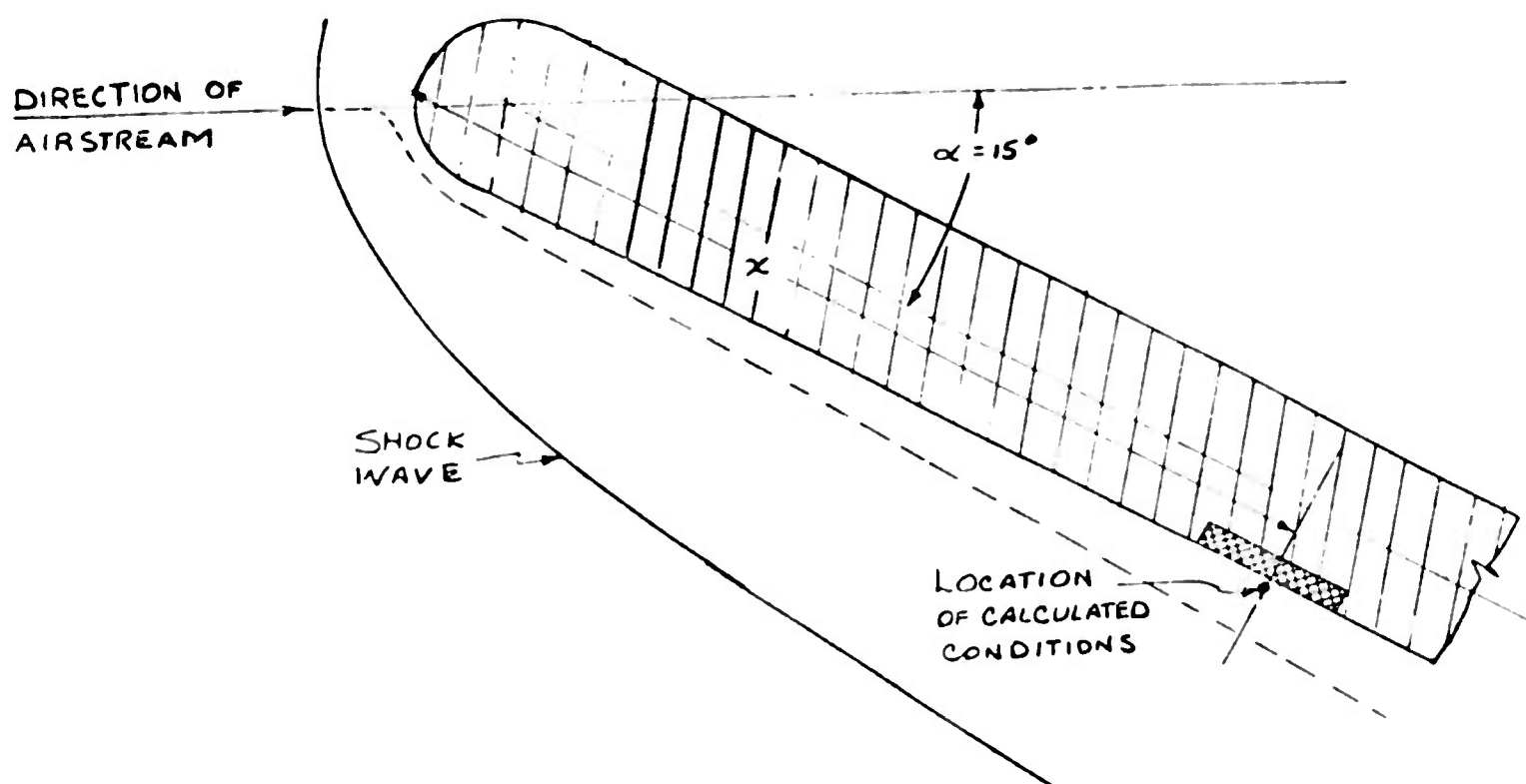
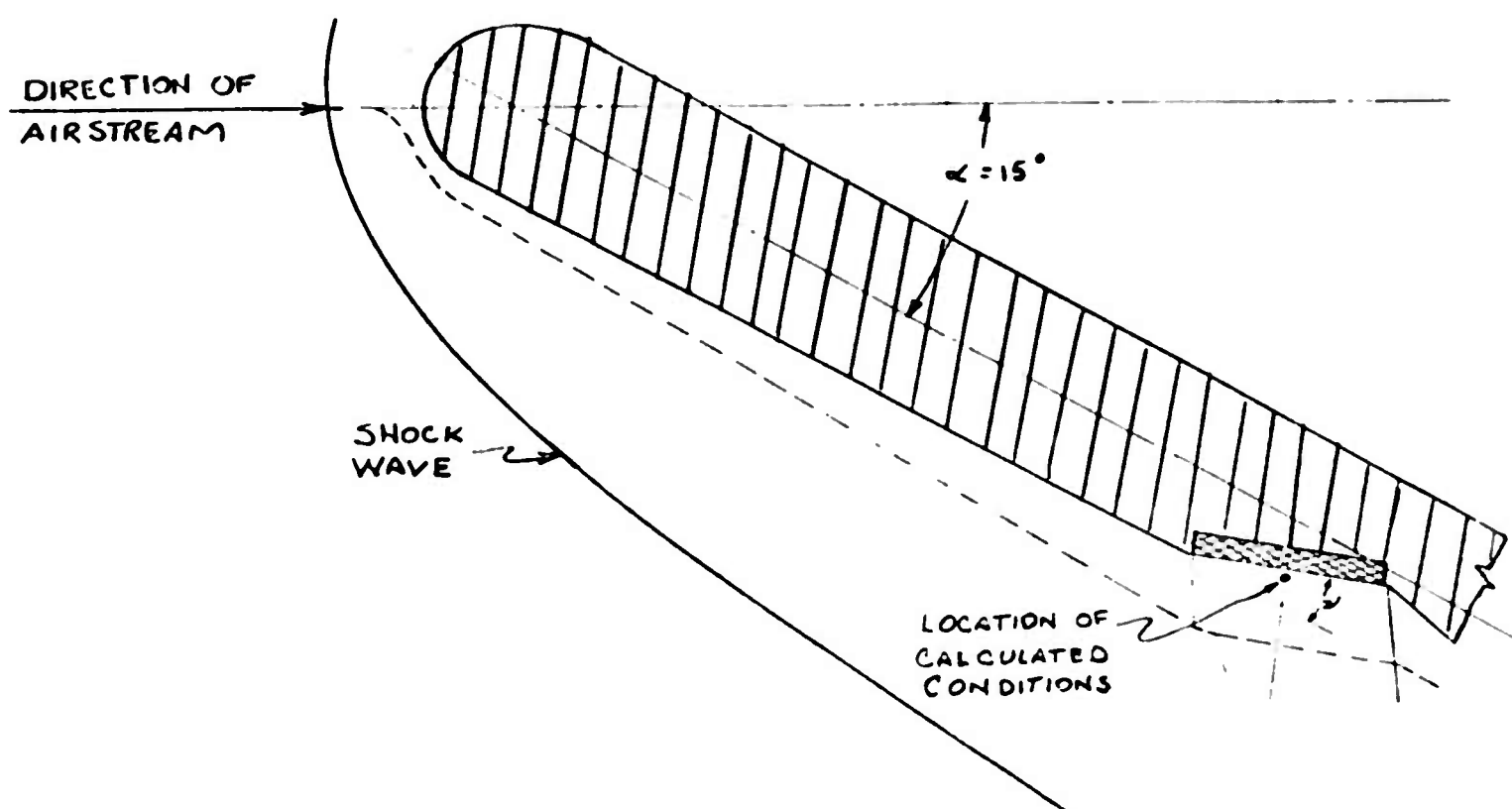
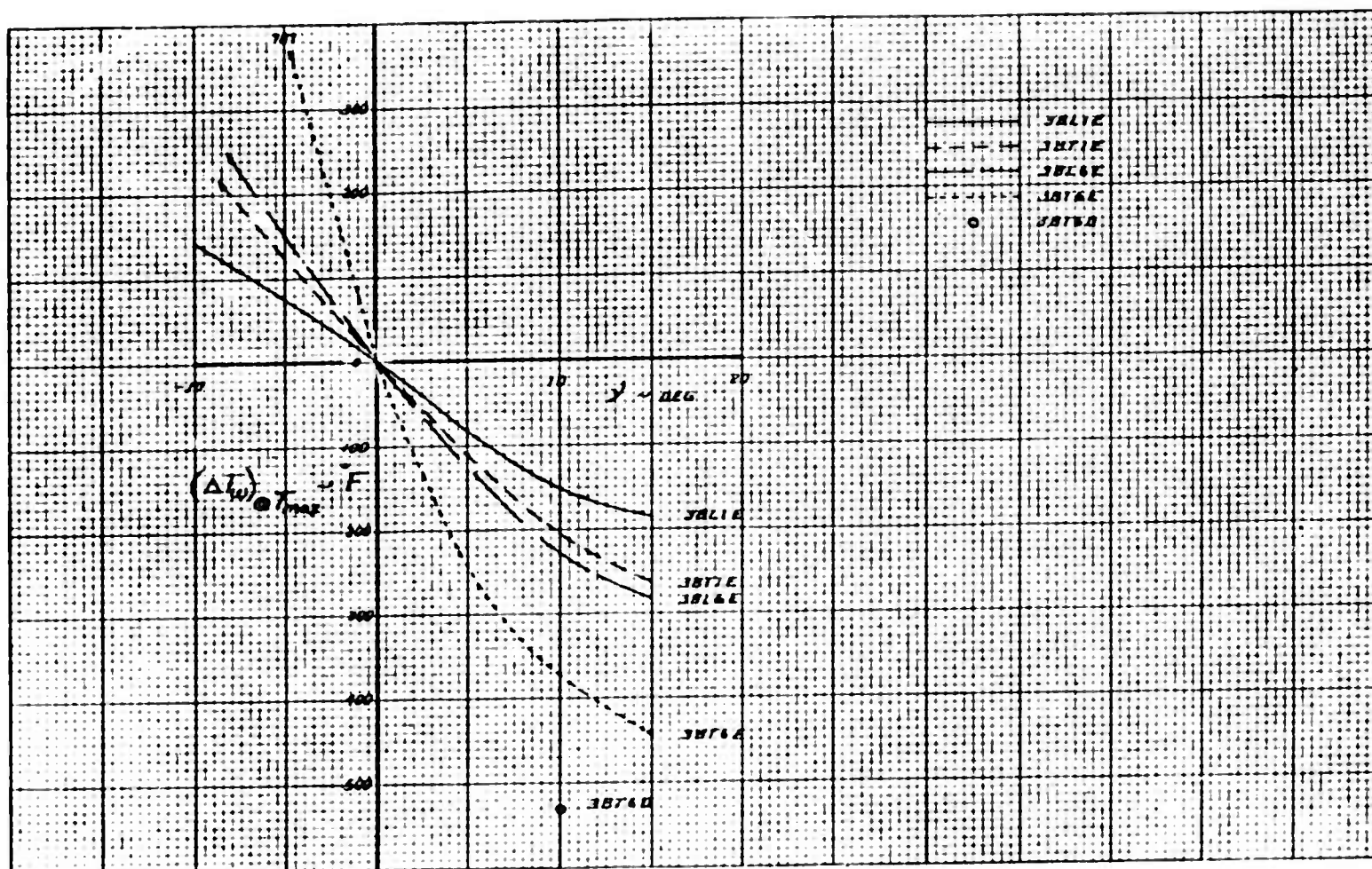


Figure 50 Effect of Location Along the Lower Surface Upon the Maximum Opaque Window Surface Temperatures Calculated for 3B Trajectory with Turbulent and Laminar Flow





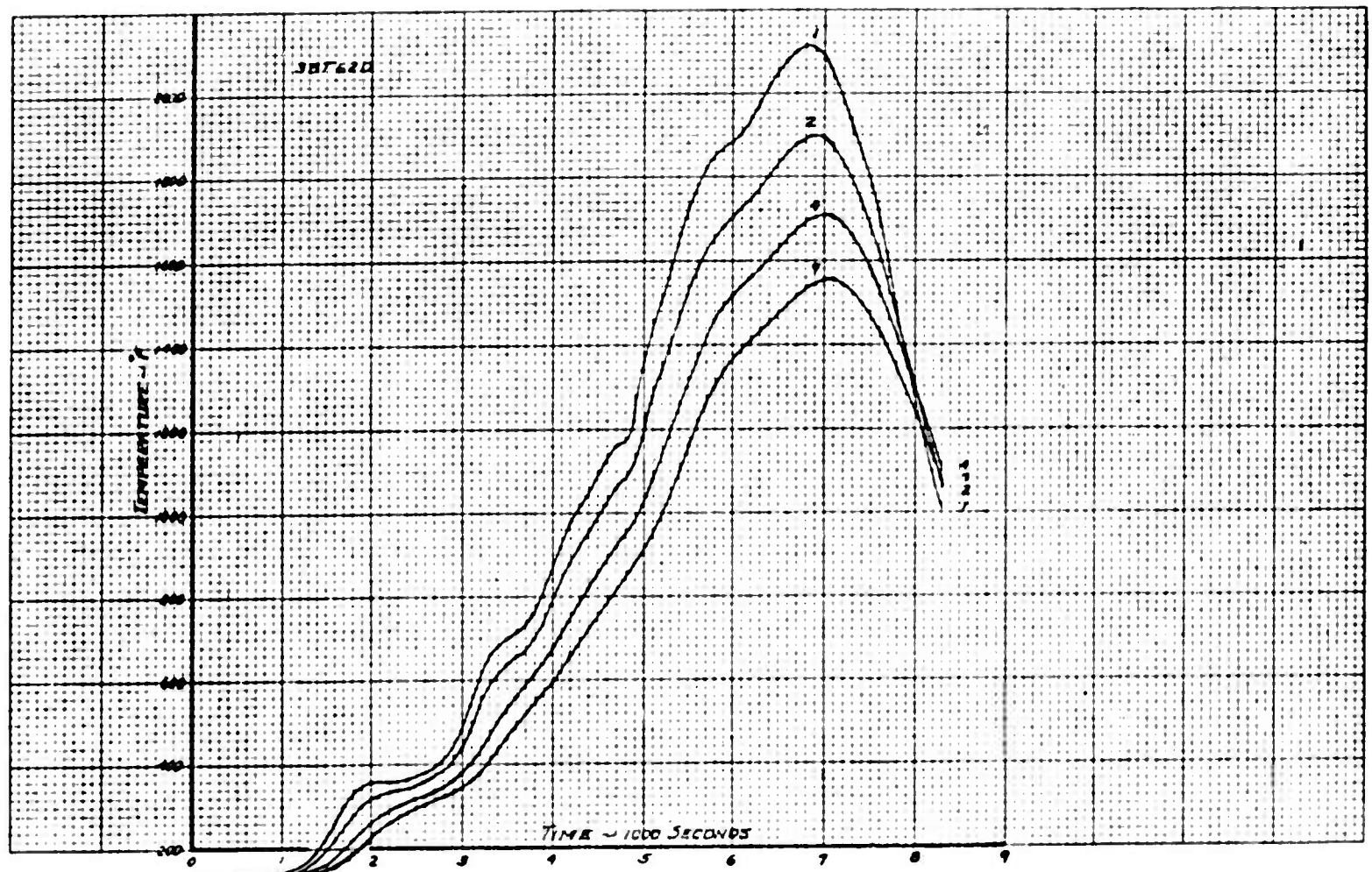
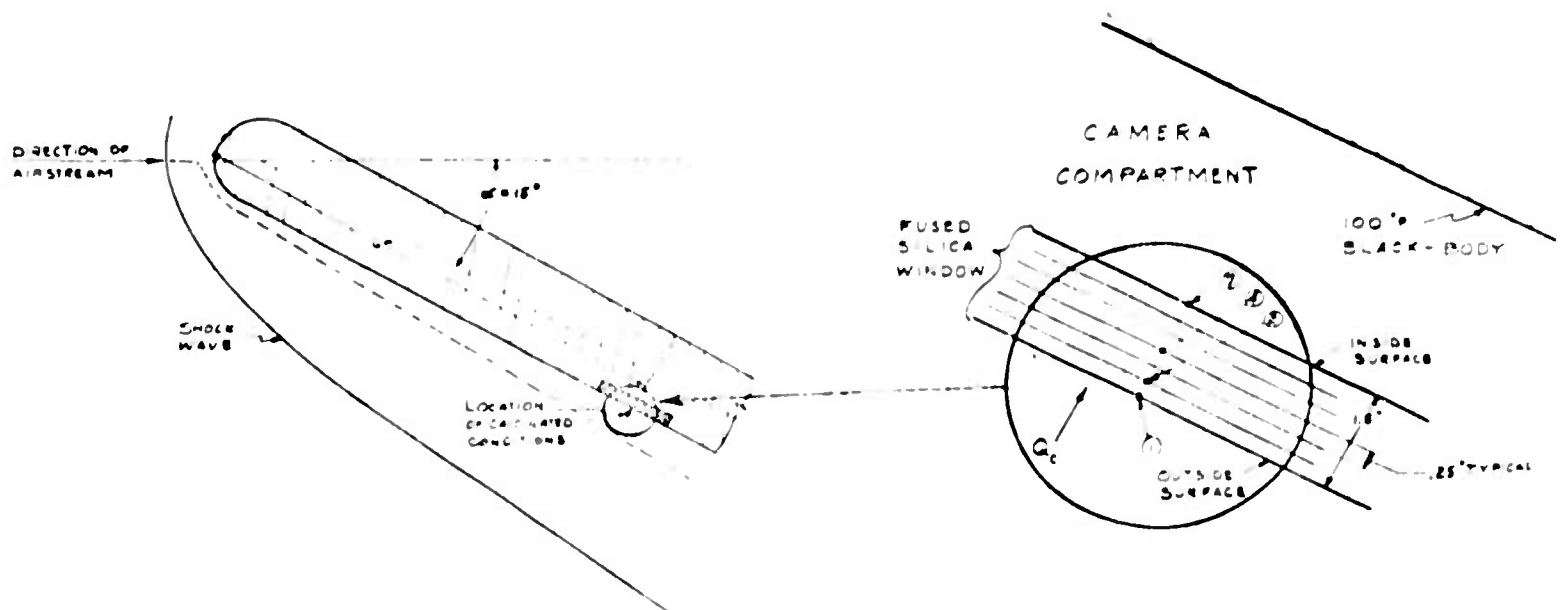


Figure 52 Trajectory 3BT62D Temperature-Time Distribution Through a Diathermanous Fused Silica Window, 1 1/2" Thick, Located Six-Foot Aft, Flush with Lower Wing Surface, Turbulent Flow





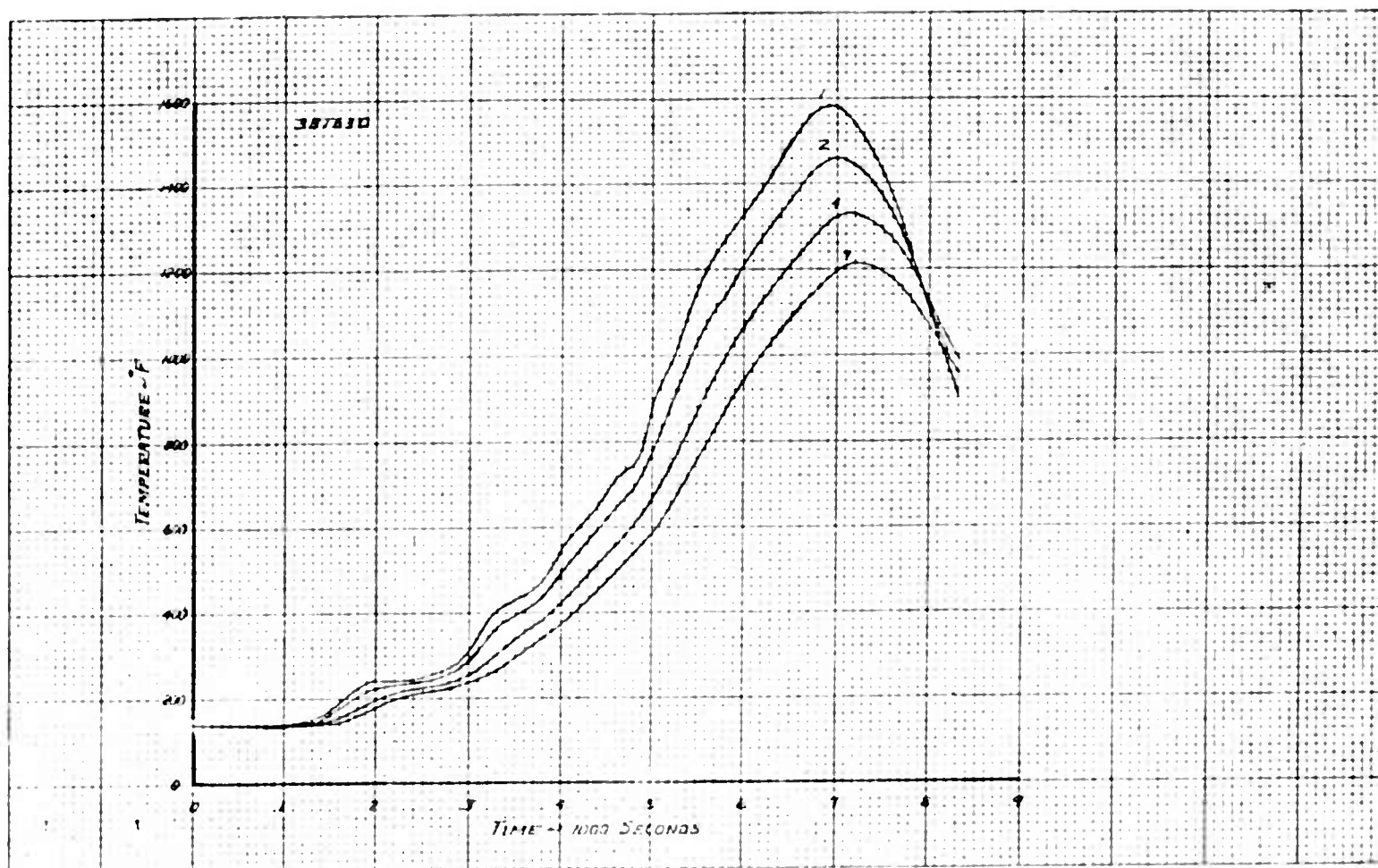
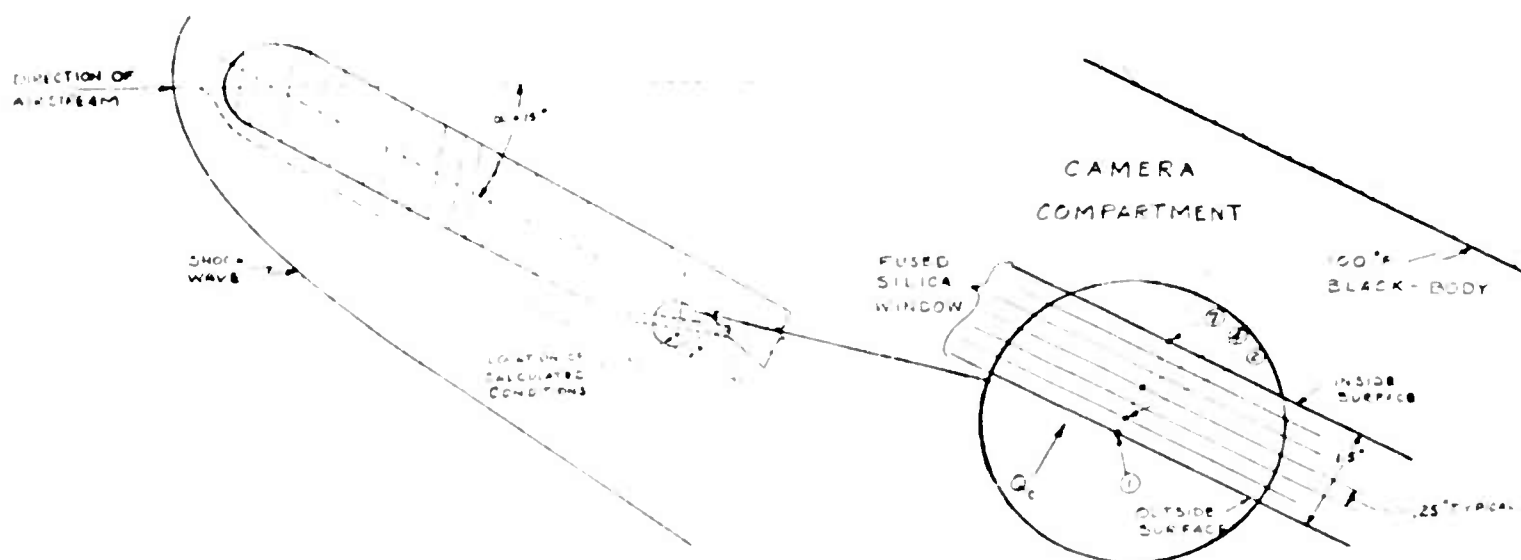


Figure 53 Trajectory 3BT63D Temperature-Time Distribution Through a Diathermanous Fused Silica Window, 1 1/2" Thick, Located Six-Foot Aft, at  $\psi = 10^\circ$  (Local Expansion Angle), Turbulent Flow



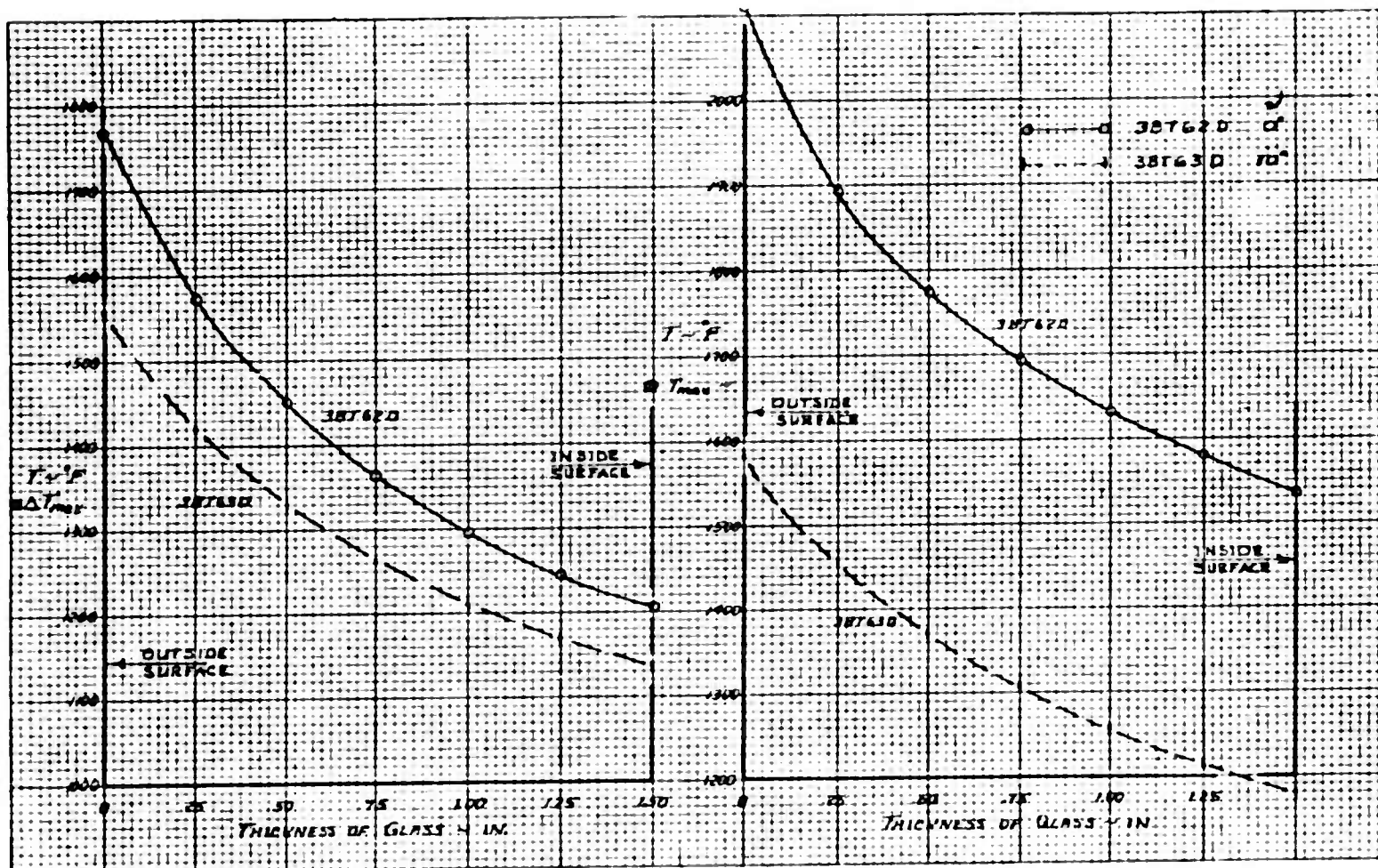
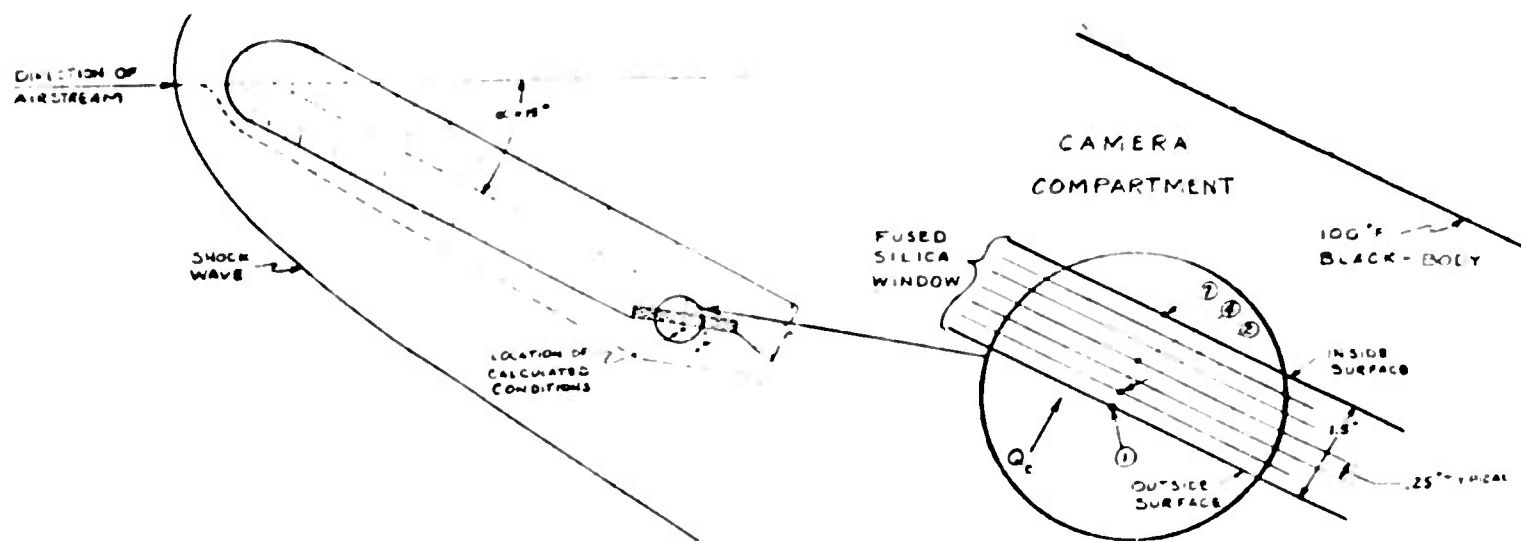


Figure 54 Temperature Distribution Through a Diathermanous Fused Silica Window, 1 1/2" Thick, Located Six-Foot Aft, Turbulent Flow, at Instant of Maximum Temperature Difference Through the Window and at Maximum Temperature of Outer Surface. 3BT6 Trajectory



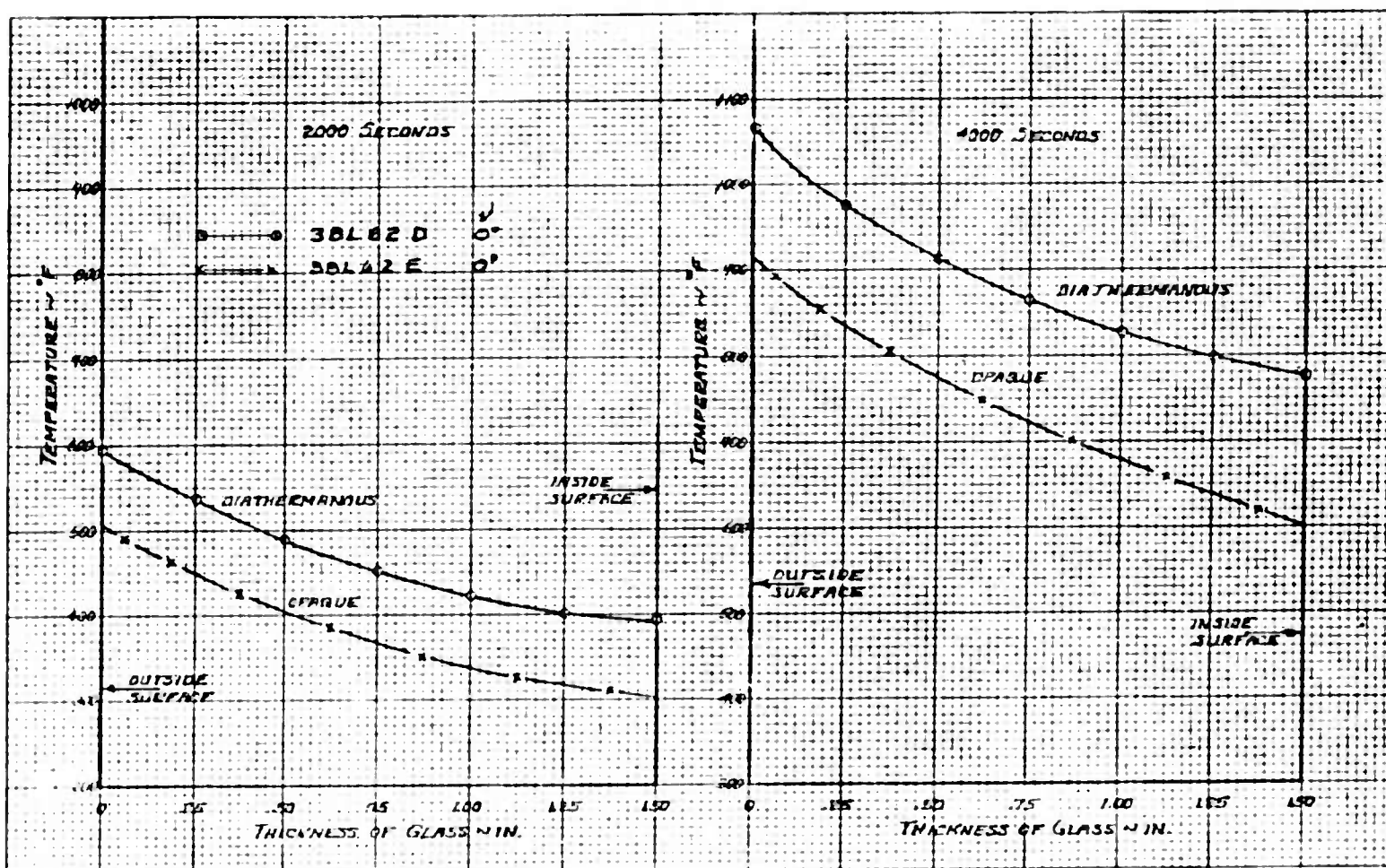
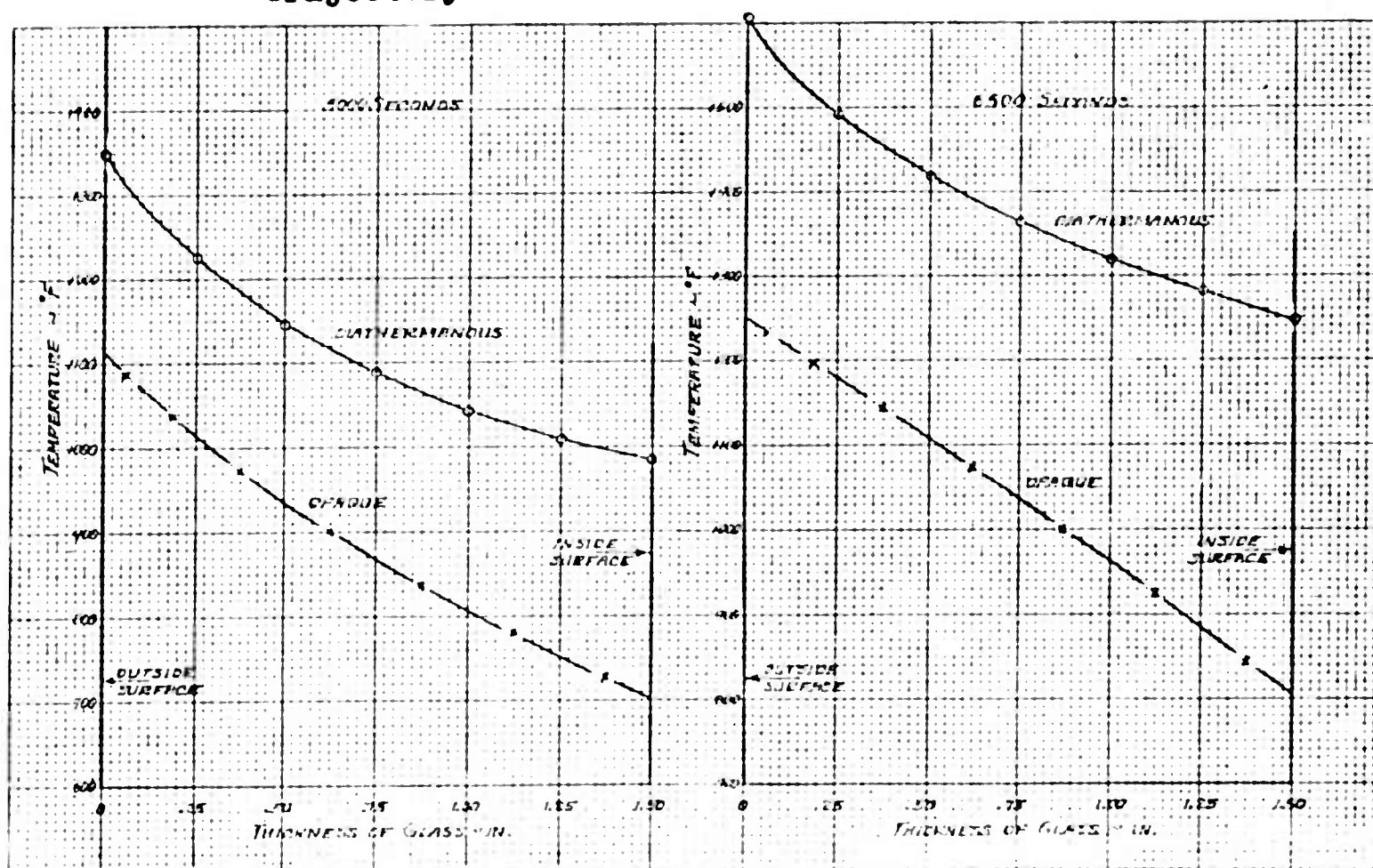


Figure 55 Comparison Between Opaque and Diathermanous Temperature Distributions Through a Fused Silica Window, 1 1/2 Thick, Located Six-Foot Aft, Flush with Lower Wing Surface, Laminar Flow at Given Times During 3BL6 Trajectory



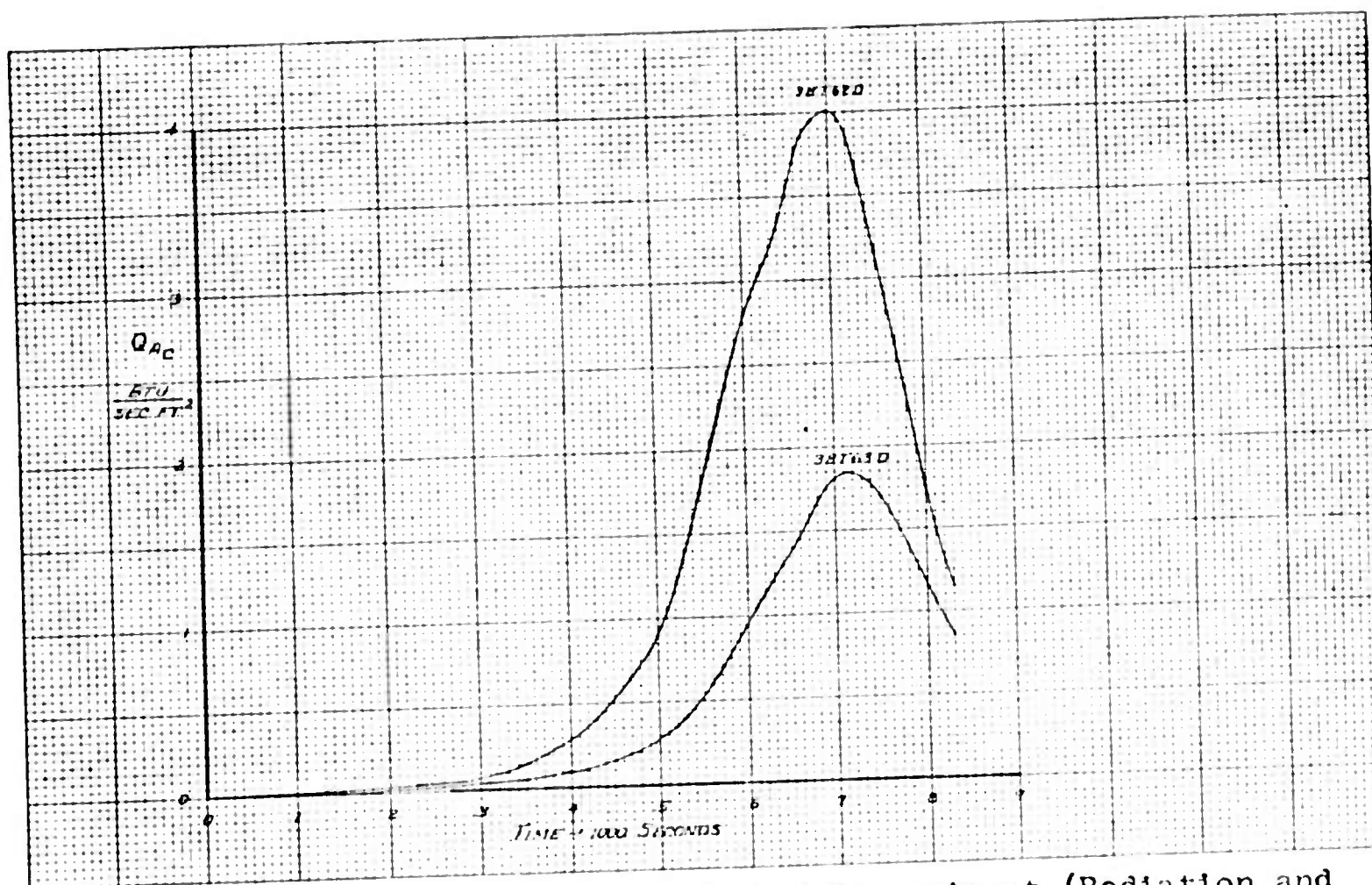
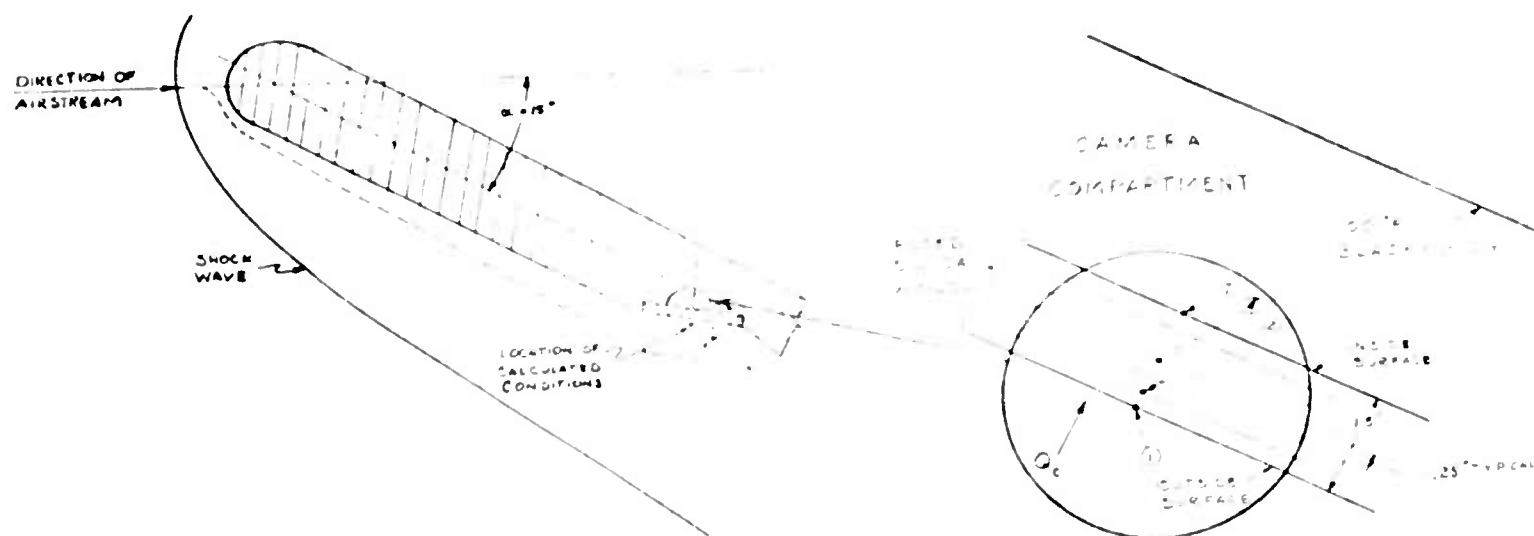


Figure 56 Heat Transfer Rates to the Compartment (Radiation and Convection) Through a Fused Silica Window, 1 1/2" Thick, During 3BT6 Trajectory with Window Flush and at a Local Expansion Angle of 10°





## Section V

### OPTICAL ANALYSIS AND TESTS

#### SECTION SUMMARY

Previous theoretical work yielded tentative predictions of the amount of bending induced in an aircraft camera window due to temperature gradients and pressure differentials arising from the aerodynamic environment. The effects of window curvature on photographic image quality have also been studied. The purpose of the present work is to verify or refute the analytical predictions on the basis of laboratory measurements of the optical effects produced by controlled changes in window curvature, and extend the analytical work if necessary.

It had first to be determined whether laboratory measurements could feasibly be utilized as a valid test of the theory. In actual flight, photographic resolution is the end product of the degrading effects of a great many factors. They include target configuration, heat waves emanating from the target, atmospheric turbulence and weather, air turbulence near the aircraft, structural properties and temperature of the window itself, camera compartment environment, camera design, film characteristics, and experience and judgment of the photointerpreters, to name a few. In the laboratory, the attempt is made to keep all parameters except one fixed, and to vary that one in a controlled manner. Also the measurement must utilize a sensor other than the high acutance camera used in the aircraft, and the relations between the laboratory sensor and the film-camera sensor must be clearly defined. The first part of the present study, therefore, was directed toward establishment of a suitable test procedure, analytical justification for this procedure, and specification of the quality required of the glass test panels.

The actual testing was divided into two parts, the measurement of optical deviation resulting from an induced window curvature due to pressure differential and the measurement of optical deviation resulting from an induced curvature due to a temperature gradient through the window along the line of sight. Pressure differential tests were made by placing small collimators inside a pressure vessel and viewing them with an external collimator as the vessel pressure was changed. In these tests the glass test panels were held at room temperature and with no temperature gradient. Temperature gradient tests were made by subjecting one surface of the panel to a radiative heat source, and viewing the deviation of a collimated beam as the temperature and gradient were altered. Initial results showed wide disagreement with the available theory. It became necessary to modify the assumptions used in the early analysis to obtain correct results. This was accomplished near the end of the project, and the experimental results show qualitative agreement with this later theory.

#### DISCUSSION OF WINDOW QUALITY

##### Required Test Window Quality

As part of the laboratory verification of effects on photographic image quality of parameters such as thermal gradient, pressure differential, and

shock wave luminosity, it was necessary to utilize glass test panels which may not be of the same quality as those used in actual aircraft. There are two basic methods of establishing the relationship between the degrading factors and the resultant image quality:

- (1) Comparison of resolution
- (2) Measurement of deviation

The first method is based on visual comparison of photographic images of bar charts specifically designed to permit subjective evaluation, or alternatively, the photometric scanning of photographic images of sine wave charts, resulting in a quantitative assessment of resolution capabilities. These techniques would be useful in evaluation of large differences of resolution resulting from the total effect of all factors contributing to the degradation. The second method, determination of deviation of light rays at selected points of a glass test panel, was proposed by the Contractor as a sensitive measure of the effects of individual environmental factors, Reference 5. Because of this sensitivity, however, the question arises as to how closely the test window must simulate the optical quality of operational photographic windows, in order that the experimental data may be validly extended to window design.

The glass ordinarily specified for use as a photographic window in Air Force programs is required to meet or exceed the optical quality prescribed in Military Specification MIL-G-1366, "Glass, Window, Aerial Photographic." The specification stipulates, among other things, the following optical characteristics.

- (a) A surface finish equivalent to that typical of high grade plate glass.
- (b) A wedge tolerance ranging from 4 arcseconds to 6 arcminutes, depending on the application and to be specified by the procuring activity.
- (c) No striae visible when observed at distances from  $1/2$  to  $1-1/2$  meters, depending on the wedge tolerance.
- (d) No bubbles larger than  $1/32$  inch in diameter.
- (e) For Group M glass only, a flatness of one wave length per 6 inches diameter area.

The characteristics of importance, which might set apart such glass from selected plate glass, are parallelism and index variations.

In the work that follows, the precise amount of flatness and freedom from inhomogeneity is determined for windows used in conjunction with high resolution aerial photographic cameras. This work served as an initial starting point for defining the quality of the glass. The work was completed in the early stages of the program and was developed only to give an indication of the quality necessary for good optical images. Later analysis was necessary to establish the exact quality needed for laboratory work.

Variations in index and parallelism can be accounted for as contributing power to the optical system. These defects would cause defocusing of a certain percentage of the energy incident upon the optical system. By studying these variations in an interferometer, it can be determined how much power will be contributed and what percent of the energy will be effected. It should be noted at this time that the effect of a window on an image forming system depends upon the type of system involved and the quality of the image. An exact analysis of the optical effects of a window on the image forming ability of a photographic lens is a function of the characteristics of the lens. Thus it becomes necessary to evaluate a great many parameters before exact analysis can be performed.

In the mathematical analysis that follows, the effect of adding power to an optical system is investigated. From the results of this investigation, the amount of power that can be tolerated will be determined. In the absence of precise data about the optical system in use, several assumptions will be made about the lens, and the image forming capability of the lens:

- (a) It will be assumed that defects in the glass are small in character, and that the total effect of all of the defects in the window can be treated as if it were the result of placing several very long focal length thin lenses, which vary in power between selected limits, in the optical path (this is identical to adding power to the system).
- (b) The form of the energy distribution of a point response in the image plane will be assumed to be gaussian both for the photographic lens and the effect resulting from the window. This assumption is made to facilitate analysis. In general, the energy distribution can only be found for a specific lens, and may differ considerably from that of a gaussian function (especially for off axis images). However, near the axis the gaussian function serves as a good approximation to the image energy distribution even for diffraction-limited systems (provided one does not consider the secondary maxima). This assumption may have more validity for the effects resulting from the window defects, since these will be, in all probability, random in nature.

Because of the number of parameters involved, a graphical presentation will be made for characteristic parametric values.

To begin, let us find what the effect of adding power is. To do this, let the window have an equivalent focal length of  $f_w$ , the lens have a focal length  $f_l$ , the principal planes of the window and the lens be separated by  $t$ , and the combined focal length be  $F$ . From Figure 57 we see

$$q = -1/V'E'_w + F \quad (1)$$

and

$$p = -1/V'E'_l + f_l$$

Furthermore,

$$\begin{aligned}
 p - q = \Delta f &= -|VE'_l| + f_l - (-|VE'_w| + F) \\
 &= -|VE'_l| + f_l + |VE'_l| + \frac{tF}{f_w} + (-F) \\
 &= f_l + \frac{tF}{f_w} - F
 \end{aligned} \tag{2}$$

But

$$F = \frac{f_l f_w}{f_l + f_w - t} \tag{3}$$

Hence

$$\begin{aligned}
 \Delta f &= f_l + \frac{t f_l f_w}{f_w(f_l + f_w - t)} - \frac{f_w f_l}{f_l + f_w - t} \\
 &= \frac{f_l^2}{f_l + f_w - t}
 \end{aligned} \tag{4}$$

Now if  $u$  is the angle of emergence of the ray, and  $r_c$  is the radius of the blur circle (see Figure 58) in the image plane, then

$$r_c = \Delta f \tan u = \Delta f \frac{D}{2F}$$

where  $D$  is the diameter of the exit pupil. Or we may write

$$\begin{aligned}
 r_c &= \frac{f_l^2}{f_l + f_w - t} \cdot \frac{D}{\frac{2 f_l f_w}{f_l + f_w - t}} = \frac{D}{2} \frac{f_l}{f_w} \\
 &= \frac{f_l^2}{2N f_w}
 \end{aligned} \tag{5}$$

where  $N$  is the  $f$ -number.



If the energy spread were constant and all of the energy coming into the lens were effected in this way,  $1/2 \Gamma_c$  would be the resolution limit. However, we shall assume that only a limited amount of the energy will be affected, and that the intensity distribution will be gaussian. We have then assumed that a point response function will be of the form

$$I_w(x) = I_{w_{max}} \exp(-ax^2) \quad (6)$$

To find the constant  $a$ , let us assume  $I_w(x)$  is down by  $1/e$  when  $x$  is equal to  $\Gamma_c$ . This is the same as saying that most of the energy falls inside of a circle of radius  $\Gamma_c$ . This can be shown by integration. Our assumption implies that

$$ax = a\Gamma_c^2 = 1 \quad \text{or} \quad a = 1/\Gamma_c^2 \quad (7)$$

For the image formed by the lens itself (or with an ideal window in place) we again assume a gaussian function:

$$I_L(x) = I_{L_{max}} \exp(-bx^2) \quad (8)$$

This time, instead of being somewhat arbitrary about the constant  $b$ , we shall make a connection between  $b$  and the resolution. According to the Rayleigh criterion, the image of two points is said to be resolved when the minimum of one distribution function corresponds to the maximum of the other. The reciprocal of the distance between the two primary maxima is said to be the resolution. However, since a gaussian function does not have a minimum, a more intimate knowledge of what is required to resolve two points is necessary. What is actually desired is the ability to discern two points. That is, that there be sufficient contrast between the two maxima and the minimum formed by the composite of the two distribution functions so that the two maxima can be observed. This will be seen in Figure 59. If one uses the Rayleigh criterion for a diffraction-limited optical system with a square aperture, this contrast is 18.83%. For a circular aperture the contrast is 37.71%. Since studies have shown that the human eye is capable of detecting contrasts of 2%, the Rayleigh criterion is conservative. For the purpose of this analysis, we shall make a compromise and say that a 10% contrast will be assumed to be necessary. The composite, or sum, of the two functions will be given by:

$$I_{TOTAL} = I_{L_1} e^{-bx^2} + I_{L_2} e^{-b(x-c)^2} \quad (9)$$

where  $C$  is the separation between the maxima. In most cases of interest,  $I_{L_1}$  is equal to  $I_{L_2}$ . Furthermore, it is obvious from Figure 59 that the minimum occurs at  $C/2$ . Let us define contrast by the equation

$$G = \frac{I_{MAX} - I_{MIN}}{I_{MAX}} \quad (10)$$

Letting  $I_{L_1} = I_{L_2}$  we have

$$G = \frac{(e^{-0} + e^{-bc^2}) - (2e^{-\frac{bc^2}{4}})}{e^{-0} + e^{-bc^2}}$$

or

$$G = \frac{1 - 2e^{-\frac{bc^2}{4}}}{1 + e^{-bc^2}} \quad (11)$$

Since  $1/C$  is the resolution, and  $G$  is the contrast,  $b$  can be found by numerical analysis. For convenience, let  $e^{-bc^2}$  be small compared to 1. Equation (11) becomes

$$\frac{1-G}{2} = e^{-\frac{bc^2}{4}} \quad (12)$$

or

$$b = \frac{4}{C^2} \ln \frac{2}{1-G} \quad (13)$$

As an example, let the resolution be 45 lines/mm.

$$b = 45 \cdot 45 \cdot 4 \ln \frac{2}{0.9} = 6.46 \times 10^3 / \text{mm}^2$$

A substitution of this quantity into  $e^{-bc^2}$  gives a value of .041, which is small compared to 1 as in our assumption.

We now want to limit the energy that is affected by the window defects. This can be easily accomplished by limiting the allowable percentage area, as seen by the lens, that contains defects. The total energy in any point response will be given by

$$E = \int_0^{\infty} I \, dA \quad (14)$$

Because of the symmetry of the gaussian function, we may simplify the integration by rotating the function about the axis of symmetry and integrating by the method of cylindrical elements. Thus in general

$$E = \int_0^{\infty} 2\pi x I(x) dx \quad (15)$$

or by substituting Eq (6) into the above

$$E_w = \int_0^{\infty} 2\pi x I_{w_{MAX}} e^{-ax^2} dx \quad (16)$$

Equation (16) is easily integrated to give (see Reference 15)

$$E_w = I_{w_{MAX}} \frac{\pi}{Q} \quad (17)$$

Similarly if Eq. (8) is substituted in Eq. (15)

$$E_L = I_{L_{MAX}} \frac{\pi}{b} \quad (18)$$

results. If the energy affected by power in the window is to be limited to some percentage Q, then

$$\frac{E_w}{E_L} = \frac{Q}{100-Q} \quad (19)$$

By substituting Eq. (17) and (18), we get

$$\frac{I_{wM}}{I_{LM}} = \frac{Q}{100-Q} \frac{a}{b} \quad (20)$$

The problem now is using all of the above information to determine the resolution that results from the combined effects. To achieve this result we write the function for the combined effect as the sum of the distribution functions:

$$I_{COMBINED} = I_{wI} + I_{LI} + I_{LII} + I_{wII} \quad (21)$$

The subscripts I and II refer to the two points to be resolved. W and L refer to the distribution functions that result from the window and lens respectively. From Eqs. (6), (8) and (20) we get

$$I_{\text{COMBINED}} = \left( \frac{Q}{100-Q} \frac{a}{b} e^{-ax^2} + e^{-bx^2} + \frac{Q}{100-Q} \frac{a}{b} e^{-a(x-c)^2} + e^{-b(x-c)^2} \right) I_{L_{\text{MAX}}}$$

Now we must solve for C when the contrast between maximum and minimum is the proper value for discerning between the two point response functions. Again,

$$G_{\text{COMBINED}} = \frac{I_{\text{COMBINED}_{\text{MAX}}} - I_{\text{COMBINED}_{\text{MIN}}}}{I_{\text{COMBINED}_{\text{MAX}}}} \quad (22)$$

Substitution of these quantities into the above equations gives

$$G_{\text{COMBINED}} = 1 - \frac{2 \left[ \frac{Q}{100-Q} \frac{a}{b} e^{-\frac{ac^2}{4}} + e^{-\frac{bc^2}{4}} \right]}{1 + \frac{Q}{100-Q} \frac{a}{b} + \frac{Q}{100-Q} \frac{a}{b} e^{-ac^2} + e^{-bc^2}} \quad (23)$$

A simple approach to understanding this equation is to solve for Q. This will give us the amount of energy that can be affected before a certain percentage degradation of resolution will result. Also it will be simpler to write C in terms of this degradation and substitute this directly into our equation. Solving for  $\frac{Q}{100-Q}$  we get

$$\frac{Q}{100-Q} = \frac{b}{a} \frac{e^{-bc^2} - \left( \frac{1-G_{\text{COMB.}}}{2} \right) - \left( \frac{1-G_{\text{COMB.}}}{2} \right) e^{-bc^2}}{-e^{-ac^2} + \left( \frac{1-G_{\text{COMB.}}}{2} \right) + \left( \frac{1-G_{\text{COMB.}}}{2} \right) e^{-ac^2}} \quad (24)$$

Let us define the fraction degradation by the relation

$$\text{deg} = \frac{\text{RESOLUTION} - 1/C}{\text{RESOLUTION}}$$

This implies that

$$C = \frac{1}{\text{RESOLUTION} (1 - \text{deg})} \quad (25)$$



Furthermore, since  $b = 4(\text{resolution})^2 \ln \frac{2}{1-G}$

$$bc^2 = \frac{4}{(1-\text{deg})^2} \ln \frac{2}{1-G} \quad (26)$$

By substitution of Eqs. (25) and (26) into Eq. (24), we can find the tolerable amount of energy affected in terms of the resolution, fraction degradation and the quantity  $a$ , which is related to the quality of window and the properties of the photographic lens. A close look at Eq. (24) with reference to our example for  $b$  reveals that the quantity  $b/a$  is dominant for small values of  $a$  (i.e. high amounts of power in the window). This implies that it would require almost 100% of the energy to be affected before significant degradation of the image would result. At first this seems quite unreasonable, but what is being said is that a large amount of power in the window will cause the energy to spread out resulting in lower intensity. Thus if only a small amount of energy is unaffected by the window, it may still be enough to result in distribution functions that meet our contrast requirements. In essence it means that resolution is not a good way to judge image quality. This is why many have gone to contrast response to evaluate photographic lenses.

Another look at Eq. (24) shows a discontinuity. That is for a given value of degradation and resolution, there is a value of  $\frac{Q}{100-Q}$  approaching infinity. This means that there exists a point where all of the incident energy must be affected by the window before it will result in the given percent degradation. Or any more improvement of the window will not result in image improvement greater than specified by the degradation.

This value occurs at

$$-e^{-\frac{ac^2}{4}} + \left( \frac{1-G_{\text{COM}}}{2} \right) + \left( \frac{1-G_{\text{COM}}}{2} \right) e^{-ac^2} = 0$$

or

$$\frac{e^{-\frac{ac^2}{4}}}{1 + e^{-ac^2}} = \frac{1-G_{\text{COM}}}{2} \quad (27)$$

This is quite similar to Eq. (11) in which we assumed that  $e^{-bc^2}$  was small compared to 1. If we make the same assumption in Eq. (27), we find

$$a = \frac{4}{c^2} \ln \frac{2}{1-G_{\text{COM}}} \quad (28)$$

and substitution of Eq. (25) into (28) gives

$$a = 4 [\text{resolution}(1-\text{deg})]^2 \ln \left( \frac{2}{1-G_{\text{COM}}} \right) \quad (29)$$

This equation gives an upper limit to  $a$ , and from it can be determined the quality of the glass that will not degrade the resolution. Equation (29) has been plotted in Figures 60, 61, 62, 63. The abscissae of these graphs represent the power in the window measured in fringes in an interferometer. The relation between window power and the fringes observed in an interferometer is easily computed if the power is relatively small. If the value obtained is substituted into Eq. (5) and the resulting value of  $a$  substituted into Eq. (29) then the graphs in Figures 60, 61, and 62 and 63 result.

To use these figures, one must know the value of the focal length and the  $f$ -number of the lens to be used with the window. He must also know the resolution of the lens. By looking at the abscissa that corresponds to these three values on the graph, he can determine the number of fringes that can be tolerated over a two inch aperture. Then by scanning the window in the interferometer using the value obtained from the graph, it can be determined if the glass is good enough to be used as a window in the optical system. The solid line in these figures represents no degradation of the resolution, while the broken line represents a 10% degradation.

To determine how good the glass should be, let us take some typical examples. A report entitled A Survey of Modern Aerial Cameras (Reference 16) gives some information that should be helpful. The report is dated 29 June 1960, and may be somewhat behind in its information, but it probably can be assumed that no drastic changes have been made in the state-of-the-art in the past two years. In the text of the report, it suggests that the upper limit of photographic resolution will be for some time around 100 lines/mm. If we assume that a lens with this capability has been constructed, and that the focal length is 12 inches at a setting of  $f/4$ , reference to Figure 61 reveals that we can stand about 1.1 fringes over a 2 inch diameter aperture before any degradation of the image will result. The report also states that a camera has been designed and built that is capable of 75 lines/mm. If we assume then the same focal length and  $f$ -number, Figure 61 shows that 1.5 fringes is tolerable. The list of lens characteristics shows that most of the lenses do not exceed 45 lines/mm. Again using the same lens parameters, a 2.5 fringe tolerance is allowed.

#### Optical Quality Necessary For Laboratory Tests

In preceding work, the quality of optical glass for use as windows in conjunction with high resolution aerial cameras was determined. This high quality will probably not be necessary for laboratory experiments involving deviation measurements. It will be necessary to assure that the deviations are not severely masked because of the fact that the image quality of the measuring device is reduced. In the analysis that follows the tolerance for the quality of glass is determined.

Since an interferometer is to be used to measure glass quality, it is necessary to establish a correlation between the quality of the image seen in the theodolite or measuring autocollimator and the shape and density of fringes seen in the interferometer.

The amount of spherical power tolerable can be computed by limiting the amount of blurring of the image in the collimator to less than the dimension subtended by the measuring bifilar. This condition is established because it is necessary to see the image of the cross hair clearly in the bifilar to make accurate readings.

Let the bifilar of the collimator subtend an angle of  $\beta$ , the focal length of the collimator be  $f_c$ , the diameter of the collimator objective be  $D$ , and the equivalent focal length of the window be  $f_w$ . Now for light of wave length  $\lambda$  in an interferometer, dark fringes appear for a difference in optical path of  $1$  such that

$$n \lambda = 1 \quad (30)$$

If the difference in optical path is the sagitta of the wave that has become curved due to spherical power, then

$$1 = \frac{D/2}{2 f_w / 2} \quad (31)$$

Here the expression for sag is given in terms of the parameters defined above. By substitution of Eq. (30) into (31), we have

$$n = \frac{D^2}{4 f_w \lambda} \quad (32)$$

From Eq. (5) we have

$$r_c = \frac{D}{2} \frac{f_c}{f_w} \quad (33)$$

If  $2r_c$  is equated to the image width necessary to fill the bifilar, then

$$r_c = \frac{f_c \beta}{2} \quad (34)$$

where  $\beta$  is measured in radians. Substitution of (34) into (33) gives

$$f_w = \frac{D}{\beta} \quad (35)$$

Thus we get the result

$$n = \frac{D}{4} \frac{\beta}{\lambda} \quad (36)$$

$D$  for the Watts autocollimator (shown in Figure 65 on the left) is 1.5 inches,  $\beta$  is about 20 seconds and  $\lambda$  is  $5.461 \times 10^{-4}$  millimeters. Substituting these values into Eq. (36) results in

$$\begin{aligned} n &= \frac{(1.5 \times 25.4) \times (20 \times 4.85 \times 10^{-6})}{4 \times 5.461 \times 10^{-4}} \\ &= 1.7 \text{ fringes of power over } D = 1.5 \text{ inches} \end{aligned}$$

Variation of fringe density is another problem however. This may be treated as a variation of wedge over a certain area. It is easily shown that if  $\delta$  is the angle of deviation resulting from a piece of glass, then

$$n = \frac{2\delta h}{\lambda} \quad (37)$$

fringes will be seen in the interferometer, where  $h$  is the height at which fringes are measured. If we divide  $n$  by  $h$  we get

$$\frac{n}{h} = N = \frac{2\delta}{\lambda} \quad (38)$$

fringes per unit length which we shall identify as the fringe density. Since we want the difference in fringe density to correspond to less than half of the tolerable angle we get

$$\begin{aligned} \Delta\delta &= \frac{\beta}{2} \\ \text{or} \\ \Delta n &= \frac{\beta}{\lambda} \end{aligned} \quad (39)$$

where  $\Delta n$  here represents the difference in fringe density over the aperture measured in fringes per inch. We have, using the numbers above

$$\Delta n = \frac{20 \times 4.85 \times 10^{-6}}{\frac{5.461 \times 10^{-4}}{25.4}} = 4.8 \text{ fringes/inch}$$

To find this value, we simply count the number of fringes in any one section of the aperture and divide by the width or height in which the fringes occur. Then by repeating the operation in another section of the aperture and subtracting the two values, the difference in fringe density results. Comparing the value obtained with the value above serves as a tolerance.

#### Quality of Glass Test Panels as Received

The Corning Glass Works, Corning, New York, generously offered to supply glass test panels, finished to the best of their ability, at a very reasonable cost so that they could "share in the development of a concept" of interest to them. Eight panels were purchased:



#1723 glass, 9 inches diameter, 1/2 inch thick

#1723 glass, 9 inches diameter, 1 inch thick

#1723 glass, 9 inches diameter, 2 inches thick

#1723 glass, 9 inches square, 1/2 inch thick

#1723 glass, 9 inches square, 1 inch thick

#1723 glass, 9 inches square, 2 inches thick

#7740 glass, 9 inches square, 1 inch thick

#7940 glass, 9 inches square, 1 inch thick

This particular combination was selected so that the relative effects of glass type, shape, and thickness could be studied with a minimum number of tests.

In studying the glass received it was discovered that there were defective areas of the glass that would make precise deviation measurements extremely difficult if not impossible. These defects caused multiple images and blurring when used in an optical system. Figure 65 shows how this initial inspection was accomplished. The two collimators were aligned so that a sharp image of the illuminated collimator reticle at left was observed in the collimator on the right. The window glass was placed in the collimated beam, and the effect of the window defects on the image observed as shown.

Inspection of the glass in an interferometer (Figure 66) revealed that there was considerable power and wedge in the window; more than enough to cause the effect observed in the collimator (see calculation below). On one particularly offensive piece of glass, it was also noticed that in the region that caused the maximum blurring, there was a rapid variation in the fringe pattern over the area that corresponded to where the collimator beam passed through glass. Readjustment of the interferometer resulted in a fringe pattern that indicated two high ridges very close together in the surface of the glass (Figure 68). This formation causes part of the beam to be deviated in one direction and the other part in another, producing a blurring and doubling of the image. A close inspection of the collimator image showed that this was indeed the case.

Several of the pieces received had these conditions, and in several the defects extended over the entire piece of glass. Wedge, spherical power or the above mentioned irregularity were common to each piece received (see Figures 68 through 75). Wedge can usually be accounted for and adjusted out of any reading for study purposes. Calculation shows that severe spreading of the image will result for large amounts of spherical power observed. However, the worst condition results from the large degree of irregularity, or rapid variation in fringe density. This results in multiple images, blurring and spread that make accuracy impossible. Investigation of the surface flatness showed that surface irregularity was the major contributor

to the glass defects (See Figures 76 through 85). In all cases the glass revealed no objectionable variations in index when viewed through the polariscope. Since the defects were on the surface, it was suggested that those glasses which exhibited large amounts of power and rapid variation in fringe density be repolished and recoated.

Using the above calculations, it is easily seen in Figure 68 through 75 that only two of the pieces of glass received were even close to being useable. (Figure 71 and certain sections of Figure 70). Figures 68 through 75 are photographs of the patterns seen in the interferometer. These figures may be used for comparison with the calculations for quantitative results. The scale of the photographs is such that what is shown is smaller than actual size. Consequently a circle equivalent in diameter to the collimator objective (1.5 inches) is shown to the right of each page.

Figures 78 through 85 are photographs of the fringes that result from placing a test flat on top of each sample. The photographs were taken using the arrangement shown in Figure 76. These may be used for qualitative evaluation of each sample. It is not suggested that these photographs represent a sufficient test for rejection of any one piece, but simply that there is an indication of surface irregularity or power. The sections photographed were chosen at random and no attempt was made to make any correlation with the interferometer data.

Table II is a description of the pieces received. Included are sizes, shapes and glass types along with the code furnished by Corning Glass Co. The letter to the left of each description is the same for each sample as the letter identifying each of the photographs.

It was decided that six of the eight panels were inadequately polished, and these panels were repolished by Thompson Optical Company, Los Angeles, to a flatness of two fringes over a two inch aperture.

## RELATIONSHIP BETWEEN DEVIATION AND RESOLUTION

### Deviation Differential

One of the basic premises by which the program was conducted was the valid application of deviation measurements to the determination of changes in system resolution. The problem of relating the image quality of an optical system to the information given about the object space has many solutions, most of which are mathematically tedious and/or highly sophisticated. The most ideal approach is to use the expressions for the wave functions incident upon the system, and by application of Huygen's principle or the Kirchhoff integral at the boundaries, together with the diffraction theory of aberrations, one obtains the precise light distribution in the image plane. However, this technique is extremely complicated and requires an intimate knowledge of the lens characteristics.

Another approach is to use the method of tracing rays through the system. This technique does not take into account the effect of the boundaries, but neither does it require the mathematical sophistication necessary in the ideal approach. From the data obtained by ray tracing, a plot of the intersection points of the rays with the image plane can be made. This is called a spot diagram. The density of points in an elemental area is related to the light intensity, and by making a plot of this intensity as a function of the image plane coordinates, the point response function is obtained. Again the mathematics is tedious, and a very intimate knowledge of the lens system is required. Herzberger has developed techniques for deriving very accurate approximations to the distribution functions using the equations of Hamilton together with Taylor's expansion, Reference 19. This method requires much less ray tracing, but again the lens formula must be known precisely. Also the algebra becomes so complicated that, for most optical systems, no explicit relation can be found for the precise ray trace, and the system can only be evaluated numerically.

Another approach involves cascading individual transfer functions of the elements that make up the optical system. By cascading, it is meant that the transfer function for the system is just the product of individual system element transfer functions. This technique has proved very useful in the past few years, and is presently being accepted as a standard method of evaluation. However, there are restrictions placed upon the use of this method. First the system must be linear: that is, if the intensity of the signal is doubled, then the response of the system must double, also the sum of two inputs must give the same response as the sum of the response of the individual inputs. Secondly, the system elements must act independently of one another. For example, in an optical system, the transfer function of a compound lens is not equal to the product of the transfer functions of the sub-elements that make up the lens. In some instances it is possible to relax this second requirement, but great care must be taken when this is done to assure that the results are valid. It is this second restriction that limits the degree to which transfer function analysis may be applied to the case of photographic windows. For only if the window introduces only first order aberrations into the photographic system or causes only simple defocusing, can a transfer function be written. Even then the expression for the window transfer function contains first order parameters of the photographic lens.

Thus, the approaches outlined above will be avoided, and a simpler method of correlating image quality to the experimental data will be used.

The effect of light deviation by a photographic window will not necessarily cause degradation of the resolution. Degradation of resolution will only result when the deviation is not constant over the aperture. Reference to the Vidya report (Reference 2), page VI-7, shows what happens to a ray that is deviated by a small amount  $\delta$ . For convenience this derivation is repeated below and the figure in that report is shown as Figure 86 of this report. Figure 87 shows the ray direction for the undeviated principle ray (i.e., the ray in the meridional plane passing through the nodal points of the lens), and for a similar ray deviated by a small amount  $\delta$ . If we assume that the lens is a high quality lens, then all rays incident upon the lens at an angle with the optical axis of  $\phi_0$  will also intersect the image plane very near the same point. From Figure 87 it can be seen that the distance from the nodal point to the point of intersection with the image plane is:

$$F / \cos \phi_0 \quad (40)$$

where  $F$  is the focal length of the lens. Also the distance  $\Delta S$  is given by:

$$\Delta S = F \delta / \cos \phi_0 \quad (41)$$

The projection of  $\Delta S$  onto the image plane will be:

$$\Delta s / \cos \phi_0 = \delta F / \cos \phi_0 \cos \phi_0 = F \delta \sec^2 \phi_0 \quad (42)$$

This is Eq. VI-7 of the Vidya report for  $\Delta z$ .

If the deviation resulting from the window is not constant, then there will be a maximum,  $\delta_a$ , and a minimum,  $\delta_b$ , such that the difference in deviation will be  $(\delta_a - \delta_b)$ . This will cause a spreading of the light energy into a circle of diameter  $\epsilon$ , where:

$$\epsilon = F (\delta_a - \delta_b) \sec^2 \phi_0 \quad (43)$$

The limit of resolution resulting from this effect will be the reciprocal of this number

$$\text{Res} = \frac{\cos^2 \phi_0}{F(\delta_a - \delta_b)} \quad (44)$$

A graph of  $F - \text{Res}$  is shown in Figure 88. To use this figure, choose the angle of incidence of interest,  $\phi_0$ , and the corresponding value of  $F - \text{Res}$  on the ordinate. By dividing this number of  $F$  in inches, the resolution limit in lines per millimeter results.

#### Analytical Assumptions

The initial optical analysis in this program was based upon the basic deviation equation derived by Vidya:

$$\delta = \frac{t}{n} \left\{ \frac{\sin \phi_0}{(N^2 - \sin^2 \phi_0)^{1/2}} - \tan \phi_0 \right\} \quad (45)$$

The validity of this equation is reliant upon several assumptions:

- (1) The inside and outside radius of curvature,  $r_1$ , and  $r_2$  are equal,
- (2) The variation in index of refraction is small compared to 1,
- (3) All other physical parameters undergo very small changes with temperature.

The validity of the first assumption will be challenged later. Information about the second assumption is available on page 420 of Reference 17. Here the index of refraction of silica glass has been measured at several wavelengths for several temperatures. For the helium green line ( $\lambda = 501.568 \text{ m}\mu$ ), it is seen that the index at  $-160 \text{ C}$  is 1.4617, and at  $1000 \text{ C}$  is 1.4772. This is a difference of .0155 for a temperature range of 1160 C. Thus the validity of the second assumption is established. See Figure 89 for another wavelength.

Figure 90 gives a good idea of the validity of the third assumption. Here we see that a large difference in temperature at the surfaces is necessary to cause substantial changes in the glass resulting from the physical constants being functions of temperature.



If we accept the above assumptions, we may accomplish a considerable amount of analysis using Eq. 45.

It was shown previously in Eq. 43 that if  $F$  is the focal length,  $\phi_0$  the proper angle of incidence, and  $\delta_a$  and  $\delta_b$  the two extreme angles of deviation of the rays, then

$$\epsilon = F \sec^2 \phi_0 (\delta_a - \delta_b) \quad (46)$$

where  $\epsilon$  is the diameter of the blur circle caused by the difference in deviation.

By a simple Taylor's expansion about  $b$  we have

$$\delta_a = \delta_b + \left. \frac{\partial \delta}{\partial \phi_0} \right|_b (\phi_a - \phi_b) + \frac{1}{2!} \left. \frac{\partial^2 \delta}{\partial \phi_0^2} \right|_b (\phi_a - \phi_b)^2 + \dots \quad (47)$$

Neglecting higher order terms, since the difference ( $\phi_a - \phi_b$ ) is small, we have

$$\delta_a - \delta_b \approx \left. \frac{\partial \delta}{\partial \phi_0} \right|_b (\phi_a - \phi_b) \quad (48)$$

From Eq. 45 we have

$$\frac{\partial \delta}{\partial \phi_0} = \frac{t}{r_i} \left\{ \frac{\cos \phi_0}{(N_0^2 - \sin^2 \phi_0)^{1/2}} + \frac{\sin^2 \phi_0 \cos \phi_0}{(N_0^2 - \sin^2 \phi_0)^{3/2}} - \sec^2 \phi_0 \right\} \quad (49)$$

Simplification of Eq. (49) results in

$$\frac{\partial \delta}{\partial \phi_0} = \frac{t}{r_i} \left\{ \frac{N_0^2 \cos \phi_0}{(N_0^2 - \sin^2 \phi_0)^{3/2}} - \sec^2 \phi_0 \right\} \quad (50)$$

Since the angle ( $\phi_a - \phi_b$ ) is small, and since the window is slightly curved, ( $\phi_a - \phi_b$ ) is easily shown to be

$$\phi_a - \phi_b = \frac{d}{r_i} \quad (51)$$

where  $d$  is the diameter of the bundle of rays of interest. Letting  $N$  be the  $f$ -number of the photographic lens we can show that

$$d = \frac{F}{N} \cos \phi_0 \quad (52)$$

Finally, substitution of Eqs. (48), (50), (51) and (52) into (45) gives the result:

$$\epsilon = \frac{F^2}{N} \frac{t}{r_i^2} \left\{ \frac{N_0^2}{(N_0^2 - \sin^2 \phi_0)^{3/2}} \sec^3 \phi_0 \right\} \quad (53)$$

C is the reciprocal of the resolution, and if  $r_i$  can be found, then the effect on resolution can be determined.

Window curvature is assumed to result from three different causes:

1. intrinsic surface curvature
2. temperature gradients
3. loads on the window (including the window weight, thermal stress, and pressure differentials).

No surface is perfectly flat and some curvature will be present in any window. Although this curvature by itself may not be enough to cause damage to the optical image, it, together with other effects, may result in enough to cause degradation. Some value for this curvature should therefore be included in any calculation. We shall refer to this as  $R_0$ .

The value of  $R_i$  that results from linear temperature distributions across the window thickness is probably the most important contribution of optical degradation. It can be shown, see Vidya Eq. (VI-31), that the resultant radius of curvature is:

$$R_i = \frac{t}{\alpha(T_0 - T_i)} \quad (54)$$

Here  $\alpha$  is the coefficient of expansion and  $T_0$  and  $T_i$  represent the temperature on the outside and inside surface of the window respectively. We shall refer to the radius of curvature as  $R_{\Delta t}$ .

Finally, the calculation for deflection resulting from loads due to the window's own weight and the pressure differential can be made. On page 194 of Reference 18 is an equation for the maximum deflection of a circular plate due to a uniform distribution of force over the surface of the plate. This is given as

$$y = \frac{3W(m-1)(5m+1)a^2}{16 E m^2 t^3 \pi} \quad (55)$$

where  $m$  is the reciprocal of Poisson's ratio,  $E$  is Young's Modulus,  $w$  the force,  $a$  the radius of the plate and  $t$  the thickness. Let us approximate the surface of a sphere of large radius (this assumption is open to challenge); we have then

$$y = a^2 = \frac{3(\pi \alpha^2 \rho t + \pi \alpha^2 \Delta p)(m-1)(5m+1)a^2}{2\Delta R_{\Delta p} 16\pi E m^2 t^3} \quad (56)$$

or

$$R_{\Delta p} = \frac{8Em^2t^3}{3\alpha^2(\rho t + \Delta p)(m-1)(5m+1)} \quad (57)$$

Here  $\rho$  is the density of the glass,  $\Delta p$  the pressure differential and  $R_{\Delta p}$  the radius of the curvature of the surface.

In most cases the physical constants of the glass,  $E$  and  $m$ , vary considerably with temperature. Hence to be accurate, the above parameters should be written as  $m=m(T)$  and  $E=E(T)$ . These functions are empirical in nature because they differ radically depending upon the type of glass of interest. No theoretical model gives sufficient accuracy to be considered.

In computing the total effect we shall add together the reciprocals of the radii resulting from each effect,  $R_{\Delta t}$ ,  $R_{\Delta p}$  and  $R_0$ . That is

$$\frac{1}{R_i} = \frac{1}{R_0} + \frac{1}{R_{\Delta p}} + \frac{1}{R_{\Delta t}} \quad (58)$$

From this equation and Eq. (54) it is seen that the parameter that gives the largest radius of curvature is the one that contributes the least to degradation of image quality.

As a final step we shall combine the effect resulting from the window together with the lens' own resolution to obtain the final resolution. We use the relation:

$$\frac{1}{R^2} = \frac{1}{R_{lf}^2} + \epsilon^2 \quad (59)$$

$$R = R_{lf} \left( \frac{1}{\epsilon^2 R_{lf}^2 + 1} \right)^{1/2} \quad (60)$$

where  $R_{lf}$  is the resolution of the film-lens combination.

As an example of the surface power inherent in photographic windows let us consider glass normally required for aerial photography. The test flat quality is usually 1 fringe power over a 2 inch diameter flat. We can compute the radius of curvature by the equation:

$$R_0 = y^2 / k\lambda \quad (61)$$

Here  $y$  is the radius of the flat,  $k$  the number of fringes and  $\lambda$  the wave length of the light used.

Thus

$$R_0 = \frac{25.4 \times 25.4}{1 \times 5.461 \times 10^{-4}} = 1.18 \times 10^6 \text{ mm}$$

The pressure expected is around 15 pounds per square inch. The specific gravity of aluminosilicate is 2.53. The density would be  $2.53 \times .03611$  pounds per cubic inch. We choose a temperature of 500 F as the temperature of the window. Young's modulus at this temperature is  $1264 \times 10^6$  pounds per square inch. Poisson's ratio is .2575. Substituting into Eq. (57) we get

$$R_{ap} = \frac{8 \times 12.64 \times 10^6 (1/0.2575)^2}{3 (4.5)^2 (2.53 \times .03611 \times 1 + 15) (1/.2575 - 1) (5/.2575 - 1)}$$

$$= 3.135 \times 10^4 \text{ inches} = 7.96 \times 10^5 \text{ mm}$$

The temperature inside may be significantly different from the outside. Let us assume that a 200 F gradient exists across the window thickness. From Eq. (54) we have:

$$R_{\Delta T} = \frac{25.4}{2.4 \times 10^6 (200)} = 5.3 \times 10^4 \text{ mm}$$

This is about a factor of 20 less than the radius due to pressure and weight. Hence we see that the pressure effect contributes much less to the image degradation than does the temperature even at the relatively high temperature of 500 F. Using Equation (58) we get for the total effect:

$$\frac{1}{R_i} = \frac{1}{1.18 \times 10^6} + \frac{1}{5.3 \times 10^4} + \frac{1}{7.96 \times 10^5}$$

or

$$R_i = 4.769 \times 10^4 \text{ mm}$$

Substituting this value into Eq. (53) and assuming an f/4 lens of 24 inches focal length viewing at  $20^\circ$  off axis, we have

$$\epsilon = \frac{(24 \cdot 25.4)^2 25.4}{4 (4.82 \times 10^4)} \left\{ \frac{(1.53)^2}{(1.53^2 - \sin^2 20^\circ)^{3/2}} - \sec^3 20^\circ \right\}$$

$$= 5.18 \times 10^{-4} \text{ mm}$$

Finally, if the resolution of the film lens combination is 150 lines per millimeter, the resultant film-lens-window combination will be from Eq. (60):

$$R = 150 \left\{ \frac{1}{(5.18 \times 10^{-4})^2 150^2 + 1} \right\}^{1/2}$$

$$= 149.5 \text{ lines/mm}$$



The above discussion assumes a linear distribution of temperature through the window. Results from the diathermanous temperature distribution program indicate that the temperature distribution is quite non-linear in transient situations and even non-linear in equilibrium. Opaque materials retain the linear character in equilibrium, but not under transient conditions. As a result a slightly different approach is necessary to predict the shape of the glass that results from non-linear temperature distributions. Let us assume that the temperature distribution is symmetrical and that it only varies with thickness.

On page 279 of Reference 23, an equation is derived that describes the deflections of a free plate under the above conditions. The equation that gives the displacement of a point in the axial direction may be used to determine the surface curvatures of the window. The above reference gives

$$W = \Delta z = -\frac{3M_T}{4(t/2)^3 E} (x^2 + y^2) + \frac{1}{(1-\nu)E} \left\{ (1+\nu) \alpha E \int_0^z T(z) dz - \frac{\nu z}{t/2} N_T - \frac{3\nu z^2}{2(t/2)^2} M_T \right\} \quad (62)$$

Here  $\nu$  is Poisson's ratio,  $M_T$  is given by

$$M_T = \alpha E \int_{-t/2}^{t/2} z T(z) dz ,$$

$$N_T = \alpha E \int_{-t/2}^{t/2} T(z) dz$$

and the other quantities are as defined previously.

Reference 21, page 359, gives the curvature,  $K$ , as

$$K = \frac{1}{R} = \frac{|Z''|}{(1 + Z'^2)^{3/2}} \quad (63)$$

Since  $Z'$  is a very small number,

$$K \approx \frac{d^2 z}{dz^2} = \frac{12 M_T}{E t^3} \quad \text{or} \quad R = \frac{E t^3}{12 M_T} \quad (64)$$

for meridional rays. Thus even under non-linear temperature distributions along the axis of the optical system, the glass plate forms a section of a spherical shell whose radius is given by Eq. (64).

For the case where the temperature distribution and mechanical constraints are arbitrary functions of the spatial coordinates, the problem becomes much more difficult, and the surface curvature can only be determined by numerical analysis for most problems. Since in most real cases the temperature distribution will not correspond to that treated in the cases above, one is left with the difficult problem of surface curvature determination. This has not been attempted here, but an alternate approach was tried to discover what would happen to the light rays if the two surface curvatures were not the same due to mechanically or thermally induced stresses. This approach was motivated by early experimental results from pressure-induced deflection. It was found that the ray deviations measured were an order of magnitude higher than would be predicted from the thin shell theory described above.

## MODIFIED THEORY

### Unequal Curvatures

The following is a derivation of the deviation of a ray passing through glass when the surface curvatures are unequal and the index of refraction inside the glass is not constant. It is desired to calculate the deviation of a ray of light through a glass window when the radii of curvature are not equal or concentric on the surfaces, and the index of refraction varies along the thickness of the glass. To arrive at this result the methods of vector analysis will be used throughout the derivation.

To begin, it is necessary to consider the situation shown in Figure 91. Here the path of the ray of light is shown as it passes through the window. Also the vectors and most of the symbols used in the analysis that follows are shown diagrammatically. It will be noted that the situation is drawn in only two dimensions. Because of the increased difficulty of performing tedious algebraic manipulation for the three dimensional problem, the tracing of skew rays will not be attempted, and only meridional rays will be considered.

The radii of curvature,  $R_1$  and  $R_2$ , are assumed to be very large so that in performing the algebraic simplification values of  $(1/R_1)^2$ ,  $(1/R_2)^2$ , and  $1/R_1 R_2$  will be neglected. It will be assumed that the index variation is small and that it only changes along the thickness of the glass and not the height. The index variation will be treated as though the glass were made up of a series of parallel thin laminae each with different index. Thus if Snell's law is applied at the air-glass surface,

$$\sin i = n_1 \sin i'$$

results. Here  $i$  is the angle of incidence,  $n_1$  is the index of the first lamina and  $i'$  is the angle of reflection. If the laminae are parallel, then the angle  $i'$  becomes the new angle of incidence of the next lamina and hence application of Snell's law gives

$$n_1 \sin i' = n_2 \sin i'' \quad (65)$$

It will be seen that

$$\sin i = n_2 \sin i''$$

Successive application of Snell's law gives

$$\sin i = n_f \sin i_f \quad (66)$$

where  $n_f$  is the index nearest the inside surface and  $i_f$  is the final angle of refraction near the surface in the final lamina.

It is now necessary to set up a coordinate system relative to which the ray vectors will be established. The origin will be placed in the center of symmetry of the window, or what would correspond to the vertex of an equivalent lens. The abscissa will be taken as normal to the surface at this point.

The propagation vector  $\vec{S}$  is defined as one which has the direction cosines of an incoming ray of interest, but a magnitude equal to the index of refraction of the medium in which the light is propagating. Taking  $\vec{S}$  to be in the air medium outside the glass, and  $\vec{O}$  to be the unit normal at the point of incidence of  $\vec{S}$  with the glass surface, then a vector analysis equivalent expression to Eq. (66) is given by:

$$\vec{S} \times \vec{O} = \vec{S}_f \times \vec{O} \quad (67)$$

Here  $\vec{S}_f$  is the light propagation vector nearest the inner surface of the window before refraction. Equation (67) may be rewritten to give:

$$(\vec{S}_f - \vec{S}) \times \vec{O} = 0$$

If the above expression is accepted, then from vector analysis,

$$\vec{S}_f - \vec{S} = \Gamma \vec{O} \quad (68)$$

must be true if  $\Gamma$  is some scalar quantity. Equation (68) is a general result of Snell's law, and can be applied wherever the use of Snell's law is required. Letting  $\vec{S}'$  be the propagation vector in the air to the right of the window, then another application of Eq. (68) results in

$$\vec{S}' - \vec{S}_f = \Gamma' \vec{O}' \quad (69)$$

where  $\vec{O}'$  is the normal at the second surface of the window and  $\Gamma'$  is the new proportionality constant.

Since it is desired to find the angle between  $\vec{S}'$  and  $\vec{S}$ , (i.e., the angle of deviation) it will be necessary to write an explicit expression for  $\vec{S}'$  in terms of  $\vec{S}$  and the window parameters. Combining Eqs. (68) and (69) one obtains

$$\vec{S}' = \vec{S} + \Gamma \vec{O} + \Gamma' \vec{O}' \quad (70)$$

The vector or cross product provides a simple way for finding the magnitude of the angle between  $\vec{S}$  and  $\vec{S}'$ .

$$\begin{aligned} |\vec{S}' \times \vec{S}| &= |\vec{S}'| |\vec{S}| \sin(\angle \vec{S}' \vec{S}) \\ &= 1 \cdot 1 \sin \delta \\ &\approx \delta \end{aligned} \quad (71)$$

if  $\delta$  is a small angle,



Using Eqs. (70) and (71)

$$\vec{S}' \times \vec{S} = \vec{S} \times \vec{S} + \Gamma \vec{O} \times \vec{S} + \Gamma' \vec{O}' \times \vec{S}$$

or

$$\delta = \Gamma \vec{O} \times \vec{S} + \Gamma' (\vec{O}' \times \vec{S}) \quad (72)$$

All that is required now is to set up expressions for the above quantities in terms of the window parameters. Let  $R_1$  be the first radius of curvature,  $R_2$  that for the second surface,  $d_1$  the height that the ray strikes the first surface,  $d_2$  the height on the second and  $n_f$  the index of refraction near the inside surface. If

$$\vec{S} = \alpha \hat{i} + \beta \hat{j} \quad (73)$$

where  $\hat{i}$  and  $\hat{j}$  are unit vectors along the x and y axes respectively and  $\alpha$  and  $\beta$  are the direction cosines of the ray relative to those axes, then it is possible to also write

$$\vec{O} = \frac{-\sqrt{R_1^2 - d_1^2} \hat{i} + d_1 \hat{j}}{R_1}$$

and

$$\vec{O}' = \frac{\sqrt{R_2^2 - d_2^2} \hat{i} + d_2 \hat{j}}{R_2}$$

or, applying the approximation

$$\frac{d_1^2}{R_1^2} \approx \frac{d_2^2}{R_2^2} \approx 0$$

and

$$\vec{O} = -1 \hat{i} + \frac{d_1}{R_1} \hat{j} \quad (74)$$

$$\vec{O}' = -1 \hat{i} + \frac{d_2}{R_2} \hat{j} \quad (75)$$

Herzberger, Reference 19, shows in general that if

$$\vec{S}' = \vec{S} + \Gamma \vec{O}$$

then

$$\Gamma = \sqrt{n^2 - n^2 + (\vec{O} \cdot \vec{S})^2} - (\vec{O} \cdot \vec{S}) \quad (76)$$

Applying Eq. (76) to (68) and (69), it is shown by direct substitution that

$$\Gamma = \sqrt{n_f^2 - 1 + (\vec{O}' \cdot \vec{S})^2} - (\vec{O}' \cdot \vec{S}) \quad (77)$$

and

$$\Gamma' = \sqrt{1 - n_f^2 + (\vec{O}' \cdot \vec{S}_f)^2} - (\vec{O}' \cdot \vec{S}_f) \quad (78)$$

Equation (77) is a straightforward expression for the proportionality constant and only involves the substitution of the quantities defined above. However, Eq. (78) can be simplified considerably by algebraic manipulation. First

$$\begin{aligned} \vec{O}' \cdot \vec{S}_f &= \vec{O}' \cdot (\vec{S} + \Gamma \vec{O}) = \vec{S} \cdot \vec{O}' + \Gamma \vec{O} \cdot \vec{O}' \\ &= -a + \beta \frac{d_2}{R_2} + \Gamma \left(1 + \frac{d_1 d_2}{R_1 R_2}\right) \\ &\approx -a + \beta \frac{d_2}{R_2} + \Gamma \\ &= -a + \beta \frac{d_2}{R_2} + \sqrt{n_f^2 - 1 + (\vec{O} \cdot \vec{S})^2} - (-a + \beta \frac{d_1}{R_1}) \\ &= \sqrt{n_f^2 - 1 + (\vec{O} \cdot \vec{S})^2} + \beta \left( \frac{d_2}{R_2} - \frac{d_1}{R_1} \right) \end{aligned} \quad (79)$$

Hence

$$\begin{aligned} (\vec{O}' \cdot \vec{S}_f)^2 &= \left[ \sqrt{n_f^2 - 1 + (\vec{O} \cdot \vec{S})^2} + \beta \left( \frac{d_2}{R_2} - \frac{d_1}{R_1} \right) \right]^2 \\ (\vec{O}' \cdot \vec{S}_f)^2 &= n_f^2 - 1 + (\vec{O} \cdot \vec{S})^2 \pm 2\beta \left( \frac{d_2}{R_2} - \frac{d_1}{R_1} \right) \sqrt{n_f^2 - 1 + (\vec{O} \cdot \vec{S})^2} \\ &\quad + \text{higher order terms} \end{aligned} \quad (80)$$

Substitution of Eq. (80) into Eq. (78) results in

$$\begin{aligned}
 \Gamma' &= \sqrt{(\vec{O} \cdot \vec{S})^2 + 2\beta \left( \frac{d_2}{R_2} - \frac{d_1}{R_1} \right) \sqrt{n_f^2 - 1 + (\vec{O} \cdot \vec{S})^2} - \sqrt{n_f^2 - 1 + (\vec{O} \cdot \vec{S})^2}} \\
 &\quad - \beta \left( \frac{d_2}{R_2} - \frac{d_1}{R_1} \right) \\
 &= \sqrt{\alpha^2 - 2\alpha\beta \frac{d_1}{R_1} + 2\beta \left( \frac{d_2}{R_2} - \frac{d_1}{R_1} \right) \sqrt{n_f^2 - 1 + (\vec{O} \cdot \vec{S})^2}} - \dots \\
 &= \pm \alpha \sqrt{1 - \frac{2\beta}{\alpha} \frac{d_1}{R_1} + \frac{2\beta}{\alpha^2} \left( \frac{d_2}{R_2} - \frac{d_1}{R_1} \right) \sqrt{n_f^2 - 1 + (\vec{O} \cdot \vec{S})^2}} - \dots \\
 &\approx \pm \alpha \left( 1 - \frac{\beta}{\alpha} \frac{d_1}{R_1} \pm \frac{\beta}{\alpha^2} \left( \frac{d_2}{R_2} - \frac{d_1}{R_1} \right) \sqrt{n_f^2 - 1 + (\vec{O} \cdot \vec{S})^2} \pm \right. \\
 &\quad \left. \sqrt{n_f^2 - 1 + (\vec{O} \cdot \vec{S})^2} - \beta \left( \frac{d_2}{R_2} - \frac{d_1}{R_1} \right) \right)
 \end{aligned} \tag{81}$$

It can be shown that

$$\vec{O} \times \vec{S} = \left( -\beta - \alpha \frac{d_1}{R_1} \right) \hat{k} \tag{82}$$

$\hat{k}$  is a unit vector normal to  $\hat{i}$  and  $\hat{j}$

and

$$\vec{O}' \times \vec{S} = \left( -\beta - \alpha \frac{d_2}{R_2} \right) \hat{k} \tag{83}$$

When Eqs. (73), (74), (77), and (81) are substituted into Eq. (72), the resulting expression is

$$\begin{aligned}
 \sin \delta &= \left[ \pm \sqrt{n_f^2 - 1 + (\vec{O} \cdot \vec{S})^2} - \left( -\alpha + \beta \frac{d_1}{R_1} \right) \right] \left[ -\beta - \alpha \frac{d_1}{R_1} \right] + \\
 &\quad \left[ -\alpha + \beta \pm \frac{\beta}{\alpha} \left( \frac{d_2}{R_2} - \frac{d_1}{R_1} \right) \sqrt{n_f^2 - 1 + (\vec{O} \cdot \vec{S})^2} \pm \sqrt{n_f^2 - 1 + (\vec{O} \cdot \vec{S})^2} \right. \\
 &\quad \left. - \beta \left( \frac{d_2}{R_2} - \frac{d_1}{R_1} \right) \right] \left[ -\beta - \alpha \frac{d_2}{R_2} \right]
 \end{aligned} \tag{84}$$

Multiplication and algebraic simplification give the final result:

$$\sin \delta = \left( \frac{d_2}{R_2} - \frac{d_1}{R_1} \right) \left( 1 \pm \frac{1}{a} \sqrt{n_1^2 - \beta^2} \right) \quad (85)$$

In Eq. (85) the "plus or minus" sign of the radical has been carried through the calculation because it is necessary to determine which sign gives physically consistent answers. To aid in this determination, let us make the approximation that  $d_2$  is given by

$$d_2 = d_1 + t \tan \phi' \quad (86)$$

Here  $\phi'$  is the angle that the ray makes with the axis after entrance into glass. If we approximate  $\phi'$  by

$$\sin \phi' = n_1 \sin \phi \quad (87)$$

we get

$$\tan \phi' = \frac{\sin \phi'}{\sqrt{n_1^2 - \sin^2 \phi}} \quad (88)$$

Now

$$a = \cos \phi \quad \text{and} \quad \beta = \sin \phi$$

hence

$$\sin \delta = \left( \frac{d_1}{R_2} + \frac{t}{R_2} \frac{\sin \phi}{\sqrt{n_1^2 - \sin^2 \phi}} - \frac{d_1}{R_1} \right) \left( 1 \pm \frac{1}{\cos \phi} \sqrt{n_1^2 - \sin^2 \phi} \right)$$

Multiplying out this result gives

$$\begin{aligned} \sin \delta = d_1 \left( \frac{1}{R_1} - \frac{1}{R_2} \right) & \left( 1 \pm \frac{\sqrt{n_1^2 - \sin^2 \phi}}{\cos \phi} \right) \\ & + \frac{t}{R_2} \left( \frac{\sin \phi}{\sqrt{n_1^2 - \sin^2 \phi}} \pm \tan \phi \right) \end{aligned} \quad (89)$$

The result quoted in the Vidya report was

$$\sin \delta = \frac{t}{R} \left( \frac{\sin \phi}{\sqrt{n_1^2 - \sin^2 \phi}} - \tan \phi \right) \quad (90)$$



If  $R_1 = R_2 = R$ , and the negative sign is chosen in Eq. (89), then the first term vanishes and what remains is the same as Eq. (90). This alone should be sufficient evidence of the validity of Eq. (85) and (89). However, there is more proof that this equation is accurate. Suppose  $\phi$  is set equal to zero. Then the second term vanishes and we are left with

$$\sin \delta = d_1 \left( \frac{1}{R_2} - \frac{1}{R_1} \right) (1 \pm n_1) \quad (91)$$

A close look at Figure 91 reveals that

$$\frac{d_1}{R_2} - \frac{d_1}{R_1} = -\alpha$$

where  $\alpha$  is the angle that exists between the first and second surface if the angle of incidence is approximately zero degrees. Substitution into Eq. (91) results in

$$\sin \delta \approx \delta = (\mp n_1 - 1) \alpha$$

which is the same as

$$\delta = \alpha (n_1 - 1) \quad (92)$$

if the negative sign is chosen in Eq. (89). Referring to Eq. (2m) of Jenkins and White, Reference 20, the deviation of a ray for a thin wedge in air at near normal incidence, is

$$\delta = (n - 1) \alpha$$

which of course is identical to Eq. (92) above. Thus there exist two entirely different proofs that verify Eq. (89) if the negative sign is chosen. Hence the final result is

$$\delta = d \left( \frac{1}{R_1} - \frac{1}{R_2} \right) \left( \frac{\sqrt{n_1^2 - \sin^2 \phi}}{\cos \phi} - 1 \right) + \frac{t}{R_2} \left( \frac{\sin \phi}{\sqrt{n_1^2 - \sin^2 \phi}} - \tan \phi \right) \quad (93)$$

Equation (93) is a very important result since it predicts a position-coordinate dependence for deviation. That is, the angle of deviation not only depends on the angle of incidence, but also on where the ray passes through the window with respect to the "vertex" of the window. Furthermore, this first term may be an order of magnitude greater than the second (the Vidya-line term). This positional dependence also indicates that the ray will be deviated positively or negatively from the incident ray depending upon whether the ray passes through the window above or below the vertex. This will be very important when considering resolution.

### Sample Calculation

This calculation will be limited to an examination of the effect of pressure on the deviation of the incoming light. This is because the calculation is much easier to accomplish and there are fewer unknowns. Eq. (93) will be used to determine deviations because a flat circular plate does not form a spherical surface under pressure. The exact shape of these surfaces is not important for use in Eq. (93), but the radius of curvature at each point where the ray passes through the air-glass interface is. The value of this radius is shown as a function of  $x$ , the distance from one of the supporting edges, in Figures 92 and 93. In both cases, the physical constants for fused silica were used and the pressure applied was ten pounds per square inch. It will be noted that these figures show that the reciprocal of the radius of curvature is not constant but obeys a parabolic function. The square plate was nine by nine inches, simply supported at two of its edges, and the circular plate was nine inches in diameter, simply supported about its circumference.

The radius of curvature for the flat plate was found by applying the equation

$$\frac{1}{R} = \frac{M}{EI} \quad (94)$$

where  $M$  is the moment about the point of interest,  $E$  is the Young's Modulus and  $I$  is the moment of inertia of the area of a cross section through the point of interest. Roark, Reference 18, page 102, gives the moment at the point  $x$  for a simply supported beam under uniform loading as

$$M = \frac{1}{2} \left( x - \frac{x^2}{l} \right) \quad (95)$$

$W$  is the total load and  $l$  is the length. For a square piece  $W$  is equal to

$$W = p l^2 \quad (96)$$

where  $P$  is the pressure.  $I$  is simply given by

$$I = \frac{1}{12} l t^3 \quad (97)$$

Thus

$$\frac{1}{R} = \frac{6 p l (x - x^2/l)}{E t^3} \quad (98)$$

This equation has been plotted in Figure 92.

For the circular plate, the situation is a little more complicated. On page 194, Roark gives an equation that relates the deflection of the plate for a uniform load as a function of the distance from the center,  $r$ . Again, use is made of Eq. (63), i.e.,

$$K = \frac{1}{R} = \frac{|y''|}{(1 + y'^2)^{3/2}} \quad (99)$$

Roark's equation is

$$y = \frac{-3W(m^2-1)}{8\pi E m^2 t^3} \left\{ \frac{(5m+1)a^2}{2(m+1)} + \frac{r^4}{2a^2} - \frac{(3m+1)r^2}{m+1} \right\} \quad (100)$$

Then  $y'$  is given by

$$y' = \frac{dy}{dr} = \frac{-3W(m^2-1)}{8\pi E m^2 t^3} \left\{ \frac{4r^3}{2a^2} - 2 \frac{(3m+1)r}{m+1} \right\} \quad (101)$$

and

$$y'' = \frac{-3W(m^2-1)}{8\pi E m^2 t^3} \left\{ \frac{6r^2}{a^2} - \frac{2(3m+1)r}{m+1} \right\} \quad (102)$$

Now  $\frac{3W(m^2-1)}{8\pi E m^2 t^3}$  is of the order of  $10^{-6}$

Thus  $y' \approx 10^{-12}$  and hence  $(1 + y'^2)^{3/2} \approx 1$

It is a good approximation then that

$$\frac{1}{R} = |y''| = \frac{3W(m^2-1)}{8\pi E m^2 t^3} \left\{ \frac{6r^2}{a^2} - \frac{(3m+1)2}{m+1} \right\} \quad (103)$$

Of course  $m$  is the reciprocal of Poisson's ratio and  $a$  is the radius of the plate. The rest of the symbols are defined above. This equation is plotted in Figure 93 for the same parameters as Figure 92.

Considering a ray passing through a square window one inch from the center at an angle of  $22.5^\circ$ , it is easily shown that the ray will pass through a point 0.73 inches from the center as it emerges from the glass. Figure 93 shows the radii of curvature at these two points to be

$$\frac{1}{R_1} = 115.5 \times 10^{-6} \text{ inch}^{-1}$$

and

$$\frac{1}{R} = 118.5 \times 10^{-6} \text{ inch}^{-1}$$

Substitution into Eq. (93) gives:

$$\delta = \left\{ (115.5 - 118.5) \frac{(1.418 - 1)}{0.923} + 118.5 \left( \frac{.3827}{1.418} - .4142 \right) \right\} \times 10^{-6} \text{ rad.}$$

$$= 3.9 \approx 4 \text{ sec. of arc.}$$



## OPTICAL TESTS

rad. Two types of optical tests were performed: pressure was applied to the window from the back, and heat was applied from the front. In both cases the deviation was measured by projecting a collimated beam of light through a glass panel and measuring the shift of the beam with an autocollimator or theodolite. Most of the deviations resulting from pressure were measured with the autocollimator, and all of those resulting from the heating of the glass were made with the theodolite. It was found, in the latter set of experiments, that the theodolite gave greater accuracy than the autocollimator, and was much easier to use and interpret.

### Pressure Test Equipment

The pressure tests were performed in two ways. The first tests were made with the glass sample mounted in the front of a large pressure vessel. Nine collimators were placed in back of the window so each beam of light passed through one of five points on the glass. This is shown schematically in Figure 94. Only square pieces of glass were used in the pressure tests. On the original test fixture three pieces of glass were tested. The first two were one inch thick and the third was one half inch thick. Before the tests were completed on the third piece, the glass ruptured, injuring the technician performing the investigation. A new pressure chamber was constructed by adapting a large steel pipe so that the window mount could be attached to the front, and an aluminum plate bolted to the back. A nozzle was attached to the back, and a piece of aluminum placed on the inside to diffuse the incoming air. A single collimator was placed inside the chamber and supported by a steel plate across the bottom. The pressure was controlled by a pressure regulator from the plant air source.

In each case, the glass was clamped such that the clamps extended vertically along the two edges. The glass was sealed from the inside against leakage by filling the void between the glass and the opening in the window mount with RTV-60 silicone. Also a gasket was placed between the window mount and the pipe to prevent leakage.

In the early experiments, the collimator design was such that the lens was potted in place with RTV-60, a rubbery compound that has some bubbles in its structure when it cures. It was felt that these bubbles were compressing under pressure and shifting the position of the collimating lens. This could lead to large measured values of deviation even though they were not the result of changes in window curvature. To correct this situation, the RTV-60 was removed from the lens mount and replaced by a metal amalgam that was tamped firmly in place. It was felt that no significant compression of this material would result. The collimator is shown in Figure 95.

This collimator was placed in the second chamber such that the angle of incidence of the collimated beam was  $22.5^\circ$  in the first case, and  $0^\circ$  in the second. The deviations were measured and found to be essentially the same as were measured in the earlier tests using the large pressure chamber. These results indicated that the earlier measurements were valid and that the large deviations were fundamental as was shown by later analysis

(See page 93 of this report). The most convincing demonstration of this was that the same collimator was used for both  $0^\circ$  incidence and  $22.5^\circ$  incidence, and the two sets of measurements were entirely different (See Figure 102 of this report).

#### Pressure Test Results

Figures 96 through 102 are a presentation of the test data in graphical form. The curves show the data points and a broken line indicating the trend of the data. The solid line is the predicted value of deviation for that position on the glass at the corresponding angle of incidence. This curve is based upon Eq. (93) and the calculation of the radii of curvature derived in Equation (98). The last curve in the set, Figure 102 shows the reading made for  $\phi = 22.5$  degrees in the small chamber using the modified collimator. Another reading was made at  $0^\circ$  with the same collimator in the same aperture but no deviation was observed.

#### Conclusions

Qualitative agreement between experimental results and later theory has been established:

- (a) Measured deviations are in proper direction.
- (b) Deviations are a direct function of angle of incidence.
- (c) Deviations are functions of the radial distance from the window "vertex" at which the light passes through. Both the magnitude and direction of the measured deviations agree with theory.

Quantitatively, the test results are in fair agreement with predicted values, the largest discrepancy being a factor of 3. It is believed that the discrepancy may arise because an approximation is used in the prediction of deviation by the method of thin shells. Since the experimental measurement is quite sensitive, it may be that this approximation is not sufficiently accurate. Another possibility is that the physical property data for the glass are not accurate.

#### Temperature Test Equipment

In the temperature tests the glass panels were heated by radiation from several quartz lamps. Thermocouples were attached at eight locations on each panel, Figure 103, by means of Sauereisen cement, and covered with aluminum insulating tape. The temperature measured by each thermocouple was monitored every two minutes on a Minneapolis-Honeywell multichannel recorder. As the temperature and temperature gradient changed over a period of time, deviation

of light through the panel was measured with a Wild theodolite. Several difficulties were encountered in making measurements of the effect of temperature. First the image of the collimator cross hair as seen through the theodolite was not stationary. This was due to the fact that the heated air through which the collimated beam passed was very turbulent. However by aligning the theodolite to the "average" position of the projected image, a fairly accurate trend was established. To verify that this trend was a result of window curvature, and was not due to index variations in the air, the window was mounted inside a vacuum chamber, and the deviations were read by viewing the deviated beam as it emerged through a small window in the chamber. A check was made on this chamber window to verify that it did not contribute to the deviation. The trend established in these tests was about the same as those read in the open atmosphere. Another problem that produced reading errors was the washing out of the image due to visible light reflected by the window into the theodolite from the quartz lamp. This resulted in severe contrast reduction and caused difficulty in reading the deviations accurately. This situation was improved by increasing the brightness of the collimator image. Finally, some of the temperature readings were inaccurate because the cement holding the thermocouples to the glass did not adhere throughout the test. However, near the center where the beam passed through the glass, the thermocouples did not break away. Thus it is felt that the temperature at these points were fairly accurate. In the vacuum chamber tests, the thermocouples adhered to the glass throughout the tests. The setup is shown in Figures 104 and 105.

#### Temperature Test Results

Figures 106 through 128 are graphical presentation of the data obtained in the temperature tests. The temperatures are shown as a function of time for eight points on the window. The positions of these eight points are shown in Figure 129. The solid line in each case is the temperature curve, the triangles represent the optical deviation data points, and the connecting line represents the trend of the deviation data. The data were plotted in such a way that if the angle measured was greater than the initial angle, the deviation was recorded as positive. If the angle measured was less than the initial angle, then the deviation was recorded as negative. The legend on each page describes the conditions under which the test was conducted.

#### Conclusions

Qualitative agreement between experimental results and the modified theory described in this report has been established:

- (a) Measured deviations are in proper direction.
- (b) Deviations are a direct function of angle of incidence.
- (c) The radial distance from the center of the panel at which the light passes through the window influences the degree of deviation. Both the magnitude and direction of this effect is corroborated by the tests.

Quantitatively, agreement is difficult to obtain because the precise temperature distribution is not known through the glass. Before exact calculations can be obtained, these distributions must be known. Additionally, the edges of the glass panels were constrained because of the necessity of holding the panel upright. It is believed that this constraint prevents the glass from expanding linearly, and thus causes it to bow. This results in a greater surface curvature than would be expected from temperature distribution alone.



Identifying Letter	Glass Type	Corning Code
A	1723 Glass 1" thick 9" diameter	586017
B	1723 Glass 1/2" Thick 9" diameter	586015
C	1723 Glass 1" Thick 9" square	586018
D	7740 Glass 1" Thick 9" square	586018
E	1723 Glass 1/2" Thick 9 square	586016
F	7940 Glass 1" Thick 9" square	586018
G	1723 Glass 2" Thick 9" diameter	586019
H	1723 Glass 2" Thick 9" square	586020

Table II

DESCRIPTION OF GLASS TEST PANELS

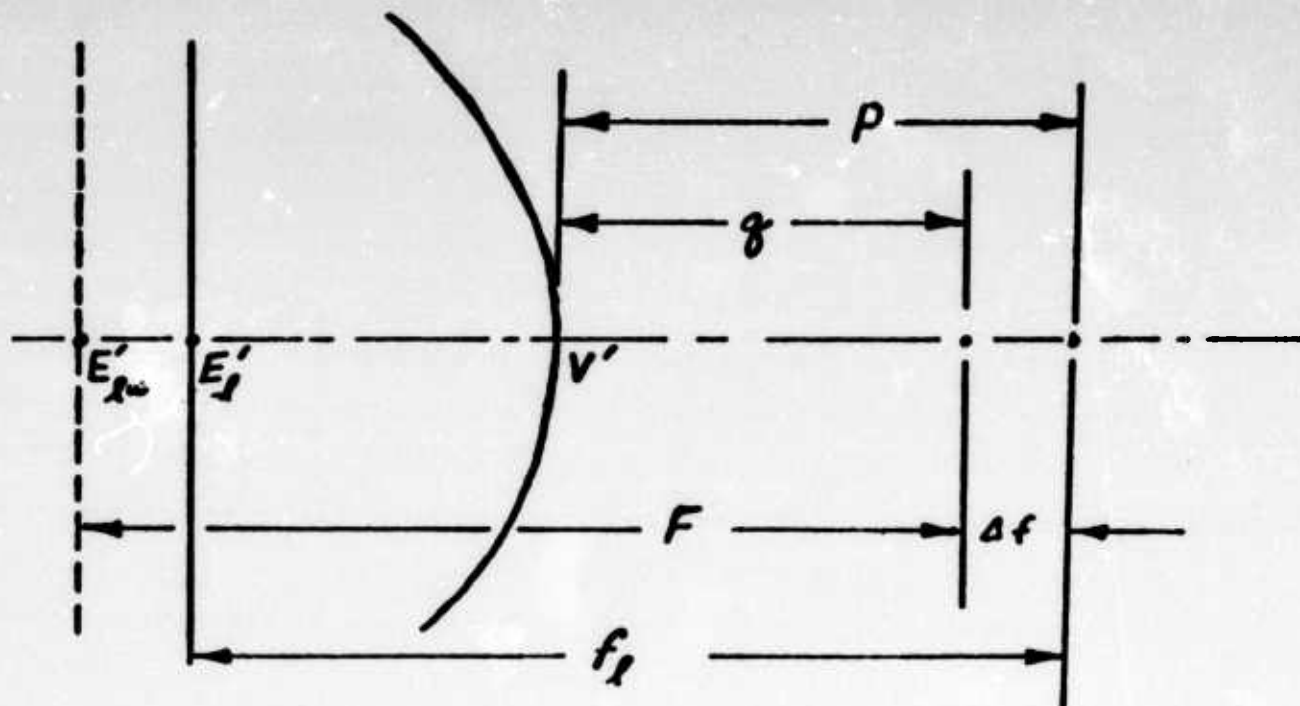


FIGURE 57

SCHEMATIC DRAWING OF THE IMAGE SPACE SHOWING THE BACK PRINCIPAL PLANE AND THE FOCAL POINT, BEFORE AND AFTER FOWER IS INTRODUCED TO THE SYSTEM. THE POINT  $V'$  REPRESENTS THE VERTEX OF THE LENS, AND  $E$  THE POSITION OF THE PRINCIPAL PLANE BEFORE IOWER IS INTRODUCED.

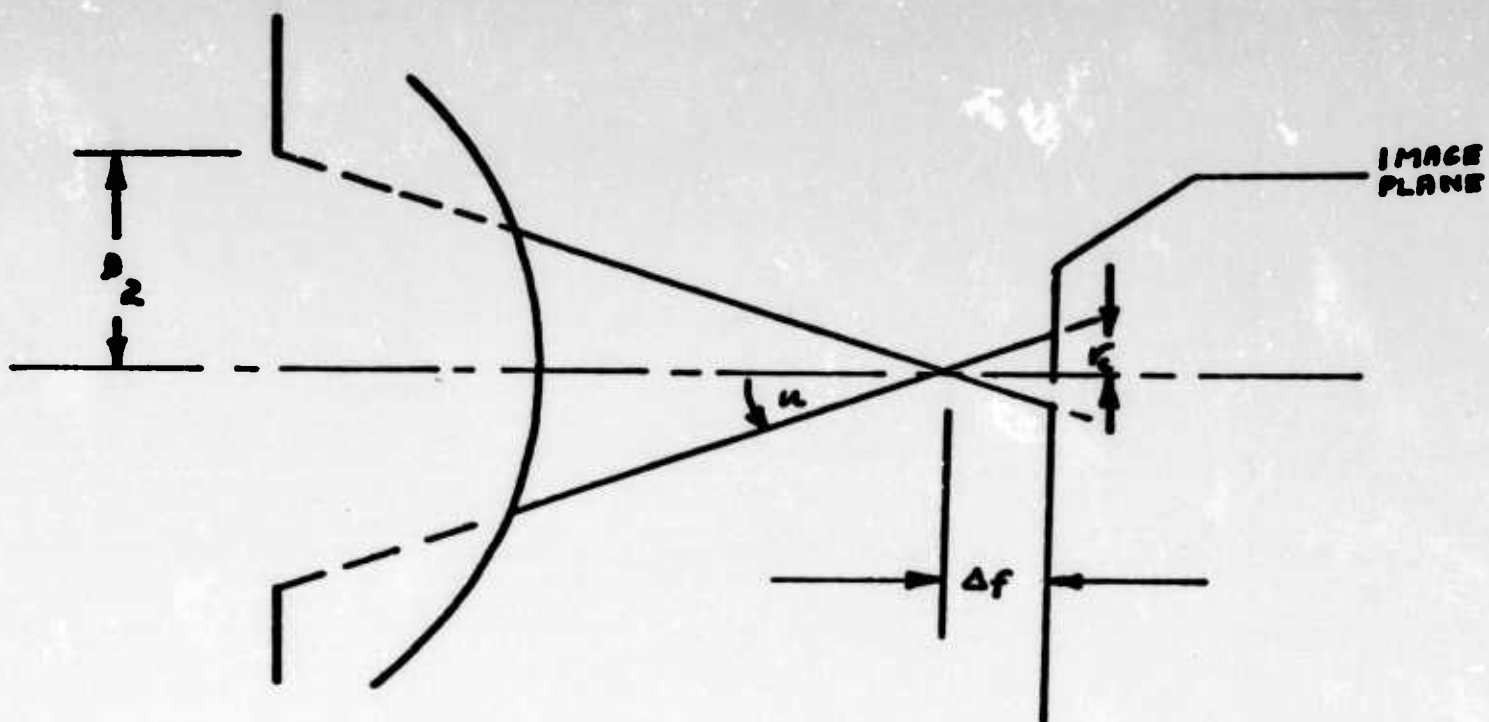


FIGURE 58

SCHMATIC DRAWING OF THE IMAGE SPACE SHOWING THE POSITION AND DIAMETER OF THE EXIT PUPIL, THE ANGLE OF CONVERGENCE, THE RADIUS OF THE BLUR CIRCLE, AND THE POSITION OF THE IMAGE PLANE

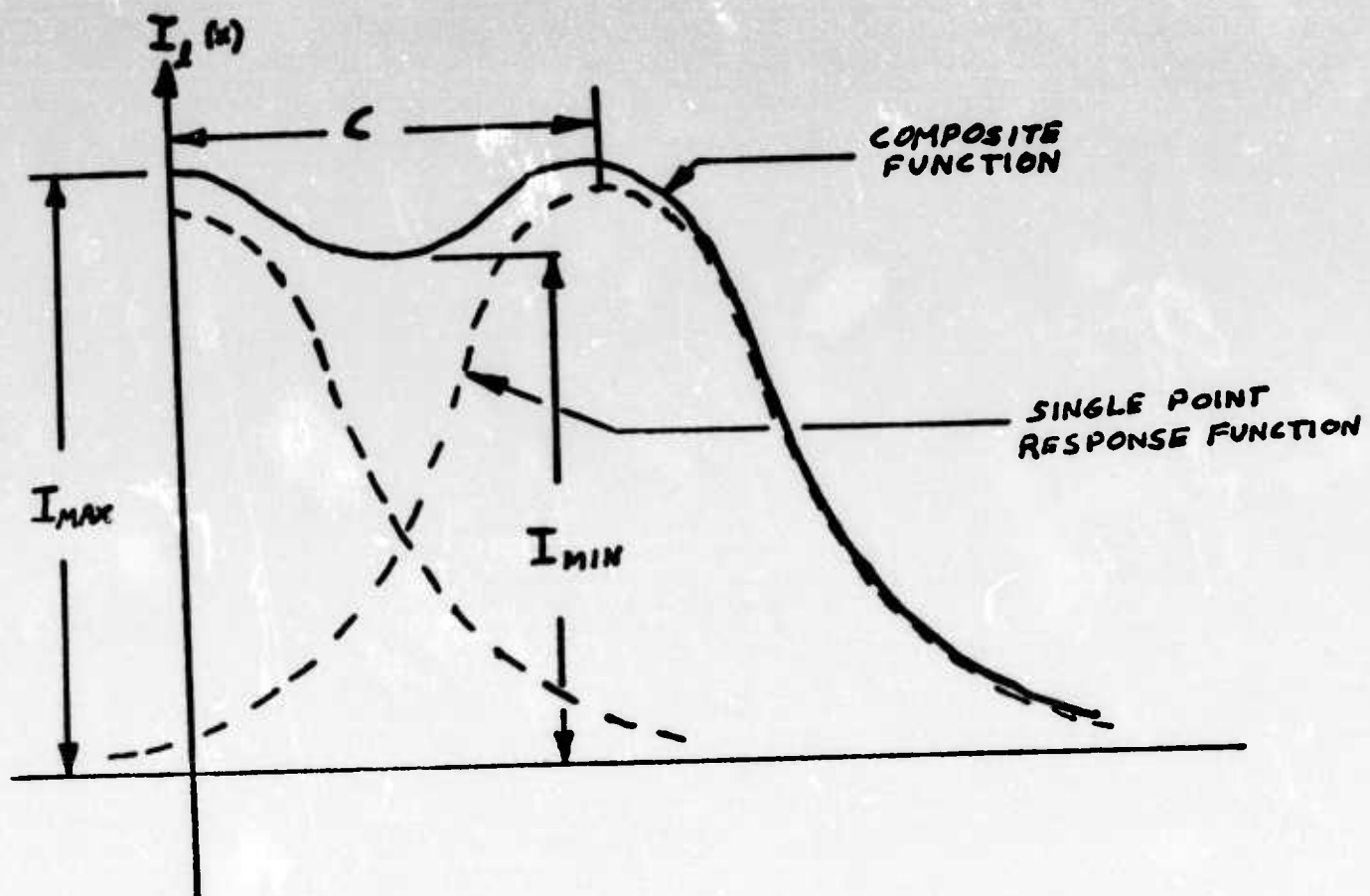


FIGURE 59

THE INTENSITY DISTRIBUTION FUNCTIONS FOR SINGLE  
POINT RESPONSE AND THE COMPOSITE FUNCTION



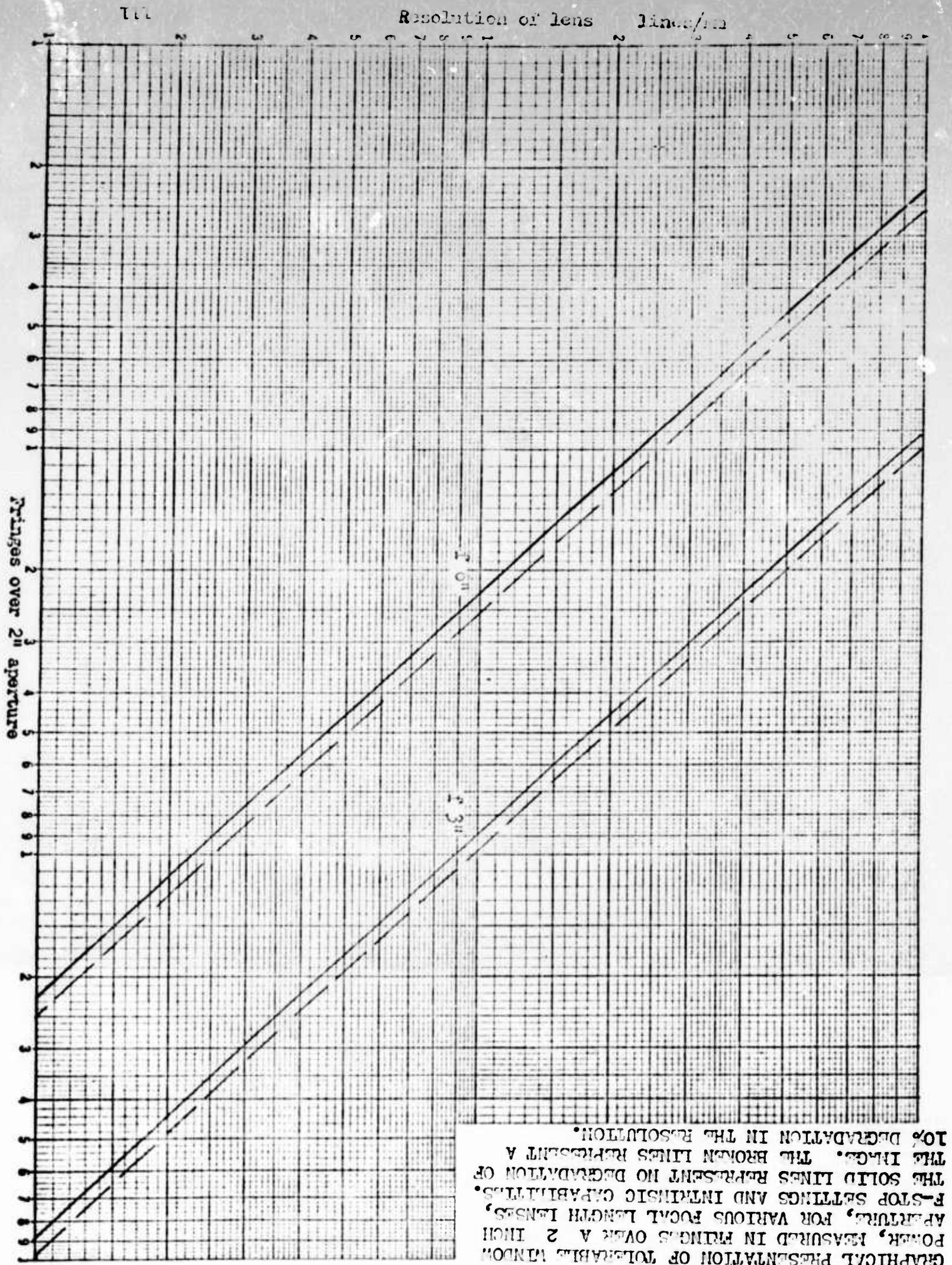


FIGURE 60

GRAPHICAL PRESENTATION OF TOLERABLE RANDOM FOCUS, MEASURED IN FRINGES OVER A 2 INCH APERTURE, FOR VARIOUS FOCAL LENGTH LENSES, F-STOP SETTINGS AND INTRINSIC CAPABILITIES. THE SOLID LINES REPRESENT NO DEGRADATION OF THE IMAGE. THE BROKEN LINES REPRESENT A 10% DEGRADATION IN THE RESOLUTION.



FIGURE 61

GRAPHICAL PRESENTATION OF TOLERABLE WINDOW POWER, MEASURED IN FRINGES OVER A 2 INCH APERTURE, FOR VARIOUS FOCAL LENGTH LENSES, F-STOP SETTINGS AND INTRINSIC CAPABILITIES. THE SOLID LINES REPRESENT NO DEGRADATION OF THE IMAGE. THE BROKEN LINES REPRESENT A 10% DEGRADATION IN THE RESOLUTION.

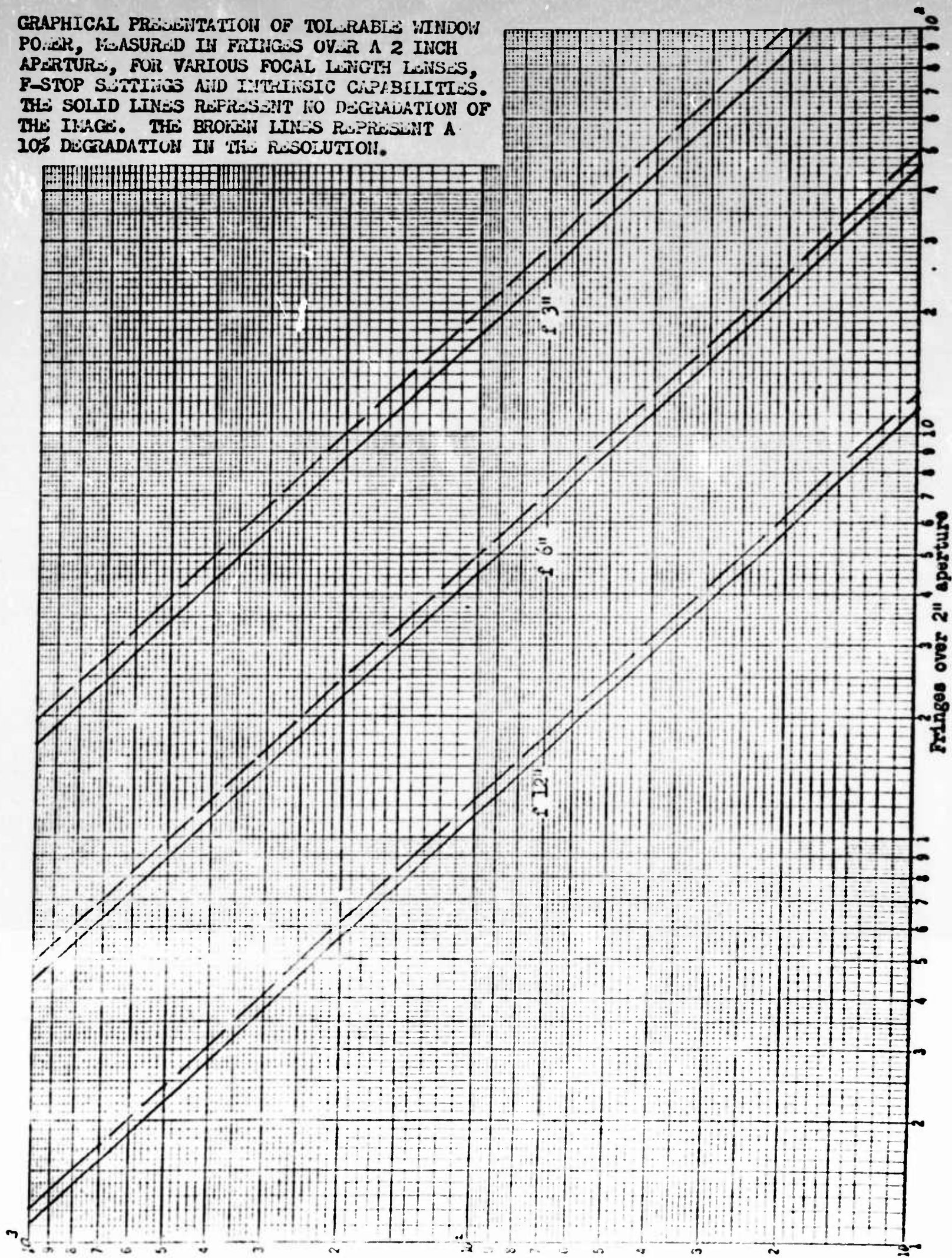




FIGURE 62

GRAPHICAL PRESENTATION OF TOLERABLE WINDOW POWER, MEASURED IN FRINGES OVER A 2 INCH APERTURE, FOR VARIOUS FOCAL LENGTH LENSES, F-STOP SETTINGS AND INTRINSIC CAPABILITIES. THE SOLID LINES REPRESENT NO DEGRADATION OF THE IMAGE. THE BROKEN LINES REPRESENT A 10% DEGRADATION IN THE RESOLUTION.

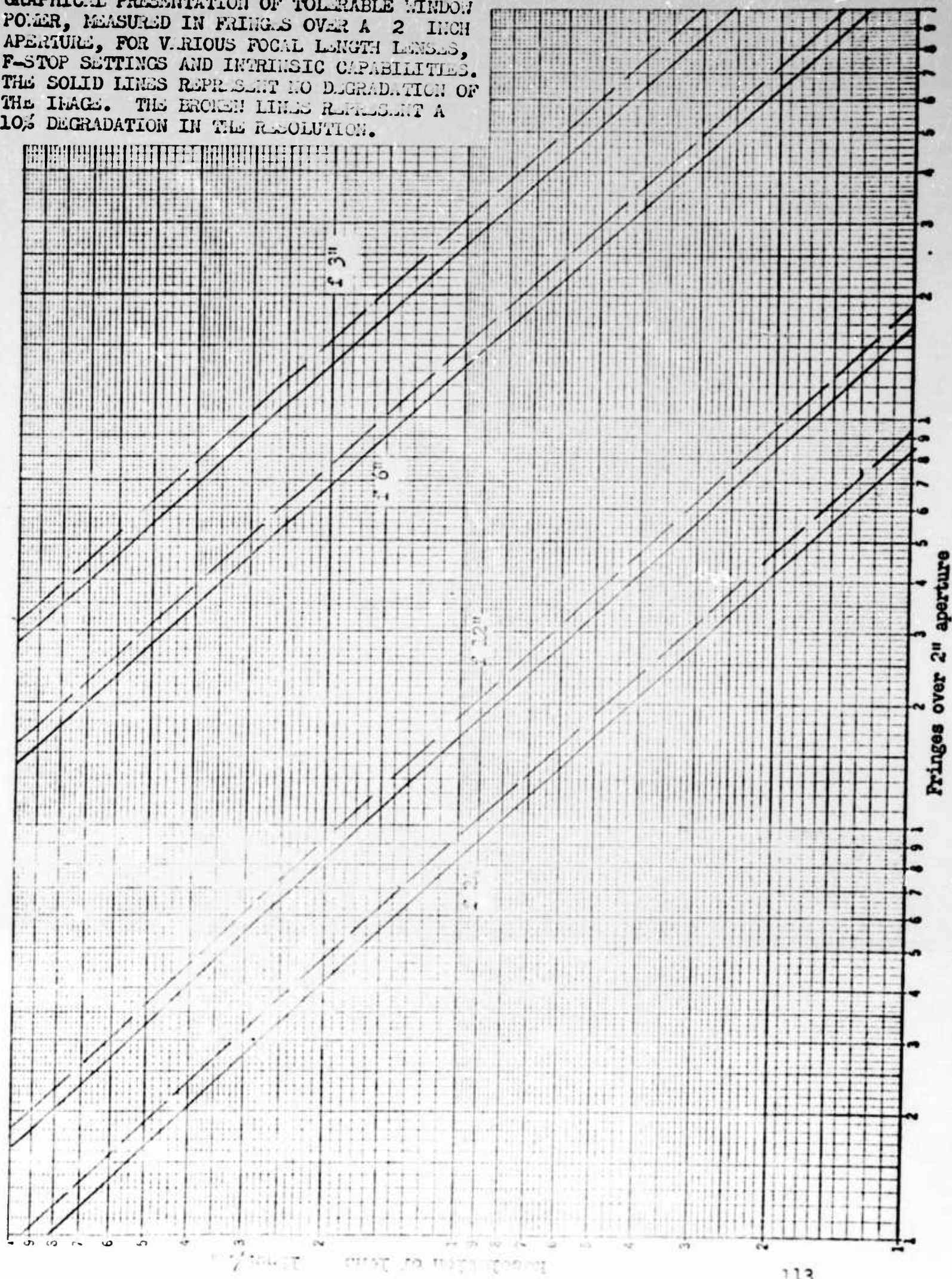




FIGURE 63

GRAPHICAL PRESENTATION OF TOLERABLE WINDOW POWER, MEASURED IN FRINGES OVER A 2 INCH APERTURE, FOR VARIOUS FOCAL LENGTH LENSES, F-STOP SETTINGS AND INTRINSIC CAPABILITIES. THE SOLID LINES REPRESENT NO DEGRADATION OF THE IMAGE. THE BROKEN LINES REPRESENT A 10% DEGRADATION IN THE RESOLUTION.

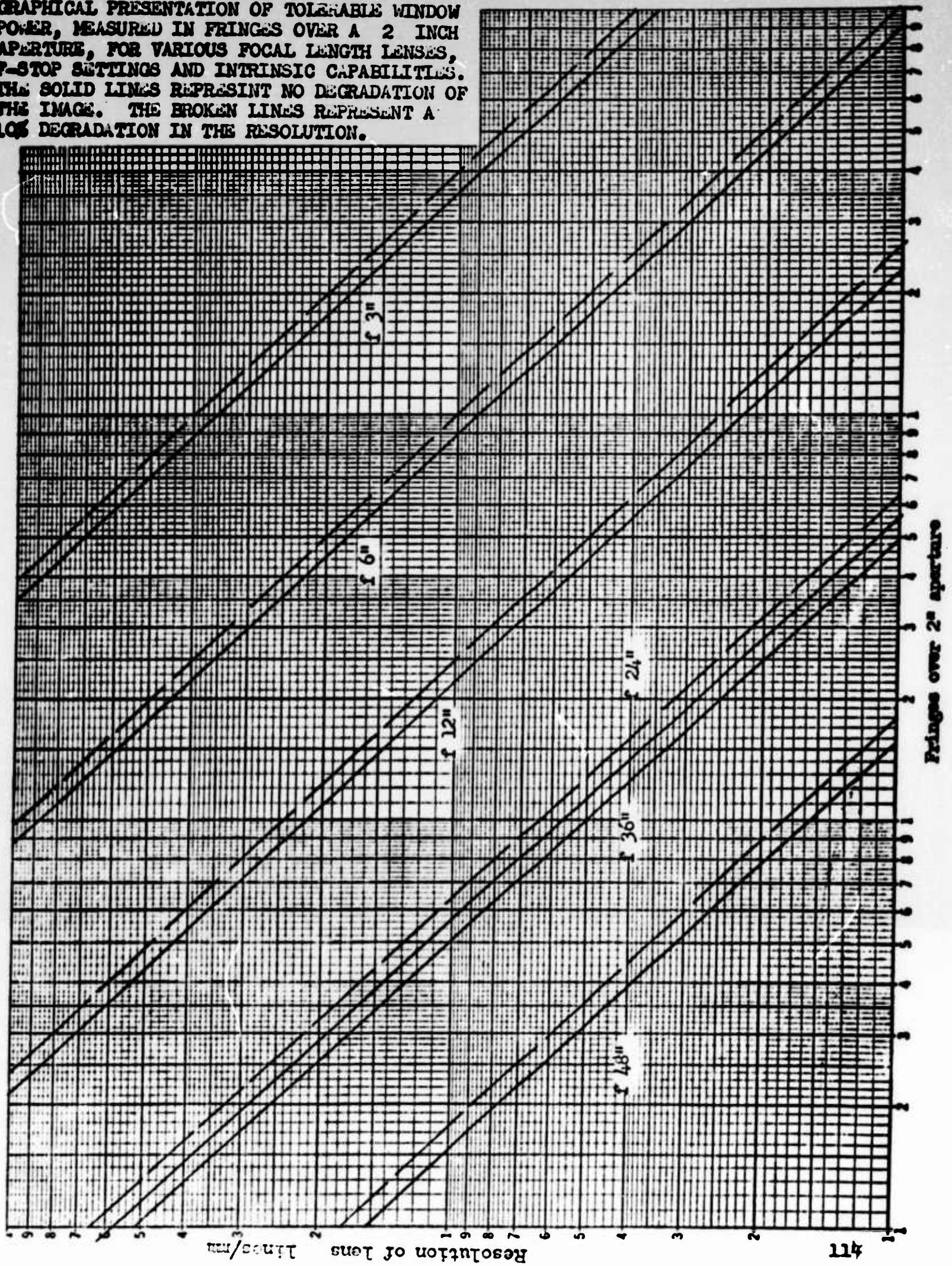




Figure 64 has been deleted.



FIGURE 65 Test arrangement to check the effect of window samples on the image formed from a collimator beam.



FIGURE 66 Interferometer with window sample in test position.



FIGURE 67 Interferometer fringe pattern without window glass in test position. This represents the ideal pattern for spherical power.

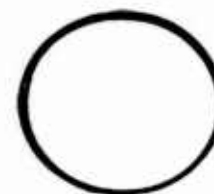
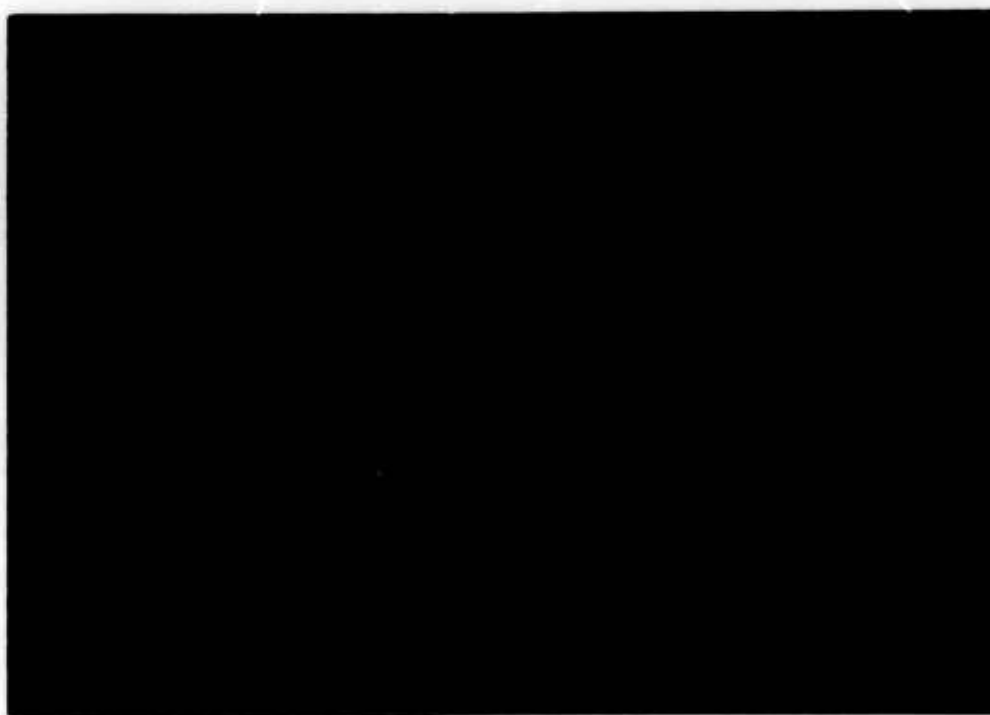


FIGURE 68 Window sample A in test position. Circle at right represents collimator objective diameter (1.5 in.) on the scale of the photograph.

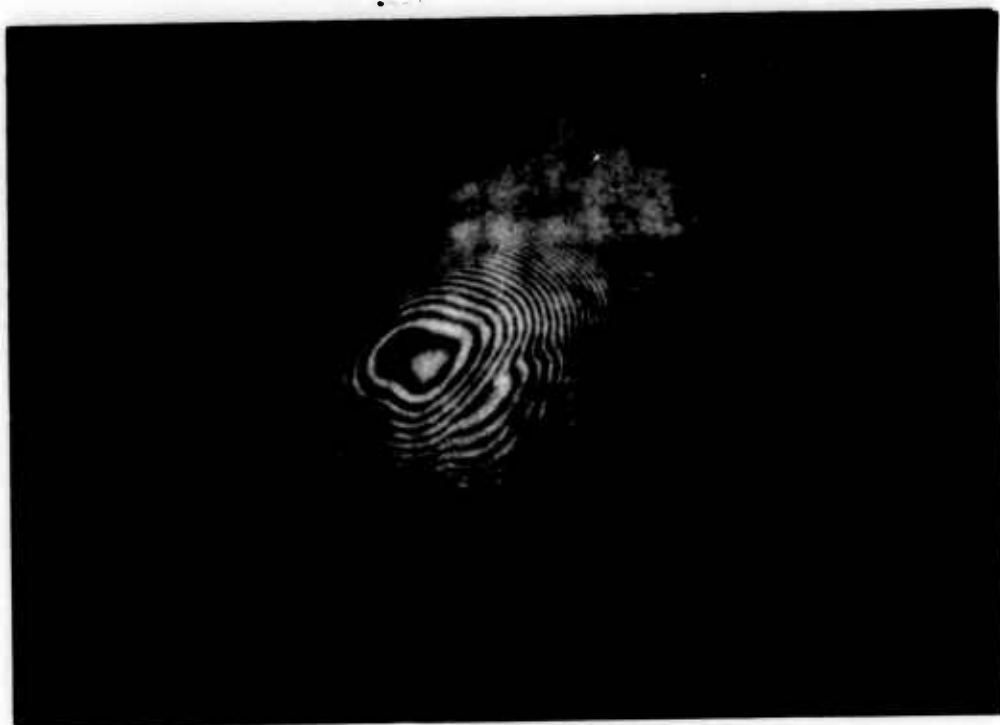


FIGURE 69 Window Sample B in interferometer test position

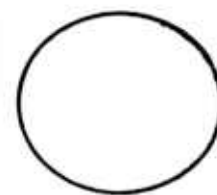
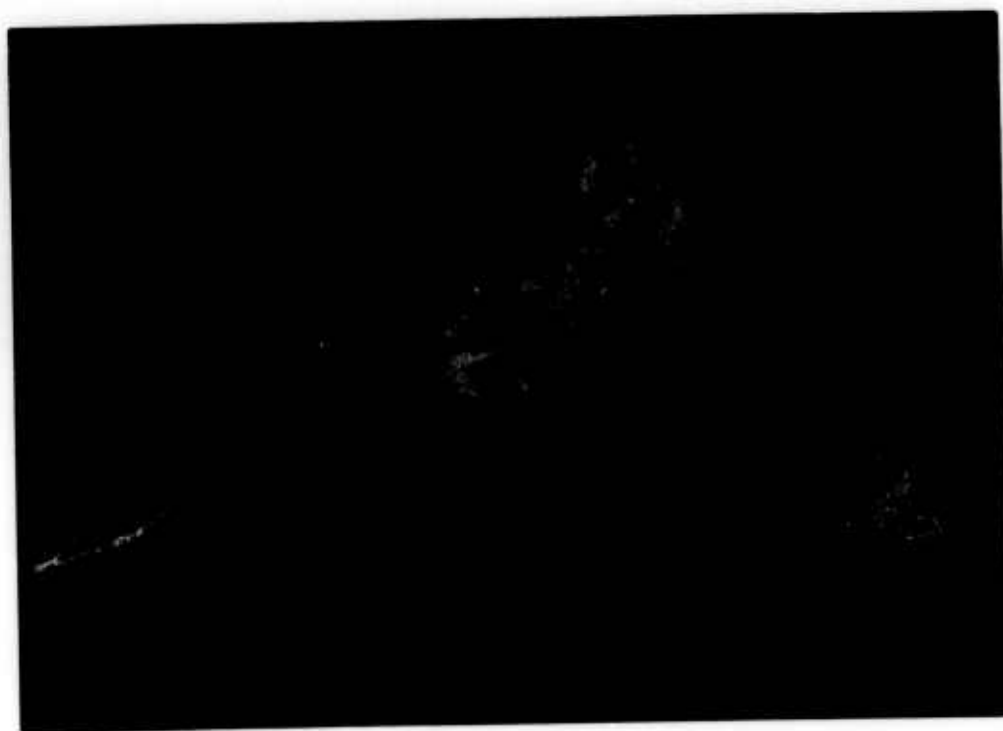


FIGURE 70 Window Sample C in interferometer test position.  
Circle at right represents the diameter of the  
collimator objective (1.5)





FIGURE 71 Interferometer pattern for window sample D



FIGURE 72 Interferometer pattern for window sample E.  
Circle at right represents the collimator  
objective diameter.

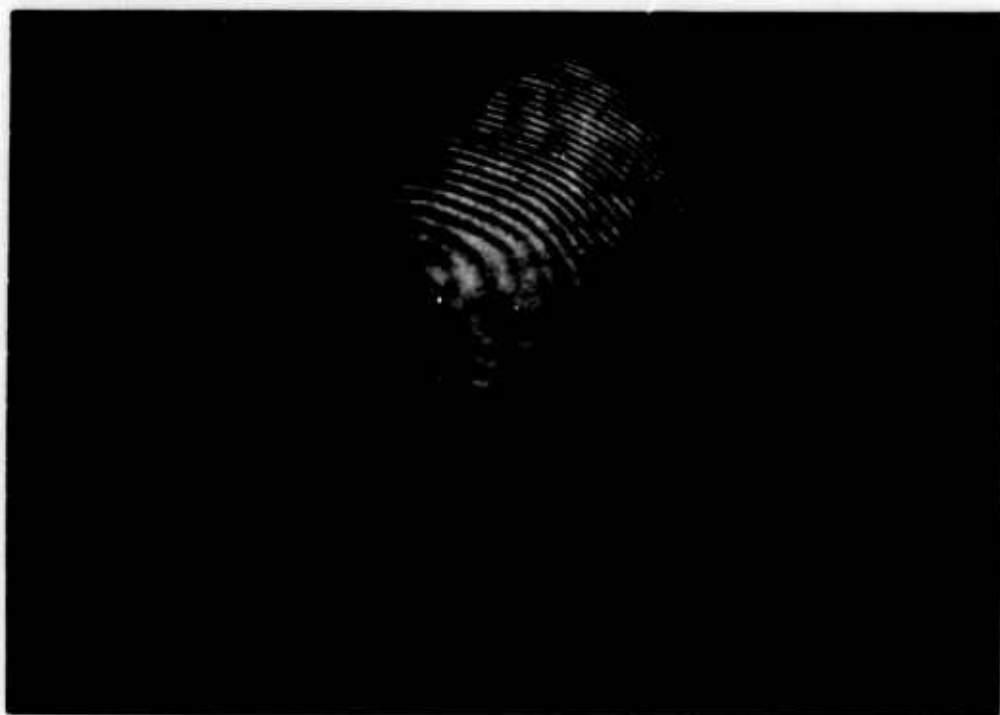


FIGURE 73 Interferometer pattern for glass sample F.

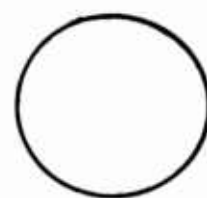


FIGURE 74 Interferometer pattern for glass sample G.  
Circle at right represents the diameter of  
the collimator objective.

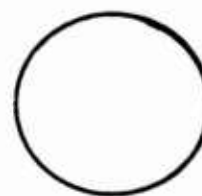
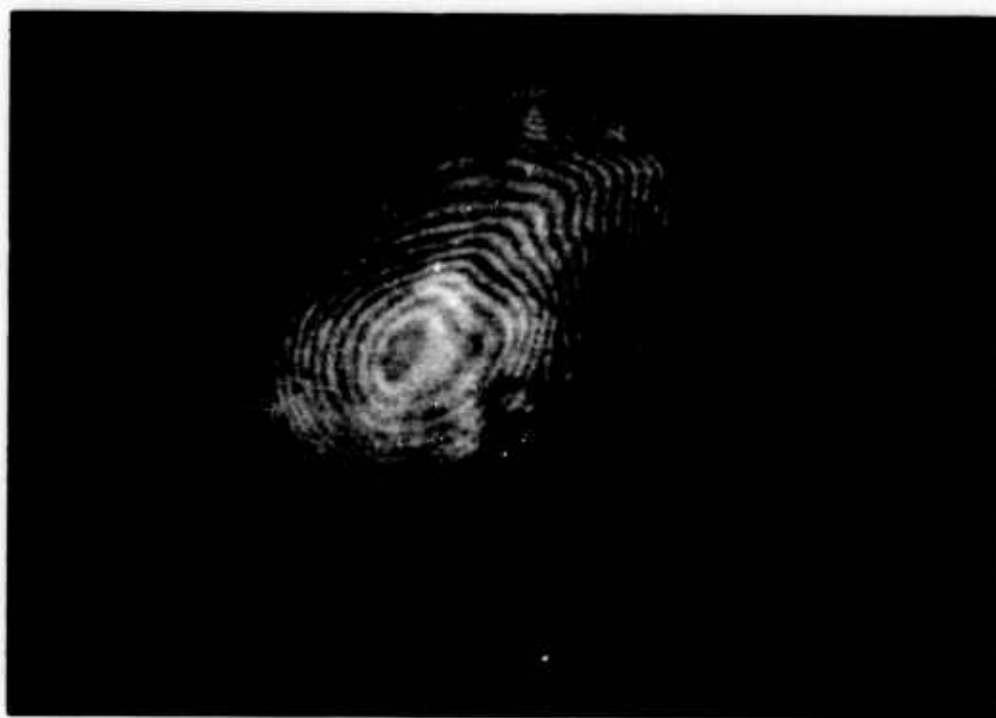


FIGURE 75 Interferometer pattern for glass sample H.  
Circle at right represents collimator  
objective diameter.

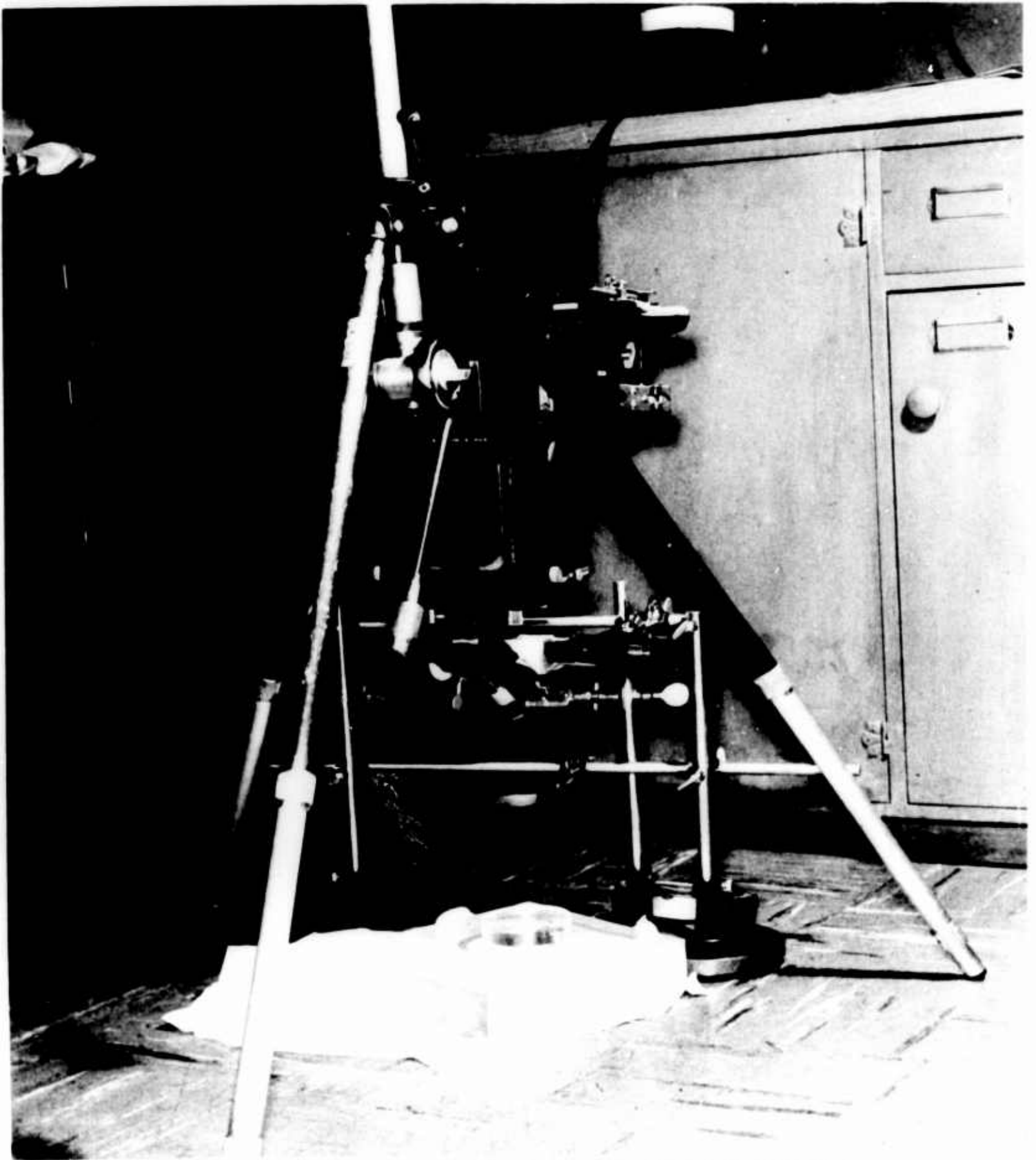


Figure 76

Test Setup for Photographing Test  
Fringe Pattern



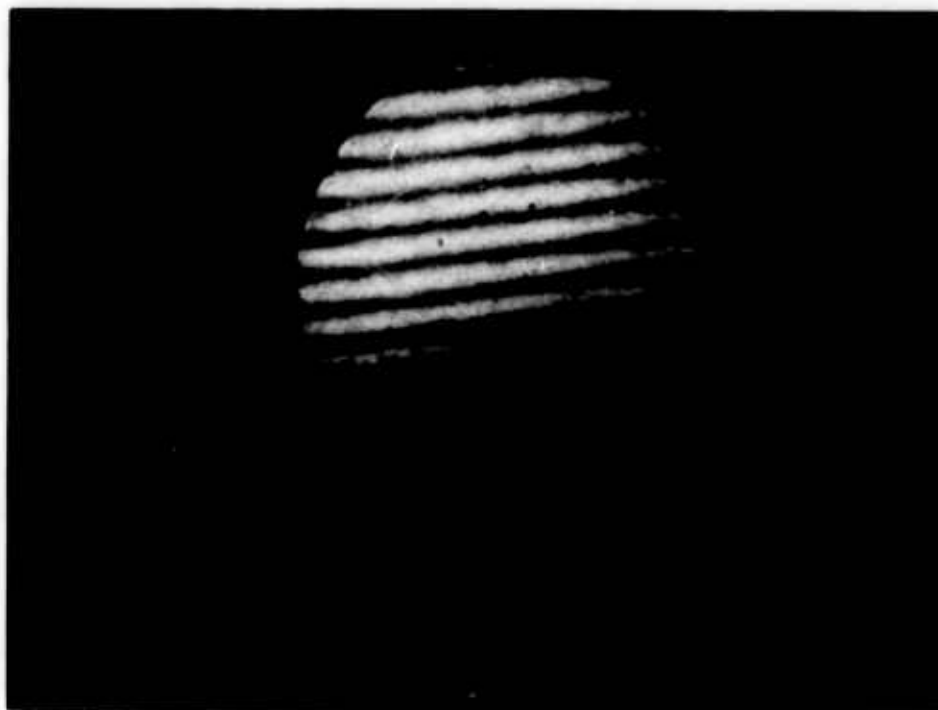


FIGURE 77 Fringe pattern produced by two test flats.



FIGURE 78 Fringe pattern produced by test flat and uncoated surface of window sample A.

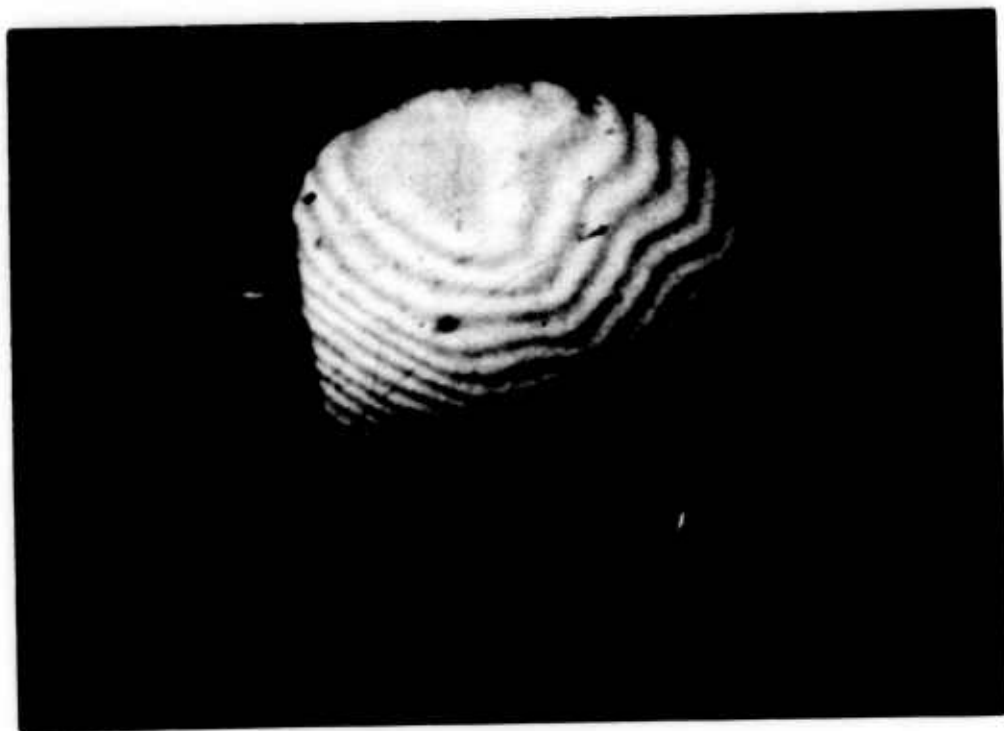


FIGURE 79 Fringe pattern produced by test flat and window sample B.

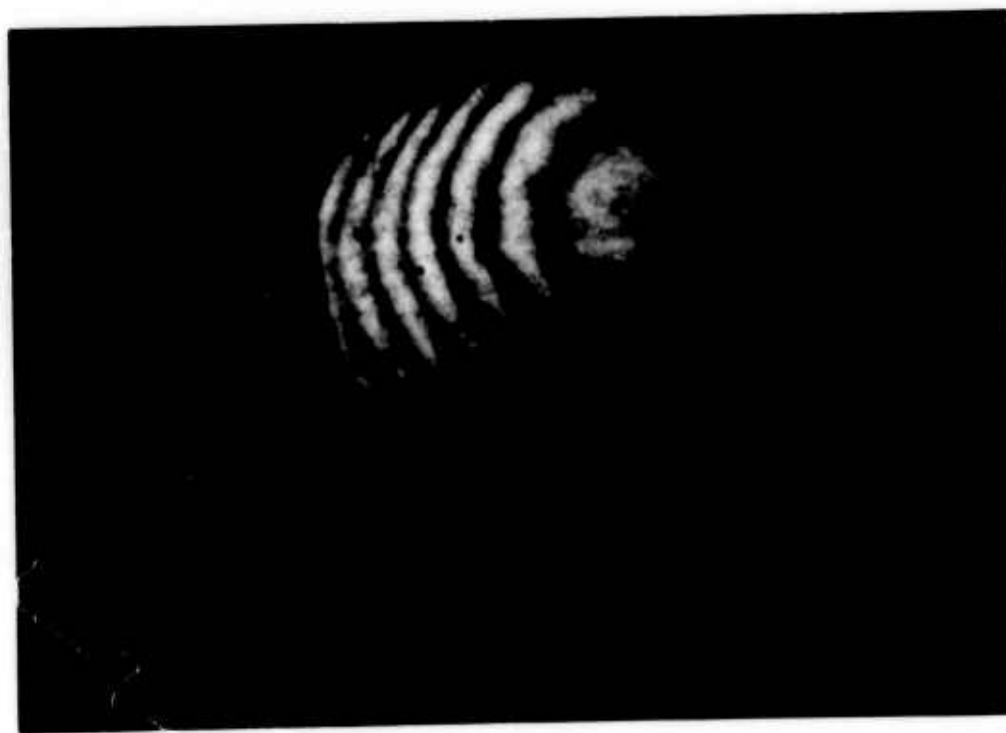


FIGURE 80 Fringe pattern produced by test flat and window sample C.



FIGURE 81 Fringe pattern produced by test flat and window sample D.



FIGURE 82 Fringe pattern produced by test flat and Window E.

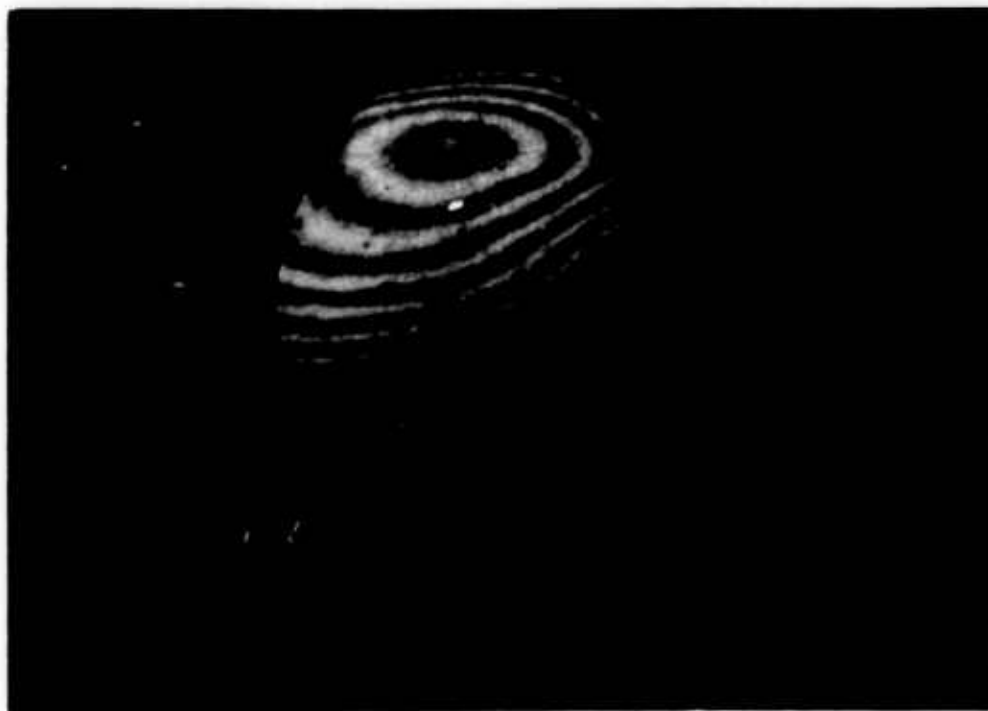


FIGURE 83 Fringe pattern produced by test flat and window sample F.

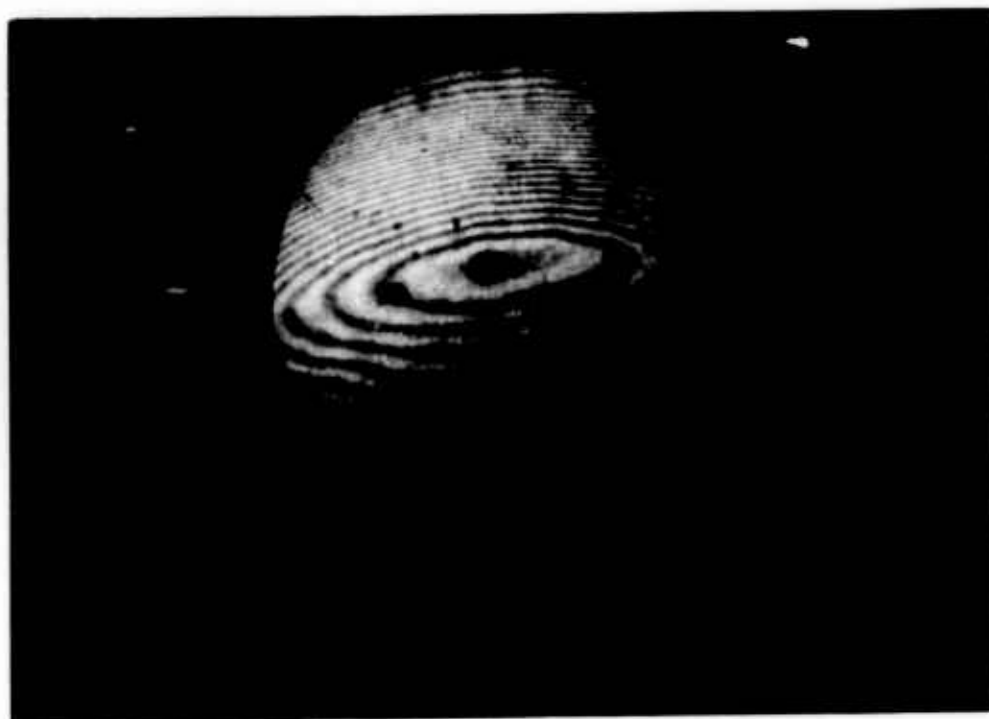


FIGURE 84 Fringe pattern produced by test flat and window sample G.





**FIGURE 85** Fringe pattern produced by test flat and Window sample H.

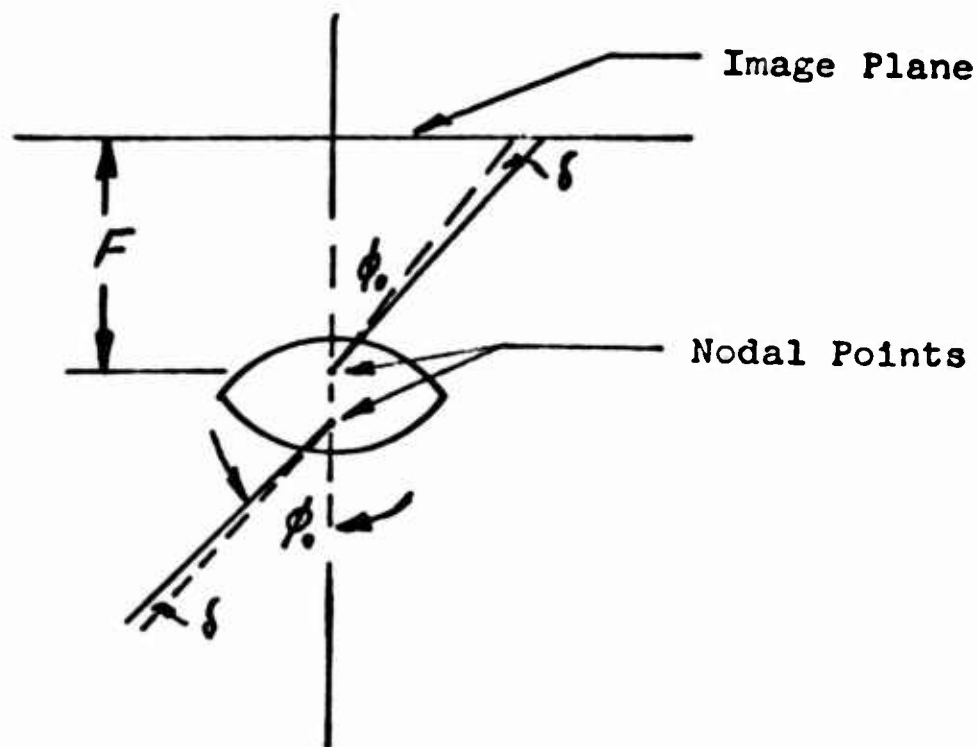


FIGURE 86 GEOMETRY OF THE OPTICAL SYSTEM FOR DEVIATED AND UNDEVIATED RAYS.

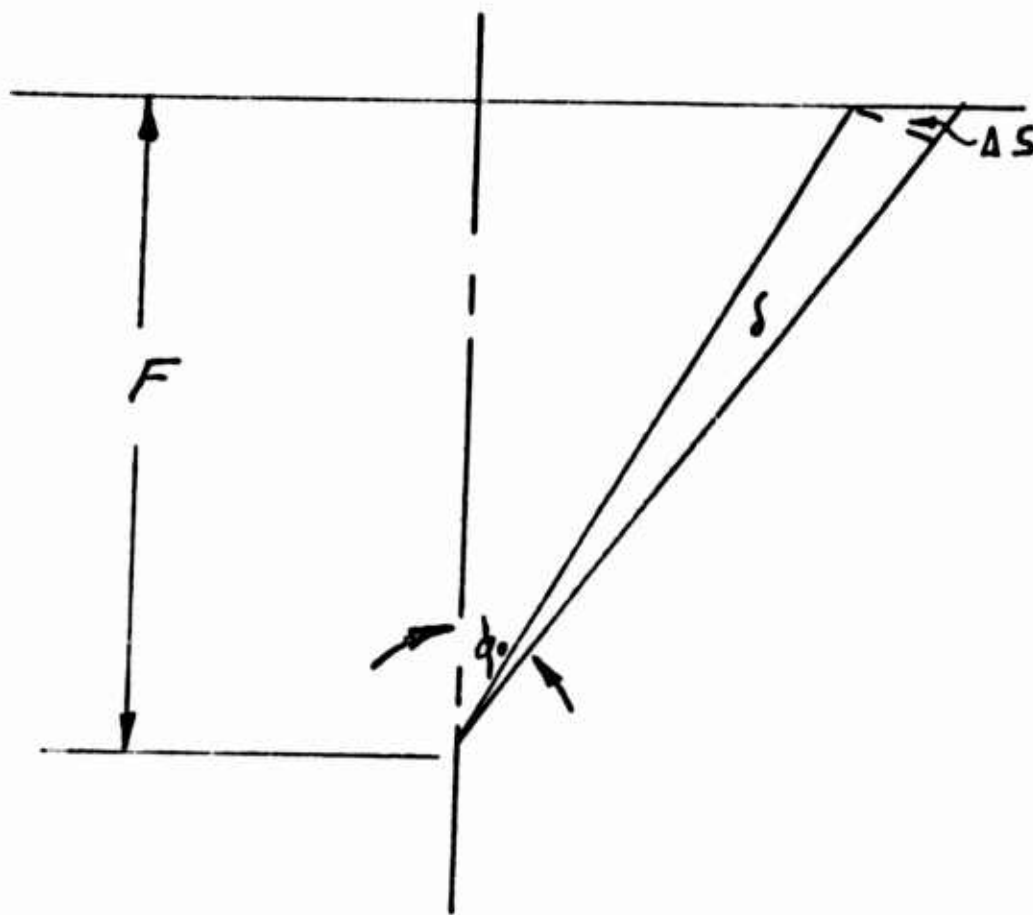


FIGURE 87 GEOMETRY OF THE DEVIATED AND UNDEVIATED RAYS IN THE IMAGE SPACE.

FIGURE 88

Graph of the Product of Resolution and Focal  
Length as a Function of the Difference in  
Deviation. The Parameter is  $\phi_0$ .

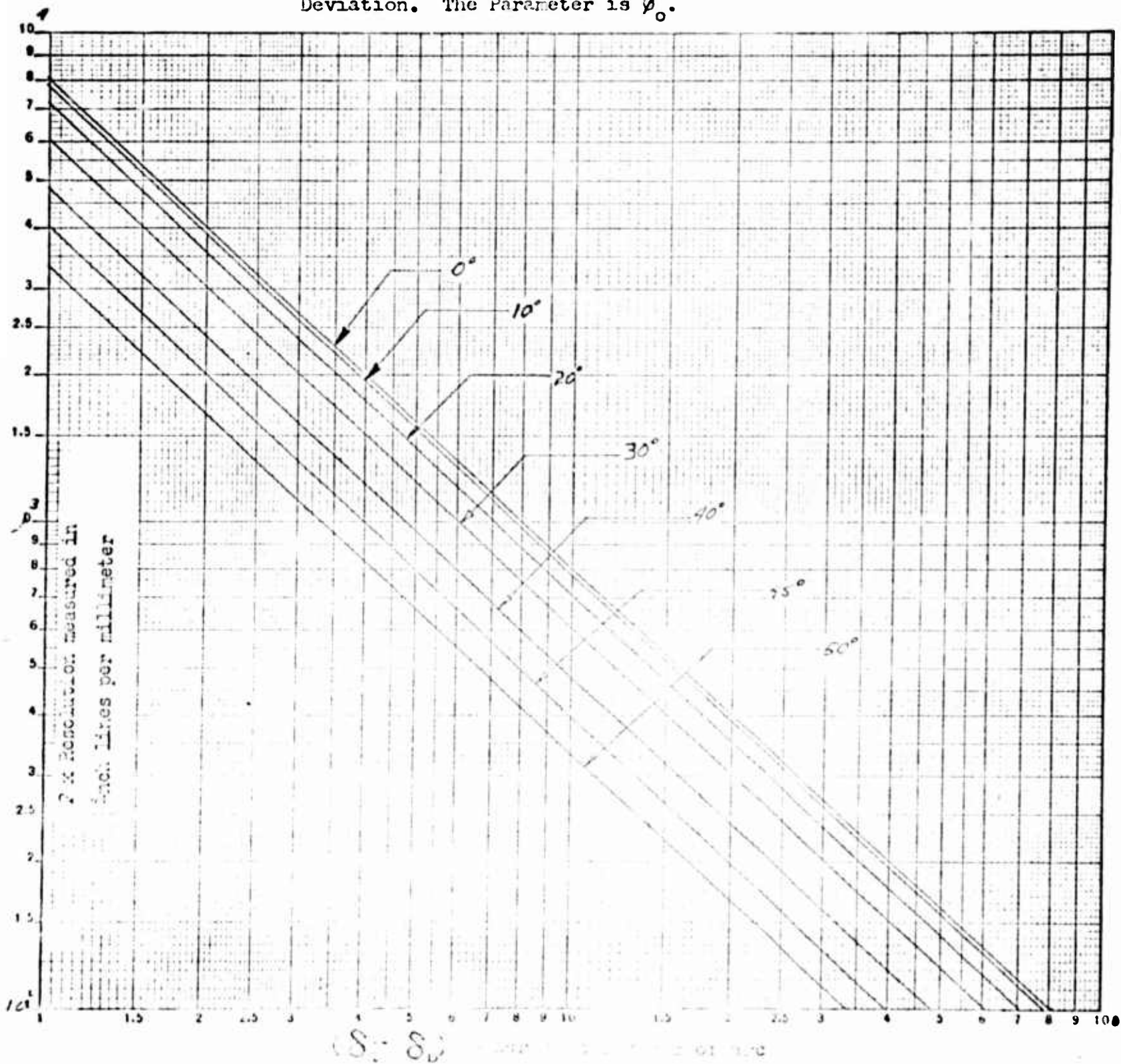
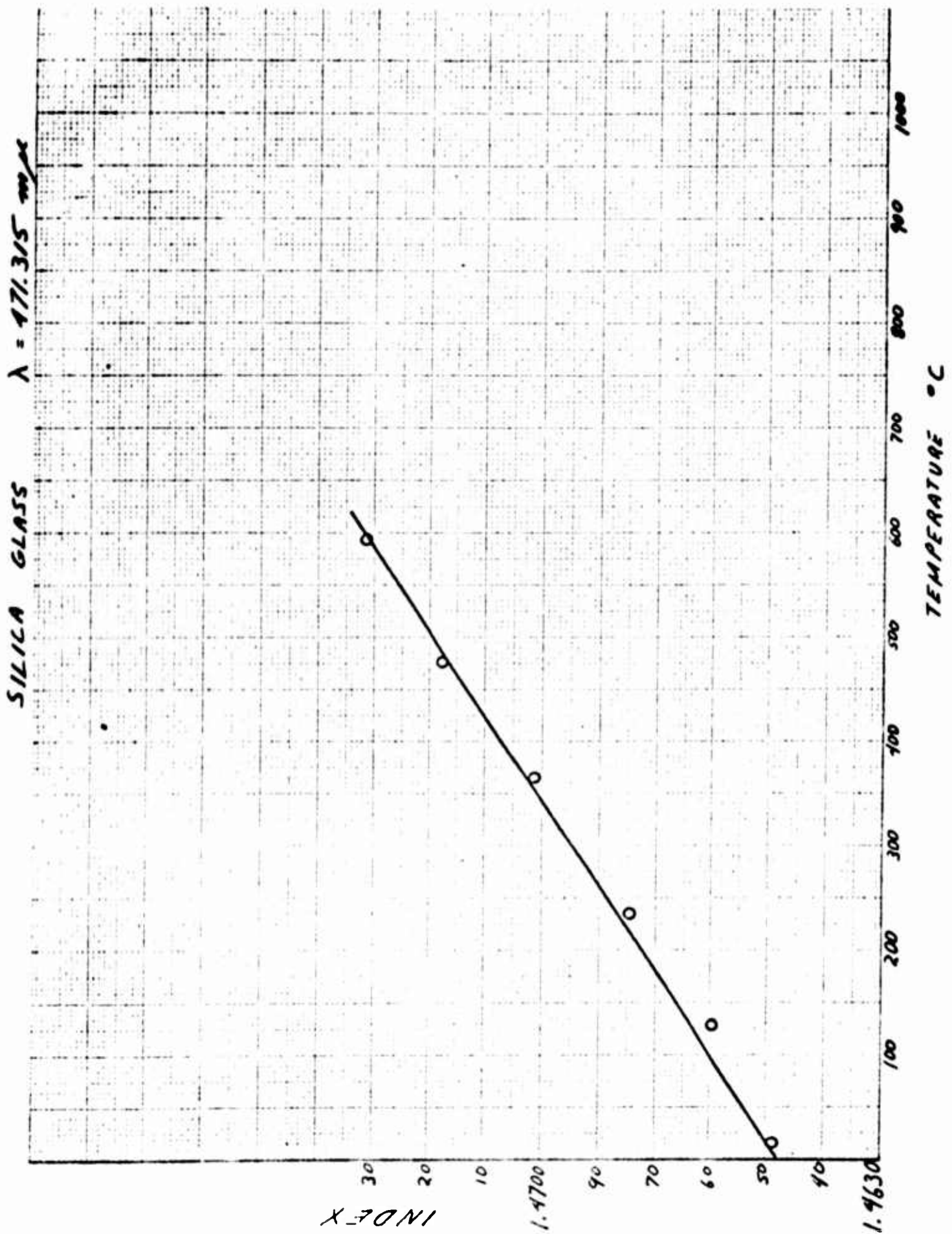


FIGURE 89

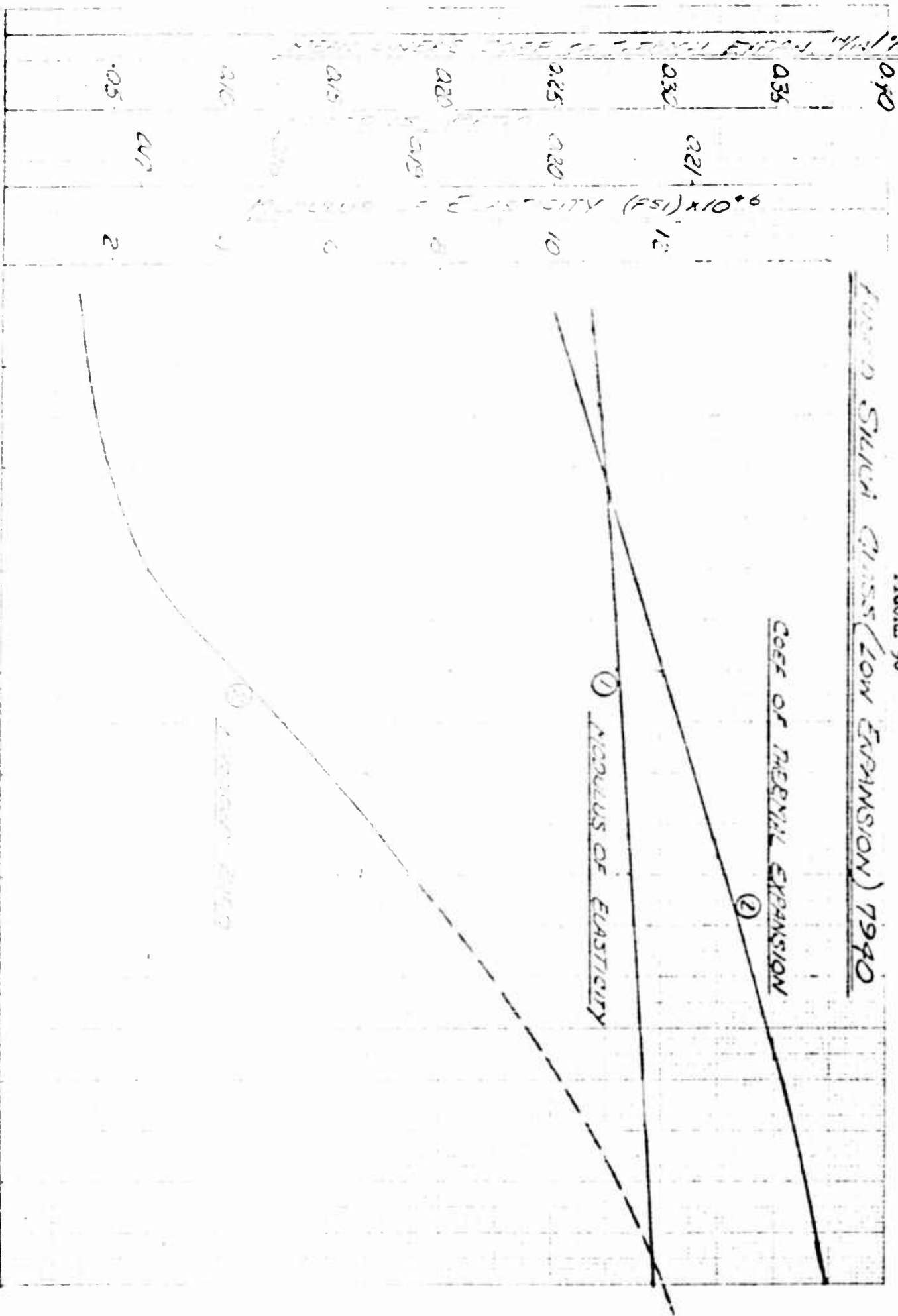
Graph of Index of Refraction versus Temperature for Fused Silica Glass #7940



Graph of Thermal Expansion Coefficient, Modulus of Elasticity, and Poisson's Ratio versus Temperature for Fused Silica Glass #7940



FIGURE 90  
Fused Silica Glass (Low Expansion) 7940



Coefficient of Thermal Expansion Coefficient, Modulus of Elasticity, and Poisson's Ratio versus

① Fused Silica Glass 7940  
② Fused Silica Glass 7940  
③ Fused Silica Glass 7940

**FIGURE 91**  
**Diagram of Ray Trace Showing Propagation Vectors, Normal Vectors,**  
**the Coordinate System, and the Angle of Deviation.**

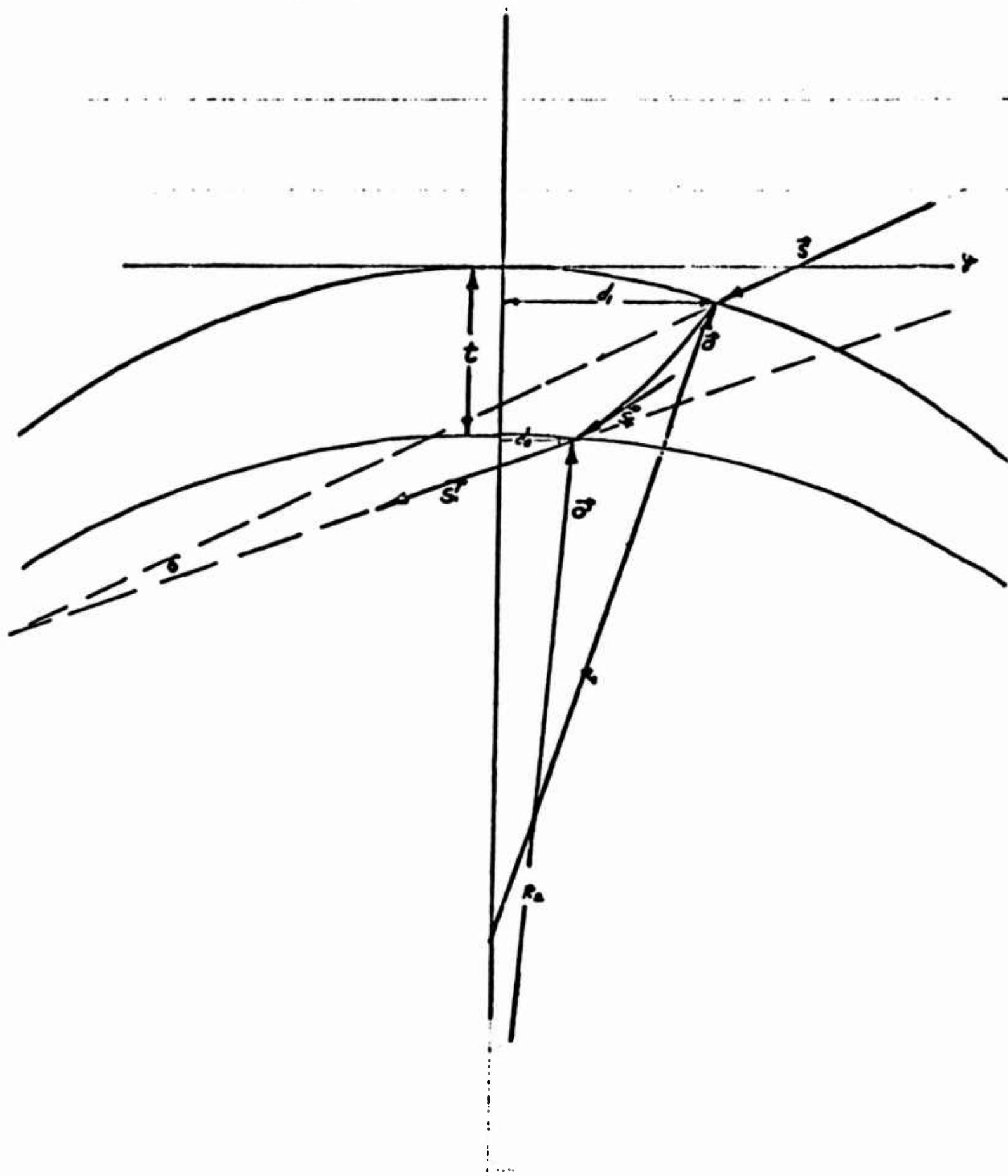


FIGURE 92

Curve of the Equation of Curvature  
for a Square Plate

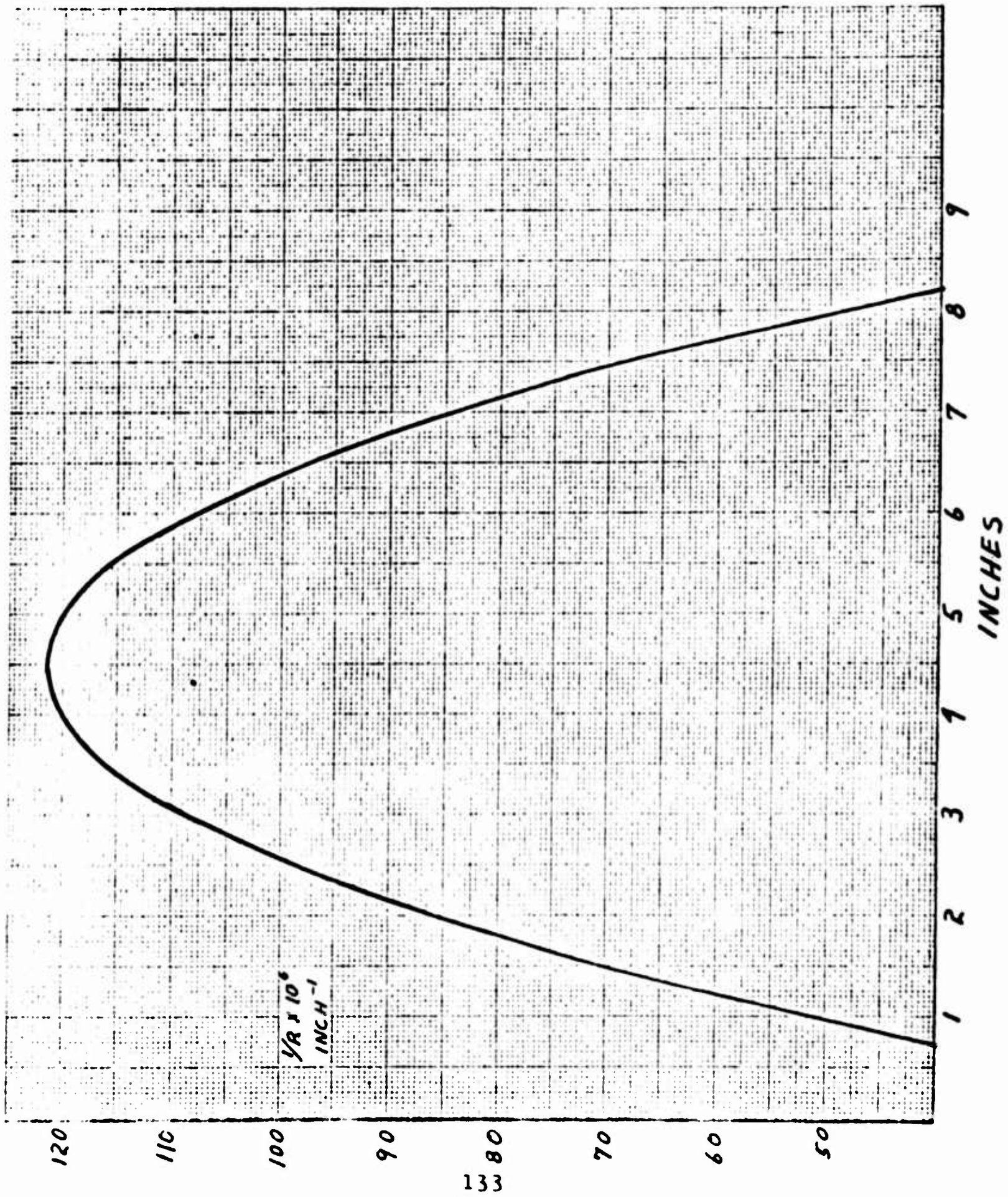
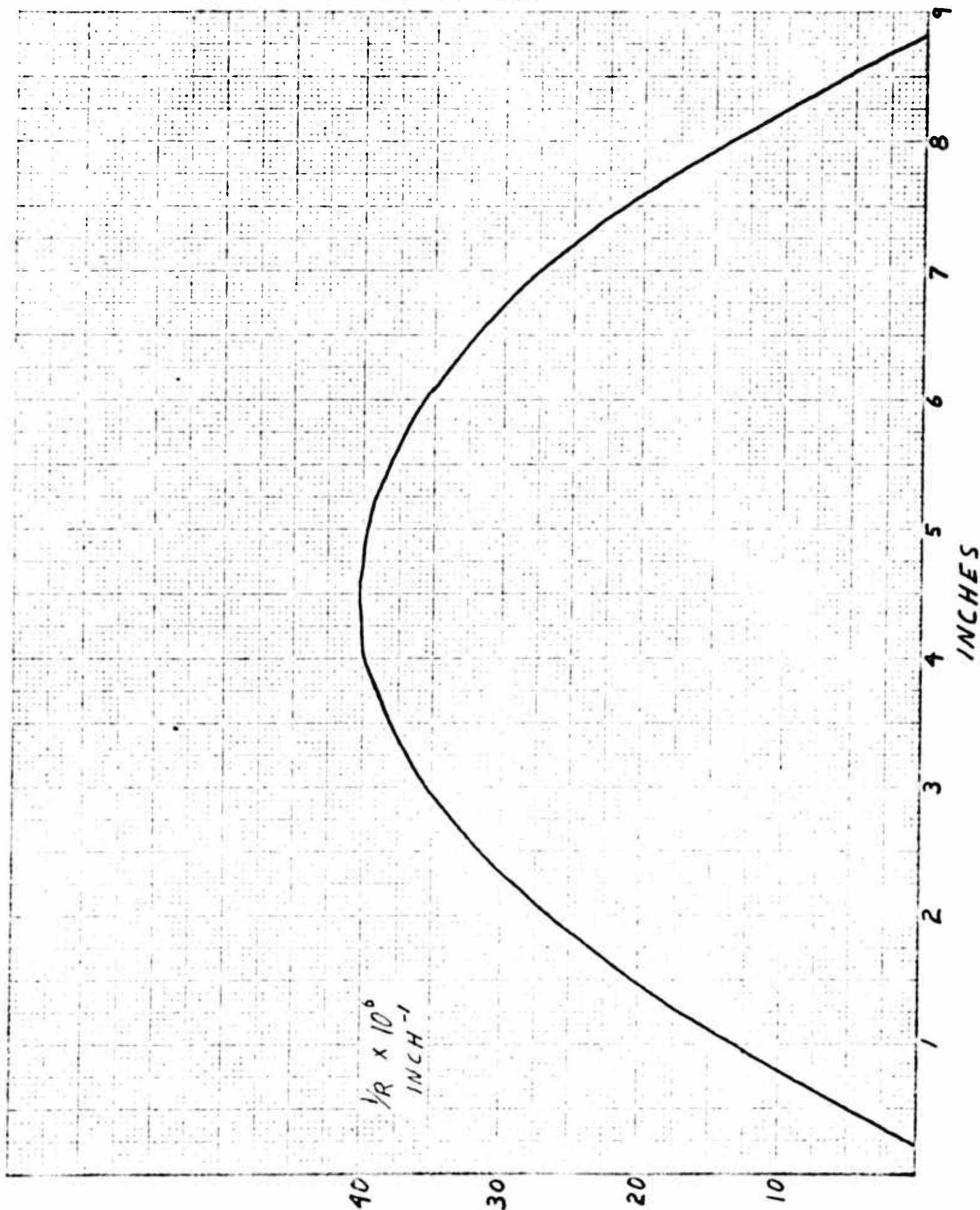
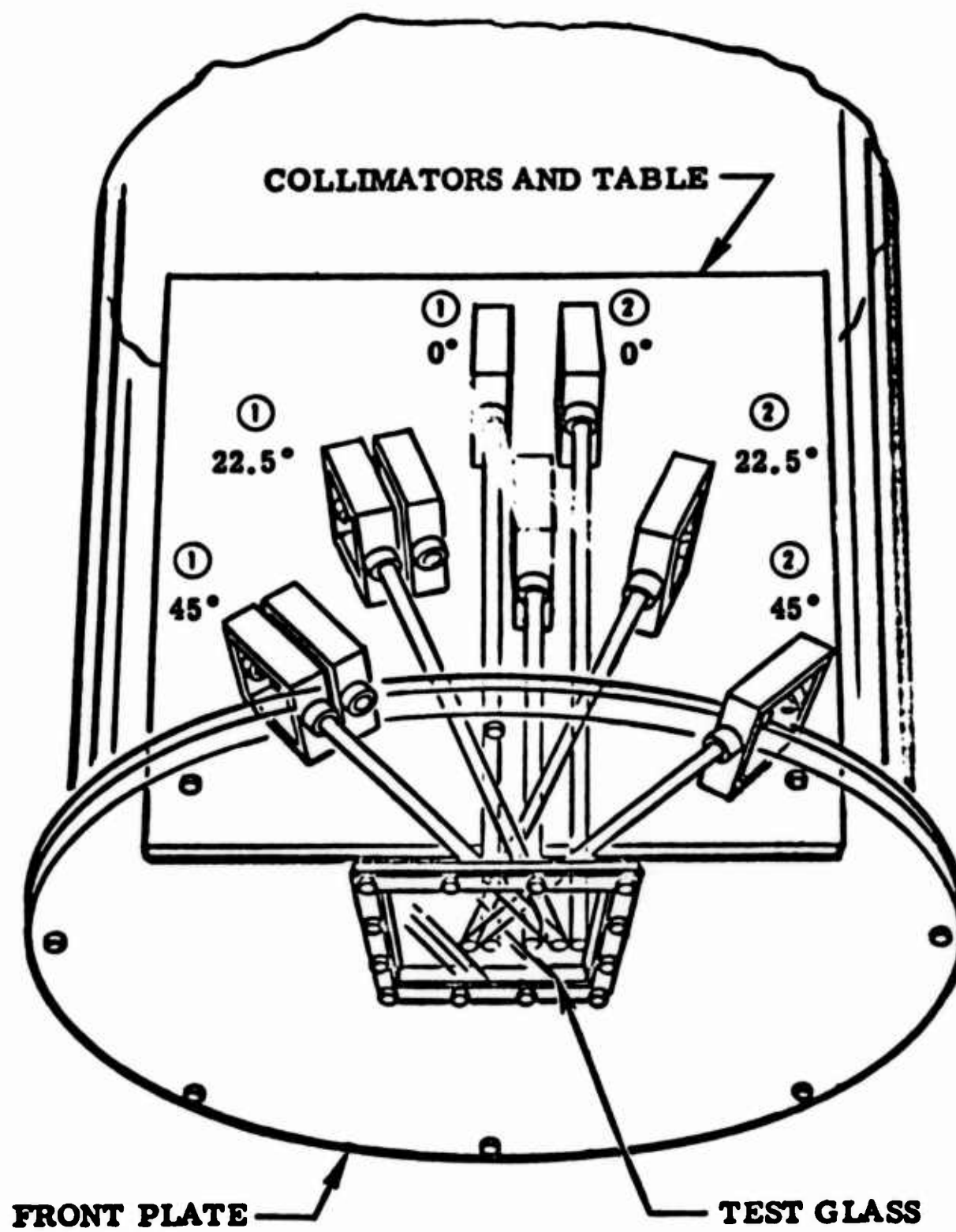


FIGURE 93

Curve of the Equation of Curvature  
for a Circular Plate







**Figure 94** Diagram of Pressure Test Setup, Showing Location of Collimators in Pressure Vessel

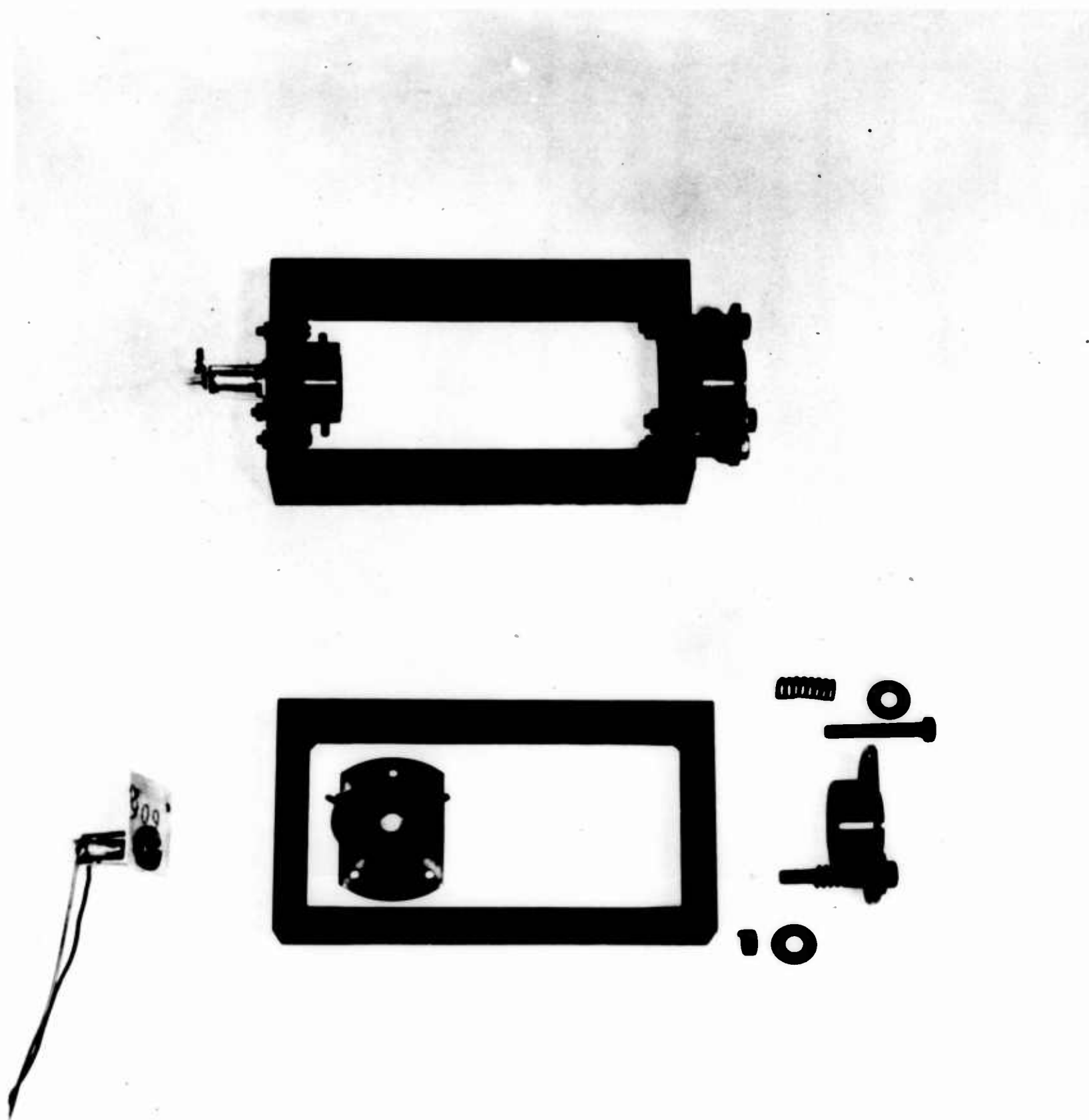


Figure 95

Test Collimator

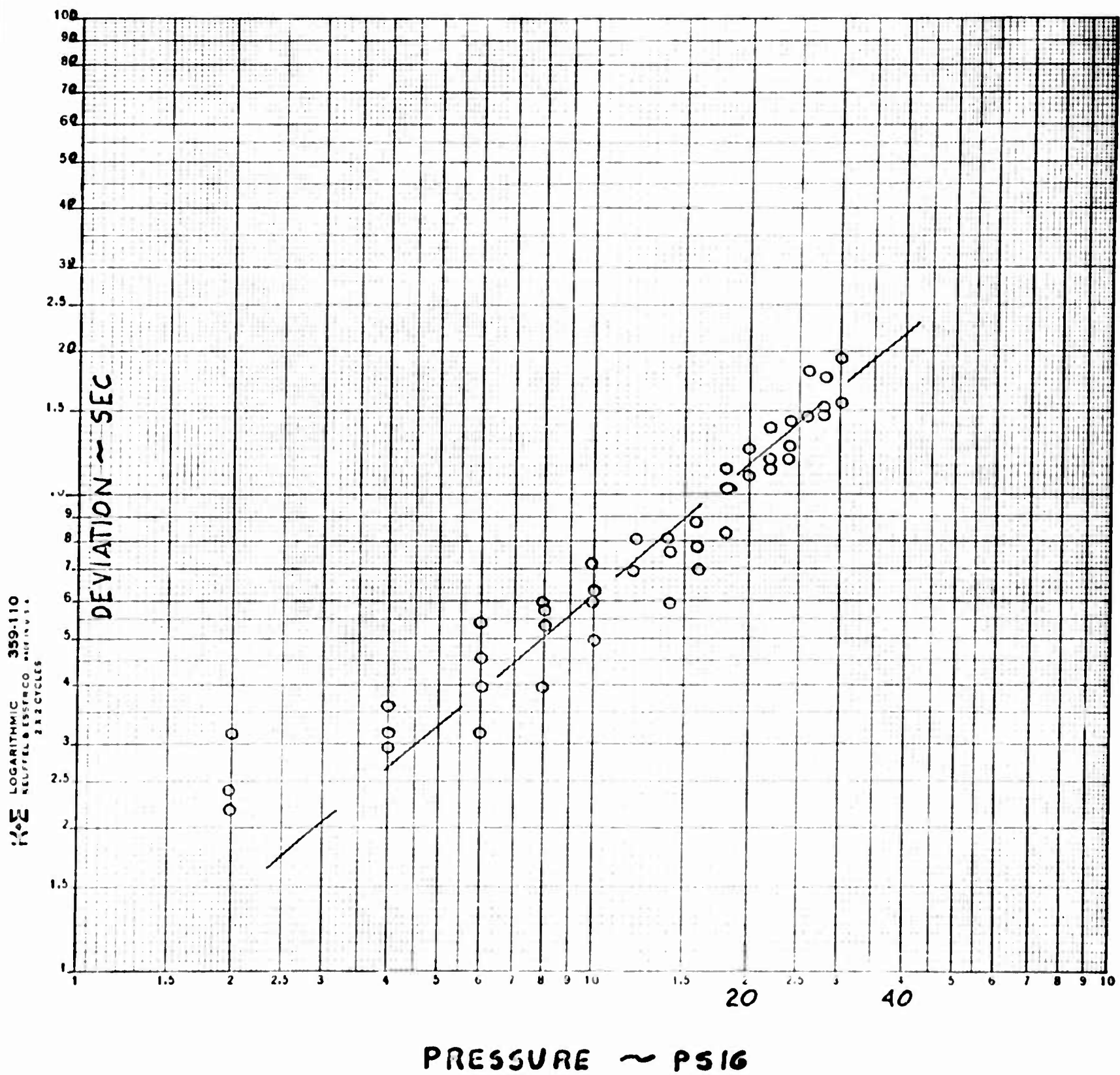


FIGURE 96-  
Light Deviation versus Pressure for Fused Silica #7940  
Glass, 9" x 9" x 1", at 90° Angle of Incidence, for  
Deposited 2" Gray Varnish

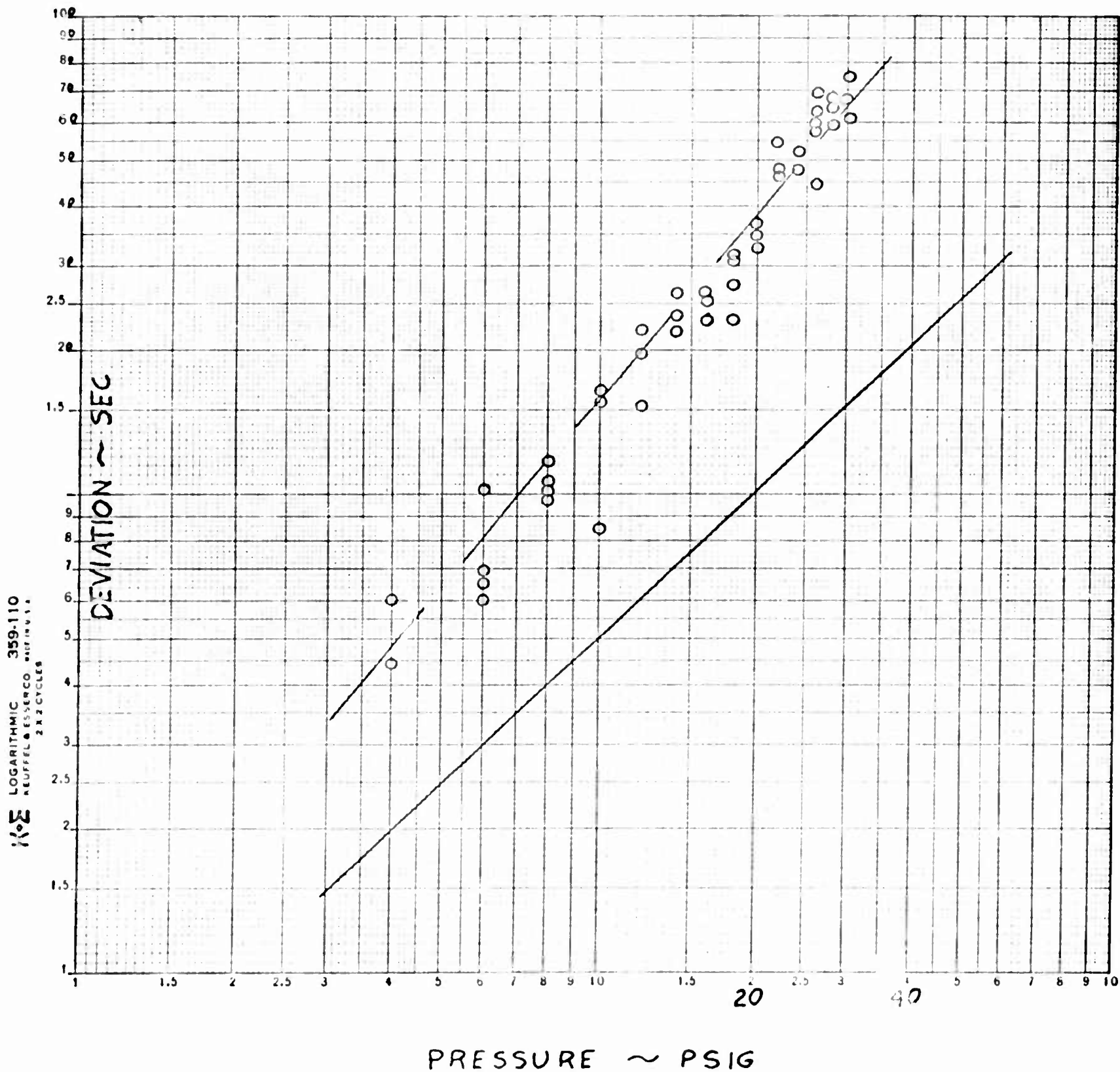


FIGURE 97  
Light Deviation versus Pressure for Fused Silica AT40  
Glass, 9" x 9" x 1". At 22.5 Degrees Angle of Incidence,  
For a 1" Spot 1" from Vertex



Light deviation versus pressure for fused Silica #7940 Glass,  
9" x 9" x 1", at 45 Degrees Angle of Incidence, for a point  
3" from Vertex

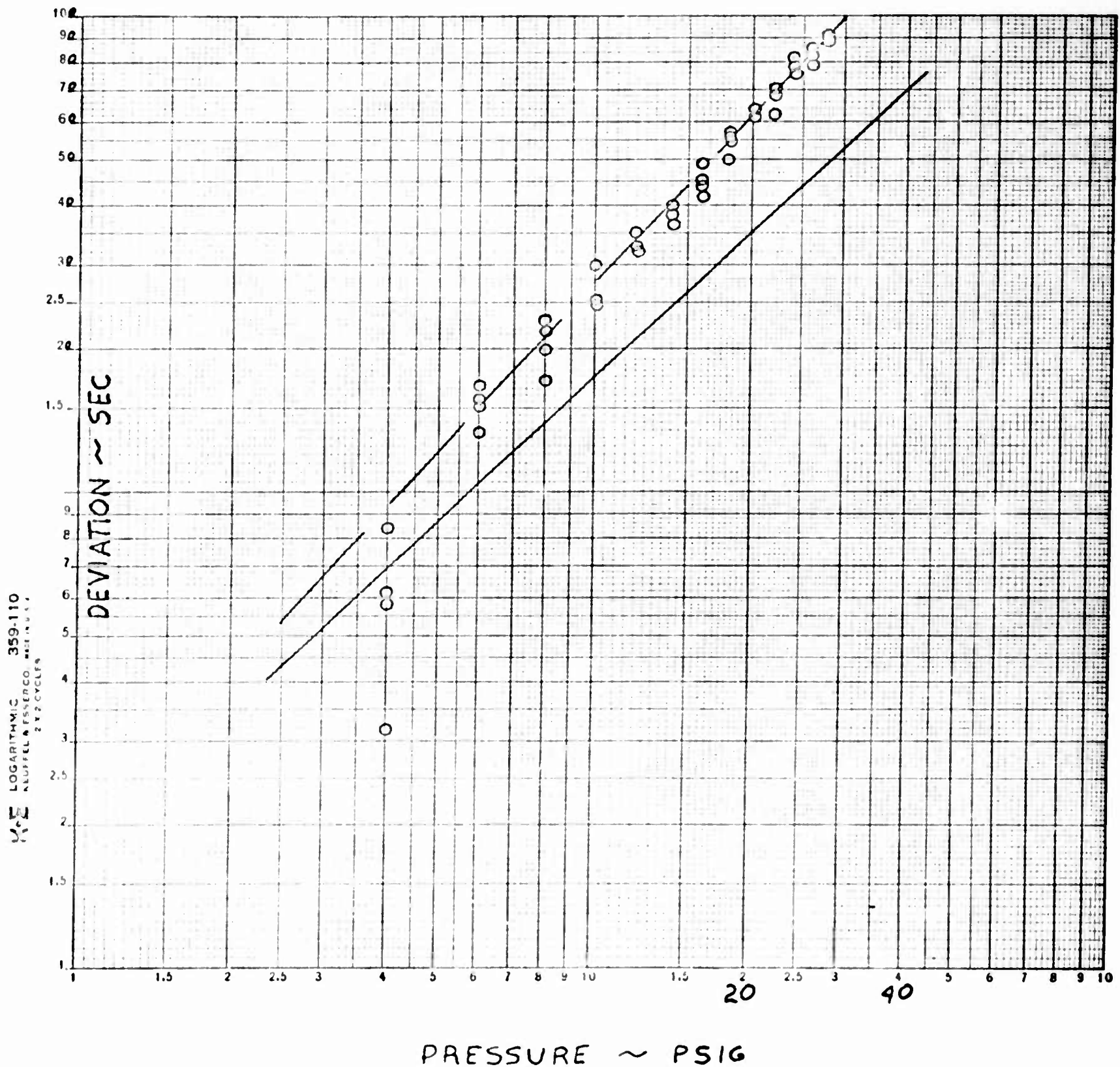


FIGURE 98  
Temperature and Light Deviation versus Time, Test #2

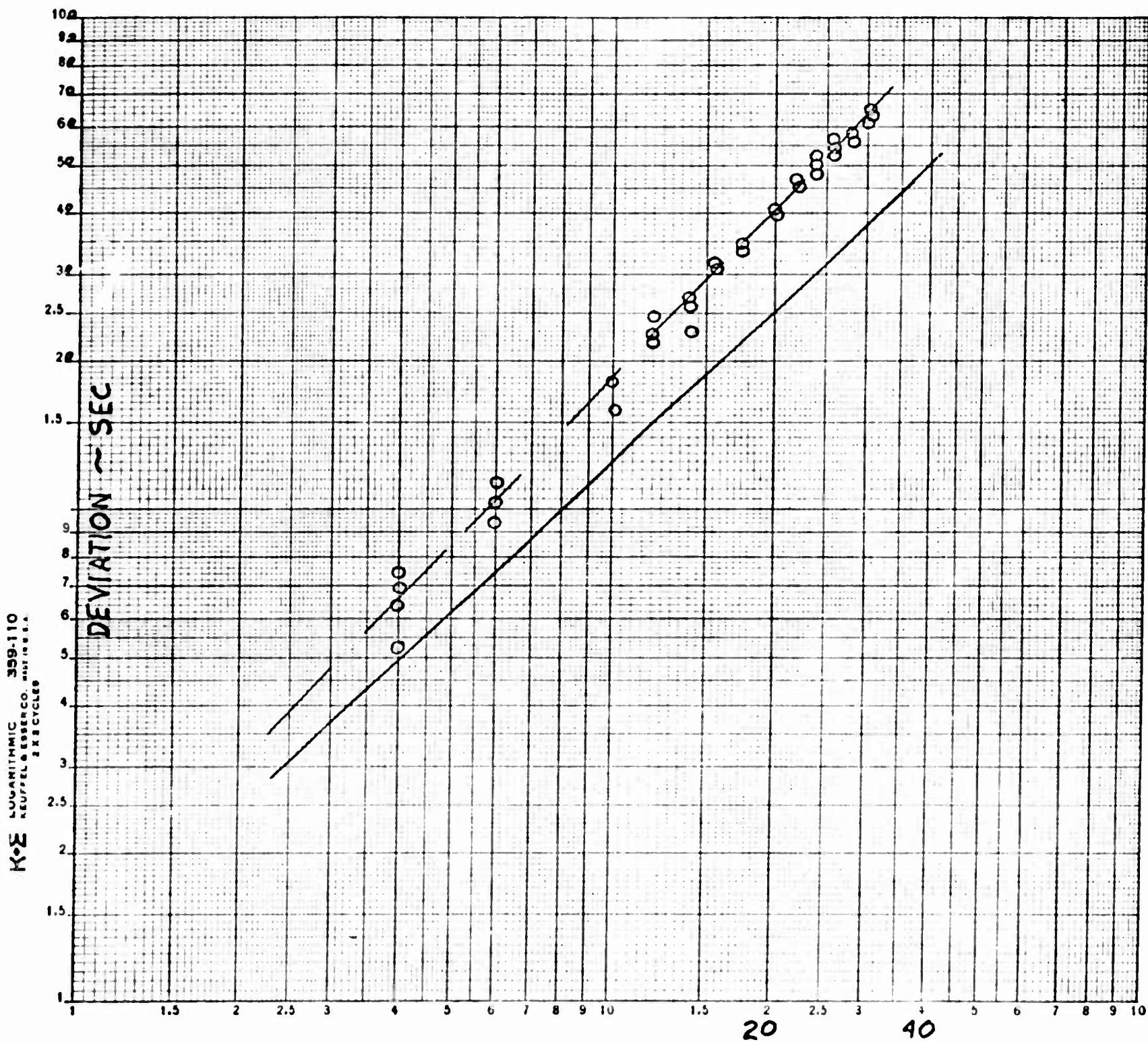
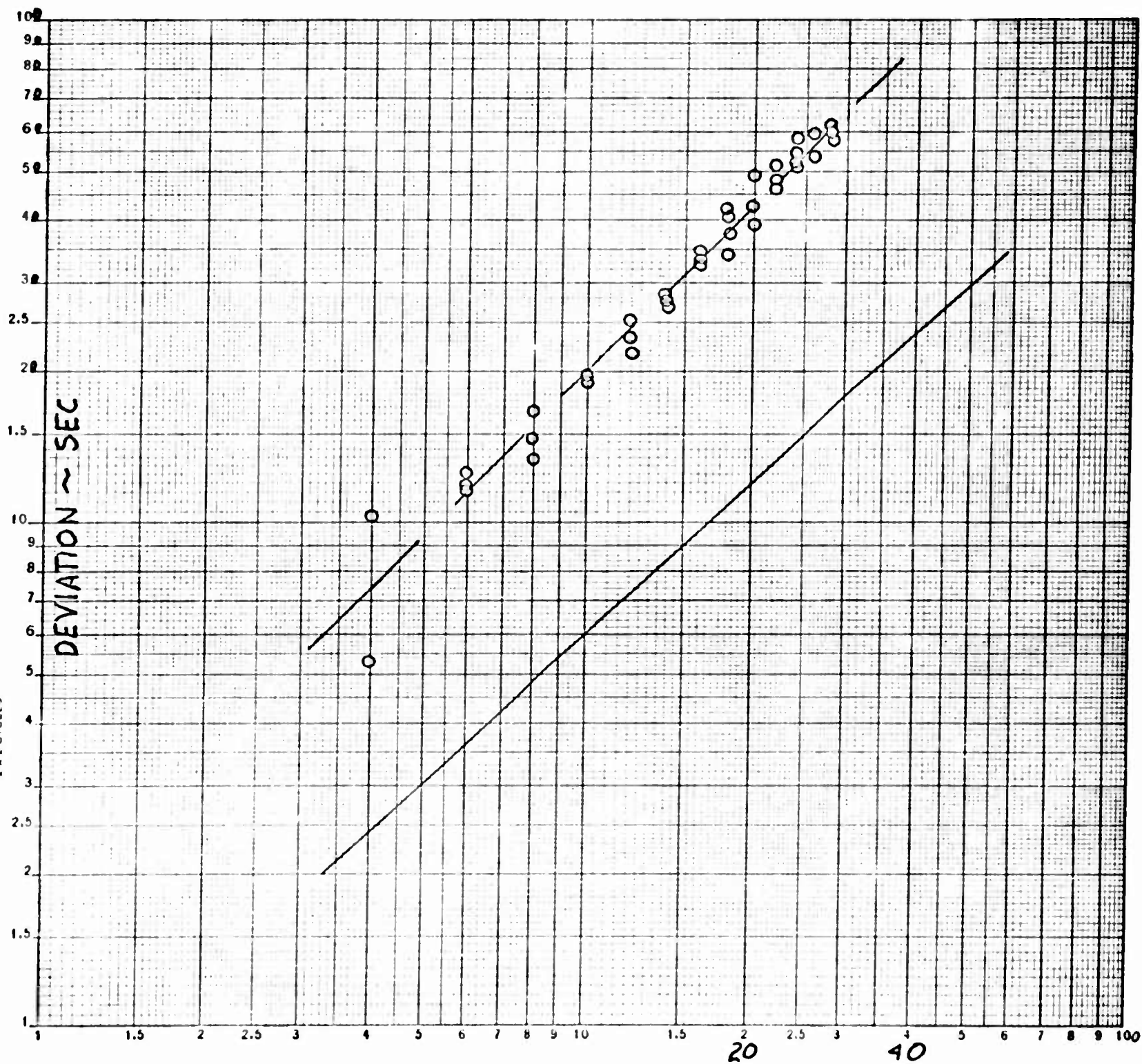


FIGURE 99  
Light Deviation versus Pressure for Fused Silica  
#7940 Glass, 9" x 9" x 1", at 45 Degrees Angle of  
Incidence, for a Point 1" from Vertex  
140



PRESSURE ~ PSIG

FIGURE 100

Light Deviation versus Pressure for Aluminosilicate  
#1723 Glass, 9" x 9" x 1" at 22.5 Degrees Angle of  
Incidence, for a Point 3" from Vertex



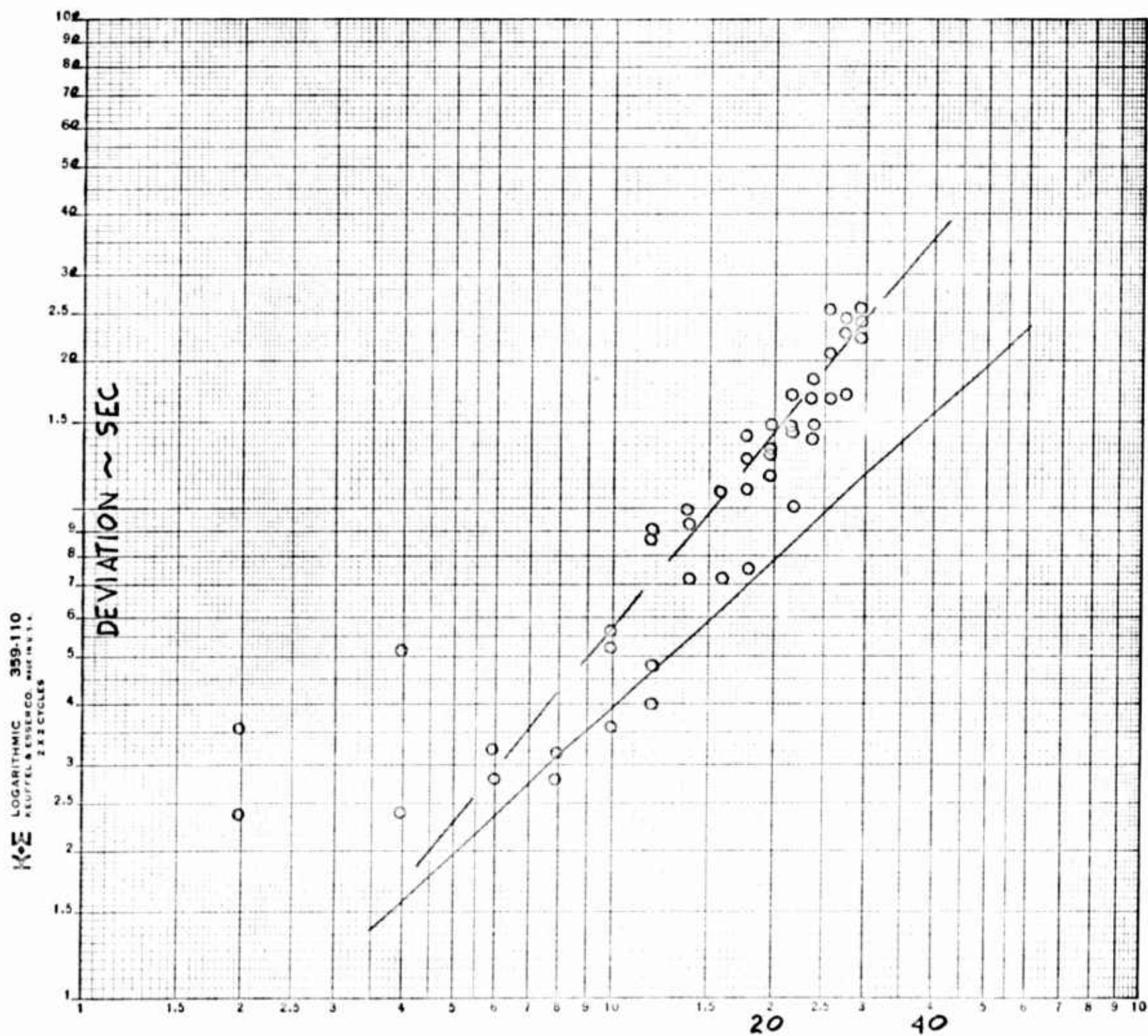


FIGURE 101  
Light Deviation versus Pressure for 17%inosilicate  
J1723 Glass, 9" x 9" x 1/2" at 42.5 l. Angle of  
Incidence, for a Point 1" from Vertex



Light Deviation versus pressure for fused Silica #940 Glass,  
 9" x 9" x 1", at 22.5 Degrees Angle of Incidence, for a Point  
 1" from Vertex. (Second Chamber)

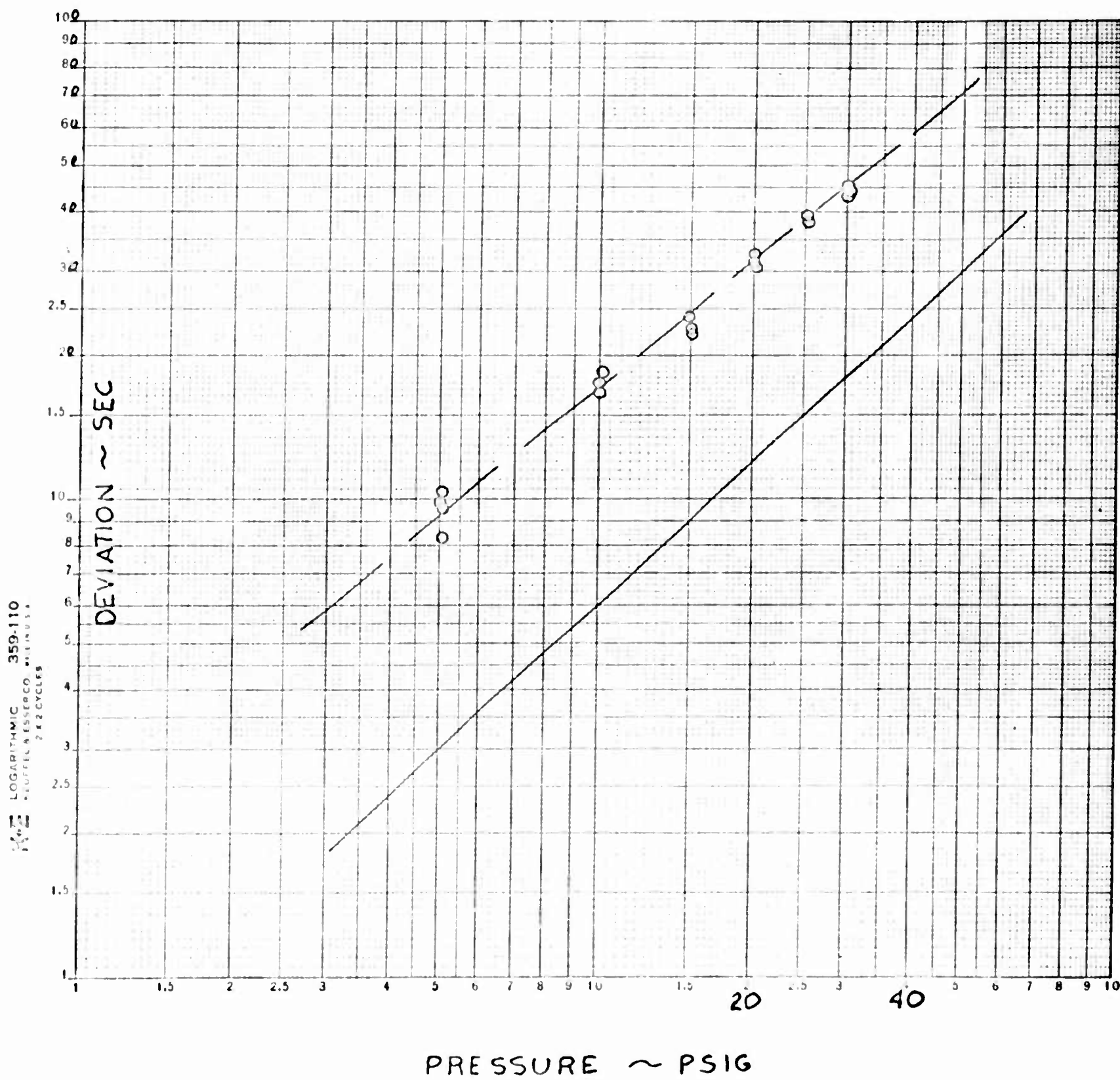


FIGURE 102

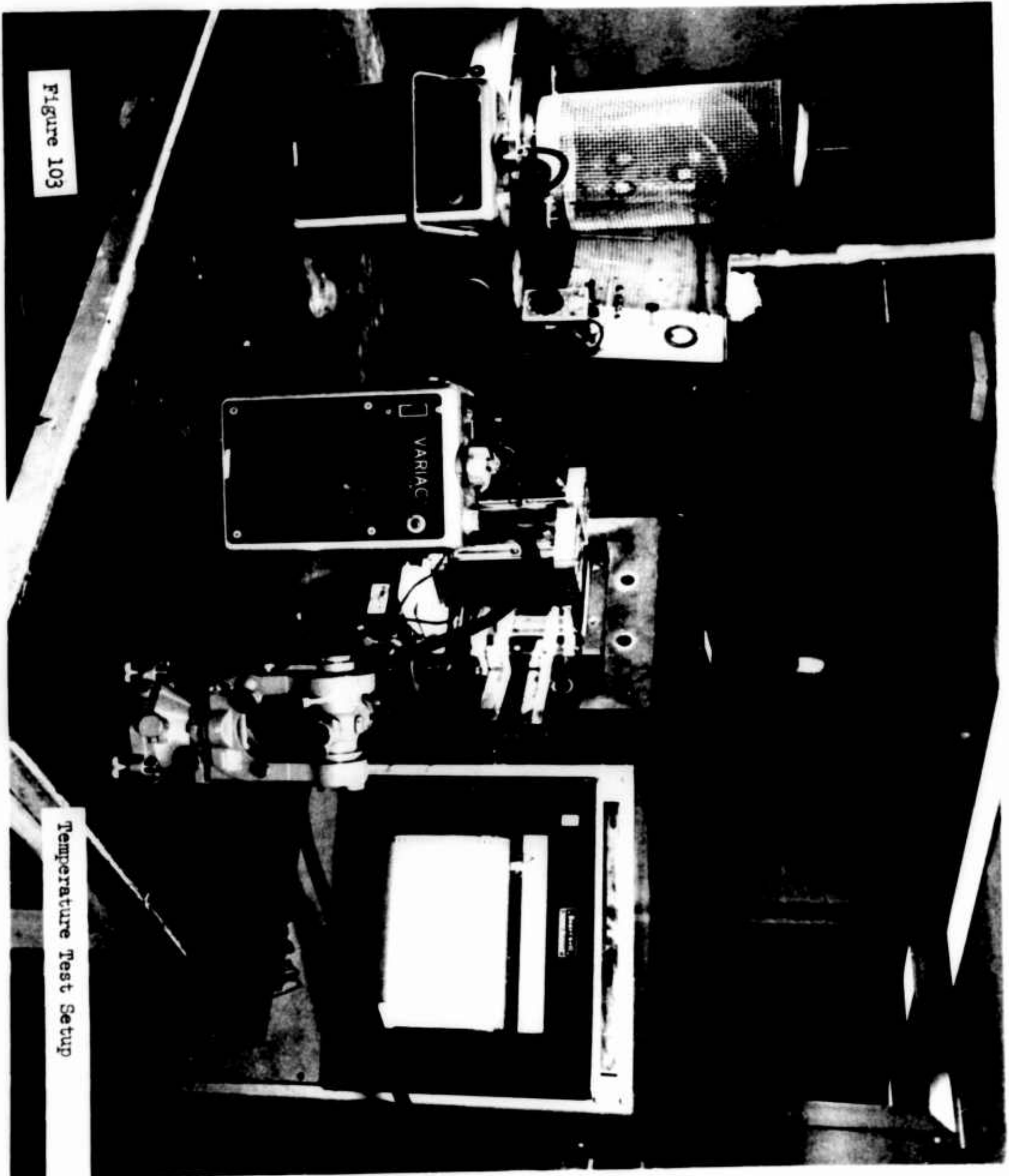
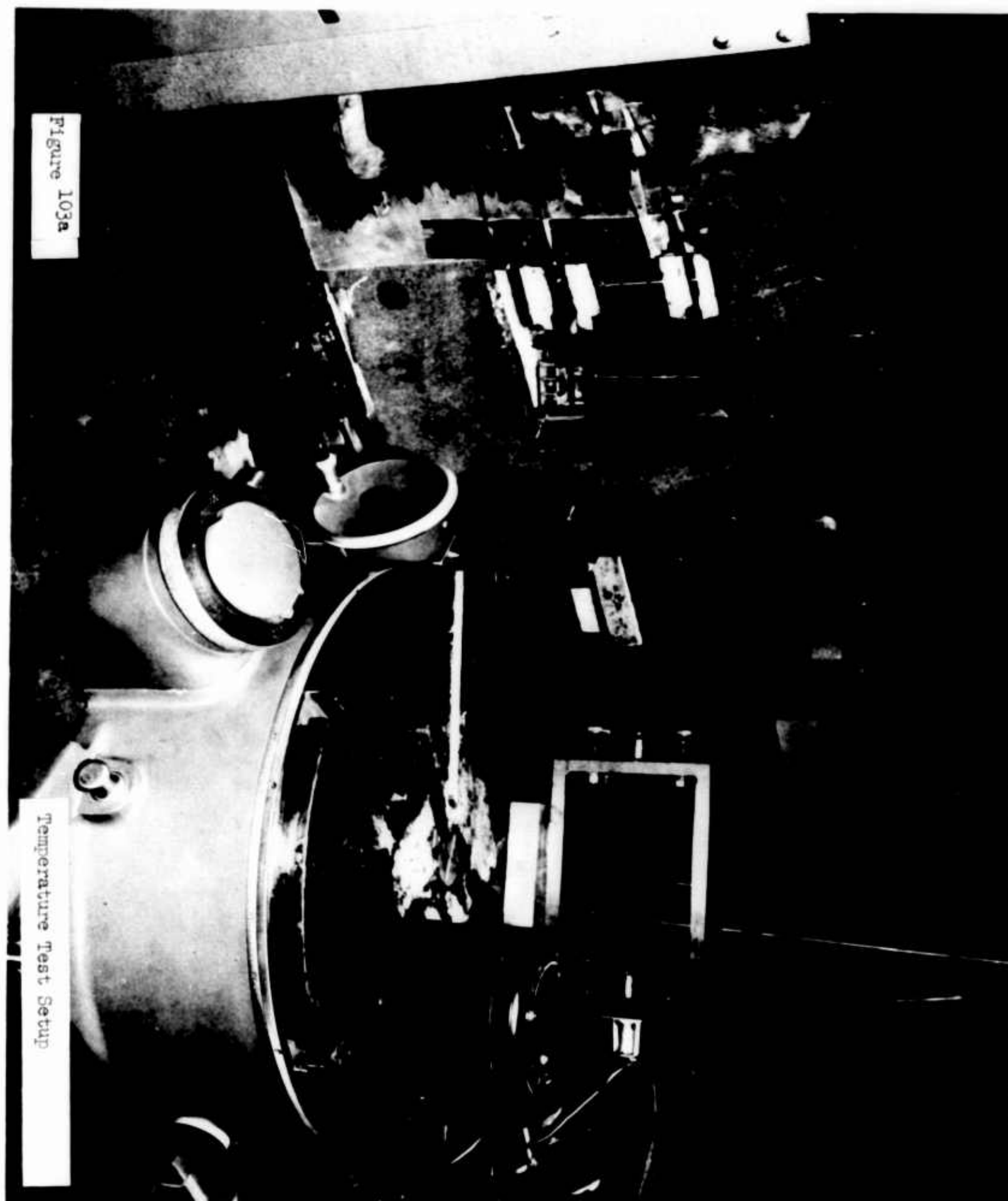


Figure 103

Temperature Test Setup



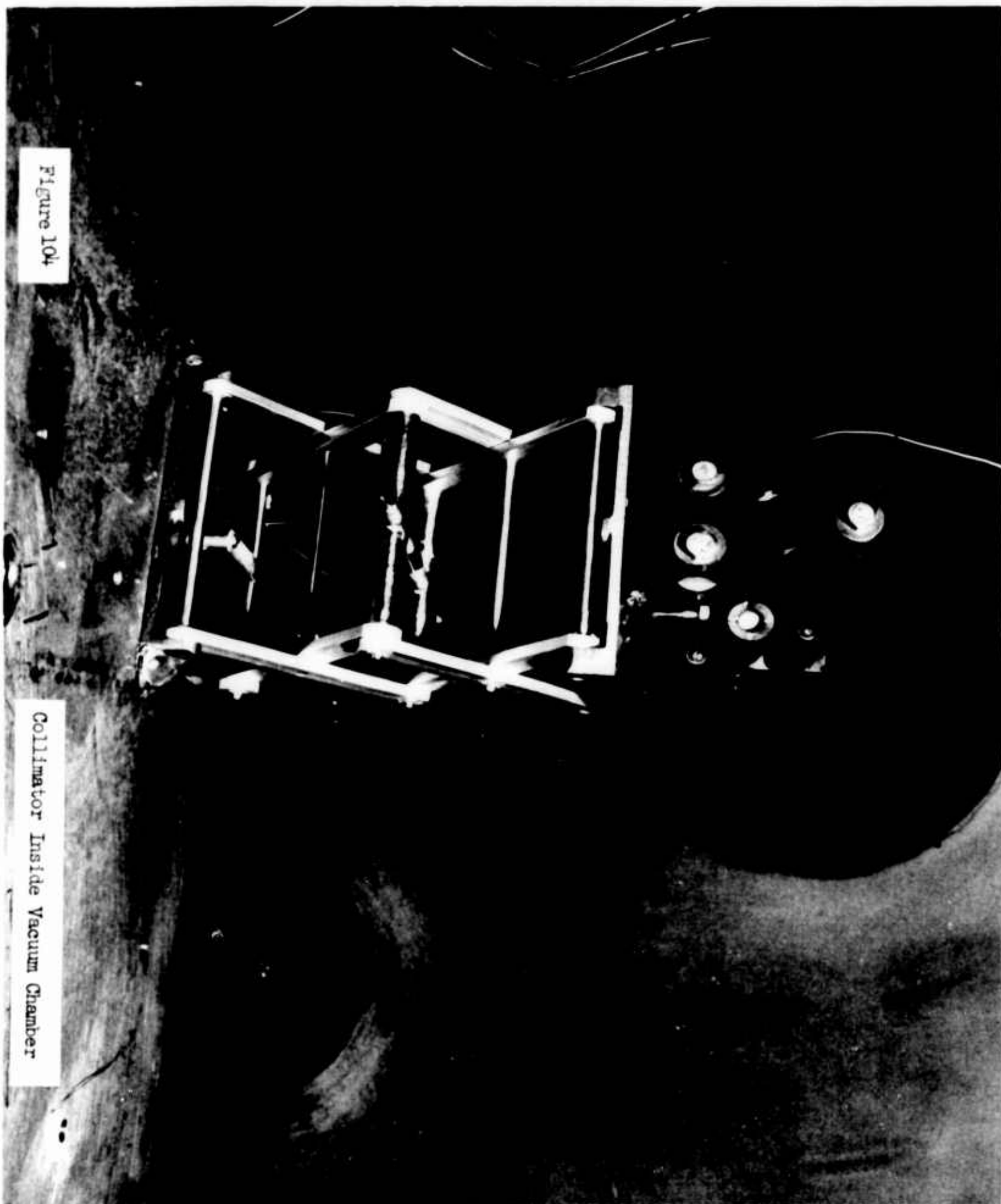


Figure 104

Collimator Inside Vacuum Chamber



247

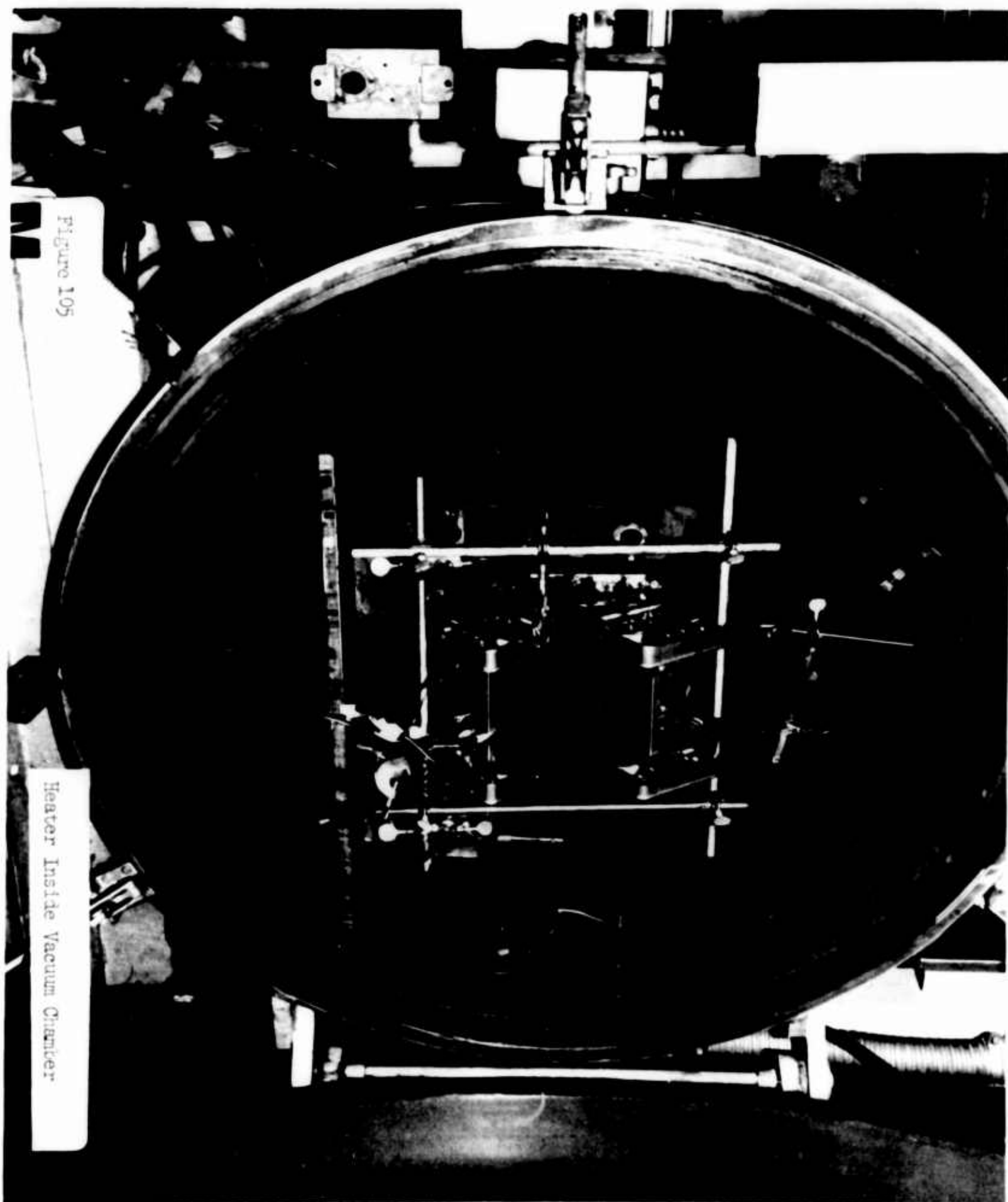


Figure 105

Heater Inside Vacuum Chamber

Figure 106. Temperature and Light Deviation versus Time, Test No. 1

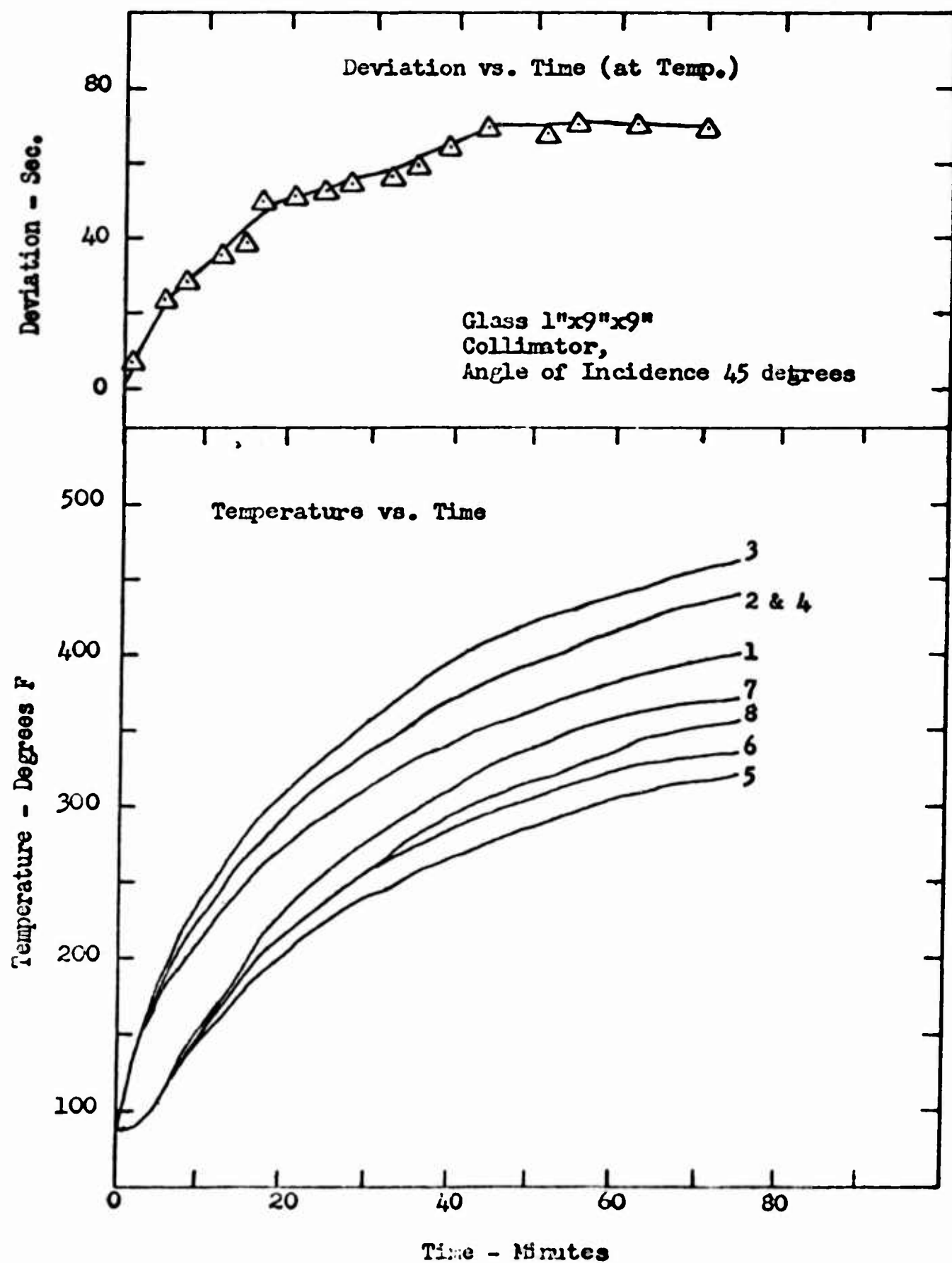


Figure 107. Temperature and Light Deviation versus Time, Test No. 2

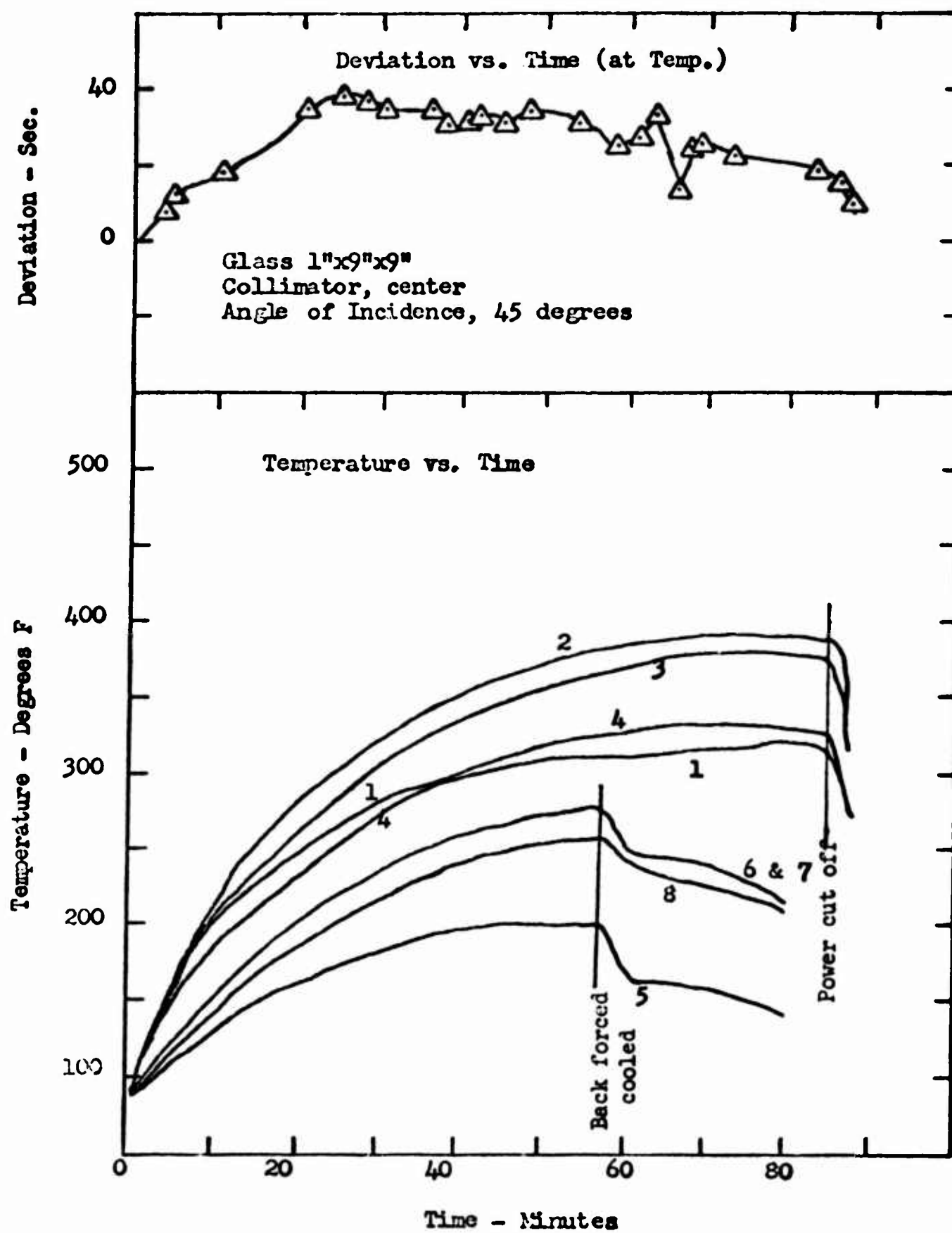


Figure 108. Temperature and Light Deviation versus Time, Test No. 3

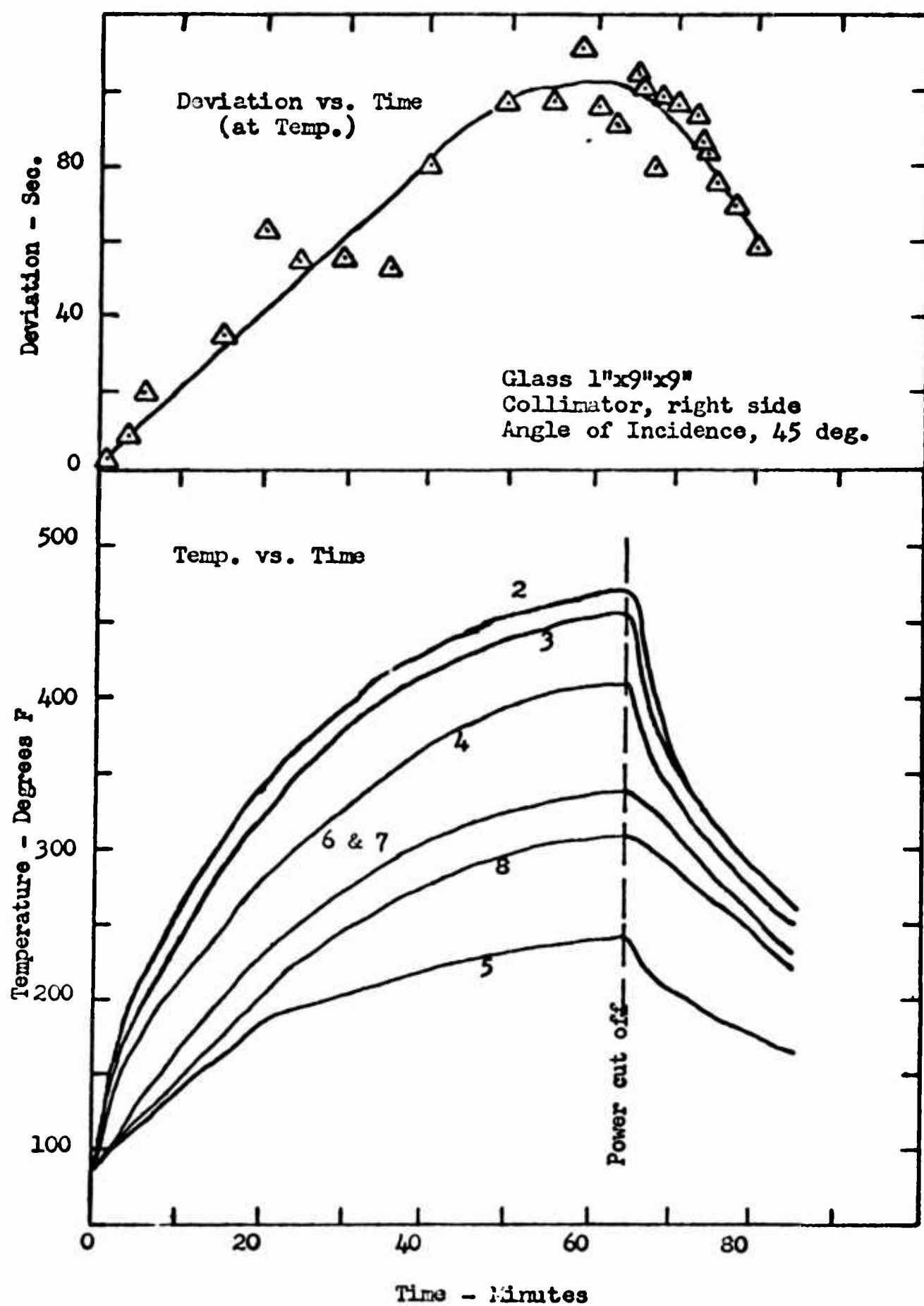




Figure 109. Temperature and Light Deviation versus Time, Test No. 4

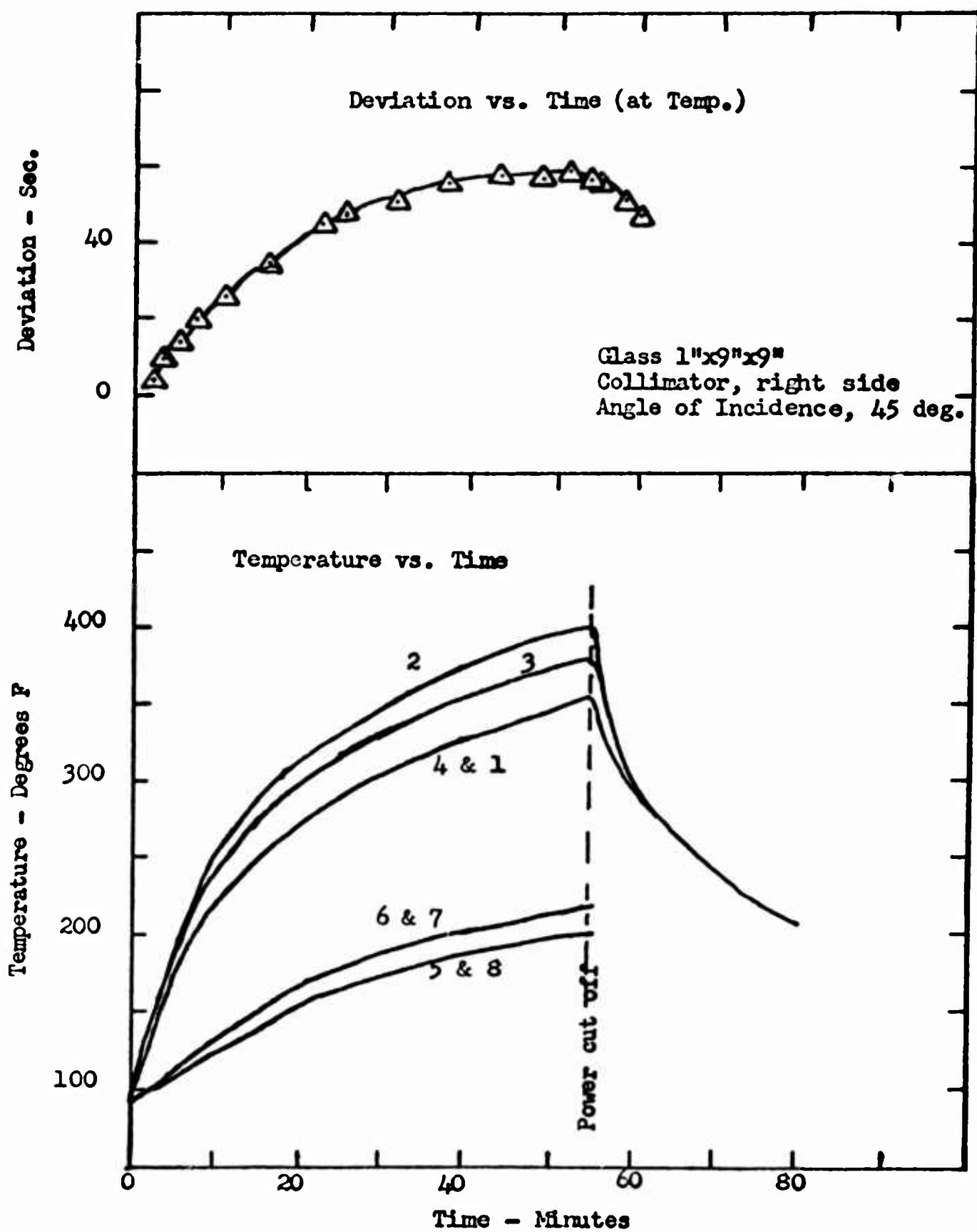


Figure 110. Temperature and Light Deviation versus Time, Test No. 5

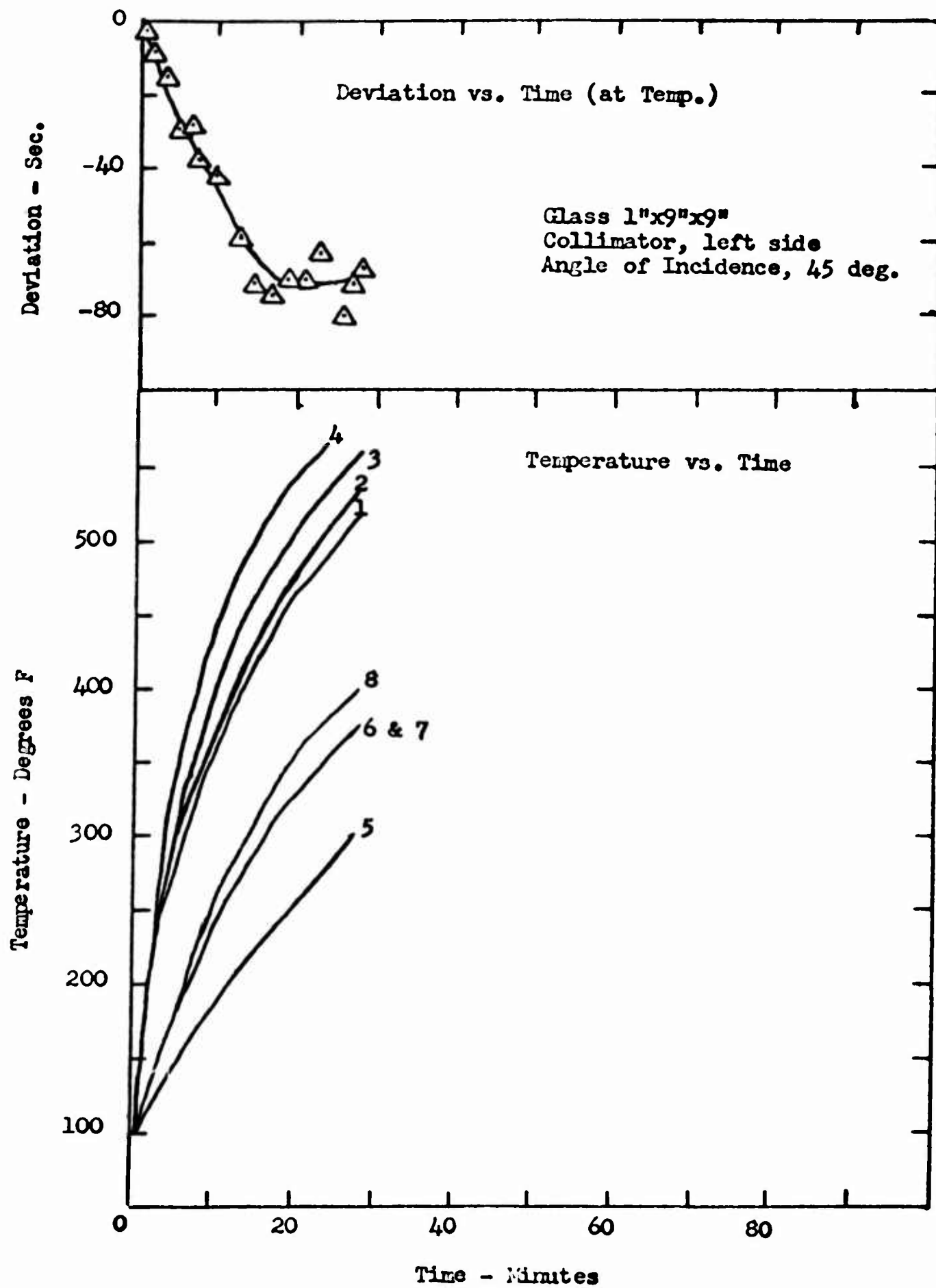


Figure 111. Temperature and Light Deviation versus Time, Test No. 6

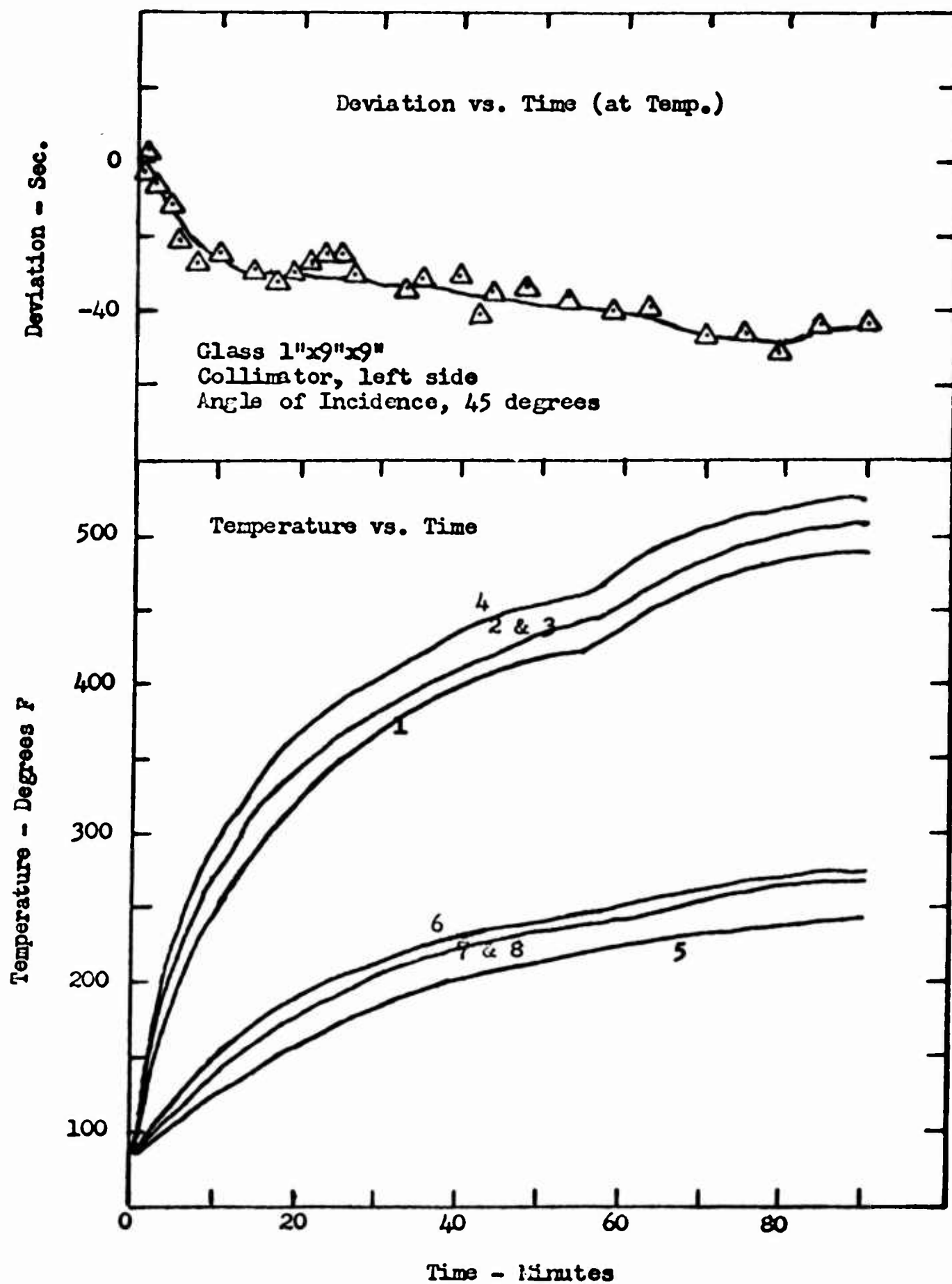


Figure 112.. Temperature and Light Deviation versus Time, Test No. 7

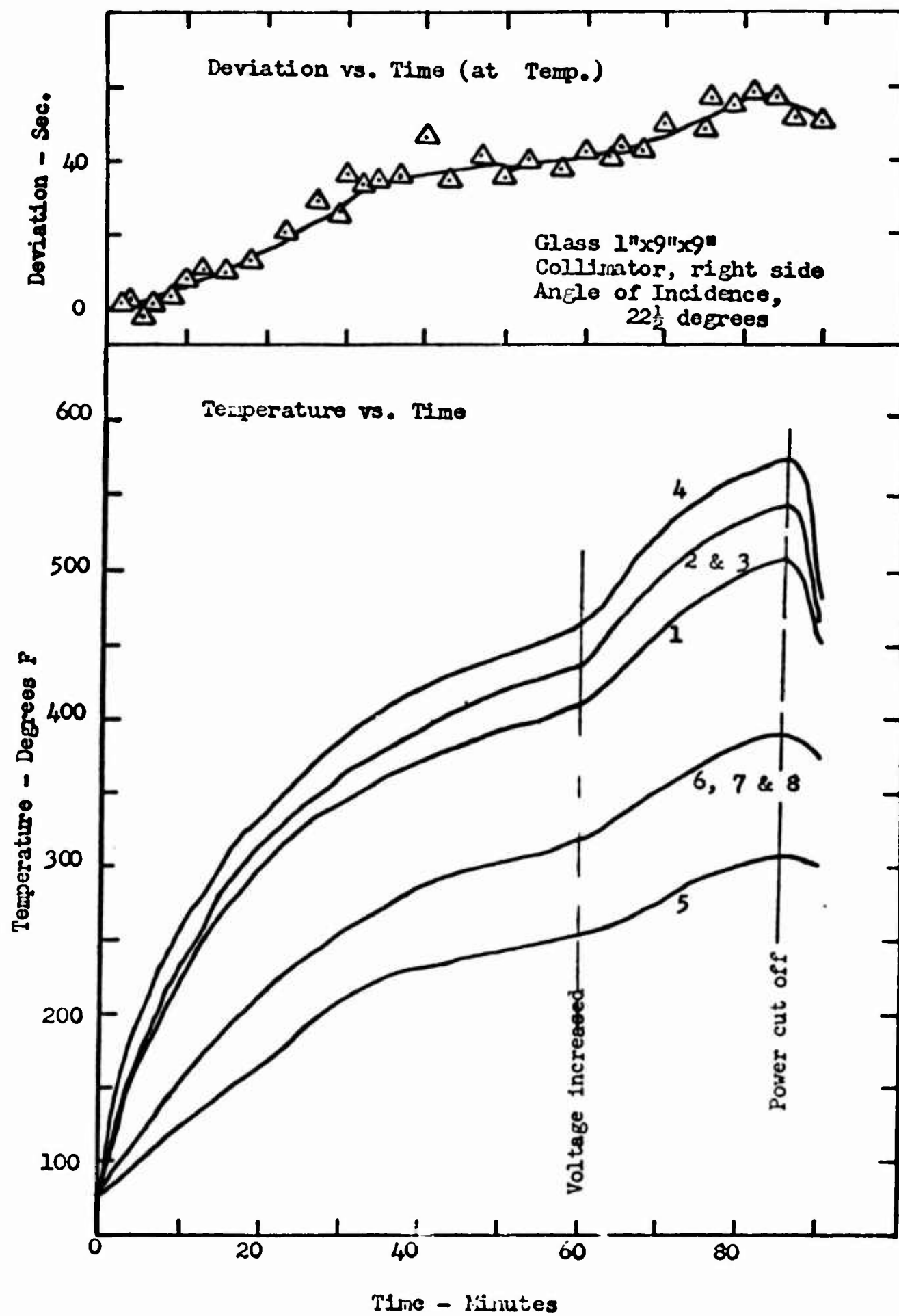


Figure 113. Temperature and Light Deviation versus Time, Test No. 8

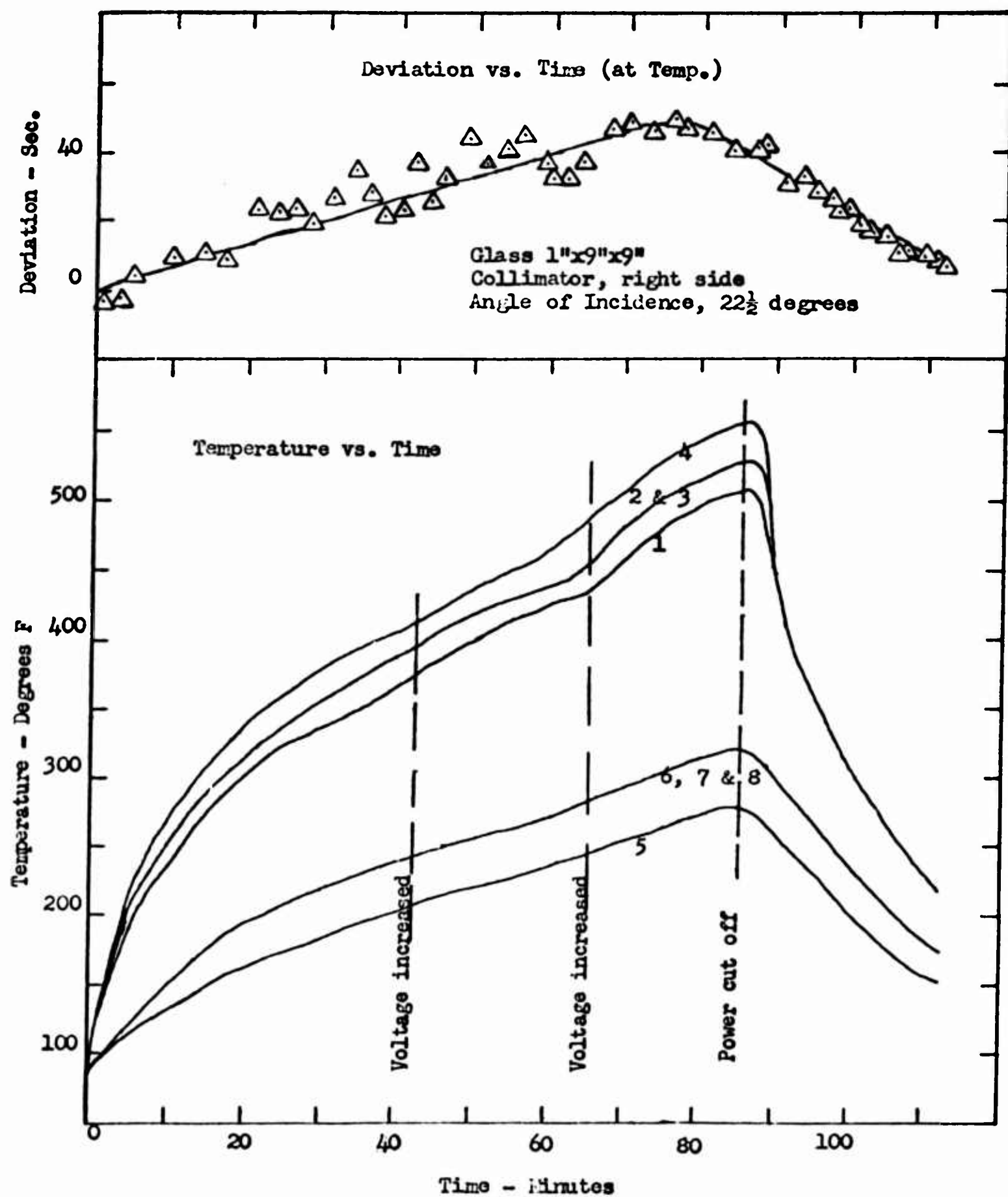




Figure 114. Temperature and Light Deviation versus Time, Test No. 9

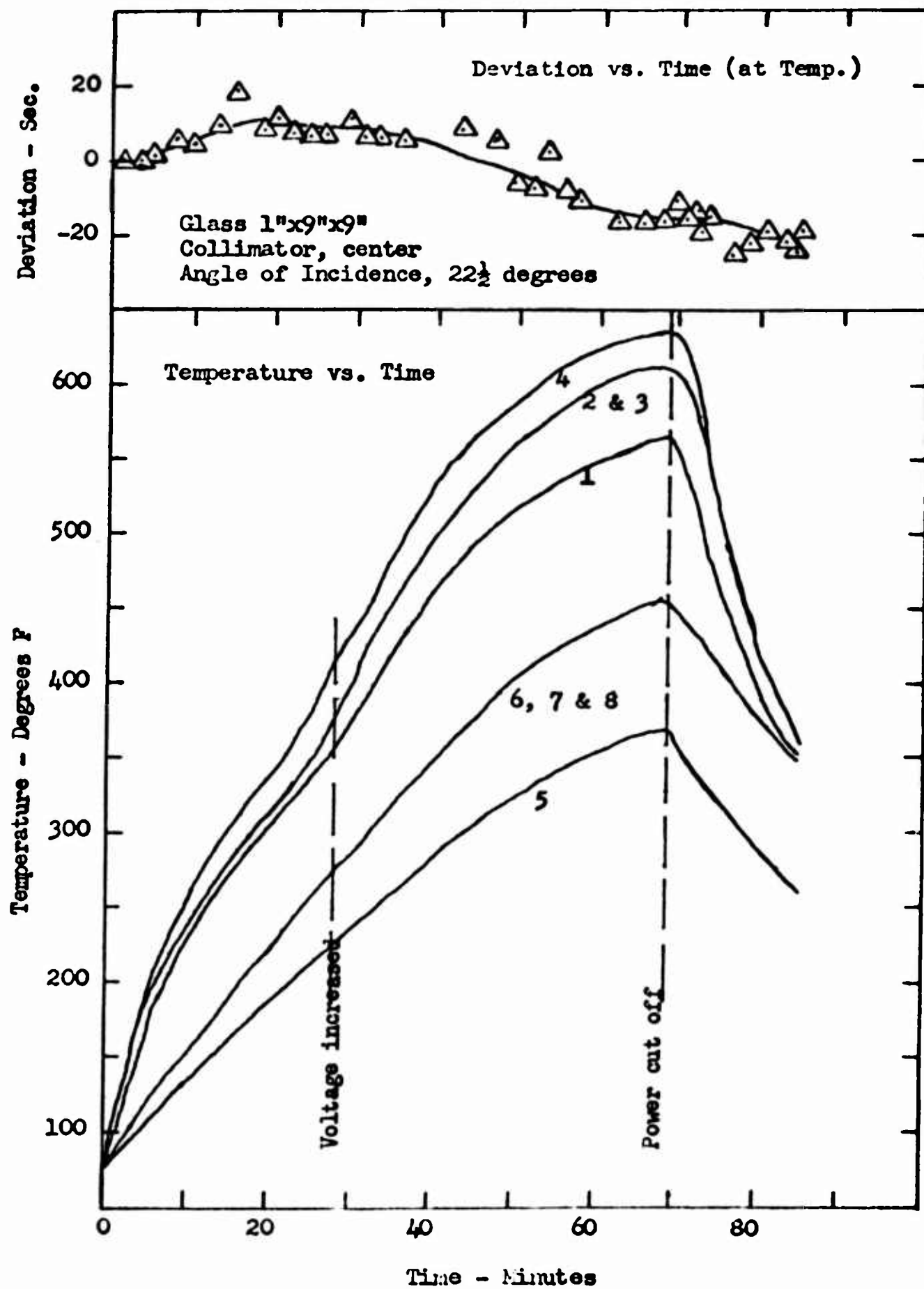


Figure .115. Temperature and Light Deviation versus Time, Test No. 10

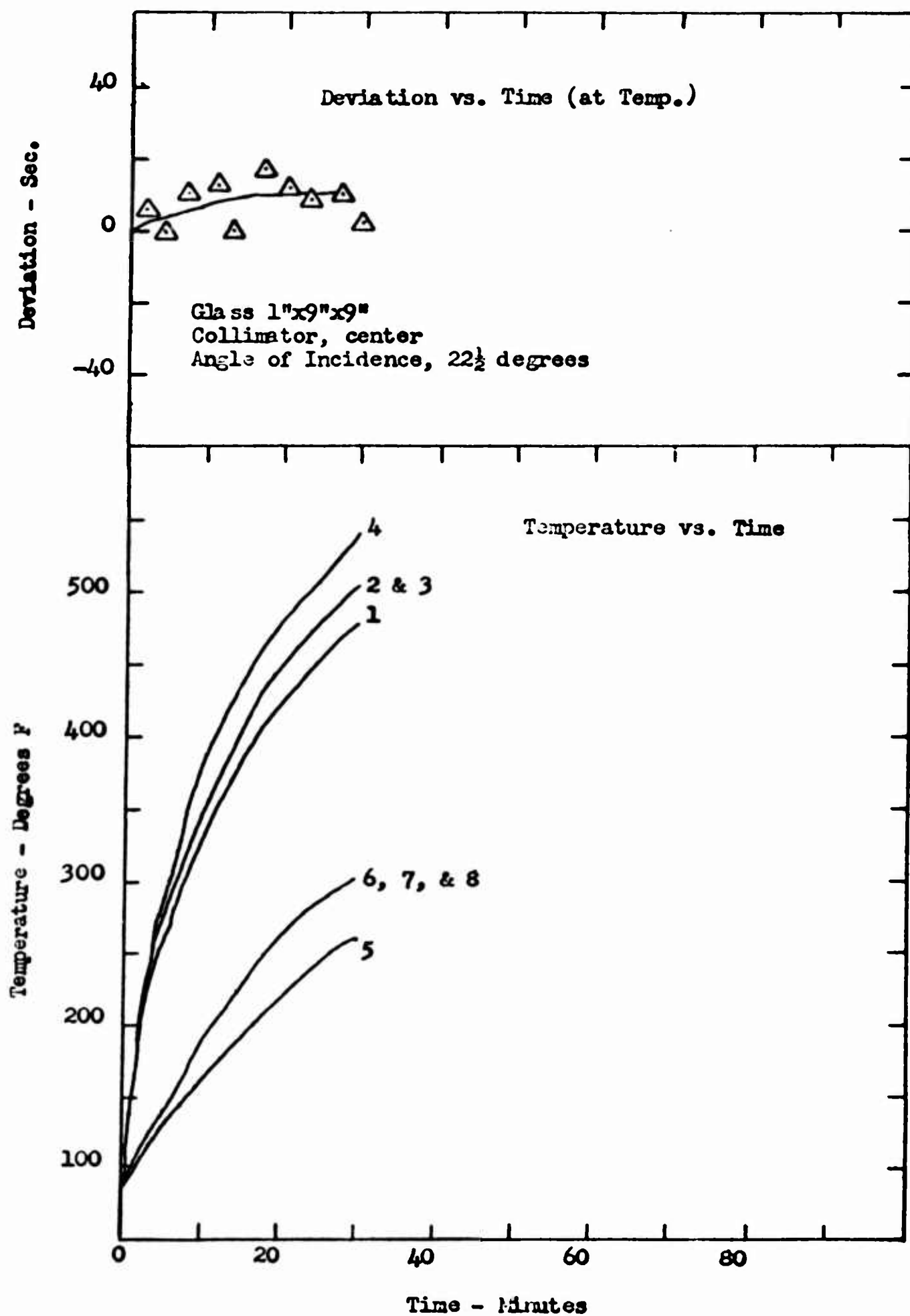


Figure 116. Temperature and Light Deviation versus Time, Test No. 11

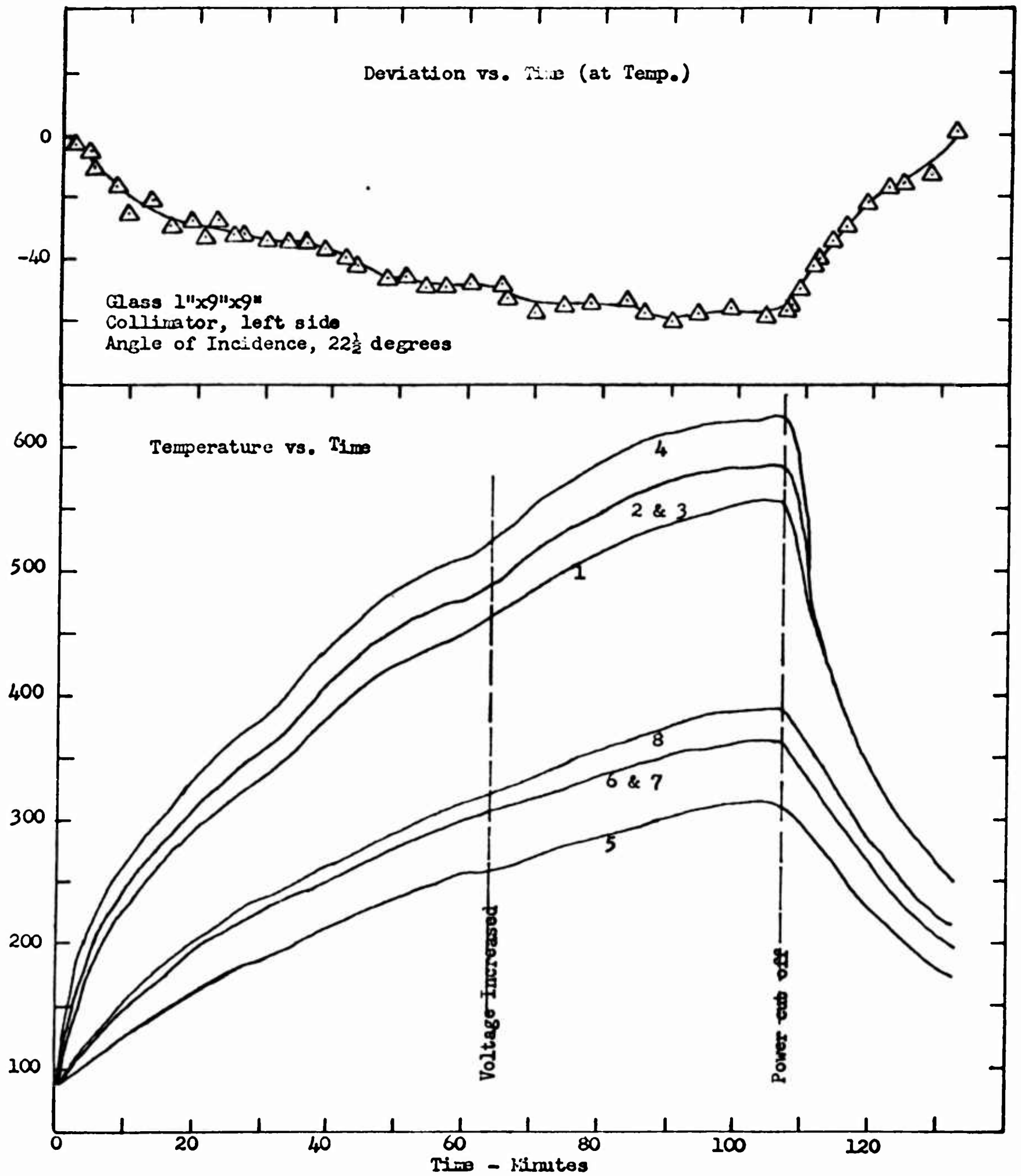


Figure 117. Temperature and Light Deviation versus Time, Test No. 12

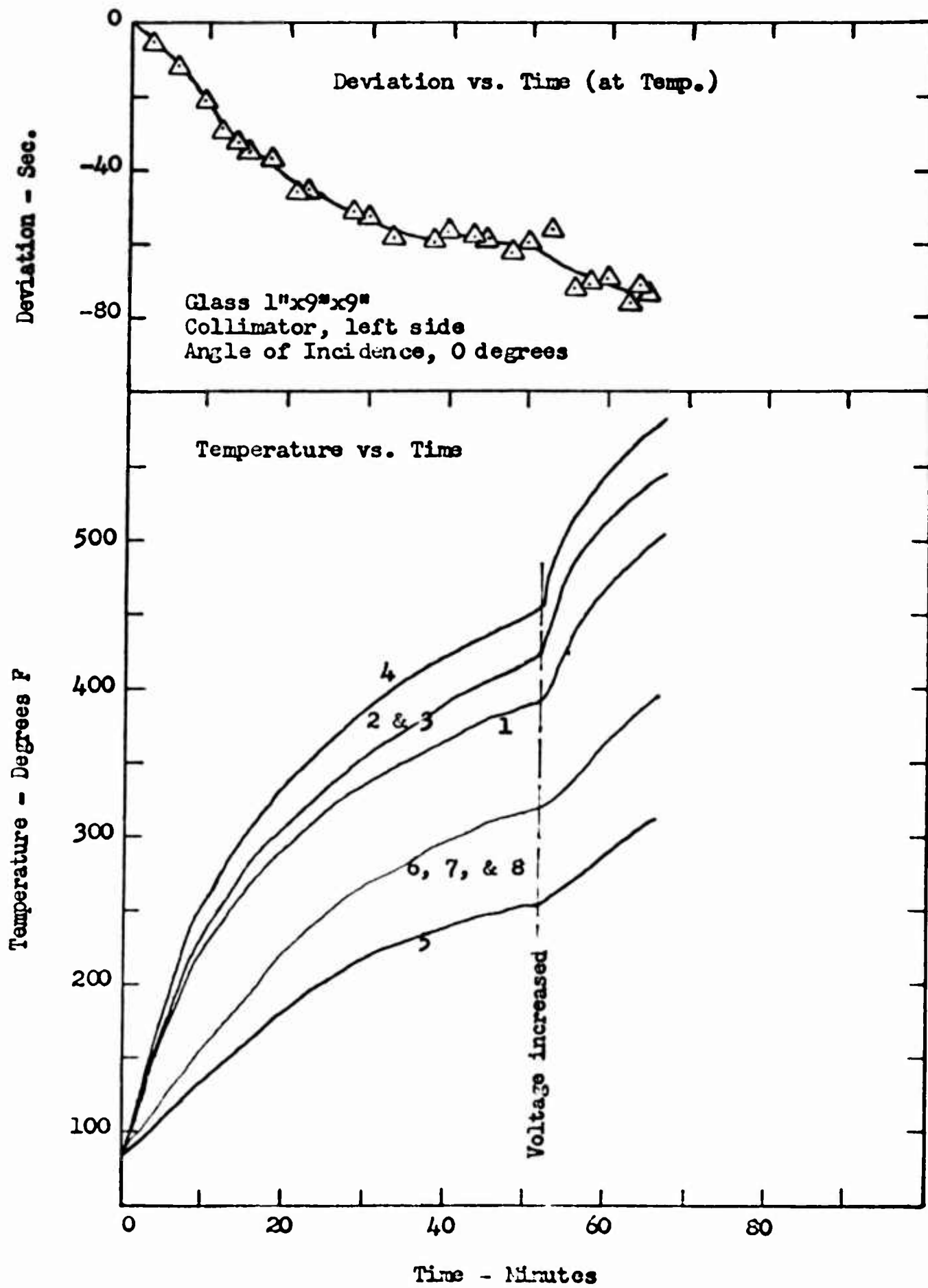


Figure 118. Temperature and Light Deviation versus Time, Test No. 13

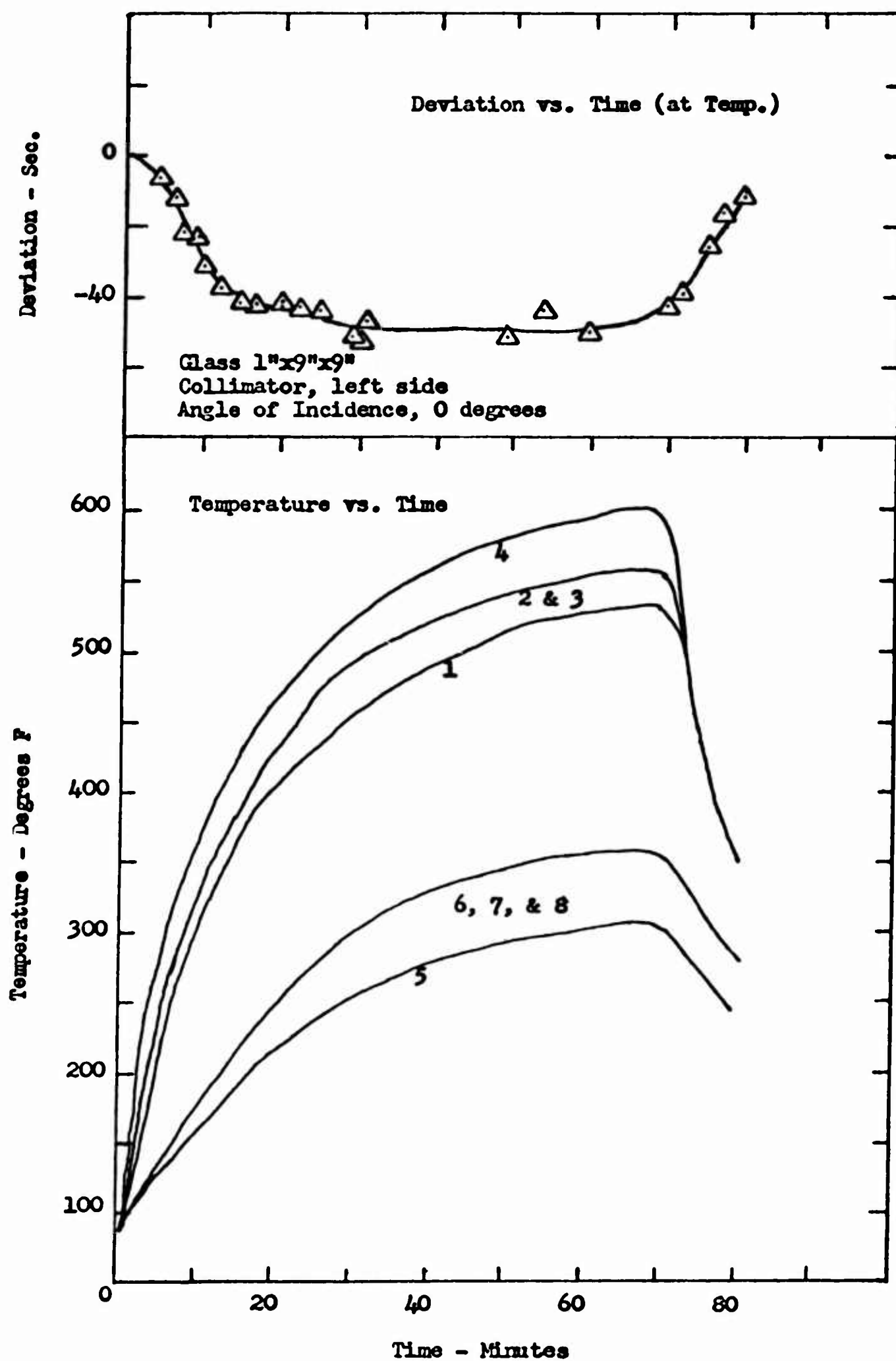




Figure 119. Temperature and Light Deviation versus Time, Test No. 14

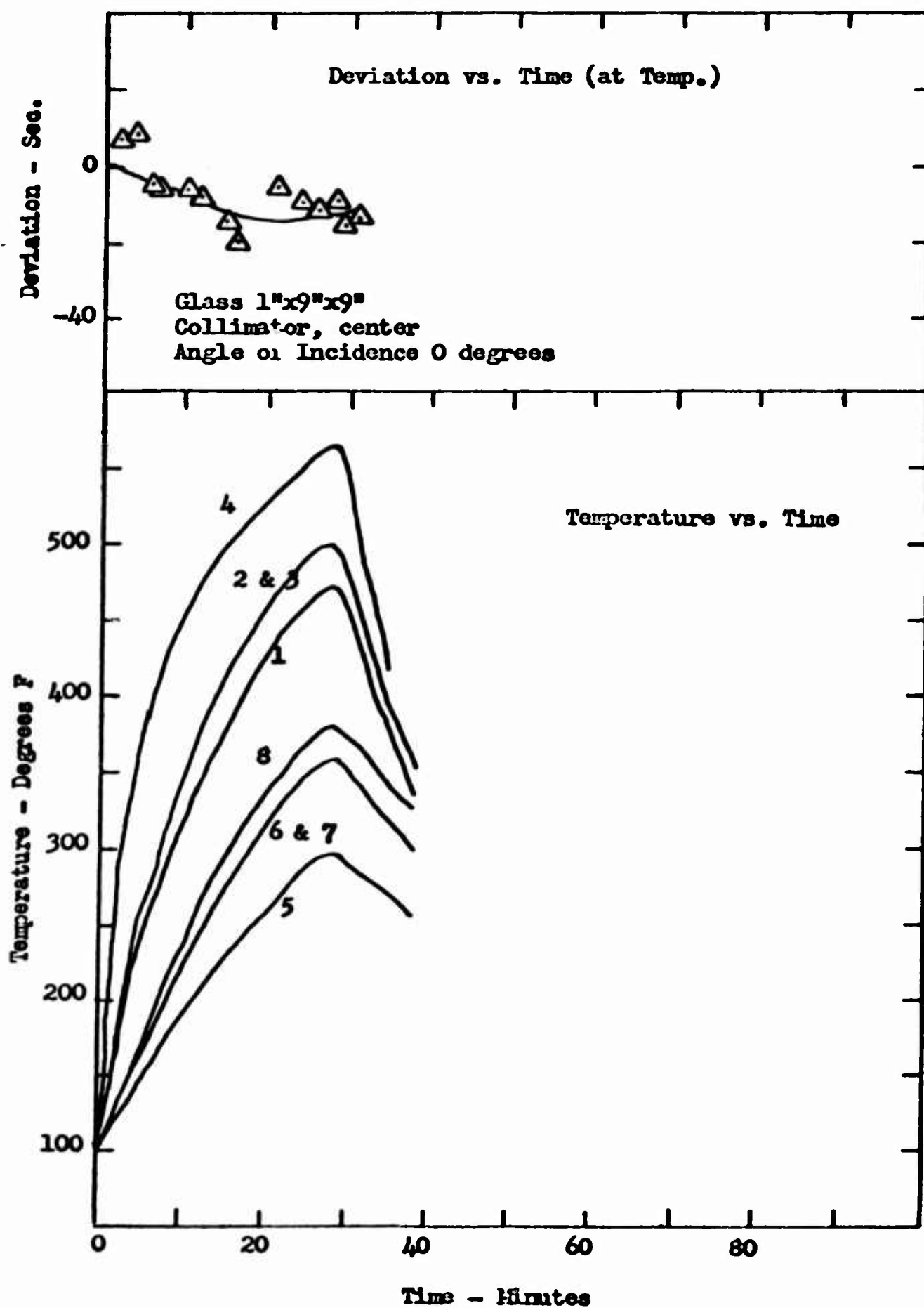


Figure 120. Temperature and Light Deviation versus Time, Test No. 15

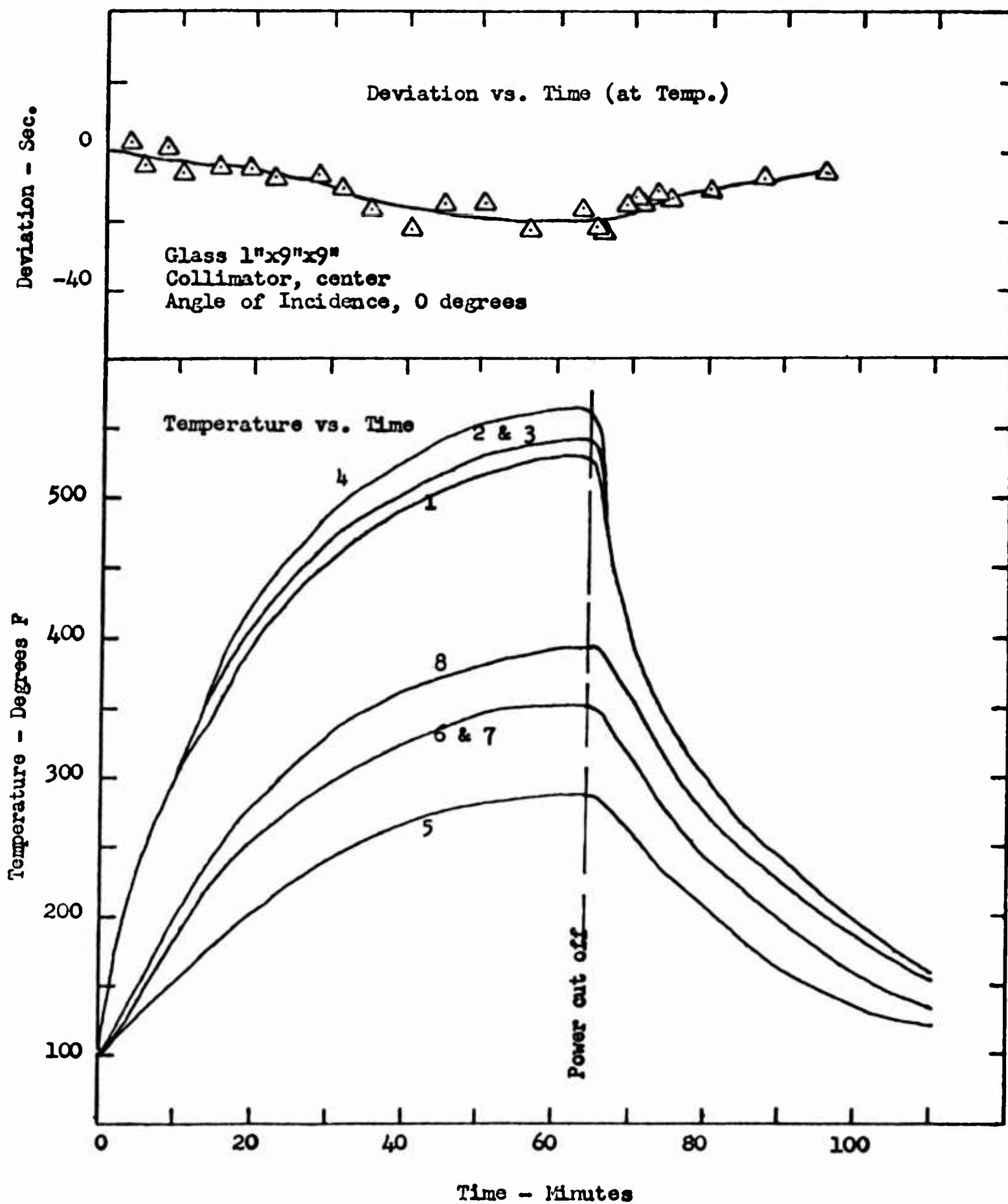


Figure 121. Temperature and Light Deviation versus Time, Test No. 16

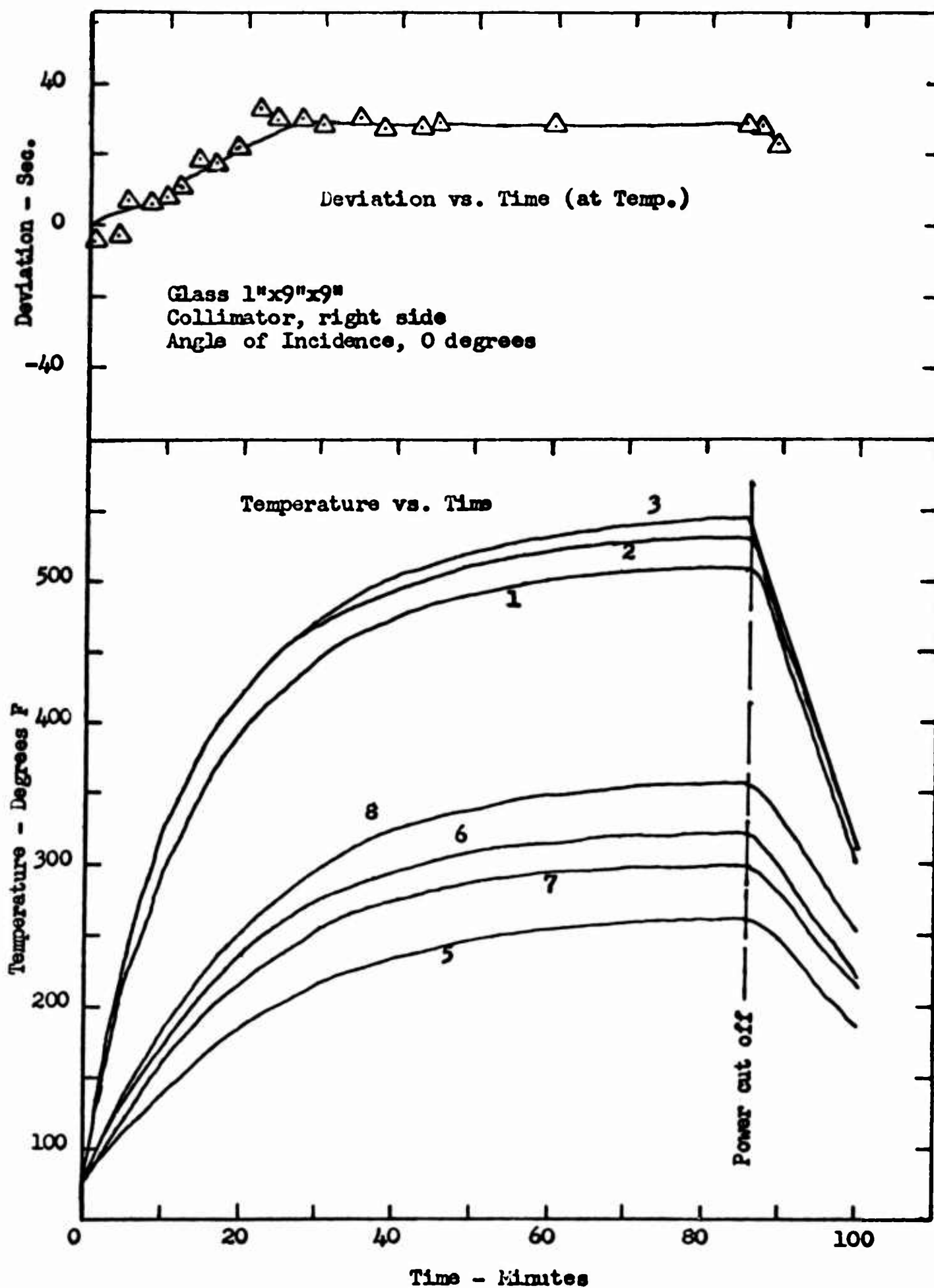


Figure 122. Temperature and Light Deviation versus Time,  
Test No. 19

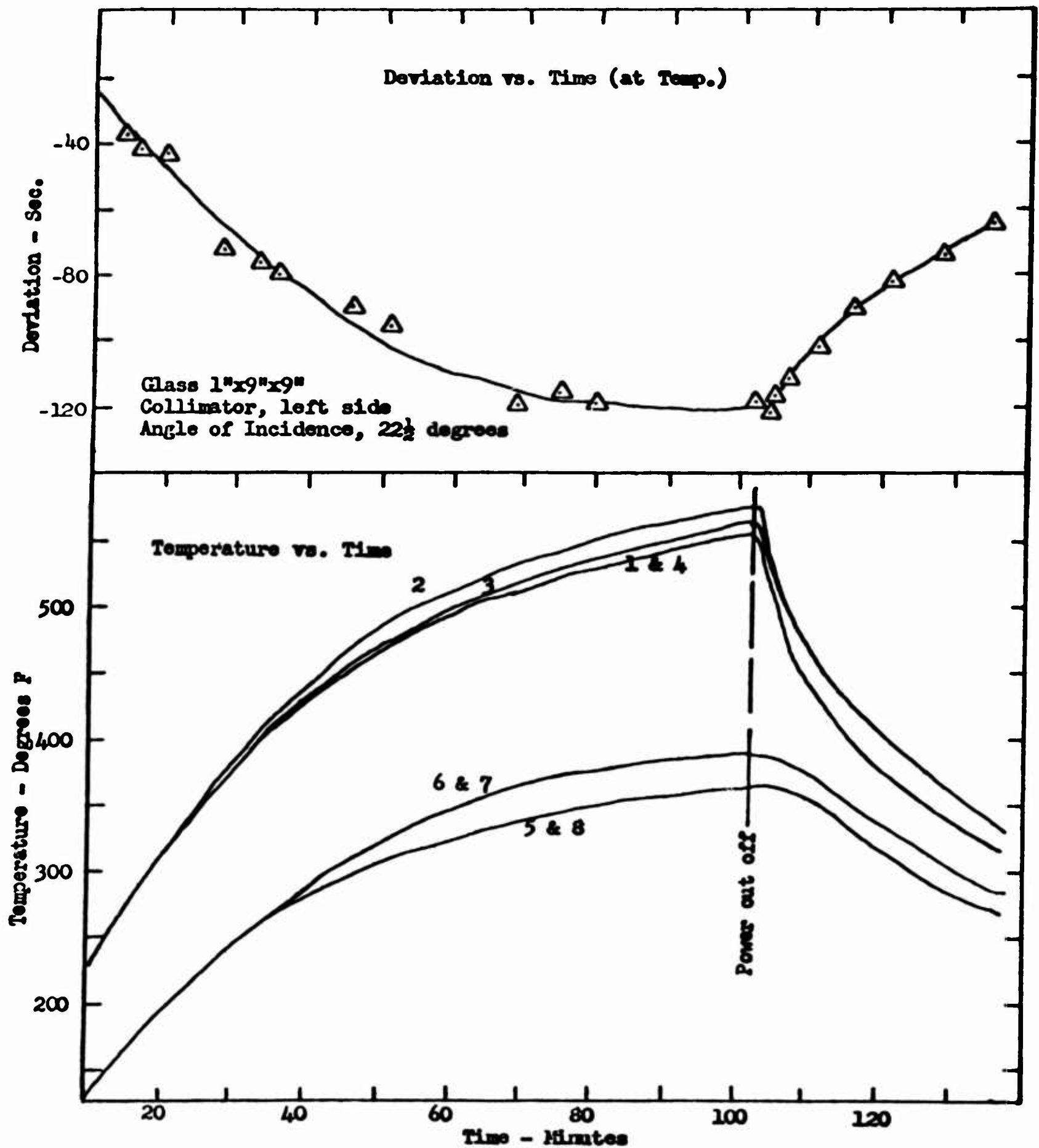


Figure 123. Temperature and Light Deviation versus Time, Test No. 20

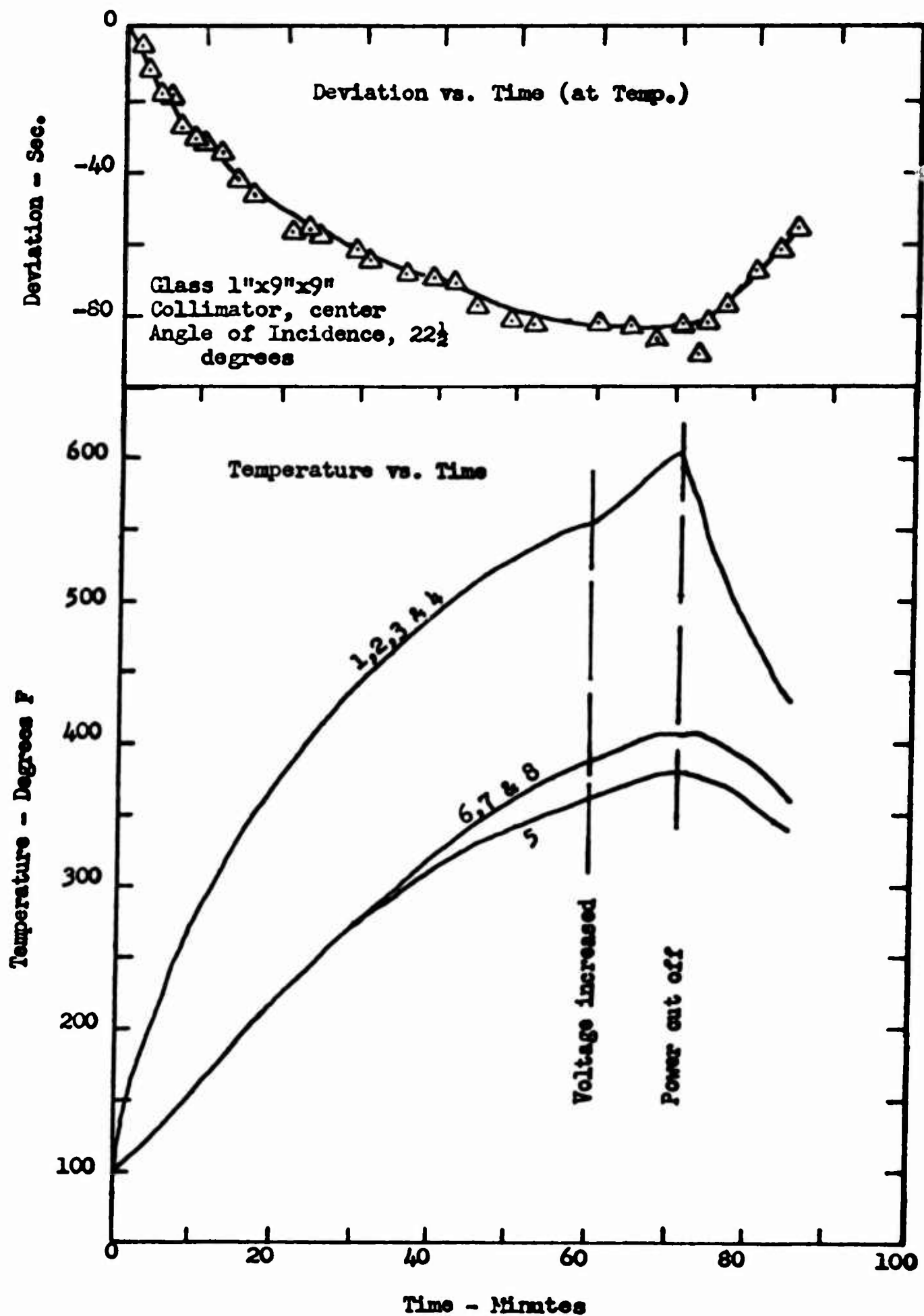




Figure 124. Temperature and Light Deviation versus Time, Test No. 21

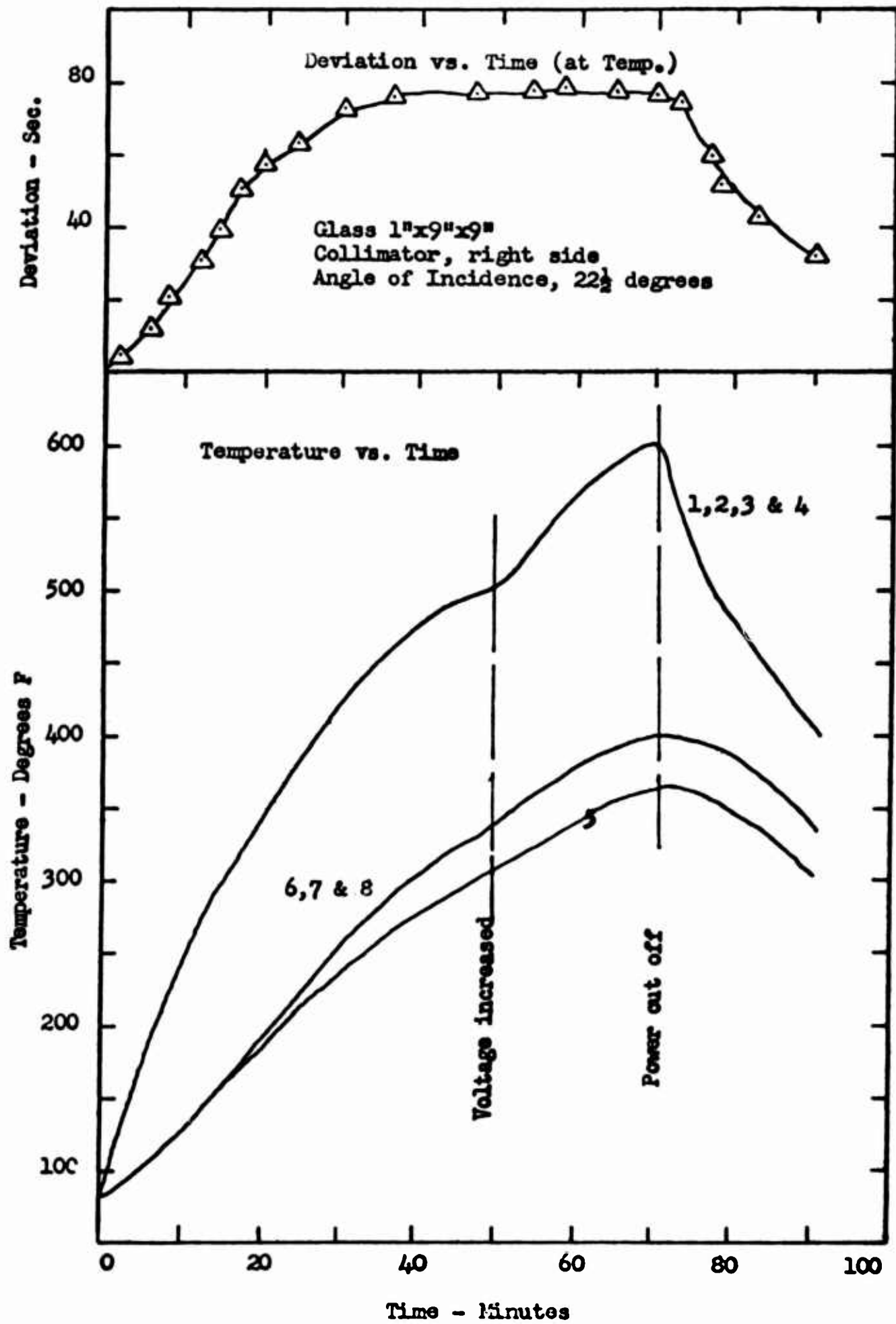


Figure 125. Temperature and Light Deviation versus Time, Test No. 22

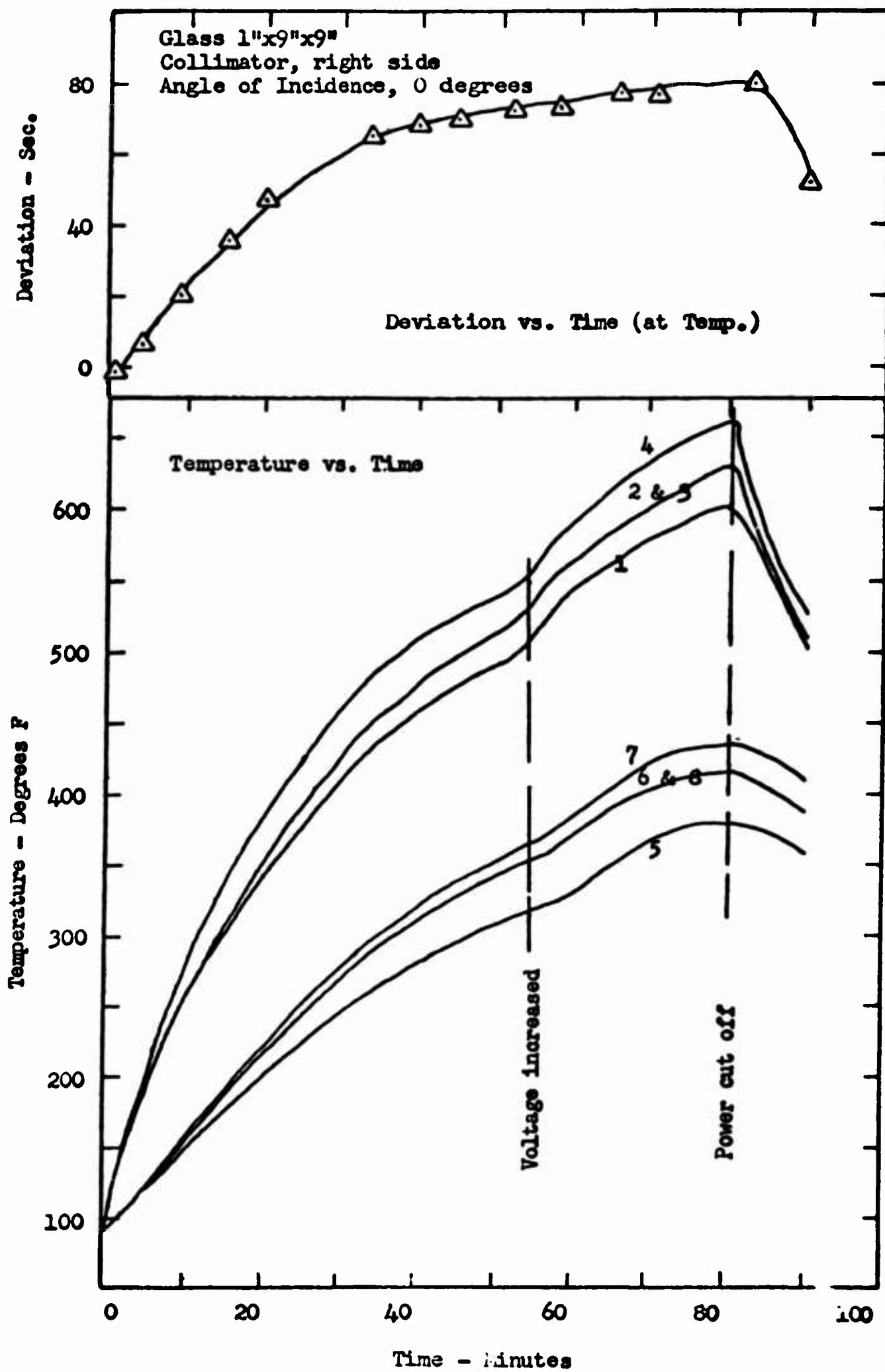


Figure 126. Temperature and Light Deviation versus Time, Test No. 23

Glass 1"x9"x9"  
Collimator, center  
Angle of Incidence, 0 degrees

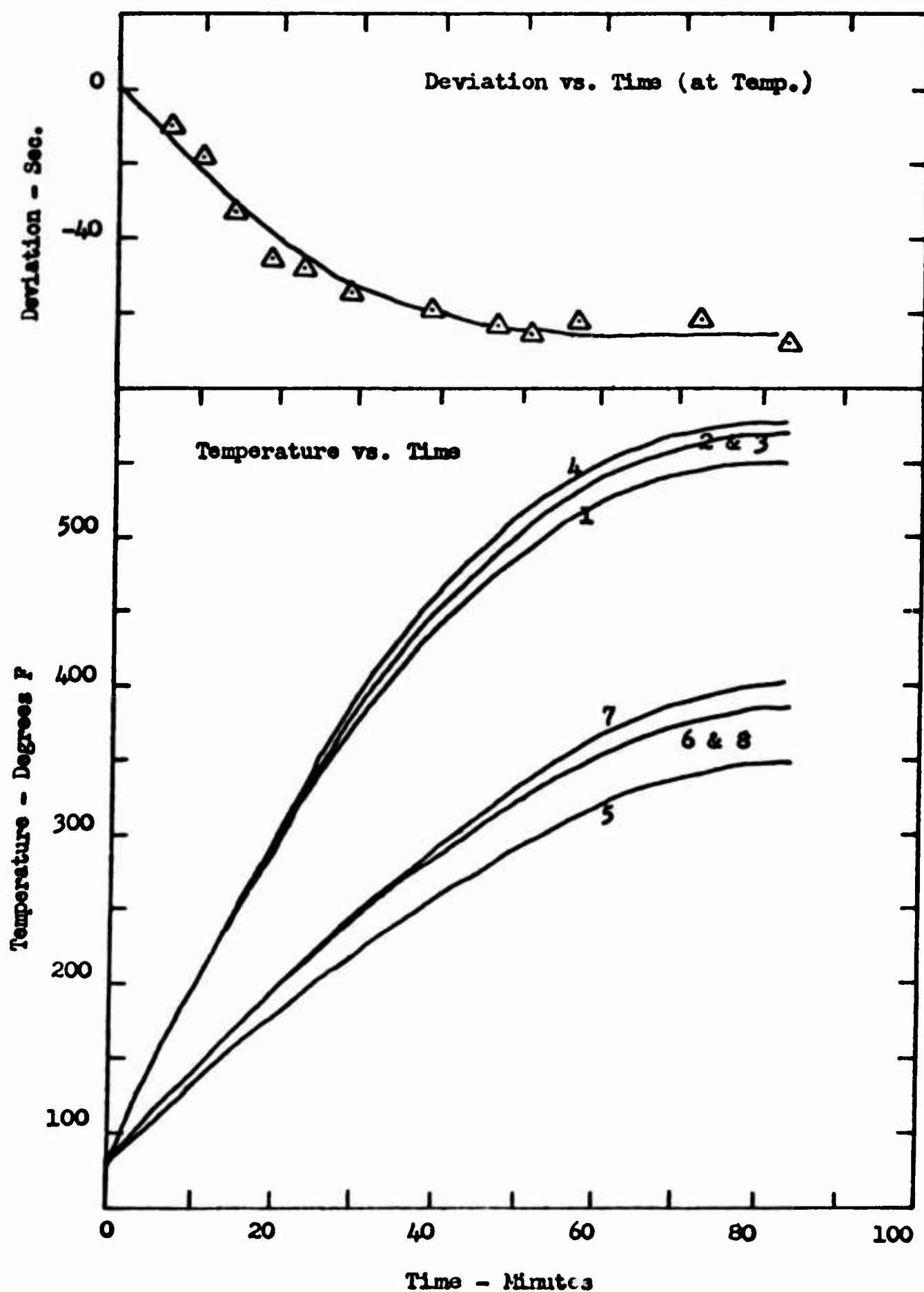


Figure 127. Temperature and Light Deviation versus Time, Test No. 24

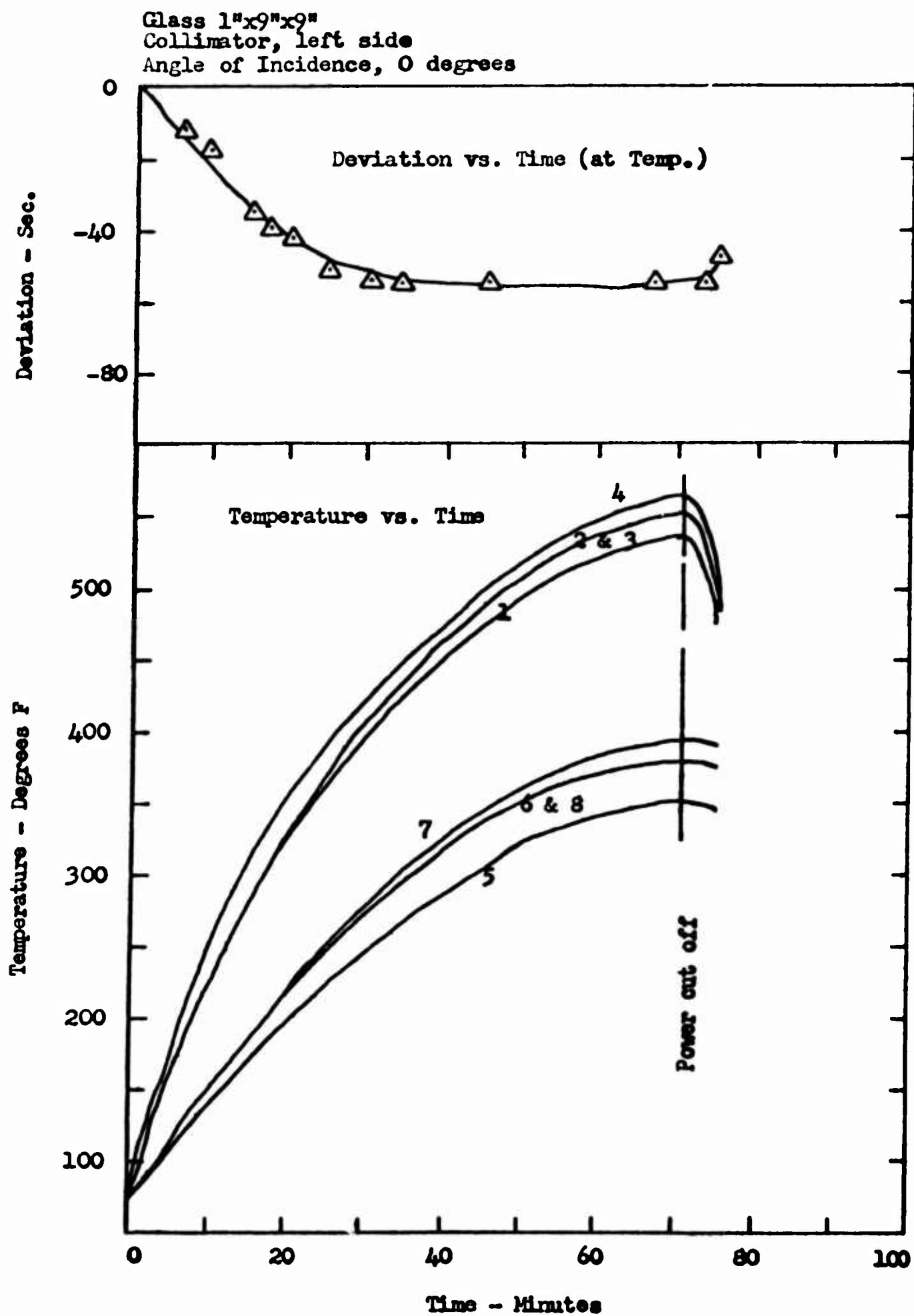
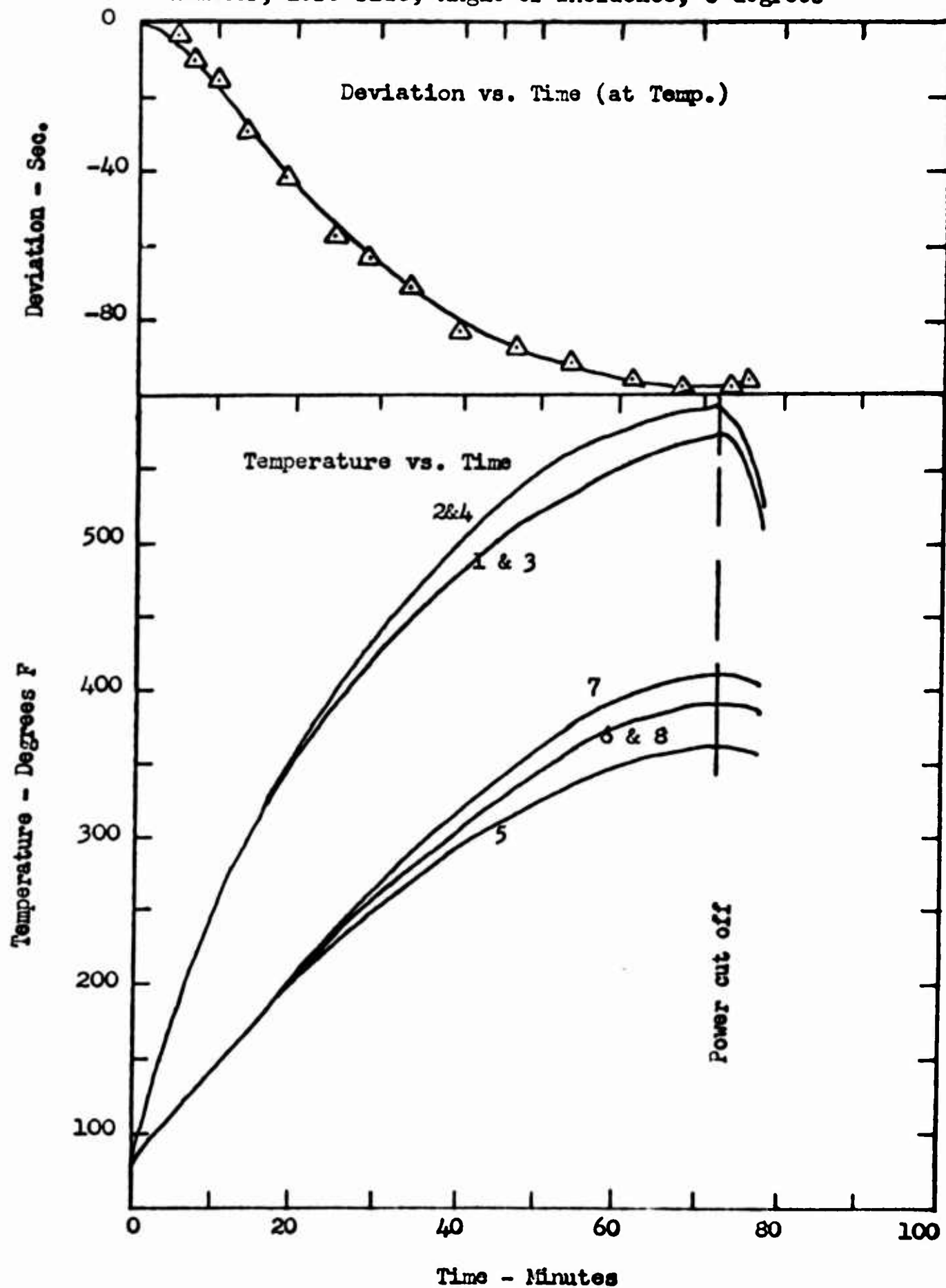


Figure 128. Temperature and Light Deviation versus Time, Test No. 25

Glass 1"x9"x9"

Collimator, left side; Angle of Incidence, 0 degrees





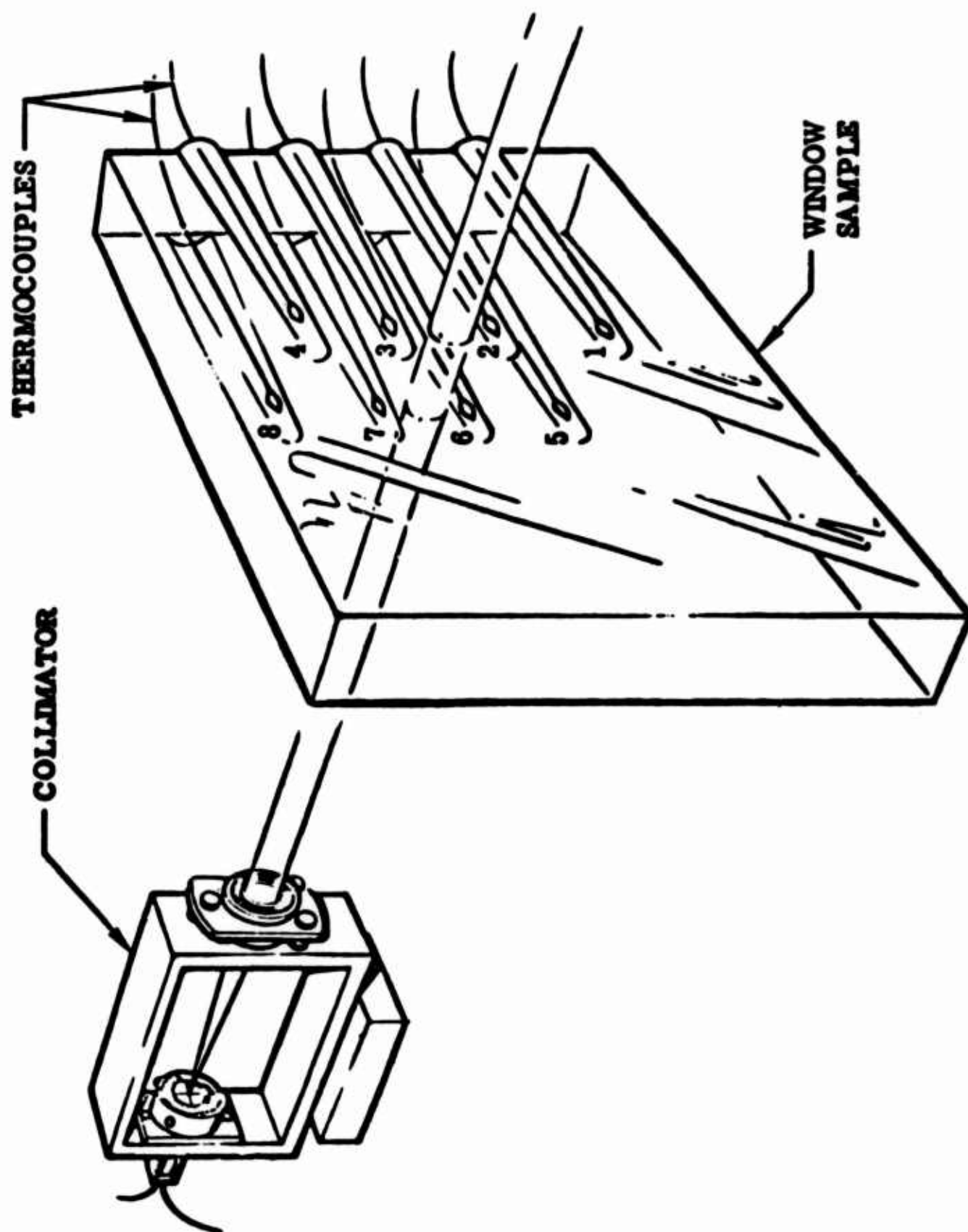


**Figure 129** Diagram Showing Location of Thermocouples on Panel

## Section VI

### LUMINOSITY TEST PROGRAM

One phase of the laboratory testing was an attempt to determine experimentally the dependence of optical deviation and resolution on boundary layer refraction, shock wave interference, and luminosity. It was intended to produce luminosity in the gas layer over a window in a shock tube, and measure the effects of this luminosity on photographic image quality. Unfortunately, the cost of the experiment became prohibitive and the tests were not carried to completion. That portion which was completed may contain useful information for subsequent related programs, and is reported in the following paragraphs.

#### TEST CONDITIONS

With the test facilities available it seemed feasible to produce a luminous condition with full flight simulation in the NAA shock tunnel. It was also intended to run a higher Mach number, which would not provide full simulation, but would produce greater luminosity. The luminous region for the particular test conditions to be used was based upon the work done by Vidya, Inc., References 1 and 2. Since the accuracy of these computations was not claimed to be better than one order of magnitude, it was not possible to determine beforehand whether luminous conditions would actually be obtained.

Test conditions and goals established for the testing program were as follows:

Observations through a non-luminous boundary layer will utilize a low-temperature gas in the shock tunnel. This observation will be made by collimator readings through a boundary layer created by a thick, blunt leading edge, and comparing them with readings taken through a layer created by a sharp leading edge. Similar observations will be made for a higher Mach number luminous layer. In addition it is intended to determine the fogging produced on photographic film by the luminous layer, to experimentally verify predictions of the amount of luminosity exhibited by a high Mach number boundary layer.

The model should be as simple as possible, with three angles of attack (0, 15, and 50). The test section will require a transparent section through which a lighted resolution target can be photographed. It is estimated that the laminar boundary layer surface, sharp leading edges and window fit in the surfaces should be made with an approximate surface roughness of less than five microinches, to keep the growth of the laminar boundary layer and the number of shock lines to a minimum. The model mounting should be so designed that the flat plates with windows on each side may be used to observe a two-dimensional heat transfer model between them (solid opaque material) which has the same internal surface as presented by the test surfaces except rotated 90 degrees.

This is in the expectation of providing a photograph of the shock profile for the luminous tunnel conditions as well as heat transfer data for the several angles of attack. The use of gages will be required along the centerline to get a chordwise distribution of the heat transfer to the surface of interest.

#### TEST PROCEDURES

Preliminary tests were conducted on a dummy model before construction of the actual model. The purpose of the test was to determine the blow time after a satisfactory start. This test showed that blockage of the model was too large to obtain satisfactory tunnel starts at the desired stagnation temperatures. Theoretical calculations also showed that full flight simulation could not be achieved in the 16 inch square nozzle being used, due to the short run time and large throat requirements, but duplication could be obtained at M 10 in the 12 inch round nozzle.

The model was redesigned to reduce tunnel blockage, and provisions were made to allow the model to be installed in either the 12 inch round nozzle or the 16 inch square nozzle. Thus, if the blockage were too large in the round nozzle, data could still be obtained, albeit imperfect, in the larger apparatus.

During this entire period it was confidently expected that useful experimental data would accrue from this admittedly secondary aspect of the program. However, with model construction approximately 50% complete, a re-assessment of costs was made and, in view of the limited budget of the overall program, the value of pursuing the shock tunnel testing at the expense of other aspects of the program became difficult to justify. Since there was no guarantee that further tests would be entirely successful in either of the two nozzles, it was decided to discontinue further work in this area. The ASD Program Manager concurred that, while the experimental measurement of luminosity would have been of wide interest, it was impossible to sustain the rate of investment for that work within the funding of the present contract.

## Section VII

### STRUCTURAL DESIGN

#### SECTION SUMMARY

Based on the experience accumulated during previous designs of windows for supersonic and hypersonic vehicles at North American Aviation, design criteria were evolved for use in this particular program. These criteria, against which the design ideas were to be judged, included:

- a) Maintenance of aerodynamic smoothness at high temperatures
- b) Continuous maintenance of a pressure seal
- c) Maintenance of structural integrity of the window material

With these guide lines, and with the thermodynamic data previously accumulated for the various trajectories of interest, several designs were produced for high-temperature window mounts. The best of these designs are included in this report, Figures 130 - 134. These designs are believed to be structurally sound, and should be applicable for use in a Dynasoar-type vehicle.

#### DESIGN CRITERIA

The design of a high-temperature window mount is complicated by the requirement that the system withstand a wide range of temperatures during a fairly brief time cycle. Thus, in addition to being resistant to damage by heat, it must also maintain its structural integrity when exposed to thermal shock. Tempered glass is generally used in structural applications because of its ability to withstand high tensile loadings which occur during pressurization or thermal shock. This ability is due to the stress distribution of unloaded tempered glass which has high compressive stresses on the surfaces balanced by internal tensile stresses. Since pressurized glass structure almost always fails in tension at an edge (more rarely at a surface) but almost never internally or in compression, tempered glass is able to withstand comparatively high tensile loading. This has the effect of reducing the compressive stresses in the fail-prone surfaces while increasing tension internally where failure virtually never occurs. As tempered glass cannot be used in an optical system because of its refractive properties, extra care must be taken to design for lower-strength glass under highly-loaded conditions. Specifically, a window mount for a hypersonic, Dynasoar-type vehicle must be judged according to three basic criteria:

- (a) Maintenance of aerodynamic smoothness
- (b) Maintenance of pressure seal
- (c) Maintenance of structural stability

Without aerodynamic smoothness the flow of air past the window would be seriously impeded, resulting in excessive turbulence and excessive heating of the vehicle. As the vehicle velocity increases, the smoothness becomes more critical. If the thermal expansion of the glass could be made to match the expansion of the surrounding structure, the smoothness could be easily maintained. Unfortunately, the glass is part of an optical system, and a low expansion is desirable. The best approach is to design the window to be flush with the surrounding structure during that part of the trajectory when the window is hottest, at its extreme expansion. At other points in the trajectory, when the glass is cooler and the adverse effects of air turbulence are less detrimental to the vehicle, there will be a slight gap in the contour.

If the pressure seal around the window were not maintained for the duration of the flight, the compartment air supply system would become overloaded. It is also necessary to maintain the seal in order to prevent explosive decompression, which would result in possible damage to vehicle and camera.

Loss of structural stability is taken to mean breaking or cracking of the glass due to thermal or mechanical stress imposed on the glass by the mount. It is assumed that the glass itself will withstand the thermal environment. Breaking or cracking of the glass would result in a pressure leak and/or a degrading of image quality. The mount must be designed to be flexible and strong under all conditions to be encountered during any specific flight.

## WINDOW MOUNT DESIGN

### Basic Mount

Evolution of a typical basic window mount design for a Dynasoar-type vehicle is shown in Figure 130 reading from the right-hand part of the drawing to the left. Type B-66 columbium was selected as the mount material because of its strength and durability at fairly high temperatures. The primary mount is H-shaped in section, with rounded surfaces contacting the glass. At room temperature the outer surface of the window is slightly indented and bevelled with respect to the plane of the mount. The slack is taken up when the glass expands with temperature and rides up the inclined surface. The periphery of the glass is surrounded by a resilient insulator such as "Fiberfrax." (Recent tests at North American indicate that a ceramic insulator such as "Kaowool" has even better stability at temperatures to 2800 F). Actual support of the glass at its periphery is accomplished by means of columbium springs at the bend on each surface. Contact between spring and glass is avoided through the use of insulation, in order to prevent hot spots.

The pressure seal is maintained by means of a columbium foil pressed flat along the outer edge of the inboard glass surface. Internal or environmental air pressure on the foil forces it into intimate contact with the glass over a relatively large surface area, preventing leakage. The foil is held flat by a wire hoop ring attached at the inside diameter of the foil washer. This also prevents the possibility of rupturing of the foil due to



hoop tension loads. The design is self-adjusting, i.e., as the temperature changes, the mount configuration also changes, in a direction which maintains the seal. The only feature of the design that could be considered undesirable is the concave radius which must be ground at the edge of the outside surface. This necessary feature increases the cost of the window and, if the grinding procedure is not performed correctly, could weaken the glass. However, if reasonable care is exercised in the grinding, and if the sharp edge at the outer surface is very lightly chamfered, no damage should be expected.

#### Extensions of Basic Design

Figures 131 through 134 are logical progressions of the basic mount of Figure 130. In the design of Figure 131 the formed columbium retainer is modified in configuration in order to provide a more positive retention of the glass panel at all temperatures. The other design features of Figure 130 are retained.

Figure 132 is an imaginative approach to solving the problem of differential expansion of glass and metal. Here small cylindrical tubes are placed around the periphery of the ring mount, each tube having an expandable bellows at one end. The tubes and bellows are filled with nitrogen gas, which expands at elevated temperatures. As the glass expands, it exerts force against the ring mount, and the resultant clamping action of the mount on the glass holds the glass steady even at higher temperatures.

At higher temperatures columbium may tend to lose its spring constant. Figures 133 and 134 show how a graphite tape may be used as an additional support. The "Fiberfrax" insulation takes up shock, and the resilient "Graphoil" tape holds the insulation in place. In Figure 133 a segmented graphite strap is used, while in Figure 134 a full strap is shown as the holding mechanism to keep the glass steady. The full strap may be easier to fabricate.

#### Conclusions

The designs presented in Figures 130 through 134 are for a typical hypersonic vehicle. The mounts provide for the maintenance of structural stability, aerodynamic smoothness, and pressurization during flight. These concepts are flexible enough to be used in a wide range of environments. Further detail must await establishment of more precise operating conditions.

Mounts for a hypersonic short-flight vehicle and a low-altitude supersonic vehicle are shown schematically in Figures 7 and 13. Since this type of mount has already been demonstrated on the X-15 research vehicle, no further design effort was indicated in this program.

#### Proposed Method for Protecting Window

Since the effect of a heated window on the image quality of high acuity systems is so severe, some method should be devised to protect the window from becoming hot. A possible protective device would be a louver-type shutter that opens only when a picture is to be taken. It would then close,

shutting off the heat supply to the window. It is felt that this configuration is the most suitable, because it would open and close rapidly and would not disrupt the airflow as seriously as the other openings.

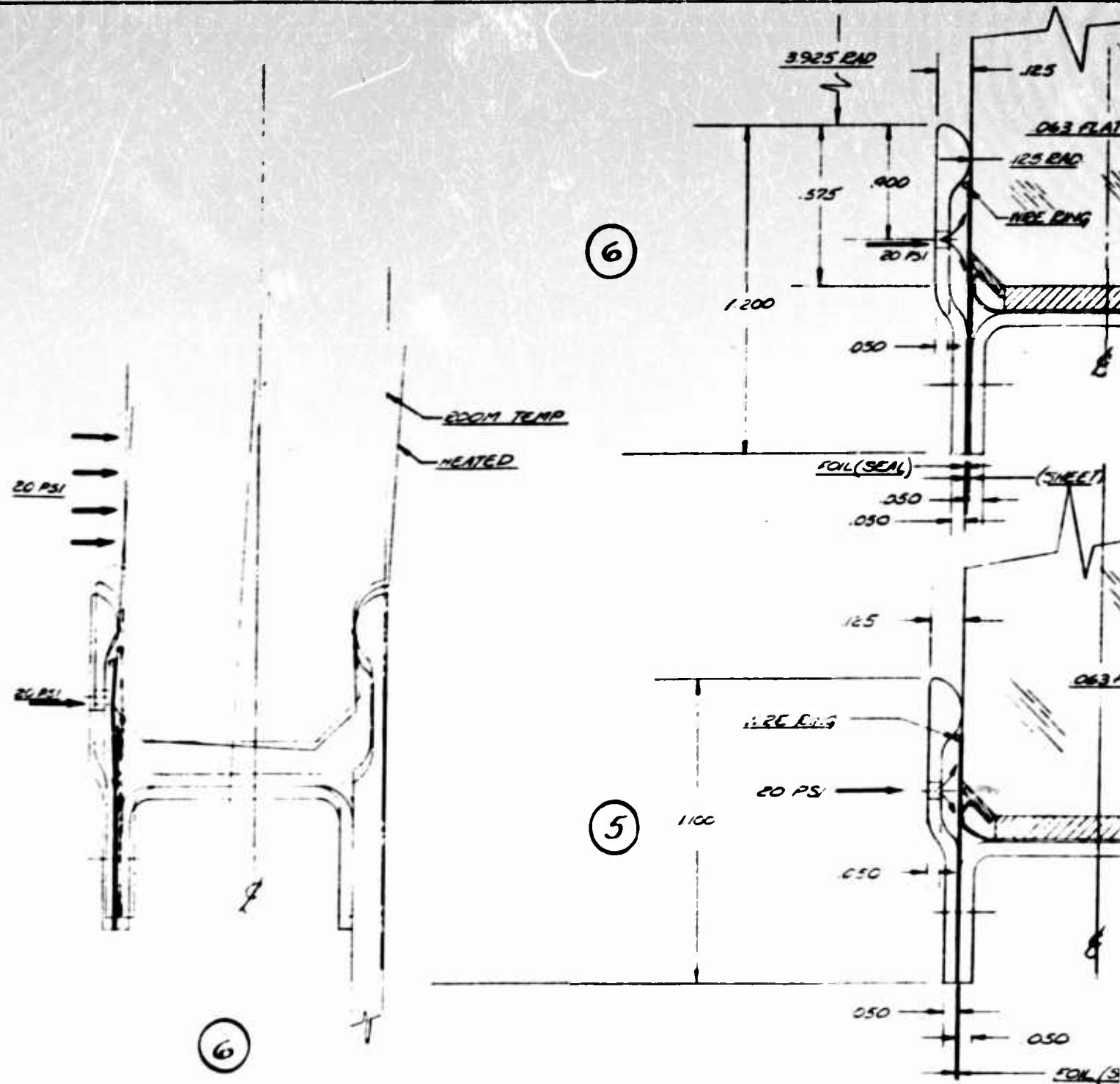
Figure 135 is a sketch of a possible configuration. This figure illustrates the shape and geometry of the system. It is recommended that a coolant be circulated into the cavity between the window and the shutter when the shutter is closed to keep the window temperature as close as possible to that of the camera cavity. It is assumed that for the short period of time that the shutter would be open, the window would not be significantly heated to cause degradation of resolution.

The mechanism for actuating the louvers should be a mechanical device. Electromagnetic devices, such as activating solenoids, lose many of their properties above the curie temperature. This temperature will probably be far below the operating temperature of the shutter.

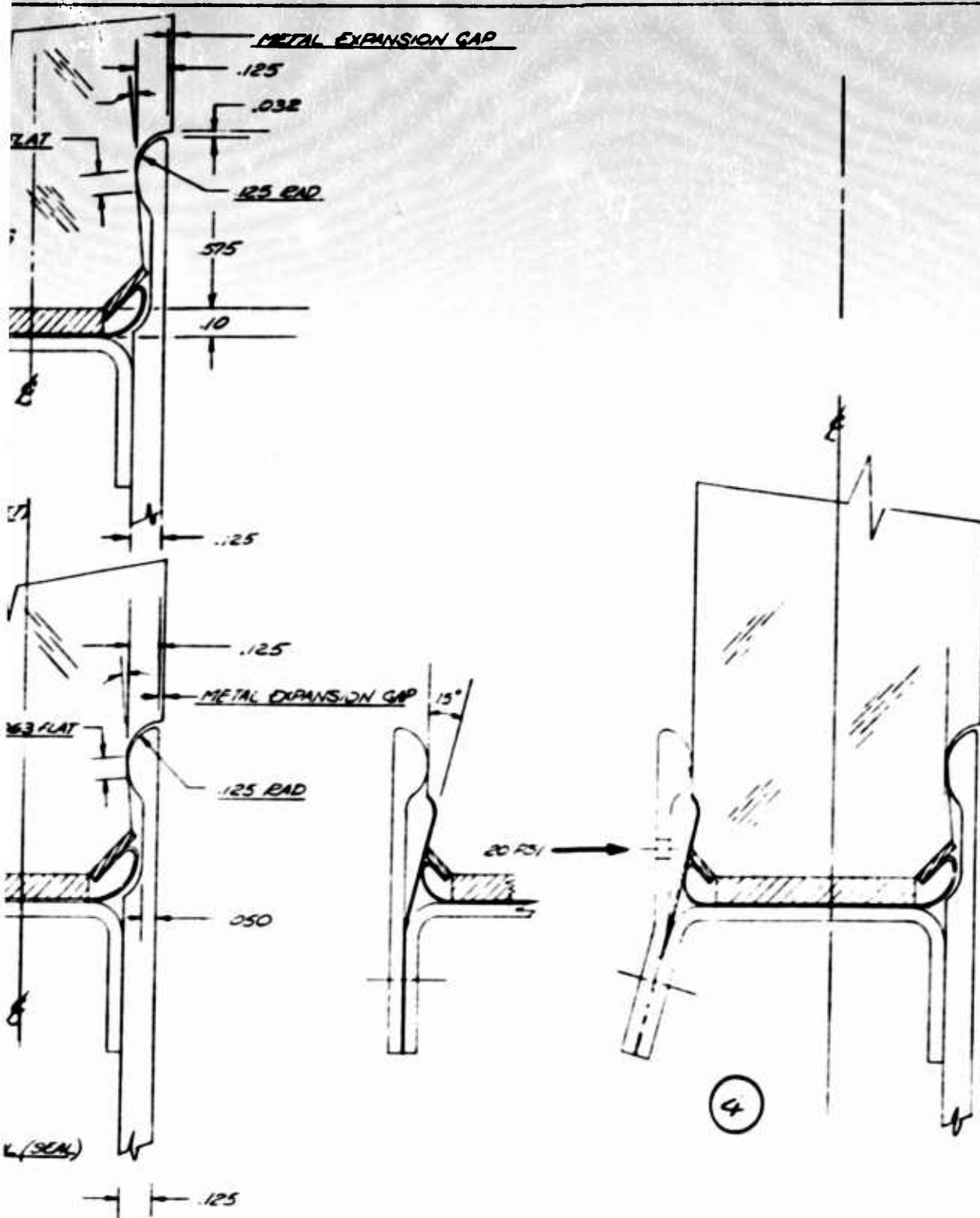
#### FEASIBILITY OF PROTECTING THE WINDOW

The aerothermodynamic analysis (Section IV) indicates that considerable protection can be provided for the window by controlling the expansion of the air layer over the window. This can be effected by sloping the window relative to the vehicle mold line. If the window is located on an aft position and is sloped to an angle of about 30 degrees, the convective heating rate is reduced by some 30 percent in laminar flow and over 40 percent in turbulent flow. These are theoretical values for a blunted two-dimensional wing, and may not reflect accurately the situation in a three-dimensional problem. However, there is no reason to believe that three-dimensional data would not be of the same order of magnitude, and so a considerable degree of optimism is warranted. A study of the particular flow characteristic of specific vehicles and missions would, of course, be necessary in any case, but it is believed that the feasibility of protection has been clearly established.

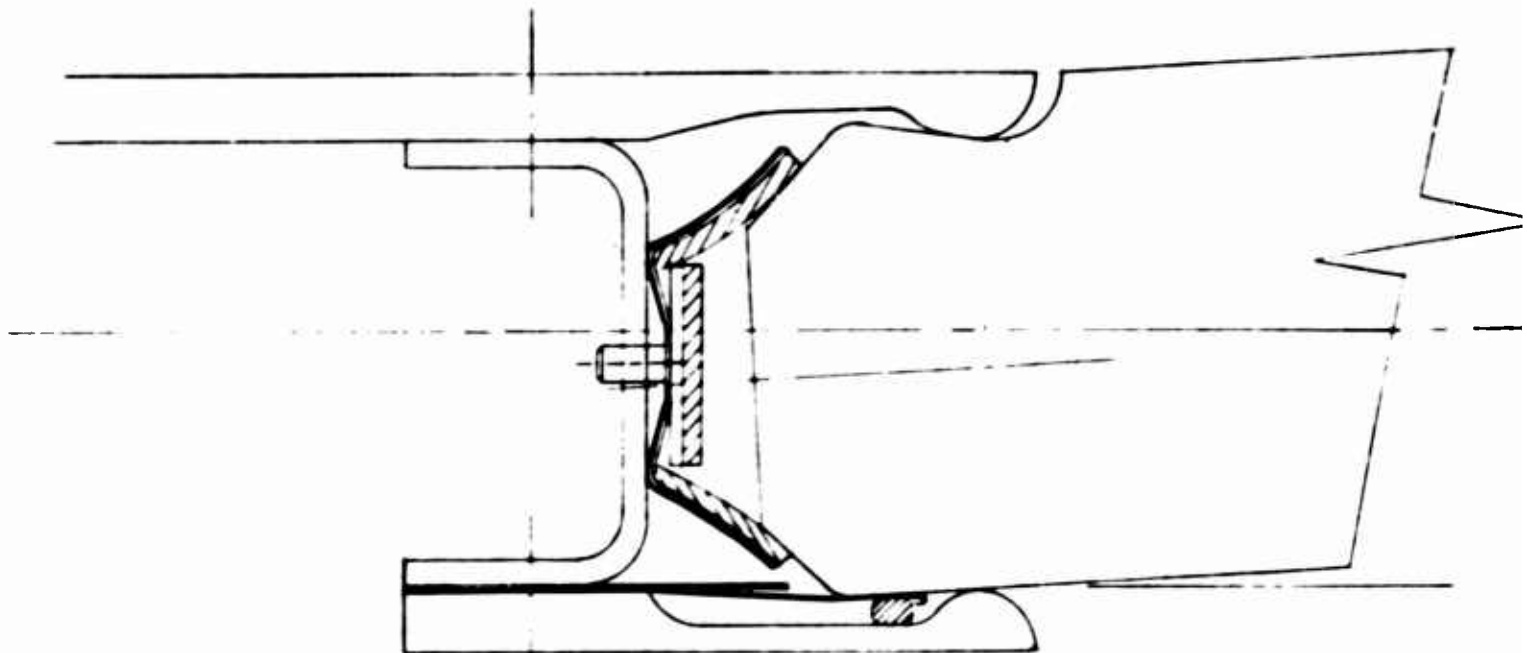
FRAMES



EDGE MOUNT - GLASS RELATIVE LOCATIONS  
@ ROOM TEMP & ELEVATED TEMP



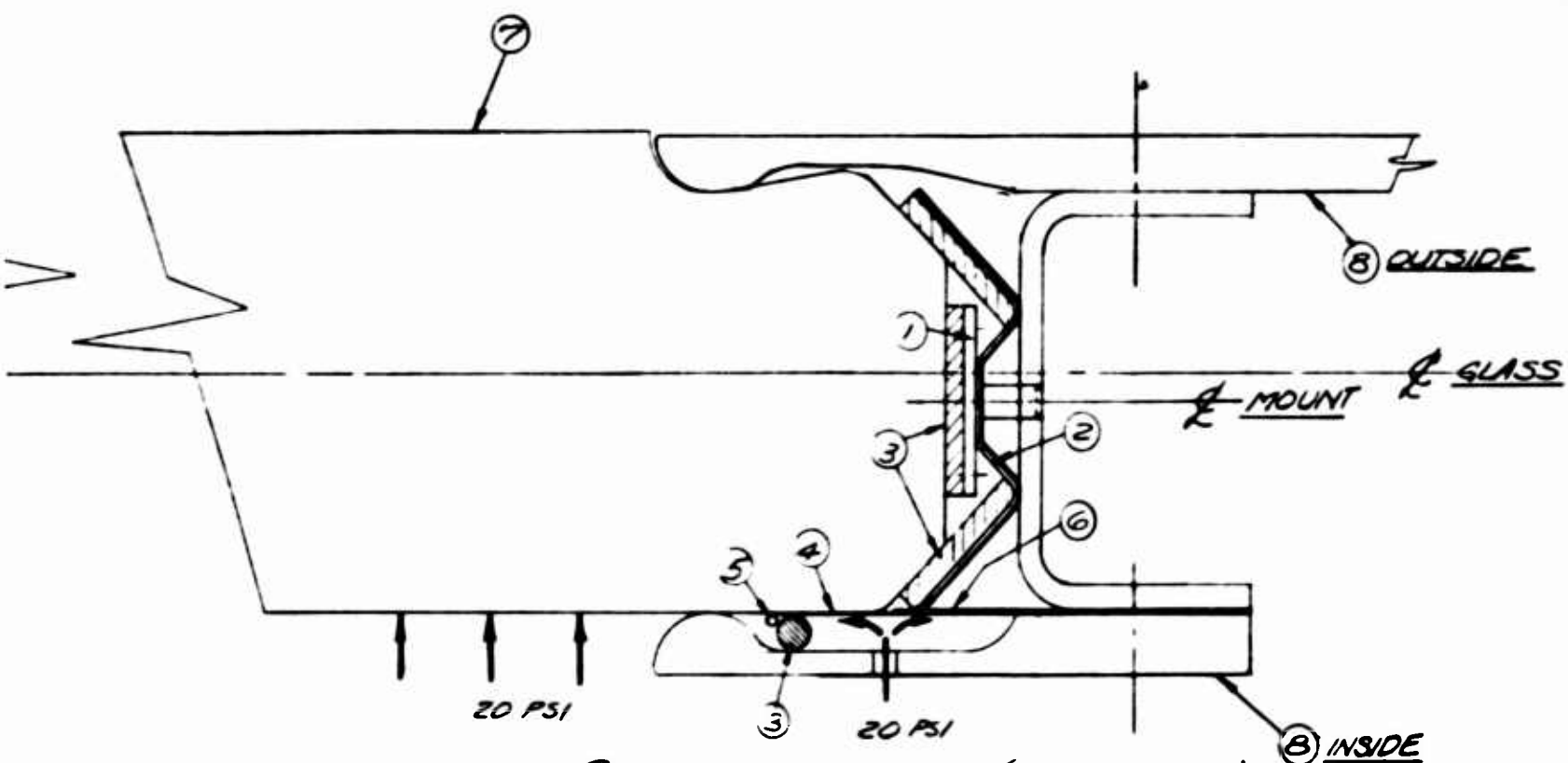
2  
FRAMES



SECTION B-B (@ELEVATED TEMP)  
4 TIMES SIZE

**A**

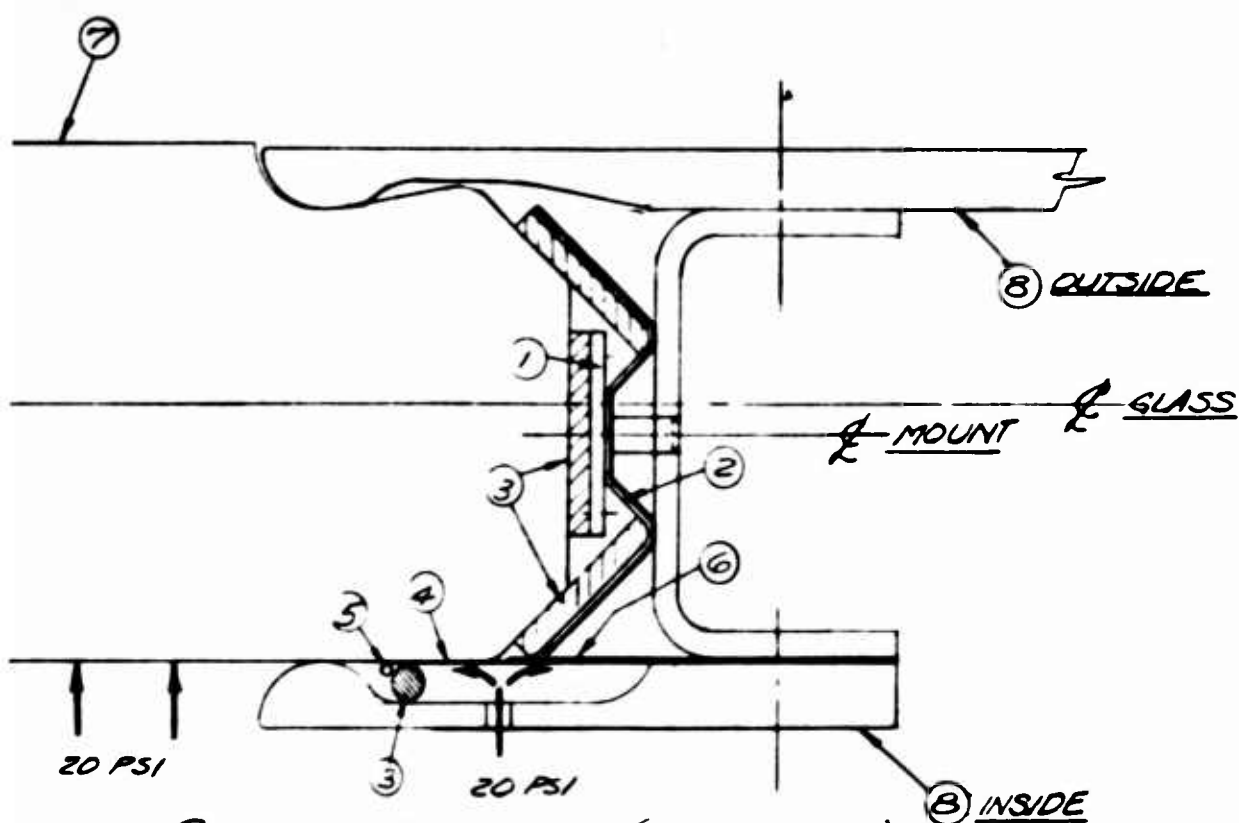




SECTION A-A (ROOM TEMP)  
4 TIMES SIZE

- ① CLOSED RING (NICKEL BASED ALLOY)
- ② FORMED RETAINER (B-66 COLUMBIUM) COMPOSED OF SEGMENTS TO ALLOW FOR EXPANSIONS
- ③ INSULATION / CUSHIONING MATERIAL (FIBERFRAX)
- ④ PRESSURE SEAL (B-66 COLUMBIUM FOIL)
- ⑤ WIRE RING ATTACHED TO ID. OF FOIL (B-66 COLUMBIUM)
- ⑥ SHEET WASHER (B-66 COLUMBIUM) (SUPPORT FOR FOIL UNDER PRESSURE)
- ⑦ GLASS (FUSED SILICA 794Q)
- ⑧ EDGE MOUNT (B-66 COLUMBIUM)

- ① CLOSED
- ② FORMED
- ③ INSULA
- ④ PRESS
- ⑤ WIRE
- ⑥ SHEET
- ⑦ GLASS
- ⑧ EDGE



# SECTION A-A (ROOM TEMP)

4 TIMES SIZE

SEAL RING (NICKEL BASED ALLOY)

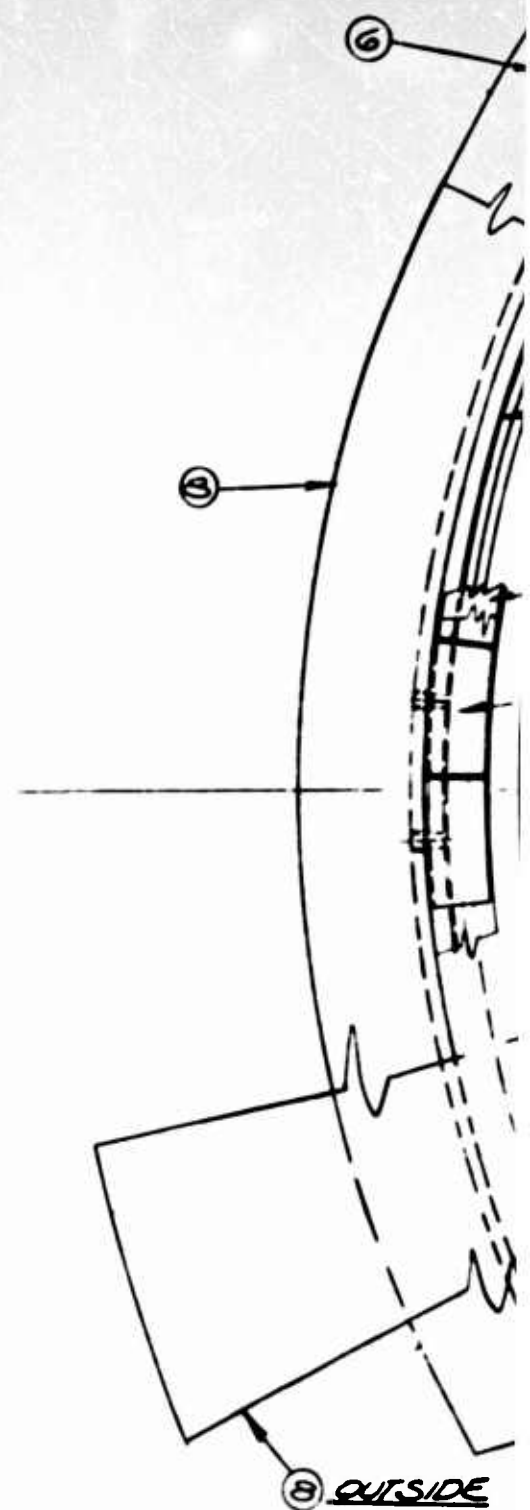
FORMED RETAINER (B-66 COLUMBIUM) COMPOSED OF  
MENTS TO ALLOW FOR EXPANSIONS  
ULATION / CUSHIONING MATERIAL (FIBERTRAK)

PRESSURE SEAL (B-66 COLUMBIUM FOIL)

PIPE RING ATTACHED TO ID. OF FOIL, B-66 COLUMBIUM)

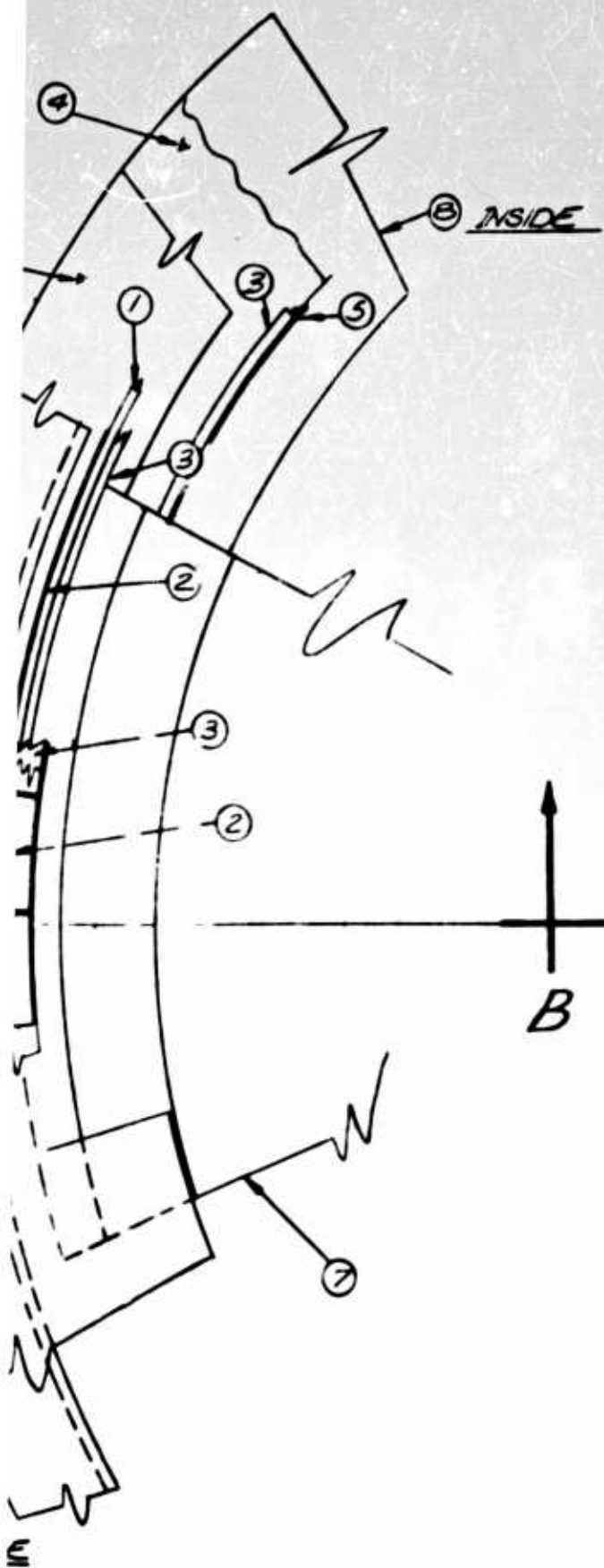
WET WASHER (B-66 COLUMBIUM)  
SUPPORT FOR FOIL UNDER PRESSURE)  
GLASS (FUSED SILICA 7949)

GLASS MOUNT (B-66 COLUMBIUM)

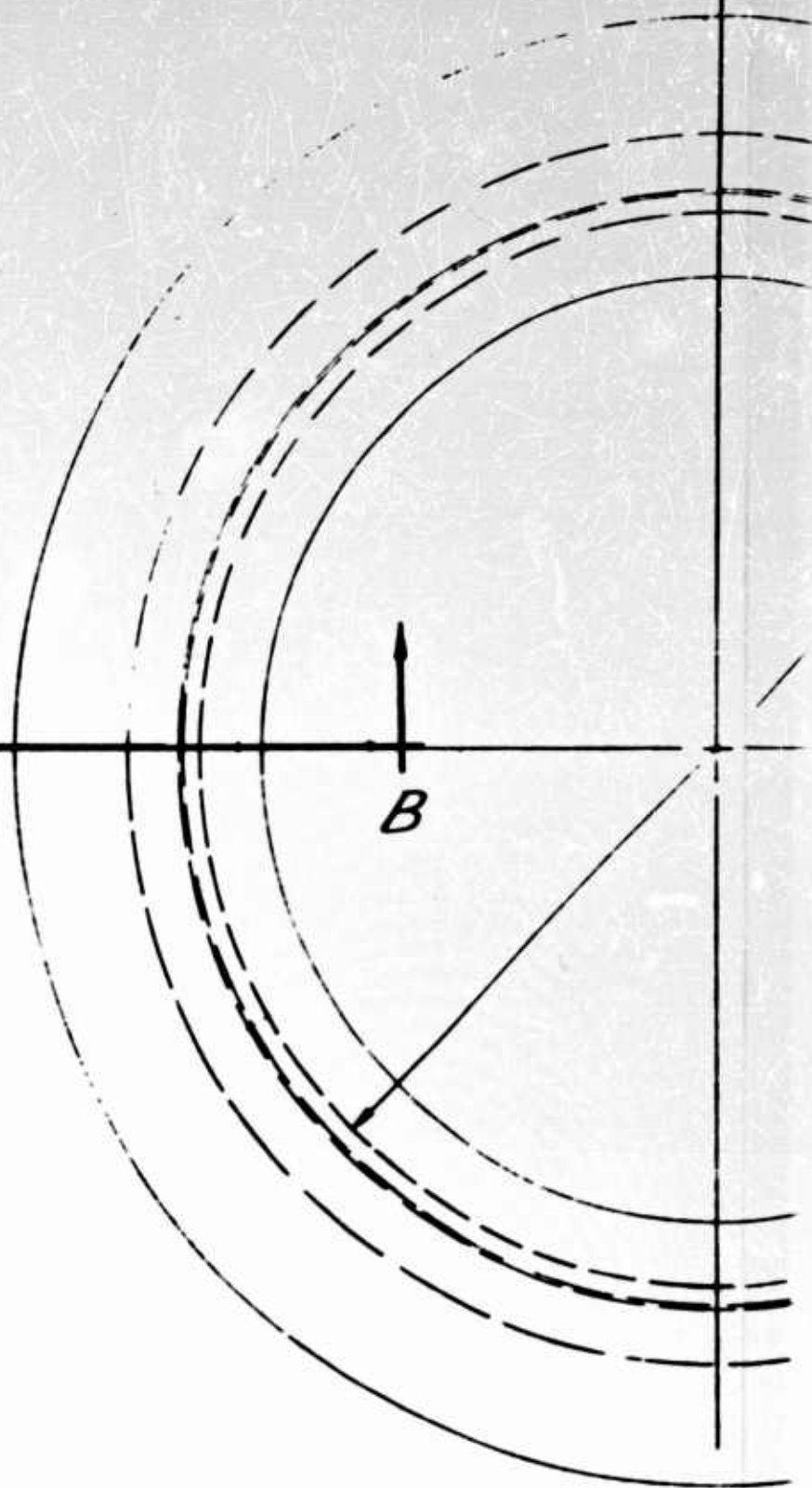


VIEW  
27

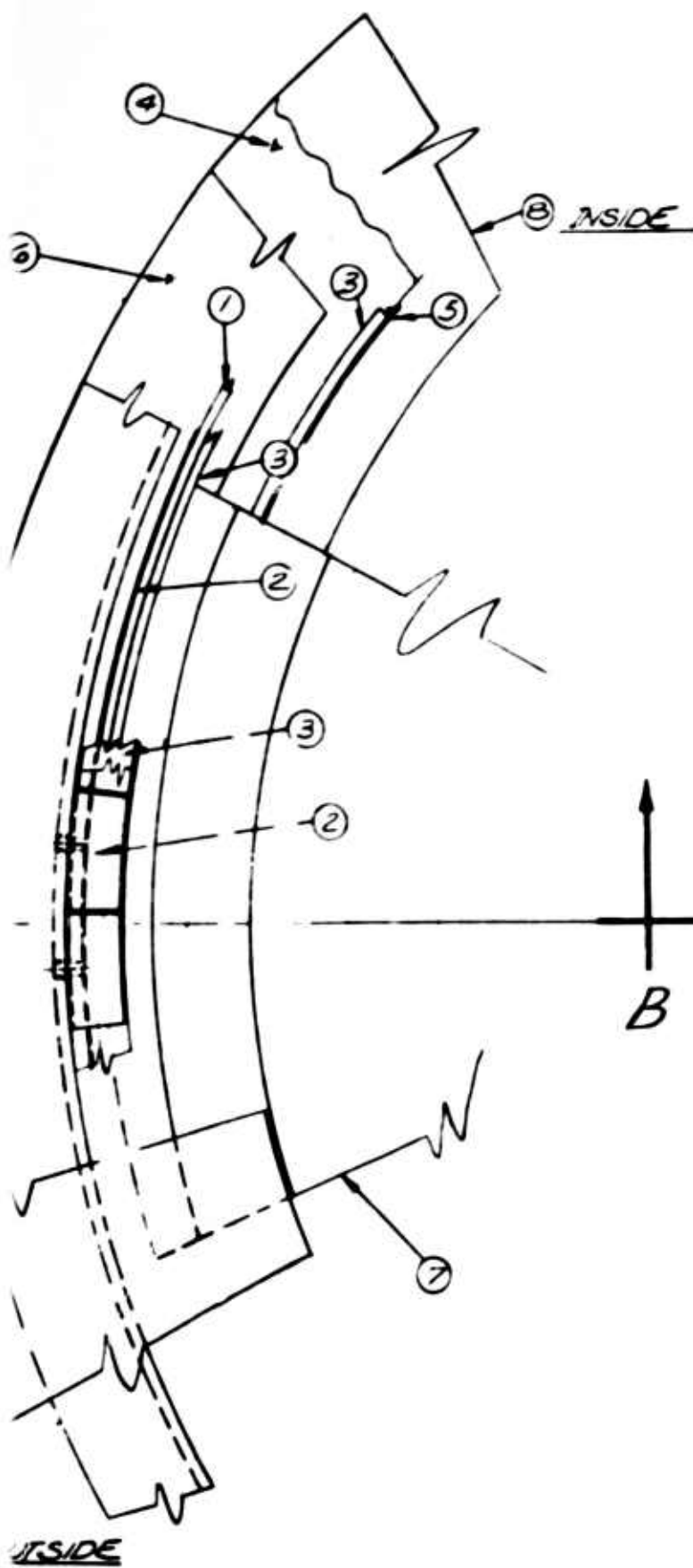
**8**



VIEW LOOKING UP  
2 TIMES SIZE



VIEW LOOKING  
FULL SCALE

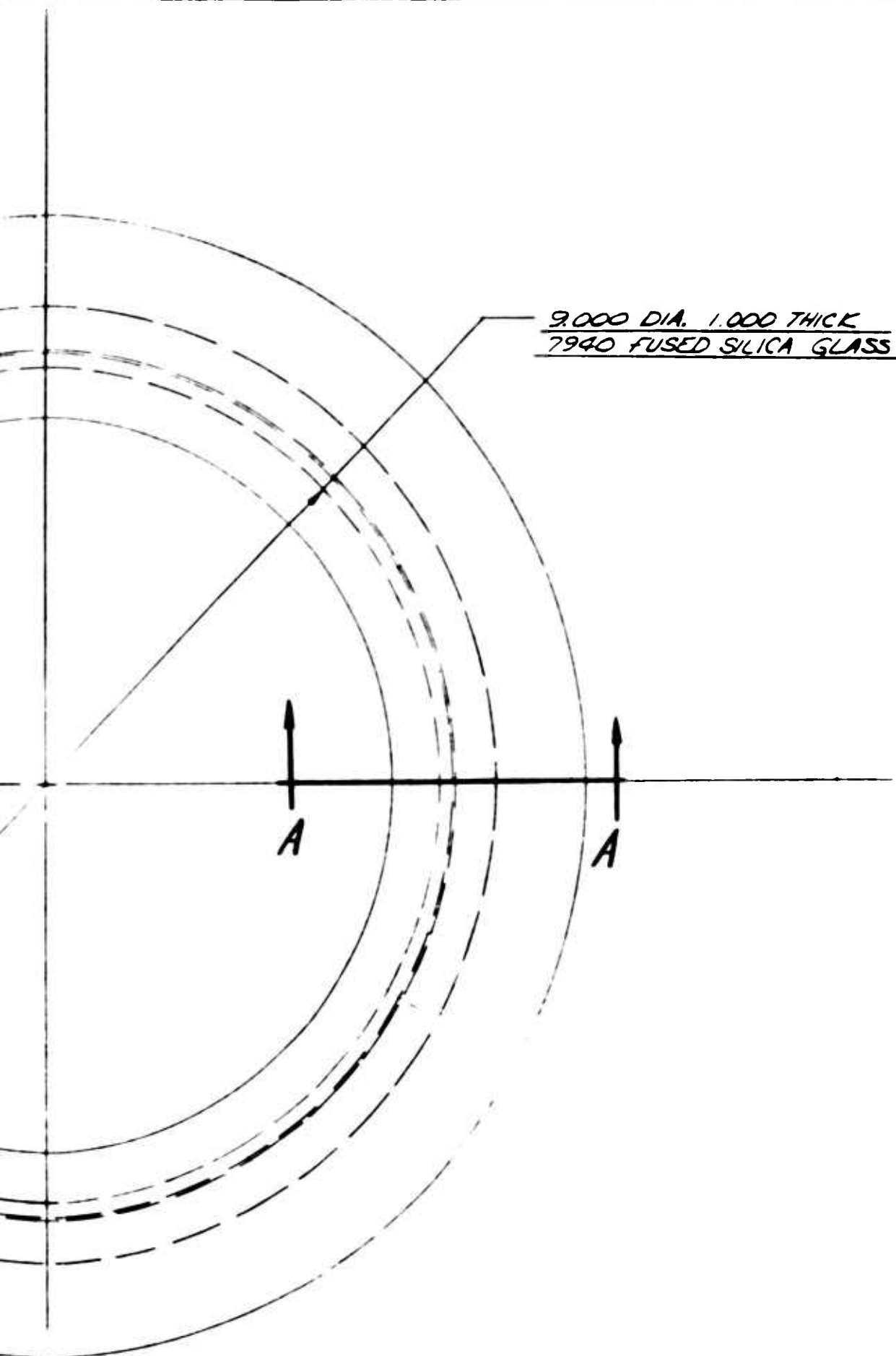


VIEW LOOKING UP  
2 TIMES SIZE



VIEW LOOK  
FULL SCALE

LOOKING UP  
LE



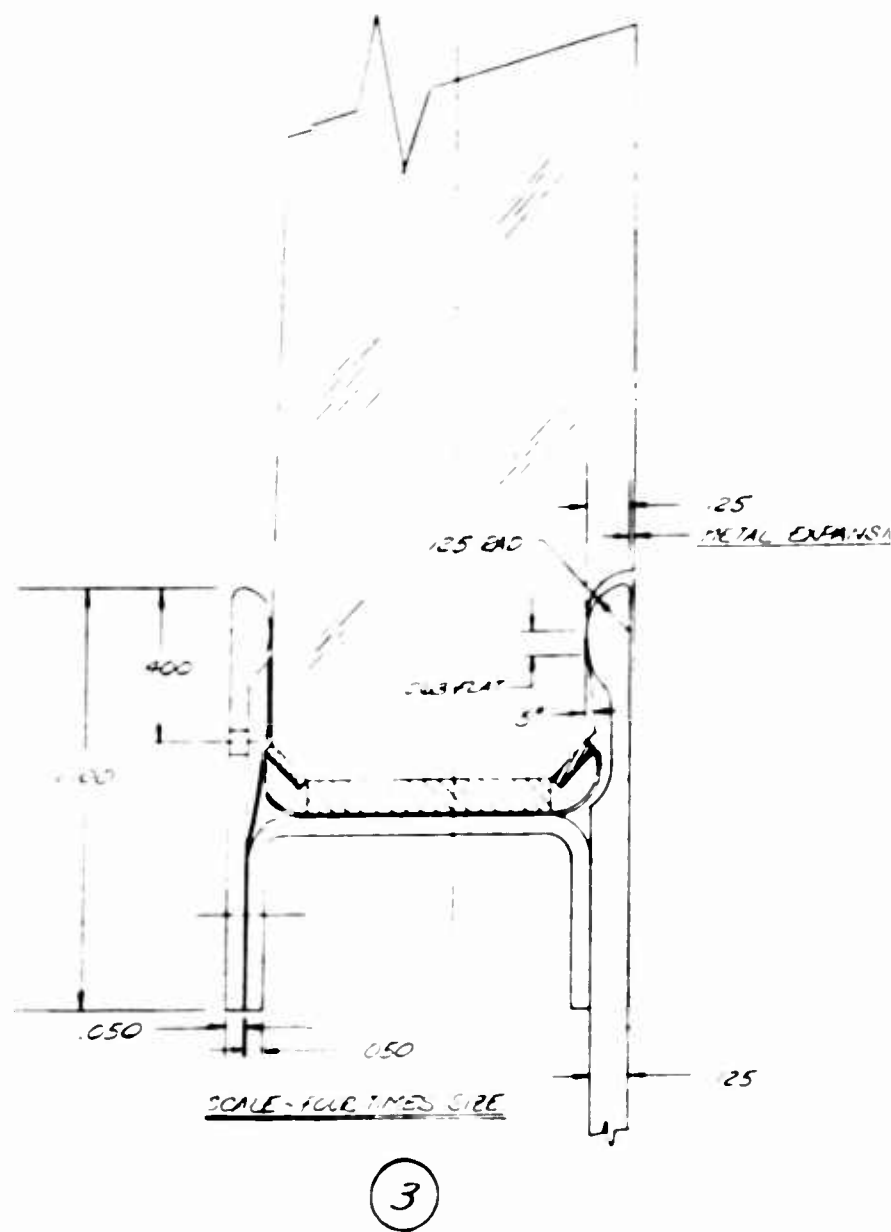
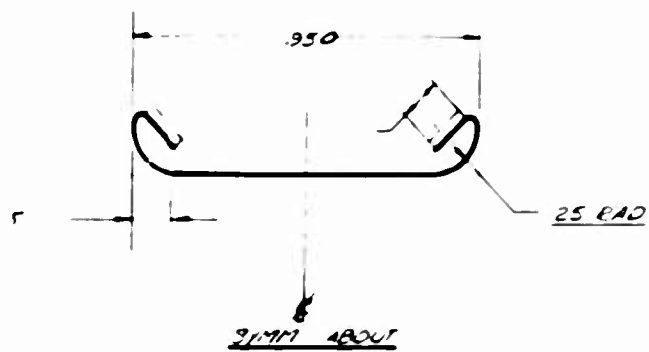
9.000 DIA. 1.000 THICK  
7940 FUSED SILICA GLASS

Figure 131 Window Mount Design 2

C

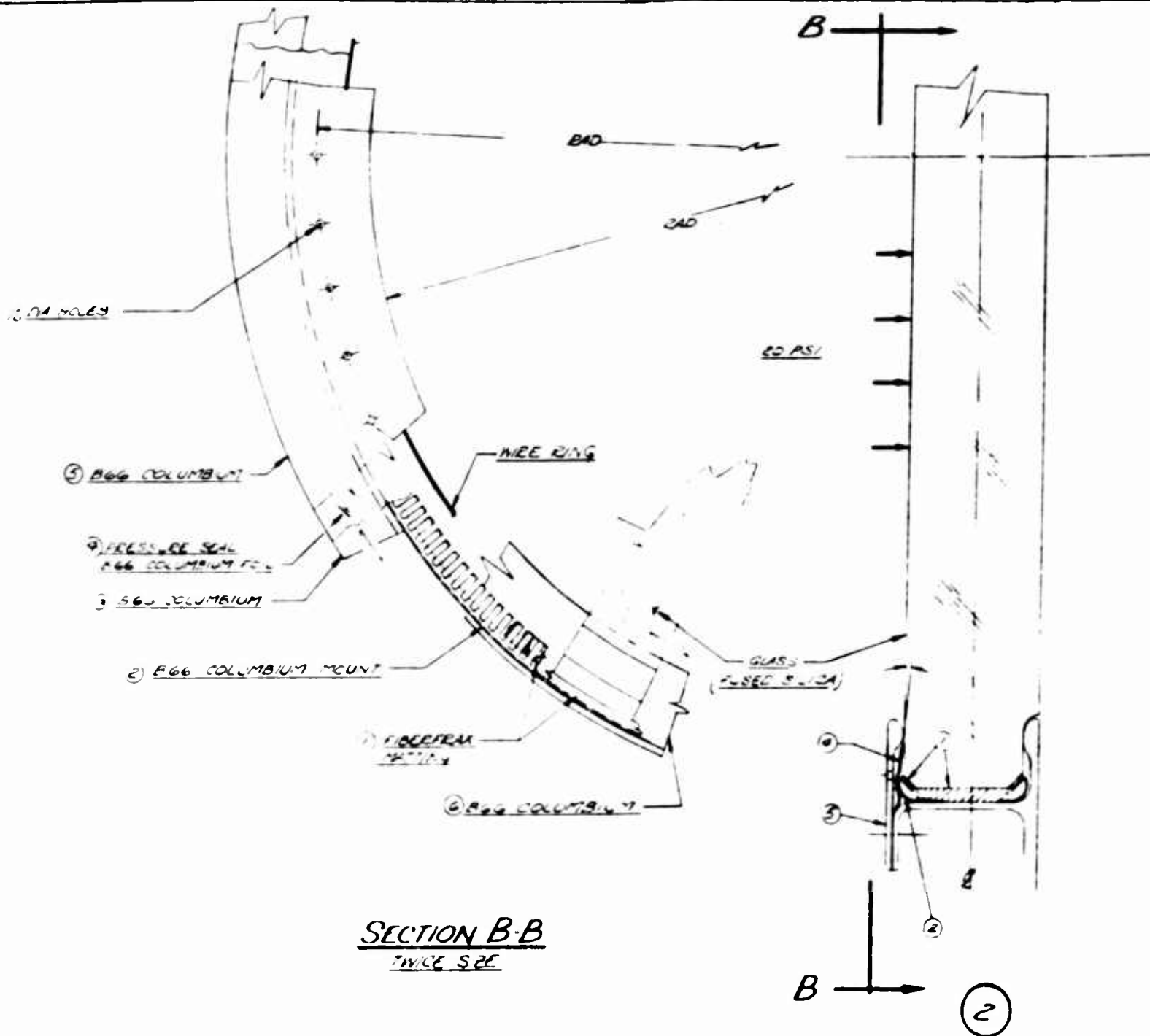


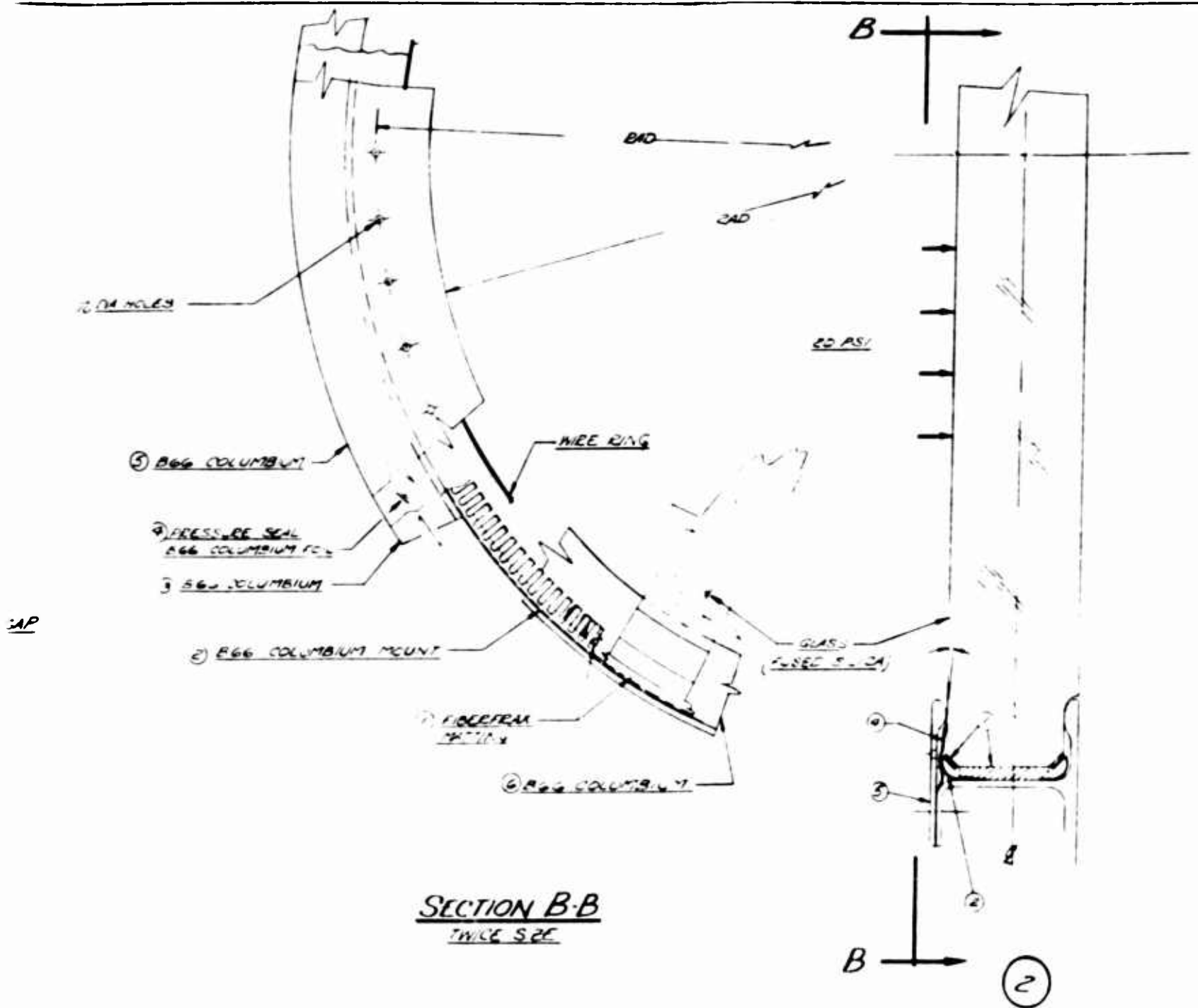
2  
FRAMES

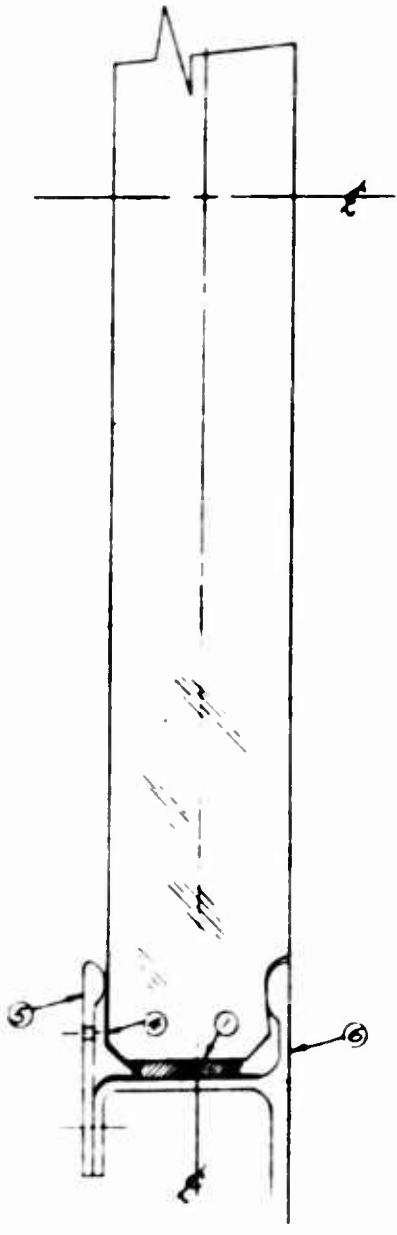


A

EXPANSION GAP

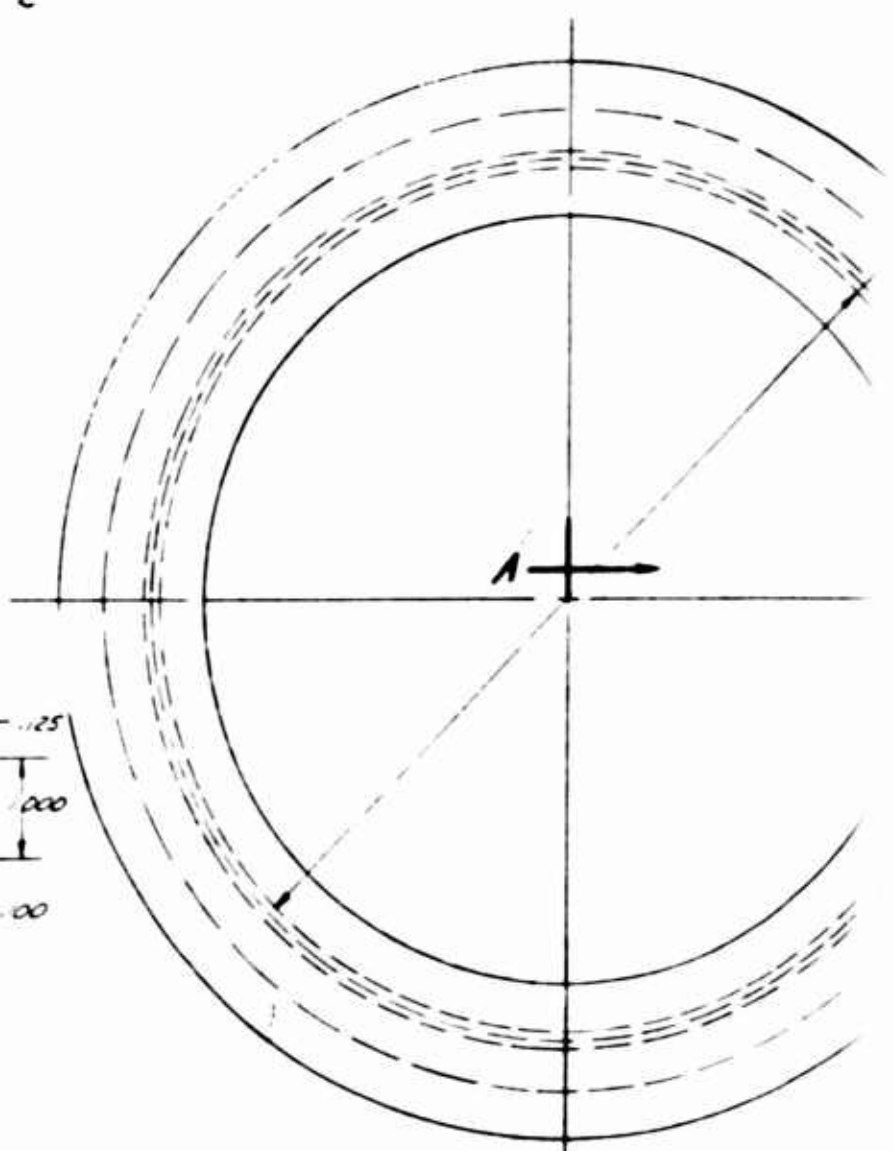
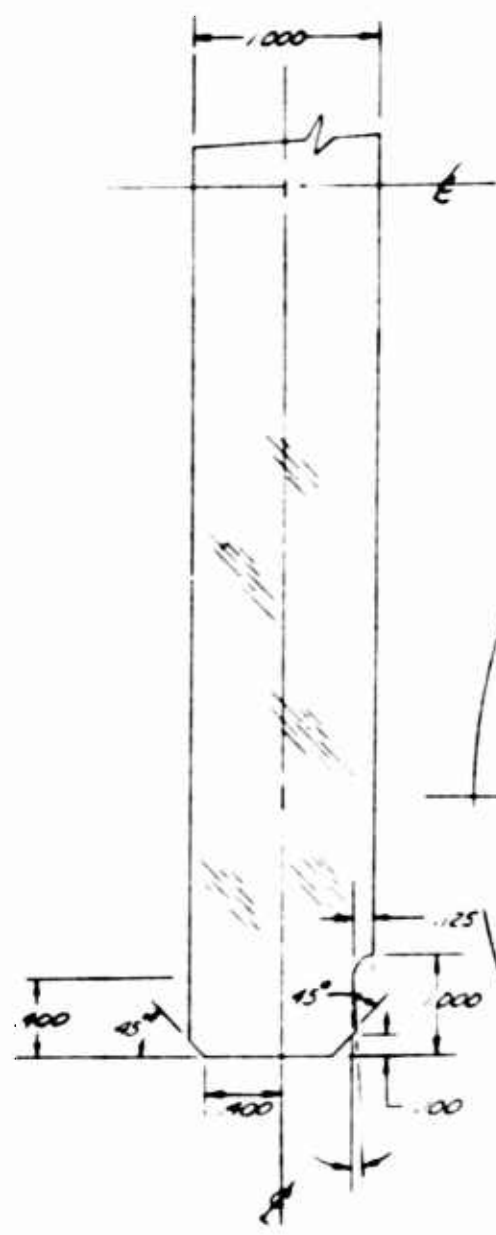






①

SECTION A-A  
WIDE SIZE



VIEW LOOKING UP  
FULL SIZE

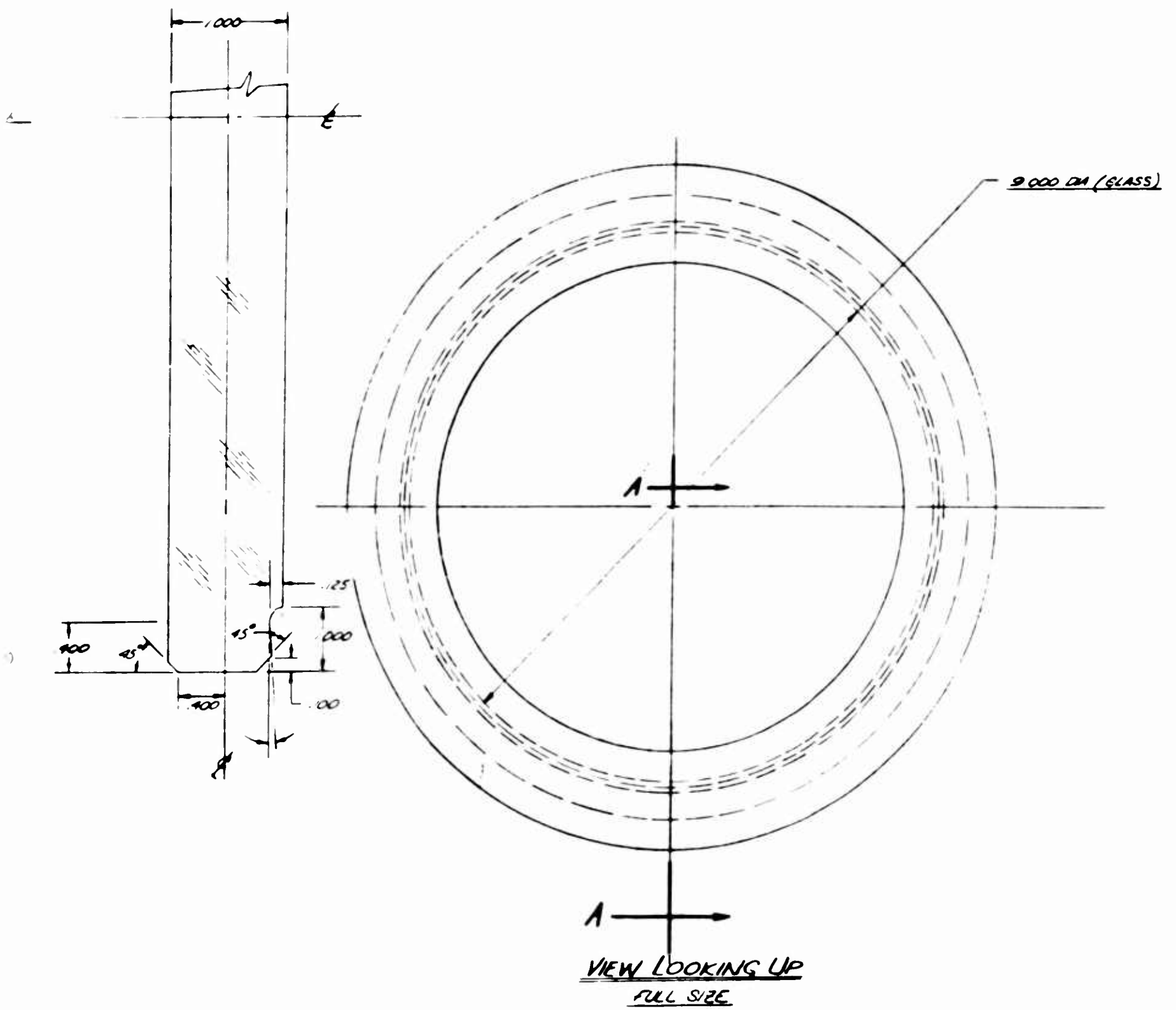




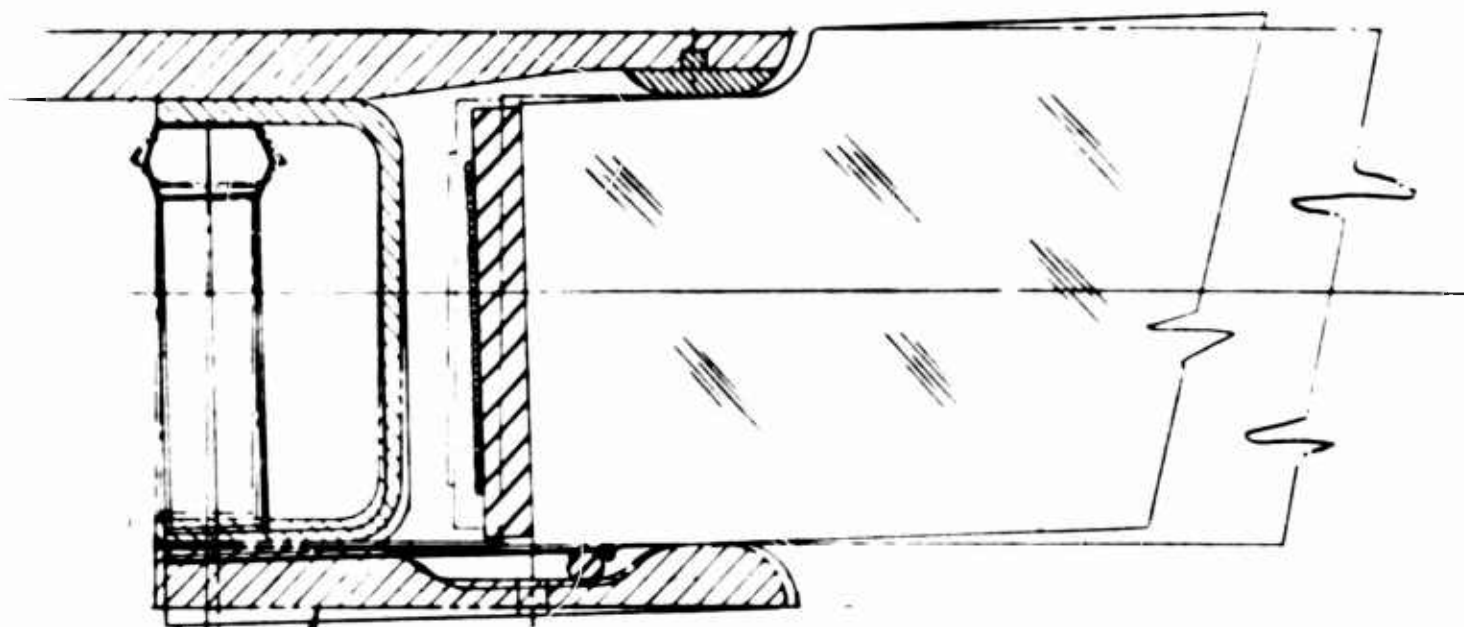
Figure 130 Basic Window Mount Design

C

2  
FRAMES™

# COMPONENT

- ① GLASS (7940 F)
- ② UPPER MOUNTING
- ③ RING MOUNT (B-
- ④ GRAPHITE CLOTH
- ⑤ WASHER FOR SU
- ⑥ LOWER MOUNTING
- ⑦  $\frac{1}{16}$  DIA. HOLE (FO
- ⑧ FOIL PRESSURE
- ⑨ RING FIBERFRA
- ⑩ CONTINUOUS FIB
- ⑪ INSULATION & C
- ⑫ RETAINER FOR
- ⑬  $\frac{1}{16}$  DIA. PLUG
- ⑭ CERAMIC OR C
- ⑮ TUBE
- ⑯ BELLOWS
- ⑰ FILL TUBE & BA  
FORCE AND CLA.  
GLASS



A

ROOM TEMPERATURE  
ELEVATED TEMPERATURE  
@ ELEVATED TEMPERATURE

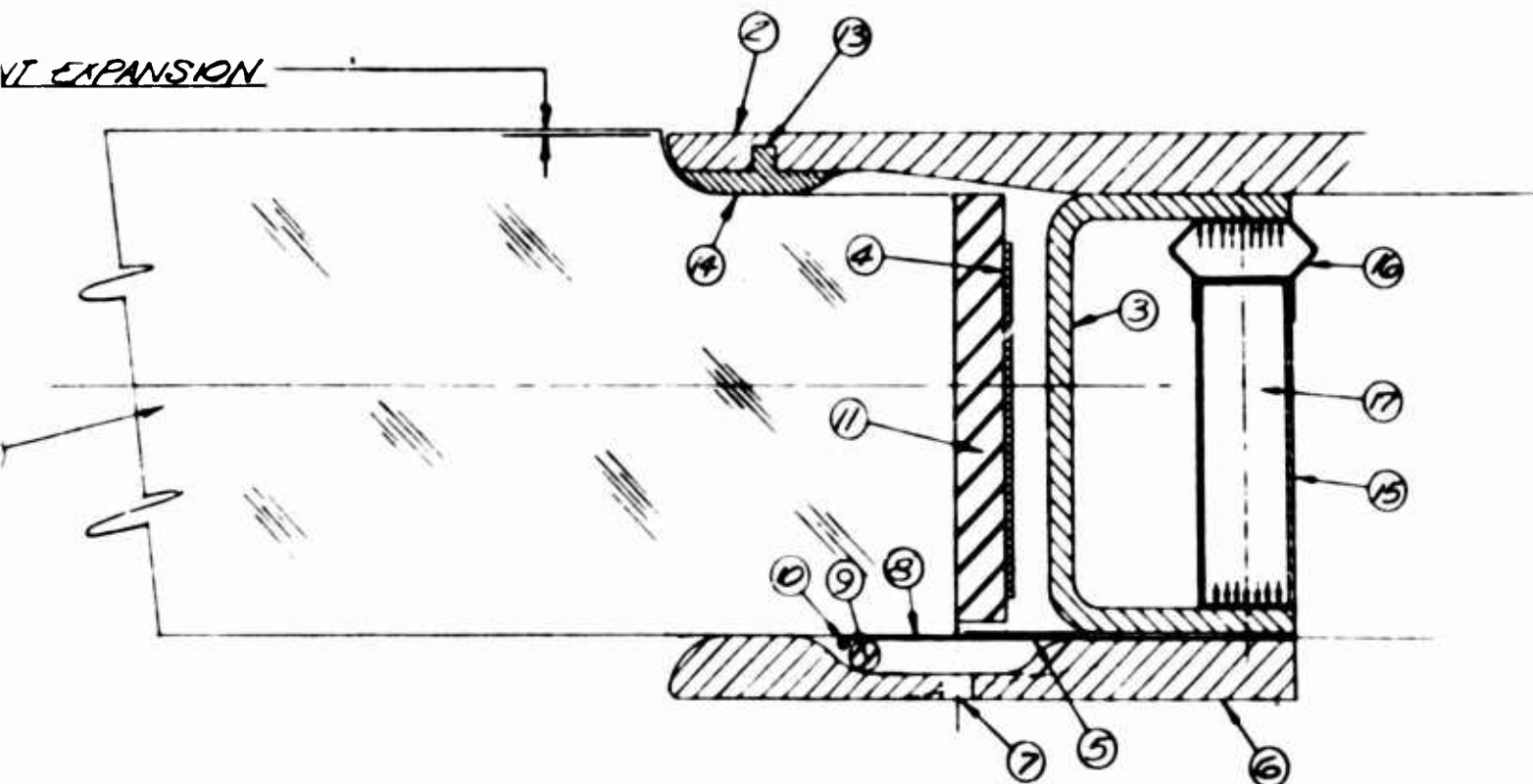
SECTION B-B  
4 TIMES SIZE

## MENTS

- FUSED SILICA - CORNING GLASS)
- TING (B-66 COLUMBIUM)
- (B-66 COLUMBIUM)
- TH (REF - NATIONAL CARBIDE COMPANY - BULLETIN NO 101 DA.)
- SUPPORTING FOIL SEAL (B-66 COLUMBIUM)
- TING (B-66 COLUMBIUM)
- FOR INTRODUCING AMBIENT PRESSURE)
- IRE SEAL (B-66 COLUMBIUM)
- FRAX) PREVENTS VIBRATION & FLUTTER OF SEAL
- WIRE TENSION RING (B-66 COLUMBIUM) (PREVENTS WRINKLING OF SEAL)
- & CUSHION (FIBERFRAX)
- ER GRAPHITE CLOTH STRAP (B-66 COLUMBIUM - WELD TO RING MOUNT)
- GRAPHITE INSULATION

BELLOWS WITH N<sub>2</sub> (GAS EXPANDS AT ELEVATED TEMPERATURES & EXERTS  
DAMPING ACTION TO TAKE UP DIFFERENTIAL IN EXPANSIONS OF MOUNT

NT EXPANSION



@ ROOM TEMPERATURE

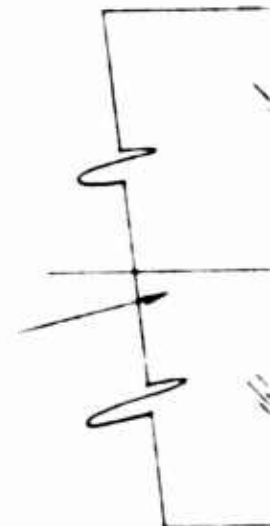
## NTS

- FUSED SILICA -
- ING (B-66 COL
- 66 COLUMBIU
- 4 (REF - NATION
- SUPPORTING FOI
- IG (B-66 COL
- OR INTRODUCIN
- E SEAL (B-G
- AX) PREVENTS
- BE TENSION E
- CUSHION (FIB
- GRAPHITE CU

GRAPHITE IN

BELLOWS WITH  
DAMPING ACTION

EXPANSION



4 - CORNING GLASS)

COLUMBIUM)

BIUM)

ATIONAL CARBIDE COMPANY - BULLETIN NO 101 DA.)

FOIL SEAL (B-66 COLUMBIUM)

COLUMBIUM)

ICING AMBIENT PRESSURE)

B-66 COLUMBIUM)

NTS VIBRATION & FLUTTER OF SEAL

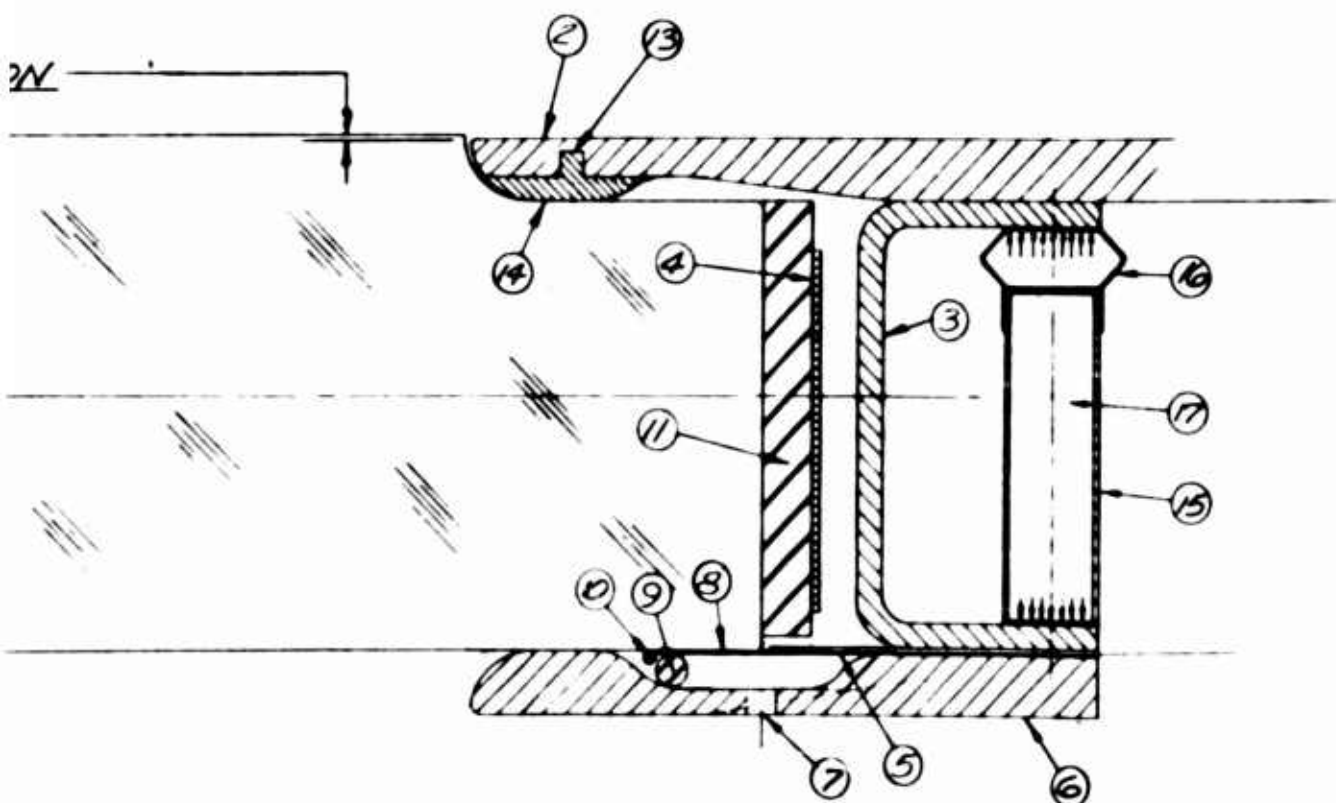
1 RING (B-66 COLUMBIUM (PREVENTS WRINKLING OF SEAL)

FIBERFRAX)

CLOTH STRAP (B-66 COLUMBIUM - WELD TO RING MOUNT)

INSULATION

WITH N<sub>2</sub> (GAS EXPANDS AT ELEVATED TEMPERATURES & EXERTS  
TION TO TAKE UP DIFFERENTIAL IN EXPANSIONS OF MOUNT

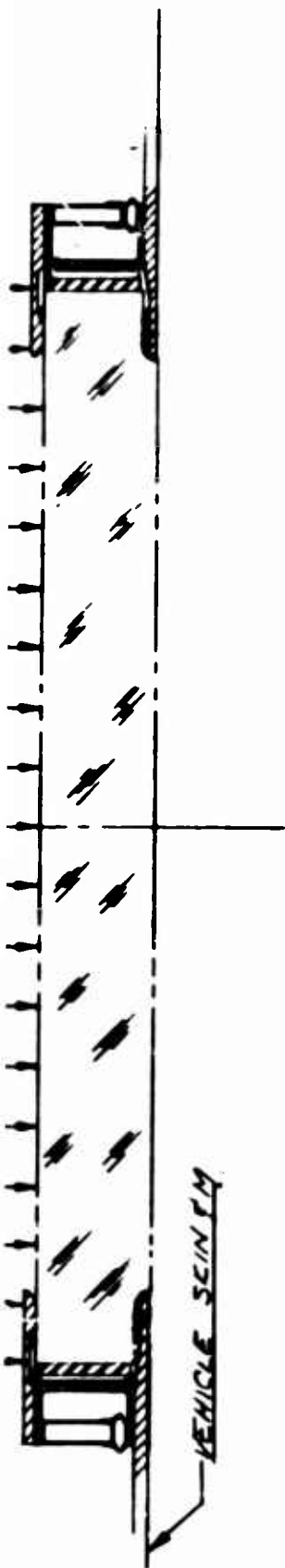


@ ROOM TEMPERATURE

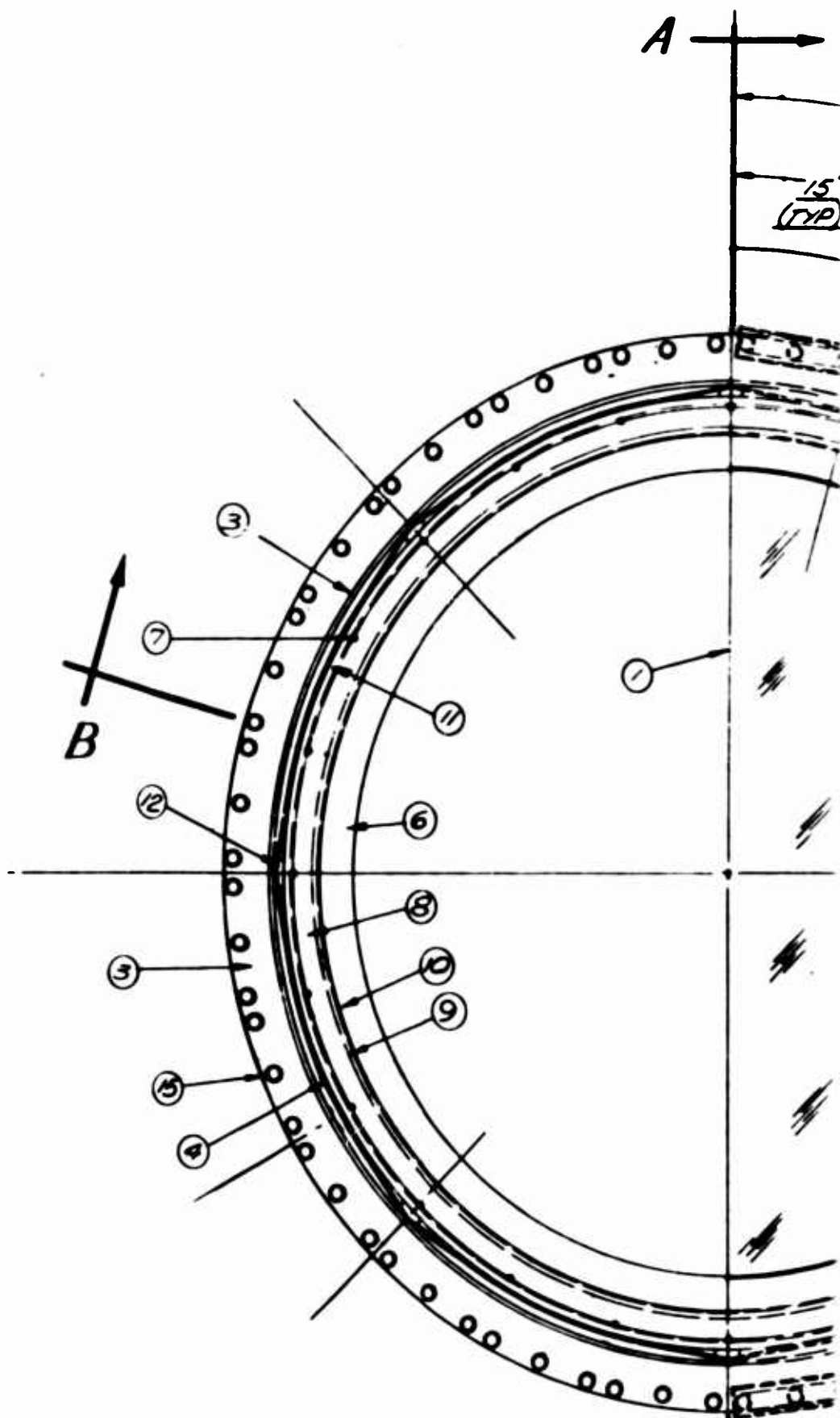
**B**

SECTION  
FULL

AMBIENT PRESSURE

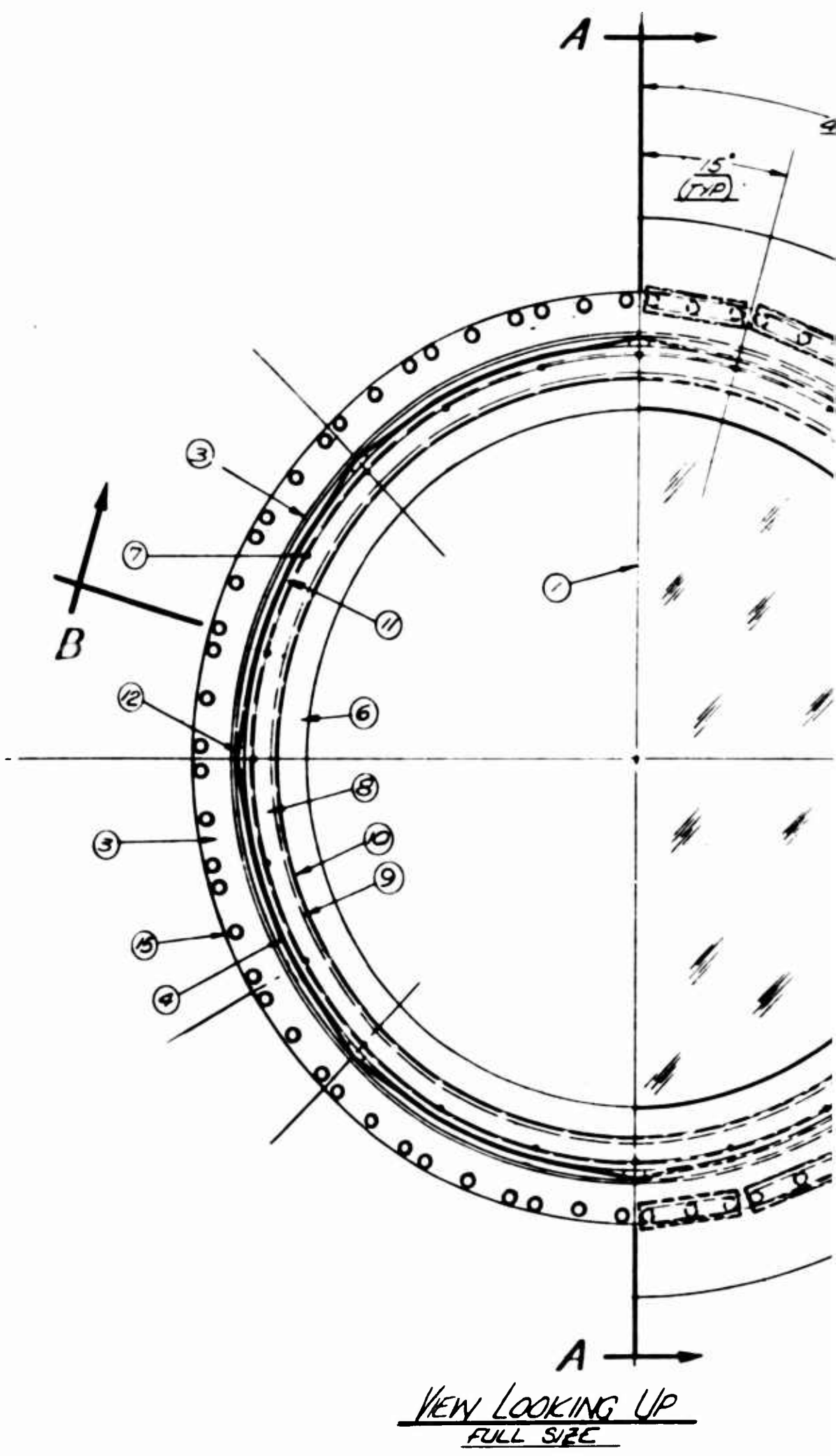
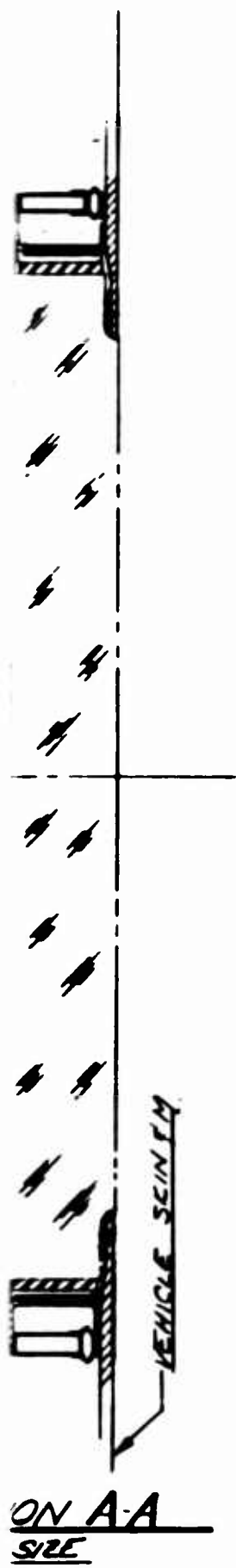


SECTION A-A  
FULL SIZE



VIEW LOOKING UP  
FULL SIZE





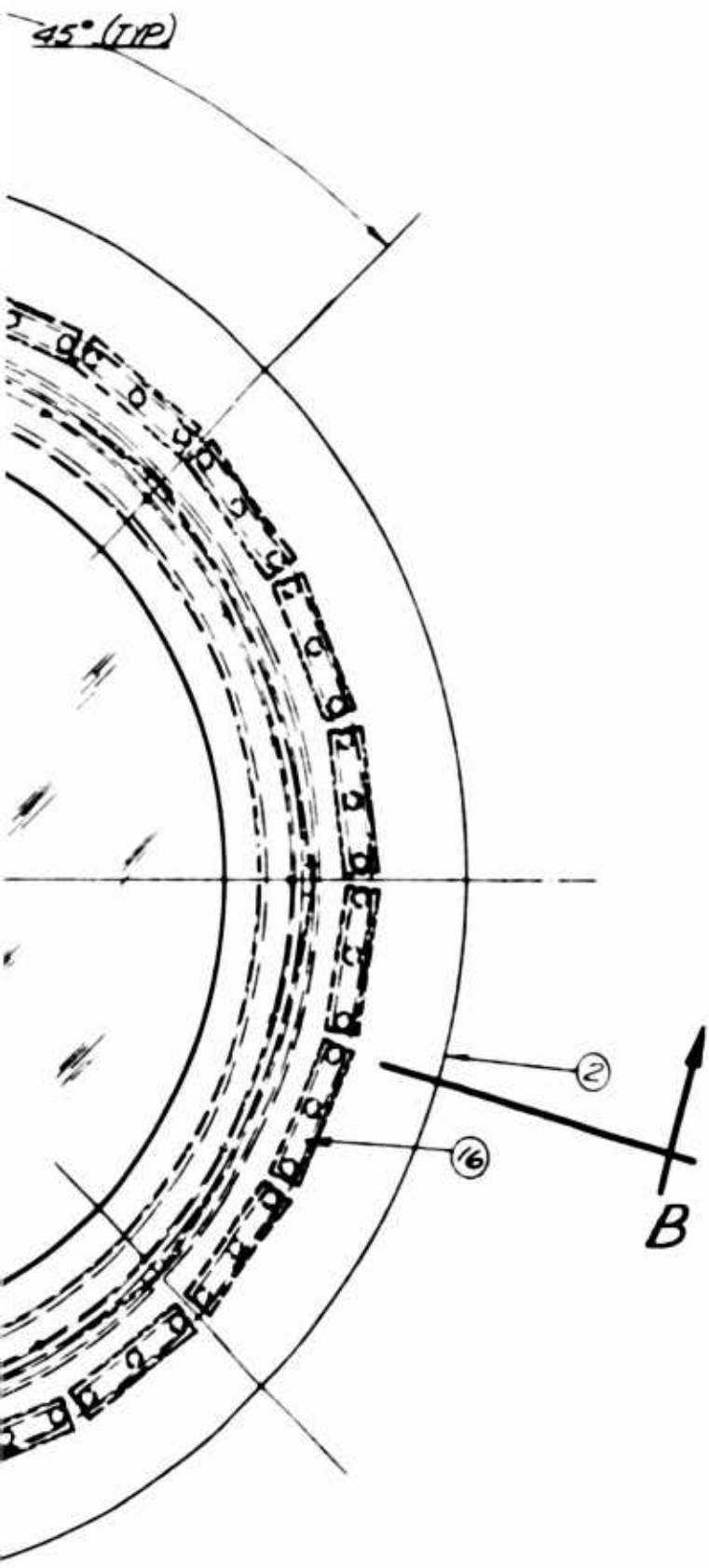
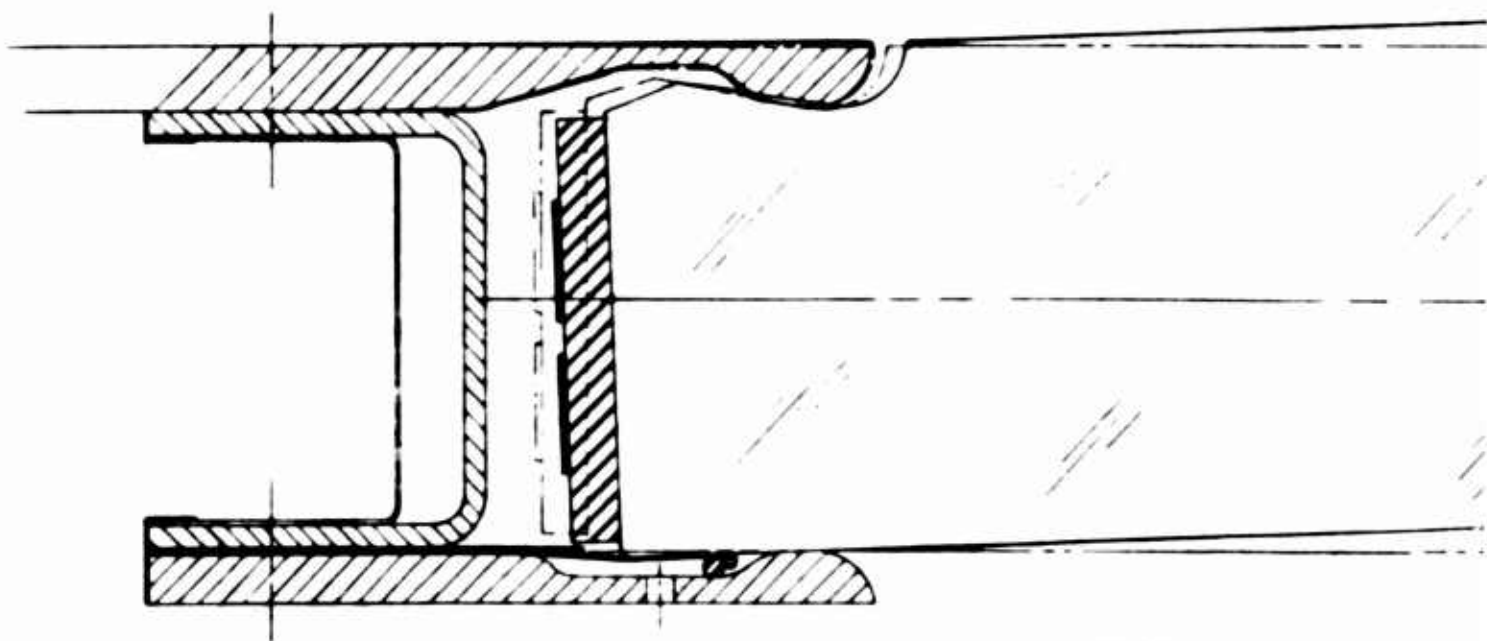


Figure 132 Window Mount Design 13

2  
FRAMES

## COMPONENTS

- 1 GLASS (7940 FUSED SILICA)
- 2 UPPER MOUNTING (B-66 COLUMBIUM)
- 3 RING MOUNT (B-66 COLUMBIUM)
- 4 GRAPHITE CLOTH (REF - NATIONAL CARBIDE COMPANY BULLETIN NO 101 DA)
- 5 EXPANSION PLUG (B-66 COLUMBIUM)
- 6 RETENSION STRAP FOR GRAPHITE CLOTH
- 7 WASHER FOR SUPPORTING FOIL SEAL (B-66 COLUMBIUM)
- 8 LOWER MOUNTING (B-66 COLUMBIUM)
- 9  $\frac{1}{16}$  DIA HOLE FOR INTRODUCING AMBIENT PRESSURE
- 10 FOIL PRESSURE SEAL (B-66 COLUMBIUM)
- 11 RING (FIBERFRAX) PREVENTS VIBRATION & FLUTTER OF SEAL
- 12 CONTINUOUS RING (B-66 COLUMBIUM) PREVENTS WRINKLING OF SEAL
- 13 INSULATION AND CUSHION (FIBERFRAX)
- 14 C-RING FOR SEALING
- 15 GRAFOIL - A GRAPHITE TAPE (REF - HIGH TEMPERATURE MATERIALS INC DA)
- 16 BEVEL GLASS TO TAKE UP DIFFERENTIAL DUE TO EXPANSIONS OF GLASS



SECTION B-B  
GLASS & MOUNTING @ ELEVATED  
4 TIMES SIZE

A

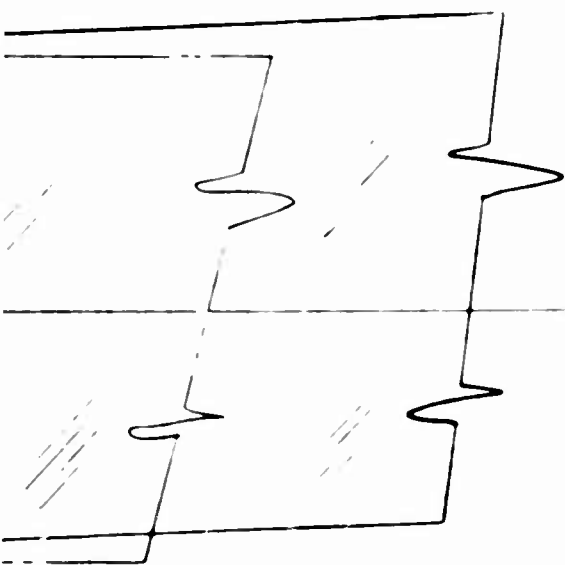
20 PSI AMBIENT PRESSURE



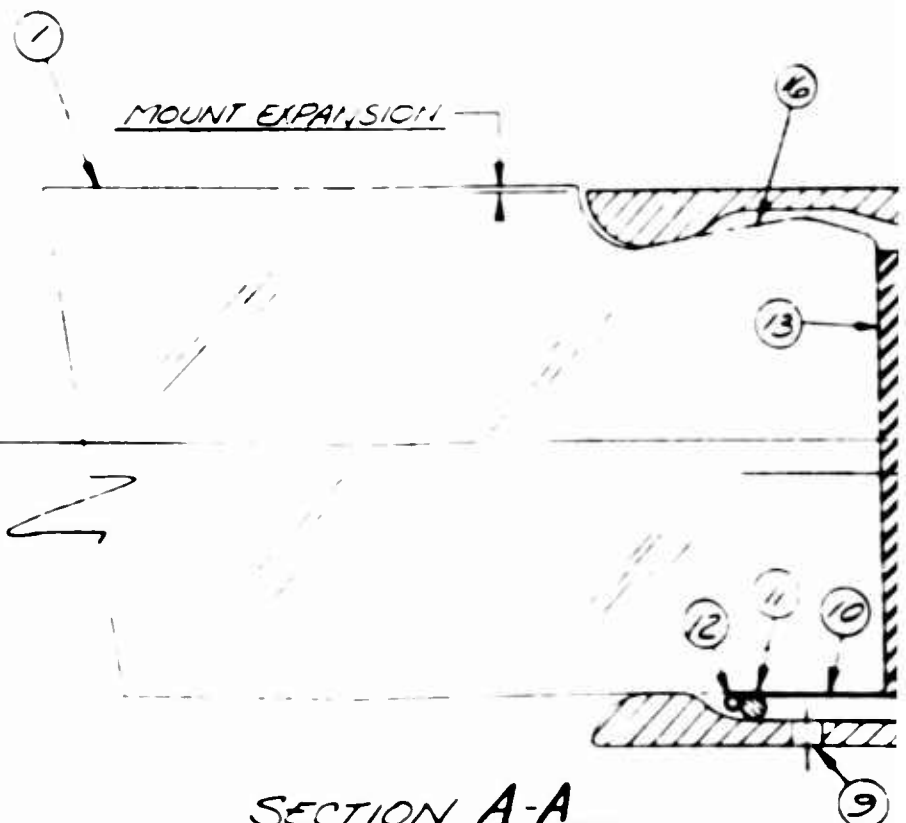
SECTION CUT @ DIA.  
FULL SIZE

IL (TENSION RING)

DATA SHEET 10-1-62)  
GLASS & MOUNTING

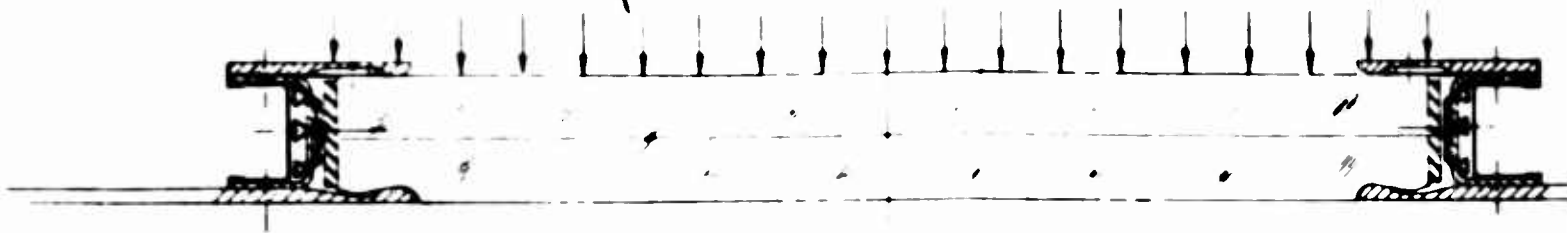


ATED TEMP



SECTION A-A  
GLASS & MOUNTING @ ROOM  
4 TIMES SIZE

20 PSI AMBIENT PRESSURE

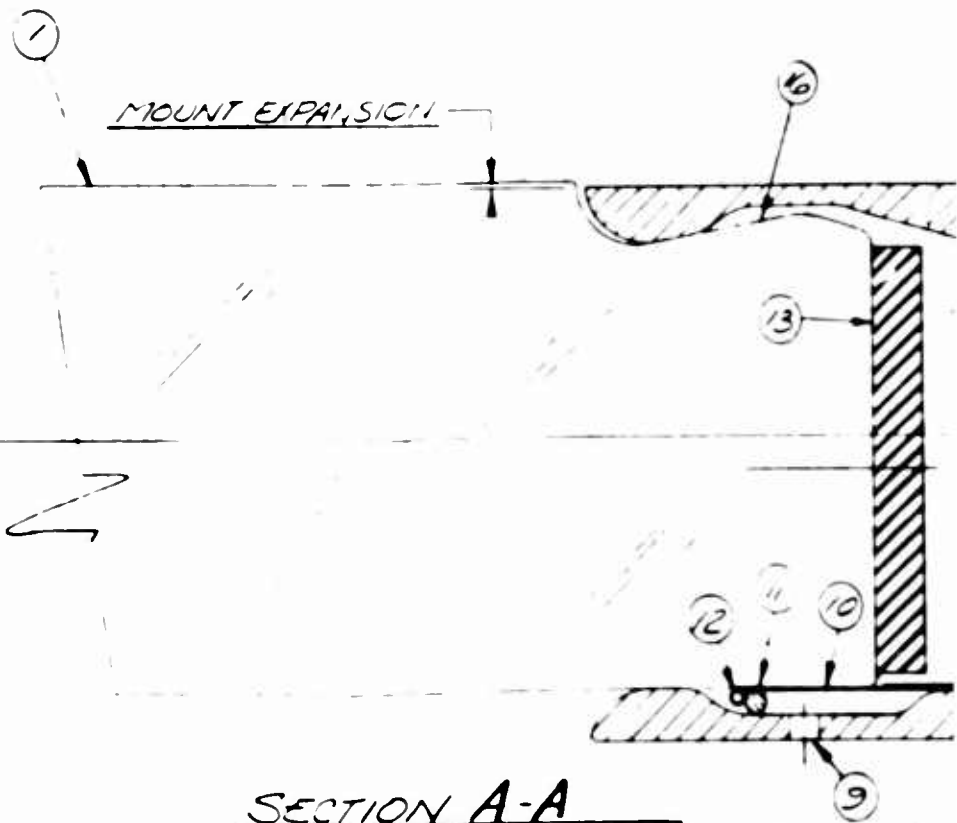


SECTION CUT @ DIA.  
FULL SIZE

(RING)

10-1-62)

INTING



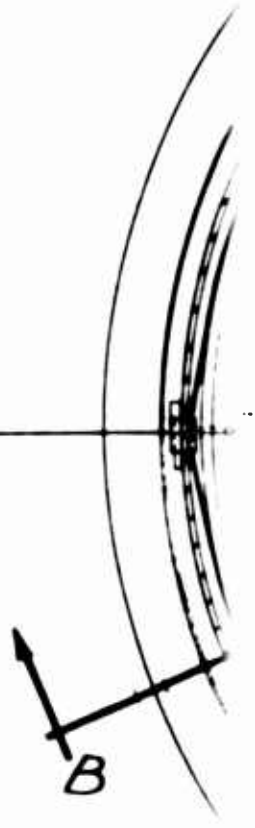
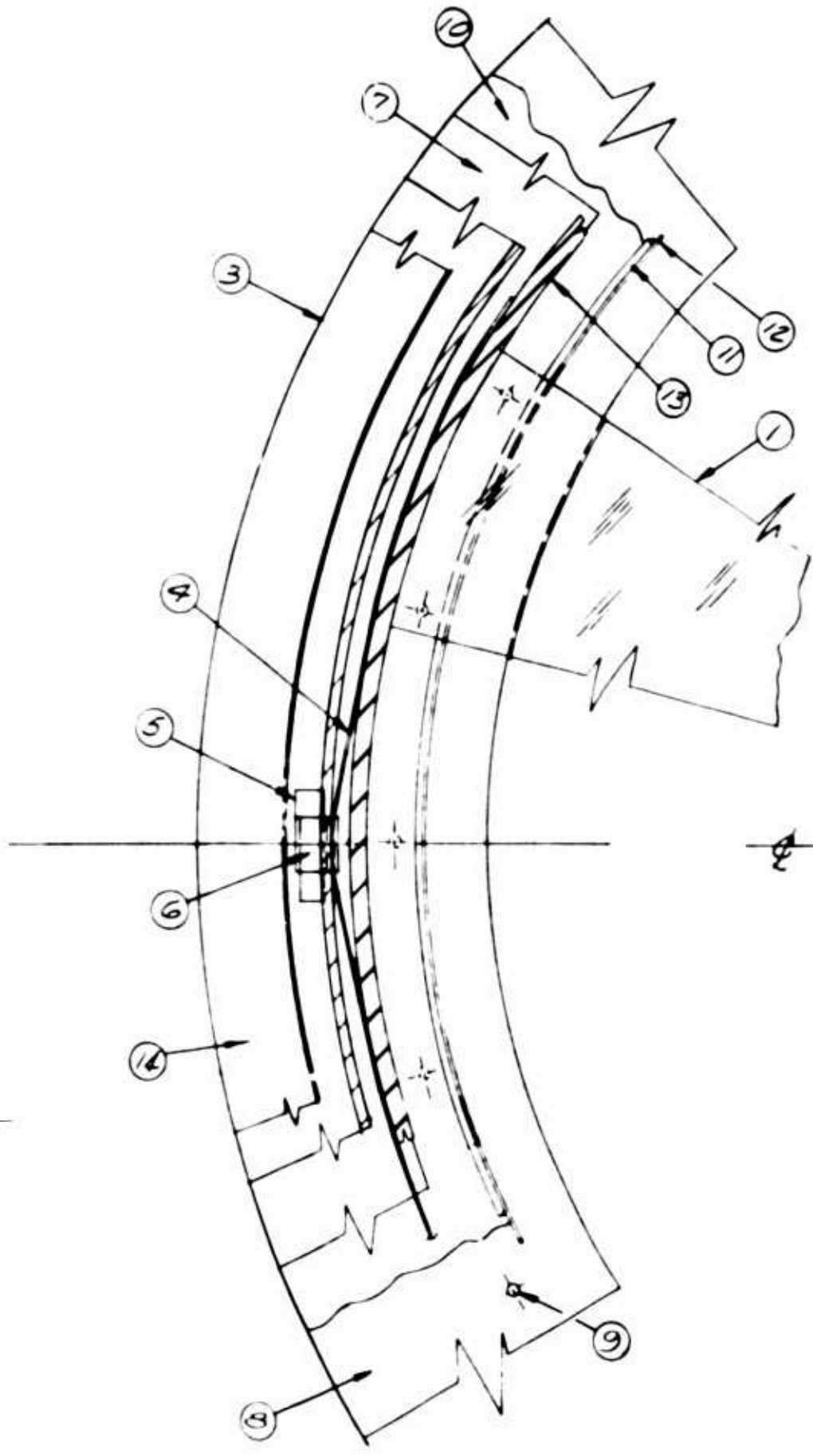
SECTION A-A  
GLASS & MOUNTING @ ROOM TEM  
4 TIMES SIZE



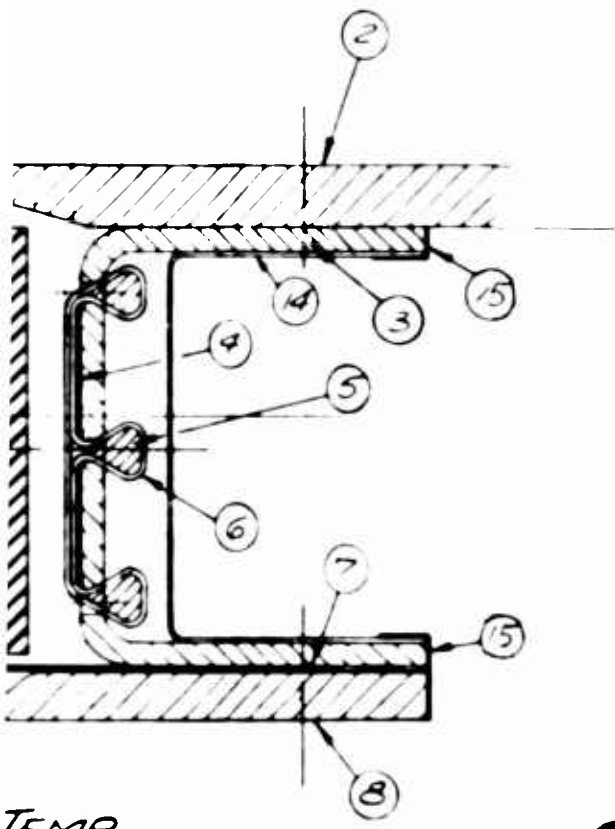
2



VEHICLE SKIN 17

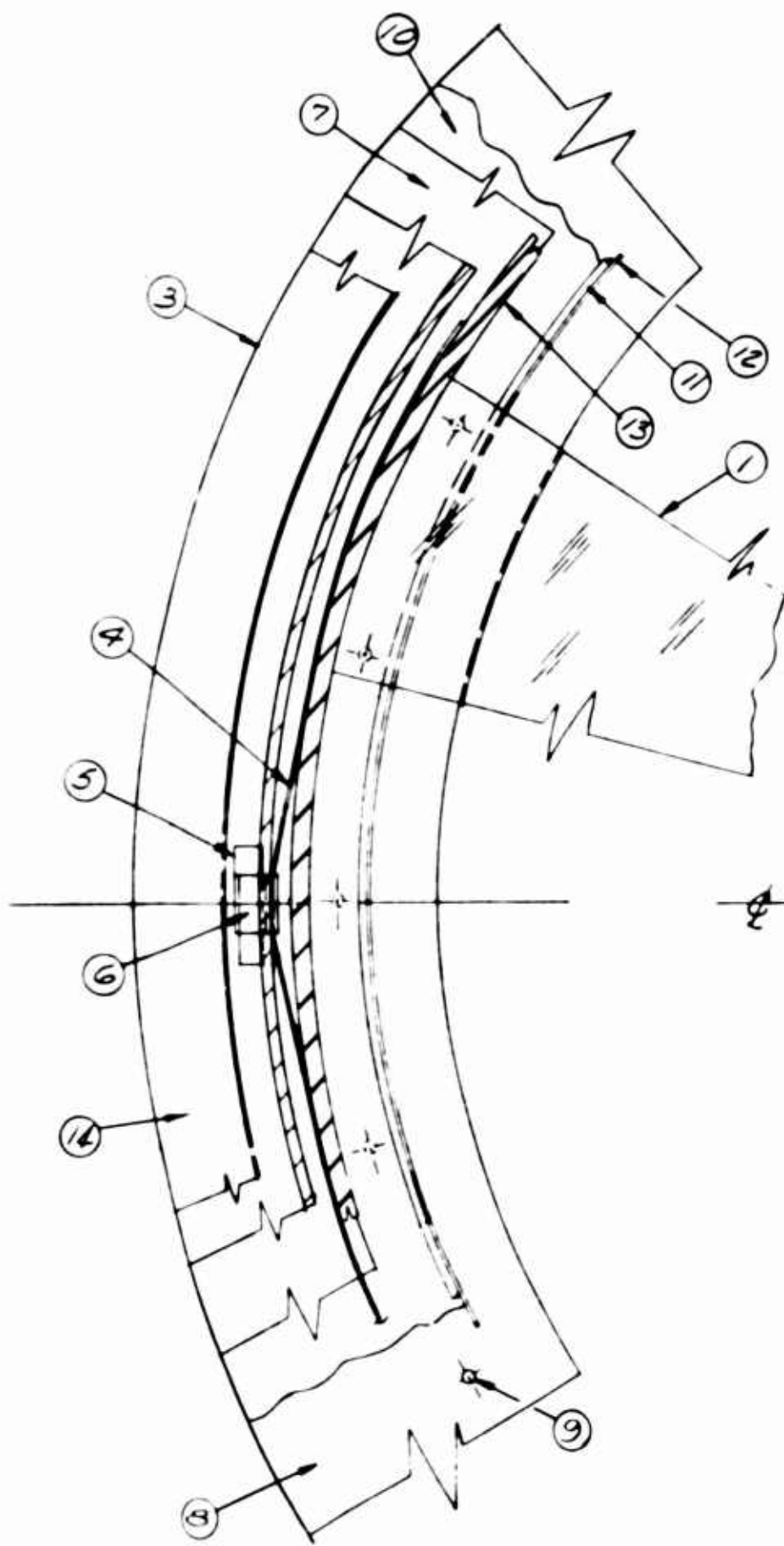


TWICE SIZE

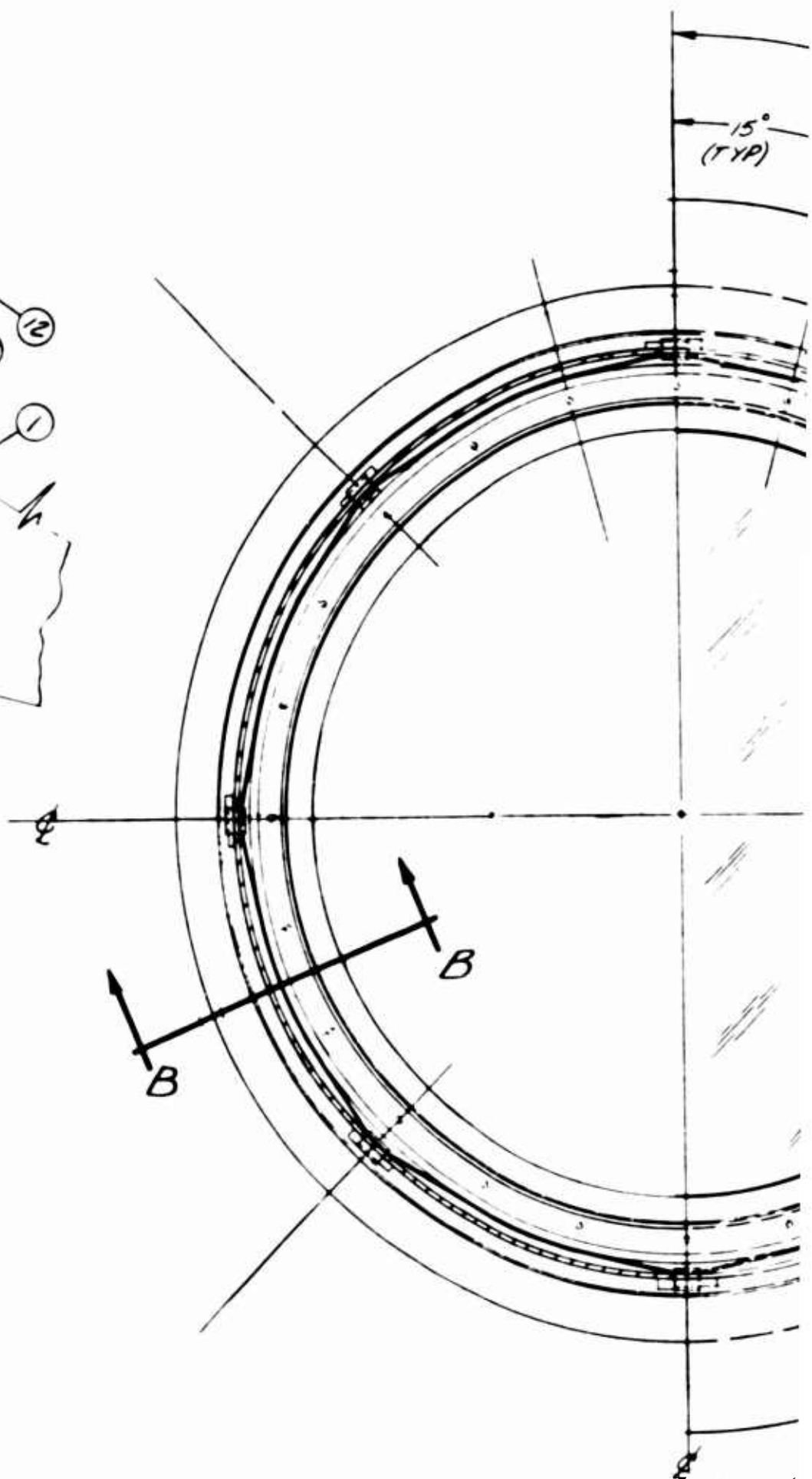


TEMP.

8



TWICE SIZE



VIEW LOOKING UP (1)

FULL SIZE

NOTE - LEFT SIDE IS CUTAWAY

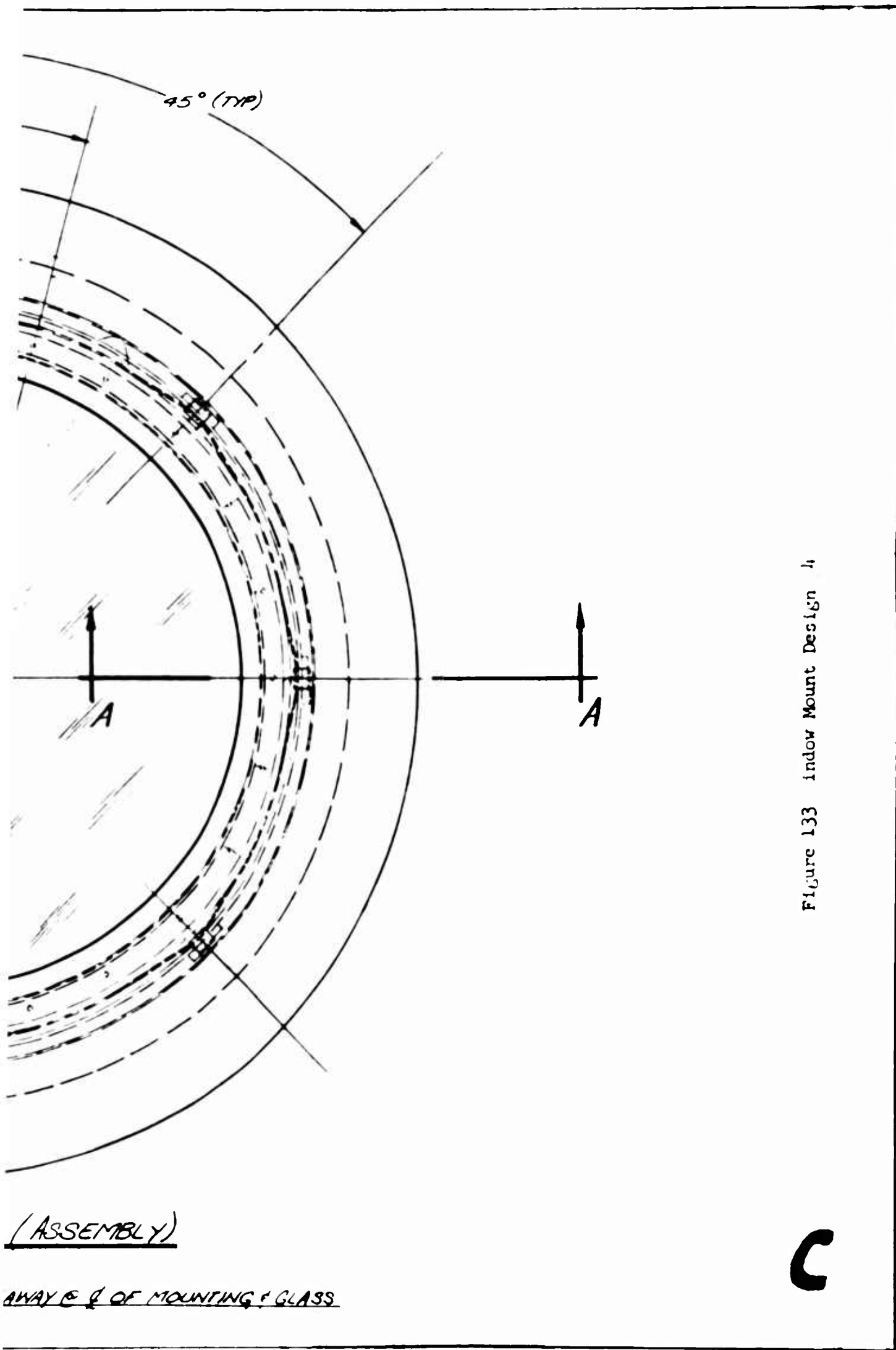
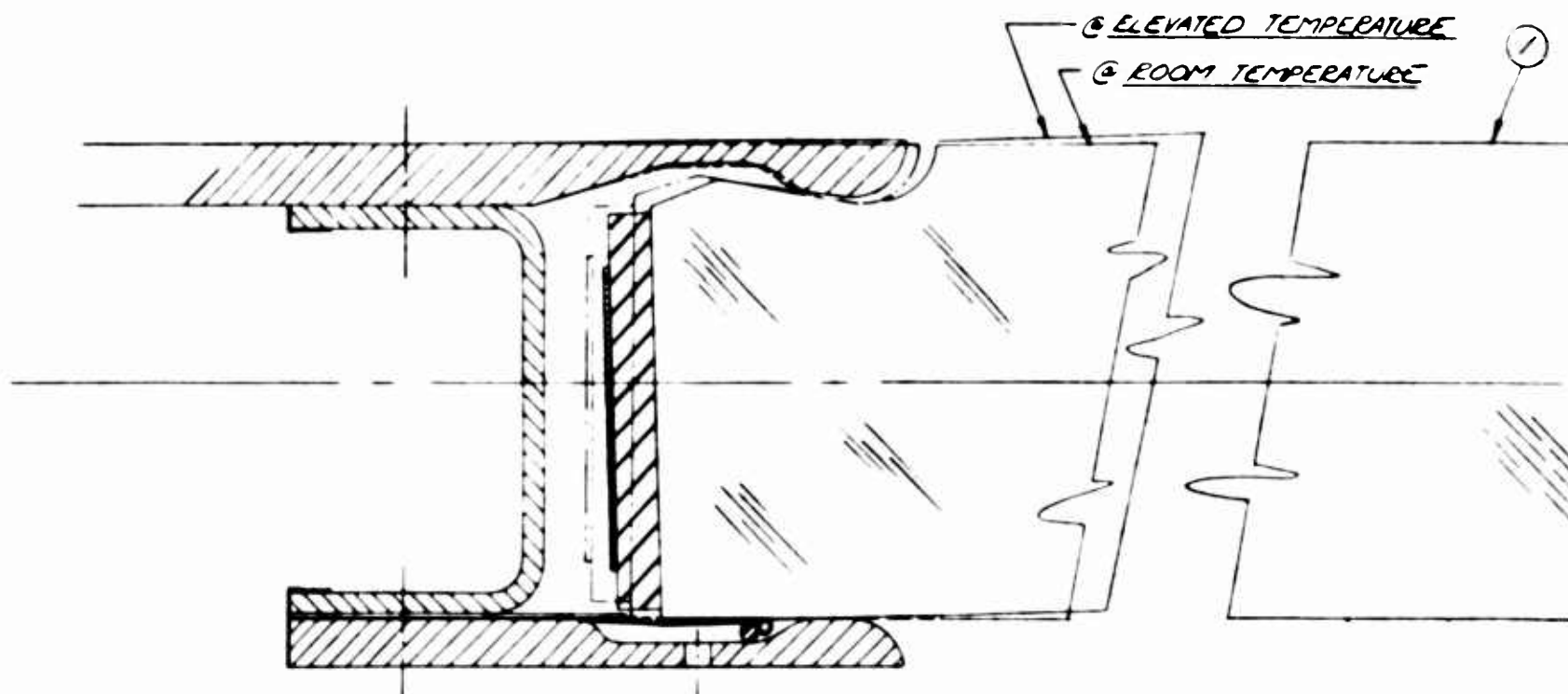


Figure 133 Indow Mount Design 4

3  
FRAMES

### COMPONENTS

- ① GLASS (7940 FUSED SILICA - CORNING GLASS)
- ② UPPER MOUNTING (B-66 COLUMBIUM)
- ③ RING MOUNT (B-66 COLUMBIUM)
- ④ GRAPHITE CLOTH (REF - NATIONAL CARBIDE COMPANY - BULLETIN NO. 101 DA)
- ⑤ WASHER FOR SUPPORTING FOIL SEAL (B-66 COLUMBIUM)
- ⑥ LOWER MOUNTING (B-66 COLUMBIUM)
- ⑦ 1/16 DIA HOLE (FOR INTRODUCING AMBIENT PRESSURE)
- ⑧ FOIL PRESSURE SEAL (B-66 COLUMBIUM)
- ⑨ RING (FIBERFRAX) PREVENTS VIBRATION & FLUTTER OF SEAL
- ⑩ CONTINUOUS RING (B-66 COLUMBIUM) PREVENTS WRINKLING OF SEAL (TENSION RING)
- ⑪ INSULATION AND CUSHION (FIBERFRAX)
- ⑫ END ATTACHMENT & MOUNTING FOR GRAPHITE CLOTH STRAP (B-66 COLUMBIUM)
- ⑬ RETAINER FOR GRAPHITE CLOTH STRAP (B-66 COLUMBIUM - WELD TO RING MOUNT)
- ⑭ GRAFOIL - A GRAPHITE TAPE (REF - HIGH TEMPERATURE MATERIALS, INC. DATA SHEET)
- ⑮ BEVEL GLASS TO TAKE UP DIFFERENTIAL DUE TO EXPANSIONS OF GLASS



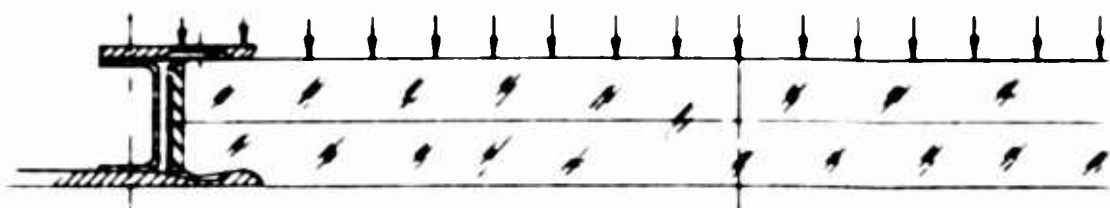
A

@ELEVATED TEMPERATURE

SECTION B-B  
4 TIMES SIZE

20.1

20 PSI AMBIENT PRESSURE



SECTION A-A  
FULL SIZE

RING)

BIUM)

5 MOUNT)

SHEET 10-1-62)

CLASS E MOUNTING



2

12

3

4

3

12

5

6

VT)

10-1-62)

MOUNTING

WELD (TOP & BOTTOM)

EXPANSION

13

2

10

4

13

3

14

10

5

14

9

8

7

6

@ ROOM TEMPERATURE

0 PSI

EXP

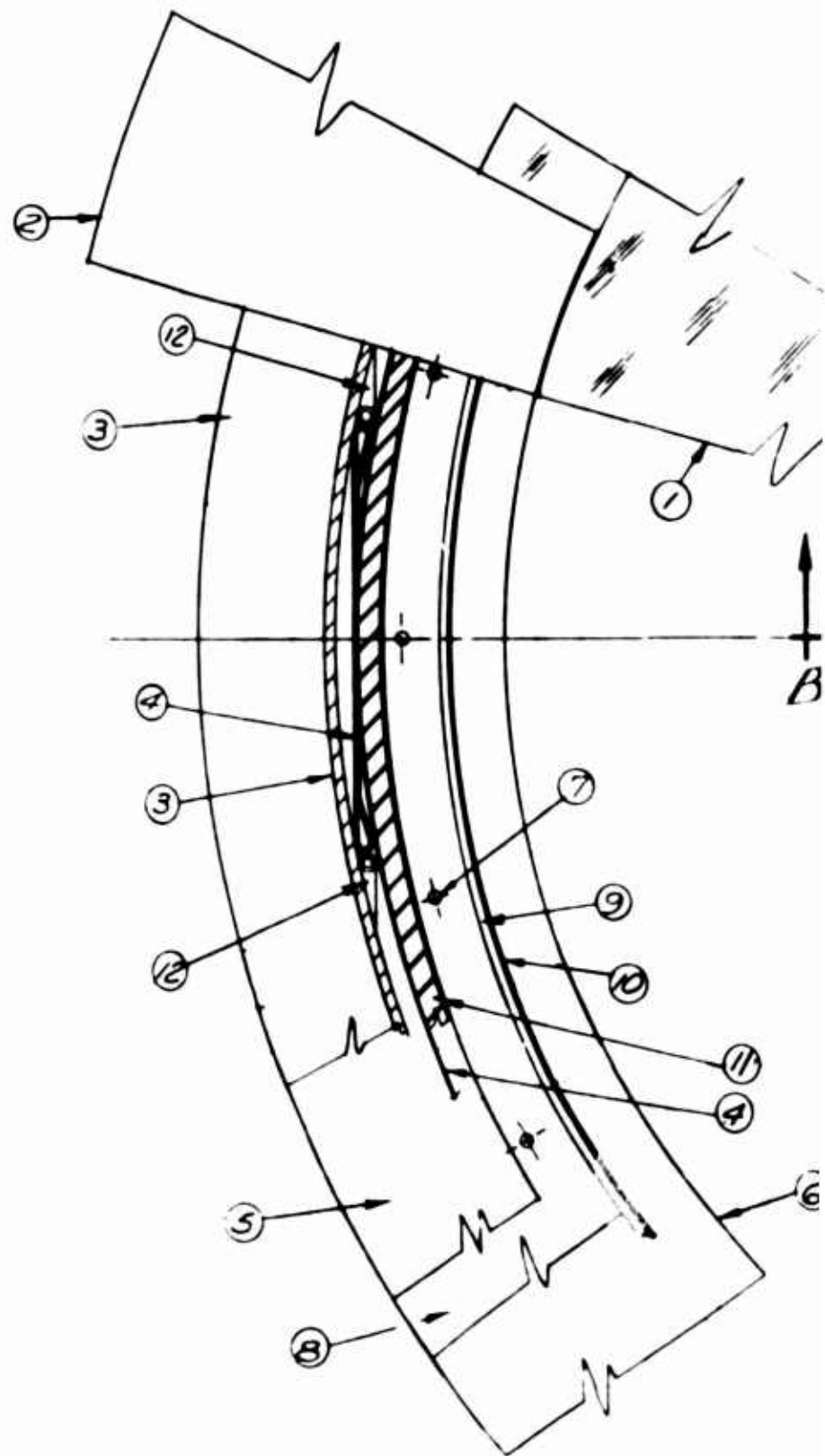




20 PSI AMBIENT PRESSURE

Diagram illustrating a beam under 20 PSI ambient pressure. The beam is supported by two vertical supports. The pressure is applied uniformly across the top surface of the beam, indicated by downward arrows. The beam is labeled "VEHICLE" on the right side.

SECTION A-A  
FULL SIZE



WELD (TOP & BOTTOM)

EXPANSION

CONTRACTION

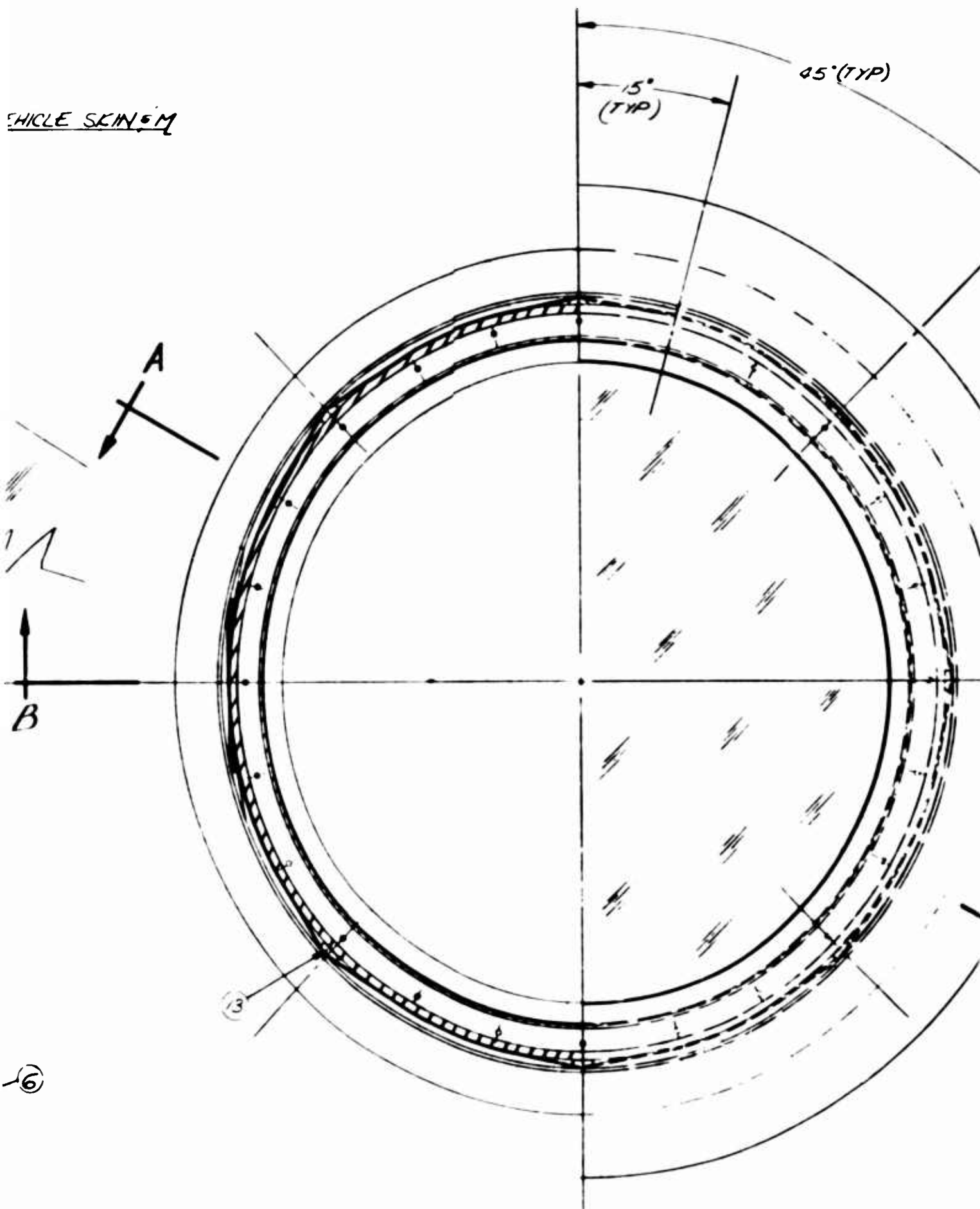
1 2 3 4 5 6 7 8 9 10 11 12 13 14 15

@ ROOM TEMPERATURE

8

Two

THICK SKIN 5M



VIEW LOOKING UP (GLASS & MOUNTING)  
FULL SIZE

TWICE SIZE



ae)

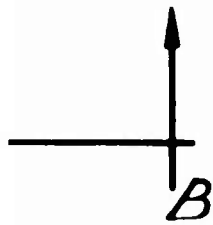
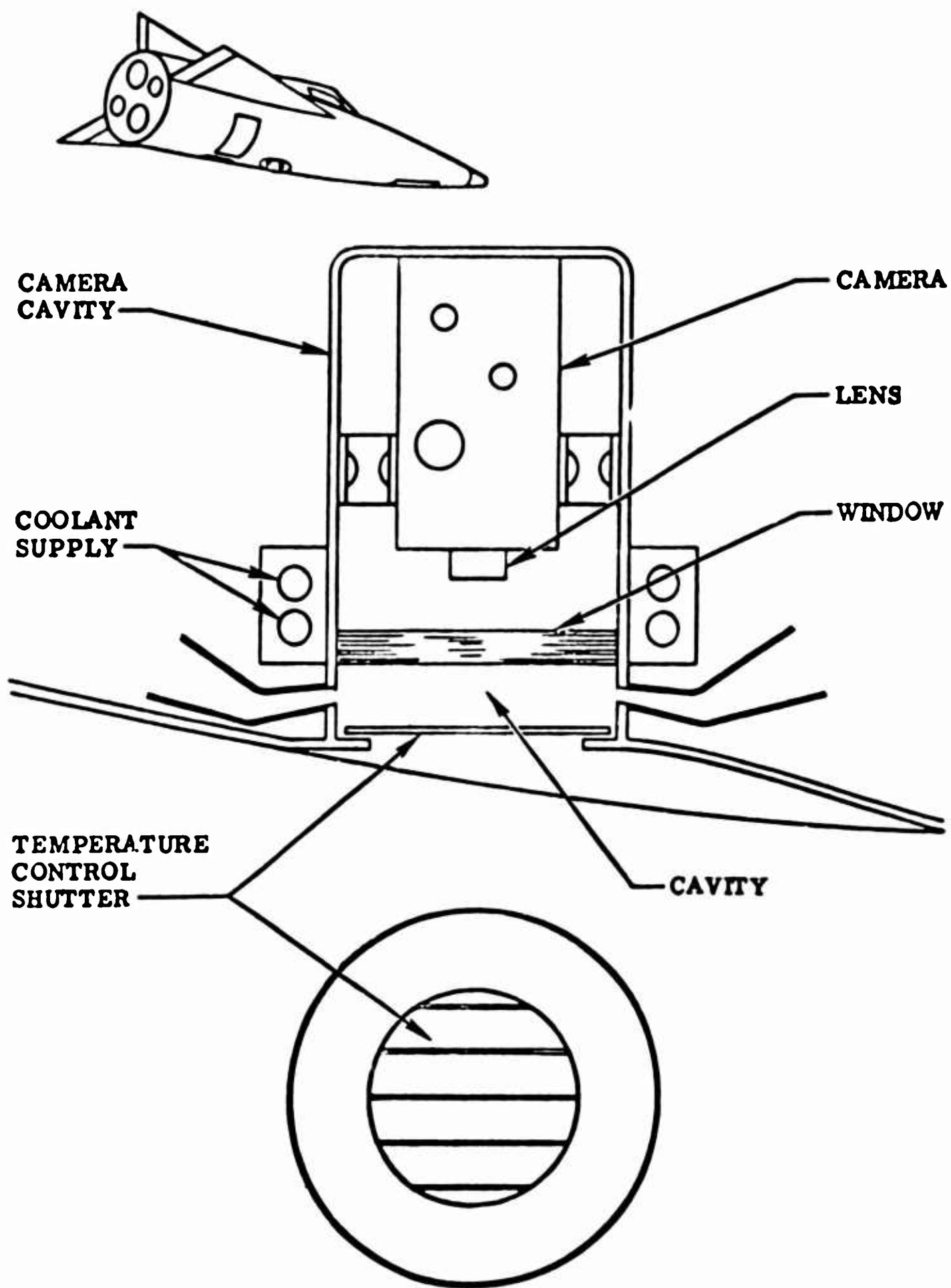


Figure 134 Window Mount Design /5

C



**Figure 135** Possible Means of Protecting a Photographic Window from the Heat Generated During Hypersonic Re-Entry



## Section VIII

### CONCLUSIONS AND RECOMMENDATIONS

#### HYPERSONIC RECONNAISSANCE PHOTOGRAPHY

The deviation of image forming rays through a window depends directly on the temperature-time parameters of the trajectory. If the temperature-time parameters of the trajectories calculated in Section IV of this report are correct, then it is relatively easy to determine the effect of the thermally curved window since the temperature distribution calculated varies only with thickness. This means that Eq. (64) can be used to determine the surface curvatures, and these results can be substituted into Eq. (93), to obtain ray deviations. If the deviations are known, then the resolution can be determined by the method outlined in Section V. However, if the temperature-time results are incorrect, or if mechanical or dynamic pressure effects are present, then the situation will be seriously altered and predictions of resolution will be very difficult.

During orbital flight the outside surface temperature of the window will probably never exceed 140 F. The temperature gradient through the glass will be essentially zero. Light rays will not be deviated by the glass, and degradation of image quality can be considered insignificant. The information-gathering capacity of the photographic system will then depend on lens quality, film resolution capabilities, and other parameters not directly related to the window, and will be equivalent to that of other satellite vehicles.

During re-entry, on the other hand, the outside surface temperature of the window rises sharply. The inside surface, protected from the heat by the window's own absorption capabilities, is generally at a lower temperature. The difference in temperature induces a curvature in the window which then acts as an unwanted additional optical element in the camera system. If the radii of curvature of the two window surfaces are not concentric or are not equal, the image quality of the photograph may be seriously degraded. The extent to which it is degraded is not easily calculable without knowledge of the exact internal temperature distribution for a particular environment and window mounting.

On the basis of the work presented herein, reconnaissance photography during hypersonic re-entry is not recommended, unless some provision is made to protect the window.

#### SUMMARY OF PROGRAM ACCOMPLISHMENTS

- 1) Assessment of analytical predictions - The validity of previous analyses concerning the effects of induced curvature on image quality has been refuted by experimental test.
- 2) Explanation of discrepancies - Discrepancies between calculated values and measured values are due to inadequacy of certain assumptions in the analyses. The theory has been modified so that more accurate predictions can be made.

3) Diathermanous window calculations - A computer program has been developed, which can be used with other programs to provide more accurate temperature distributions through partially-transparent materials.

4) Controlled-expansion flow - The feasibility of protecting camera windows from extreme thermal environments by means of controlled expansion flow has been established. Controlled expansion is achieved when the aft end of the window is tilted inward from the vehicle moldline. The density of the air passing by the tilted window is reduced by a controlled amount, resulting in a net reduction of heat transfer to the window.

5) Window mount design - Several designs have been prepared for a window mount to be used in a 2000-2500°F environment. These mounts achieve structural stability of the window-mount system while maintaining aerodynamic smoothness and an adequate pressure seal.

6) Deviation measurements - Measured values of optical deviation through a photographic window have been obtained as functions of temperature, pressure differential, distance of the light beam from the center of the window, and angle of incidence of the light beam with respect to the normal to the window.

7) Dynasoar window properties - Temperature-time curves and heat transfer curves for a camera window have been prepared for typical Dynasoar trajectories. These values are believed to be considerably more precise than previously available data.

#### RECOMMENDATIONS

In order to more closely simulate the environmental factors which affect window performance, it is recommended that flight testing be seriously considered in any subsequent program. The reasons for this recommendation are as follows:

- (1) Protecting the window from the thermal environment by means of a controlled expansion surface has been shown theoretically to be feasible. However, some of the assumptions used in the analysis are necessarily imprecise, and a verification of the results by means of operational tests would be valuable.
- (2) The laboratory tests which verified the analytical predictions were necessarily confined to lower temperatures than would be encountered in flight. In addition, the laboratory tests were designed to investigate the effects of a single parameter at one time. A flight test is desirable for simulation of several contributing factors simultaneously, at temperatures more closely approximating the expected operational conditions to be encountered.
- (3) The design for a window mount is based on design experience gained in previous aircraft programs. A prototype should be designed in detail, fabricated, tested in the laboratory,

modified as necessary, and finally proof-tested in actual flight. A method for measuring local temperatures within transparent materials has recently been developed (not under this contract), at North American, Reference 22.

It is proposed that consideration be given to a follow-on combined analytical, laboratory, and flight testing program, the flight test utilizing the X-15 research aircraft or some other vehicle capable of simulating the desired environment. The recommended program would include the following areas of investigation:

- 1) Continuation of the analytical work in aerothermodynamics and optics, to more precisely define the structural problems.
- 2) Detail design of window and mount to comply with specific requirements of hypersonic vehicles. Window material, size, and shape would be optimized. A stress analysis would be performed on the window-mount system.
- 3) Fabrication of a prototype window and mount, and laboratory environmental testing of the system.
- 4) Installation of the system on a suitable aircraft, (e.g. X-15), and instrumentation as necessary to acquire useful operational data.
- 5) Flight test, and interpretation of accrued data.

Recommended analytical work in aerothermodynamics includes the following activities:

- a) Checking out the computer programming techniques more rigorously.
- b) Defining the flow field and luminosity effects by simulation of flight conditions in a shock tunnel. This will establish the relative importance of window radiation, and also provide experimental data on the effectiveness of protection methods in reducing local flow heat transfer.

Recommended analytical work in optics includes:

- a) Construction of an apparatus to incrementally move the image plane of an optical collimator system of which a heated window is an integral component. This will permit separation of defocusing effects from degradation-of-resolution effects, and will provide greater insight into the mechanisms involved. It may be possible, for example, to employ a feedback circuit from window to camera, to maintain the focal plane at optimum position.
- b) Continuation of the analytical work presented herein, to the investigation of skew rays and curved image "planes". The mathematics could be kept reasonably simple by assuming specific camera parameters.

- c) Construction of an apparatus for direct recording of transfer functions of heated windows.
- d) Investigation into the practicability of directly measuring internal temperatures of a glass panel having a temperature gradient between surfaces. A method developed at NAA/LAD appears feasible, Reference 22, but has not been proven experimentally.\*

\*Note: Headquarters AFSC Aeronautical Systems Division Letter Request for Proposal, number ASD PR 5977-N-10, dated 9 October 1963, is directed toward this type of investigation.

## Section IX

### REFERENCES

1. Nielsen, J. N., et al, Effects of Supersonic and Hypersonic Aircraft Speed upon Aerial Photography, Final Technical Report, Phase I, Vidya Report No. 17, March 1960.
2. Nielsen, J. N., et al, Effects of Supersonic and Hypersonic Aircraft Speed upon Aerial Photography, Final Report, Phase II, Vidya Report No. 37, January 1961.
3. Armour Research Foundation Progress Reports, Contract AF33(616)-6322.
4. ASFC ASD Request for Proposal 33(657)-62-5064-Q, 4 October 1961.
5. Technical Proposal for Study of Photographic Window Problem in Supersonic and Hypersonic Aircraft, North American Aviation, Inc., Report NA-61-1156, 3 November 1961.
6. Monroe, S. G., "A Transient Skin Temperature program for the IBM 704," North American Aviation, Inc., Report NA-57-1170, 6 September 1957.
7. Monroe, S. G., "A Computer Program for Hypersonic and Supersonic Temperature Evaluation," North American Aviation, Inc., Report NA-62-794, 3 August 1962.
8. Larson, H. K., "Heat Transfer in Separated Flows," Journal of the Aerospace Sciences, Vol. 26, No. 11, November 1959.
9. Chapman, D. R., "A Theoretical Analysis of Heat Transfer in Regions of Separated Flow," NACA TN-3792, October 1956.
10. Charwat, Dewey, Roos & Hitz, "Transfer" Journal of the Aerospace Sciences, Vol. 28, No. 7, July 1961.
11. Creager, M. O., "High Altitude Hypervelocity Flow Over Swept Blunt Glider Wings," I.A.S. Paper #59-113.
12. Monroe, S.G., "The Transient Temperature Solution of a Diathermanous Optically - Thick Skin of a Hypersonic Vehicle," North American Aviation, Inc., Report NA-63-451, 17 February 1963.
13. Gardon, R., "Calculation of Temperature Distribution in Glass Plates Undergoing Heat-Treatment," Journal of the American Ceramic Society, Vol. 41, No. 6, June 1958.
14. Goebel, T. P., "A Digital Program for Calculating Aerodynamic Heat Flux - Discussion of Equations," North American Aviation, Inc., Report NA-62-795, 23 July 1962.



15. Dwight, Tables of Integrals and Other Mathematical Data, MacMillan & Co., 1957.
16. A Survey of Modern Aerial Cameras, North American Aviation, Inc., Report MSL 60-6-19, 28 June 1960.
17. Morey, Properties of Glass, Reinhold, 1950.
18. Roark, Formulas for Stress and Strain, McGraw-Hill, 1954.
19. Herzberger, Modern Geometrical Optics, Interscience, 1958.
20. Jenkins & White, Fundamental of Optics, McGraw-Hill, 1957.
21. Smail, Analytic Geometry and Calculus, Appleton-Century, 1953.
22. North American Aviation, Inc., Internal Letter FS-63-5-13, 20 May 1963.
23. Boley and Weiner, Theory of Thermal Stress, Wiley, 1960.